Physics of the Solid State, Vol. 44, No. 10, 2002, pp. 1809–1832. Translated from Fizika Tverdogo Tela, Vol. 44, No. 10, 2002, pp. 1729–1751.

REVIEWS

Electromagnetic and Fluctuation-Electromagnetic Forces of Interaction of Moving Particles and Nanoprobes with Surfaces: A Nonrelativistic Consideration

G. V. Dedkov and A. A. Kyasov

Kabardino-Balkarian University, Nal'chik, 360004 Russia

e-mail: gv_dedkov@mail.ru

Received August 9, 2001

Abstract—The most complete nonrelativistic theory of dynamic fluctuation electromagnetic interactions between particles of various types (charges, dipoles, neutral atoms, nanoparticles) and the surfaces (flat or cylindrical) of a polarizable medium (the boundary of a solid) is reported for the first time. The theory is based on the application of the Maxwell equations and the formalism of fluctuation–dissipation relations. For a flat surface, effects of spatial dispersion are also taken into account. Papers of other authors are analyzed critically. The results of recent investigations in which dissipative fluctuational forces could be observed are considered briefly. *© 2002 MAIK "Nauka/Interperiodica".*

CONTENTS

1. INTRODUCTION

By electromagnetic and fluctuation-electromagnetic forces are meant dynamic forces of interaction of electric dipoles (a charge, dipole, quadrupole, etc.) and neutral systems (a spherical atom or a nanoparticle, including the tip of a scanning probe microscope (SPM)) with surfaces. In the first case, the interaction is due to a dielectric response of the surface to the external electric field of a moving multipole of constant magnitude; in the second case, the interaction is caused by spontaneous fluctuational electric fields of the moving neutral particle and the surface, which induce electric fields and currents in both parts of a given system. The conservative forces of attraction of neutral particles to the surface are usually called the van der Waals (vdW) forces. For brevity, we will call all these interactions fluctuation-electromagnetic interactions (FEMIs).

The investigation of FEMIs has large fundamental and practical importance. In particular, the processes of interaction of charged particles and multipoles with a surface were the subject of intense investigations in connection with the problem of damage of the first wall of nuclear reactors (see [1, 2] and references therein). The FEMIs are responsible for the effects of adsorption and desorption, optical properties of atomic particles and films formed at surfaces, friction properties of contacting surfaces, etc. In recent years, the interest in this problem has been stimulated by the intense development of scanning probe microscopy, which permit one to perform quantitative measurements of conservative and dissipative forces between nanoparticles (nanoprobes) and surfaces of solids and liquids [3, 4].

The aim of this work is a theoretical analysis of corresponding problems in terms of a unified nonrelativis-

1063-7834/02/4410-1809$22.00

tic approach developed in our previous works and based on the Maxwell equations and on the theory of electromagnetic fluctuations in a polarizable medium. This approach ensures a comprehensive quantum-statistical description of the system. The discussion of some relativistic and classical aspects of the theory of FEMIs can be found in well-known review papers and monographs [5–10]. Note, however, that even the nonrelativistic part of the problem under consideration concerning dissipative FEMIs is up to now a subject of intense theoretical developments [11–22] whose results frequently contradict one another. As to the relativistic theory and the relation between it and the nonrelativistic theory, this problem is even less clear (see, e.g., [10, 23–25]).

The nonrelativistic formulation of the problem means the fulfillment of two restrictions: (1) it is assumed that the velocity of particles is small as compared to the speed of light and (2) the retardation of electromagnetic interactions can be neglected. In typical problems of nanotribology and nanoprobe microscopy, the first condition is fulfilled with a large margin. Of more importance is the second condition, which restricts the range of characteristic distances between the particles and the surface to approximately 20 nm; however, it is this range that can be efficiently probed with the help of an SPM, as well as in the processes of passage of neutral particles and molecular beams near a surface. In any case, since a correct relativistic solution to a problem should ensure a limiting transition to a nonrelativistic case, the results obtained in this work should be taken into account upon the corresponding generalization of the theory.

The paper has the following structure. In Sections 2 and 3, we consider historical aspects of the development of the nonrelativistic theory of FEMIs and critically analyze works of other authors. Sections 4 and 5 are devoted to the general theory of conservative and dissipative FEMIs for flat and cylindrical surfaces, respectively. We consistently consider the interaction of a surface with charged particles, dipole molecules, and spherical neutral particles (atoms). For a flat surface, we also take into account effects of spatial dispersion. In Section 6, we discuss friction and heat exchange in nanoprobe–surface systems and friction in systems of flat surfaces. In view of the mathematical complexity of the problem of finding the spectrum of electromagnetic fluctuations between bodies of an arbitrary shape, in this case we additionally introduce the approximation of additivity of interactions. Upon more exact calculations, the numerical magnitudes of some force constants can change, but the dependences of forces on the distance and velocity will remain unaltered. In the given variant of the theory, the temperatures of the particle (nanoprobe) and the surface may, in general, be different. If the particle is an atom, the particle temperature is assumed to be zero, while the temperature of the surface may be arbitrary. In Section 7, we discuss experiments in which FEMIs can manifest themselves. At present, however, no reliable data on the measurements of FEMIs are available, since the energy dissipation appears to be caused by several competing mechanisms. In the last section, the main conclusions are given.

As a rule, we use the Gaussian system of units, but in sections concerning the allowance for spatial dispersion, some formulas are written in atomic units ($e = \hbar = m = 1$). In the formulas that contain multiple integrals over wave vectors and frequencies, infinite limits $(-\infty, +\infty)$ of integration are meant for each variable, except for the resulting formulas for forces and potentials of interaction, in which the integration limits were reduced to the interval $(0, \infty)$, as, e.g., in (44), (45), (54), and some other. The functions marked by one or two primes mean the real and imaginary components, respectively. In Section 5 in the formulas that contain sums of cylindrical functions at $0 \le n < \infty$ (e.g., (85), (86), (88)), the term with a zero summation index is taken with a weighting factor equal to 1/2.

2. HISTORICAL ASPECTS OF THE PROBLEM

To our knowledge, the first attempts of the application of the model of Brownian motion to particles moving near a surface were made in [26–29]. In the approximation that is linear in the velocity, the drag force acting on a particle is equal to $F = -\eta V$, and the coefficient of viscous friction η is determined by the relation

$$\eta = \frac{1}{MV}\frac{dW}{dR}, \tag{1}$$

where M is the mass of the particle and dW/dR is the retarded force of the medium reaction generated by polarization charges. In the case of interaction between a localized and extended systems, the general expression for η has the form [26, 30]

$$\eta = (k_B T)^{-1}\mathrm{Re}\int_0^\infty dt\langle \hat{F}(t)\hat{F}(0)\rangle_R, \tag{2}$$

where $\langle \hat{F}(t)\hat{F}(0)\rangle_R$ is the thermal average value of the operator correlator of the fluctuational force in the stationary approximation, corresponding to the distance R between the systems. Formula (2) is a modification of the Kubo formula [31].

The calculation of the coefficient η is part of a more general problem of the calculation of dynamic interactions between moving particles and surfaces, which in the case of charges and multipoles was developed by many authors using classical and quantum approaches [32–43]. An important role in the development of the theory belongs to the so-called specular-reflection model [44, 45] (see below, in Section 4), which permits one to consider the interaction of particles with surfaces in the most illustrative manner.

As long as we deal with the interaction of charges and multipoles, we speak of a "Hartree" coupling between the systems. In the case of neutral moving systems, the FEMI is executed by weaker vdW forces.

The problem of the calculation of dissipative FEMIs was considered by Teodorovich [46, 47], Mahanty [48], and Schaich and Harris [49]. Even these first works have demonstrated the inconsistency of the results obtained and triggered a long theoretical discussion, which has not yet been finished to day [11–25].

Thus, Teodorovich considered friction in a system of two plane-parallel plates separated by a distance z and obtained (at $T = 0$ K) the following expression for the coefficient of friction:

$$\eta \approx S\frac{3\hbar}{64\pi^2 z^4}\frac{\varepsilon_{01}-1}{\varepsilon_{01}+1}\frac{\varepsilon_{02}-1}{\varepsilon_{02}+1}, \quad (3)$$

where S is the area of the plates, ε_{01} and ε_{02} are the static dielectric constants of the contacting materials, and $\hbar$ is Planck's constant. Schaich and Harris [49] obtained for two metallic plates the relation $\eta \sim T^2/z^6$ in the simplest "jellium" model and $\eta \sim T^2/z^4$ in the "jellium" model with allowance for electron scattering according to the Drude model, i.e., a zero friction at the zero temperature (in both cases). The coefficient of friction of a neutral particle near a metal surface proved to be

$$\eta \sim \frac{\hbar}{z^2}\frac{\alpha(0)^2}{z^6}\left(\frac{e^2/z}{\hbar\omega_s}\right)^2, \quad (4)$$

where $\alpha(0)$ is the static polarizability and ω_s is the frequency of a surface plasmon. At the same time, Mahanty [48] obtained for the interaction of a neutral particle with a surface

$$\eta = \frac{\hbar\alpha(0)\Delta_s(0,0)}{32z^5}, \quad (5)$$

where $\Delta_s(0, 0)$ is the limit of the function of the dielectric response of the surface (FDRS) at $\omega \longrightarrow 0$, $\mathbf{q} \longrightarrow 0$ (for the definition of the FDRS, see Section 4.1). Mahanty [48] was also the first who considered the problem of dynamic corrections to the long-range potential of interaction of atomic particles. Note (this is important) that no restrictions were imposed in [48] on the magnitude of the (nonrelativistic) velocity, whereas only linear approximations in velocity were considered in many later works. In the case of the interatomic repulsive potentials, the problem of dynamic corrections was considered in our works [50].

Schaich and Harris [49] concluded that Eq. (3) was erroneous based on the following argument. If we take into account that the main process that contributes to the correlator in Eq. (2) (at $T = 0$) is the process of generation of electron–hole pairs—whereas in the jellium model, the "screening charge" is time-independent and, therefore, the perturbation produced by the parallel motion of the plates is absent—the decay of the electric current due to the generation of electron–hole pairs should violate the law of momentum conservation.

We will address this problem in the next section; here, we simply note that the overwhelming majority of authors of later works [11–15, 41, 51, 52] mainly support the principal conclusion made in [49]: at $T = 0$, the friction of metallic plates (in the approximation that is linear in velocity) is absent and the friction of a neutral atom (particle) against the surface is determined by higher orders of quantum perturbation theory.

In the works by Levitov [23], Polevoĭ [24], Mkrtchian [25], and Dorofeev *et al.* [53], a relativistic approach was developed, but the formulas obtained in these works give a zero friction force in the limit of $c \longrightarrow \infty$. Possibly, in these works only relativistic corrections to this force were obtained, whereas the main (nonrelativistic) component independent of V/c was lost. This problem requires an independent consideration, which is beyond the scope of this review.

The situation with the calculation of dissipative forces became even more complex after our works [16–18, 54–56] in which the tangential force acting on a particle was determined via the integral of dissipative energy losses of the fluctuational electromagnetic field taken over the particle volume and divided by the particle velocity. The results of these works predict the existence of a linear-in-velocity contribution to the friction coefficient of the moving particle at $T = 0$: $\eta \sim V/z^5$ (cf. Eq. (4)). The corresponding approach somewhat resembles the technique that was applied in [24, 53], where the authors expressed the power of the tangential force through the rate of heating (cooling) of contacting bodies. On the other hand, in [15, 57], the authors identified the local heating of the surface with the probe of the scanning microscope and the work of the fluctuational electromagnetic field done on the electrons of the probe. However, a more detailed analysis shows [58] that, although the dissipative forces between the bodies upon their relative (noncontact) motion and heat exchange are internally related, the relationship between them is by no means simple. It turns out (see Section 4.4 below) that in the nonrelativistic case the general relation between the integral of dissipative losses of the fluctuational electromagnetic field, the tangential (dipole) force, and the rate of heating of the particle has the form

$$\frac{1}{V}\int \langle \mathbf{j}\mathbf{E}\rangle d^3r \equiv \langle (\mathbf{d}\nabla)E_x\rangle + \frac{1}{V}\langle \dot{\mathbf{d}}\mathbf{E}\rangle, \quad (6)$$

where $\mathbf{d}$ is the resulting vector of the dipole momentum of the particle caused by spontaneous fluctuations of the particle itself and by the fluctuations of the field of the surface (induced contribution), $\mathbf{E}$ is the vector of the electric field, and $\mathbf{j}$ is the current density; the angular brackets mean the complete quantum–statistical averaging. As usual in the fluctuation-electromagnetic theory, all vector quantities are considered as Heisenberg operators.

As follows from Eq. (6), the identical equality of the power of the tangential force and the integral of dissipation (taken over the particle volume) occurs only at $\mathbf{d} = 0$, i.e., for particles that do not possess a fluctuational dipole moment. Unfortunately, the existence of general formula (6) and its relativistic generalization (see Conclusion) has not received due attention, which has led to many contradictions [12–16, 21–25, 53–57].

3. DISCUSSION OF THEORETICAL RESULTS OF OTHER AUTHORS

The subject of discussion in this section are papers [11–15, 46–49] that are devoted to the nonrelativistic theory of FEMIs. Note, however, that the authors of [14, 15] also took into account retardation effects. As to the earlier works [46–48], it is commonly assumed that they are erroneous [11–15, 49]; however, we found no comprehensive discussion of these problems in the literature, except for the above-mentioned critical remark of Schaich and Harris [49]. In our opinion, a modification of the Lifshitz theory [5] concerning moving plates, which was made by Teodorovich [46, 47] using the concept of convective spatial dispersion [59], is insufficiently correct, since the dissipative lateral force is obtained in it from the expression for conservative interaction. Friction appears as a consequence of the anisotropy of spatial dispersion. The same feature is characteristic of Mahanty's work [48], in which the conservative interaction is expressed through a secular determinant and the tangential force is obtained by the corresponding differentiating of the energy with respect to the lateral coordinate.

The starting point of calculations in [49] is Eq. (2), but the authors note that although Eq. (2) yields a formally exact result, no strict calculation is possible using this formula and even an approximate calculation in the case of the vdW interaction seems to be difficult. For this reason, the authors make a number of additional approximations, the most important of which is the factorization of the correlation function of the Heisenberg operators of the electron density of interacting systems 1 and 2 (see [49, Eq. (24)]):

$$\begin{aligned} &T_\tau\langle\hat\rho^1(t)\hat\rho^2(t)\hat\rho^1(0)\hat\rho^2(0)\rangle \\ &\sim T_\tau\langle\hat\rho^1(t)\hat\rho^1(0)\rangle T_\tau\langle\hat\rho^2(t)\hat\rho^2(0)\rangle, \end{aligned} \quad (7)$$

where T_τ is the chronological operator. This cardinal simplification means that the electron densities of the systems do not correlate with one another. At the same time, it is well known that the existence of such a correlation lies in the basis of the conservative vdW interaction (!). Subsequent calculations for the friction coefficient of a neutral atom yield Eq. (4), which predicts a very low result. In reality, Eq. (7) restricts the interaction to the allowance for a second-order perturbation theory contribution, which follows from the presence of the squared polarizability in Eq. (4). Note also that upon the parallel motion of two metallic plates, the friction force only appears at a nonzero temperature.

Recently, more detailed calculations of the coefficients of friction for charges, dipole molecules, and neutral atoms for the case of motion over a flat surface (with a local FDRS) were performed by Tomassone and Widom [13]. For the first two types of particles, they used the temperature theory of second-order perturbations, Coulomb Green's functions, and the fluctuation-dissipation theorem for the correlator of the fluctuational fields of the surface. As a result, well-known nonrelativistic formulas for the potentials of interaction of charges and dipoles with the surface were obtained. The lateral force was then calculated using formula (2). However, when performing an analogous calculation for the fluctuating atomic dipole, the authors of [13] did not calculate the correlator entering into Eq. (2) but applied a modification of the nonstationary perturbation theory (without sufficient grounds), in which the squared matrix element of the Hamiltonian of the interaction was replaced by the squared matrix element of the operator of the force that acts on the dipole from the fluctuational field of the surface. The subsequent calculation includes an additional approximation analogous to (7) (see the passage from Eq. (49) to (54) in [13]), and the final result for the force of friction of a neutral atom (in the linear-in-velocity approximation) predicts its absence at $T = 0$:

$$F = \frac{3\hbar V}{2\pi z^5}\int_0^\infty \alpha''(\omega)\Delta''(\omega)\frac{d}{d\omega}\frac{1}{\exp(\omega\hbar/k_BT)-1}d\omega, \quad (8)$$

where $\alpha''(\omega)$ and $\Delta''(\omega)$ are the imaginary components of the atomic polarizability and the FDRS $\Delta(\omega) = (\varepsilon_2(\omega) - 1)/(\varepsilon_2(\omega) + 1)$, $\varepsilon_2(\omega)$ is the dielectric function of the medium, z is the distance to the surface, and the other quantities have the usual sense. On the whole, this work is characterized by the absence of a general theoretical basis that would permit calculations of fluctuation-electromagnetic interactions for all types of particles in an unified manner.

In the private communication [60] given as an answer to our remarks on the derivation of Eq. (8) by the authors of [13], Persson states that the equation is correct and gives another derivation of the same formula based on the transformation of Eq. (2) using an integral variant of the fluctuation–dissipation theorem. In the course of this calculation, however, again the central point of our objections arises, i.e., the "splitting" of the correlator of the components of the operator of the dipole moment of the atom and the electric field of the surface (cf. Eq. (7)).

The nonzero (at $T = 0$) contribution to the friction coefficient obtained in the second-order perturbation theory by Persson and Volokitin [11] has the form

$$\eta = e^2 m \frac{[k_F^3 \alpha(0)]^2}{(k_F d)^{10}} \frac{\omega_F}{\omega_p} k_F I(d), \quad (9)$$

where d is the distance from the atom to the edge of the jellium of the metal; e and m are the charge and mass of the electron, respectively; k_F, ω_F, and ω_p are the Fermi vector, Fermi frequency, and plasma frequency, respectively; and the function $I(d)$ weakly depends on d at $d >$ 0.4 nm for the parameters of the jellium model $r_s = 2$ to 4 times $I(d) = 7$–13 [41]. Formula (9), as we see, agrees with the result of Schaich and Harris (4).

A somewhat different treatment of the problem of deceleration of an atom moving over a surface (in the case of FEMI) was used in the works of Annett and Echenique [51, 52], who resorted to the formalism of a complex effective potential ("self energy"). The real part of this potential corresponds to the conservative vdW attraction of the atom to the surface, and the imaginary part, to the probability of anelastic excitations of the surface caused by the interaction. As follows from the calculations of the authors (see [52, Eq. (11)]), at $V < 2M\omega_{n0}$, where M is the atomic mass and ω_{n0} is the frequency of transition of the atom from the ground (0) into an excited (n) state, no imaginary part of the self-energy is present and, consequently, friction is also absent. However, one should take into account that this theory is based on the Born–Oppenheimer approximation for the many-electron wave function of the atom–surface system, in which the change in the wave functions of separate parts upon interaction is neglected; i.e., in fact, the correlation disturbances imposed by the FEMIs are ignored.

The works of Pendry [12] and Volokitin and Persson [14, 15] are devoted to a related problem of friction of ideally smooth (reflecting electromagnetic radiation) surfaces separated by a plane vacuum gap of width d. In these calculations, the contact shear stress was calculated on the basis of the Maxwell tensor of stresses in vacuum.

Pendry [12] considered the case of $T = 0$ using an heuristic expression for the electric field in the gap consisting of two parts: (1) the contribution of the fluctuational electric field from the immobile plate; and (2) the contribution of the electromagnetic wave reflected from the moving (with a velocity V) plate, which takes into account the Doppler shift of the frequency of the Fresnel reflection coefficient $R_{1pp}(\omega + k_x V)$. The corresponding wave has a polarization of the P type with the electric vector lying in the same plane that contains the vector normal to the surface and the wave vector. After the substitution of the amplitude of the resulting field into the tensor of stresses and integration with respect to the projections of the wave vectors k_x, k_y (the z axis is directed perpendicular to the surface), the following expression was obtained for the contact stress applied to the immobile plate from the mobile plate (see [12, Eq. (18)]):

$$F_x/S = \frac{2\hbar}{4\pi^3} \int_0^\infty k_x dk_x \int_{-\infty}^\infty \exp(-2kd) dk_y \times \int_0^\infty (\Delta_1''(\omega + k_x V) - \Delta_1''(\omega - k_x V)) \Delta_2''(\omega) d\omega, \quad (10)$$

where $\Delta_{1,2}''(x)$ are the imaginary components of the FDRS for the immobile (1) and mobile (2) plates; $k^2 = k_x^2 + k_y^2$; and S is the area of the interface. In the nonrelativistic limit, the FDRS coincides with the Fresnel coefficient for the P waves. At $V \longrightarrow 0$, it follows from (10) that

$$F_x/S = \frac{3\hbar V}{16\pi^2 d^4} \int_0^\infty \Delta_2''(\omega) \frac{d}{d\omega} \Delta_1''(\omega) d\omega. \quad (11)$$

Equation (11) appears to correspond to a nonzero friction force between plates of different materials. For plates of like materials, this force is zero, but one should not attach much importance to this result because of the approximate character of the model. Pendry [12], however, did not obtain formula (11), since an additional symmetrization of formula (10) was made. Indeed, formula (10) does not take into account the contribution from the second plate. But when constructing this contribution proceeding from this formula, one should take into account the fundamental asymmetry of (10) with respect to the related Fresnel coefficients. Therefore, if we formally change the order of considering the plates (as was done in [12]), the resulting formula proves to be nonidentical to (10). Upon subsequent transformations, mutual annihilation of linear-in-velocity contributions to the tangential force occurs (see [12, Eq. (25)]):

$$F_x/S = \frac{1}{2\pi^2} \int_0^\infty k_x dk_x \int_{-\infty}^\infty \exp(-2kd) dk_y \times \int_0^{k_x V} \mathrm{Im} \frac{\varepsilon_1(\omega) - 1}{\varepsilon_1(\omega) + 1} \mathrm{Im} \frac{\varepsilon_2(k_x V - \omega) - 1}{\varepsilon_2(k_x V + \omega) + 1} d\omega. \quad (12)$$

It follows from (12) that the contribution to friction that does not vanish at $V \longrightarrow 0$ is $F_x \sim V^3/d^6$, and in the case of frequency-independent dielectric functions, formula (12) coincides in form with the result of Teodorovich (3).

The more tedious quantum calculations of the author in the second part of [12] led to the same results for the lateral force (cf. Eqs. (15) and (55) in [12]).

Volokitin and Persson [14, 15] extended Pendry's calculation to the case of $T \neq 0$ by applying a dynamic modification of the Lifshitz theory for finding the amplitude of the electric field in the gap between the bodies. Their initial equations contain retardation effects, but since the relative motion of the plates under consideration is slow, additional simplifying assumptions are made (see, e.g., [15, Eqs. (23) and (24)]). In these works, the conservative and dissipative forces are treated in a completely identical manner and the tangential (dissipative) force arises as a result of the relative motion of the bodies due to the Doppler shifts of the field amplitudes. This idea, however, is by no means new, since (in a somewhat different form) it was applied by Teodorovich. The calculations of the authors of [15] confirmed the result obtained by Pendry [12] at $T = 0$; at $T \neq 0$, the final formula of [15] is close to that obtained by Schaich and Harris [49].

To complete the discussion, we may say that the problem of dissipative FEMIs was mainly considered from two different viewpoints: as the problem of friction of moving particles (charges, dipoles, fluctuating dipoles) and as the problem of friction of plane-parallel plates. In the last case, the general electrodynamic problem for moving bodies have not yet been solved. The main strategy was the adaptation of the Lifshitz theory for conservative FEMIs to the calculation of dissipative FEMIs (!). As to the first part of the problem (especially, the case of a fluctuating dipole), here a tendency is traced of reducing the complex (dissipative) process of friction to a standard quantum-mechanical problem, in which elementary excitations can be related to the model Hamiltonian of a perturbation. Thus, for sliding friction, it is assumed that the main elementary dissipative process is the process of decay of electron–hole excitations [3, 11, 13, 41, 49]. In the calculations of deceleration of charged particles and dipoles of constant strength, this does nor lead to complications, since one of the interacting fields is Coulomb, and the arising correlator (see (2)) can be split in approximation (7) without affecting the final result. In the final analysis, the quantum theory simply reduces to the application of the "Fermi golden rule" and the results obtained using this theory, as well as using Eq. (2) (in the approximation linear in velocity) and via classical electrodynamics, prove to be completely identical. As to the case of fluctuating dipoles (and multipoles), no constructive derivation of the formula for the tangential force that would be free from additional simplifying assumptions has virtually existed up to now. In particular, no general expression for the tangential force with allowance for the nonlinear dependence on the velocity at arbitrary temperatures of the particle and surface has existed so far.

On the whole, the complexity of the problem of dissipative FEMIs for neutral systems was caused, in our opinion, by the absence of a clear understanding of the relation between fundamental physical quantities concerning this problem, such as the power of the fluctuation-electromagnetic field, the tangential force, the rate of heat exchange, the role of spontaneous and induced components of electric fields and currents, etc. It is this reason that determines the variety of theoretical schemes applied by different authors and, as a consequence, the presence of a fundamental discordance of opinions. The suggested theory, in our opinion, lifts all contradictions in a simple and natural way.

4. INTERACTION OF MOVING ATOMIC AND MOLECULAR PARTICLES WITH FLAT SURFACES

4.1. Physical Processes in a Moving-Particle–Surface System in the Regime of Small Velocities and the Dielectric Response of the Surface

Upon the motion (scattering) of a moving particle near a surface, various inelastic processes are possible. Using a quantum treatment, we may expect that the particle can lose its energy due to the generation of phonons, surface plasmons and polaritons, electron–hole pairs, and any other elementary excitations of the surface. If single plasmons are generated, they decay by decomposing into separate electron–hole excitations.

A static charge placed near a polarizable medium interacts with the induced potential of the image charge. Inside the medium, there arises a cloud of a screening charge around it, which has a spherically symmetric form. When the charge moves with a velocity V, the electric potential induced in the plasma acquires a cylindrical symmetry; therefore, the charge is subject to a lateral drag force. The energy of the translational motion is spent on Joule losses related to the electric current induced in the plasma. In the case of a moving dipolar molecule, the cause of retardation is the same. As a result, ohmic heating of the medium occurs (the final result of friction). When particles move near a medium, the motion of charges induced on its surface is also accompanied by energy dissipation due to ohmic losses.

In the absence of a spatial dispersion of the FDRS, the energy losses of slowly moving multipoles can be related to the damping of surface plasmons, since the generation of single undamped plasmons at small velocities is impossible (for particles whose energy is smaller than the threshold energy of plasmon generation).

For a moving neutral atom in the ground state (nanoparticles), the process of retardation is more complex, since the energy of translational motion can be spent not only on the excitation (heating) of the surface, but also on the heating of the particle itself. In the case of an atom, such a "heating" can be treated as an analog of the Lamb shift of levels. On the whole, the moving-particle–surface system, in a certain sense, is similar to a system of two coupled mechanical oscillators, in which energy can pass from one oscillator to another. If the moving multipole of a constant magnitude can only be

retarded upon interaction with a surface, a neutral particle (see below) can also receive energy from surface excitations, i.e., can be accelerated.

In a theoretical description of FEMIs, the key role is played by the FDRS, for which the most general expression (with allowance for spatial dispersion) can be introduced in terms of the specular-reflection model (SRM) [44, 45]. This model was successfully applied by many authors to describe dynamic effects of the interaction of charged particles with metallic surfaces [1, 34–36, 61–63]. According to the SRM, the medium–vacuum interface is assumed to be sharp and the induced potential is determined by the external field of the particle, its mirror image, and the field of fictitious surface charges at the interface that should be introduced to ensure boundary conditions for continuity of the potential and of the normal component of the vector of electric displacement. For a charged particle (Fig. 1a), the Fourier components of the scalar electric potential are equal to [1]

$$\phi(\mathbf{k}, \omega) = (8\pi^2 Ze/k^2) \times [\delta(\omega - \mathbf{kV}) + \delta(\omega - \mathbf{kV}') + \rho_s(\mathbf{q}, \omega)], \quad z < 0, \tag{13}$$

$$\phi(\mathbf{k}, \omega) = -8\pi^2 Ze\rho_s(\mathbf{q}, \omega)/k^2\varepsilon(\mathbf{k}, \omega), \quad z > 0, \tag{14}$$

where $\mathbf{V}$ is the velocity of the particle with parallel ($\mathbf{V}_\parallel$) and perpendicular ($\mathbf{V}_\perp$) components; $\mathbf{V} = (\mathbf{V}_\parallel, \mathbf{V}_\perp)$; and $\mathbf{V}' = (\mathbf{V}_\parallel, -\mathbf{V}_\perp)$; and $\mathbf{k} = (\mathbf{q}, k_z)$. The minus sign in Eq. (14) allows for the continuity of the electric displacement at the medium–vacuum interface ($z = 0$). The condition of the continuity of the potential itself determines the density of the surface charge $\rho_s(\mathbf{q}, \omega)$:

$$\rho_s(\mathbf{q}, \omega) = -\frac{q}{\pi + qI_0} \times \int_{-\infty}^{+\infty} \frac{dk_z}{q^2 + k_z^2}[\delta(\omega - \mathbf{kV}) + \delta(\omega - \mathbf{kV}')], \tag{15}$$

$$I_0 = \int_{-\infty}^{+\infty} \frac{dk_z}{k^2\varepsilon(\mathbf{k}, \omega)}. \tag{16}$$

With allowance for Eqs. (13), (15), and (16), we obtain for the induced potential

$$\phi^{\text{ind}}(\mathbf{r}, t) = \frac{Ze}{2\pi^2}\int d\mathbf{q}\int d\omega \frac{|\mathbf{V}_\perp|\exp(-q|z|)}{(\omega - \mathbf{V}_\parallel \cdot \mathbf{q})^2 + (V_\perp q)^2} \times \left(\frac{qI_0 - \pi}{qI_0 + \pi}\right)\exp(i(\mathbf{qV}_\parallel - \omega)t). \tag{17}$$

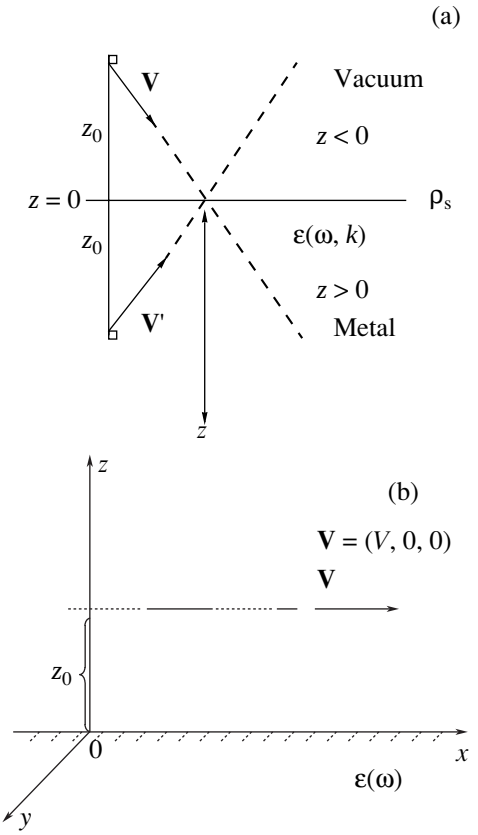

Fig. 1. (a) Specular-reflection model. The particle intersects the surface of the medium at the time instant $t = 0$. (b) Schematic of the lateral interaction of a neutral atom with a flat surface.

It is convenient to define the FDRS that enters into (17) as

$$\Delta_s(q, \omega) = \frac{\pi - qI_0}{\pi + qI_0}. \tag{18}$$

In a local case, it is easy to show, using Eqs. (16) and (18), that

$$\Delta_s(\omega, q) = \Delta(\omega) = \frac{\varepsilon(\omega) - 1}{\varepsilon(\omega) + 1}. \tag{19}$$

The drag force on the particle upon its parallel motion is obtained from (17) in the limit $V_\perp \longrightarrow 0$ [1] as

$$F = -(Ze/V)[\partial\phi^{\text{ind}}(\mathbf{r}, t)/\partial t]_{\mathbf{r} = \mathbf{V}t} = \frac{2(Ze)^2}{\pi V_\parallel^2}\int_0^\infty dq_y \int_0^\infty d\omega \frac{\omega}{q}\exp(-2qz_0)\Delta_s''(\omega, q), \tag{20}$$

where z_0 is the distance from the particle to the surface and $q^2 = q_y^2 + \omega^2/V_\parallel^2$.

For the dielectric function $\varepsilon(\mathbf{k}, \omega)$, there exist a number of analytical approximations, which take into

account various properties of the polarizable medium. We give some of them, which will be used below.

(1) An approximation for the case of a conducting medium and small particle velocities, when the energy transferred to the plasma is much smaller than the Fermi energy (here and in Eqs. (22)–(27), we use atomic units) [64]

$$\varepsilon(k, \omega) = 1 + \frac{\omega_p^2}{V_F^2 k^2 [1 - i\pi\omega\theta(2k_F - k)/2kV_F]/3 - \omega(\omega + i\gamma)}, \quad (21)$$

where $\theta(x)$ is the unit Heaviside function.

Formula (21) generalizes the hydrodynamic Lindhard approximation [65] for the case where the velocity of plasmons is equal to $V_F/\sqrt{3}$. The term proportional to the θ function in the denominator describes damping because of electron–hole excitations, and the term proportional to γ describes the damping of collective modes. Upon the expansion in frequencies, formula (21) agrees with the well-known dielectric Lindhard function $\varepsilon^L(k, \omega)$. The presence of the θ function in (21) takes into account that $\mathrm{Im}(1/\varepsilon^L(k, \omega))$ vanishes at $k > 2k_F$, since low-energy electron–hole excitations are absent for the corresponding wave vectors. Substituting (21) into (16) and integrating, we obtain for the FDRS in the limit of low frequencies [1]

$$\Delta_s(q, \omega) = \frac{1 - q(A + B + C)}{1 + q(A + B + C)}, \quad (22)$$

$$A = \frac{1}{(q^2 + q_{TF}^2)^{1/2}}, \quad (23)$$

$$B = \frac{-i\omega q_{TF}}{4V_F}\left[\frac{2q_{TF}^2 + q^2}{q_{TF}^2(q^2 + q_{TF}^2)^{3/2}} \times \ln\left(\frac{(q^2 + q_{TF}^2)^{1/2} + q_{TF}}{(q^2 + q_{TF}^2)^{1/2} - q_{TF}}\right) - \frac{2}{(q^2 + q_{TF}^2)q_{TF}}\right], \quad (24)$$

$$C = \frac{-i\omega\gamma q_{TF}^2}{s^2} \times \left[\left(\frac{(q^2 + q_{TF}^2)^{1/2} - q}{q_{TF}^4 q(q^2 + q_{TF}^2)^{1/2}}\right) - \frac{1}{2q_{TF}^2(q^2 + q_{TF}^2)^{3/2}}\right], \quad (25)$$

where $s = V_F/\sqrt{3}$ and $q_{TF} = \omega_p/s$.

Of certain interest is also the long-wavelength expansion of the FDRS corresponding to (21) in wave vectors without restrictions on the frequency. In this limit ("weak dispersion"), Eq. (18) has the form [66] ($\omega_s = \omega_p/\sqrt{2}$)

$$\Delta_s(\omega, q) = \frac{\omega_s^2}{\omega_s^2 - \omega^2 - i\omega\gamma} \times \left(1 - \frac{i}{3}\frac{\omega V_F}{\omega^2 - \omega_s^2 + i\omega\gamma} q \ln(4q_F/q)\right), \quad (26)$$

where q_F is the Fermi wave vector. By definition,

$$V_F = q_F = \pi q_{TF}^2/4, \quad q_{TF} = \sqrt{3}\omega_p/V_F, \quad \gamma = \omega_p^2/4\pi\sigma, \quad (27)$$

where σ is the static conductivity.

(2) The FDRS in the Drude approximation

$$\varepsilon(\omega) = 1 - \frac{\omega_p^2}{\omega(\omega + i/\tau)}, \quad (28)$$

where τ is the time of relaxation of conduction electrons. With allowance for (18) and (28), we obtain for the FDRS

$$\Delta(\omega) = \frac{\omega_p^2(\omega_p^2 - 2\omega^2)}{(\omega_p^2 - 2\omega^2) + 4\omega^2/\tau^2} + i\frac{2\omega_p^2\omega/\tau}{(\omega_p^2 - 2\omega^2) + 4\omega^2/\tau^2}. \quad (29)$$

(3) A weakly nonlocal approximation [67, 68]

$$\Delta(q, \omega) = \frac{1 - \varepsilon(\omega)}{1 + \varepsilon(\omega)}\left(1 + \frac{2\varepsilon(\omega)}{\varepsilon(\omega) + 1} q d(\omega) + \ldots\right), \quad (30)$$

where $\varepsilon(\omega)$ is the Drude function (28) and $d(\omega)$ is the shift of the centroid of the induced screening charge of metal. In the case of low frequencies under the condition $q \ll \omega/V_F$, it follows from (30) [41]

$$\Delta''(q, \omega) = 2I(q)\frac{\omega}{\omega_p}\frac{q}{q_F}, \quad (30a)$$

where $I(q)$ is a function of order unity weakly dependent on q. Formula (30a) was frequently used in investigations into sliding friction [11, 40, 41, 68, 69].

(4) The low-frequency approximation for a conductor

$$\varepsilon(\omega) = 1 + \frac{4\pi\sigma i}{\omega}, \quad (31)$$

$$\Delta''(\omega) = \frac{2\pi\sigma\omega}{\omega^2 + 4\pi^2\sigma^2}. \quad (31a)$$

(5) The Debye approximation for an insulator

$$\varepsilon(\omega) = 1 + \frac{\varepsilon(0) - 1}{1 - i\omega\tau}, \quad (32)$$

$$\Delta''(\omega) = \frac{2(\varepsilon(0)-1)\omega/\tau}{\omega^2 + \left(\frac{\varepsilon(0)+1}{2\tau}\right)^2}, \quad (32a)$$

where τ is the time of dipole relaxation and $\varepsilon(0)$ is the static dielectric constant.

(6) The model of the optical absorption line with a Lorentzian profile

$$\varepsilon_i(\omega) = \varepsilon_{i\infty} + \frac{(\varepsilon_{i0}-\varepsilon_{i\infty})\omega_{0i}^2}{(\omega_{0i}^2-\omega^2) - i\gamma_i\omega}, \quad (33)$$

where the index i denotes the type of the material; ε_{i0} and $\varepsilon_{i\infty}$ are the corresponding static and high-frequency values of the dielectric constant, respectively; and ω_{0i} and γ_i are the frequencies and the line widths, respectively.

Now, we pass to a consistent consideration of conservative and nonconservative FEMI forces acting on moving particles without, first, allowance for the spatial dispersion of the FDRS. The corresponding calculations are based on the exact solution to the Poisson equation for the Fourier components of the induced electric potential due to the moving particle and on the fluctuation–dissipation theorem; this makes it possible to easily reproduce all results for FEMIs available in the literature in the case of charges and dipole particles [16–18, 21]. For a fluctuating dipole, the derivation of the general formula for a tangential force is given for the first time.

4.2. Charged Particles

In the case of the parallel motion of a charge (Ze), the general formulas for the normal and tangential forces have the form [16–18]

$$F_z(z, V) = -\frac{2(Ze)^2}{\pi}\int_0^{\pi/2} d\phi \int_0^\infty q\,dq \times \exp(-2qz)\Delta'(qV\cos\phi), \quad (34)$$

$$F_x(z, V) = -\frac{2(Ze)^2}{\pi}\int_0^{\pi/2} \cos\phi\, d\phi \int_0^\infty q\,dq \times \exp(-2qz)\Delta''(qV\cos\phi). \quad (35)$$

Using the designation $\omega = qV\cos\phi$, formulas (34) and (35) can easily be reduced to a form coinciding with that obtained in [70]:

$$F_z(z, V) = -\frac{2(Ze)^2}{\pi V^2}\int_0^\infty d\omega\,\omega K_1(2\omega z/V)\Delta'(\omega), \quad (36)$$

$$F_x(z, V) = -\frac{2(Ze)^2}{\pi V^2}\int_0^\infty d\omega\,\omega K_0(2\omega z/V)\Delta''(\omega), \quad (37)$$

where $K_0(x)$ and $K_1(x)$ are the modified Bessel functions.

For the dielectric function (21) without damping ($\tau \longrightarrow \infty$), formula (37) is simplified as follows [1, 71]:

$$F_x(z, V) = -\frac{(Ze)^2\omega_s^2}{V^2}K_0\left(\frac{2\omega_s z}{V}\right). \quad (38)$$

For the dielectric function (29), we can, using an expansion in powers of the velocity and retaining the first terms of the expansion that do not vanish at $V = 0$, reduce formulas (34) and (35) to the following form:

$$F_x(z, V) = -\frac{(Ze)^2}{16\pi\sigma z^3}V + \ldots, \quad (39)$$

$$F_z(z, V) = -\frac{(Ze)^2}{4z^2}\left(1 - \frac{3}{16\pi^2}\frac{V^2}{\sigma^2 z^2} + \ldots\right). \quad (40)$$

Formulas analogous to (39) were obtained in [1, 13, 72]. In order to show the identity of (39) and Eq. (32) from [1], it is sufficient to perform standard substitutions $\gamma = 1/\tau$, $4\pi\sigma/\tau = \omega_p^2$, and $\omega_s = \omega_p/\sqrt{2}$. All of the above results can also be obtained from (17) and the first part of (20), using the local FDRS.

In the case of motion in the direction perpendicular to the surface, the normal component of the force of interaction includes conservative and dissipative components simultaneously (here, it is assumed that $V > 0$):

$$F_z(z, V) = \frac{i(Ze)^2}{\pi V^2}\int_{-\infty}^\infty d\omega\,\omega\Delta(\omega)\exp(-i\omega z/V) \times \int_0^\infty \frac{dq\,q\exp(-qz)}{q^2 + \omega^2/V^2} = -(Ze)^2\int_0^\infty dq\,q\Delta(-iqV)\exp(-2qz). \quad (41)$$

The separation of the force into conservative and dissipative components can easily be seen by expanding (41) in powers of the velocity and using FDRS (32a):

$$F_z(z, V) = -\frac{(Ze)^2}{4z^2}\left(1 + \frac{V}{2\pi\sigma z} + \frac{3V^2}{8\pi^2\sigma^2 z^2} + \ldots\right). \quad (42)$$

As in the case of parallel motion, it follows from (42) that the dissipative contributions to the force of interaction contain odd components of the velocity, whereas the conservative contributions contain even components (beginning from V^0). The first term in (42) describes the attraction of the charge to its image.

4.3. Dipole Molecules

The force that acts on a dipole from the induced field of the surface is written as follows [17, 18]:

$$\mathbf{F} = (\mathbf{d}\nabla)\mathbf{E}^{\text{ind}}. \quad (43)$$

In the case of the lateral motion of the dipole, we obtain ($\mathbf{d} = (d_x, d_y, d_z)$)

$$F_z(z, V) = \frac{-2}{\pi}\int\int dq_x dq_y \exp(-2qz) \times (q_x^2 d_x^2 + q_y^2 d_y^2 + q^2 d_z^2)\Delta'(q_x V), \quad (44)$$

$$F_x(z, V) = \frac{-2}{\pi}\int\int dq_x dq_y q_x \exp(-2qz) \times (q_x^2 d_x^2 + q_y^2 d_y^2 + q^2 d_z^2)\Delta''(q_x V)/q. \quad (45)$$

In the case of normal motion, we have

$$F_z(z, V) = -\frac{d_x^2 + d_y^2 + 2d_z^2}{2}\int_0^\infty dq q^3 \Delta(-iqV)\exp(-2qz), \quad z = Vt. \quad (46)$$

Expanding (44)–(46) in powers of the velocity V, we obtain

(a) for lateral motion

$$F_z(z, V) = -\frac{3(d_x^2 + d_y^2 + 2d_z^2)}{16z^4} \times\left(\Delta'(0) + \frac{5V^2}{8z^2}\frac{d^2\Delta'(\omega)}{d\omega^2}\bigg|_{\omega = 0}\frac{(3d_x^2 + d_y^2 + 4d_z^2)}{(d_x^2 + d_y^2 + 2d_z^2)} + \ldots\right), \quad (47)$$

$$F_x(z, V) = -\frac{3(3d_x^2 + d_y^2 + 4d_z^2)V}{32z^5}\frac{d\Delta''(\omega)}{d\omega}\bigg|_{\omega = 0} + \ldots; \quad (48)$$

(b) for normal motion

$$F_z(z, V) = -\frac{3(d_x^2 + d_y^2 + 2d_z^2)}{16z^4} \times\left(\Delta(0) + \frac{2V}{z}\frac{d\Delta''}{d\omega}\bigg|_{\omega = 0} + \ldots\right), \quad z = Vt. \quad (49)$$

In particular, for the FDRS corresponding to Eq. (32a), formulas (47)–(49) take on the following form:

$$F_z(z, V) = -\frac{3(d_x^2 + d_y^2 + 2d_z^2)}{16z^4} \times\left(1 - \frac{5V^2}{16\pi^2\sigma^2 z^2}\frac{3d_x^2 + d_y^2 + 2d_z^2}{d_x^2 + d_y^2 + 2d_z^2} + \ldots\right), \quad (50)$$

$$F_x(z, V) = -\frac{3(3d_x^2 + d_y^2 + 4d_z^2)V}{64\pi\sigma z^5} + \ldots, \quad (51)$$

$$F_z(z, V) = -\frac{3(d_x^2 + d_y^2 + 2d_z^2)}{16z^4}\left(1 + \frac{V}{\pi\sigma z} + \ldots\right). \quad (52)$$

The numerical coefficients and the dependences on the distance in Eqs. (50)–(52) exactly correspond to the results obtained in [13]. In addition, note that the friction forces in the case of normal motion of charges are twice as large, and in the case of dipoles, fourfold as large as those upon lateral motion.

4.4. Neutral Atoms

In the case of fluctuating dipoles (multipoles), the general method [16–18] does not permit one to separate spatial and temporal variables in the Poisson equation upon the perpendicular motion of the particle; therefore, in what follows, we give the results only for lateral motion (most important for practical applications). An atom under consideration is characterized by a dynamical polarizability $\alpha(\omega)$, and the distance z_0 to the surface is restricted by the condition $r_0 \ll z_0 \ll c/\omega_0$, where r_0 is a characteristic dimension of the atomic dipole and ω_0 is the characteristic frequency of the electromagnetic spectrum (Fig. 1b). This condition justifies the application of the approximation of a point dipole and permits one to neglect the retardation effect. Naturally, all the results that will be obtained below are equally applicable to the case of an arbitrary spherically symmetric particle. The potential of interaction with the surface is written in the form [7, 73]

$$U = -\frac{1}{2}\langle \mathbf{dE}\rangle = -\frac{1}{2}\langle \mathbf{d}^{sp}\mathbf{E}^{ind}\rangle - \frac{1}{2}\langle \mathbf{d}^{ind}\mathbf{E}^{sp}\rangle = U_1 + U_2, \quad (53)$$

where the first term (U_1) is due to spontaneous fluctuations of the atomic dipole $\mathbf{d}^{sp}(t)$ and the second term (U_2) is due to the fluctuations of the electric field of the surface $\mathbf{E}^{sp}(t)$. The procedure for performing corresponding calculations is described in our previous works [16–18, 21 58, 66]. It uses the fluctuation-dissipative relations given in [74]. As a result, we have for the attractive potential

$$U(z_0, V) = -\frac{\hbar}{\pi^2}\int\int\int d\omega dk_x dk_y k \exp(-2kz_0) \times \coth\frac{\omega\hbar}{2k_B T}\{\alpha''(\omega)[\Delta'(\omega - k_x V) + \Delta'(\omega + k_x V)] + \Delta''(\omega)[\alpha'(\omega - k_x V) + \alpha'(\omega + k_x V)]\}. \quad (54)$$

At $T = 0$ and $V = 0$, Eq. (54) yields the well-known formula for the static potential of the vdW attraction of a particle to the surface [7]

$$U(z_0) = -\frac{\hbar}{4\pi z_0^3}\int_0^\infty d\omega\alpha(i\omega)\Delta(i\omega). \quad (55)$$

Dynamic corrections to the potential are obtained upon the expansion of Eq. (54) in powers of the velocity

(note that only even powers of V have nonzero values). Thus, the correction quadratic in V in the general case will have the form

$$\Delta U^{(2)}(z_0, V) = -\frac{V^2}{z_0^5}\frac{3\hbar}{16\pi}\int_0^\infty d\omega \coth\frac{\omega\hbar}{2k_BT} \times\left(\alpha''(\omega)\frac{\partial^2\Delta'(\omega)}{\partial\omega^2} + \Delta''(\omega)\frac{\partial^2\alpha'(\omega)}{\partial\omega^2}\right). \quad (56)$$

Before we pass to the calculation of the lateral force, we consider in more detail the derivation of the main formula (6). Following [58], we obtain the following expression for the vector of polarization produced by a neutral particle upon its motion in vacuum with a velocity V at a distance z_0 from the flat boundary that bounds a semiinfinite medium with a dielectric constant $\varepsilon(\omega)$ (Fig. 1b):

$$\mathbf{P}(\mathbf{r}, t) = \delta(x - Vt)\delta(y)\delta(z - z_0)\mathbf{d}(t), \quad (57)$$

where $\mathbf{d}(t)$ is the fluctuational dipole moment of the particle. The density of the electric current related to $\mathbf{P}(\mathbf{r}, t)$ is, by definition, $\mathbf{j} = \partial\mathbf{P}(\mathbf{r}, t)/\partial t$. In the absence of radiation, it follows from the law of conservation of the energy of the particle–surface system that

$$-\frac{dW}{dt} = \int\langle\mathbf{jE}\rangle d^3r, \quad (58)$$

where the left-hand side represents the rate of energy losses for the fluctuational electromagnetic field and the right-hand side corresponds to the averaged work of the field $\mathbf{E}$ done on the moving particle per unit time. With allowance for Eqs. (57) and (58), we obtain

$$\int\langle\mathbf{jE}\rangle d^3r = V\left\langle\frac{\partial}{\partial x}(\mathbf{dE})\right\rangle + \langle\dot{\mathbf{d}}\mathbf{E}\rangle. \quad (59)$$

We should especially say that, first, we should perform differentiation $(\partial/\partial x)$ in (59) and only after this insert the Cartesian coordinates of the particle at the time instant t, i.e., $(Vt, 0, z_0)$. Then, after a simple transformation of the first term on the right-hand side of Eq. (59), with allowance for the fact that in the nonrelativistic case we have $\mathrm{rot}\mathbf{E} = 0$, we obtain identity (6), which is the main one in further calculations of the dissipative tangential force. In this identity, the first term on the right-hand side represents the tangential component of the "dipole" force acting on the particle, while the second term is related to the rate of heating the particle; note that the integral of dissipation (on the left-hand side) is taken over the volume of the particle. Upon the motion of a neutral atom, which is considered as a system of coupled charges, the rate of heating can be treated as a modification of the Lamb shift of levels due to the fluctuational electromagnetic field. As follows from the identity, the equality of the power of the tangential force and the rate of dissipation of the energy of the fluctuational field is strictly fulfilled only for a particle with a constant dipole moment. Unfortunately, this circumstance has not been earlier taken into account in a due way [16–18, 21, 53–56].

The calculation of the lateral force F_x is performed similar to the calculation of the attractive potential. It is convenient to write the initial formula so that it would explicitly contain spontaneous and induced components of the dipole moment of the particle and of the fluctuational electric field of the surface (cf. with Eqs. (53)):

$$F_x = \langle(\mathbf{d}\nabla)E_x\rangle = \langle(\mathbf{d}^{\mathrm{sp}}\nabla)E_x^{\mathrm{ind}}\rangle + \langle(\mathbf{d}^{\mathrm{ind}}\nabla)E_x^{\mathrm{sp}}\rangle.$$

The course of the further calculation is analogous to the calculation of the conservative potential [18, 21]. At arbitrary temperatures of the particle (T_1) and surface (T_2), the resulting formula has the form [58]

$$F_x = \langle(\mathbf{d}\nabla)E_x\rangle = -\frac{2\hbar}{\pi^2}\iiint d\omega dk_x dk_y k_x k \times\exp(-2kz_0)\left\{\coth\left(\frac{\omega\hbar}{2k_BT_1}\right)\alpha''(\omega) \times[\Delta''(\omega + k_xV) - \Delta''(\omega - k_xV)] + \coth\left(\frac{\omega\hbar}{2k_BT_2}\right)\Delta''(\omega)[\alpha'(\omega + k_xV) - \alpha''(\omega - k_xV)]\right\}. \quad (60)$$

At $T_1 = T_2 = T$, Eq. (60) in the linear approximation in the velocity reduces to the form

$$F_x = \langle(\mathbf{d}\nabla)E_x\rangle = \frac{3\hbar V}{4\pi z_0^5} \times\int_0^\infty d\omega a''(\omega)\Delta''(\omega)\frac{d}{d\omega}\coth\left(\frac{\omega\hbar}{2k_BT}\right), \quad (60a)$$

which coincides with the result obtained in [13]. Thus, formula (8) obtained by Tomassone and Widom [13] is correct, but, in contrast to these authors, we obtained it without resorting to any additional approximations. As to formula (60), it was obtained for the first time in [58] and yields the most general expression for the dipole force at arbitrary temperatures of the particle and surface (in the nonrelativistic case).

A fundamentally new and important consequence of the theory is the possibility of accelerating the particle by the field of surface excitations at $T_1 \neq T_2$. Physically, this is due to the fact that a neutral particle (atom) has natural frequencies. For dipole molecules and charged particles, only deceleration is observed. Thus, in the approximation linear in the velocity, after directly integrating Eq. (60) with respect to the wave vectors and

integrating in parts with respect to the frequency in the second term of the integrand, we obtain

$$F_x = -\frac{3\hbar V}{4\pi z_0^5}\int_0^\infty d\omega\left[\frac{1}{\left[\exp\left(\frac{\omega\hbar}{k_B T_1}\right)-1\right]}\right.$$

$$\left.-\frac{1}{\left[\exp\left(\frac{\omega\hbar}{k_B T_2}\right)-1\right]}\right]\alpha''(\omega)\frac{d}{d\omega}\Delta''(\omega)-\frac{3\hbar V}{4\pi z_0^5}\frac{\hbar}{k_B T_2} \quad (61)$$

$$\times\int_0^\infty d\omega\alpha''(\omega)\Delta''(\omega)\frac{\exp\left(\frac{\omega\hbar}{k_B T_2}\right)}{\left[\exp\left(\frac{\omega\hbar}{k_B T_2}\right)-1\right]^2}.$$

It follows from (61) that the sign of the lateral force depends on the relationship between the temperatures of the particle and surface, as well as on the sign of the derivative of the FDRS. Acceleration is also possible for a neutral atom ($T_1 = 0$) near a heated surface ($T_2 = T$). These problems will be discussed below.

4.5. Effects of Spatial Dispersion

The presence of spatial dispersion, as follows from Eqs. (35), (45), and (54), should be taken into account under the condition $qz \approx 1$ (where q is the wave vector of the surface excitation), i.e., at distances from the surface $z \le l_0 = 1/q$. For charged particles, the effects of dispersion are taken into account by using Eqs. (17) and (20); when using Eqs. (34) and (35), it is sufficient to replace the local FDRS in them by a nonlocal one in accordance with Eq. (18). The formulas for the conservative FDRSs are modified in a similar way.

The passage to dipoles and fluctuating dipoles requires an additional substantiation, which was done in [20, 66] with the use of the SRM. The SRM equations analogous to (13), (14) have the form

$$-k^2\phi_{\omega\mathbf{k}} = 8\pi^2$$
$$\times[i\delta(\omega-\mathbf{qV})\mathbf{kd}+i\delta(\omega-\mathbf{qV}')\mathbf{kd}+\rho_s(\mathbf{q},\omega)],$$
$$z<0, \quad (62)$$
$$\phi_{\omega\mathbf{k}} = \frac{8\pi^2\rho_s(\mathbf{q},\omega)}{\varepsilon(\mathbf{k},\omega)k^2}, \quad z>0,$$

where

$$\rho_s(\mathbf{q},\omega) = -2i\frac{\delta(\omega-\mathbf{qV})}{(\pi/k+I_0)}\int_{-\infty}^{+\infty}dk_z\frac{\mathbf{kd}}{k_z^2+q^2}, \quad (63)$$

I_0 is determined from Eq. (16), and $\mathbf{V} = \mathbf{V}'$ (in the case of parallel motion). A disadvantage of the SRM is the divergence of the integral in Eq. (63) and in the corresponding formula for the z component of the electric field in the presence of a nonzero d_z projection of the dipole moment ($d_z \neq 0$). No difficulties exist for other projections; therefore, assuming $d_z = 0$, we can obtain the formula for the induced potential directly from Eq. (62), subtracting the Fourier component of the unscreened potential $4\pi\rho_s(\mathbf{q},\omega)/k^2$. As a result, we have

$$\phi^{\text{ind}}_{\omega\mathbf{q}}(z_0) = \frac{4\pi^2 i}{q}\Delta_s(q,\omega)\mathbf{dq}\exp(-2qz_0)\delta(\omega-\mathbf{qV}). \quad (64)$$

Comparison of this formula with an analogous formula for the local case [18, 21] shows that the allowance for spatial dispersion (as in the case of charges) reduces to the formal replacement of the local FDRS by a nonlocal one. Since upon the replacement $\mathbf{dq} \longrightarrow \mathbf{dq} - id_z k_z$ Eq. (64) ensures a correct solution in the case of the local FDRS, this formula can be extended, with such a modification, to the general case with arbitrary orientations of the dipole moment of the particle. The correctness of such a replacement follows from the coincidence of the formulas obtained in the case of $d_z \neq 0$ with the exact calculation [1]. The authors of the cited work solved the corresponding problem for a dipole particle by using the available results for a moving charge and representing the dipole as two charges located at distances z and $z + d_z$ from the surface.

The further calculations of conservative and nonconservative forces in the case of all types of particles are completely analogous to those done in the local case; therefore, the general formulas for the FEMIs obtained in the preceding sections are modified by the replacement of the local FDRS by a nonlocal one.

For example, consider the contribution of spatial dispersion to the lateral force for a moving dipole of constant magnitude with allowance for the interaction with surface plasmons. For simplicity, we restrict ourselves to an asymptotics $z_0 \gg q_{\text{TF}}^{-1}$. Passing to a long-wavelength limit in Eqs. (22)–(25), we write

$$\text{Im}\Delta_s(q,\omega = q_x V) \approx \frac{2q_x\gamma V}{\omega_p^2}$$
$$+\frac{2qq_x V}{V_F q_{\text{TF}}^2}\left(\ln 2-\frac{1}{2}-\ln q/q_{\text{TF}}\right). \quad (65)$$

Substituting (65) into (35) and taking into account the relations $V_F = \pi q_{\text{TF}}^2/4$ and $\gamma = \omega_p^2/4\pi\sigma$, we obtain

$$F \approx -\frac{15}{8\pi}\frac{(3d_x^2+d_y^2+4d_z^2)q_{\text{TF}}^2 V}{(q_{\text{TF}}z_0)^6}\ln(0.44q_{\text{TF}}z_0)$$
$$-\frac{3}{64\pi\sigma}\frac{(3d_x^2+d_y^2+4d_z^2)V}{z_0^5}. \quad (66)$$

As can be seen from (66), the allowance for the dispersion of plasmons leads to the appearance of an additional contribution to the lateral force (first term) apart from the second term, which is responsible for the local FDRS (cf. with Eq. (51)).

A similar result is obtained upon the use of FDRS (26). Indeed, at $z_0 \gg q_{TF}^{-1}$ and $V/z_0 \ll \omega_s$, we have $\omega \ll \omega_s$; therefore, separating the term that is responsible for dispersion in (26), we obtain

$$\mathrm{Im}\Delta_s^{(2)}(\omega, q) \approx \frac{V_F q \ln(4q_F/q)}{3}\omega\omega_s^2. \quad (67)$$

Then, substituting (67) into (35) and using the tabulated integral [75]

$$\int_0^\infty x^n \exp(-mx)\ln x dx = \frac{n!}{m^{n+1}}\left(\sum_{k=1}^{n}(1/k) - 0.577 - \ln m\right),$$

we find

$$F^{(2)} \approx -\frac{15}{8\pi}\frac{(3d_x^2 + d_y^2 + 4d_z^2)}{q_{TF}^4 z_0^6}\ln(1.45 q_F z_0). \quad (68)$$

Comparing (68) with the first term of (66), we conclude that they coincide, except for the numerical factor under the sign of the logarithm (by definition, $V_F = q_F = \pi q_{TF}^2/4$).

Similarly, for a charged particle, the corrections to the lateral force due to the dispersion of plasmons (corresponding to FDRSs (65) and (67)) have the form

$$F^{(2)} \approx -\frac{3}{2\pi}\frac{(Ze)^2 V}{(q_{TF}z_0)^4}\ln(0.692 q_{TF} z_0), \quad (69)$$

$$F^{(2)} \approx -\frac{3}{2\pi}\frac{(Ze)^2 V}{(q_{TF}z_0)^4}\ln(2.27 q_{TF} z_0). \quad (70)$$

Formulas (66) and (69) coincide exactly with those given in [1].

In the case of a neutral particle with a fluctuating dipole moment, using the SRM, we obtain for the Fourier component of the induced potential the following expression, instead of (64),

$$\phi_{\omega\mathbf{q}}^{\mathrm{ind}}(z_0) = \frac{2\pi i}{q}\Delta_s(q, \omega)\mathbf{d}^{\mathrm{sp}}(\omega - \mathbf{qV})\mathbf{q}\exp(-2qz_0), \quad (71)$$

where $\mathbf{d}^{\mathrm{sp}}(\omega - \mathbf{qV})$ is the Fourier component of the spontaneous dipole moment. As in the case of a constant dipole, to obtain correct results with allowance for the presence of a normal projection of the vector of the dipole moment in (69), we should make a substitution

$$\mathbf{d}^{\mathrm{sp}}(\omega - \mathbf{qV})\mathbf{q} \longrightarrow \mathbf{d}^{\mathrm{sp}}(\omega - \mathbf{qV})\mathbf{q} - id_s^{\mathrm{sp}}(\omega - \mathbf{qV})k_z. \quad (72)$$

After this modification and the replacement of the FDRS by a nonlocal one, all general formulas of Section 4 remain valid.

In the case of interaction of a neutral atom with surface plasmons in metals, the contribution of high (plasma) frequencies is suppressed due to the presence of exponential factors in (60) and (60a). Restricting ourselves to a low-frequency limit, we write for the complex part of the atomic polarizability

$$\alpha''(\omega) = \omega\frac{e^2}{m}\sum_n \frac{f_{0n}\gamma_{0n}}{\omega_{0n}^3}, \quad (73)$$

where f_{0n}, ω_{0n}, and γ_{0n} are the oscillator force, frequency, and line width for the transition $0 \longrightarrow n$, respectively. In turn, the FDRS is determined by Eqs. (22)–(25), from which it follows at $\omega \longrightarrow 0$ that

$$\Delta_s''(q, \omega) \approx \omega\frac{i}{\omega}\frac{2q(B + C)}{(1 + qA)^2} \equiv \omega D(q). \quad (74)$$

In the asymptotic limit $z_0 \gg 1/2k_{TF}$, the expression for $D(q)$ reduces to the form

$$D(q) \approx \frac{2}{\sqrt{3}\omega_p}\frac{q}{q_{TF}}\left(\ln(2q_{TF}/q) - \frac{1}{2}\right) + \frac{1}{2\pi\sigma}, \quad (75)$$

where $\sigma = \omega_p^2/(4\pi\gamma)$ is the static conductivity. In the approximation linear in the velocity, we obtain after the substitution of (73) into (60) (using atomic units and the condition $2\pi\sigma > k_B T$)

$$F = -\frac{3}{2\pi}k_1 k_2 V(k_B T_2)^2 \times\left[\frac{5}{\sqrt{3}\omega_p}\frac{q_{TF}^5}{(q_{TF}z_0)^6}\ln(0.441 q_{TF} z_0) + \frac{1}{2\pi\sigma z_0^5}\right], \quad (76)$$

where

$$k_1 = -\int_0^\infty \frac{x dx}{\exp(x) - 1} + \int_0^\infty \frac{x^2 dx}{\exp(x) - 1} + \int_0^\infty \frac{x^2 dx}{(\exp(x) - 1)^2} = 1.645, \quad (77)$$

$$k_2 = \sum_n f_{0n}\gamma_{0n}/\omega_{0n}^3. \quad (78)$$

Using the FDRS (26), the resulting formula coincides with (76) after the replacement of the argument of the logarithm by $1.645 q_F z_0$. Note also that formula (76) is only applicable at $V \ll 2\pi\sigma z_0$, whereas at greater velocities, an obligatory procedure is the allowance for nonlinear terms in the expansion in powers of the velocity.

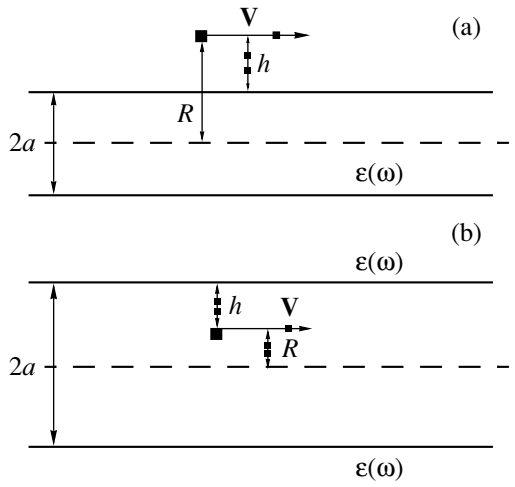

Fig. 2. Schematic of the particle motion (a) parallel to the generatrix of a convex cylindrical surface and (b) inside a cylindrical channel.

In a similar way we may consider, e.g., dispersion effects upon the interaction of particles with surface polaritons and excitons. In this case (as well as at enhanced temperatures), we may expect a stronger interaction of particles with the surface due to the effect of the resonance structure of the FDRS.

5. INTERACTION OF MOVING ATOMIC AND MOLECULAR PARTICLES WITH CYLINDRICAL SURFACES

The investigation of FEMIs between particles and curved surfaces is of interest not only in connection with the problems of retardation and friction, but also due to the possibilities of controlling and transporting atomic beams in microchannels and nanotubes [76, 77] as well as upon the investigations of the adsorption ability of fullerenes and porous substances.

In the mathematical respect, this problem is more complex than in the case of a flat surface; therefore, the number of available reports is much smaller (see, e.g., the reviews [73, 78] on the vdW forces). Physical adsorption at curved surfaces was considered by Schmeits and Lucas [79, 80]; in a recent work [57], Dorofeev *et al.* calculated vdW forces and heat flows between bodies of various curvature using the conformal mapping method in a two-dimensional formulation.

For cylindrical surfaces (at $T = 0$), the calculation of dissipative forces of FEMIs was first calculated in our works [55, 56]. Below, we give more general results [22, 66, 81] obtained in a nonrelativistic approximation for both conservative and dissipative forces of FEMIs at an arbitrary temperature but without allowance for spatial dispersion.

The scheme of calculations and the restrictions are the same as for flat surfaces. Figure 2a shows the geometry of the interaction for a convex cylindrical surface bounding the medium under consideration; Fig. 2b illustrates the interaction of a particle in a cylindrical channel. The condition of the applicability of a dipole approximation and neglecting the effect of retardation is written in the form $r_0 \ll h \ll c/\omega_0$, where $h = |R - a|$; R and a denote the radial distance from the particle to the cylinder axis and the cylinder radius, respectively; r_0 is the characteristic size of the atom; and ω_0 is the characteristic frequency of the spectrum. As in the case of a flat surface, the calculations are based on the exact solutions to the Poisson equation for a particle–surface system and the fluctuation–dissipative relations (for details, see [22, 66, 81]).

5.1. Charged Particles

In the case of a charged particle moving parallel to the symmetry axis of a convex cylindrical surface, the components of the conservative and dissipative forces are

$$F_r(R, V) = \frac{4(Ze)^2}{\pi} \times \sum_{n=0}^{\infty} \int_0^{\infty} dk k K_n(kR) K_n'(kR) \Delta_n'(kV), \quad (79)$$

$$F_z(R, V) = -\frac{4(Ze)^2}{\pi} \sum_{n=0}^{\infty} \int_0^{\infty} dk k K_n^2(kR) \Delta_n''(kV), \quad (80)$$

$$\Delta_n(\omega) = \frac{(\varepsilon(\omega) - 1) I_n(ka) I_n'(ka)}{\varepsilon(\omega) I_n'(ka) K_n(ka) - I_n(ka) K_n'(ka)}, \quad (81)$$

where $K_n(x)$ and $I_n(x)$ are the cylindrical functions of order n (primes mark their derivatives); the argument ka, which is an analog of the FDRS for a flat surface, is omitted for simplicity; and Δ_n' and Δ_n'' are the real and imaginary components of $\Delta_n(\omega)$, respectively. Taking into account (79), the conservative potential of attraction of the charge to the surface can be written as

$$U(R, V) = -\frac{2(Ze)^2}{\pi} \sum_{n=0}^{\infty} \int_0^{\infty} dk K_n^2(kR) \Delta_n'(kV). \quad (82)$$

For a charge moving inside a cylindrical channel parallel to its axis, formulas (79)–(82) are modified by the substitution $K_n(x) \longleftrightarrow I_n(x)$.

5.2. Dipole Molecules

For a dipole molecule moving parallel to the symmetry axis of a convex cylindrical surface, the compo-

nents of the tangential and radial forces of interaction with the surface are determined by the relations

$$F_z = \langle \nabla_z(\mathbf{dE})\rangle, \quad F_R = \langle \nabla_R(\mathbf{dE})\rangle, \tag{83}$$

with the radial component being related to the conservative attractive potential as

$$F_R = -\frac{\partial U}{\partial R}, \quad U = -1/2\langle \mathbf{dE}\rangle. \tag{84}$$

The same formulas are used below for calculating forces for fluctuating dipoles. The resulting formulas for U and F_z are written as

$$U(R, V) = -\frac{2}{\pi R^2}\sum_{n=0}^{\infty}{}'\int_0^\infty dk K_n^2(kR) \times [n^2 d_\phi^2 + (kR)^2 d_z^2 + (kR)^2 \Phi_n^2(kR) d_r^2]\Delta_n'(kV), \tag{85}$$

$$F_z(R, V) = -\frac{4}{\pi R^2}\sum_{n=0}^{\infty}{}'\int_0^\infty [n^2 d_\phi^2 + (kR)^2 d_z^2 + (kR)^2 \Phi_n^2(kR) d_r^2]\Delta_n''(kV) dk K_n^2(kR), \tag{86}$$

where d_ϕ, d_r, and d_z are the components of the dipole moment in the cylindrical coordinate system (Fig. 2a) and the function $\Phi_n(x)$ is a logarithmic derivative of the MacDonald function:

$$\Phi_n(z) \equiv \frac{d}{dz}\ln K_n(z). \tag{87}$$

In the case of motion inside a cylindrical channel parallel to its axis, as in the case of a charged particle, the substitution $K_n(x) \longleftrightarrow I_n(x)$ should be done in Eqs. (85)–(87).

5.3. Neutral Atoms

In the most general case, taking into account the difference in the temperatures of the particle (T_1) and surface (T_2), the resulting formulas have the form

$$U(R, V) = -\frac{\hbar}{\pi^2 R^2}\sum_{n=0}^{\infty}{}'\int\int d\omega dk K_n^2(kR) \times [n^2 + (kR)^2 + (kR)^2 \Phi_n^2(kR)] \times \{\coth(\omega\hbar/2k_B T_1)\alpha''(\omega)[\Delta_n'(\omega + kV) + \Delta_n'(\omega - kV)] + \coth(\omega\hbar/2k_B T_2)\Delta_n''(\omega)[\alpha'(\omega + kV) + \alpha'(\omega - kV)]\}, \tag{88}$$

$$F_z(R, V) = -\frac{\hbar}{\pi^2 R^2}\sum_{n=0}^{\infty}{}'\int\int d\omega dk k K_n^2(kR) \times [n^2 + (kR)^2 + (kR)^2 \Phi_n^2(kR)] \times \{\coth(\omega\hbar/2k_B T_1)\alpha''(\omega)[\Delta_n''(\omega + kV) - \Delta_n''(\omega - kV)] + \coth(\omega\hbar/2k_B T_2)\Delta_n''(\omega)[\alpha''(\omega + kV) - \alpha''(\omega - kV)]\}. \tag{89}$$

Formula (88) generalizes the well-known expression for the stationary potential of the vdW attraction of an atom to a cylindrical surface at $T = 0$. Indeed, assuming $T = 0$ and $V = 0$ in this formula, the contour of integration with respect to frequencies can be rotated in such a manner that it will coincide with the imaginary semiaxis. Then, with allowance for the relation

$$\mathrm{Im}\int_0^\infty d\omega\alpha(\omega)\Delta_n(\omega) = \int_0^\infty d\omega\alpha(i\omega)\Delta_n(i\omega), \tag{90}$$

the result can be written in a form coinciding with that given in [79, 80, 82], i.e.,

$$U(R) = -\frac{\hbar}{\pi^2 R^2}\sum_{n=0}^{\infty}{}'\int_0^\infty dk K_n^2(kR) \times [n^2 + (kR)^2 + (kR)^2 \Phi_n^2(kR)] \times \frac{\alpha(i\omega)(\varepsilon(i\omega) - 1)I_n'(ka)I_n(ka)}{\varepsilon(i\omega)K_n(ka)I_n'(ka) - K_n'(ka)I_n(ka)}. \tag{91}$$

The dynamic corrections to the potential, as in the case of a flat surface, contain only even powers of the velocity.

The formula for the tangential force in the approximation linear in the velocity is obtained by expanding functions entering into (89) into a Taylor series. As a result, we obtain

$$F_z(R, V) = -\frac{2\hbar V}{\pi^2 R^2}\sum_{n=0}^{\infty}{}'\int_0^\infty dk k^2 K_n^2(kR) C_n(k) \times [n^2 + (kR)^2 + (kR)^2 \Phi_n^2(kR)], \tag{92}$$

$$C_n(k) = \int_0^\infty d\omega\left\{\left[\coth\left(\frac{\omega\hbar}{2k_B T_1}\right) - \coth\left(\frac{\omega\hbar}{2k_B T_2}\right)\right] \times \left[\alpha''(\omega)\frac{d\Delta_n''(\omega)}{d\omega} - \Delta_n''(\omega)\frac{d\alpha''(\omega)}{d\omega}\right] + \alpha''(\omega)\Delta''(\omega)\left(-\frac{d}{d\omega}\right)\left[\coth\left(\frac{\omega\hbar}{2k_B T_1}\right) + \coth\left(\frac{\omega\hbar}{2k_B T_2}\right)\right]\right\}. \tag{93}$$

Thereby, the tangential force is represented in the form of a sum of two summands, one of which is alternates

sign and corresponds to the first term in brackets in the integrand of Eq. (93), and the second one is of fixed sign. At $T_1 = T_2$, only the sign-constant part is retained, and $F_z < 0$. Such a situation was also observed in the case of the flat surface (see Eq. (61)).

Passage to the case of a concave cylindrical surface for the case of the motion of the particle in a cylindrical channel is trivial and also is done by the modification of formulas (86)–(96), namely, by the substitution $K_n(x) \longleftrightarrow I_n(x)$.

5.4. Interaction of a Neutral Atom with a Thin "Filament"

It follows from general formula (89) that at $V \longrightarrow 0$ the main contribution to the integral in k comes from the region of $k \le 1/R$; therefore, at $a \ll R$, we have $ka \ll 1$ and can expand $\Delta_n(\omega)$ in powers of ka. In this case, with allowance for the asymptotics of the cylindrical functions at small values of the argument in the sum over n, it is sufficient to retain only two terms proportional to

$$\Delta_0(\omega) = \frac{(ka)^2}{2}\frac{\varepsilon(\omega)-1}{1-\varepsilon(\omega)\dfrac{(ka)^2}{2}\ln(\gamma ka/2)}, \qquad (94)$$

$$\Delta_1(\omega) = \frac{(ka)^2}{2}\frac{\varepsilon(\omega)-1}{\varepsilon(\omega)+1} = \frac{(ka)^2}{2}\Delta(\omega). \qquad (95)$$

In the case of a dielectric filament, we also can omit the term proportional to $\varepsilon(\omega)$ in the denominator of Eq. (94). As a result, we obtain

$$F = -\frac{\hbar a^2 V}{R^7}\int_0^\infty d\omega\left\{0.33\left[\alpha''(\omega)\varepsilon''(\omega)\left(-\frac{d}{d\omega}\right)\right.\right.$$
$$\times[\coth(\hbar\omega/2k_BT_1)+\coth(\hbar\omega/2k_BT_2)]$$
$$+[\coth(\hbar\omega/2k_BT_1)-\coth(\hbar\omega/2k_BT_2)]$$
$$\left.\times\left(\alpha''\frac{d\varepsilon''}{d\omega}-\varepsilon''\frac{d\alpha''}{d\omega}\right)\right]+1.1\left[\alpha''(\omega)\Delta''(\omega)\left(-\frac{d}{d\omega}\right)\right. \qquad (96)$$
$$\times[\coth(\hbar\omega/2k_BT_1)+\coth(\hbar\omega/2k_BT_2)]$$
$$+[\coth(\hbar\omega/2k_BT_1)-\coth(\hbar\omega/2k_BT_2)]$$
$$\left.\left.\times\left(\alpha''(\omega)\frac{d\Delta''(\omega)}{d\omega}-\Delta''(\omega)\frac{d\alpha''(\omega)}{d\omega}\right)\right]\right\}.$$

At $T_1 = T_2 = T$, Eq. (96) reduces to a simpler form

$$F = -\frac{2\hbar a^2 V}{R^7}\int_0^\infty d\omega\alpha''(\omega)(0.33\varepsilon''(\omega)+1.1\Delta''(\omega))$$
$$\times\left(-\frac{d}{d\omega}\coth\left(\frac{\hbar\omega}{2k_BT}\right)\right). \qquad (97)$$

In the case of an insulating filament, the denominator in (94) should be taken into account as a whole, since at $\omega \longrightarrow 0$ we have $\varepsilon(\omega) \approx 4\pi\sigma i/\omega$. In this case, we obtain $F \propto \dfrac{a^2\sigma V}{R^7}$. The parameter a may be considered as a characteristic dimension of the electron shell of the filament atoms

6. DISSIPATIVE FORCES AND HEAT EFFECTS IN NANOPROBE–SURFACE SYSTEMS AND BETWEEN FLAT SURFACES

6.1. Additivity Approximation

When calculating FEMIs between bodies of an arbitrary shape, we should know the equilibrium spectrum of electromagnetic fluctuations in the gap between the bodies. The arising geometrical restrictions affect this spectrum and reflect the fundamental feature of fluctuational forces: they cannot be expressed through the sum of pair interparticle potentials. Fortunately, the additivity approximation in the case of vdW forces is sufficiently correct: upon more exact calculations, only interaction constants change rather than the dependences of the forces on the distance [83, 84]. For example, for the case of a convex probe and a flat surface, the error is 5–20% [83]; therefore, this approximation can be used as an acceptable working hypothesis. In experiments with the application of a scanning probe microscope, the typical situation is the contact of a parabolic probe with a flat surface; therefore, below we will consider precisely this case, as well as the contact of a spherical particle (cluster) with a flat surface, and restrict ourselves to an approximation linear in velocity. In addition, we consider friction of flat surfaces.

For solids with a cubic lattice, the polarizability is related to the dielectric constant of the material by the Clausius–Mossotti equation; therefore, we have

$$\alpha''(\omega) = \frac{3}{4\pi N}\mathrm{Im}\frac{\varepsilon_1(\omega)-1}{\varepsilon_1(\omega)+2}, \qquad (98)$$

where N is the volume concentration of atoms of the probe. After the substitution of (98) into (61) and integration over the volume of the parabolic probe (with the equation of its surface $z = (x^2 + y^2)/2R + d$, where R is the curvature radius of the probe near the apex and d is the distance from the apex to the surface), we obtain

(assuming that the ratio of the height of the probe to its radius is large) [19]

$$F = -\frac{3}{16\pi}\frac{\hbar RV}{d^3}J(\varepsilon_1(\omega), \varepsilon_2(\omega)), \quad (99)$$

where the integral of overlap of the spectrum $J(\varepsilon_1(\omega), \varepsilon_2(\omega))$ has precisely the same structure as the frequency integrals in (61) with the replacement of the imaginary part of the particle polarizability by the function

$$\tilde{\Delta}''(\omega) = \mathrm{Im}\frac{\varepsilon_1(\omega)-1}{\varepsilon_1(\omega)+2}. \quad (100)$$

In the optical (infrared) range of the spectrum or at sufficiently high temperatures, when $\hbar\omega \ll k_B T$, Eq. (99) with allowance for (61) and (100) reduces to a simpler form:

$$F = -\frac{3}{16\pi}\frac{k_B TRV}{d^3}J(\varepsilon_1(\omega), \varepsilon_2(\omega)), \quad (101)$$

$$J(\varepsilon_1(\omega), \varepsilon_2(\omega))$$

$$= \begin{cases} \int_0^\infty d\omega \dfrac{\tilde{\Delta}_1''(\omega)\Delta_2''(\omega)}{\omega^2}, & T_1 = T_2 = T, \quad (102a) \\ \int_0^\infty \dfrac{d\omega}{\omega}\tilde{\Delta}_1''(\omega)\dfrac{d}{d\omega}\Delta_2''(\omega), & T_1 = T,\ T_2 = 0, \quad (102b) \\ \int_0^\infty \dfrac{d\omega}{\omega}\Delta_2''(\omega)\dfrac{d}{d\omega}\tilde{\Delta}_1''(\omega), & T_1 = 0,\ T_2 = T. \quad (102c) \end{cases}$$

In the case of arbitrary temperatures of the probe and surface, the required modification of Eqs. (101) and (102) is obvious. When using the nonlocal FDRSs, we should proceed from the general formula (60).

For a small spherical particle, under the condition $R \ll z < c/\omega_0$, the friction force is determined by Eqs. (60) and (61) in which the imaginary part of the polarizability is,

$$\alpha''(\omega) = R^3\tilde{\Delta}_1''(\omega). \quad (103)$$

At $R \approx z$, formula (103) appears to become invalid, but for a metallic cluster of an arbitrary shape we can use an analytical formula for the polarizability $\alpha(\omega)$ obtained in terms of the Thomas–Fermi model [85]:

$$\alpha(\omega) = R^3 \times \left\{1 + \frac{3(1-\kappa R\coth(\kappa R))}{2(\varepsilon(\omega)-1)(1-\kappa R\coth(\kappa R)+\varepsilon(\omega)(\kappa R)^2)}\right\}, \quad (104)$$

where $\kappa^2 = \frac{4}{\pi}\frac{(9\pi/4)^{1/3}}{r_s}$ and r_s are the parameters of the jellium model (in atomic units). For example, at R = 10 nm (a typical value of the radius of nanoprobes in SPM), we have $\kappa R \gg 1$ and, therefore, $\coth(\kappa R) \approx 1$. Then, as can easily be shown using Drude approximation (28), it follows from (104) that $\alpha''(\omega) \sim R^2$ (cf. (103)); note that the resonance frequency of absorption coincides with the plasma frequency of the metal ω_p rather than with the Mie frequency $\omega_p/\sqrt{3}$ (as follows from (103)). And even at $\kappa R \ll 1$, formula (104) differs from (103), although $\alpha''(\omega) \sim R^3$. Thus, allowance for screening in the case of conducting clusters and nanoprobes can be of fundamental importance.

6.2. Fluctuation–Dissipation Forces for Various Mechanisms of Absorption of Contacting Materials

First, we consider the contribution to the lateral force from absorption in the low-frequency part of the electromagnetic spectrum, i.e., for the case of contacts of bad conductors (with a low conductivity) and insulators (dielectric functions (31) and (32)). In this case, the integrals $J(\varepsilon_1(\omega), \varepsilon_2(\omega))$, as can easily be shown, can be calculated in a similar way. For example, for a contact of conductors, we obtain (indices 1 and 2 refer to the probe and surface, respectively), using (101) and (102),

$$\int_0^\infty d\omega \frac{\tilde{\Delta}_1''(\omega)\Delta_2''(\omega)}{\omega^2} = \frac{3}{4(2\sigma_1+3\sigma_2)}, \quad (105)$$

$$\int_0^\infty \frac{d\omega}{\omega}\tilde{\Delta}_1''(\omega)\frac{d}{d\omega}\Delta_2''(\omega) = \frac{9\sigma_1}{4(2\sigma_1+3\sigma_2)^2}, \quad (106)$$

$$\int_0^\infty \frac{d\omega}{\omega}\Delta_2''(\omega)\frac{d}{d\omega}\tilde{\Delta}_1''(\omega) = \frac{3\sigma_2}{(2\sigma_1+3\sigma_2)^2}. \quad (107)$$

Formulas (101), (102), and (105)–(107) are valid under the condition $k_B T/2\pi\hbar \gg \max(\sigma_1, \sigma_2)$. In another limit, at $k_B T/2\pi\hbar \ll \min(\sigma_1, \sigma_2)$, it follows from (99) that $F_x \propto T^2$ and the magnitude of the overlap integral [see Eq. (61)] proves to be smaller. In the general case, the exponent of the $F_x(T)$ dependence (for a given type of materials) changes in the range of 1–2 if we neglect possible temperature variation of the dielectric characteristics of the probe and the surface.

The maximum magnitudes of integrals (106) and (107) is reached at $2\sigma_1 = 3\sigma_2$. Then, with allowance for (101) and (102), we obtain

$$F_x = -0.022\frac{k_B TRV}{\sigma_1 d^3}. \quad (108)$$

At the magnitudes of the parameters typical of the SPM (R = 30 nm, d = 0.5 nm, T = 300 K, and V = 1 m/s), we

obtain $F_x = -0.022/\sigma_1(N)$. In the case of the contact of materials with metallic conductivity ($\sigma_1 = 10^{17}$ s^{-1}), F_x is negligible. But already for amorphous carbon ($\sigma_1 = 10^9$ s^{-1}), the magnitude of F_x becomes noticeable and, for the contacts of insulators with bad conductors, can reach values of about 1 nN, characteristic of the contact mode of SPM.

Upon the resonance character of absorption in materials with a dielectric response of the type of (28) and/or (33), formulas (102) also can be reduced to a universal form. Thus, e.g., for a contact of conductors described by Drude formulas (28), the tangential force acting on the probe is equal (in the case of the overlap integral (102b)) to

$$F_x = -\frac{3}{16\pi}\frac{k_B T R V\sqrt{3}}{d^3\omega_{p1}} G\left(\frac{\sqrt{3}}{\omega_{p1}\tau_1}, \frac{\sqrt{2}}{\omega_{p2}\tau_2}, \frac{\omega_{p2}}{\omega_{p1}}\sqrt{\frac{3}{2}}\right), \quad (109)$$

$$G(x, y, z) = \int_0^\infty \frac{dt}{(1 - t^2z^2)^2 + x^2z^2t^2}\frac{d}{dt}\frac{t}{(1 - t^2) + y^2t^2}, \quad (109a)$$

where the quantities ω_p and τ with indices 1 and 2 denote plasma frequencies and relaxation time of the probe and surface, respectively. In addition, one should take into account that the range of applicability of (109) is restricted to the condition $k_B T/\hbar \gg \max(\omega_{p1}, \omega_{p2})$. Formulas of the same type can be written for the integrals given in (102a) and (102c).

It is essential that, in contrast to the above-considered case (see (105)–(108)), integrals (102b) and (102c) alternate sign for the contacts of unlike materials and integral (102a) is always of s fixed sign. Note that $G < 0$ at $\omega_{p1}/\sqrt{3} > \omega_{p2}/\sqrt{2}$ and, consequently, the "hot" probe is accelerated by the tangential force. On the contrary, integral (102c) is negative at $\omega_{p1}/\sqrt{3} < \omega_{p2}/\sqrt{2}$ and the acceleration of the "cold" probe occurs at the expense of the heated surface. For the contacts of like materials, as well as for unlike materials at the same temperature, the tangential force is always retarding. Note that the possibility of the appearance of such effects was indicated by Polevoĭ [24] when considering the relativistic problem of friction of flat surfaces. Numerical calculations yield for the $G(x, y, z)$ function values of an order of 10–10^3 upon a noticeable overlap of the absorption bands; otherwise, its value is negligible. However, a resonance effect is possible even in the case of a significant discordance in the positions of the absorption peaks if at certain values of the particle velocity and certain distance to the surface, the overlap integral is not small (see Section 6.4 below). In order to obtain correct results in the last case, it is necessary to use general formula (60) and to take into account the shape of the absorption lines and the nonlocality of the FDRS, since the approximation linear in velocity is inadequate in this case.

Under the above-indicated conditions of the SPM experiments ($G = 10^3$ and $\omega_{p1} = 10^{13}$ s^{-1}, which corresponds to semiconductors such as germanium), we obtain an estimate $F_x = 5$ pN. To calculate the contribution to the tangential force from absorption at higher frequencies, we should apply the general formula (99), but even if the resonance region of frequencies is close to the Wien frequency $k_B T/\hbar$, the corresponding contribution to the force F_x turns out to be less significant because of the presence of exponential factors in (61). Thus, the above estimates of the tangential forces are close to maximum possible ones.

In the case where normal metals are in contact, a noticeable contribution at low frequencies can come from the nonlocal correction to the dielectric function. As a result, we obtain the following dependence: $F_x \propto VT^2/d^6$. At $d = 0.4$–0.5 nm, this contribution may be somewhat greater than follows from formulas (108), but, in any case, it is very small. For the contact of flat surfaces, the corresponding results are given in Section 6.3.

6.3. Friction of Flat Surfaces

When using the additivity approximation, the transition to the case of the contact of flat surfaces is trivial: integration over the volume of the probe is replaced by integration over the distance z_0 (from 0 to ∞) and multiplying by the area of the contacts. As a result, the formulas analogous to (99), (101), and (109) for the contact shear stress between two plane-parallel thick plates separated by a gap d take on the form

$$F/S = -\frac{9\hbar V}{32\pi^2 d^4} J(\varepsilon_1(\omega), \varepsilon_2(\omega)), \quad (110)$$

$$F/S = -\frac{9k_B T V}{32\pi^2 d^4} J(\varepsilon_1(\omega), \varepsilon_2(\omega)), \quad (111)$$

$$F/S = -\frac{9}{32\pi^2}\frac{k_B T V\sqrt{3}}{d^4\omega_{p1}} G\left(\frac{\sqrt{3}}{\omega_{p1}\tau_1}, \frac{\sqrt{2}}{\omega_{p2}\tau_2}, \frac{\omega_{p2}}{\omega_{p1}}\sqrt{\frac{3}{2}}\right), \quad (112)$$

where the integrals of overlapping of the spectra have the same meaning. The domain of the validity of Eqs. (111) and (112) is the same as that for formulas (101) and (109).

As was noted in Section 3, the friction of flat surfaces was recently considered in [12, 14, 15, 69]. In particular, the case of $T \neq 0$ was discussed in [14, 15, 69], and it was noted in [69] that a large contribution to the stress F/S for metallic surfaces can come from nonlocal effects. The results of the present work agree with this conclusion as well as with the earlier result of [49] and the statement of the authors of the above-cited works that, at $T = 0$, the linear-in-velocity contribution to the

friction force vanishes (without allowance for the possible relativistic corrections and structural effects).

Note, however, that formulas (60) and (61) laid in the basis of our work predict a number of new effects that are absent in the existing theory developed in [12, 14, 15, 49, 69]: (1) at various temperatures of the plates, as in the case of a parabolic nanoprobe and a surface, acceleration of the moving plate is possible; (2) heating of the "cold" plate is possible (see Subsection 6.4); and (3) the character of the temperature dependence of F/S depends on the type of contacting materials—in particular, the higher friction is accompanied by a linear dependence $F/S \sim T$, which can be characteristic of both the homogeneous and inhomogeneous contacts between semiconductors and insulators. Thus, at $T_1 = T_2 = 300$ K, $\omega_p = 10^{13}$ s^{-1}, $d = 1$ nm, $G = 10^3$, and $V = 1$ m/s, formula (112) yields $F/S = -3 \times 10^4$ N/m^2. This value is higher by 11 orders of magnitude than follows from Eq. (41) of [15] corresponding to the Drude approximation for the contact of metallic surfaces.

The calculation of the low-frequency nonlocal contribution to the friction force for metallic surfaces can conveniently be performed using FDRSs (73) and (74). Restricting ourselves, for simplicity, to the case of like materials and assuming $\Delta_1''(q, \omega) = \Delta_2''(q, \omega) = \tilde{\Delta}_1''(q, \omega)$ and $\omega \ll \omega_s$, we obtain (in atomic units), after the corresponding integration of Eq. (60),

$$F/S \approx -2.16 k_B^2 (T_1^2 + T_2^2) \frac{1}{\omega_p^4 q_{TF}^2} \frac{V}{d^5} \times [\ln^2(1.21 q_{TF}) + \ln^2(2d) + 2\ln(1.21 q_{TF})\ln(2d) - 3.74\ln(0.89 q_{TF} d)]. \quad (113)$$

Then, at typical values of the parameters $T_1 = T_2 = 300$ K, $\omega_p = 9$ eV, $q_{TF} = 1.07$ au, $d = 1$ nm, and $V = 1$ m/s, we estimate from (113) that $F/S = -3.4 \times 10^{-4}$ N/m^2. This is three orders of magnitude greater than was obtained in [69], but is much smaller than in the case of the atomic contact of surfaces (~10^8 N/m^2) and in the case of the sliding friction of nonmetallic surfaces.

6.4. Thermal Effects

The thermal effects of the nonradiative modes of a fluctuational electromagnetic field upon the contact of an immobile probe with the surface and the possibility of their practical utilization ("thermal stamping") was recently discussed in [57, 86–88]. The theory developed in this paper also permits one to discuss the case of a moving probe (dynamic regime).

Thus, in the general case, the rate of heating (cooling) of a moving particle ($\dot{Q}$) is determined by the second term in (59). Performing statistical averaging in such a way as was done in Section 4.4 upon the calculation of the normal and tangential forces, we obtain [58]

$$\dot{Q} = \langle \dot{\mathbf{d}}\mathbf{E} \rangle = \langle \dot{\mathbf{d}}^{sp}\mathbf{E}^{ind} \rangle + \langle \dot{\mathbf{d}}^{ind}\mathbf{E}^{sp} \rangle = -\frac{2\hbar}{\pi^2} \iiint d\omega dk_x dk_y k \exp(-2kz_0) \times \left\{ \coth\left(\frac{\omega\hbar}{2k_B T_1}\right) \alpha''(\omega)[\omega\Delta''(\omega + k_x V) + \omega\Delta''(\omega - k_x V)] - \coth\left(\frac{\omega\hbar}{2k_B T_2}\right)\Delta''(\omega) \times [(\omega + k_x V)\alpha''(\omega + k_x V) + (\omega - k_x V)\alpha''(\omega - k_x V)] \right\}. \quad (114)$$

In particular, at $V = 0$, Eq. (114) reduces to the form

$$\dot{Q} = -\frac{\hbar}{\pi z_0^3} \int_0^\infty \omega d\omega \alpha''(\omega)\Delta''(\omega) \times \left[\frac{1}{\exp(\hbar\omega/k_B T_1) - 1} - \frac{1}{\exp(\hbar\omega/k_B T_2) - 1} \right], \quad (115)$$

which coincides with the nonrelativistic limit of the result obtained in [88]. As could be expected in this case, the particle is cooled if its temperature is higher than the temperature of the surface. For bad conductors with a dielectric response (33) under the condition $k_B T/2\pi\hbar \gg \max(\sigma_1, \sigma_2)$ and in the case of the contact of a parabolic probe with the surface, we obtain from (115) (assuming $\sigma_1 = \sigma_2 = \sigma$)

$$\dot{Q} = -\frac{3\pi}{10} k_B (T_1 - T_2) \frac{R\sigma}{d}. \quad (116)$$

At $T_1 = 300$ K, $T_2 = 0$ K, $R/d = 30$ and $\sigma = 1$ $(\Omega\ \text{m})^{-1}$ (silicon), it follows from (116) that $\dot{Q} = -3.5 \times 10^{-10}$ W. Consequently, if we take into account that the effective area of the surface heated by the probe is on the order of $d^2 = 10^{-18}$ m^2, the heat flux to the surface will be equal to 3.5×10^8 W/m^2, which is much higher than the flux of radiation from a blackbody with the same temperature (4.6 W/m^2). In the case where $k_B T/2\pi\hbar \ll \sigma$, we similarly obtain

$$\dot{Q} = -\frac{3\pi}{160} \frac{R}{d} \frac{k_B^4 (T_1^4 - T_2^4)}{\hbar^3 \sigma^2}. \quad (117)$$

Formula (117) coincides to the accuracy of a numerical coefficient of order unity with the result of [88].

For the contact of normal metals at $T_1 = 300$ K, $T_2 = 0$ K, $R/d = 30$, and $\sigma = 10^7$ $(\Omega\ \text{m})^{-1}$, Eq. (117) yields $\dot{Q} = -1.8 \times 10^{-14}$ W. In this case, as was shown in [88], a greater contribution to heating may come from the

relativistic correction, which is absent in (115). Note, however, that the additivity approximation used by the authors of [88] is insufficiently correct for metals, since it does not take into account the effects of screening of the electron gas (see Section 6.1 and Eq. (104)); therefore, the optimum choice of contacting materials with the purpose of obtaining maximum heating requires a more detailed analysis.

Qualitatively new effects are possible in the dynamic regime. We perform a simplified consideration for this case, assuming that the functions $\alpha''(\omega)$ and $\Delta''(\omega)$ are of resonant type: $\alpha''(\omega) = A\delta(\omega - \omega_0)$ and $\Delta''(\omega) = B\delta(\omega - \omega_s)$. After substitution of these functions into Eq. (114) and integration over all variables, we obtain (here $K_{0,1}(x)$ are the Bessel functions)

$$\dot{Q} = -\frac{4\omega_0\hbar}{\pi^2}AB\frac{(\omega_0-\omega_s)^2}{V^3}\left[K_0\left(\frac{2z_0|\omega_0-\omega_s|}{V}\right) + \frac{V}{2z_0|\omega_0-\omega_s|}K_1\left(\frac{2z_0|\omega_0-\omega_s|}{V}\right)\right] \times\left[\left(\exp\left(\frac{\omega_0\hbar}{k_BT_1}\right)-1\right)^{-1}-\left(\exp\left(\frac{\omega_s\hbar}{k_BT_2}\right)-1\right)^{-1}\right]. \quad (118)$$

It follows from Eq. (118) that in the limit of high temperatures the sign of $\dot{Q}$ depends on the difference $(T_1/\omega_0 - T_2/\omega_s)$; therefore, the particle (probe) can be heated even if it has a greater temperature as compared to the temperature of the surface; $\dot{Q}$ reaches a maximum (in the absolute value) at $V = 0.94z_0|\omega_0 - \omega_s|$. This condition may be considered as the condition for thermal resonance. Since the main contribution to the integral in wave vectors in (114) comes from the range of $k \sim 1/z_0$, this means that at corresponding velocities of the particles we cannot neglect nonlinear velocity-dependent effects. In the equal extent, this also refers to the calculation of the tangential force using Eq. (60).

It is important to emphasize that the nonlinear effects can manifest themselves in the dynamic regime of SPM (i.e., at velocities of 1–100 m/s) at distances of about 1 nm from the surface if the characteristic range of frequencies falls into the interval of 10^{10}–10^{12} s^{-1}. For faster particles, the nonlinear effects can be noticeable at greater distances (proportional to the velocity) from the surface.

In the conclusion of this section, we note that even a short consideration of FEMIs in the case of interaction of nanoparticles with surfaces reveals many new interesting features related to the change in the sign of the lateral force and the rate of heat exchange depending on the dielectric properties of the contacting materials, their temperatures, distances, and relative velocities.

7. DISCUSSION OF SOME RESULTS

7.1. Sliding Friction of Adsorbates (Experiments with a Quartz Microbalance)

The technique of the quartz crystal microbalance (QCM) in the investigations of nanostructural friction was first applied by Krim and Widom [89] (see also [3, 4]). A QCM represent a quartz plate oscillating due to the piezoelectric effect along the normal to the surface or along the surface with a quality factor of about 10^5. When a metallic film is applied onto the plate, the frequency of the oscillator changes, and this permits one to control the mass of the film with a high accuracy. When, additionally, atoms of a gas (air, inert gases) are adsorbed on the film, this changes the frequency and Q factor of the QCM, which makes it possible to study vibration modes of the adsorbates. The main experimental parameters are changes in the frequency and quality factor of the oscillator, which determine the decay time of the vibrational motion of the adsorbate τ. Thus, upon the adsorption of xenon on the Ag/Au(100) surface, the typical vibration-decay time is 2–3 ns.

At present, no common basis exists for a theoretical interpretation of these results. Thus, Krim *et al.* [90] believe that the main mechanism of damping is phonon, whereas the authors of [11, 41, 91, 92] assume that, in the systems of these types, the dominating mechanism is FEMI and use the theory based on Eq. (9) or its modifications. In related experiments, however, the distance d from the adsorbate to the surface has not been controlled and, since formula (9) has a very strong dependence on d, even small changes in d can lead to a sharp change in τ. In terms of our theory (with allowance for the difference in the temperatures of the particles and the surface), the dependence on the distance is far less strong ($\tau \sim d^5$); therefore, to match the theoretical value of the damping time with experimental data, the particle should be located at a somewhat greater distance from the surface. In our opinion, for a critical choice of a theoretical model, additional data characterizing the temperature and dielectric properties of contacting materials are required.

It is, e.g., known that a solidified xenon film is characterized by strong exciton absorption peaks (as well as peaks due to interband transitions) [93], and the presence of the surface leads to the appearance of surface excitons. On the other hand, in a solid film, new phonon modes arise, and its cooling with respect to the substrate may be accompanied by a positive contribution to the tangential force (see the first term in Eq. (61)). In particular, heat exchange via nonradiative modes can lead to freezing of the film. Similar effects can be responsible for the experimentally observed weak friction of solidified films of adsorbates that are incommensurate with the substrate [94], since any structural changes cause changes in the dielectric properties and, correspondingly, in the overlap integrals of the absorption spectra that determine friction forces of fluctuational nature.

An intriguing problem is also the interpretation of recent experiments [95] that show a sharp (approximately twofold) decrease in τ for nitrogen molecules adsorbed on a lead substrate upon a superconducting transition. The critical frequency corresponding to the energy gap of lead, $\omega_c = 4k_BT_c/\hbar = 3.8 \times 10^{12}$ s^{-1} falls into the range of phonon frequencies; therefore, if in the normal state of lead there is a contribution to the interaction with the adsorbate related to this range of electromagnetic spectrum, a sharp decrease in the FEMI is possible below the critical temperature. This assumption is favored by the experimental results on the frequency dependence of the density of electron states in lead $N(\omega)$ [96], which reveal a nonmonotonic character at $\omega > 2k_BT_c$.

7.2. Dissipative Forces in the Modulation Regime of Scanning Probe Microscopes

Measurements of forces of interaction between the probes of an SPM and the surfaces was performed in many works [97–102]. Thus, the conservative forces in the normal mode of SPM were studied in [97–99], while dissipative forces were investigated in [100–102]. Since the main subject of our work are dissipative FEMIs, we restrict ourselves to a brief discussion of the results of [100–102].

Gotsmann *et al.* [100] studied the interaction between a silicon probe and the surface of mica in the normal vibration mode (in vacuum, at $T = 300$ K) at the following parameters: the rigidity of the console $k = 40$ N/m, the radius of the nanoprobe $R = 20$ nm, the amplitude of vibrations of the oscillator $A = 32$ nm, the fundamental frequency $f = 296.6$ kHz, and $Q = 22815$. It follows from the measurements that the average power of energy dissipation is approximately 0.1 and 0.02 pW at the distances from the probe apex to the surface 0.1 and 0.5 nm, respectively. Thus, the dependence on the distance approximately follows the law $\bar{P} \sim d^{-1}$. At these parameters of the oscillator, the internal dissipation of energy upon free vibrations is $P^{(i)} = \pi kA^2 f/Q = 0.17$ pW. We have not yet obtained an exact expression for the friction force in the normal mode of probe vibrations; therefore, for estimates, we use formula (101) for the lateral motion with a doubled coefficient (which is valid for charges). In this case, at typical parameters for the silicon + mica pair ($\sigma = 0.01\ \Omega^{-1}$ m^{-1}, $\varepsilon = 6$, $\tau = 10^{-9}$ s) and $T = 300$ K, we obtain from (102a) that $F = -C\dot{z}/z^3(N)$ and $C = 6.6 \times 10^{-39}$ N m^2 s. Then, for the harmonic law of vibrations of the probe and the condition $d \ll A$ (d is the distance from the probe apex to the surface), we obtain for the average power of dissipation

$$\bar{P}(d) \approx \sqrt{\frac{A}{2}}\frac{\pi^2 f^2 C}{d^{3/2}}. \qquad (119)$$

Using (119), we find that $\bar{P}(0.1\text{ nm}) = 3.6 \times 10^{-4}$ pW and $\bar{P}(0.5\text{ nm}) = 3.2 \times 10^{-5}$ pW, which is three orders of magnitude smaller than in the experiment. For agreement with experimental data, we should accept $\tau = 10^{-6}$ s and decrease the conductivity of the probe by two–three orders of magnitude. For this type of contact, such a change in the parameters is problematic.

In the lateral vibration regime, we have

$$\bar{P}(d) = \frac{2\pi^2 A^2 f^2 C}{d^3}, \qquad (120)$$

instead of (119); therefore, at $d = 0.5$ nm we obtain $\bar{P} = 0.047$ pW and, consequently, dissipation due to FEMIs in this case should be more noticeable.

These estimates show that, for the normal vibration mode, more significant dissipative forces appear to exist, e.g., caused by the destruction of adhesion bonds [4, 103], which contribute significantly to damping even if no snap in contact occurs.

Experimental measurements of the forces were performed [101] for the Al (probe)–Au (surface) contacts under the following conditions: $f = 267.2$ kHz, $k = 40$ N/m, $R = 35$ nm, and $Q = 19050$. The damping observed is satisfactorily described by the dependence $F = -C\dot{z}/z^3$ at $C = 8 \times 10^{-35}$ N m^2 s. However, in this case as well, the theoretical estimates of dissipative forces of FEMI prove to be much lower than the experimental ones. Thus, using Eq. (108), we obtain $C = 10^{-49}$–10^{-48} N m^2 s. The calculation of C with allowance for the nonlocal contribution from the FDRS may yield a value that is greater by several orders of magnitude, but nevertheless it will be too small. Moreover, the values of the forces in this experiment turn out to be too great even for the contact regime of SPM.

Dorofeyev *et al.* [102] studied Brownian motion of an aluminum-coated nanoprobe near the surface of gold. Here also, very large values of dissipative forces were registered (even at distances of about 5 nm from the point of contact with the probe), which unlikely can be considered as dissipative forces of FEMI.

On the whole, we see that the available measurements of dissipative forces cannot be interpreted in terms of the theory of FEMI. The authors of [88] agree with this conclusion. We believe that, for the investigation of dissipative FEMIs, the use of the lateral vibration regime is more promising, in which case the probe moves at a constant controlled height from the surface.

7.3. Normal and Lateral Interaction of Neutral Beams of Particles with a Flat Surface

There is another way of experimentally studying FEMIs, which is related to the investigation of normal and lateral interactions with the surface upon motion of neutral atomic–molecular beams and clusters near the surface [104]. As follows from theory, the motion of

particles not only causes the appearance of dissipative FEMIs but also affects the conservative forces of attraction to the surface. Such forces were studied experimentally in [105–107]. The authors of [105, 106] found that in the case of atoms of alkali metals scattered by metallic cylinders, the vdW attractive forces are somewhat weaker than those predicted by the theory. In [107], on the contrary, a stronger dynamic attraction of semiconductor plates was revealed.

In this connection, we note that our recent calculations of the forces of dissipative FEMIs upon the interaction of beams of helium atoms with a metallic surface [104] need to be corrected, since they were based on the formula for the tangential force obtained in [16], which differed from Eq. (60) in the character of temperature dependence. To experimentally study the dissipative FEMIs (upon the passage of particles over the surface), it is more expedient to use neutral molecular and cluster beams, since the temperature and structural effects in this case are pronounced more strongly. For example, for hot molecules with a temperature of about 10000 K, the frequency range of effective interaction with the surface expands to 10^{15} s^{-1}; therefore, the magnitude of dissipative forces may be much higher. In addition, resonance effects are possible (see Section 6.4). The performance of such measurements is of fundamental importance for testing the theory.

8. CONCLUSION

The limited volume of the paper prevented the consideration of many important aspects of FEMIs, such as friction in 2D electron systems [109], the interaction of multipoles with a surface [110], structural effects of the surface [66, 69], etc. Nevertheless, we believe that the suggested nonrelativistic theory of FEMI can serve as a basis for understanding all basic physical processes in contacts of particles and nanoprobes with surfaces. In essence, the theory is based only on the Maxwell equations and the formalism of fluctuation–dissipation relations.

It is very important that all our formulas for conservative and dissipative forces coincide with those known from the literature for both the flat and cylindrical surfaces (in the nonrelativistic limit). For the interaction of neutral systems (atom–surface, nanoprobe–surface, surface–surface), our formulas not only lead in special cases to known results obtained by other authors [12–15, 49, 87, 88] but also predict new effects (see Eqs. (60) and (114)). Note that all these results directly follow from statistically averaged electrodynamic formulas for the power of the fluctuational electromagnetic field, as well as for the normal and tangential forces acting on moving particles (in full accordance with the spirit of the Lifshitz–Pitaevskiĭ theory).

In particular, we obtained the most general formula for the tangential force acting on a moving particle with allowance for the fact that its temperature differs from the temperature of the surface (see Eq. (60)), and the linear-in-velocity formula (8) that was first obtained in [13] found a strict substantiation without resorting to Eq. (2). For the first time, we obtained analogous results for cylindrical surfaces and formulas for the heating of moving particles.

The theory predicts the possibility of an acceleration of a moving particle in the field of surface excitations, as well as of the appearance of an "anomalous" flux of heat from a cold to a hot body. Physically, this is caused by the fact that the particles have natural frequencies, for which reason the energy exchange with the surface is by no means a trivial process, in contrast to the case of a charge and a dipole molecule, when the lateral force can only be retarding and the surface is always heated. The effect of spatial dispersion complicates the interaction picture even more, since the dispersion equations of surface excitations depend on the geometry of the contact zone and any structural changes in this zone dramatically affect the dielectric characteristics of the surfaces and forces of FEMI.

Unfortunately, no reliable experimental data are available at present that could permit us to unambiguously identify dissipative forces of FEMIs and test theoretical models. In this connection, the most promising methods, in our opinion, are those based on measurements of dissipative forces in the lateral vibration regime in a scanning probe microscope and on the passage of neutral beams near a smooth surface.

Among the most important theoretical problems that are of interest for the physics of FEMIs and can be solved in terms of our theory are the following: (1) the calculation of FEMIs upon the normal motion of a neutral particle toward the surface; (2) a more detailed investigation of the role of spatial dispersion and the near structure of electromagnetic fields near curved surfaces; (3) the investigation of the relation of electromagnetic and phonon mechanisms upon friction; and (4) the allowance for the effects of retardation and, more widely, the development of a consistent relativistic theory of sliding friction. The fundamentals of this theory were laid in our recent works [111]. In particular, relativistic generalizations of formulas (6), (60), and (114) have been obtained in these works.

At the final stage of preparing this paper for publication, we obtained the possibility of being acquainted with the last work of Volokitin and Persson [112], who kindly supplied us with a preprint of their paper. In that paper, the authors obtained a formula analogous to our formula (60) at equal temperatures of the particle and surface; however, the key identity (6), which is fundamentally necessary for the calculation of the force of friction and flux of heat between a moving particle and surface in the laboratory coordinate system is absent in both [112] and in their earlier paper [88]. Therefore, Volokitin and Persson have calculated the heat flux only at the zero relative velocity of the bodies and its relation

to the friction force was only noted as followed from the similar structure of the final equations.

REFERENCES

1. R. Nunez, P. M. Echenique, and R. H. Ritchie, J. Phys. C **13**, 4229 (1980).
2. P. M. Echenique, F. J. Garcia de Abajo, V. H. Ponce, and M. E. Uranga, Nucl. Instrum. Methods Phys. Res. B **96**, 583 (1995).
3. B. N. J. Persson, *Sliding Friction: Physical Principles and Applications* (Springer, Heidelberg, 1998).
4. G. V. Dedkov, Usp. Fiz. Nauk **170** (6), 543 (2000); Phys. Status Solidi A **179** (1), 2 (2000).
5. E. M. Lifshits, Zh. Éksp. Teor. Fiz. **29**, 94 (1955) [Sov. Phys. JETP **2**, 73 (1956)]; I. E. Dzyaloshinskii, E. M. Lifshitz, and L. P. Pitaevski, Adv. Phys. **10**, 165 (1961).
6. J. Mahanty and B. W. Ninham, *Dispersion Forces* (Academic, London, 1976).
7. Yu. S. Barash, *Van der Waals Forces* (Nauka, Moscow, 1988).
8. S. Weinberg, Rev. Mod. Phys. **61**, 1 (1989).
9. V. M. Mostepanenko and N. N. Trunov, *The Casimir Effect and Its Applications* (Clarendon, Oxford, 1997).
10. M. Kardar, Rev. Mod. Phys. **71**, 1233 (1999).
11. B. N. J. Persson and A. I. Volokitin, J. Chem. Phys. **103**, 8679 (1995).
12. J. B. Pendry, J. Phys.: Condens. Matter **9**, 10301 (1997).
13. M. S. Tomassone and A. Widom, Phys. Rev. B **56**, 4938 (1997).
14. A. I. Volokitin and B. N. J. Persson, Phys. Low-Dimens. Struct. **7** (8), 17 (1998).
15. A. I. Volokitin and B. N. J. Persson, J. Phys.: Condens. Matter **11**, 345 (1999).
16. G. V. Dedkov and A. A. Kyasov, Phys. Lett. A **259**, 38 (1999).
17. G. V. Dedkov and A. A. Kyasov, Pis'ma Zh. Tekh. Fiz. **25** (12), 10 (1999) [Tech. Phys. Lett. **25**, 466 (1999)].
18. G. V. Dedkov and A. A. Kyasov, Fiz. Tverd. Tela (St. Petersburg) **43** (1), 169 (2001) [Phys. Solid State **43**, 176 (2001)].
19. G. V. Dedkov and A. A. Kyasov, Fiz. Tverd. Tela (St. Petersburg) **43** (3), 536 (2001) [Phys. Solid State **43**, 556 (2001)].
20. G. V. Dedkov and A. A. Kyasov, Pis'ma Zh. Tekh. Fiz. **27** (8), 68 (2001) [Tech. Phys. Lett. **27**, 338 (2001)].
21. A. A. Kyasov and G. V. Dedkov, Surf. Sci. **463**, 11 (2000).
22. A. A. Kyasov and G. V. Dedkov, Fiz. Tverd. Tela (St. Petersburg) **43** (3), 554 (2001) [Phys. Solid State **43**, 574 (2001)].
23. L. S. Levitov, Europhys. Lett. **8**, 488 (1989).
24. V. G. Polevoĭ, Zh. Éksp. Teor. Fiz. **98**, 190 (1990) [Sov. Phys. JETP **71**, 1119 (1990)].
25. V. E. Mkrtchian, Phys. Lett. **207**, 299 (1995).
26. E. G. D'Agliano, W. Schaich, P. Kumar, and H. Suhl, in *Collective Properties of Physical Systems: Proceedings of the 24th Nobel Symposium*, Ed. by B. I. Lundqvist and S. Lundqvist (Academic, New York, 1973).
27. E. G. D'Agliano, P. Kumar, W. Schaich, and H. Suhl, Phys. Rev. B **11**, 2122 (1975).
28. W. L. Schaich, Solid State Commun. **15**, 357 (1975).
29. W. L. Schaich, Surf. Sci. **49**, 221 (1975).
30. W. Schaich, J. Chem. Phys. **60**, 1087 (1974).
31. J. M. Ziman, *Principles of the Theory of Solids* (Cambridge Univ. Press, Cambridge, 1972).
32. M. Sunjic, G. Toulouse, and A. A. Lucas, Solid State Commun. **11**, 1629 (1972).
33. R. Ray and G. D. Mahan, Phys. Lett. A **42**, 301 (1972).
34. J. Heinrichs, Phys. Rev. B **8**, 1346 (1973).
35. J. Harris and R. O. Jones, J. Phys. C **6**, 3585 (1973).
36. D. Chan and P. Richmond, Surf. Sci. **39**, 437 (1973).
37. G. D. Mahan, in *Collective Properties of Physical Systems: Proceedings of the 24th Nobel Symposium*, Ed. by B. I. Lundqvist and S. Lundqvist (Academic, New York, 1973), p. 164.
38. D. L. Mills, Phys. Rev. B **15**, 763 (1977).
39. G. Barton, Rep. Prog. Phys. **42**, 963 (1979).
40. B. N. J. Persson, Phys. Rev. B **44**, 3277 (1991).
41. A. Liebsch, Phys. Rev. B **55**, 13263 (1997).
42. F. Garcia-Moliner and F. Flores, *Introduction to the Theory of Solid Surfaces* (Cambridge Univ., Cambridge, 1979).
43. F. J. Garcia de Abajo and P. M. Echenique, Phys. Rev. B **46**, 2663 (1992).
44. R. H. Ritchie and A. L. Marusak, Surf. Sci. **4**, 234 (1966).
45. D. Wagner, Z. Naturforsch. A **21**, 634 (1966).
46. E. V. Teodorovich, in *Proceedings of the National USSR Conference on the Theory of Friction, Wear, Lubrication, Tashkent, 1975.*
47. E. V. Teodorovich, Proc. R. Soc. London, Ser. A **362**, 71 (1978).
48. J. Mahanty, J. Phys. B **13**, 4391 (1980).
49. W. L. Schaich and J. Harris, J. Phys. F **11**, 65 (1981).
50. G. V. Dedkov, Radiat. Eff. **103**, 157 (1987); Usp. Fiz. Nauk **165** (8), 919 (1995) [Phys. Usp. **38**, 877 (1995)].
51. J. A. Annett and P. M. Echenique, Phys. Rev. B **34**, 6853 (1986).
52. J. A. Annett and P. M. Echenique, Phys. Rev. B **36**, 8986 (1987).
53. I. A. Dorofeyev, H. Fuchs, and J. Jersch, Phys. Rev. B **64**, 35403 (2001).
54. A. A. Kyasov, in *Collection of Scientific Works of Institute of High Temperature Physics, Academy of Sciences of USSR*, Ed. by V. E. Fortov and E. A. Kuz'menkov (Inst. Fiz. Vys. Temp. Akad. Nauk SSSR, Moscow, 1991), p. 122.
55. A. A. Kyasov, Available from VINITI, No. 1407-B91 (1991).
56. A. A. Kyasov, Author's Abstract of Candidate's Dissertation (Nal'chik, 1993).
57. I. Dorofeyev, H. Fuchs, B. Gotsmann, and G. Wenning, Phys. Rev. B **60**, 9069 (1999).
58. G. V. Dedkov and A. A. Kyasov, Pis'ma Zh. Tekh. Fiz. **28** (8), 79 (2002) [Tech. Phys. Lett. **28**, 346 (2002)].

59. B. N. Bolotovskiĭ and S. N. Stolyarov, Usp. Fiz. Nauk **114**, 569 (1973) [Sov. Phys. Usp. **17**, 875 (1973)].
60. B. N. J. Persson, private communication (2000).
61. D. M. Newns, Phys. Rev. B **1**, 3304 (1970).
62. J. I. Gersten and N. Tzoar, Phys. Rev. B **8**, 5671 (1993).
63. V. Celli, in *Surface Science: Lectures Presented at an International Course, Trieste, 1974* (IAEA, Vienna, 1975), p. 393.
64. T. L. Ferrell, P. M. Echenique, and R. H. Ritchie, Solid State Commun. **32**, 419 (1979).
65. J. Lindhard and K. Dan, Vidensk. Selsk. Mat.-Fys. Medd. **28**, 8 (1954).
66. G. V. Dedkov and A. A. Kyasov, submitted to Phys. Rep.
67. P. J. Feibelman, Prog. Surf. Sci. **12**, 287 (1982).
68. B. N. J. Persson and E. Zaremba, Phys. Rev. B **31**, 1863 (1985).
69. B. N. J. Persson and Zh. Zhang, Phys. Rev. B **57**, 7327 (1998).
70. R. Garcia-Molina, A. Gras-Marti, A. Howie, and R. Ritchie, J. Phys. C **18**, 5335 (1985).
71. F. Sols, P. Mirango, and F. Flores, Surf. Sci. **161**, 33 (1985).
72. J. S. Shier, Am. J. Phys. **36**, 245 (1968).
73. Yu. S. Barash and V. L. Ginzburg, Usp. Fiz. Nauk **143** (3), 345 (1984) [Sov. Phys. Usp. **27**, 467 (1984)].
74. L. D. Landau and E. M. Lifshitz, *Course of Theoretical Physics*, Vol. 5: *Statistical Physics* (Nauka, Moscow, 1976; Pergamon, Oxford, 1980), Part 1.
75. I. S. Gradshtein and I. M. Ryzhik, *Table of Integrals, Series, and Products* (Nauka, Moscow, 1962; Academic, New York, 1980).
76. G. V. Dedkov, Nucl. Instrum. Methods Phys. Res. B **143**, 584 (1998).
77. G. V. Dedkov and B. S. Karamurzov, Surf. Coat. Technol. **128–129**, 51 (2000).
78. D. Langbein, Phys. Kondens. Mater. **15**, 61 (1972).
79. M. Schmeits and A. A. Lucas, Surf. Sci. **64**, 176 (1977).
80. M. Schmeits and A. A. Lucas, Surf. Sci. **14** (1), 1 (1983).
81. A. A. Kyasov and G. V. Dedkov, Surf. Sci. **491**, 124 (2001).
82. V. M. Nabutovskiĭ, V. R. Belosludov, and A. M. Korotkikh, Zh. Éksp. Teor. Fiz. **77** (2), 700 (1979) [Sov. Phys. JETP **50**, 352 (1979)].
83. P. Johansson and A. Apell, Phys. Rev. B **56**, 4159 (1997).
84. Yu. N. Moiseev, V. M. Mostepanenko, and V. I. Panov, Phys. Lett. A **132**, 354 (1988).
85. M. B. Smirnov and V. P. Krainov, Laser Phys. **9**, 943 (1999).
86. I. A. Dorofeyev, J. Phys. D **31**, 600 (1998).
87. J. B. Pendry, J. Phys.: Condens. Matter **11**, 6621 (1999).
88. A. I. Volokitin and B. N. J. Persson, Phys. Rev. B **63**, 205404 (2001).
89. J. Krim and A. Widom, Phys. Rev. B **38**, 12184 (1988).
90. M. S. Tomassone, J. B. Sokoloff, A. Widom, and J. Krim, Phys. Rev. Lett. **79** (24), 4798 (1997).
91. B. N. J. Persson and A. Nitzan, Surf. Sci. **367**, 261 (1996).
92. J. B. Sokoloff, Phys. Rev. B **52**, 5318 (1995).
93. G. Baldini, Phys. Rev. **128**, 1562 (1962).
94. G. M. McClelland and J. M. Glosli, in *Fundamentals of Friction: Macroscopic and Microscopic Processes*, Ed. by I. L. Singer and H. M. Pollock (Kluwer, Dordrecht, 1992), p. 405.
95. A. Dayo, W. Alnasrallah, and J. Krim, Phys. Rev. Lett. **80**, 1690 (1998).
96. V. M. Svistunov, M. A. Belogolovskiĭ, and A. I. Khachapurov, Usp. Fiz. Nauk **163** (1), 61 (1993) [Phys. Usp. **36**, 65 (1993)].
97. F. Giessibl, Phys. Rev. B **56**, 16010 (1997).
98. H. Holscher, W. Allers, U. D. Schwarz, and R. Wiesendanger, Phys. Rev. Lett. **83** (23), 4780 (1999).
99. B. Gotsmann, B. Anczykowski, C. Seidel, and H. Fuchs, Appl. Surf. Sci. **140**, 314 (1999).
100. B. Gotsmann, C. Seidel, B. Anczykowski, and H. Fuchs, Phys. Rev. B **60**, 11051 (1999).
101. B. Gotsmann and H. Fuchs, Phys. Rev. Lett. **86**, 2597 (2001).
102. I. Dorofeyev, H. Fuchs, G. Wenning, and B. Gotsmann, Phys. Rev. Lett. **83**, 2402 (1999).
103. G. V. Dedkov, Wear **232** (2), 145 (1999); Mater. Lett. **38**, 360 (1999).
104. G. V. Dedkov and A. A. Kyasov, Nucl. Instrum. Methods Phys. Res. B **183**, 241 (2001).
105. A. Shih and V. A. Parsegian, Phys. Rev. A **12**, 835 (1975).
106. J. Mehl and W. L. Schaich, Phys. Rev. A **16**, 921 (1977).
107. W. Arnold, S. Hunklinger, and K. Dransfeld, Phys. Rev. B **19**, 6049 (1979).
108. B. N. J. Persson and A. I. Volokitin, Phys. Rev. Lett. **84**, 3504 (2000).
109. T. J. Gramila, J. P. Eisenstein, A. H. MacDonald, *et al.*, Phys. Rev. Lett. **66**, 1216 (1991); Phys. Rev. B **47**, 12957 (1993); Physica B (Amsterdam) **197**, 442 (1994).
110. A. A. Kyasov and G. V. Dedkov, Fiz. Tverd. Tela (St. Petersburg) **44** (9), 1700 (2002) [Phys. Solid State **44** (9), 1779 (2002)].
111. A. A. Kyasov and G. V. Dedkov, Pis'ma Zh. Tekh. Fiz. (in press) [Tech. Phys. Lett. (in press)]; Nucl. Instrum. Methods Phys. Res. (in press).
112. A. I. Volokitin and B. N. J. Persson, Phys. Rev. B **65**, 115419 (2002).

Translated by S. Gorin

Physics of the Solid State, Vol. 44, No. 10, 2002, pp. 1833–1839. Translated from Fizika Tverdogo Tela, Vol. 44, No. 10, 2002, pp. 1752–1757.

METALS AND SUPERCONDUCTORS

Band Structure of ZrB_2, VB_2, NbB_2, and TaB_2 Hexagonal Diborides: Comparison with Superconducting MgB_2

I. R. Shein and A. L. Ivanovskiĭ

Institute of Solid-State Chemistry, Ural Division, Russian Academy of Sciences, Pervomaĭskaya ul. 91, Yekaterinburg, 620219 Russia

e-mail: irshein@mail.ur.ru

Received September 26, 2001

Abstract—The band structure and Fermi surface parameters of ZrB_2, VB_2, NbB_2, and TaB_2 hexagonal diborides are considered in the framework of the self-consistent full-potential LMTO method in comparison with the relevant parameters of a MgB_2 isostructural superconductor. The factors responsible for the superconducting properties of AlB_2-like diborides are analyzed, and the results obtained are compared with previous calculations and available experimental data. *© 2002 MAIK "Nauka/Interperiodica".*

1. INTRODUCTION

The recent discovery of the critical transition ($T_c \approx$ 40 K) in magnesium diboride (MgB_2) [1] and preparation of a series of promising superconducting MgB_2-based materials (ceramics, films, long wires, and tapes) [2] have stimulated an active search for new superconductors among the related compounds having structural or chemical elements in common with MgB_2.

The group of hexagonal (AlB_2-like) diborides that are isostructural to MgB_2 are considered to be the first superconductor candidates. Detailed investigations of the band structure and the pairing mechanism in MgB_2 [2–7] have demonstrated that the most promising superconductor candidates are diborides of Group I and II metals, for example, metastable CaB_2 [6], LiB_2, and ZnB_2 [7]. Moreover, Kwon *et al.* [8] predicted the possible critical transition ($T_c > 50$ K) in AgB_2 and AuB_2.

It is highly unlikely that new superconductors (with $T_c > 1$ K) will be revealed among the AlB_2-like *d* metal diborides (VB_2) [2–7]. In 1970, Cooper *et al.* [9] published the first data on the superconductivity of NbB_2 ($T_c = 3.9$ K). However, these data were not confirmed by systematic investigations of the superconductor properties for a series of MeB_2 diborides (*Me* = Ti, Zr, Hf, V, Nb, Ta, and Cr) [10]. According to [10], MeB_2 diborides are characterized by $T_c < 0.7$ K.

The sufficiently high temperatures T_c reported in recent publications [11–13] for ZrB_2 (5.5 K [11]), TaB_2 (9.5 K [12]), and NbB_2 (5.2 K [13]) appeared to be quite unexpected. It is worth noting that, although different research groups have investigated identical series of diborides (for example, TiB_2, ZrB_2, HfB_2, VB_2, NbB_2, and TaB_2 [12] and ZrB_2, NbB_2, and TaB_2 [11]), each group discovered its own superconductor (ZrB_2 [11] or TaB_2 [12]), whereas all the other MeB_2 phases were considered to be nonsuperconducting.

The results obtained by Kaczorowski *et al.* [12] prompted Rosner *et al.* [14] to investigate in detail the temperature dependences of the magnetic susceptibility and electrical conductivity of TaB_2. It was revealed that the superconducting transition in TaB_2 is not observed down to $T \sim 1.5$ K. The difference in the superconducting properties of MgB_2 and TaB_2 was discussed in [14, 15] on the basis of the band structure calculations. It was noted that these properties differ significantly due to strong effects of hybridization of the Ta 5*d* and B 2*p* states in TaB_2 and a weak (compared to that in MgB_2) electron interaction with the E_{2g} mode of the phonon spectrum [14]. Singh [15] explained the drastic decrease in T_c for TaB_2 (and the absence of superconductivity in VB_2) in terms of the considerable decrease in the contributions of the B 2*p* states to the density of states $N(E_F)$ at the Fermi level: MgB_2 (0.494) > TaB_2 (0.114) > VB_2 (0.043 states/eV). When analyzing fine features in the soft x-ray B *K* emission and absorption spectra of MgB_2, NbB_2, and TaB_2 compounds, Nakamura *et al.* [16] noted the fundamental difference in structure of their near-Fermi edges with dominant contributions of the B $2p_\sigma$ (MgB_2) or B $2p_\pi$ states (NbB_2, TaB_2). To the best of our knowledge, no work has reproduced the results obtained in [11].

As was shown in [2–7], the superconductivity of MgB_2 and related borides is adequately described in the framework of the electron–phonon interaction theory. Therefore, the specific features of the electronic spectrum (primarily, the composition and the structure of the near-Fermi bands) are important factors responsible for superconductivity.

This paper reports on the results of a detailed analysis of the band structure of Zr, V, Nb, and Ta diborides

Table 1. Lattice parameters (Å) of Mg, Zr, V, Nb, and Ta diborides according to our FLMTO calculations in comparison with the available experimental and calculated data

Diboride	Our data			Data of other authors		
	a	*c*	*c*/*a*	*a*	*c*	*c*/*a*
MgB_2	3.04869	3.46637	1.1370	3.083	3.521	1.142 [23]
ZrB_2	3.16932	3.53126	1.1142	3.170	3.532	1.114 [11]
				3.165	3.547	1.12 [23]
VB_2	3.00678	3.04768	1.0136	2.997	3.056	1.0196 [15]
				2.998	3.057	1.02 [23]
NbB_2	3.18141	3.35693	1.0550	3.116	3.264	1.06 [23]
				3.082	3.243	1.0522 [12]
TaB_2	3.16421	3.32337	1.0503	3.098	3.224	1.0407 [14]
				3.083	3.244	1.0522 [15]
				3.097	3.225	1.041 [23]

in comparison with the available data on superconducting MgB_2.

2. OBJECTS OF INVESTIGATION AND CALCULATION TECHNIQUE

It is known that the aforementioned diborides are isostructural (AlB_2 type, space group $P6/mmm$) and their crystal lattices are formed by alternating hexagonal monolayers of the metal and graphitelike boron networks [17]. The unit cell contains three atoms: one metal atom and two boron atoms. The fundamental difference between these atoms is associated with the type of metal sublattice involved; i.e., this difference stems from the electronic configurations of the metal atoms ($3s^2 3p^0$ for Mg; $5s^2 4d^2$ for Zr; and $(n+1)s^2 nd^3$ for V, Nb, and Ta, where $n = 3$, 4, and 5, respectively), which are responsible for both the increase in the electron concentration, namely, MgB_2 (8 electrons per unit cell) < ZrB_2 (10 electrons per unit cell) < VB_2, NbB_2, and TaB_2 (11 electrons per unit cell), and the change in the interatomic bonds (see [2, 18, 19]).

The band structure calculations for MeB_2 were performed in the framework of the local-electron-density (LDA) functional theory using the self-consistent full-potential linearized muffin-tin orbital (FLMTO) method with allowance made for relativistic effects and spin–orbit interactions [20, 21] with the exchange–correlation potential [22]. In our calculations, we obtained the equilibrium unit-cell parameters from the condition of the minimum total energy of the system. The calculated parameters of MeB_2 are listed in Table 1.

3. RESULTS AND DISCUSSION

3.1. MgB_2. Analysis of the data presented in Figs. 1 and 2 demonstrates that the specific features of the band structure of superconducting MgB_2 are determined by the B $2p$ states involved in the formation of four $\sigma(2p_{x,y})$ and two $\pi(p_z)$ energy bands. The B $2p_z$ states are oriented normally to the boron atom networks and form weak interlayer π bonds. The B $2p_{x,y}$ bands are of the quasi-two-dimensional ($2D$) type and form plane regions aligned along the Γ–A direction of the Brillouin zone. The small variance of the σ bands also suggests weak interactions between the Mg–B layers. Two B $2p_{x,y}$ bands cross E_F and significantly contribute to the density of states at the Fermi level. It should be noted that these bands are responsible for the metal-like properties of MgB_2 (Table 2). An important feature of MgB_2 is the occurrence of the B $2p_{x,y}$ hole states: in the Γ–A direction, these states reside above E_F and form hole-type cylindrical elements of the Fermi surface (Fig. 1).

Thus, the band spectrum of MgB_2 is characterized by the following elements, which are critical with respect to its superconducting properties and to the effects of intralayer and interlayer interactions (see also [2–7]): (1) the position of the $\sigma(p_{x,y})$ bands with respect to E_F (the occurrence of hole states), (2) the variance of these bands in the Γ–A direction [$\Delta E^{\sigma}(\Gamma$–$A)$ is determined by the degree of interaction between the metal–boron layers], and (3) the magnitude and orbital composition of the density of states $N(E_F)$ to which the B σ states of graphitelike boron networks make a dominant contribution. In this context, we consider the band structure of Zn, V, Nb, and Ta diborides. It should be noted that, in the diboride series, the most evident consequence of changes in the composition of the metal sublattice is an increase in the electron concentration with sequential filling of the energy bands. In this case, the Fermi level for ZrB_2 is located in the pseudogap between the completely occupied bonding states and unoccupied antibonding states, which is responsible for both the highest stability of ZrB_2 (and isoelectronic and isostructural TiB_2 and HfB_2) in the series of AlB_2-like

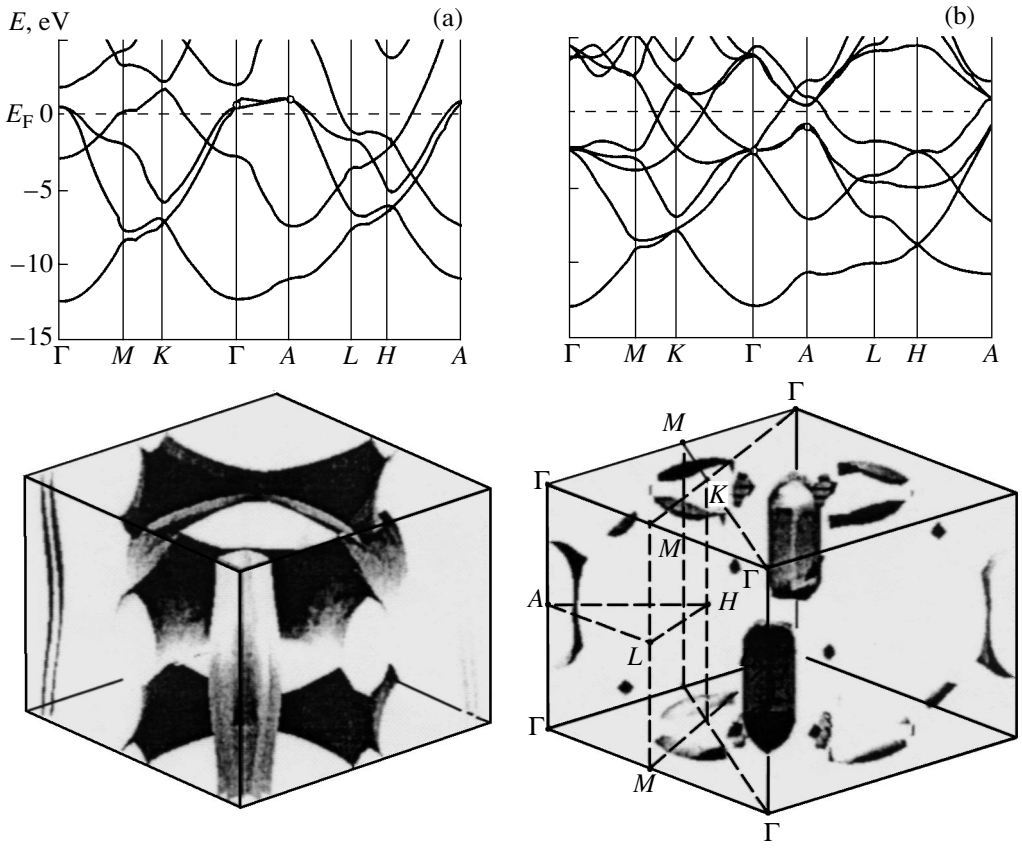

Fig. 1. Energy bands and Fermi surfaces of (a) MgB_2 and (b) ZrB_2.

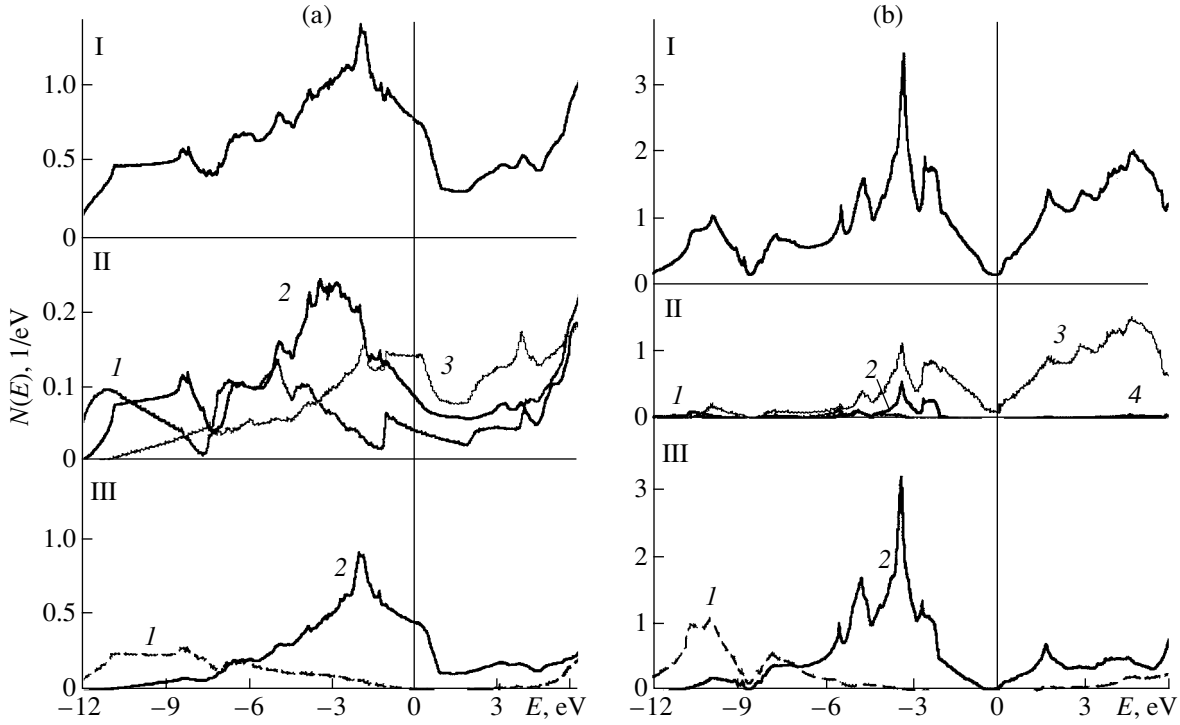

Fig. 2. (I) Total and (II, III) local densities of valence (*1*) *s* states, (*2*) *p* states, (*3*) *d* states, and (*4*) *f* states of (II) metal and (III) boron sublattices of (a) MgB_2 and (b) ZrB_2.

Table 2. Variance of the σ (B $p_{x,y}$) bands in the Γ–*A* direction and orbital contributions to the density of states at the Fermi level (states/eV per cell) of MeB_2 phases

Phase	$\Delta E^{\sigma}(\Gamma$–$A)$, eV	Density of states at E_F						
		total	*Me s*	*Me p*	*Me d*	*Me f*	B *s*	B *p*
MgB_2	0.72	0.719	0.040	0.083	0.138	–	0.007	0.448
ZrB_2	1.73	0.163	0.001	0.002	0.130	–	0.00019	0.030
VB_2	2.69	1.379	0.024	0.013	1.255	–	0.002	0.085
NbB_2	2.49	1.074	0.037	0.017	0.818	–	0.012	0.190
TaB_2	2.61	0.910	0.003	0.016	0.664	0.038	0.011	0.178

phases and their extreme thermomechanical characteristics [23]. This inference was confirmed by recent FLMTO calculations of the cohesion energy for a series of MeB_2 phases (where *Me* are 3*d*, 4*d*, or 5*d* metals) [18, 19].

3.2. ZrB_2. As follows from the data presented in Table 2 and Figs. 1 and 2, the near-Fermi edges of the electronic spectra of ZrB_2 and MgB_2 differ radically. The following features are characteristic of ZrB_2: (1) the boron $\sigma(p_{x,y})$ bands are located below E_F (at –1.1 eV, i.e., at the *A* point of the Brillouin zone), and the relevant hole states are absent; (2) the σ bands are characterized by a considerable variance in the Γ–*A* direction [$\Delta E^{\sigma}(\Gamma$–$A) = 1.73$ eV] and cease to be of the 2*D* type due to the formation of strong covalent *d*–*p* bonds between the metal–boron layers, which involve only the partially occupied $\pi(p_z)$ bands; and (3) compared to MgB_2, the density of states $N(E_F)$ for ZrB_2 decreases drastically (from 0.719 to 0.163 states/eV); in this case, the Zr 4*d* states make the largest contribution (~80%) to the density of states $N(E_F)$, whereas the contribution of the boron states is considerably smaller (~18%). A comparison of the Fermi surfaces of MgB_2 and ZrB_2 demonstrates a pronounced change in the type of near-Fermi states (2*D* ⟶ 3*D*) (Fig. 1). It is seen that the Fermi surface of ZrB_2 consists of three types of figures, which are associated with mixed Zr 4*d* and B 5*p*–B *p* states: (i) the 3*D* figure of rotation around the straight line along the Γ–*A* direction with hole conduction, (ii) the 3*D* figure near the midpoint of the *M*–*K* segment with electron conduction, and (iii) small segments of the 3*D* type with electron conduction.

3.3. VB_2, NbB_2, and TaB_2. The energy bands, Fermi surfaces, and densities of states of these isoelectronic and isostructural diborides are shown in Figs. 3 and 4. Some parameters of the electronic structure are given in Tables 2 and 3. The aforementioned differences between ZrB_2 and MgB_2 [such as the population of the

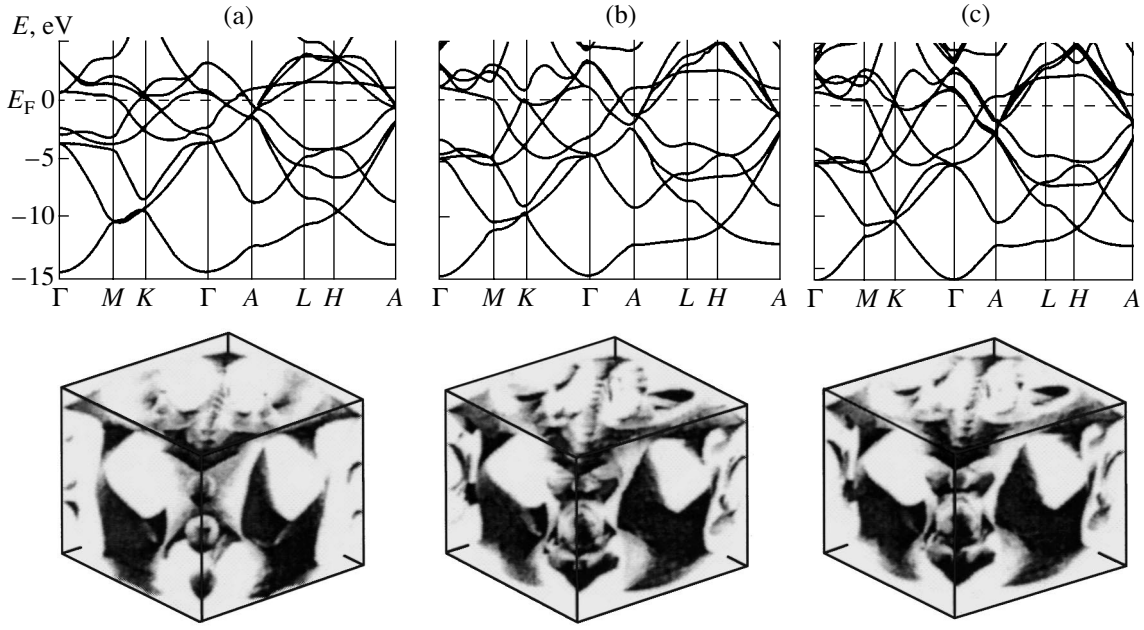

Fig. 3. Energy bands and Fermi surfaces of (a) VB_2, (b) NbB_2, and (c) TaB_2.

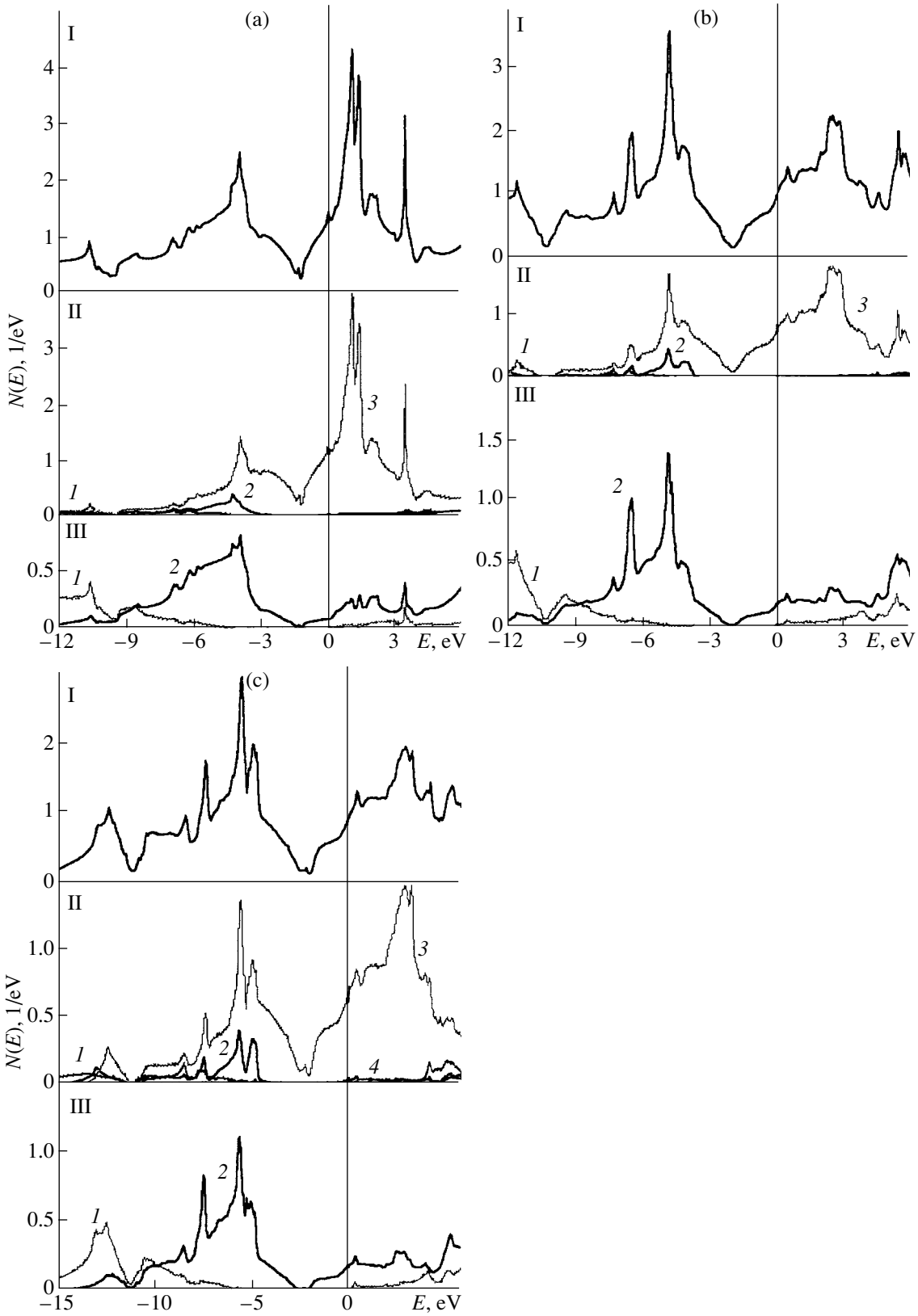

Fig. 4. (I) Total and (II, III) local densities of valence (*1*) *s* states, (*2*) *p* states, (*3*) *d* states, and (*4*) *f* states of (II) metal and (III) boron sublattices of (a) VB_2, (b) NbB_2, and (c) TaB_2.

Table 3. Densities of states at the Fermi level (states/eV) of Mg, Ta, and V diborides according to our FLMTO calculations in comparison with the data taken from [14, 15]

Phase	$N(E_F)$		
	our data	FP [15]	FPLO [14]
MgB_2	0.719	0.691	0.71
B 2*p*	0.448	0.494	
TaB_2	0.910	0.966	0.91
Ta 5*d*	0.664	0.647	
B 2*p*	0.178	0.114	
VB_2	1.379	1.359	
V 3*d*	1.255	1.235	
B 2*p*	0.085	0.043	

Note: The total density of states and partial contributions of the *Me d* and B 2*p* states are given.

$\sigma(p_{x,y})$ bands, the decrease in the contributions of the B 2*p* states to the density of states $N(E_F)$, and the $2D \longrightarrow 3D$ crossover of the type of near-Fermi states in $N(E_F)$] are also characteristic of VB_2, NbB_2, and TaB_2. Moreover, unlike ZrB_2, these diborides have common features: (1) a partial population of the antibonding *d* band, which provides the metallic type of conduction; (2) a considerable increase in the density of states $N(E_F)$; and (3) an increase in the population of $\pi(p_z)$ bands. The Fermi surface can undergo a characteristic transformation. For example, the Fermi surface of TaB_2 (Fig. 3) contains double nonintersecting (internal and external) electron-type spheroids of rotation around the *A* point which are determined by the 3*D* B 2*p* and Ta $5d_{xz,yz}$ states, respectively. The B $\sigma(p_{x,y})$ bonding bands are located below E_F (for VB_2, NbB_2, and TaB_2, the energies at the *A* point of the Brillouin zone are equal to –1.3, –2.5, and –2.6 eV, respectively) and, as in the case of ZrB_2, exhibit a considerable energy variance $\Delta E^{\sigma}(\Gamma\text{–}A)$, which is maximum for VB_2 (Table 2).

In the isoelectronic series $VB_2 \longrightarrow NbB_2 \longrightarrow TaB_2$, the density of states $N(E_F)$ decreases gradually and its largest value (for VB_2) is associated with the contribution of the near-Fermi quasi-flat vanadium $3d_{xz,yz}$ band in the Γ–*M* direction. By contrast, the contribution of B 2*p* states of the antibonding σ and π bands to the density of states $N(E_F)$ in this series changes nonmonotonically: it reaches a maximum (0.190 states/eV) for NbB_2 but remains considerably smaller than that for MgB_2 (0.448 states/eV). The high density of B 2*p* states in the vicinity of E_F for NbB_2 (as compared to TaB_2) has been confirmed by spectroscopic measurements [16].

4. CONCLUSIONS

Thus, the analysis of the band structure and Fermi surface parameters of *d* metal (Zr, V, Nb, Ta) isostructural diborides has revealed fundamental differences between the aforementioned compounds and MgB_2. These differences are as follows: (1) population of the $p_{x,y}$ bonding bands and the absence of the σ hole states, (2) enhancement of the covalent interactions between boron and metal layers (due to hybridization of the B 2*p*–*Me d* states) and loss of the quasi-two-dimensional type by the energy bands, and (3) changes in the magnitudes and orbital composition of the density of states $N(E_F)$ when the *d* valence states of the metals become predominant. The last feature is characteristic of low-temperature superconductors, for example, metal-like compounds of these *d* elements with carbon, nitrogen, and silicon (NbN, V_3Si, etc.), whose temperatures T_c correlate with the densities of states $N(E_F)$ [24]. In this case, reasoning from the results obtained, we can infer that low-temperature superconductivity is more probable in V, Nb, and Ta diborides; among these compounds, the highest temperature T_c should be expected for VB_2. Under the assumption (by analogy with MgB_2 [2–7]) that the near-Fermi density of B 2*p* states is the main electronic factor responsible for the superconducting properties of MeB_2 diborides, NbB_2 should possess the highest temperature of the critical transition. Note that, according to the pairing model proposed earlier in [25, 26], the population of not only the σ bands but also the π bands of boron must be taken into consideration. In any case, the superconducting transition in ZrB_2 is less probable and the results obtained in [11] need revision.

REFERENCES

1. J. Nagamatsu, N. Nakagawa, T. Muranaka, *et al.*, Nature **410**, 63 (2001).
2. A. L. Ivanovskiĭ, Usp. Khim. **70** (9), 811 (2001).
3. J. Kortus, I. I. Mazin, K. D. Belaschenko, *et al.*, Phys. Rev. Lett. **86** (20), 4656 (2001).
4. J. M. An and W. E. Pickett, Phys. Rev. Lett. **86** (19), 4366 (2001).
5. N. I. Medvedeva, A. L. Ivanovskii, J. E. Medvedeva, and A. J. Freeman, Phys. Rev. B **64**, 020502 (2001).
6. K. D. Belashchenko, M. van Schilfgaarde, and V. A. Antropov, cond-mat/0102290 (2001).
7. V. P. Antropov, K. D. Belashchenko, M. van Schilfgaarde, and S. N. Rashkeev, cond-mat/0107123 (2001).
8. S. K. Kwon, S. J. Youn, K. S. Kim, and B. I. Min, cond-mat/0106483 (2001).
9. A. S. Cooper, E. Corenzest, L. D. Longinotti, *et al.*, Proc. Natl. Acad. Sci. USA **67** (4), 313 (1970).
10. L. Leyarovska and E. Leyarovski, J. Less-Common Met. **67** (3), 249 (1979).
11. V. A. Gasparov, N. S. Sidorov, I. L. Zver'kova, and M. P. Kulakov, Pis'ma Zh. Éksp. Teor. Fiz. **73** (10), 601 (2001) [JETP Lett. **73**, 532 (2001)].

12. D. Kaczorowski, A. J. Zaleski, O. J. Zogal, and J. Klamut, cond-mat/0103571 (2001).
13. J. Akimitsu, in *Abstracts of 2001 Annual Meeting of Physical Society of Japan, 2001*, Vol. 3 (4), p. 533.
14. H. Rosner, W. E. Pickett, S.-L. Drechsler, *et al.*, cond-mat/0106092 (2001).
15. P. P. Singh, cond-mat/0104580 (2001).
16. J. Nakamura, N. Yamada, K. Kuroki, *et al.*, cond-mat/0108215 (2001).
17. Yu. B. Kuz'ma, *Crystal Chemistry of Borides* (Vishcha Shkola, L'vov, 1983).
18. A. L. Ivanovskiĭ, N. I. Medvedeva, G. P. Shveĭkin, and Yu. E. Medvedeva, Metallofiz. Noveĭshie Tekhnol. **20** (1), 41 (1998).
19. A. L. Ivanovskiĭ, N. I. Medvedeva, and Yu. E. Medvedeva, Metallofiz. Noveĭshie Tekhnol. **21** (1), 19 (1999).
20. M. Methfessel, C. Rodriquez, and O. K. Andersen, Phys. Rev. B **40** (3), 2009 (1989).
21. S. Y. Savrasov, Phys. Rev. B **54** (23), 16470 (1996).
22. J. P. Perdew and Y. Wang, Phys. Rev. B **45** (23), 13244 (1992).
23. G. V. Samsonov and I. M. Vinitskiĭ, *Refractory Compounds* (Metallurgiya, Moscow, 1976).
24. S. V. Vonsovskiĭ, Yu. A. Izyumov, and É. Z. Kurmaev, *Superconductivity of Transition Metals, Their Alloys and Compounds* (Nauka, Moscow, 1977).
25. M. Imada, cond-mat/0103006 (2001).
26. K. Furukawa, cond-mat/0103184 (2001).

Translated by N. Korovin

Physics of the Solid State, Vol. 44, No. 10, 2002, pp. 1840–1844. Translated from Fizika Tverdogo Tela, Vol. 44, No. 10, 2002, pp. 1758–1761.

METALS AND SUPERCONDUCTORS

Effect of Ion Irradiation on the Upper Critical Magnetic Field in Electronic and Hole *d*-Wave Superconductors

N. P. Shabanova, S. I. Krasnosvobodtsev, A. V. Varlashkin, and A. I. Golovashkin

Lebedev Physical Institute, Russian Academy of Sciences, Leninskiĭ pr. 53, Moscow, 119991 Russia

e-mail: varlash@sci.lebedev.ru

Received November 13, 2001

Abstract—The effect of ion irradiation on the upper critical magnetic field H_{c2} in electronic and hole high-temperature superconductors is studied. It is shown that the variation of H_{c2} may be connected with the *d*-wave symmetry of the order parameter. © *2002 MAIK "Nauka/Interperiodica".*

1. INTRODUCTION

Studies of various groups of high-temperature superconductors (HTSC) subjected to ion irradiation have revealed an anomalous character of variation of the upper critical magnetic field with increasing radiation defect concentration [1, 2]. The classical growth of H_{c2}, which is usually caused by electron scattering from radiation-induced defects, was not observed. Attempts to noticeably increase H_{c2} even by irradiating high-quality epitaxial films to doses that did not change in the critical temperature with increasing electrical resistivity were unsuccessful.

Studies of conventional superconductors featuring the phonon mechanism have shown that scattering from defects plays a dominant role in the variation of the upper critical field in the cases where irradiation does not produce noticeable changes in the electronic structure. This situation can be exemplified using the NbC superconducting compound [3, 4]. In other cases, for instance, in Nb_3Sn, where the electronic characteristics undergo a strong variation, it is this variation that determines the behavior of H_{c2} under irradiation [5].

This publication reports on a study of the effect of radiation defects on the variation of electronic characteristics and conduction-electron scattering in electronic and hole cuprate HTSCs, as well as of the part that these variations play in the anomalous behavior of H_{c2}.

2. EXPERIMENT

We studied *c*-oriented epitaxial films of $YBa_2Cu_3O_{7-\delta}$ (YBCO), $HoBa_2Cu_3O_{7-\delta}$ (HBCO), and $Nd_{2-x}Ce_xCuO_{4-\delta}$ (NCCO) prepared *in situ* by two-beam laser ablation [6, 7]. The films were irradiated by energetic helium ions at room temperature and at T = 77 K [8]. We measured temperature dependences of the electrical resistivity in a normal state and investigated the resistive superconducting transitions in a dc magnetic field oriented perpendicular to the film surface. The temperature dependence of the upper critical field $H_{c2}(T)$ was determined from the shift of the resistive transition.

3. RESULTS AND DISCUSSION

Figure 1 shows the superconducting resistive transitions in an NCCO epitaxial film observed in a magnetic field before and after irradiation of the film to a low helium ion dose. We see that although the electrical resistivity ρ of the material increased almost twofold as a result of the irradiation, the temperature dependence of H_{c2} virtually did not change. Irradiation to higher doses changed the slope $-dH_{c2}/dT$ of the temperature dependence of the upper critical magnetic field only

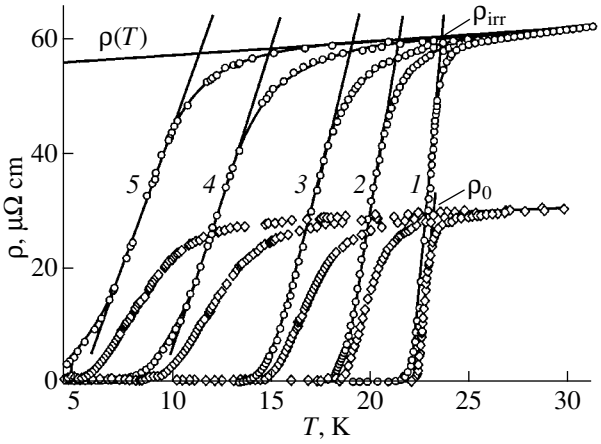

Fig. 1. Superconducting transitions in an epitaxial NCCO film in a magnetic field before and after irradiation by energetic He^+ ions to a dose of 1×10^{13} cm^{-2}. Curves *1*–*5* were obtained in magnetic fields 0, 5, 10, 20, and 30 kOe, respectively. Determination of the electrical resistivity in a normal state near T_c of the original (ρ_0) and irradiated (ρ_{irr}) samples is shown.

1063-7834/02/4410-1840$22.00

weakly even when the critical temperature T_c decreased strongly.

The broadening of the superconducting transition in the YBCO and HCCO films in a magnetic field was stronger [5]. Under irradiation, the slope $-dH_{c2}/dT$ decreased approximately proportional to the critical temperature.

The variation in H_{c2} of the cuprate HTSCs observed to occur under irradiation was found to be very similar to that of the part of H_{c2} of conventional superconductors, which is commonly called the clean-base term (Fig. 2).

In the absence of scattering, the slope $(-dH_{c2}/dT)$ corresponds to the clean-base term determined by the quantity $T_c/\langle v^2\rangle$, where $\langle v^2\rangle$ is the Fermi surface-averaged square of the Fermi velocity [9, 10]. Scattering from defects increases the upper critical magnetic field [11, 12]. The slope of the temperature dependence $-dH_{c2}/dT$ near T_c can be written, with inclusion of scattering, as

$$-dH_{c2}/dT \sim \frac{T_c}{\langle v^{*2}\rangle}(1 + \lambda_{tr}). \qquad (1)$$

The quantity λ_{tr} grows with decreasing electron mean free path l or relaxation time $\tau = l/v^*$:

$$\lambda_{tr} = \frac{\hbar}{2\pi k T_c \tau^*} = 0.882\frac{\xi_0}{l}. \qquad (2)$$

Here, $\hbar$ is the Planck constant, k is the Boltzmann constant, and $\xi_0 = 0.18\hbar v^*/kT_c$. The above expressions are written for a strong-coupled superconductor, where $\tau^* = \tau(1 + \lambda)$ and $v^* = v/(1 + \lambda)$, with λ being the electron–phonon coupling constant.

The effect of electron scattering from radiation defects on H_{c2} was demonstrated in the case of the conventional superconductors NbC and Nb_3Sn in [3, 5]. In the case where defects do not affect the electronic structure and T_c noticeably, the variation of the $T_c/\langle v^{*2}\rangle$ factor (or the clean-base term) in Eq. (1) is relatively small. The increase in H_{c2} is caused by the growth of λ_{tr}, which is a result of the decrease in the mean free path.

We note that scattering from normal impurities and defects in conventional superconductors does not affect the critical temperature (Anderson's theorem) [13]. The variation in T_c is connected in this case with a variation in the electronic characteristics.

Unlike T_c of conventional superconductors, the critical temperature of high-temperature cuprates is sensitive to scattering. This is connected with the odd *d*-wave symmetry of the order parameter [14], which has been revealed in both hole and electronic HTSCs [15, 16]. Estimates made for a fairly pure superconductor with an odd order parameter suggest that the critical temperature in the case of scattering from defects can be written as $T_c = T_{c0}(1 - \pi\hbar/2kT_{c0}\tau)$ [17]. Here, T_{c0} is the critical temperature in the absence of scattering and $\hbar/(\pi kT_{c0}\tau) \ll 1$. In view of Eq. (2), we can recast this as $T_c = T_{c0}/(1 + \pi^2\lambda_{tr})$.

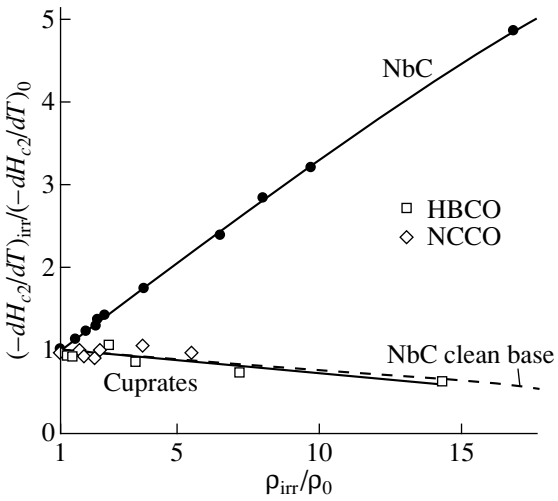

Fig. 2. Reduced slope $(-dH_{c2}/dT)_{irr}/(-dH_{c2}/dT)_0$ plotted vs. reduced electrical resistivity ρ_{irr}/ρ_0 for NbC, HBCO, and NCCO films irradiated by He^+ ions. $(-dH_{c2}/dT)_0$ and ρ_0 are the characteristics of the original sample. The dashed line shows the variation of the clean-base term for NbC.

Thus, the scattering-induced decrease in the critical temperature of a *d*-wave superconductor lowers the upper critical magnetic field rapidly, so that the factor $(1 + \lambda_{tr})$ in Eq. (1) can be neglected. As a result, the scattering-induced variation of the slope $-dH_{c2}/dT$ for a *d*-wave superconductor can be qualitatively described by the expression

$$-dH_{c2}/dT \sim \frac{T_c}{\langle v^{*2}\rangle} \sim \frac{T_{c0}}{\langle v^{*2}\rangle(1 + \pi^2\lambda_{tr})}. \qquad (3)$$

Equation (3) shows that the variation of the slope $-dH_{c2}/dT$ for a *d*-wave superconductor is determined by the ratio $T_c/\langle v^{*2}\rangle$ in both cases of variation of the electronic characteristics and changes in scattering.

This accounts qualitatively for the observed character of variation of the upper critical magnetic field of cuprate HTSCs with decreasing electron mean free path.

HTSC irradiation changes not only the mean free path but also the conduction electron concentration N. The relation

$$\rho = \frac{mv}{Ne^2 l} \qquad (4)$$

(m and e are the effective mass and charge of an electron, respectively) shows that the electrical resistivity ρ can grow both as a result of a decrease in the mean free path caused by radiation defects and through a change in the electronic characteristics.

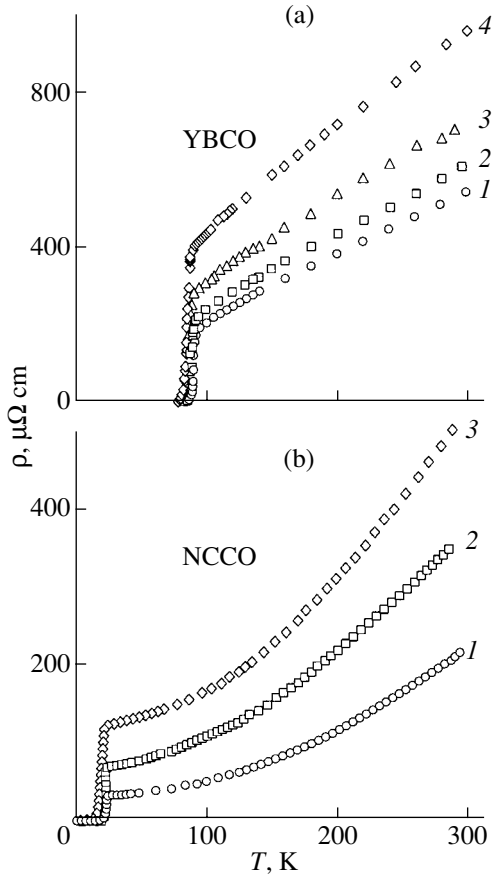

Fig. 3. Temperature dependences of the electrical resistivity of epitaxial films of high-temperature superconductors irradiated by He^+ ions to various doses F equal to (a) (*1*) 0, (*2*) 6×10^{14}, (*3*) 1.6×10^{15}, and (*4*) 2.6×10^{15} cm^{-2}; and (b) (*1*) 0, (*2*) 1×10^{13}, and (*3*) 1×10^{14} cm^{-2}.

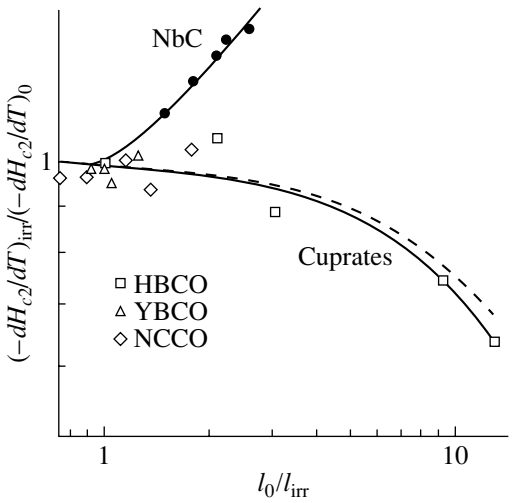

Fig. 4. Variation of reduced slope $(-dH_{c2}/dT)_{irr}/(-dH_{c2}/dT)_0$ with increasing reduced reciprocal mean free path of electrons l_0/l_{irr} measured for epitaxial films of the high-temperature cuprate superconductors HBCO, YBCO, and NCCO irradiated by He^+ ions. $(-dH_{c2}/dT)_0$ and l_0 are the characteristics of the original sample. Shown for comparison are data for the conventional superconductor NbC; dashed line is the clean-base term.

Irradiation of cuprates brings about not only a growth of the residual resistivity associated with defects but also an increase in the slope $d\rho/dT$ of the temperature dependence of the electrical resistivity $\rho(T)$ (Fig. 3). The temperature dependence of ρ is determined by that of the mean free path. If $\rho(T)$ follows a linear dependence, the slope $d\rho/dT$ can be considered as a measure of the variation of the quantity mv/N under irradiation. The ratio of $d\rho/dT$ to the resistivity ρ_n close to T_c varies in proportion to the electron mean free path under irradiation:

$$\frac{1}{\rho_n}\frac{d\rho}{dT} \sim l. \qquad (5)$$

This permits one to estimate the irradiation-induced variation in l and mv/N from data on the temperature dependence of $\rho(T)$.

The irradiation-induced variation of mv/N and of the electron mean free path l near T_c was directly estimated for YBCO (Fig. 3) and HBCO [5], as well as for NbC, which feature a close-to-linear dependence of the electrical resistivity on temperature. In the case of NCCO, for which the $\rho(T)$ dependence is nonlinear, qualitative estimates were obtained.

It was shown that irradiation of YBCO, HBCO, and NCCO brings about a noticeable decrease in the electron mean free path in these HTSCs. Unlike conventional superconductors, however, the slope $-dH_{c2}/dT$ was not found to increase (Fig. 4).

The decrease in the upper critical magnetic field observed in HBCO may be due to a strong effect of scattering on the critical temperature of the *d*-wave superconductor. The small coherence length of hole HTSCs, $\xi(0) \sim 20$ Å, makes realization of the pure-superconductor approximation $\lambda_{tr} \ll 1$ possible, where Eq. (3) becomes valid.

At the same time, estimates made for YBCO and HBCO for low irradiation doses and for zinc substituting for copper [18] showed that the relative variation of mv/N is comparable to that of $1/l$ or exceeds it. The dependence of H_{c2} on electronic characteristics may turn out to be substantial in this case. In particular, a decrease in the conduction electron concentration may result in a fast decrease in T_{c0} in Eq. (3) as the Fermi level passes through the singularity in the density of states [17]. In all cases, hole HTSCs exhibit a common pattern of H_{c2} variation; namely, the slope $-dH_{c2}/dT$ decreases approximately in proportion to the critical temperature (Fig. 5). One may think that the variation of the quantity $T_c/\langle v^{*2}\rangle$ for these superconductors is determined by that of T_c.

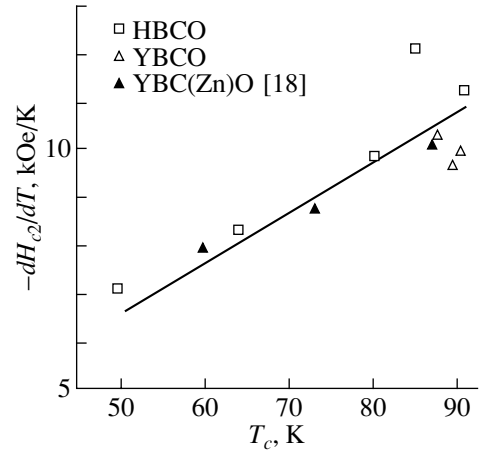

Fig. 5. Slope $-dH_{c2}/dT$ plotted vs. critical temperature T_c for epitaxial films of the hole high-temperature superconductors HBCO and YBCO irradiated by helium ions and of zinc-doped YBCO [18].

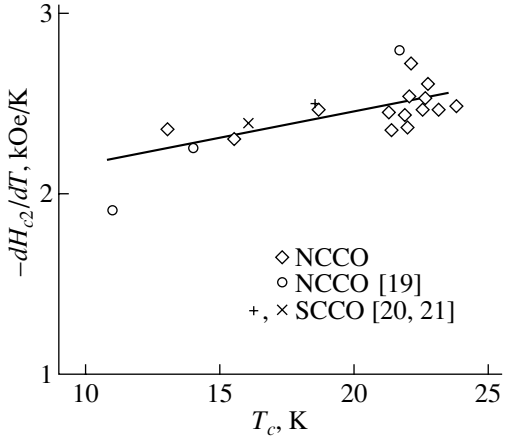

Fig. 6. Slope $-dH_{c2}/dT$ plotted vs. critical temperature T_c for electronic high-temperature superconductors, namely, for NCCO epitaxial films irradiated by helium ions, with different Nd/Ce contents and with different oxygen composition [19], as well as for SmCeCuO [20, 21].

Electronic high-T_c superconductors NCCO and SmCeCuO (SCCO) exhibit a weak tendency to a decrease in the slope $-dH_{c2}/dT$ with decreasing critical temperature as a result of irradiation or a change in the oxygen content [19] and in the rare-earth content ratio (Fig. 6). The values of the critical field near T_c (and of the slope $-dH_{c2}/dT$) obtained for these compounds practically coincide [20, 21]. It is not possible to enhance scattering considerably in these cuprates using irradiation (Fig. 4). Even very low irradiation doses bring about a decrease in the critical temperature, because these compounds are superconducting within a very narrow oxygen content interval. The quantity mv/N also exhibits a noticeable variation. A decrease in the conduction electron concentration (a change in the Fermi level) can cause a decrease not only in T_c but also in v^*. Therefore, the observation of a small irradiation-induced decrease in the slope $-dH_{c2}/dT$ for electronic superconductors may be assigned to features in the electronic structure which govern the variation of the quantity $T_c/\langle v^{*2}\rangle$.

4. CONCLUSIONS

Thus, it has been shown that the absence of growth of the upper critical magnetic field in hole and electronic HTSCs observed to occur with a decreasing electron mean free path under irradiation by energetic ions may be accounted for by the *d*-wave symmetry of the order parameter. The change in the conduction electron concentration caused by radiation-induced defects should play a substantial role in the variation of the upper critical magnetic field. Under variation of the electronic characteristics, the quantity H_{c2} behaves qualitatively similar to the clean-base term in the expression for the upper critical magnetic field of a conventional superconductor.

ACKNOWLEDGMENTS

The support of the Russian Scientific Council "Topical Problems in the Physics of Condensed Matter" (subprogram "Superconductivity," project no. 98027), is gratefully acknowledged.

REFERENCES

1. S. I. Krasnosvobodtsev, N. P. Shabanova, V. S. Nozdrin, and A. I. Golovashkin, Fiz. Tverd. Tela (St. Petersburg) **41**, 1372 (1999) [Phys. Solid State **41**, 1256 (1999)].
2. J. Y. Lin, S. J. Chen, S. Y. Chen, *et al.*, Phys. Rev. B **59**, 6047 (1999).
3. S. I. Krasnosvobodtsev, N. P. Shabanova, E. V. Ekimov, *et al.*, Zh. Éksp. Teor. Fiz. **108**, 970 (1995) [JETP **81**, 534 (1995)].
4. N. P. Shabanova, S. I. Krasnosvobodtsev, V. S. Nozdrin, *et al.*, Czech. J. Phys. **46**, 853 (1996).
5. N. P. Shabanova, S. I. Krasnosvobodtsev, V. S. Nozdrin, and A. I. Golovashkin, Fiz. Tverd. Tela (St. Petersburg) **38**, 1969 (1996) [Phys. Solid State **38**, 1085 (1996)].
6. A. I. Golovashkin, E. V. Ekimov, S. I. Krasnosvobodtsev, *et al.*, Physica C (Amsterdam) **162–164**, 715 (1989).
7. V. S. Nozdrin, S. I. Krasnosvobodtsev, O. M. Ivanenko, *et al.*, Pis'ma Zh. Tekh. Fiz. **22** (24), 1 (1996) [Tech. Phys. Lett. **22**, 996 (1996)].
8. N. P. Shabanova, V. S. Nozdrin, S. I. Krasnosvobodtsev, *et al.*, Kratk. Soobshch. Fiz., No. 12, 35 (1999).
9. L. P. Gor'kov and T. K. Melik-Barkhudarov, Zh. Éksp. Teor. Fiz. **45**, 1493 (1963) [Sov. Phys. JETP **18**, 1031 (1964)].

10. B. J. Dalrymple and D. E. Prober, J. Low Temp. Phys. **56**, 545 (1984).
11. L. P. Gor'kov, Zh. Éksp. Teor. Fiz. **37**, 1407 (1959) [Sov. Phys. JETP **10**, 998 (1960)].
12. N. R. Werthamer, in *Superconductivity*, Ed. by R. D. Parks (Marcel Dekker, New York, 1969), Vol. 1, p. 321.
13. P. W. Anderson, J. Phys. Chem. Solids **11**, 26 (1959).
14. H. Won and K. Maki, Physica C (Amsterdam) **282–287**, 1837 (1997).
15. C. C. Tsuei, J. R. Kirtley, C. C. Chi, *et al.*, Phys. Rev. Lett. **73**, 593 (1994).
16. C. C. Tsuei and J. R. Kirtley, Phys. Rev. Lett. **85**, 182 (2000).
17. A. A. Abrikosov, Int. J. Mod. Phys. B **13**, 3405 (1999).
18. J. Schroeder, M. Ye, J. F. Marneffe, *et al.*, Physica C (Amsterdam) **278**, 113 (1997).
19. J. Herrmann, M. C. Andrade, C. C. Almasan, *et al.*, Phys. Rev. B **54**, 3610 (1996).
20. M. C. Andrade, C. C. Almasan, Y. Dalichaouch, and M. B. Maple, Physica C (Amsterdam) **184**, 378 (1991).
21. M. A. Crusellas, J. Fontcuberta, and S. Pinol, Phys. Rev. B **48**, 4223 (1993).

Translated by G. Skrebtsov

Physics of the Solid State, Vol. 44, No. 10, 2002, pp. 1845–1849. Translated from Fizika Tverdogo Tela, Vol. 44, No. 10, 2002, pp. 1762–1765.

SEMICONDUCTORS AND DIELECTRICS

Thermopower of Lead Chalcogenides at High Pressures

V. V. Shchennikov, S. V. Ovsyannikov, and A. Yu. Derevskov

Institute of Metal Physics, Ural Division, Russian Academy of Sciences, ul. S. Kovalevskoĭ 18, Yekaterinburg, 620219 Russia

Received October 1, 2001; in final form, December 24, 2001

Abstract—Thermopower measurements on Pb*X* crystals (*X* = Te, Se, S) at high hydrostatic pressures of up to 35 GPa are reported. New data were obtained on the magnitude and on the pressure dependence of the thermopower of high-pressure semiconducting and metallic phases. The phase transitions occurring in Pb*X* are treated in terms of a model in which the transition to an insulator electronic spectrum is caused by the Peierls lattice distortion. © *2002 MAIK "Nauka/Interperiodica".*

1. INTRODUCTION

Lead chalcogenides [1, 2], which are semiconducting compounds of Group IV and VI elements, undergo pressure-induced phase transitions from rock-salt to germanium sulfide-type structure [3–5]. In Pb*X* (*X* = Te, Se, S), unlike in the majority of other substances, the electrical resistivity, rather than decreasing at the phase transition, increases by several orders of magnitude [6–8], as in the mercury chalcogenides [9]. At still higher pressures ($P \geq 15$ GPa), Pb*X* compounds were observed to transfer to a CsCl-type bcc structure [5]. Judging from the literature, the thermoelectric properties of the new phases have not been studied. Much the same, the behavior of the thermopower *S* is seen to reflect the variation of the electronic structure and carrier parameters of semiconductors under pressure [9, 10]. This fact was employed, in particular, in studying the pressure-induced transformation of the electronic structure of the initial phases of PbS, PbSe, and PbTe [11, 12]. The purpose of this study was to investigate the thermopower of the high-pressure phases of lead chalcogenides.

2. EXPERIMENTAL TECHNIQUES

The high quasi-hydrostatic pressure *P* was produced in anvil-type chambers made of the VK6 hard alloy (up to 10 GPa) and synthetic diamonds (up to 30–40 GPa) [9]. The pressure-transmitting medium was catlinite, of which the sample containers were made. The pressure was estimated to within ±10% from a calibration graph (relating the pressure to the force applied) constructed using the phase transformations in the reference substances Bi, ZnS, GaP, etc., for each of the chambers employed [9, 13–17]. The high-pressure setup made it possible to measure simultaneously the force, sample compression, anvil temperatures, temperature drop ΔT, and the electrical signal from the sample [16, 17]. The results of the measurements were entered into a nonvolatile memory and transferred subsequently to a computer [16, 17]. The technique used in the thermoelectric measurements at pressures of up to 30–40 GPa was described in [9, 15]. The temperature distribution in the anvils for different sample sizes and thermal conductivities was calculated in [18]; this distribution is used to estimate the error of ΔT determination in a sample. To take into account the error introduced by the anvils, the sample was replaced by lead as a reference material, whose thermopower at room temperature is close to zero (–1.27 μV/K [10]). The thermoelectric measurements were conducted both in stationary conditions at a fixed temperature drop and in a nonstationary thermal regime [16, 17]. The diamond anvils served as the heater and cooler in the thermoelectric measurements [9]. The temperature gradient was produced by heating the anvil, the heater being located in the chamber. Earlier measurements of *S* made at up to 30 GPa on a large number of semiconducting compounds [13] have shown satisfactory agreement with the studies performed at hydrostatic pressures of up to 2–10 GPa carried out using the standard technique.

The materials chosen for the study were *p*-PbSe and *n*-PbTe single crystals and *p*-PbSe and *n*-PbS polycrystalline samples. The room-temperature electron concentration and electrical resistivity ρ of the crystals were 1.5×10^{18} cm^{-3} and 4×10^{-3} Ω cm in PbTe and 6.5×10^{18} cm^{-3} and 2.2×10^{-3} Ω cm in PbS, respectively. The hole concentration and electrical resistivity of single-crystal and polycrystalline *p*-PbSe samples were ~1.1×10^{18} cm^{-3} and 8×10^{-3} Ω cm, and 6×10^{18} cm^{-3} and 2×10^{-3} Ω cm, respectively. The crystal structure and lattice parameter were characterized by x-ray diffraction. The samples of the crystals studied in the diamond chamber measured typically ~$0.2 \times 0.2 \times 0.1$ mm; these samples were placed into a hole 0.3 mm in diameter drilled in the center of the catlinite container. The samples studied in the hard-alloy chamber were ~$0.4 \times 0.4 \times 0.2$ mm in size. We either used platinum–silver, spring-loaded contacts of a 5-μm-thick ribbon or employed diamond anvils (which had a low elec-

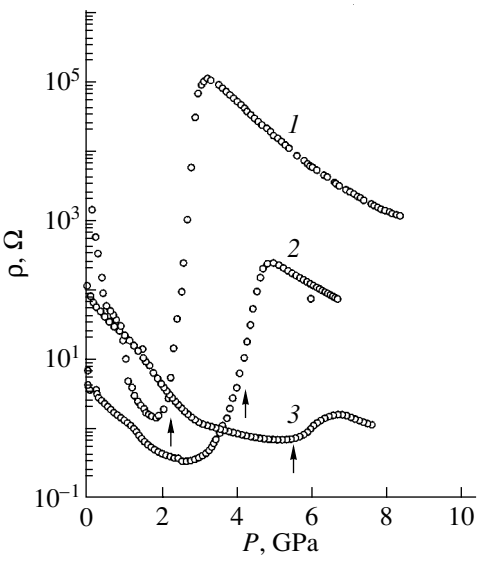

Fig. 1. Pressure dependences of the electrical resistivity for polycrystalline samples of (*1*) PbS and (*2*) PbSe and (*3*) a single-crystal sample of PbTe measured in a hard-alloy chamber at $T = 293$ K. The arrows identify the structural phase transitions derived from x-ray diffraction data [3–5] (see text).

trical resistivity due to metallic inclusions) as electrical probes contacting the samples [9, 15]. The relative errors with which the resistivity ρ and S were determined did not exceed 3 and 20%, respectively.

3. RESULTS AND DISCUSSION

The pressure dependences of electrical resistivity reveal jumps indicating reversible phase transitions (the reverse course of the curves is not shown) in the interval from 2 to 6 GPa (Fig. 1), which is in good agreement with earlier measurements [4, 6–8]. The structural phase transitions occurring at $P \approx 2.2$–2.5, 4.2–4.5, and 5.2–6.5 GPa have been observed in PbS, PbSe, and PbTe from measurements of the electrical resistivity [4, 6–8] and in x-ray diffraction experiments [5]. The electrical resistivity of different lead chalcogenides behaves in a qualitatively similar way with pressure, which is a consequence of their having similar electronic structure [1, 2]. The $S(P)$ dependences are substantially different for these samples, which reflects the different behavior of the partial contributions of electrons and holes to the conductivity (Fig. 2). The results of measurements carried out in stationary and nonstationary regimes almost coincided. While the values of S obtained in the diamond and hard-alloy chambers correlate, on the whole, with one another, the data obtained in the region of phase transitions, where S undergoes strong variations, exhibit a scatter associated with nonuniform pressure distribution. The values of $S(P)$ obtained for the PbTe crystal at low pressures P coincided to within experimental error with the figure $S = -230$ μV/K, which was

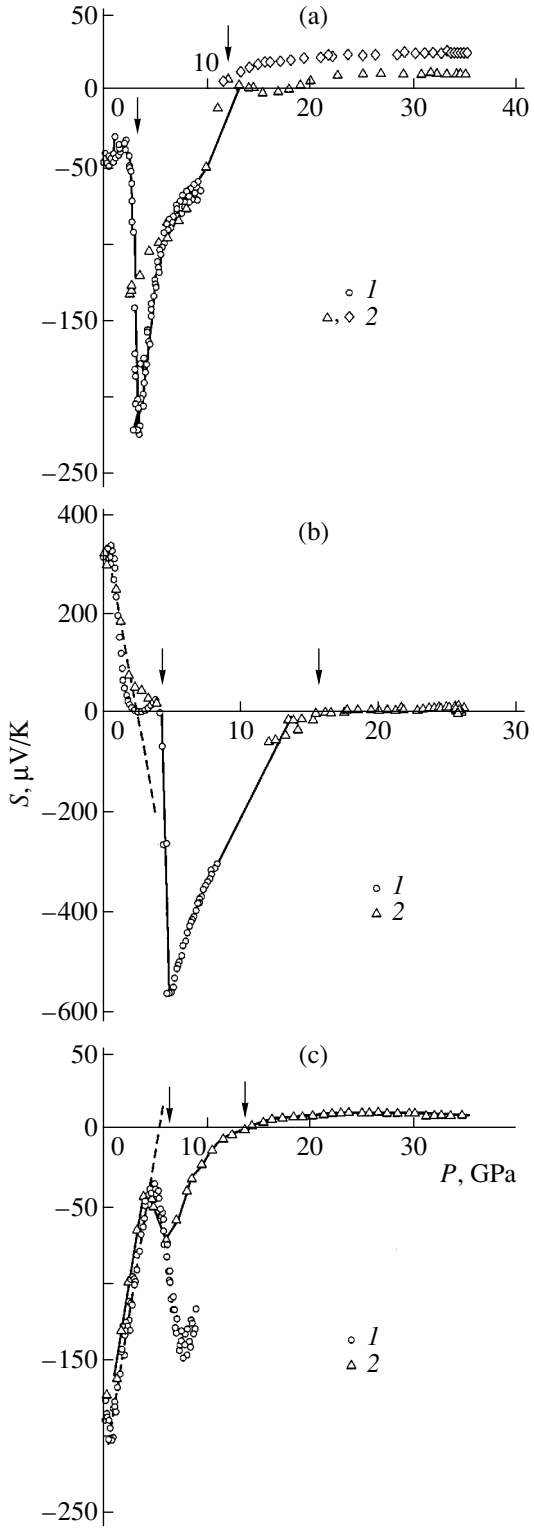

Fig. 2. Pressure dependences of the thermopower of (a) a polycrystalline PbS sample and single-crystal samples of (b) PbSe and (c) PbTe measured at $T = 298$ K in (*1*) hard-alloy and (*2*) diamond-anvil chambers. The data for PbS refer to two samples; sample *1* is characterized by the pressure dependence of electrical resistivity shown in Fig. 1. The arrows point to phase transitions. The dashed lines for the PbSe and PbTe samples show the calculated pressure dependences of thermopower (see text).

found at atmospheric pressure using the standard technique. The thermopower of the PbS sample decreased irreversibly after the first cycle of raising the pressure; this should probably be attributed to the growth in the concentration of defects and the associated charge carriers. The $S(P)$ graphs displayed in Fig. 2 exhibit a reversible character.

At atmospheric pressure, PbX compounds (X = Te, Se, S) with a rock-salt structure are narrow-gap semiconductors, with the band gap E_g being equal to 0.286, 0.16, and 0.19 eV, respectively [1, 2], which decreases with increasing pressure (dE_g/dP = –55 to –70, –60 to –86, and –70 to –90 meV/GPa for PbS, PbSe, and PbTe, respectively [4, 9]). The pressure-induced decrease in ρ and S in the initial NaCl-structure phase is in accord with the pressure dependence of E_g. Taking into account the above pressure-dependence coefficients, the band gap should vanish before the onset of the structural phase transitions. As follows from the magnitude of thermopower $|S| < 50$ μV/K, the samples under study are indeed in the gapless or metallic state at these pressures (Fig. 2). The thermopower of an intrinsic semiconductor can be written as [10]

$$S = \frac{k_0}{|e|}\left\{\frac{\sigma_n}{\sigma}(r_n + 2) - \frac{\sigma_p}{\sigma}(r_p + 2) + \frac{\sigma_n - \sigma_p}{\sigma}\frac{E_g}{2k_0T} - \frac{3}{4}\ln\frac{m_p}{m_n}\right\}, \quad (1)$$

where σ is the conductivity, which is the sum of the electronic, σ_n, and hole, σ_p, conductivities; k_0 is the Boltzmann constant; e is the electronic charge; m_p and m_n are the effective masses of the electron and the hole, respectively; and $0 \le r_n \le 2$ and $0 \le r_p \le 2$ are the scattering parameters, which determine the energy dependences of the momentum relaxation time for the electrons and holes, respectively [10]. The effective masses of electrons and holes in the initial phase of PbX are anisotropic, particularly in PbTe, where the anisotropy parameter (the ratio of the mass along the axis of the constant-energy ellipsoid $m_\parallel$ to that in the perpendicular direction $m_\perp$) is 10 times that in PbS and PbSe [2]. Therefore, Eq. (1) should contain, in place of m_p and m_n, effective density-of-states masses at the L point of the Brillouin zone: $m_{\text{eff}} = N_c^{2/3}(m_\perp^2 m_\parallel)^{1/3}$, where N_c is the number of equivalent ellipsoids [10].

The behavior of $S(P)$ of the PbX samples both in the initial and high-pressure phases is described by the $E_g(P)$ variation, i.e., by the third term in Eq. (1); however, the effect of compensation of the electronic and hole contributions to the thermopower is also substantial. The $S(P)$ relation for PbSe in the initial phase is in agreement with the one calculated using Eq. (1), if we take $\sigma_p = \sigma$ ($\sigma_n = 0$) and use the known pressure coefficient dE_g/dP = –86 meV/GPa [4]. For PbTe, agreement with calculations for dE_g/dP = –70 meV/GPa [4] is reached for $\sigma_n/\sigma_p = 1.8$ (Fig. 2). In the PbS sample, the electron concentration after the application of pressure is substantially in excess of the intrinsic value and, therefore, thermopower in the initial phase varies only weakly. We note that the $S(P)$ relations also have features that are possibly associated with the pressure-induced variation of other parameters in Eq. (1). The jump of S in the new phase (Fig. 2), as well as the growth of the resistivity (Fig. 1), reflects the opening of the semiconducting gap in the high-pressure phases. Measurements showed that all lead chalcogenides are electronic semiconductors in the new phase and have a negative pressure coefficient of $|S|$. The latter fact correlates with the pressure dependences of ρ in these phases [4, 6–8]. Obviously enough, the $|S(P)|$ and $\rho(P)$ dependences in the new phase are associated with the decrease in E_g, which is characterized by approximately the same pressure coefficient as in the original NaCl-structure phases.

The relations obtained and the phase transitions in PbX can be interpreted within a model taking into account the major role played by the p bands in chemical-bond formation and the Peierls lattice distortion [19]. This model reproduces well the type of the crystal and electronic structure of some elements of Groups V, VI, and VII of the Periodic table, as well as of the mercury, indium, gallium, and bismuth chalcogenides at normal and high pressures [13, 19–21]. The model accounts for the opening of the semiconducting gap and its closure under pressure in compounds with different crystal structures, namely, cubic crystals, layered and chain structures, and molecular and liquid phases [19, 20]. This model is applicable for both qualitative description and precise quantitative calculation of the electronic structure [2, 19].

This model was also used to find the energy spectrum of the original NaCl-structure phase of PbX [2]. As shown by numerical calculations, energy bands near the Fermi level group to form triplets, which do not overlap with other bands; in other words, the crystal-field splitting of the atomic p levels is smaller than the distance to bands of other symmetry, so that the bands in the vicinity of the Fermi level derive primarily from the p states [2]. In the prephase with a simple cubic lattice (assuming the nearest neighbor atoms to be equivalent), all PbX compounds must be metals, because the p band is half-filled (with three electrons per six states). The exact electronic structure of PbX at the L point of the Brillouin zone was derived from the electronic structure of the metallic praphase by successively taking into account the ionicity, hybridization, and spin–orbit interaction [2]. The inclusion of ionicity (doubling of the period) of crystals leads to p-band splitting and the opening of a semiconducting gap between the filled and unoccupied p states in the original rock salt structure [2].

As follows from the experimental data obtained in this study and [4, 6–8] and calculations from [2, 4], $E_g \longrightarrow 0$ in the NaCl-structure phase as the pressure increases. According to the *p*-band model, however, the metallic state of Pb*X* crystals must be unstable in the cubic NaCl structure, because the Peierls lattice distortion is energetically favorable, and the energy of the system decreases as a result of the opening of the semiconducting gap [19]. The metallic state induced in Pb*X* by high pressure favors doubling of the lattice period and the opening of a semiconductor band gap at the Fermi level which separates the filled from unoccupied electronic states [19–21]. Indeed, the high-pressure Pb*X* phases have an orthorhombic structure whose parameter *a* is approximately twice that of the initial cubic phase [3, 4]. (We note that the structure of these phases was not established reliably in [5].) Thus, the opening of a semiconductor gap E_g in the high-pressure Pb*X* phases is well described by this model. The band gap in the new semiconductor phases can be estimated from the change in the resistivity and thermopower. Assuming the jump in the electrical resistivity to be due primarily to the carrier concentration drop, i.e., to the increase in E_g, we use the ratio of the resistivities of the second and first phases (both at $P = 0$ and before the phase transition) to obtain the estimates $E_g \approx 0.6$, 0.4, and 0.1 eV for PbS, PbSe, and PbTe, respectively, near the phase transition points, which, for lead selenide and telluride, is in accord with the data derived from $S(P)$. The underevaluation of $S(P)$ obtained for the sulfide, as well as for the initial phase, is probably due to an excess impurity or defect electrons.[1]

The density of Peierls structures is lower than that of an undistorted lattice; therefore, the application of a certain pressure will remove the distortion, i.e., will cause metallization [20]; this exactly was observed to occur in the above compounds [13, 14, 20]. Such transitions to a metallic state with a further increase in pressure are also seen to take place in the lead chalcogenides and are indicated by a sharp change in the pressure coefficient of $S(P)$ (Fig. 2) and in the resistivity [4, 6–8]. For PbSe (Fig. 2), a drop in magnitude of the thermopower and a reversal of the sign to positive occur near $P = 16$ GPa, which is in agreement with the data suggesting a transition to the bcc structure [5]. In PbTe, the sign of *S* changes to positive at ~10–12 GPa, which is likewise close to the transition point to the bcc lattice $P = 13$ GPa, the value derived from synchrotron data [5]. In PbS, the drop in magnitude of *S* and the change of the sign to positive were observed by us to take place at a pressure $P \approx 12$ GPa, which is lower than that at which the transition to the bcc structure was detected in x-ray diffraction experiments ($P = 21.5$ GPa [5]). Resistance measurements [8] also revealed the transition of PbS to a metallic state to occur at a lower pressure (18 GPa).

The thermopower of the high-pressure metallic phases, which have tentatively the CsCl-type bcc structure [5], is positive, with $S \approx 10$–20 μV/K being in agreement with the values typical of metals. Interestingly, in most of the high-pressure phases of elements of Groups IV and VI and of the II–VI compounds exhibiting metallic properties, the thermopower has the same sign and values [4]. The Hg*X* and Pb*X* semiconductor compounds, having different initial structures, follow similar pressure behavior. In Pb*X*, the Peierls instability sets in in the NaCl structure, where the semiconductor band gap opens under pressure, whereas in the gapless Hg*X* semiconductors, the pressure first initiates a transition from the tetrahedral sphalerite lattice, which is unstable for the given ratio of the cationic and anionic radii of Hg and *X* (like ions come in contact), to an octahedral (NaCl) lattice [3], which is distorted, in accordance with the *p*-band model, into a cinnabar structure [13, 14, 19]. As a result, the pressure-induced change in the electrophysical properties in materials of these two groups is nearly the same.

[1] Already after this paper had been submitted to press, we found the $S(P)$ relation for a single-crystal PbS sample, which agrees qualitatively with the one presented here; the value of *S* for the second phase corresponds to the band gap $E_g \approx 0.6$ eV.

ACKNOWLEDGMENTS

The authors are indebted to N.N. Stepanov for providing the samples.

This study was supported by the Russian Foundation for Basic Research (project no. 01-02-17203) and the Russian Physical Society.

REFERENCES

1. Yu. I. Ravich, B. A. Efimova, and I. A. Smirnov, *Semiconducting Lead Chalcogenides* (Nauka, Moscow, 1968; Plenum, New York, 1970).
2. B. A. Volkov, O. A. Pankratov, and A. V. Sazonov, Zh. Éksp. Teor. Fiz. **85** (4), 1395 (1983) [Sov. Phys. JETP **58**, 809 (1983)].
3. L. F. Vereshchagin and S. S. Kabalkina, *X-ray Diffraction Studies under High Pressure* (Nauka, Moscow, 1977).
4. N. M. Ravindra and V. K. Srivastava, Phys. Status Solidi A **58**, 311 (1980).
5. T. Chattopadhyay, H. G. von Schnering, W. A. Grosshans, and W. A. Holzapfel, Physica B & C (Amsterdam) **139–140**, 356 (1986).
6. G. A. Samara and H. G. Drickamer, J. Chem. Phys. **37** (5), 1159 (1962).
7. A. A. Semerchan, N. N. Kuzin, L. N. Drozdova, and L. F. Vereshchagin, Dokl. Akad. Nauk SSSR **152**, 107 (1963).
8. N. B. Brandt, D. V. Gitsu, N. S. Popovich, *et al.*, Pis'ma Zh. Éksp. Teor. Fiz. **22**, 225 (1975) [JETP Lett. **22**, 104 (1975)].
9. I. M. Tsidil'kovskiĭ, V. V. Shchennikov, and N. G. Gluzman, Fiz. Tekh. Poluprovodn. (Leningrad) **17** (5), 958 (1983) [Sov. Phys. Semicond. **17**, 604 (1983)].

10. K. Seeger, *Semiconductor Physics* (Springer, Berlin, 1973; Mir, Moscow, 1977).
11. A. A. Averkin, B. Ya. Moĭzhes, and I. A. Smirnov, Fiz. Tverd. Tela (Leningrad) **3** (6), 1859 (1961) [Sov. Phys. Solid State **3**, 1354 (1961)].
12. A. A. Averkin, S. Kasimov, and E. D. Nensberg, Fiz. Tverd. Tela (Leningrad) **4** (12), 3669 (1962) [Sov. Phys. Solid State **4**, 2683 (1963)].
13. V. V. Shchennikov, Fiz. Tverd. Tela (St. Petersburg) **42** (4), 626 (2000) [Phys. Solid State **42**, 641 (2000)].
14. V. V. Shchennikov, Phys. Status Solidi B **223** (1–2), 561 (2001).
15. V. V. Shchennikov, Rasplavy, No. 2, 33 (1988).
16. V. V. Shchennikov, A. Yu. Derevskov, and V. A. Smirnov, in *High Pressure Chemical Engineering*, Ed. by Ph. Rudolf von Rohr and Ch. Trepp (Elsevier, Amsterdam, 1996), p. 604.
17. V. V. Shchennikov, A. Yu. Derevskov, and V. A. Smirnov, Proc. SPIE **3213**, 261 (1997).
18. V. V. Shchennikov and A. V. Bazhenov, Rev. High Pressure Sci. Technol. **6**, 657 (1997).
19. B. A. Volkov, O. Pankratov, and S. V. Pakhomov, Zh. Éksp. Teor. Fiz. **86**, 2293 (1984) [Sov. Phys. JETP **59**, 1336 (1984)].
20. J. P. Gaspard, F. Marinelli, and A. Pellegatti, Europhys. Lett. **3** (10), 1095 (1987).
21. P. B. Littlewood, Crit. Rev. Solid State Mater. Sci. **11** (3), 229 (1984).

Translated by G. Skrebtsov

Physics of the Solid State, Vol. 44, No. 10, 2002, pp. 1850–1853. Translated from Fizika Tverdogo Tela, Vol. 44, No. 10, 2002, pp. 1766–1769.

SEMICONDUCTORS AND DIELECTRICS

Electrophysical Properties and Electronic Structure of Tin-Doped Antimony Telluride

I. V. Gasenkova*, M. K. Zhitinskaya, S. A. Nemov**, and L. D. Ivanova*****

** Institute of Electronics, National Academy of Belarus, Minsk, Belarus*

*** St. Petersburg State Technical University, Politekhnicheskaya ul. 29, St. Petersburg, 195251 Russia*

**** Baĭkov Institute of Metallurgy and Materials Sciences, Russian Academy of Sciences, Leninskiĭ pr. 49, Moscow, 117911 Russia*

Received October 3, 2001; in final form, December 24, 2001

Abstract—The effect of Sn atoms on the electrophysical properties and x-ray photoelectron spectra of Czochralski-grown Sb_2Te_3 single crystals is studied. The character of the temperature dependences of the kinetic coefficients is shown to depend noticeably on the structure of the valence band, which consists of two valence subbands. Estimates of the effective density-of-states masses of holes and of the gap between the valence-band extrema in Sb_2Te_3 : Sn agree with the data available for the Sb_2Te_3 not doped with tin. X-ray photoelectron spectra of Sb_2Te_3 : Sn single crystals do not exhibit noticeable core-level shifts and electron density redistribution in the valence band. *© 2002 MAIK "Nauka/Interperiodica".*

1. INTRODUCTION

The effect of tin atoms on the electrical properties of Sb_2Te_3 has been studied in a number of works [1–3]. Sn was established to act as a deep acceptor in this compound [1, 2]. In Sb_2Te_3, tin revealed unusual properties, namely, negative magnetoresistance, anomalies in the temperature dependence of the Hall coefficient, and its dependence on the applied magnetic field [3]. It was not reported in [3] whether these anomalies are related to any features in the energy spectrum.

We showed in [4] that a coordinated investigation of the kinetic coefficients, namely, of the electrical conductivity, Hall, Seebeck, and Nernst–Ettingshausen effects, as well as of x-ray photoelectron spectra, permits one to draw conclusions as to the presence or absence of features in the energy spectrum of a compound.

This communication reports on a study of the effect of Sn on transport phenomena and x-ray photoelectron spectra of Sb_2Te_3 single crystals.

2. SAMPLES

Sb_2Te_3 single crystals were Czochralski grown in a floating crucible, which served to feed the growing crystal with a liquid melt, using the technology developed at the Baĭkov Institute of Metallurgy and Materials Sciences [5]. This method permits one to grow sufficiently large, high-quality crystals with a given crystallographic orientation. The uniformity of the samples in concentration was estimated from local values of the thermopower on the surface of the single crystals. The scatter in the values of thermopower did not exceed 2–3%. The experiment was carried out on samples of two types, namely, on those of stoichiometric composition and on those doped by a heterovalent Sn impurity. The crystals were prepared from Te, Sb, and Sn of 99.9999 wt % purity. The impurity content was estimated through chemical analysis. All of the grown crystals exhibited hole conduction.

3. THE EXPERIMENT AND DISCUSSION OF THE RESULTS

3.1. Kinetic Effects

On each of the Sb_2Te_3 samples studied, we measured the following independent transport coefficients: S_{11} and S_{33} (Seebeck), R_{123} and R_{321} (Hall), Q_{123} (Nernst–Ettingshausen), and σ_{11} and σ_{33} (electrical conductivity). The measurements were conducted in the temperature interval 77–350 K. The charge carrier concentration was determined, as in [4], from the larger Hall tensor component R_{321} at 77 K from the relation

$$p = (eR_{321})^{-1}. \quad (1)$$

As follows from our data, the tin impurity acts as a deep acceptor in Sb_2Te_3, which is in agreement with [1, 2].

The observed temperature dependences of the transport coefficients in Sb_2Te_3 : Sn are qualitatively similar to those for undoped Sb_2Te_3. Therefore, the experimental data found for crystals with tin can be interpreted as in the case of stoichiometric Sb_2Te_3; namely, the discussion of results should take into account the complex valence-band structure and the existence of carriers of at least two types (with noticeably different mobilities) involved in the transport phenomena.

1063-7834/02/4410-1850$22.00

Introduction of the tin impurity made it possible to shift the Fermi level into the valence band by $\Delta\varepsilon_F \sim 0.1$ eV as compared to samples that were not doped by Sn. This doping left the main relations governing the transport phenomena unchanged. While the concentration dependences of the Hall mobility and of the Seebeck coefficient do not exhibit the pronounced effects characteristic of band-to-band or resonance scattering, certain quantitative differences are, however, seen because of the increased hole concentration.

Using our data on the above transport coefficients, we found the effective density-of-states mass at the Fermi level $m_d^*(\varepsilon_F)$ and the scattering parameter r [the exponent in the energy dependence of the relaxation time $\tau(\varepsilon) \sim \varepsilon^{r-1/2}$]. The parameters $m_d^*(\varepsilon_F)$ and r were estimated from the totality of the four measured kinetic coefficients:

$$m_d^*(\varepsilon_F) = A(S_{11} - Q_{123}/R_{123}\sigma_{11}), \quad (2)$$

$$Q_{123}/R_{123}\sigma_{11}S_{11} = (r - 1/2)/(r + 1), \quad (3)$$

where $A = (3/\pi)^{2/3}h^2/Tp^{2/3}e/k_0$; σ_{11} and S_{11} are the electrical conductivity and the Seebeck coefficient, respectively, in the direction perpendicular to the trigonal axis; and Q_{123} and R_{123} are the Nernst–Ettingshausen and Hall coefficients, respectively, measured in a magnetic field aligned with the trigonal axis c_3. These relations are valid for degenerate carrier statistics, and their application is justified in this case by the high hole concentration of the samples. According to the Hall measurements, this concentration was $(1.2–4.0) \times 10^{20}$ cm^{-3}.

The values of m_d^* calculated within the one-band model vary from $(0.8–0.9)m_0$ (m_0 is the free-electron mass), a value characteristic of Sb_2Te_3 ($p = 1.2 \times 10^{20}$ cm^{-3}), to $0.6m_0$ for Sb_2Te_3 : Sn ($p = 3.7 \times 10^{20}$ cm^{-3}). In this model, the values of m_d^* derived using Eq. (2) are intermediate between the effective masses of light and heavy holes. The decrease in the effective mass can be explained in terms of the two-band model by the Fermi level ε_F shifting into the additional valence-band extremum and by the possible effect of the band-to-band scattering or band nonparabolicity. For samples with tin, the scattering parameter r as calculated from Eq. (3) was negative. This might also indicate both the effect of interband scattering and the band nonparabolicity. The existence of an additional extremum in the Sb_2Te_3 valence band with a smaller hole effective mass is argued for not only by our measurements but also by the data reported in [6–9].

We used the data on the Seebeck coefficient anisotropy to estimate the energy gap between the main and additional extrema $\Delta\varepsilon_v$ in the same way as was done in our earlier study [6]. In the temperature region where the holes of the second band of concentration p_2 just begin to contribute to conductivity, i.e., when $\nu = p_2/p_0 \ll 1$ ($p_0 = p_1 + p_2$ is the total hole concentration), the Seebeck coefficient anisotropy depends exponentially on the energy gap between the two valence subbands:

$$\Delta S \sim \nu \sim \exp(-\Delta\varepsilon_v/k_0T).$$

The energy gap $\Delta\varepsilon_v$ found for Sb_2Te_3 : Sn is equal to $\Delta\varepsilon_v \sim 0.1$ eV and virtually does not differ from that determined for Sb_2Te_3. Thus, the energy spectrum parameters derived from experimental data on the transport coefficients indicate the absence (in contrast to Bi_2Te_3) of a noticeable effect of the Sn impurity on the energy spectrum of Sb_2Te_3.

3.2. Electronic Structure as Determined from X-ray Photoelectron Spectra

The conclusion that Sn has no resonance states, which was drawn from the data on the transport coefficients, needs to be checked independently. In order to study features in the distribution of the total density of states in the valence band of Sb_2Te_3, both undoped and doped by tin, we measured x-ray photoelectron spectra of the valence band using an ÉS-2401 electron spectrometer with Mg K_α radiation. The valence electron distribution in the tin-doped Sb_2Te_3 is almost the same as that in the undoped antimony telluride. The top of the Sb_2Te_3 valence band derives primarily from the $5p_{3/2}$ states of Te and $5p$ states of Sb, which are localized at 1.7 eV. The (Te $5p_{1/2}$ + Sb $5p$) states are located at 3.4 eV; they are the strongest (the main maximum) and make up, together with the above-mentioned maximum, a band about 5 eV wide. If tin atoms are introduced, the $5p$ states of Sn also contribute to the band top. However, this does not initiate either a shift of the states relative to the Fermi level (the maxima of the Sb_2Te_3 : Sn spectrum lie at the same energy as those of Sb_2Te_3) or a change in the density of the states.

The core level spectra of Sb_2Te_3 represent narrow peaks with a binding energy E_b of 538.6 eV for Sb $3d_{3/2}$ (the peak FWHM = 1.3 eV), E_b = 529.4 eV for Sb $3d_{5/2}$ (FWHM = 2.1 eV), E_b = 573.0 eV for Te $3d_{5/2}$ (FWHM = 1.5 eV), and E_b = 583.3 eV for Te $3d_{3/2}$ (FWHM = 1.4 eV). The Te $4d$ spectra with FWHM = 3.2 eV were decomposed into two maxima, with one of them corresponding to Te $4d_{5/2}$ with E_b = 40.3 eV and the other to Te $4d_{3/2}$ with E_b = 41.7 eV. A similar deconvolution of the Sb $4d$ spectra (FWHM = 2.6 eV) yielded values of 33.1 and 34.2 eV for the Sb $4d_{5/2}$ and Sb $4d_{3/2}$ maxima, respectively. The binding energies are given relative to the C $1s$ level at 284.6 eV. Introduction of the tin impurity did not produce any core-level chemical shifts, changes in the shape of the spectra, or their broadening. The binding energies of the above levels in Sb_2Te_3 : Sn remained unchanged within the reproducibility of the values of the binding energy, from 0.1–0.2 eV.

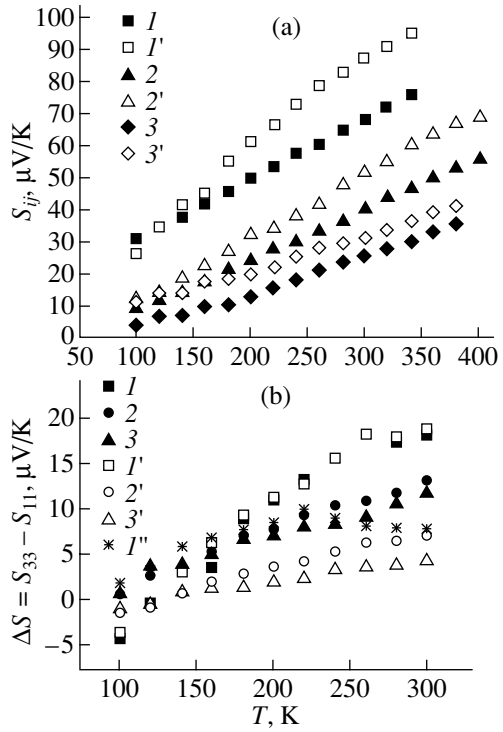

Fig. 1. (a) Temperature dependences of the Seebeck coefficient components (*1*–*3*) S_{11} and (*1*'–*3*') S_{33} for Sb_2Te_3 samples with different initial hole concentrations *p* equal to (*1*, *1*') 1.21×10^{20}, (*2*, *2*') 2.58×10^{20}, and (*3*, *3*') 3.68×10^{20} cm^{-3}. (b) Temperature dependences of the Seebeck coefficient anisotropy $\Delta S = S_{33} - S_{11}$: (*1*–*3*) experimental data, (*1*'–*3*') two-band model calculations, and (*1*") one-band model calculation with inclusion of scattering anisotropy and band nonparabolicity (from [10]). The parameters of the two-band model used are $\Delta\varepsilon_v \sim 0.1$ eV, $m^*_{d1} = 0.3m_0$, $m^*_{d2} = 0.9m_0$, $b_a = 0.9$, $b_c = 0.5$, $A_a^{(2)} = 0.83$, $A_c^{(2)} = 0.76$, $\chi_c = 1.1$, and $\chi_a = 1.2$.

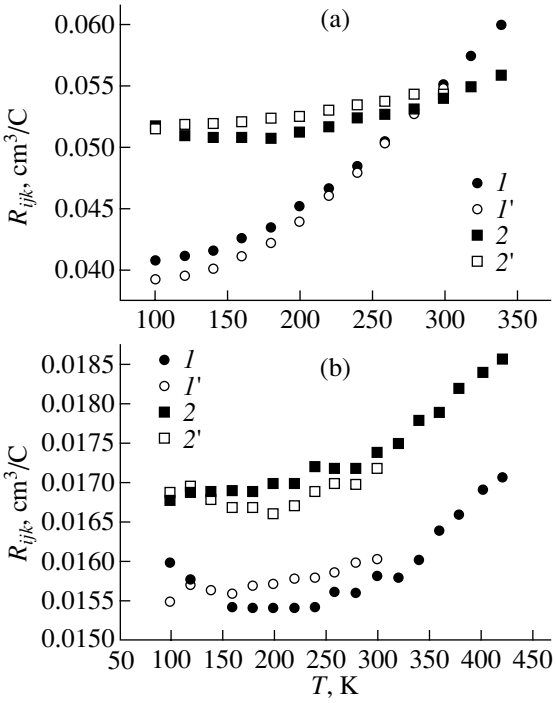

Fig. 2. Temperature dependences of the Hall coefficient components (*1*, *1*') R_{123} (**j** ⊥ **c** ∥ **B**) and (*2*, *2*') R_{321} (**j** ⊥ **c** ⊥ **B**) measured for two Sb_2Te_3 samples with hole concentrations *p* equal to (a) 1.21×10^{20} and (b) 2.58×10^{20} cm^{-3}; (*1*, *2*) are experiment and (*1*', *2*') are two-band model calculation.

3.3. Anisotropy of the Seebeck and Hall Coefficients

As already mentioned, introduction of Sn permitted us to shift the Fermi level ε_F into the valence band, where the effect of the additional extremum on the kinetic coefficients should be more distinct. We observed a change in the anisotropy of the Seebeck coefficient (Fig. 1) and in the relative magnitude of the Hall tensor components (Fig. 2). The observed change in both the absolute and relative thermopower anisotropy with increasing temperature and hole concentration, as well as the absence of crossing of the Hall tensor components R_{123} and R_{321} in the sample with the highest hole concentration, finds explanation in terms of a model involving an additional extremum (with a lighter effective mass) and inclusion of a mixed scattering mechanism. The calculations were performed using the formulas [6, Eqs. (A14), (A17)]

$$\Delta S = S_c - S_a = [S^{(1)} - S^{(2)}]\nu(1-\nu)$$
$$\times (b_c - b_a)/\{[(1-\nu)b_c + \nu][(1-\nu)b_a + \nu]\},$$

$$R_c = [A_c^{(1)}/p_0][(1-\nu)b_a^2 + \nu/\chi_c]/[(1-\nu)b_a + \nu]^2,$$

$$R_a = [A_a^{(1)}/p_0][(1-\nu)b_c b_a + \nu/\chi_a]/\{[(1-\nu)b_c + \nu]$$
$$\times [(1-\nu)b_a + \nu]\}.$$

Here, the index *c* refers to the trigonal axis of the crystal and index *a* refers to the direction in the crystal cleavage plane. The notation used is as follows: $\nu = p_2/p_0$ is the ratio of the hole concentration in the second band to their total concentration in both bands, $p_0 = p_1 + p_2$, so that $p_1/p_0 = 1 - \nu$; $b_a = u_a^{(1)}/u_a^{(2)}$ and $b_c = u_c^{(1)}/u_c^{(2)}$ are the ratios of the hole mobilities in the first and second bands in the direction of the cleavage plane and in the perpendicular direction, respectively; $\chi_c = A_c^{(1)}/A_c^{(2)}$ and $\chi_a = A_a^{(1)}/A_a^{(2)}$; and $A_c^{(1)}$, $A_c^{(2)}$, $A_a^{(1)}$, and $A_a^{(2)}$ are the structural Hall factors of the first and second bands for **H** ∥ **c** (index *c*) and **H** ⊥ **c** (index *a*).

Figure 1 displays experimental data on the thermopower S_{11} and S_{33} and its absolute anisotropy (ΔS), and Fig. 2 shows the temperature dependences of the Hall coefficient components for Sb_2Te_3 samples, stoichiometric and tin-doped, and the data as compared

with calculations. The changes in the thermopower anisotropy and in the relation between the Hall tensor components observed to occur with increasing hole concentration are related to the Fermi level shifting into the additional valence-band extremum and to a change in the relative influence of this extremum. As seen from Fig. 1, both the experimental and theoretical relations indicate a decrease in ΔS with increasing hole concentration. The function approximating ΔS within the two-band model [6, Eq. (A14)] passes through a maximum at the ratio of the main and additional hole concentrations such that $\nu^2/(1 + \nu)^2 = b_a b_c$. A shift of ν toward smaller or larger values results in a decrease in ΔS; exactly this is observed in experiment. The observed difference between the experimental and calculated values can be accounted for by the fact that our calculations took into account only the two-band effect on the thermopower anisotropy. If, however, one includes the thermopower anisotropy that is associated with the mixed scattering mechanism, as was done in [10], then the agreement between the theory and experiment becomes substantially better.

In addition, an increase in the hole concentration p results in a relative increase in the role played by acoustic scattering, which is more isotropic. Let us consider this point in more detail. In the case of the mixed scattering mechanism and degenerate statistics, the reciprocal of the observed (total) mobility is the sum of the inverse partial mobilities governed by various scattering mechanisms. The partial contribution of impurity scattering remains constant with increasing hole concentration, whereas the mobility due to acoustic scattering of holes scales as $u_{ac} \sim p^{-1/3}$. The noticeable part played by acoustic scattering in the Sn-doped samples is also indicated by the temperature dependence of the Hall mobility $u \sim T^{-\nu}$, with an exponent ν close to unity.

Our estimates show that better agreement of calculations with experiment can be reached by assuming that the additional valence-band extremum (with a lighter effective mass) is substantially nonparabolic, with a nonparabolicity parameter $\lambda = d\ln m^*/d\ln p \approx 0.3$.

4. CONCLUSION

Thus, it has been confirmed that tin in antimony telluride acts as a deep acceptor. This made it possible to carry out studies of the band structure of Sb_2Te_3 : Sn for the Fermi energy ε_F being shifted by about ~0.1 eV into the valence band as compared to undoped Sb_2Te_3. This shift did not entail any noticeable changes in the band parameters. The data obtained on the anisotropy of the Seebeck and Hall coefficients supported the existence of an additional extremum with a light effective mass in the valence band.

The absence of features in the electronic structure of Sb_2Te_3 : Sn, unlike Bi_2Te_3 : Sn, shows that the electronic structure of the Sb_2Te_3 valence band is not changed by tin doping and, hence, does not contain resonance states of Sn.

REFERENCES

1. J. Horak, P. Lostak, and M. Matyas, Phys. Status Solidi B **129**, 381 (1985).
2. L. D. Ivanova, Yu. V. Granatkina, and Yu. A. Sidorov, Neorg. Mater. **34**, 34 (1998).
3. P. N. Sherov, E. I. Shvedkov, and N. V. Timofeeva, Neorg. Mater. **26** (2), 275 (1990).
4. I. V. Gasenkova, M. K. Zhitinskaya, S. A. Nemov, and T. E. Svechnikova, Fiz. Tverd. Tela (St. Petersburg) **41** (11), 1969 (1999) [Phys. Solid State **41**, 1805 (1999)].
5. L. D. Ivanova, S. A. Brovikova, G. Zussmann, and P. Renskhaus, Neorg. Mater. **31** (6), 739 (1995).
6. M. K. Zhitinskaya, S. A. Nemov, and L. D. Ivanova, Fiz. Tverd. Tela (St. Petersburg) **44** (1), 41 (2002) [Phys. Solid State **44**, 42 (2002)].
7. A. Middendorf, K. Dietrich, and G. Landwehr, Solid State Commun. **13**, 443 (1973).
8. I. A. Smirnov, A. A. Andreev, and V. A. Kutasov, Fiz. Tverd. Tela (Leningrad) **10** (6), 1782 (1968) [Sov. Phys. Solid State **10**, 1403 (1968)].
9. B. Rönlund, O. Beckman, and H. Levy, J. Phys. Chem. Solids **26**, 1281 (1965).
10. M. Stordeur, Phys. Status Solidi B **124**, 439 (1984); **124**, 799 (1984).

Translated by G. Skrebtsov

Physics of the Solid State, Vol. 44, No. 10, 2002, pp. 1854–1858. Translated from Fizika Tverdogo Tela, Vol. 44, No. 10, 2002, pp. 1770–1774.

SEMICONDUCTORS AND DIELECTRICS

Secondary Anti-Stokes Emission from the Bulk of Gallium Phosphide at 4.2 K

V. S. Gorelik, A. L. Karuzskiĭ, and P. P. Sverbil'

Lebedev Institute of Physics, Russian Academy of Sciences, Leninskiĭ pr. 53, Moscow, 117924 Russia

Received September 17, 2001; in final form, January 9, 2002

Abstract—Secondary radiation (photoluminescence and Raman scattering) emitted by gallium phosphide single crystals at helium temperatures is investigated. It is established for the first time that, in the case when the secondary emission spectra are excited by a cw low-power He–Ne laser, whose linewidth lies in the transparency region of GaP, anti-Stokes photoluminescence from the bulk of the sample occurs due to interband and impurity recombination. The results obtained make it possible to carry out a qualitative and quantitative analysis of impurities which are present in the bulk of a semiconductor by recording the bulk anti-Stokes photoluminescence spectra at low temperatures. © *2002 MAIK "Nauka/Interperiodica".*

1. INTRODUCTION

If the quantum energy E_0 of exciting radiation is larger than the forbidden gap of a semiconductor, secondary emission takes place only in a thin surface layer of the material under investigation. An analysis of the photoluminescence (PL) and Raman spectra in this case provides information on the electron and vibration spectra of only a thin surface layer of the semiconductor.

This work is devoted to an analysis of the low-temperature characteristics of the anti-Stokes secondary radiation in gallium phosphide crystals excited by a laser source whose photon energy does not exceed the forbidden gap E_g of GaP (photoexcitation of carriers takes place in the bulk of the crystal).

2. EXPERIMENTAL TECHNIQUE

We studied the PL and Raman spectra of gallium phosphide single crystals with the (100) orientation of the surface grown without deliberate introduction of impurities. The spectra were recorded on an automated DFS-24 spectrometer [1] with an instrument function width of 0.7 cm^{-1}. During measurements, the sample was immersed in liquid helium (at temperature $T = 4.2$ K) in an optical helium cryostat. Secondary radiation was excited by a 5-mW He–Ne laser with a wavelength of 632.8 nm and by an argon laser with lasing wavelengths of 488.0 and 476.5 nm and a power of 20 and 5 mW, respectively. For measuring reflection spectra, a 40-W halogen incandescent lamp was used.

3. RESULTS

We studied the photoluminescence and Raman spectra of gallium phosphide in the Stokes and anti-Stokes ranges. For the first time, we observed anti-Stokes photoluminescence (ASPL) with an intensity considerably higher than the intensity of secondary Stokes radiation in the case of excitation of secondary emission spectra by a cw He–Ne laser of a relatively low power at 4.2 K (Fig. 1). ASPL is virtually not observed if measurements are made at liquid-nitrogen temperature. In the ASPL spectrum, a broad band with a peak near 2.2 eV dominates. In addition, a small

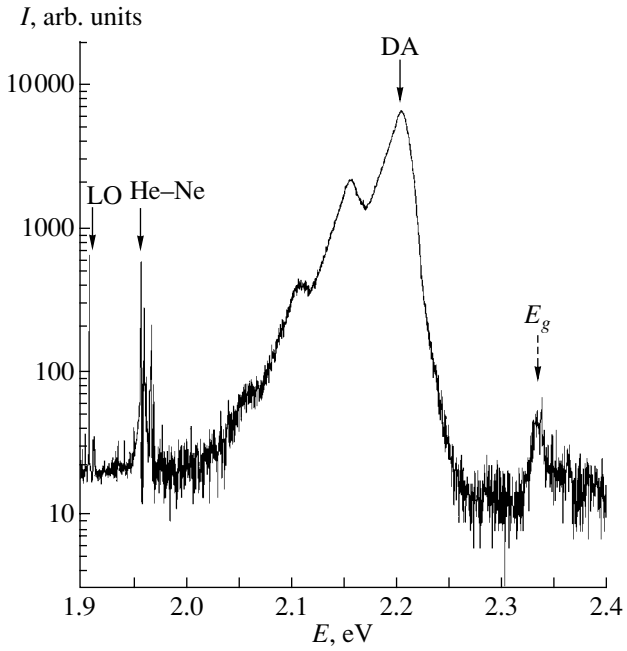

Fig. 1. Secondary emission spectrum in the Stokes and anti-Stokes region of a GaP crystal with the (100) orientation at $T = 4.2$ K. Excitation by a He–Ne laser ($\lambda_0 = 632.8$ nm, $E_0 = 1.96$ eV) in the region 1.9–2.4 eV; DA indicates the position of the intensity peak of donor–acceptor recombination; the dashed arrow on the right corresponds to interband recombination.

1063-7834/02/4410-1854$22.00

broad peak of interband ASPL with a maximum in the region of the energy band gap E_g = 2.338 eV is observed [2]. Low-intensity narrow lines observed in the spectrum in the vicinity of the exciting line of the He–Ne laser are not associated with GaP and are due to spontaneous emission from the gas discharge in the laser. The dominating broad band of ASPL at liquid-helium temperature contains several phonon replicas with a shift of 50 meV, which is close to the energy of an LO phonon at the Γ point of the Brillouin zone observed in the Stokes region of the Raman spectrum (indicated by an arrow in Fig. 1). A similar broad band modulated by phonon replicas upon the excitation of GaP by an electron beam followed by recombination of donor–acceptor (D–A) pairs was observed earlier in [3].

Figure 2 shows combined spectral–time characteristics of variation of the ASPL intensity obtained as result of periodic intermission of the exciting light beam (1-s illumination followed by 2-s blanking). The gratings of the spectrometer scanned the spectrum at a constant rate. Thus, the upper envelope of the spectrum in Fig. 2 is similar to the curve shown in Fig. 1, while the lower envelope corresponds to the afterglow intensity distribution of ASPL for a delay time of 2 s after the excitation is switched off. An increase in the delay time leads to a shift in the spectral position of the line peak (indicated by arrows) towards lower energies.

The kinetics of the ASPL decay after switching off of the exciting laser beam is shown in greater detail in Fig. 3 for three values of the ASPL energy: 2.2 and 2.15 eV (the ASPL peak and its first LO-phonon replica) and 2.175 eV in the interval between these maxima. It can be seen from Fig. 3 that the time during which the ASPL intensity decreases by two orders of magnitude from the steady-state value amounts to ~5 s for E = 2.2 eV, ~20 s for E = 2.15 eV, and to more than 60 s for E = 2.175 eV. These dependences also indicate a shift of the line maximum with a delay towards lower values of energy. It should be noted that the afterglow observable in GaP to the naked eye at helium temperature lasts for more than 1 min.

Figure 4 shows the variation of the ASPL spectra upon an increase in the intensity of excitation by a He–Ne laser (curves *1*, *2*) and of similar PL spectra upon an increase in the energy E_0 of an exciting photon to a value above the forbidden gap width E_g = 2.338 eV (curves *3*, *4*). It can be seen from Fig. 4 that an increase in the exciting photon energy leads to a systematic shift of the main peak (indicated by an arrow) towards higher energies.

In addition, series of narrow lines appear in the most intense PL spectrum (curve *4* in Fig. 4) in the interval 2.24–2.30 eV. Figure 5 illustrates, in greater detail, the presence of sharp photoluminescence peaks in the interval 2.24–2.32 eV, which should be attributed, in accordance with the available data [2], to impurity centers of the type of closely spaced S–C donor–acceptor pairs.

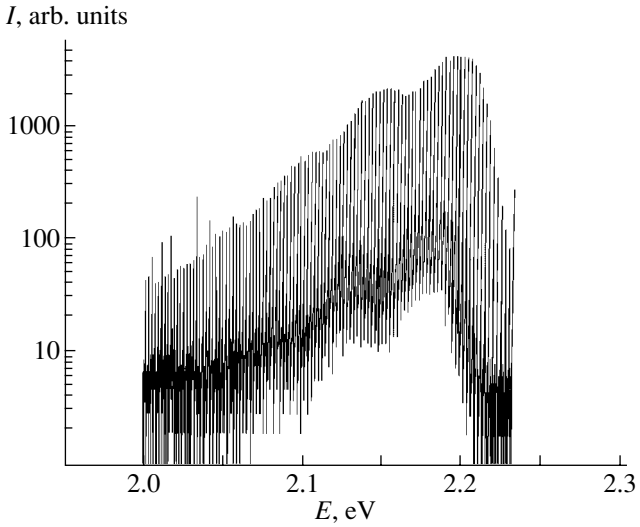

Fig. 2. Variation of the ASPL intensity in GaP at T = 4.2 K with simultaneous scanning of the spectrum and cyclic excitation by a He–Ne laser (illumination for 1 s and blanking for 2 s). Arrows mark the positions of ASPL afterglow peaks with a zero- and 2-s delay.

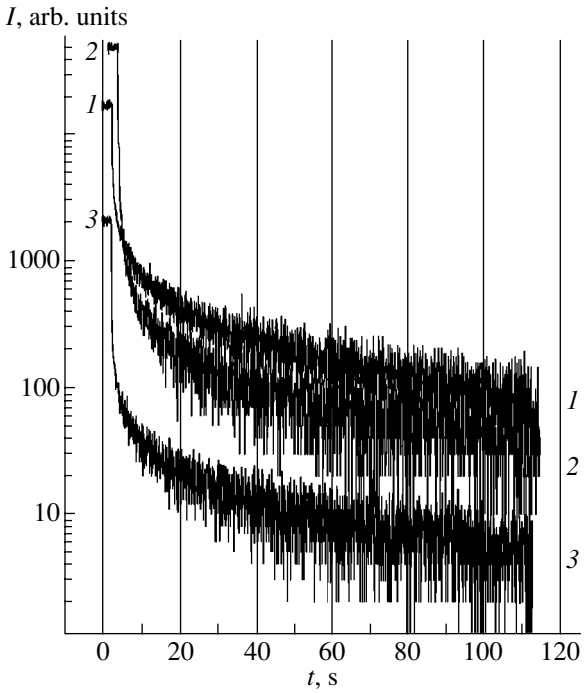

Fig. 3. Kinetics of ASPL decay in GaP at T = 4.2 K for the following three different energies E after the excited radiation is switched off (E_0 = 1.96 eV): (*1*) 2.175, (*2*) 2.2, and (*3*) 2.15 eV. Curve *3* is displaced downwards by an order of magnitude for the sake of visualization.

The PL spectrum (Fig. 5) displays a low-intensity phononless line (2.310 eV) of an exciton bound at the

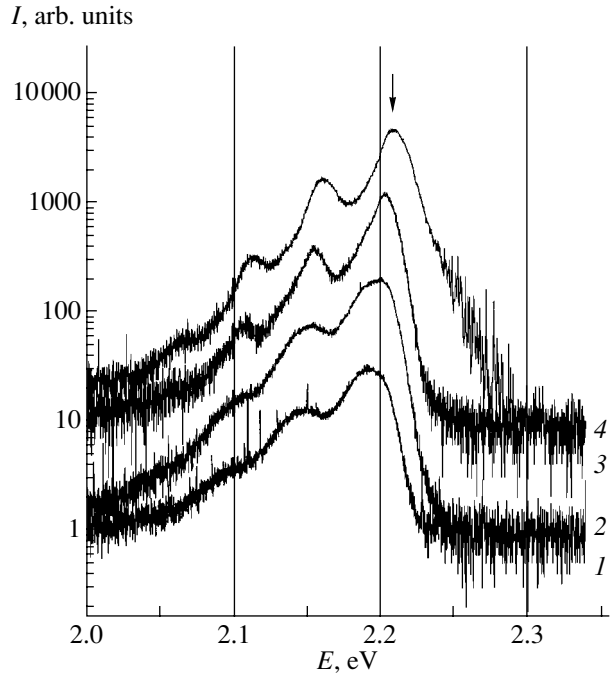

Fig. 4. ASPL and PL spectra in GaP at $T = 4.2$ K for different values of excitation energy E_0, eV: (*1*) 1.96 at a power of 0.6 mW, (*2*) 1.96 at a power of 5 mW, (*3*) 2.54, and (*4*) 2.6.

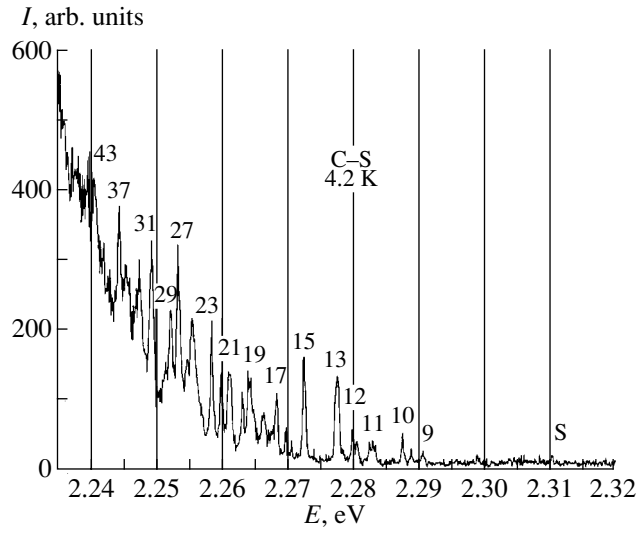

Fig. 5. Donor–acceptor recombination spectrum in GaP at $T = 4.2$ K in the energy range 2.23–2.32 eV. The numbers on peaks, in accordance with [2], correspond to the numbers of shells in the sublattices of donors S and acceptors C; a low-intensity peak (S) of an exciton bound to sulfur is shown on the right.

donor S. The reflection spectrum (Fig. 6) contains, in addition to the peak of the exciton bound at the neutral donor S, a more intense peak at 2.318 eV, which is due to a phononless transition of an exciton bound at a neutral isoelectron center, viz., a nitrogen impurity [2–7].

4. DISCUSSION

4.1. Analysis of Impurities in the Bulk of the Crystal Using the Anti-Stokes Photoluminescence Spectra

The spectral position and kinetics of the spectrum observed, illustrated in Figs. 1–3, indicate that the dominating ASPL band corresponding to the bulk of the GaP crystal is due to the donor–acceptor recombination [2, 3]. It follows from Fig. 2 that 2 s after the He–Ne laser beam is shuttered (lower envelope), the maximum of the spectrum (shown by the arrow) is shifted towards lower energies. This fact can be explained in terms of the recombination of distant electron–hole pairs with a longer lifetime upon an increase in the delay time; the Coulomb binding energy of these pairs decreases, and the photon energy of phononless radiative recombination can be represented by the expression [2, 3]

$$E(r) = E_g - (E_A + E_D) + \frac{e^2}{\varepsilon r}, \qquad (1)$$

where E_A and E_D are the ionization energies of the noninteracting donor and acceptor, e is the electron charge, ε is the relative permittivity of the crystal, and r is the distance between the donor and acceptor.

An increase in the recombination lifetime with the distance between an acceptor and a donor also explains the kinetic dependences of intensity (presented in Fig. 3) at various points in the D–A ASPL band. The intensity of phononless recombination of electrons and holes in D–A pairs located at the most probable distances and being emitted in the region of the peak of the D–A band (curve *2* in Fig. 3 for $E = 2.2$ eV) decreases by a factor of 100 over 5 s. The phononless recombination intensity for more distant D–A pairs with energy $E = 2.175$ eV (curve *1*) decreases much more slowly (by a factor of 100 over 1 min). The nonmonotonic increase in the decay time upon an increase in energy (for curve *3*, this time is 20 s for $E = 2.15$ eV) is due to the contribution from the first LO-phonon replica of the band peak.

The shift in the peak position of the D–A recombination band upon an increase in the ASPL excitation intensity and in the exciting photon energy E_0 above the forbidden gap width (see Fig. 4) corresponds to recombination of less distant electrons and holes. In the case of excitation by quanta with energy 2.54–2.6 eV, light is absorbed in a submicrometer surface layer, leading to a high concentration of carriers and a small mean distance between them. In contrast to surface excitation with the excitation energy $E_0 = 1.96$ eV, recombination occurs from the entire illuminated volume of the semiconductor. The peak of the ASPL intensity is shifted towards lower energies upon a decrease in the beam intensity of the He–Ne laser (curves *2*, *1* in Fig. 4) due to a decrease in the concentration of excited carriers.

The spectral position of the broad D–A ASPL band (see Figs. 1, 2, 4) and characteristic narrow peaks from closely spaced donor–acceptor pairs (Fig. 6) indicates

that sulfur is the major donor impurity in the bulk of the samples under investigation, while carbon is the major acceptor [2]. This is also confirmed by the fact that the PL spectrum in Fig. 5 displays an exciton bound to sulfur. The observed spectrum is close in shape to the luminescence spectrum observed in [2] corresponding to a sulfur concentration $\geq 10^{17}$ cm^{-3}. The reflection spectrum (Fig. 6) shows that samples also contain an isoelectronic nitrogen impurity in an appreciable concentration ($\geq 10^{17}$ cm^{-3}).

4.2. On the Possible Mechanism of Excitation of Anti-Stokes Photoluminescence

Anti-Stokes photoluminescence observed earlier in GaP at liquid-helium temperature [4–7] was excited by powerful ($\geq 10^{14}$ W cm^{-2}) laser pulses and exhibited a quadratic dependence of the ASPL intensity on the excitation power, which is typical of two-photon excitation. According to the results of our measurements, the ASPL spectral intensity under steady-state conditions increases linearly with the intensity of excitation from 0.05 to 5 mW (see, for example, the data presented in Fig. 4). The linear dependence indicates that the process of ASPL excitation for a relatively low power of the exciting He–Ne laser is of the step rather than of the two-photon type. Impurity centers characterized by deep energy levels in the forbidden gap, long lifetimes, and the possibility of existing in several charge states are apparently excited at the first stage of illumination of the crystal in the transparency region. Examples of such centers in gallium phosphide are donor–acceptor pairs or complexes with oxygen or copper and, probably, an isoelectron nitrogen impurity. The excitation process can be regarded as the absorption of a photon by such a center in the crystal, followed by the formation of a localized polariton of the upper polariton branch near the center of the Brillouin zone, which is characterized by an anomalously low phase velocity ($k \longrightarrow 0$). The heating of the crystal leads to rapid polariton–phonon relaxation of the excited state. In the case under investigation of low temperatures, such a polariton has a long life. The action of exciting radiation may lead to a further excitation of the center under investigation, accompanied by the formation of a free charge carrier and its subsequent recombination.

Figure 1 also shows an emission band corresponding to an interband transition ($E = E_g$). Exciton radiation is virtually not observed, which can be explained as follows. In the case of conventional PL excitation at the surface by photons with an energy higher than the band gap width, strong absorption of excited radiation leads to a high concentration of electron–hole pairs, which is sufficient for neutralizing charge impurities and for creating excitons. On the contrary, the absorption of light and the concentration of nonequilibrium charge carriers are low in the case of photoexcitation by radiation in the sample transparency region at helium temperatures,

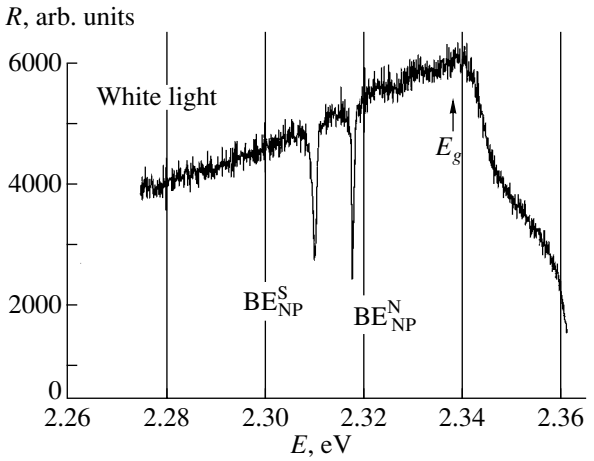

Fig. 6. Reflection spectrum for GaP at $T = 4.2$ K; E_g is the band edge, BE^S_{NP} is the no-phonon line of an exciton bound to sulfur, and BE^N_{NP} is the no-phonon line of an exciton bound to nitrogen.

leading to a high concentration of charge states of donor and acceptor ions. The concentration of the "frozen" plasma formed by such charged states suffices [8, 9] to prevent the formation of excitons characterized by a large Bohr radius. As a result, nonequilibrium charge carriers which are not bound at donors and acceptors are in the state of a plasma of free carriers and are responsible for the interband ASPL line in Fig. 1.

5. CONCLUSIONS

Thus, it has been established that the exposure of a gallium phosphide crystal at 4.2 K to He–Ne laser radiation in the transparency region of the crystal leads to electron excitation of long-lived localized impurity centers and to the formation of holes in the valence band in the bulk of the sample. At the next stage, under the action of light, the electrons from impurity centers pass to the conduction band. Subsequently, electron–hole recombination takes place.

The observed bulk ASPL spectra provide information on the impurity centers present in the bulk of semiconducting materials. We analyzed impurities in the bulk of GaP crystals under investigation. The results obtained can be subsequently used for monitoring the impurity states in actual semiconducting crystals and for improving the methods of obtaining ultrapure semiconducting materials.

Moreover, step excitation of free carriers in the region illuminated by a laser beam in a crystal makes it possible to create photostimulated conduction in the bulk of the semiconductor in the case when the wavelength of exciting radiation is larger than the wavelength corresponding to the photoconductivity threshold.

ACKNOWLEDGMENTS

The authors thank A.É. Yunovich and A.I. Gutkin for helpful discussions.

This study was supported by the Russian Foundation for Basic Research (project no. 98-02-17452) and the State Science and Engineering Program "PTUMNÉ" (grant no. 02.04.4.2.15É37).

REFERENCES

1. A. L. Karuzskiĭ, A. V. Kvit, V. N. Murzin, *et al.*, Mikroélektronika **25** (1), 13 (1996).
2. A. É. Yunovich, in *Radiative Recombination in Semiconductors*, Ed. by Ya. E. Pokrovskiĭ (Nauka, Moscow, 1972), p. 273.
3. D. C. Thomas, J. J. Hopfield, and W. M. Augustyniak, Phys. Rev. **140** (1A), A202 (1965).
4. B. M. Ashkinadze, I. P. Kretsu, S. L. Pyshkin, *et al.*, Fiz. Tverd. Tela (Leningrad) **10** (12), 3681 (1968) [Sov. Phys. Solid State **10**, 2921 (1969)].
5. B. M. Ashkinadze, I. P. Kretsu, S. L. Pyshkin, and I. D. Yaroshetskiĭ, Fiz. Tekh. Poluprovodn. (Leningrad) **2** (10), 1511 (1968) [Sov. Phys. Semicond. **2**, 1261 (1969)].
6. B. M. Ashkinadze, A. I. Bobrysheva, E. V. Vitiu, *et al.*, in *Proceedings of the IX International Conference on Physics of Semiconductors, Moscow, 1968*, Vol. 1, p. 200.
7. B. M. Ashkinadze, S. M. Ryvkin, and I. D. Yaroshetskiĭ, Fiz. Tekh. Poluprovodn. (Leningrad) **3** (4), 535 (1969) [Sov. Phys. Semicond. **3**, 455 (1969)].
8. B. G. Zhurkin, A. L. Karuzskiĭ, and V. A. Fradkov, in *Optically Excited Semiconductors under Low and Ultralow Temperatures*, Ed. by N. G. Basov (Nauka, Moscow, 1988), Tr. Fiz. Inst. Akad. Nauk SSSR, Vol. 188, p. 178.
9. M. Chiba, V. A. Fradkov, A. L. Karuzskii, *et al.*, Physica B (Amsterdam) **302–303**, 408 (2001).

Translated by N. Wadhwa

Physics of the Solid State, Vol. 44, No. 10, 2002, pp. 1859–1863. Translated from Fizika Tverdogo Tela, Vol. 44, No. 10, 2002, pp. 1775–1779.

SEMICONDUCTORS AND DIELECTRICS

On the Role Played by Bending Vibrations in Heat Transfer in Layered Crystals

N. A. Abdullaev, R. A. Suleĭmanov, M. A. Aldzhanov, and L. N. Alieva

Institute of Physics, Academy of Sciences of Azerbaijan, Baku, 370143 Azerbaijan

e-mail: farhad@azintex.com

Received October 25, 2001

Abstract—The temperature dependences of the thermal conductivity of layered crystals (LCs) of graphite, boron nitride, gallium sulfide, etc., are analyzed. It is shown that the bending branch of vibrations typical of LCs determines the behavior of the thermal conductivity only in the region of its increase. The decrease in thermal conductivity upon heating cannot be explained by taking into account the bending vibrations only, and phonon–phonon interaction processes become effective only in the case of excitation of other branches in the acoustic spectrum. © *2002 MAIK "Nauka/Interperiodica".*

1. INTRODUCTION

As early as in 1952, Lifshitz [1] indicated the important role played by a specific branch of acoustic vibrations, which he called the bending branch, in the thermal properties of layered crystals (LCs). Under the assumption of an extreme degree of anisotropy of LCs, the bending branch corresponding to vibrations propagating in the plane of layers with atomic displacements in the direction perpendicular to these layers (in the direction of the weak link) is found to make a dominant contribution to the thermal properties of LCs. Lifshitz [1] considered the heat capacity and thermal expansion of a hypothetical layered crystal in which interlayer forces are much weaker than intralayer forces. In view of the specific dispersion relation for the bending branch, characterized by the presence of a quadratic term (which was directly confirmed by neutron diffraction studies for some LCs), the heat capacity of an LC exhibits a rather specific temperature dependence: $C \sim T^3$ (at low temperatures), $C \sim T^2$ (at intermediate temperatures), and $C \sim T$ (at high temperatures). Regions of low, intermediate, and high temperatures are different for different LCs; for example, in the case of graphite, these regions correspond to $T < 1$ K, 10 K $< T <$ 80 K, and 100 K $< T <$ 250 K, respectively.

According to Lifshitz [1], the specific role of bending vibrations should be manifested most strongly in the so-called membrane effect (an increase in the frequency of bending vibrations upon an extension of the layers), leading to negative thermal expansion in the plane of the layers.

Temperature dependences of heat capacity have been studied experimentally in many layered crystals starting from the most anisotropic LC graphite and its structural analog boron nitride. For many layered crystals, temperature regions were found in which the heat capacity depends on temperature in accordance with the predictions made in [1]. However, it cannot be concluded reliably for all LCs that the observed peculiarities are associated with the contribution of bending waves, since not all of these crystals can be regarded as strongly anisotropic. Nevertheless, many LCs, except pyrolitic graphite and boron nitride (GaSe, InSe, GaTe, PbI_2, In_4Se_3, etc.), cannot be attributed to the class of strongly anisotropic crystals; consequently, the role of bending waves in each specific case requires detailed analysis [2]. In this connection, the results of analysis of thermal expansion of LCs are quite valuable, since the role of bending waves can be manifested not only in the specific temperature dependence of the corresponding linear thermal expansion coefficient (LTEC) $\alpha_{\|}(T)$ but also in its sign. The role played by bending waves in the thermal expansion of a number of LCs (graphite, boron nitride, GaSe, GaS, InSe) was studied in a series of publications [3, 4]. In particular, the temperature intervals in which bending vibrations dominate (due to their negative contribution to linear expansion) were singled out for graphite and boron nitride. For example, bending vibrations in graphite are responsible for negative values of $\alpha_{\|}$ over a wide temperature range, 30–600 K, the value of $\alpha_{\|}$ decreasing up to 200–250 K. This corresponds to an increasing contribution from bending vibrations to $\alpha_{\|}$, while the contribution from other vibrational branches with positive Grüneisen parameters starts increasing above these temperatures, which ultimately leads to positive values of $\alpha_{\|}$ at $T >$ 600 K. As regards LCs of the GaS, GaSe, and InSe type, these crystals also have regions with negative values of $\alpha_{\|}$ [although, in a much narrower temperature range than for graphite (30–50 K)]. Qualitatively, this result is in full agreement with the predictions of the Lifshitz theory, according to which a considerably smaller anisotropy of the above crystals (as compared to graphite) should sharply reduce the role of bending vibra-

1063-7834/02/4410-1859$22.00 © 2002 MAIK "Nauka/Interperiodica"

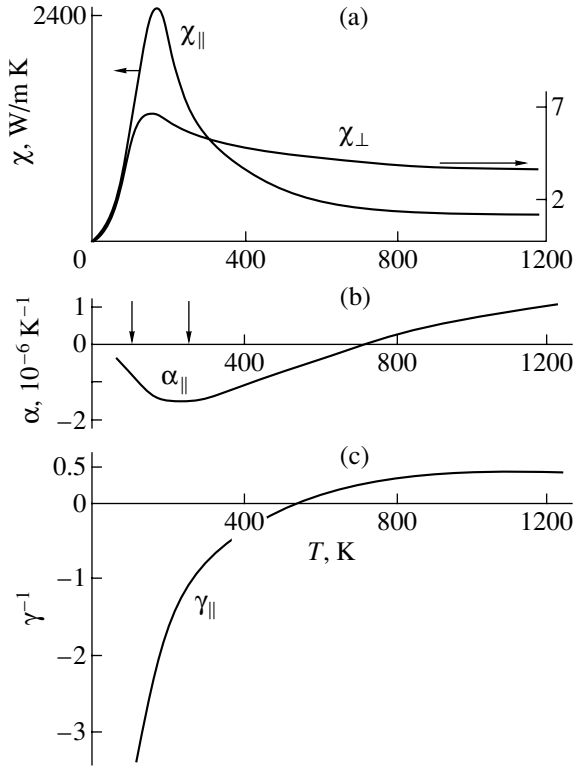

Fig. 1. Temperature dependences of (a) thermal conductivity $\chi_{\parallel}$ and $\chi_{\perp}$ in graphite in directions parallel and perpendicular to the layers, respectively; (b) thermal expansion coefficient $\alpha_{\parallel}$ in the plane of the layers; and (c) Grüneisen parameter $\gamma_{\parallel}$ in the plane of the layers. On curve (b), the temperature interval in which heat capacity $C \sim T$ is indicated by arrows.

tions in the thermal properties. However, it would be incorrect to carry out calculations based on [1] to single out the temperature intervals in which certain types of vibrations (including bending vibrations) dominate in view of the weak anisotropy of the crystals and inapplicability of the theory developed in [1] to them. Nevertheless, the results of analysis of the LTEC even in weakly anisotropic LCs are of importance in studying other LC properties.

The main conclusion that follows from the above brief analysis of the role of bending vibrations in the thermal properties of LCs is that the investigation of a specific physical parameter requires detailed analysis of the entire body of experimental data.

All that has been said above is based on the rich experimental information available on the heat capacity and thermal expansion of LCs but not on the thermal conductivity. Consequently, a clear understanding of the contribution from bending waves to heat transfer in LCs does not exist, in our opinion, even though this problem has been considered by several authors [5, 6]. This study aims at determining the role played by bending waves in the thermal conductivity of LCs on the basis of the entire body of data available on the possible role of these waves in LCs.

In our recent communication [7], we reported on the results of experimental investigations into the thermal conductivity of GaS and GaSe in the temperature range 5–300 K. Here, we analyze these data together with the available results on the temperature dependence of the thermal conductivity of LCs in order to single out and interpret the characteristic features of thermal conductivity of LCs.

2. DISTINGUISHING FEATURES OF THERMAL CONDUCTIVITY IN GRAPHITE

Thermal conductivity has been studied most thoroughly in various modifications of graphite [8–10]. We discuss here the results of analysis of pyrolitic graphite and boron nitride [11, 12], which are distinguished by the highest degree of anisotropy of physical properties exhibited among all LCs known to date. Figure 1a shows the temperature dependence of thermal conductivity of graphite measured in two directions (parallel and perpendicular to the layers).

The experimental data demonstrate the following features of the thermal conductivity of graphite (boron nitride also displays a similar behavior).

(1) Strong anisotropy in the thermal conductivity: the thermal conductivity $\chi_{\parallel}$ in the plane of the layers (close to its maximum value) is 500–600 times higher than the thermal conductivity $\chi_{\perp}$ perpendicular to the layers.

(2) In the temperature interval where the heat capacity $C \sim T^2$, the increase in thermal conductivity with temperature generally follows the law $\chi \sim T^{2+x}$, where x varies from 0.4 to 0.7 in different publications. This effect is known as a thermal anomaly.

(3) The peak value of the thermal conductivity $\chi_{\parallel}(T)$ lies in the high-temperature region 200–250 K, while the thermal conductivity above this region decreases upon an increase in temperature according to an exponential law over a wide temperature range ($T \le 1000$ K):

$$\chi = a(T/\Theta_i)^n \exp(\Theta_i/bT), \qquad (1)$$

where Θ_i is the characteristic Debye temperature and a, b, and n are constants [13].

We will not consider all the features in the behavior of χ in graphite; we will concentrate our attention only on those which were or can be explained using the concept of bending waves.

First, it has been established reliably that heat is transferred in graphite mainly by lattice waves and not by electrons. This circumstance has been mainly confirmed by numerous experimentally calculated values of the ratio $\chi/\sigma T \ge 100$, as well as by measurements of the thermal conductivity of graphite in a transverse magnetic field [10].

Anisotropy in the thermal conductivity cannot be explained on the basis of peculiarities in the acoustic spectrum alone. We must also assume that thermal conductivity in the region of its increase with temperature is limited by scattering at defects. A typical feature of practically all LCs is the presence of a considerable number of defects in their layer junctions, whose presence leads to a considerable scattering of phonons (and charge carriers [14]) during their motion across the layers but practically does not affect their motion in the plane of the layers. This results in considerably shorter mean free paths of phonons and charge carriers in the direction perpendicular to the layers and, hence, leads to a lower thermal and electrical conductivity in this direction.

In the literature, one model explaining the peculiar law of an increase in $\chi \sim T^{2+x}$ has been predominantly discussed. A distinguishing feature is the difference in the behavior of thermal conductivity from the increase in heat capacity with temperature. In view of the specific form of the phonon spectrum of LCs, the heat capacity at low temperatures for many layered crystals follows the law $C \sim T^2$ (in the "intermediate"-temperature region indicated above) or even $C \sim T$ (at "high" temperatures). According to [5], the quadratic dispersion relation typical of bending waves can make a certain contribution to the "acceleration" of the increase in the value of χ with temperature. In this case, the generally accepted assumption concerning the constancy of the group velocity of the propagation of phonons no longer holds and this velocity increases with temperature.

In our opinion, another possible reason for the accelerated growth in the thermal conductivity in LCs could be the specific behavior of the Grüneisen parameter typical of bending vibrations. Figure 1c shows the temperature dependence of the Grüneisen parameter $\gamma_\parallel$ for graphite, which was determined on the basis of experimental data on the heat capacity, thermal expansion coefficient, and elastic constants [15–17]. Since the phonon mean free path in the case of phonon scattering from dislocations is inversely proportional to the square of the Grüneisen parameter, the sharp decrease in the absolute value of the Grüneisen parameter $\gamma_\parallel$ upon an increase in temperature (according to [18], $\gamma_\parallel(T) = -A/T + B$ for the intermediate temperature range) in the case of this scattering mechanism, which is most probable in the given temperature range, can be manifested in a much faster increase in the value of χ with temperature than for the heat capacity.

It should also be noted that the temperature range in which the value of χ increases corresponds completely to the region in which bending vibrations play a dominating role in the behavior of both the heat capacity and thermal expansion. This can be seen most clearly from the thermal expansion $\alpha_\parallel(T)$ curve, where the contribution from other branches becomes noticeable at temperatures higher than 250–300 K [peak of $\chi(T)$], which is manifested in an increase in the values of $\alpha_\parallel$ (Fig. 1b).

The most interesting problem concerns the participation of bending waves in umklapp processes. It is well known [6] that the quadratic dispersion relation for bending waves makes the participation of only the bending branch in phonon–phonon scattering processes possible. If this situation is indeed realized, umklapp processes will lead to an exponential decrease in the thermal conductivity [$\sim\exp(\Theta/bT)$] with a peculiar value of coefficient b ($b \approx 1$), in contrast to the value $b \approx 2$ usually observed in LCs [6]. According to the authors of [6], this is valid for graphite, boron nitride, PbI_2, and In_4Se_3. A detailed analysis of experimental results on the exponential decrease in thermal conductivity in graphite [9, 10] proved that $b \approx 2$. A similar result was obtained from an analysis of the temperature dependence of the thermal conductivity of boron nitride [12].

In addition, in accordance with [6], the region of peculiar decay in the thermal conductivity (with $b = 1$) must correspond to the temperature region in which the heat capacity of LCs increases linearly with temperature due to the fact that the main contribution comes from the bending branch. This temperature region in graphite lies between 100 and 250 K [15], which is much lower than the region of exponential decay of the thermal conductivity.

Finally, it was proved above that the bending branch dominates in the thermal properties of graphite up to temperatures of ~250 K, after which the role of other acoustic vibrations (in particular, intralayer vibrations) becomes significant.

Thus, the decisive role of bending vibrations in the umklapp processes in graphite (as well as in boron nitride) is disputable. Apparently, the processes of phonon–phonon interaction involving only the phonons of the bending branch are ineffective; these processes are, however, allowed by conservation laws [6].

3. THERMAL CONDUCTIVITY OF GaS AND GaSe

Figure 2 shows the temperature dependences of the thermal conductivity of LCs GaS and GaSe. Thermal conductivity was measured using the steady-state method [19]. The error in measurement did not exceed 5%. Monocrystalline samples were cut in the shape of a parallelepiped with a cross-sectional area up to 0.2 cm^2 and a length of 2–3 cm.

It can be seen from Fig. 2 that the thermal conductivity in both crystals is characterized by the following features.

(1) The thermal conductivity is anisotropic: the thermal conductivity $\chi_\parallel$ in the direction perpendicular to the layers is much smaller than the thermal conductivity $\chi_\perp$ in the plane of the layers. At the same time, the anisotropy in the thermal conductivity of GaS and GaSe is

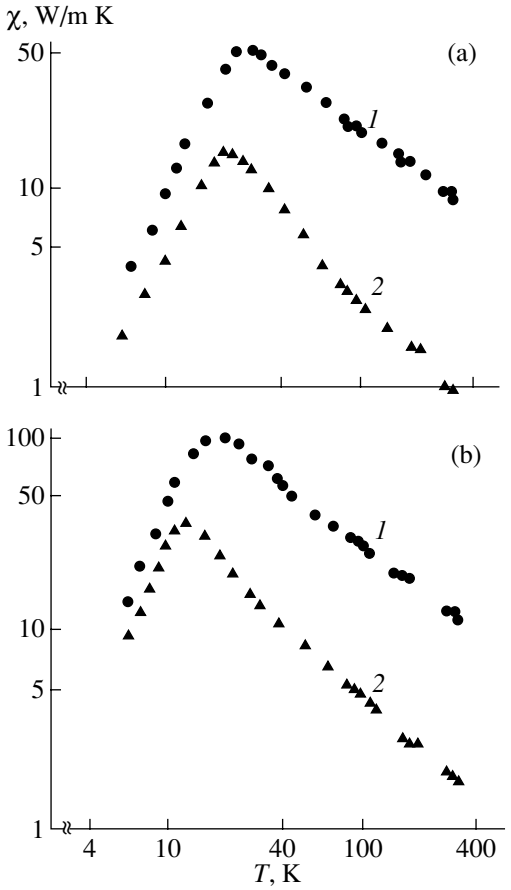

Fig. 2. Temperature dependences of the thermal conductivity of layered crystals: (a) GaS in the plane of the layers, $\chi_{\parallel}$ (curve *1*), and perpendicular to the layers, $\chi_{\perp}$ (curve *2*); and (b) GaSe in the plane of the layers, $\chi_{\parallel}$ (curve *1*), and perpendicular to the layers, $\chi_{\perp}$ (curve *2*).

considerably lower than that in graphite and decreases with temperature.

(2) The temperature dependences of the thermal conductivities $\chi_{\parallel}$ and $\chi_{\perp}$ in the region where their values increase with temperature obey the following power laws: $\chi_{\parallel} \sim T^{2.4 \pm 0.1}$ and $\chi_{\perp} \sim T^{2.1 \pm 0.1}$ in GaS and $\chi_{\parallel} \sim T^{2.5 \pm 0.1}$ and $\chi_{\perp} \sim T^{2.2 \pm 0.1}$ in GaSe.

(3) In the region where the thermal conductivity decreases with increasing temperature, χ follows the exponential law from Eq. (1) over a wide range of temperatures.

As in the case of graphite, the occurrence of anisotropy in the thermal conductivity of GaS and GaSe cannot be explained in terms of peculiarities in the acoustic spectrum and can be interpreted only by taking into account the peculiarities of scattering of charge carriers from the defects typical of LCs.

It can be seen that a peculiar increase in the thermal conductivity is typical not only of graphite but also of GaS and GaSe. It should be recalled that the mechanism proposed in [5] for explaining the thermal anomaly in graphite is based to a considerable extent on the quadratic dispersion relation for bending vibrations. It was noted above that when discussing the role of bending vibrations, we must keep in mind that GaS and GaSe exhibit, weak anisotropy. In particular, the quadratic dispersion relation was not observed for transverse acoustic waves propagating in the plane of the layers in GaSe (as well as in InSe, In_4Se_3, PbI_2, CdI_2, etc.), while only a slight deviation from linearity was observed in [20] for GaS.

Nevertheless, the temperature intervals in which the behavior of heat capacity corresponds to the predictions made in [1] were observed for all LCs listed above. For example, for GaS, the temperature intervals in which $C \sim T^2$ and $C \sim T$ are 27–37 K and 70–120 K, respectively. Thus, in contrast to graphite, the regions of peculiar behavior of thermal conductivity of GaS are above the thermal-conductivity peak, while the region in which the thermal conductivity increases corresponds to the temperature range in which $C(T) \sim T^{2-3}$. Therefore, it is reasonable, in our opinion, to assume that there is no thermal anomaly in GaS at all. This also completely applies to GaSe. Thus, the increase in the thermal conductivity of LCs GaS and GaSe with temperature, described by the law $\sim T^{2+x}$, is associated with the corresponding increase in the heat capacity of these crystals with temperature.

Let us now consider the temperature variation of the thermal conductivity of GaS and GaSe in the region of exponential decay and take into account the fact that this region corresponds to the temperature range in which the heat capacity of GaSe and GaS (as well as In_4Se_3 and PbI_2 [6]) increases according to the laws $C \sim T^2$ and $C \sim T$ (see above). A meticulous graphic analysis of $\chi_{\parallel}(T)$ in GaS and GaSe using Eq. (1) and the data on the temperature dependences of heat capacity in these crystals [21, 22] revealed that the value of Θ/b is approximately equal to 110 for GaS and 65 for GaSe. Since the results of the publications mentioned above show that the Debye temperature $\Theta_D \sim 260$ K for GaS [21] and $\Theta_D \sim 190$ K for GaSe [22], we can conclude with confidence that the value of constant b exceeds 2 both for GaS and GaSe. Taking into account the results of calculations made in [6] concerning the possibility of umklapp processes involving three phonons belonging only to the bending branch of the acoustic vibration spectrum, according to which b must be approximately equal to unity, we can state that the effectiveness of these processes in GaS and in GaSe is low, as in the case of graphite and boron nitride.

As regards the LCs In_4Se_3 and PbI_2 studied in [6], the role of bending vibrations in these crystals (which are even less anisotropic than GaS and GaSe) is rather questionable.

4. CONCLUSIONS

Thus, an analysis of the results of investigation into the thermal conductivity of layered crystals, together with an investigation of heat capacity and thermal expansion, revealed that bending vibrations determining the temperature variation of heat capacity and thermal expansion of LCs at low temperatures can determine the behavior of the thermal conductivity of LCs only in the region where this conductivity increases with temperature. The effects of phonon–phonon interaction involving phonons of the bending branch have only a low probability. Even in the most anisotropic LC graphite (and boron nitride), umklapp processes become effective only in the case of excitation of high-frequency acoustic vibrations corresponding to other branches of the acoustic spectrum of this crystal.

REFERENCES

1. I. M. Lifshitz, Zh. Éksp. Teor. Fiz. **22** (4), 475 (1952).
2. É. E. Anders, B. Ya. Sukharevskiĭ, and L. S. Shestachenko, Fiz. Nizk. Temp. **5** (7), 783 (1979) [Sov. J. Low Temp. Phys. **5**, 373 (1979)].
3. G. L. Belen'kiĭ, R. A. Suleĭmanov, N. A. Abdullaev, and V. Ya. Shteĭnshraĭber, Fiz. Tverd. Tela (Leningrad) **26** (12), 3560 (1984) [Sov. Phys. Solid State **26**, 2142 (1984)].
4. R. A. Suleymanov and N. A. Abdullayev, Carbon **31** (7), 1011 (1993).
5. B. T. Kelly, Philos. Mag. **15**, 1005 (1967).
6. É. E. Anders, I. V. Volchok, and B. Ya. Sukharevskiĭ, Fiz. Nizk. Temp. **4** (9), 1202 (1978) [Sov. J. Low Temp. Phys. **4**, 566 (1978)].
7. N. A. Abdullaev, M. A. Aldzhanov, and É. M. Kerimova, Fiz. Tverd. Tela (St. Petersburg) **44** (2), 213 (2002) [Phys. Solid State **44**, 221 (2002)].
8. C. A. Klein and M. G. Holland, Phys. Rev. **136**, A575 (1964).
9. R. Taylor, Philos. Mag. **13**, 157 (1966).
10. A. I. Lutkov, V. I. Volga, B. K. Dymov, *et al.*, Neorg. Mater. **8** (8), 1409 (1972).
11. E. K. Sichel, R. E. Miller, M. S. Adrahams, and C. J. Buiocchi, Phys. Rev. B **13** (10), 4607 (1976).
12. A. Simpson and A. D. Stuckes, J. Phys. C **4** (13), 1710 (1971).
13. J. M. Ziman, *Electrons and Phonons* (Clarendon, Oxford, 1960; Inostrannaya Literatura, Moscow, 1962).
14. G. L. Belen'kiĭ, N. A. Abdullaev, V. N. Zverev, and V. Ya. Shteĭnshraĭber, Pis'ma Zh. Éksp. Teor. Fiz. **47** (10), 498 (1988) [JETP Lett. **47**, 584 (1988)].
15. W. DeSorbo and W. W. Tyler, J. Chem. Phys. **21** (5), 1660 (1953).
16. A. C. Bailey and B. Yates, J. Appl. Phys. **41** (13), 5088 (1970).
17. W. B. Gauster and I. J. Fritz, J. Appl. Phys. **45** (8), 3309 (1974).
18. N. A. Abdullaev, Fiz. Tverd. Tela (St. Petersburg) **43** (4), 697 (2001) [Phys. Solid State **43**, 727 (2001)].
19. M. A. Aldzhanov, K. K. Mamedov, A. B. Abdullaev, and S. A. Aliev, Fiz. Tverd. Tela (Leningrad) **27**, 284 (1985) [Sov. Phys. Solid State **27**, 174 (1985)]; M. A. Aldzhanov, M. D. Nadzhafzade, and Z. Yu. Seidov, Fiz. Tverd. Tela (St. Petersburg) **41** (1), 24 (1999) [Phys. Solid State **41**, 20 (1999)].
20. B. M. Powell, S. Iandl, I. L. Brebner, and F. Levy, J. Phys. C **10** (16), 3039 (1977).
21. K. K. Mamedov, M. A. Aldzhanov, I. G. Kerimov, and M. I. Mekhtiev, Fiz. Tverd. Tela (Leningrad) **19** (5), 1471 (1977) [Sov. Phys. Solid State **19**, 857 (1977)].
22. K. K. Mamedov, M. A. Aldzhanov, I. G. Kerimov, and M. I. Mekhtiev, Fiz. Tverd. Tela (Leningrad) **20** (1), 42 (1978) [Sov. Phys. Solid State **20**, 22 (1978)].

Translated by N. Wadhwa

Physics of the Solid State, Vol. 44, No. 10, 2002, pp. 1864–1868. Translated from Fizika Tverdogo Tela, Vol. 44, No. 10, 2002, pp. 1780–1784.

SEMICONDUCTORS AND DIELECTRICS

Nonempirical Quantum-Chemical Calculation of the Electric Field Gradient at the ^{51}V Nucleus Sites in Alkali Metavanadates

L. S. Vorotilova, L. V. Dmitrieva, S. A. Lavrov, and B. F. Shchegolev

Grebenshchikov Institute of Silicate Chemistry, Russian Academy of Sciences, ul. Odoevskogo 24/2, St. Petersburg, 199155 Russia

Received December 6, 2001

Abstract—The electric-field gradient tensor at the vanadium nucleus site was calculated *ab initio* within a cluster model for chained vanadates XVO$_3$ (X = Li, Na, K). A comparison with experiment showed that it suffices to consider only small $(VO_4)^{3-}$ and $(V_3O_{10})^{5-}$ clusters in crystals of this type. The calculation scheme stability with respect to increasing cluster size was analyzed. © *2002 MAIK "Nauka/Interperiodica".*

1. INTRODUCTION

Currently, correct calculation of the NMR spectrum parameters for quadrupole nuclei in crystals within the quantum-chemical cluster models is an urgent problem. Earlier [1, 2], we showed that, when correctly chosen basis functions and sufficiently accurate structural data are used, the results fit experimental spectra well for ^{27}Al and ^{47,49}Ti nuclei in oxygen octahedra. The GAMESS [3] and GAUSSIAN-94 codes were used for these cluster nonempirical calculations.

It is of interest to extend this calculation procedure to oxygen-containing compounds of vanadium, since vanadium oxides and vanadates have been much studied using NMR. Furthermore, new compounds containing vanadium–oxygen complexes have been synthesized in recent years. These compounds are characterized by unique properties and are promising for application in various fields of engineering. Of particular interest are NaV_2O_5, CaV_2O_5, and MgV_2O_5 vanadium oxides because of their low-temperature magnetic properties and phase transitions [4, 5]; some mixed vanadates with high ionic conduction are also of interest [6].

As a rule, the coordination state of V^{5+} ions in the oxygen environment is the VO_4 tetrahedron or the VO_5 trigonal bipyramid, which can form simple or double chains, layers, and other more complex structures.

In this paper, we consider XVO$_3$ (X = Li, Na, K) crystals containing infinite simple chains of VO_4 tetrahedra. This study was aimed at *ab initio* calculations (and comparison of the results with available experimental data) of the electric field gradient (EFG) at the vanadium nucleus site for various clusters and various V and O basis functions. The small contribution from the lattice surrounding the cluster to the EFG was neglected by analogy with [1, 2].

2. STRUCTURAL MODELS AND CALCULATION PROCEDURE

Alkali metavanadates X^+VO_3 (X^+ = Li$^+$, Na$^+$, K$^+$) are characterized by a chained structure (Fig. 1). Alkali cations occupying sites of two types are arranged between

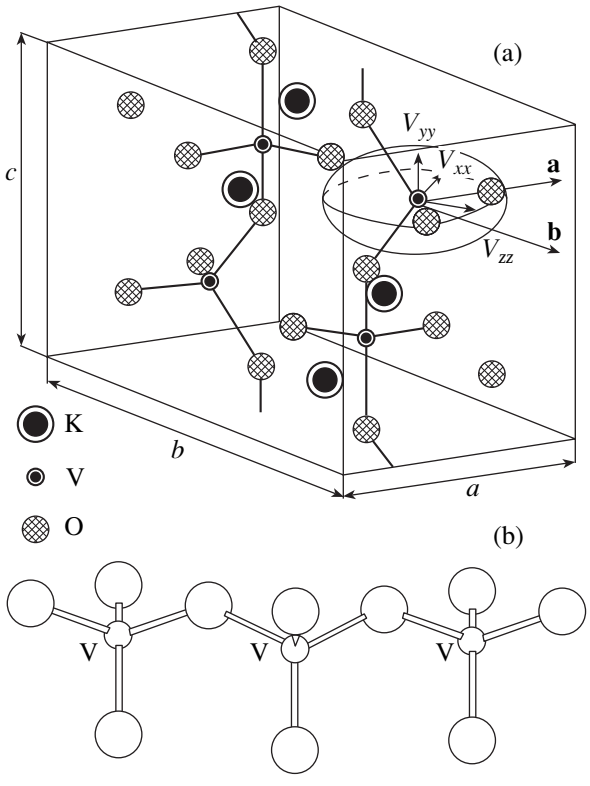

Fig. 1. Structure of the KVO_3 crystal: (a) the unit cell and the EFG tensor orientation at the ^{51}V site and (b) the $(V_3O_{10})^{5-}$ cluster.

1063-7834/02/4410-1864$22.00 © 2002 MAIK "Nauka/Interperiodica"

Table 1. Structural parameters of XVO_3 crystals

Compound	Unit cell parameters, Å	V–O bond lengths, Å	References
$LiVO_3$	a = 10.158	1.6279; 1.6617;	[7]
	b = 8.417 (γ = 110.5°)	1.7638; 1.8480	
	c = 5.885		
$NaVO_3$	a = 10.557	V1: 1.6249; 1.6442;	[8]
	b = 9.469 (γ = 108.4°)	1.8045; 1.8102	
	c = 5.880	V2: 1.6467; 1.6665; 1.7942; 1.8126	
KVO_3	a = 5.176	1.6296; 1.6432;	[9]
	b = 10.794	1.8062 × 2	
	c = 5.680		

the chains formed by VO_4 tetrahedra sharing common vertices. Lithium and sodium metavanadates[1] belong to space symmetry groups $C12/c1$ [7] and $C1c1$ [8] (monoclinic system), and potassium metavanadate belongs to *Pbcm* (orthorhombic) [9]. The V–O bond lengths in the tetrahedra are given in Table 1.

The EFG at ^{51}V nucleus sites was calculated for charged clusters of two types: a cluster of minimum size $(VO_4)^{3-}$, consisting of one tetrahedron with the bond lengths given in Table 1, and an extended cluster $(V_3O_{10})^{5-}$, containing three neighboring tetrahedra. In the latter case, the EFG was calculated at the central vanadium nucleus site. In general, because of the absence of symmetry elements at the vanadium site, the EFG tensor and the quadrupole interaction tensor have an arbitrary orientation with respect to the crystallographic axes. Therefore, in order to compare calculations with the experimental data, a code representing the EFG tensor in the crystallographic axes has to be employed. All the calculations were carried out using the GAMESS code [3] following the nonempirical MO LCAO SCF (Hartree–Fock–Roothaan) method.

Special emphasis was placed on the choice of basis functions for vanadium and oxygen atoms. For vanadium, the atomic basis (13S7P5D) [10] was checked, which, in combination with the triple-zeta basis for oxygen, was advantageously employed in cluster calculations of nucleus magnetic properties of another transition element, titanium located in an oxygen octahedron [2]. However, in the case under consideration (vanadium in the oxygen tetrahedron), the best results were achieved when using (for both V and O) built-in sets of the triple-zeta-type basis functions complemented by built-in polarization and diffusion functions (6 – 311 + +G(d)).

[1] Only the α-$NaVO_3$ modification was considered.

3. RESULTS OF CLUSTER CALCULATIONS

3.1. KVO_3

The vanadium atoms in potassium metavanadate are located in the symmetry plane perpendicular to the crystal axis **c**. Therefore, two principal axes of the EFG tensor lie in the crystalline plane **ab,** while the third axis is parallel to the axis **c**. Experiment [11] and calculations show that this third axis is the principal axis of the tensor **Y** (see Tables 2, 3). The tensor parameters calculated even for the cluster of minimum size $(VO_4)^{3-}$ have quite reasonable values. In the case of the extended cluster $(V_3O_{10})^{5-}$, the fit is improved: the differences in the tensor components and in the axis orientation in the plane **ab** between the calculations and experiment decrease to 10% and 4°, respectively (see Tables 2, 3).

Table 2. Calculated EFG tensor parameters at the ^{51}V site for XVO_3

Compound, cluster	V_{zz}, au	η	Euler angles, deg
$LiVO_3$			
$(VO_4)^{3-}$	0.3156 (3.70)*	0.55	90, 90, 46
$(V_3O_{10})^{-5}$	0.1915 (2.23)	0.78	87, 84, 70
$NaVO_3$			
$(VO_4)^{3-}$ (1)	0.3299 (3.87)	0.99	85, 80, 32
$(VO_4)^{3-}$ (2)	0.2709 (3.18)	0.81	79, 81, 24
$(V_3O_{10})^{5-}$ (1)	0.2267 (2.78)	0.91	74, 63, 42
KVO_3			
$(VO_4)^{3-}$	0.4543 (5.33)	0.48	90, 75, 0
$(V_3O_{10})^{5-}$	0.3275 (3.84)	0.58	90, 48, 0

* The values in parentheses are the quadrupole interaction constants C_Q (MHz) calculated for $Q = 0.05b$.

Table 3. Experimental [11–16] parameters of the tensor eQV_{ik}/h for ^{51}V in vanadates XVO_3

Compound	T, K	C_Q, MHz	η	Euler angles, deg	References
$LiVO_3$					
Single crystal	300	3.58 (3)	0.34 (3)	74, 67, 46	[12]
		3.30	0.82	98, 72, 47	[15]
Polycrystal (MAS NMR)	300	3.18 (7)	0.87		
$NaVO_3$					
Single crystal	77	3.70 (5)	0.52 (2)	79, 62, 41	[13]
Polycrystal (MAS NMR)	300	3.80 (10)	0.46 (4)		[15]
Polycrystal (NQR)	300	3.745 (3)	0.489 (3)		[16]
KVO_3					
Single crystal	300	4.22 (15)	0.65 (15)	90, 52, 0	[11]
Polycrystal (MAS NMR)	300	4.20 (10)	0.80 (5)		[15]
Polycrystal	77	4.16 (10)	0.87 (3)		[14]
Polycrystal (NQR)	300	4.201 (2)	0.794 (1)		[16]

3.2. $NaVO_3$ and $LiVO_3$

As indicated above, lithium and sodium metavanadates are characterized by monoclinic symmetry. All vanadium atoms in $LiVO_3$ are structurally equivalent, while there are two nonequivalent positions of vanadium in $NaVO_3$. The orthogonal coordinate axes (x, y, z) were chosen in the calculations to coincide with the crystal rotation axes (**a***, **b**, **c**) from the experiments performed in [12, 13]:

$$x \parallel \mathbf{a}^*, \quad y \parallel \mathbf{b}, \quad z \parallel \mathbf{c},$$

where **b** and **c** are the crystallographic axes and **a*** is perpendicular to the **bc** plane.

Table 2 lists the principal values of the EFG tensor at the ^{51}V sites, the asymmetry parameters, and the Euler angles between the principal tensor axes X, Y, Z and the crystal rotation axes **a***, **b**, **c** for $NaVO_3$ and $LiVO_3$. One can see that the EFG calculations for the two nonequivalent positions of ^{51}V in sodium metavanadate yield tensor parameters that are close in both magnitude and orientation. The tensors for the two positions cannot be distinguished experimentally; therefore, an average tensor is given in [13, 15].

A comparison of the calculated and experimental data for sodium metavanadate (Table 3) shows that the minimum-cluster $(VO_4)^{3-}$ model more adequately describes the quadrupole coupling constant, while the extended-cluster $(V_3O_{10})^{5-}$ model gives the orientation of the tensor principal axes to a higher degree of accuracy (1°–5°). The agreement between the calculated asymmetry parameter and its experimental value is appreciably worse. Similar results were also obtained for lithium metavanadate: the cluster size does not affect the fit appreciably (see Tables 2, 3).

4. EXPERIMENTAL PARAMETERS OF THE QUADRUPOLE TENSOR eQV_{ik}/h FOR NUCLEI ^{51}V IN XVO_3

The components of the quadrupole splitting tensor for vanadium in vanadates can be determined from NMR spectra of both single crystals and polycrystalline samples. However, the results obtained on single crystals are more appropriate for comparing with calculation, since these results contain information not only on the principal values of the EFG tensor but also on the orientations of its principal axes. This is also important from the viewpoint of cluster choice and when the general applicability of the model under study is tested for use in describing the quadrupole interaction between ^{51}V nuclei and the crystal EFG. Thus, we based our results, for the most part, on those from [11–13], where $LiVO_3$, $NaVO_3$, and KVO_3 single crystals were studied using a stationary method at low frequencies. The low-frequency (low-magnetic-field) conditions allowed us to neglect the chemical-shift tensor when calculating the quadrupole parameters.

As an example, Fig. 2 displays the orientational dependence of the position of side lines for nuclei ^{51}V and ^{23}Na in $NaVO_3$ on the rotation of the crystal about the axis **b** (the vector $\mathbf{H}_0$ was rotated in the **ac** plane through 180°). Since the ^{51}V spin is 7/2, there are three satellite pairs: $\pm 3/2 \longleftrightarrow \pm 1/2$, $\pm 5/2 \longleftrightarrow \pm 3/2$, and $\pm 7/2 \longleftrightarrow \pm 5/2$. The spectrum of ^{23}Na (spin 3/2) consists of one satellite pair $\pm 3/2 \longleftrightarrow \pm 1/2$ in addition to the central line; however, this nucleus can occupy two inequivalent crystallographic sites with different splitting parameters. Therefore, two different sodium spectra are observed.

Study of the orientational dependences of the resonance line position in three mutually perpendicular planes makes it possible to determine the principal val-

ues of the eQV_{ik}/h tensor and the direction cosines of the principal axes through diagonalization of the initial nondiagonal tensor [13]. The results are given in Table 3.

Table 3 also includes the eQV_{ik}/h tensor parameters independently determined in vanadates from spectra measured in strong fields upon rotation at the magic angle [15]. The values of $C_Q \equiv eQV_{zz}/h$ and η are close to the measurements on single crystals; an appreciably different constant C_Q for $NaVO_3$ was observed only in one work [6]. Taking into account that close values of C_Q and η were obtained at room temperature and 77 K, it can be concluded that no phase transitions exist in this temperature range. This conclusion is also confirmed by the ^{23}Na spectra.

5. DISCUSSION

A comparison of the experimental results for ^{51}V nuclei in alkali metavanadates and the calculated EFG tensor parameters has shown that the calculation procedure employed is sufficiently advantageous as applied to these compounds. Indeed, even a small-cluster model consisting of a single tetrahedron gives the correct orientation of the principal axes and a splitting constant C_Q close to the experimental value. For an extended cluster up to three tetrahedra, the corrections to the parameters are small, as a rule (Table 2), which indicates that this calculation scheme is stable. Some differences in the behavior of the parameters as the cluster grows can be detected when comparing monoclinic $LiVO_3$ and $NaVO_3$ crystals and orthorhombic KVO_3: when passing to a larger cluster, all tensor parameters for potassium vanadate simultaneously approach their experimental values.

The rather good agreement between the calculated and experimental quadrupole tensor parameters and its orientation allowed us to uniquely determine the EFG tensor in lithium metavanadate crystals. Because of the presence of twins in these crystals, the diagonalization of the tensor eQV_{ik}/h yielded two possible sets of parameters (Table 3). Comparing them with the calculated values, it can be concluded that C_Q = 3.30 MHz and η = 0.82 are the most probable values.

Since the vanadium–oxygen tetrahedra in the crystals under study differ in the V–O bond lengths only weakly (Table 1), the values of the quadrupole constant C_Q lie in a narrow range of 3–4 MHz. The values of the parameter η indicate that the symmetry differs strongly from being axial. It may be noted that the EFG principal axis makes an angle close to 90°, with the crystallographic axis **c** directed along the chain (this angle is equal to 90° in KVO_3). Thus, the direction of the principal axis of the field gradient in chained vanadates is controlled not by long bridge bonds (of length ~1.8 Å) but by shorter cross bonds (of length ~1.65 Å).

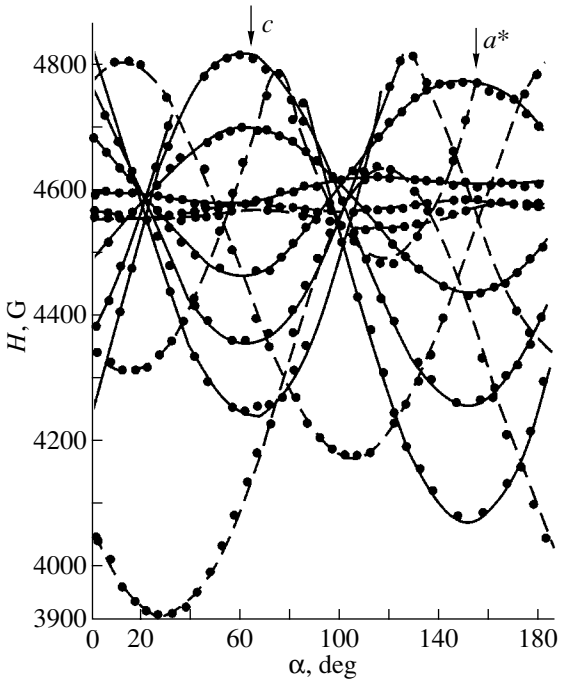

Fig. 2. Orientational dependence of the ^{51}V and ^{23}Na resonance line positions on rotation of the magnetic field vector $\mathbf{H}_0$ in the **ac** plane. Solid curves correspond to the central and side lines of the ^{51}V spectrum, and dashed curves are related to the spectra of ^{23}Na in two inequivalent positions.

We note that the calculated parameter η differs appreciably from the experimental one. Probably, the neglect of the cluster neighborhood, i.e., alkali cations, produces the basic effect on η. Disagreement can also be caused by an inaccuracy in the determination of the structural parameters; as is known, the asymmetry parameter of the EFG tensor is most sensitive to small deviations in atom coordinates.

In summary, it can be inferred that the technique described above is also applicable to other compounds with tetrahedral complexes VO_4. This is of particular interest when the experimental NMR spectra do not yield a complete set of parameters.

ACKNOWLEDGMENTS

We would like to thank V.S. Kasperovich for helpful discussions.

This study was supported in part by the RF Program "Integration" (project no. A0147) and the Russian Foundation for Basic Research (project no. 00-02-16919).

REFERENCES

1. L. S. Vorotilova, B. F. Shchegolev, and L. V. Dmitrieva, Fiz. Tverd. Tela (Leningrad) **33** (5), 1527 (1991) [Sov. Phys. Solid State **33**, 861 (1991)]; L. S. Vorotilova,

L. V. Dmitrieva, O. E. Kvyatkovskiĭ, and B. F. Shchegolev, Fiz. Tverd. Tela (St. Petersburg) **39** (4), 618 (1997) [Phys. Solid State **39**, 540 (1997)].

2. L. S. Vorotilova, L. V. Dmitrieva, and B. F. Shchegolev, Fiz. Tverd. Tela (St. Petersburg) **42** (8), 1408 (2000) [Phys. Solid State **42**, 1447 (2000)].
3. M. W. Schmidt, K. K. Baldridge, J. A. Boatz, *et al.*, J. Comput. Chem. **14** (11), 1347 (1993).
4. M. Isobe and Y. Ueda, J. Phys. Soc. Jpn. **65** (5), 1178 (1996); N. Katoh, J. Phys. Soc. Jpn. **68** (1), 258 (1999).
5. M. A. Korotin, V. I. Anisimov, T. Saha-Dasgupta, and I. Dasgupta, J. Phys.: Condens. Matter **12** (2), 113 (2000).
6. F. Delmaire, M. Rigole, E. A. Zhilinskaya, *et al.*, Phys. Chem. Chem. Phys. **2** (19), 4477 (2000).
7. R. D. Shannon and C. Calvo, Can. J. Chem. **51**, 265 (1973).
8. A. M. Shaikh, Ferroelectrics **107**, 219 (1990).
9. F. C. Hawthorrne and C. Calvo, J. Solid State Chem. **22** (2), 157 (1977).
10. I. Hyla-Kryspin, J. Demuynck, A. Strich, and M. Benard, J. Chem. Phys. **75** (8), 3954 (1981).
11. S. D. Gornostansky and S. V. Stager, J. Chem. Phys. **46** (3), 4959 (1967).
12. L. V. Dmitrieva, Z. N. Zonn, and G. A. Rump, Zh. Strukt. Khim. **14** (1), 30 (1973).
13. L. V. Dmitrieva, A. P. Vereshchagina, Z. N. Zonn, and V. A. Panteleev, in *Nuclear Magnetic Resonance* (Leningr. Gos. Univ., Leningrad, 1974), Vol. 5, p. 68.
14. S. L. Segel and R. B. Creel, Can. J. Phys. **48** (21–22), 2673 (1970).
15. J. Skibsted, N. Chr. Nielsen, H. Bildsoe, and H. J. Jakobsen, J. Am. Chem. Soc. **115** (16), 7351 (1993).
16. D. Mao, P. J. Bray, and G. L. Petersen, J. Am. Chem. Soc. **113** (18), 6812 (1991).

Translated by A. Kazantsev

Physics of the Solid State, Vol. 44, No. 10, 2002, pp. 1869–1879. Translated from Fizika Tverdogo Tela, Vol. 44, No. 10, 2002, pp. 1785–1794.

SEMICONDUCTORS AND DIELECTRICS

Second Harmonic Generation and Rectification of Space-Charge Waves in Photorefractive Crystals

V. V. Bryksin and M. P. Petrov

Ioffe Physicotechnical Institute, Russian Academy of Sciences, Politekhnicheskaya ul. 26, St. Petersburg, 194021 Russia

Received December 19, 2001; in final form, January 17, 2002

Abstract—A theory explaining the effects of second harmonic generation and rectification of space-charge waves (SCWs) in both space and time in photorefractive crystals and semi-insulating semiconductors is formulated for the first time. The theory predicts two mechanisms of SCW second harmonic excitation. An experimental technique is proposed for second harmonic detection, and the formulas required for interpreting the experimental results are derived. It is found that the effect of complete rectification of SCWs may lead to a change in the current passing through the sample by tens of percent. The results of calculations are in qualitative agreement with preliminary experimental results. © *2002 MAIK "Nauka/Interperiodica".*

1. INTRODUCTION

Space-charge waves (SCWs) can emerge in photorefractive crystals (or semi-insulating semiconductors, in general) placed in an external electric field [1]. Such waves are sometimes referred to as "trap charge-exchange waves" [1], "photorefractive waves" [2], or "photorefractons." Space-charge waves are characterized by a peculiar dispersion relation: their frequency is inversely proportional to the wave vector. As a rule, SCWs attenuate quite rapidly; their lifetime is comparable to the period of natural oscillations.

Progress in the experimental investigation of SCWs is determined to a considerable extent by the choice of the method of their excitation and detection. One of the most effective methods of SCW generation is optical excitation by producing a periodic (sinusoidal) interference pattern oscillating near the equilibrium position in the crystal. In this case, if the period of the interference pattern coincides with the spatial period of an SCW and the frequency of oscillations of the interference pattern also coincides with the eigenfrequency of the given wave, resonance SCW excitation that is easily detectable by optical methods [2] takes place.

For relatively small values of the contrast m of the interference pattern ($m \ll 1$), the effects under investigation are linear in nature. In this case, the oscillating fields and currents in the sample are linear functions of m. However, for large values of m (comparable to unity), nonlinear effects leading to the emergence of fields and currents proportional to the second and higher powers of m become significant. Nonlinearity emerges because new charge carriers excited by light experience the action of not only the electric field applied to the sample but also of the fields of static and dynamic charge gratings that have formed by this time.

Second-order effects (proportional to m^2) in a system of SCWs can be considered in terms of their interaction with each other and scattering from static gratings if the latter are formed for the chosen method of SCW excitation (e.g., excitation by an oscillating interference pattern). The interaction between SCWs resembles, to a certain extent, some second-order nonlinear effects in optics, e.g., second harmonic generation and optical rectification. It should be recalled that, in nonlinear optics, the contribution to the second-order nonlinear susceptibility $\chi^{(2)} \propto \mathbf{A} \cdot \mathbf{A}$ (where $\mathbf{A}$ is the complex amplitude of the wave) is responsible for the generation of waves with a doubled wave vector and doubled frequency of oscillations, while the contribution $\chi^{(2)} \propto \mathbf{A} \cdot \mathbf{A}^* = \text{const}(x, t)$ (independent of x and t) is responsible for optical rectification. Optical rectification results in the formation of a static uniform electric field in the sample (uniform polarization); i.e., both temporal and spatial rectification of optical oscillations take place. To our knowledge, the problem of second harmonic generation and rectification of SCWs has not been discussed in the literature.

This study aims at a rigorous theoretical analysis of these phenomena and the methods of their detection. We propose that an oscillating interference pattern be used for exciting SCWs. The numerical estimates given at the end of this paper show that SCW rectification is a strong effect causing strong (tens of percent) changes in the direct current passing through the sample. Some preliminary results were reported in [3].

2. CALCULATION OF INDUCED FIELD

Conditions of excitation and the method of SCW analysis considered below are similar to those described in [2, 4, 5]. The diagram of optical excitation is shown in Fig. 1.

A crystal is illuminated by coherent laser beams, one of which is phase-modulated with frequency Ω and

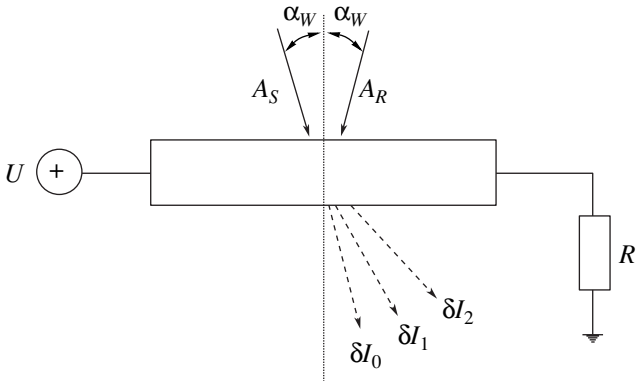

Fig. 1. Diagram of excitation of space-charge waves and recording of zeroth (δI_0), first (δI_1), and second (δI_2) non-Bragg diffraction peaks for the A_S beam. The beams δI_0, δI_1, and δI_2 are directed at the angles α_W, $3\alpha_W$, and $5\alpha_W$, respectively.

amplitude Θ. As a result, the intensity of light incident on the crystal has the form

$$W(x, t) = W_0[1 + m\cos(K_g x + \Theta\cos\Omega t)]. \quad (1)$$

Here,

$$W_0 = W_1 + W_2, \quad (2)$$

W_1 and W_2 are the intensities of the recording beams,

$$m = \frac{2\sqrt{W_1 W_2}}{W_1 + W_2} \quad (3)$$

is the interference pattern contrast, and $K_g = 2\pi/\Lambda$, Λ being the period of the interference pattern. In the case of symmetric excitation, we have

$$\Lambda = \lambda_W/(2\sin\alpha_W), \quad (4)$$

where λ_W is the wavelength of the recording light beam and α_W is the angle of incidence of the recording beams.

In order to calculate the internal induced field $E(x, t)$, we use the standard system of nonlinear differential equations [6] (see also [4, 5])

$$\frac{n(x, t)}{\tau} - \frac{1}{e}\frac{\partial j(x, t)}{\partial x} = g(x, t), \quad (5)$$

$$j(x, t) = e\mu n(x, t)[E_0 + E(x, t)], \quad (6)$$

$$\frac{\varepsilon}{4\pi}\frac{\partial E(x, t)}{\partial t} + j(x, t) = I(t), \quad (7)$$

where $j(x, t)$ is the nonuniform density of ohmic current, $n(x, t)$ is the concentration of photoelectrons, τ is the lifetime of photoelectrons in the conduction band, μ is the mobility of photoelectrons, ε is the static permittivity, E_0 is the electric field defined as $E_0 = U/L$ (U is the voltage supplied by a source and L is the distance between the electrodes), and $I(t)$ is the current density in the external circuit, which is defined as the ratio of the total current in the external circuit to the cross-sectional area S of the sample. In Eq. (6), we have omitted the contribution from diffusion processes since we assume that the diffusion contribution to the current can be disregarded in the case of large E_0 and comparatively small K_g.

Equations (5)–(7) are usually supplemented with the condition $\int_0^L E(x, t)dx = 0$ [6], which indicates the absence of a uniform electric field induced by the formed space-charge grating. This is quite justified if the circuit contains no resistances connected in series with the sample. Such resistances include the actual load resistance (shown in the diagram in Fig. 1), the internal resistance of the source, and a possible auxiliary resistance at the crystal–electrode boundaries. In our analysis, all these possible sources of resistance are taken into account by including an effective load resistance R in the circuit. We will solve the system of equations (5)–(7) under the additional condition

$$\frac{1}{L}\int_0^L dx E(x, t) = -I(t)\rho, \quad (8)$$

where $\rho = RS/L$. In fact, condition (8) implies a decrease in the applied field in the bulk of the sample as compared to E_0 (because of the voltage drop across resistance R) and the possible emergence of both a static field and a field varying in time and homogeneous in space due to the formation of space-charge gratings.

The photoelectron generation rate $g(x, t)$ in a sample illuminated by light of the intensity given by Eq. (1) is

$$g(x, t) = g_0[1 + m\cos(K_g x + \Theta\cos\Omega t)], \quad (9)$$

where $g_0 = HW_0$, H being the coefficient determined by the photon energy, quantum yield, and the absorption coefficient of the crystal.

Having eliminated the photoelectron concentration $n(x, t)$ between Eqs. (5)–(7), we obtain a closed equation for the induced field,

$$\omega\frac{\partial Y(z, T)}{\partial T} + \left[h(z, T) - d\omega\frac{\partial^2 Y(z, T)}{\partial z\partial T}\right] \times [1 + Y(z, T)] = f(T). \quad (10)$$

Here, the following dimensionless variables have been introduced: $f(T) = 4\pi\tau_M I(T)/(\varepsilon E_0)$, $d = K_g L_0$, $z = K_g x$, $T = \Omega t$, $Y(z, T) = E(z, T)/E_0$, $\omega = \Omega\tau_M$, and $h(z, T) = 1 + m\cos(z + \Theta\cos T)$. The quantities $L_0 = \mu E_0\tau$ and $\tau_M = \varepsilon/(4\pi e\mu g_0\tau)$ are the drift length and the Maxwellian relaxation time, respectively. It should be noted that here we have introduced the drift length L_0 and the so-called quality parameter d for the case when the actual applied field is equal to E_0. In the presence of resistance R, the actual value of L_0 and, hence, d must be appropriately renormalized, which will be done below.

A solution $Y(z, T)$ to Eq. (10) is a periodic function of two variables: $Y(z, t) = Y(z + 2\pi p, T + 2\pi l)$. Consequently, this function can be expanded into a double Fourier series,

$$Y(z, T) = \sum_{p, l = -\infty}^{\infty} Y_{p, l} \exp(ipz + ilT). \quad (11)$$

The equation for the Fourier components has the form

$$(i + pd)\omega l Y_{p, l} + h_{p, l} + \sum_{p', l' = -\infty}^{\infty} Y_{p - p', l - l'}[h_{p', l'} + p'\omega l' d Y_{p', l'}] = f_1 \delta_{p, 0}. \quad (12)$$

The time Fourier components f_l of the current flowing in the external circuit are determined from condition (8), which assumes the following form in the Fourier representation:

$$Y_{p = 0, l} = -\rho\sigma f_l. \quad (13)$$

Here, $\sigma = \varepsilon/(4\pi\tau_M) = e\mu g_0 \tau$ is the electrical conductivity of the sample under uniform illumination.

The Fourier components $h_{p, l}$ of the illumination intensity are given by

$$h_{p, l} = \delta_{p, 0}\delta_{l, 0} + \frac{m}{2} J_l(\Theta)[\delta_{p, l} i^l + \delta_{p, -l} i^{-l}]. \quad (14)$$

We will seek a solution to the system of nonlinear equations (12) in the weak-contrast approximation $m \ll 1$. It should be noted that $h_{p, l} \propto m^{|p|}$. We can easily verify that in this case $Y_{p, l} \propto m^{|p|}$ for $m \ll 1$.

To lowest order in m, Eq. (12) under condition (13) is simplified radically and assumes the following form for $p \geq 1$:

$$(1 + pl\omega d + i\omega l) Y_{p, l} = -h_{p, l} + \rho\sigma \sum_{l' = -\infty}^{\infty} f_{l - l'}(h_{p, l'} + pl'\omega d Y_{p, l'}) - \sum_{p' = 1}^{p} \sum_{l' = -\infty}^{\infty} Y_{p - p', l - l'}(h_{p', l'} + p'l'\omega d Y_{p', l'}). \quad (15)$$

The values of $Y_{p, l}$ for $p \leq -1$ can be found from the relations

$$Y_{-p, -l} = Y^*_{p, l}, \quad Y_{p, -l}(\omega) = Y_{p, l}(-\omega). \quad (16)$$

Equation (12) is a recurrent relation for the Fourier components $Y_{p, l}$ of the dimensionless induced field. The case when $p = 0$ requires separate consideration. Substituting $p = 0$ into Eq. (12) and taking into account Eq. (13), we can obtain an expression for the current in the external circuit,

$$f_i = \frac{\delta_{l, 0}}{1 + q}, \quad (17)$$

where $q = \rho\sigma$.

It should be emphasized that expression (17) for the current is derived to the lowest (zeroth) order in m (but is valid for any value of the phase modulation amplitude Θ).

Let us now consider the case when $p = 1$. From Eq. (15), we have

$$Y_{1, l} = -\frac{h_{1, l}}{(1 + q)(1 + \omega l\tilde{d} + i\omega l)} = -\frac{m}{2(1 + q)} \frac{i^l J_l(\Theta)}{1 + \omega l\tilde{d} + i\omega l}. \quad (18)$$

Here, $\tilde{d} = d/(1 + q)$ corresponds to the renormalization of the electric field determining the drift length due to the voltage drop across the load resistance R. In particular, in the cases $l = 0$, 1, and 2 we are interested in, for $\Theta \ll 1$, we have

$$Y_{1, 0} = -\frac{m}{2(1 + q)}, \quad (19)$$

$$Y_{1, 1} = \frac{m}{4i(1 + q)} \frac{\Theta}{1 + \omega\tilde{d} + i\omega}, \quad (20)$$

$$Y_{1, 2} = \frac{m}{16(1 + q)} \frac{\Theta^2}{1 + 2\omega\tilde{d} + 2i\omega}. \quad (21)$$

Expression (20) describes the amplitude of the field of a moving grating; the wave vector of this grating is equal to K_g, and the frequency of the driving force is $\Omega = \omega\tau_M$. When the condition $\omega\tilde{d} = 1$ is satisfied, resonance sets in, which means that the conditions for the excitation of the eigenmode of oscillations, i.e., SCWs, are satisfied.

For $\tilde{d} \gg 1$, the resonance (fundamental) frequency is given by

$$f_f = \frac{\Omega_f}{2\pi} = \frac{1}{2\pi\tau_M \tilde{d}} = \frac{1 + q}{2\pi\tau_M \mu\tau E_0 K_g}. \quad (22)$$

This expression in the approximation in question is the dispersion relation for SCWs. In resonance, the SCW field has the form

$$E_{sc}(x, t) = \frac{1}{4} E_0 m\Theta \frac{d}{(1 + q)^2} \cos(\Omega t - K_y x).$$

In expression (21), resonance also exists, but at half as high a frequency. This resonance is associated with the chosen method of SCW excitation. As a matter of fact, in the case of phase modulation of one of the beams, oscillations of the interference pattern arise not only at frequency Ω but also at higher harmonics. The amplitude of these oscillations is proportional to the corresponding power of Θ (for $\Theta \ll 1$). The amplitude of second harmonic oscillations is proportional to Θ^2,

which is in accordance with formula (21). Thus, relation (21) describes the excitation of the same waves as those discussed above but at the second harmonic of the excitation frequency.

Let us now consider second-order effects in m. In this case, we retain the terms proportional to m^2 in Eq. (6) for current density. Since $n(x, t)$ and $E(x, t)$ contain terms with coefficients of the type $m\exp(\pm iK_g x)$ and $m\Theta\exp[i(K_g x - \Omega t)]$, the product $n(x, t)\,E(x, t)$ contains terms of the type $m^2\exp(i2K_g x)$, $m^2\Theta\exp[i(2K_g x - \Omega t)]$, $m^2\Theta\exp(i\Omega t)$, $m^2\Theta^2\exp[i(2K_g x - 2\Omega t)]$, and $m\Theta\exp[i(K_g x - \Omega t)]m\Theta\exp[-i(K_g x - \Omega t)] = m^2\Theta^2$. Expression $m^2\exp(i2K_g x)$ indicates the emergence of the second spatial harmonic in the static grating. The contribution of the type $m^2\Theta\exp[i(2K_g x - \Omega t)]$ corresponds to the emergence of a running grating with a doubled wave vector (spatial doubling), while the term $m^2\Theta\exp(i\Omega t)$ indicates the emergence of a field which is homogeneous in space but oscillates in time (spatial rectification). The last two effects mentioned above were studied earlier in [3–5, 7, 8].

The term proportional to $m^2\Theta^2\exp[i(2K_g x - 2\Omega t)]$ describes the generation of the second harmonic of the traveling wave, while the last term $m^2\Theta^2$ indicates the possible emergence of a uniform direct current due to the interaction of waves, which is spatial and temporal rectification.

In order to study the process of the second harmonic generation for the traveling wave, we will now analyze the second spatial harmonics $Y_{2, l}$ of the field to within m^2. Taking into account relations (13) and (17), as well as the fact that $h_{2, l} = 0$, we obtain from Eq. (11)

$$(1 + 2\omega l\tilde{d} + i\omega l)Y_{2, l} = -\sum_{l' = -\infty}^{\infty} Y_{1, l-l'}(h_{1, l'} + \omega l' d Y_{1, l'}).$$

Using relations (14) and (10) and carrying out simple transformations, we obtain

$$Y_{2, l} = \frac{i^l(2 + i\omega l)m^2}{(1 + q)(1 + 2\omega l\tilde{d} + i\omega l)} \times \sum_{l' = -\infty}^{\infty} \frac{J_{l-l'}(\Theta)J_{l'}(\Theta)}{[1 + \omega(l - l')\tilde{d} + i\omega(l - l')][1 + \omega l'\tilde{d} + i\omega l']}. \quad (23)$$

This expression, combined with Eqs. (14) and (19)–(21) in the limit of small amplitude of phase modulation ($\Theta \ll 1$), leads to the following comparatively simple expressions for the Fourier components of the induced field we are interested in:

$$Y_{2, 0} = \frac{m^2}{4(1 + q)}, \quad (24)$$

$$Y_{2, 1} = \frac{im^2\Theta}{8(1 + q)}\frac{2 + i\omega}{(1 + 2\omega\tilde{d} + i\omega)(1 + \omega\tilde{d} + i\omega)}, \quad (25)$$

$$Y_{2, 2} = -\frac{m^2\Theta^2}{16(1 + q)}\frac{1 + i\omega}{1 + 4\omega\tilde{d} + 2i\omega} \times \left[\frac{1}{1 + 2\omega\tilde{d} + 2i\omega} + \frac{1}{(1 + \omega\tilde{d} + i\omega)^2}\right]. \quad (26)$$

Expressions (19) and (23) for the Fourier components $Y_{1, 0}$ and $Y_{2, 0}$ are in accord with the exact result obtained in [4] for $Y_{p, 0}$,

$$Y_{p, 0} = \left(\frac{\sqrt{1 - m^2} - 1}{m}\right)^{|p|} \cong \left(-\frac{m}{2}\right)^{|p|},$$

and the expressions for the first temporal Fourier components $Y_{1, 1}$ and $Y_{2, 1}$ agree with the corresponding result obtained in [4].

Expression (26) describes the amplitude of a moving grating whose wave vector is equal to $2K_g$ and whose frequency of oscillations is equal to the frequency of excitation doubled. It should be noted that the eigenfrequency of oscillations for an SCW with wave vector $2K_g$ must be equal to $\Omega/2\pi = f_f/2$.

The structure of relation (26) shows that there are three resonances (for $\omega = 1/\tilde{d}$, $\omega = 1/2\tilde{d}$, and $\omega = 1/4\tilde{d}$). The nature of these resonances can be described as follows. The resonance at $\omega = 1/4\tilde{d}$ is associated with the interaction of two forced oscillations with wave vector K_g and dimensionless frequencies equal to $\omega = 1/\tilde{d}$ (the amplitude of each of these waves is proportional to $m\Theta$). In the nonlinear regime, these oscillations (waves) generate a wave with doubled wave vector and doubled frequency, i.e., with wave vector $2K_g$ and frequency $\Omega_f/4\pi = f_f/2$, which exactly satisfies the dispersion relation. In other words, the eigenmode is excited in this case due to the generation of the second harmonic of induced oscillations. The amplitude of the eigenmode in this case is proportional to $m^2\Theta^2$.

The resonance at $\omega = 1/\tilde{d}$ is associated with the resonant excitation of two fundamental modes (with wave vector K_g and frequency $\Omega_f/2\pi = f_f$). The amplitude of these waves is proportional to $m\Theta$. The interaction of these excited eigenmodes generates a second harmonic, i.e., a wave with wave vector $2K_g$ and frequency $2f_f$. This wave is not an eigenmode since it does not satisfy the dispersion relation; nevertheless, its excitation is of resonance nature since the resonance excitation of eigenmodes occurs at the first stage of the process. The amplitude of the resultant wave is proportional to the amplitudes of the two waves generating it; consequently, this amplitude is proportional to $m^2\Theta^2$.

The resonance at the intermediate frequency is not associated with the excitation of the second harmonic of the traveling wave. This resonance [as well as the resonance at frequency $\omega = 1/\tilde{d}$, Eq. (21)] is associated

with the excitation of the main fundamental mode, but by means of the second harmonic of oscillations of the interference pattern. For this reason, the resonance emerges at a modulation frequency equal to $\Omega_f/4\pi = f_f/2$. The amplitude of this wave is proportional to $m\Theta^2$. Then, this wave interacts with the static charge grating characterized by wave vector K_g and an amplitude proportional to m. This gives rise to a wave with wave vector $2K_g$ and frequency $f = 2f_f$ whose amplitude is proportional to $m^2\Theta^2$. This wave is not an eigenmode, but its excitation is of resonance nature since the fundamental mode is excited resonantly at the first stage.

All possible processes with any combination of p and l can be considered similarly. However, for $m \ll 1$ and $\Theta \ll 1$, it is expedient to confine the analysis to processes involving only a small number of waves (one or two). It should be noted that for large values of $\tilde{d}$, near the resonance, we must ensure a more stringent condition than $m \ll 1$, namely, $m\tilde{d} \ll 1$. Otherwise, the system stability must be analyzed additionally.

3. ANALYSIS OF EXPERIMENTALLY OBSERVED QUANTITIES CHARACTERIZING SECOND HARMONIC GENERATION

It is expedient to carry out experiments on the SCW second harmonic generation on photorefractive crystals. Since these crystals exhibit the electrooptical effect, the electric field of an SCW induces a refractive-index wave. When a crystal is exposed to a laser beam, the corresponding diffraction peaks from the running wave of the refractive index can be observed. In this way, we can obtain the required complete information on the grating (its amplitude, wave vector, and oscillation frequency). One possible method of experimental investigation is based on diffraction of the recording beams themselves. This technique was used in the preliminary experiments described in [3]. The first part of this section will be devoted to this method of measurement.

Let us consider the diffraction of light from a thin hologram recorded by two beams A_S and A_R: $A_S = A_{S0}\exp(ik_S x)$ and $A_R = A_{R0}\exp(ik_R x + i\Theta\cos\Omega t)$. A hologram is regarded as thin if its thickness D satisfies the condition $D \ll \Lambda^2 n_0/\lambda_W$, where n_0 is the refractive index of light and λ_W is the wavelength of the recording and reading light beams. For a thin hologram, we can introduce the transmission coefficient $T(x, t) = \exp[i\varphi(x, t)]$ connecting the amplitude A^{out} of light immediately behind the hologram with the amplitude A^{in} of incident light, $A^{\text{out}}(x, t) = T(x, t)A^{\text{in}}(x, t)$. In our case, $\varphi(x, t) = QE(x, t)$ is the increment of the phase of the beam passing through the hologram due to the modulation of the refractive index. Here, Q is a parameter depending on the electrooptical properties of the crystal. For crystals belonging to the point group 23 and $\bar{4}3m$ and, e.g., for the cut $\langle 110\rangle$, we have $Q = \pi r_{41} n_0^3 D/\lambda_W$, where r_{41} is the electrooptical coefficient. Subsequently, we consider the case of $Q \ll 1$ and take into account linear corrections in this parameter. As a result, we obtain

$$\begin{aligned} A^{\text{out}}(z, T) &= \exp(ik_R x) \\ &\times [A_{S0}\exp(-iz) + A_{R0}\exp(i\Theta\cos T)] \\ &\times [1 + iQE_0 Y(z, T)]. \end{aligned} \tag{27}$$

In this relation, a transition has been made to the dimensionless variables z, T, and $Y(z, T)$ and $k_R - k_S = K_g$.

The spatial Fourier component of the amplitude of the output light beam has the form

$$\begin{aligned} A_p^{\text{out}}(T) &= \{A_{S0}[\delta_{p,-1} + iQEY_{p+1}(T)] \\ &+ A_{R0}\exp(i\Theta\cos T)[\delta_{p,0} + iQE_0 Y_p(T)]\}. \end{aligned} \tag{28}$$

Here, we have omitted the insignificant common phase factor $\exp(ik_R x)$. In order to avoid confusion, note that we label the observed diffraction beams with the subscript p corresponding to the first diffraction order of the beam A_R for the grating with wave vector pK_S.

The intensity of Bragg peaks with $p = 0, -1$ is proportional to the first power of Q, while the intensity of all the remaining peaks is proportional to $\propto Q^2$. For this reason, we first consider the intensity of Bragg peaks. For $p = 0$, we obtain the following expression for the zeroth-peak intensity from Eq. (28):

$$\begin{aligned} \delta I_0(T) &= \left|A_0^{\text{out}}\right|^2 - A_{R0}^2 \\ &= -A_{S0}A_{R0}QE_0 2\,\text{Im}[Y_1(T)\exp(-i\Theta\cos T)]. \end{aligned} \tag{29}$$

For the second Bragg peak with $p = -1$, we have

$$\delta I_{-1}(T) = \left|A_{-1}^{\text{out}}\right|^2 - A_{S0}^2 = \delta I_0(T). \tag{30}$$

The intensity of non-Bragg peaks is given by

$$\begin{aligned} \delta I_p(T) &= Q^2 E_0^2 \\ &\times \left|A_{S0}Y_{p+1}(T) + A_{R0}\exp(i\Theta\cos T)Y_p(T)\right|^2. \end{aligned} \tag{31}$$

In the limiting case of small contrast $m \ll 1$ considered here, this expression is simplified:

$$\delta I_p(T) = Q^2 E_0^2 A_{R0}^2 \left|Y_p(T)\right|^2, \quad p \geq 1, \tag{32}$$

$$\delta I_p(T) = Q^2 E_0^2 A_{S0}^2 \left|Y_{p+1}(T)\right|^2, \quad p < -1. \tag{33}$$

Let us now analyze the time dependence of the intensity of the zeroth Bragg peak. For this purpose, we expand expression (29) into a Fourier series in time. We confine our analysis in this section to the case of small phase modulation amplitude $\Theta \ll 1$. In this limit, we

have the following expression for the time Fourier components with $l \geq 0$:

$$\delta I_{0,l} = iQE_0A_{R0}A_{S0} \times \sum_{l'=0}^{l} [(-i)^{l'} Y_{1,l-l'}(\omega) - i^l Y^*_{1,l-l'}(-\omega)] \frac{\Theta^{l'}}{2^{l'} l'!}. \quad (34)$$

The time-dependent intensity $J_{p,l}(t)$ of the pth peak (with $p > 0$) at frequency $l\Omega$ is defined as

$$J_{p,l}(t) = C_{p,l}\cos(\Omega lt + \varphi_{l,p}), \quad (35)$$

where the amplitude $C_{p,l}$ and phase $\varphi_{l,p}$ of the signal are connected with the quantity $\delta I_{p,l}$ through the relations

$$C_{p,l} = 2\sqrt{(\mathrm{Re}\delta I_{p,l})^2 + (\mathrm{Im}\delta I_{p,l})^2}, \quad \tan\varphi_{p,l} = \frac{\mathrm{Im}\delta I_{p,l}}{\mathrm{Re}\delta I_{p,l}}. \quad (36)$$

The peaks for $p < 0$ can be obtained from the relations [see Eqs. (32), (33)]

$$J_{-1,l}(t) = J_{0,l}(t), \quad J_{-p-1,l}(t) = \frac{A_{S0}^2}{A_{R0}^2} J_{p,l}(t). \quad (37)$$

It should be noted that in the absence of auxiliary illumination, the ratio A_{R0}/A_{S0} determines the contrast of the image:

$$\frac{A_{R0}}{A_{S0}} = \frac{1 \pm \sqrt{1-m^2}}{m}. \quad (38)$$

In this case, the oscillating components of non-Bragg diffraction peaks for positive values of p are completely suppressed for $A_{R0} > A_{S0}$; on the contrary, for $A_{R0} < A_{S0}$, non-Bragg peaks with $p < 0$ are suppressed completely [4].

Thus, according to [34], the first and second temporal harmonics of Bragg peaks are defined by the relations

$$\delta I_{0,1} = A_{S0}A_{R0}QE_0 \times \left\{ \frac{\Theta}{2}[Y_{1,0}(\omega) + Y^*_{1,0}(-\omega)] + i[Y_{1,1}(\omega) - Y^*_{1,1}(\omega)] \right\}, \quad (39)$$

$$\delta I_{0,2} = A_{S0}A_{R0}QE_0 \times \left\{ \frac{\Theta}{2}[Y_{1,1}(\omega) + Y^*_{1,1}(-\omega)] + i[Y_{1,2}(\omega) - Y^*_{1,2}(\omega)] \right\}. \quad (40)$$

In accordance with Eq. (39) and Eqs. (19) and (20), for the first temporal harmonic, we have

$$C_{0,1} = A_{S0}A_{R0}Qm\Theta\omega\frac{E_0}{1+q} \times \sqrt{\frac{1+\omega^2(1+\tilde{d}^2)^2}{[1-\omega^2(1+\tilde{d})]^2 + 4\omega^2}}, \quad (41)$$

$$\varphi_{0,1} + \pi = \arctan\frac{1+\omega^2(1+\tilde{d}^2)}{\omega[1-\tilde{d}^2+\omega^2(1+\tilde{d}^2)^2]}. \quad (42)$$

The first harmonic has a single resonance peak at $\omega_r = (1+\tilde{d}^2)^{-1/2}$. This result is in accord with that obtained in [4] (for $\rho = 0$, i.e., $\tilde{d} = d$, since the short-circuiting regime is considered in [4]).

In accordance with Eqs. (40), (20), and (21), the second temporal harmonic has the form

$$C_{0,2} = A_{S0}A_{R0}Qm\Theta^2\frac{\omega dE_0}{2(1+q)}\sqrt{\frac{\omega^2[1+9\omega^2(1+\tilde{d}^2)^2]}{\{[1-\omega^2(1+\tilde{d}^2)]^2+4\omega^2\}\{[1-4\omega^2(1+\tilde{d}^2)]^2+16\omega^2\}}}, \quad (43)$$

$$\varphi_{0,2} = \arctan\left\{\frac{3\omega}{2}\frac{4-(1+\tilde{d}^2)[1-\omega^2(1+\tilde{d}^2)][1-4\omega^2(1+\tilde{d}^2)]}{14\omega^4(1+\tilde{d}^2)+4\omega^2(1-\tilde{d}^2)-1}\right\}. \quad (44)$$

Thus, while the frequency dependence of the first temporal harmonic has only one resonance peak at the frequency $\omega_r = (1+\tilde{d})^{-1/2}$, the frequency dependence of the second harmonic exhibits one more peak at the frequency $\omega_r = 1/2(1+\tilde{d})^{-1/2}$. These resonances are well resolved for $\tilde{d} \gg 1$ (i.e., in a strong external field), and the position of the resonance peaks is given by the relation $\omega_r \cong 1/(l\tilde{d})$, where $l = 1, 2$. It can be proved that the frequency dependence of the lth harmonic of Bragg peaks has l maxima corresponding to frequencies $\omega_r = 1/(l'\tilde{d})$, where $l' = 1, 2, \ldots, l$. It should be recalled that this conclusion is valid only for $m \ll 1$, $\Theta \ll 1$, when the intensity of the lth harmonic of Bragg peaks is proportional to $A_{S0}A_{R0}QE_0m\Theta^l$.

Let us now consider the frequency harmonics for non-Bragg peaks. In accordance with relation (32), we have

$$\delta I_{p,l} = Q^2E_0^2A_{R0}^2\sum_{l'=0}^{l} Y_{p,l-l'}(\omega)Y^*_{p,l'}(-\omega). \quad (45)$$

The frequency dependence of the first harmonic was studied theoretically and experimentally in [2, 4]. In the case of $l = 2$ (corresponding to signal detection at a frequency equal to the doubled frequency of modulation of the recording beam), Eq. (45) assumes the form

$$C_{1,2} = \frac{1}{8}Q^2A_{R0}^2m^2\Theta^2\omega^2\frac{E_0^2}{(1+q)^2}\sqrt{\frac{(3\tilde{d}^2-1)+4\omega^2(1+\tilde{d}^2)^2}{\{[1-\omega^2(1+\tilde{d}^2)]^2+4\omega^2\}\{[1-4\omega^2(1+\tilde{d}^2)]^2+16\omega^2\}}}. \quad (47)$$

It can be seem from this relation that the frequency dependence of the first non-Bragg peak has two resonance peaks at frequencies $\omega_r = 1/\sqrt{1+\tilde{d}^2}$ and $1/2\sqrt{1+\tilde{d}^2}$ in analogy with the Bragg peaks in Eq. (43).

Let us now consider the second frequency harmonic for the second non-Bragg peak $p = 2$. In accordance with Eqs. (46) and (23)–(25), we can write

$$\delta I_{2,2} = \frac{1}{64}Q^2A_{R0}^2m^4\Theta^2\frac{E_0^2}{(1+q)^2}$$
$$\times\left\{\frac{(2+i\omega)^2}{[(1+i\omega)^2-\omega^2\tilde{d}^2][(1+i\omega)^2-4\omega^2\tilde{d}^2]}\right.$$
$$-\frac{1+i\omega}{1+4\omega\tilde{d}+2i\omega}\left[\frac{1}{1+2\omega\tilde{d}+2i\omega}+\frac{1}{(1+\omega\tilde{d}+i\omega)^2}\right] \quad (48)$$
$$\left.-\frac{1+i\omega}{1-4\omega\tilde{d}+2i\omega}\left[\frac{1}{1-2\omega\tilde{d}+2i\omega}+\frac{1}{(1-\omega\tilde{d}+i\omega)^2}\right]\right\}.$$

In general, the analytic expression for the frequency dependence of the quantity $J_{2,2}(t)$ is too cumbersome. For this reason, we write here this expression in the most interesting limiting case of $\tilde{d} \gg 1$ in the absence of damping:

$$J_{2,2}(t) = \frac{1}{16}Q^2A_{R0}^2m^4\Theta^2\frac{E_0^2}{(1+q)^2}\cos(2\Omega t)$$
$$\times\left\{\frac{2}{(1-\omega^2\tilde{d}^2)(1-4\omega^2\tilde{d}^2)}\right.$$
$$-\frac{1+8\omega^2d^2}{(1-4\omega^2\tilde{d}^2)(1-16\omega^2\tilde{d}^2)} \quad (49)$$
$$\left.-\frac{1+9\omega^2\tilde{d}^2}{(1-\omega^2\tilde{d}^2)^2(1-16\omega^2\tilde{d}^2)}\right\}.$$

$$\delta I_{p,2} = Q^2E_0^2A_{R0}^2$$
$$\times\{Y_{p,0}[Y_{p,2}(\omega)+Y_{p,2}^*(-\omega)]+Y_{p,1}(\omega)Y_{p,1}^*(-\omega)\}. \quad (46)$$

By using Eq. (43) and taking into account relations (15)–(17), we obtain the following expression for the second temporal harmonic of the first non-Bragg peak:

It can be seen that the frequency dependence of $J_{22}(t)$ has three resonance peaks at frequencies $\omega_r = 1/\tilde{d}$, $1/2\tilde{d}$, and $1/4\tilde{d}$. The numerically calculated frequency dependence of the amplitude of the second temporal Fourier component $C_{2,2}$, determined from relations (36) and (48), is presented in Fig. 2.

It should be noted that, in accordance with relation (46), the signal $\delta I_{p,2}$ at the second-harmonic frequency contains, in addition to a contribution proportional to the second frequency harmonic $Y_{p,2}$ of the induced electric field, a second term proportional to the squared amplitude of the first frequency harmonic $Y_{p,1}$. Consequently, the resonance contribution to the frequency dependence of the second non-Bragg peak at frequencies $\omega_r = 1/\tilde{d}$ and $\omega_r = 1/2\tilde{d}$ is formed at the expense of the first and second temporal harmonics of the induced field, while the resonance at frequency $\omega_r = 1/4\tilde{d}$ is associated exclusively with the second temporal harmonic of the field.

In general, the frequency dependence of the Bragg peaks at the harmonic frequency Ωl has l resonance peaks at frequencies $\omega_r = 1/l'\tilde{d}$, $l' = 1, 2, \ldots, l$ and their amplitude is proportional to $m\Theta^l$. As regards non-Bragg peaks with index p at the lth harmonic frequency, their intensity is proportional to $m^p\Theta^l$ and possesses $l\left(p-\frac{l-1}{2}\right)$ (for $p \geq l$) or $p\left(l-\frac{p-1}{2}\right)$ (for $p \leq l$) peaks at resonance frequencies $\omega_r = 1/(\tilde{d}\,p'l')$, where $p' = 1, 2, \ldots, p$ and $l' = 1, 2, \ldots, l$. It should be emphasized here that this conclusion is valid only in the limit $m \ll 1$ and $\Theta \ll 1$. If this criterion is violated and the number of quasiparticles in intermediate states increases, then the number of resonance peaks will increase (see also [4] in this connection).

A disadvantage of the method for studying the temporal Fourier components of oscillating gratings through analysis of the diffraction of recording beams themselves is that the second component, for example, contains a contribution proportional to the product of the first temporal components [see Eq. (46)]. For this reason, we will carry out an analysis on the basis of

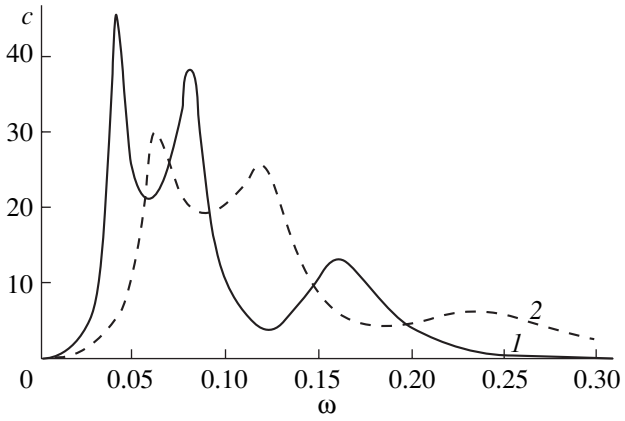

Fig. 2. Frequency dependence of the dimensionless second-harmonic amplitude $c = C_{22}\frac{64(1+q)^2}{Q^2A_{R0}^2m^4\Theta^2E_0^2}$ of the second non-Bragg peak calculated using formulas (36) and (48); $\tilde{d} = 6$ (curve *1*) and 4 (curve *2*).

another method of measurements using a probe beam. In this case, in addition to the recording beams, a probe beam is incident on the crystal at an angle α_p, ensuring Bragg diffraction with wave vector $2K_g$ (see Fig. 1). The angle α_p is chosen from the condition

$$\sin\alpha_p = \frac{2\lambda_p}{\lambda_W}\sin\alpha_W.$$

Here, λ_p is the wavelength of the probe beam. The photodetector must be placed at the diffraction peak from the grating with wave vector $2K_g$. If a thin crystal (of thickness satisfying the condition $D \ll \Lambda^2 n_0/4\lambda_p$) is used, there are no stringent limitations on the angle of incidence and the readout angle is equal to $2\alpha_p$ relative to the direction of propagation of the probe beam. A reference beam is directed to the photodetector simultaneously with the diffracted beam. The reference beam must be coherent to the diffracted beam; consequently, the formed beam must be formed by the same source as the probe beam. In addition, we must ensure that the amplitude of the reference beam is much larger than the amplitude of the diffracted beam. In order to avoid the formation of an interference pattern in the aperture of the photodetector, it is desirable that the reference and diffracted beams be focused at the photodetector. This case will be considered below.

The amplitude A_d of the diffracted beam in the low diffraction efficiency approximation has the form

$$A_d(T) = A_p iQE_0Y_2(T), \tag{50}$$

where A_p is the amplitude of the probe beam. If we denote the amplitude of the reference beam by A_r, the intensity of light at the photodetector is given by

$$\begin{aligned} W_{\rm pr}(T) &= |A_r + A_p iQE_0Y_2(T)|^2 \\ &\cong |A_r|^2 - 2QE_0\,{\rm Im}[A_r^*A_pY_2(T)]. \end{aligned} \tag{51}$$

The second temporal Fourier component of the light intensity at the photodetector is

$$\begin{aligned} W_{\rm pr}^{(2)} &= iQE_0[A_r^*A_pY_{22}(\omega) - A_rA_p^*Y_{22}^*(-\omega)] \\ &= -i\frac{QE_0m^2\Theta^2}{16(1+q)}|A_rA_p|(1+i\omega) \\ &\times\left\{\frac{\exp(i\beta)}{1+4\omega\tilde{d}+2i\omega}\left[\frac{1}{1+2\omega\tilde{d}+2i\omega}+\frac{1}{(1+\omega\tilde{d}+i\omega)^2}\right]\right. \\ &\left.-\frac{\exp(-i\beta)}{1-4\omega\tilde{d}+2i\omega}\left[\frac{1}{1-2\omega\tilde{d}+2i\omega}b+\frac{1}{(1-\omega\tilde{d}+i\omega)^2}\right]\right\}, \end{aligned} \tag{52}$$

where β is the phase difference between the amplitudes A_p and A_r.

Thus, the signal being recorded when the probe beam is used has three peaks (at $\omega = 1/\tilde{d}$, $1/2\tilde{d}$, and $1/4\tilde{d}$), as for the diffraction of the recording beams themselves [cf. Eqs. (48), (52)]. However, in the latter case, the signal also contains a "parasitic" contribution from the product of the first Fourier components described by the first term in the braces on the right-hand side of Eq. (48), while relation (52) contains no parasitic contribution. In addition, the probe beam technique makes it possible to control the signal by varying the phase β between the probe and reference beams. However, this phase affects the frequency dependence of the signal only weakly over the entire frequency range except in the low-frequency region. In particular, for $\omega = 0$, the signal is proportional to $\sin\beta$ and vanishes only for $\beta = 0$ and π.

The expression for the amplitude of the signal being recorded, which is equal to $|W_{\rm pr}^{(2)}|$ has a cumbersome form. Here, we write an analytic expression for this amplitude taking into account only the second resonance term in the braces in Eq. (52):

$$\begin{aligned} |W_{\rm pr}^{(2)}| &= \frac{QE_0m^2\Theta^2|A_rA_p|}{16(1+q)[(1-\omega\tilde{d})^2+\omega^2]} \\ &\times\sqrt{\frac{(1+\omega^2)[(2-4\omega\tilde{d}+\omega^2\tilde{d}^2-\omega^2)^2+4\omega^2]}{[(1-4\omega\tilde{d})^2+4\omega^2][(1-2\omega\tilde{d})^2+4\omega^2]}}. \end{aligned}$$

When the probe beam is used, the ratios between the signal intensities at different peaks are $I(f = f_f/4) : I(f = f_f/2) : I(f = f_f) \cong (68\tilde{d}/9) : (19\tilde{d}/3) : (\tilde{d}^2/3)$. The ration between the same intensities as functions of the applied voltage U are $(68U^2/9)$; $(19U^2/3) : (U^3/3)$. Figure 3 shows the numerically calculated [from Eq. (52)] frequency dependence of the signal in the case where the probe beam technique is used. A comparison of Figs. 2 and 3 shows that the use of a probe beam considerably suppresses the intermediate peak at frequency $f = f_f/2$, while the other two peaks are deformed comparatively weakly.

The Maxwellian relaxation time τ_M for the known materials $Bi_{12}GeO_{20}$, $Bi_{12}TiO_{20}$, and $Bi_{12}SiO_{20}$ illuminated with a laser beam of intensity 100–200 mW/cm^2 (for $\lambda_W = 530$ nm) is of the order of 10^{-4} s, and the resonance frequencies for fields of the order of 10 kV/cm and $\tilde{d} \cong 3$–5 must lie in the interval from 10 to 500 Hz, which is convenient for measurements. It should be recalled that $\Omega/2\pi$ is the phase modulation frequency for one of the reference beams, while the signal being recorded oscillates with the doubled frequency Ω/π. The intensities of the signals must be high enough for detection judging from the results of known holographic experiments on these crystals.

4. EFFECT OF SCW RECTIFICATION IN BOTH SPACE AND TIME

It was noted above that nonlinear interaction of space-charge waves can lead to the emergence of an auxiliary direct current or voltage in the circuit containing the crystal, i.e., to the complete (space and time) rectification effect. This means that the magnitude of the direct current in the circuit must depend on the frequency of oscillations of the interference pattern; in this case, a resonance singularity may emerge if the conditions for SCW excitation are satisfied.

In order to calculate the frequency dependence of the current in the external circuit, we consider Eq. (12) once again. By putting $p = 0$ into it and taking into account the contributions proportional to m^2, we retain only the terms with $p' = 0, \pm 1$ in the sum over p'. This gives

$$(1 + q + i\omega l) f_l = \delta_{l,0} + \sum_{l' = \infty}^{\infty} [(h_{1,l'} + \omega\tilde{d} l' Y_{l,l'}) Y_{-1,l-l'} + (h_{-1,l'} - \omega\tilde{d} l' Y_{-1,l'}) Y_{1,l-l'}]. \quad (53)$$

Using now the first spatial Fourier components (18) and carrying out transformations, we obtain the following closed relation for the temporal Fourier components of the current:

$$(1 + q + iq\omega l) f_l = \delta_{l,0} - i^l \frac{2 + i\omega l}{1 + q} \frac{m^2}{4} \times \sum_{l' = -\infty}^{\infty} \frac{J_{l'}(\Theta) J_{l'-l}(\Theta)}{[1 + \omega\tilde{d}(l' - l) - i\omega(l' - l)][1 + \omega\tilde{d} l' + i\omega l']}. \quad (54)$$

In particular, relation (54) for the first Fourier component $l = 1$ in the limit $\Theta \ll 1$ coincides with the result obtained in [5], where the spatial rectification of photorefractive waves was investigated:

$$f_i = i\omega\tilde{d} \frac{m^2\Theta}{4(1 + q)} \frac{2 + i\omega}{(1 + q + iq\omega)[(1 + i\omega)^2 - \omega^2\tilde{d}^2]}.$$

Let us consider in greater detail the frequency dependence of the steady-state current, which can be derived from relation (54) by setting $l = 0$. Taking into account the relation between the dimensionless parameter f_l and the Fourier component of current I_l, we obtain

$$I_0(\omega) = \frac{\sigma E_0}{1 + q} \times \left\{1 - \frac{m^2}{2(1 + q)} \sum_{l = -\infty}^{\infty} \frac{J_l^2(\Theta)}{(1 - \omega\tilde{d} l)^2 + \omega^2 l^2}\right\} = \frac{\sigma E_0}{1 + q} \quad (55)$$

$$\times \left\{1 - \frac{m^2}{(1 + q)\omega} \mathrm{Re} \int_0^{\infty} d\varphi \exp\left(-\frac{2\varphi}{\omega - i\omega\tilde{d}}\right) J_0(2\Theta \sin\varphi)\right\}.$$

This relation shows that the dependence of the steady-state current on the modulation frequency for $\tilde{d} > 1$

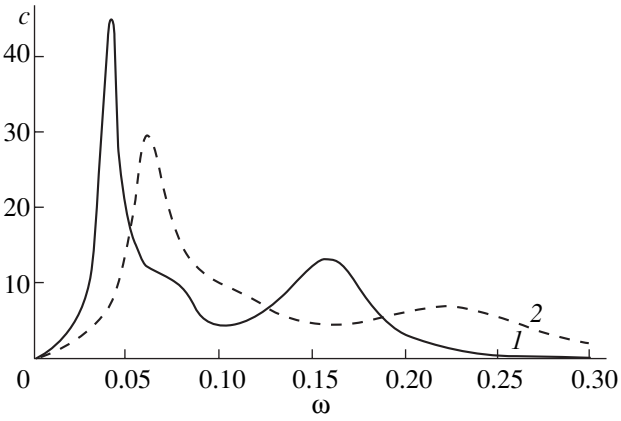

Fig. 3. Frequency dependence of the dimensionless second-harmonic amplitude $c = |W_{\mathrm{pr}}| \frac{16(1 + q)}{Q|A_r A_p| m^2 \Theta^2 E_0}$ calculated using formulas (52) in the probe beam technique geometry for $\beta = 0$; $\tilde{d} = 6$ (curve *1*) and 4 (curve *2*).

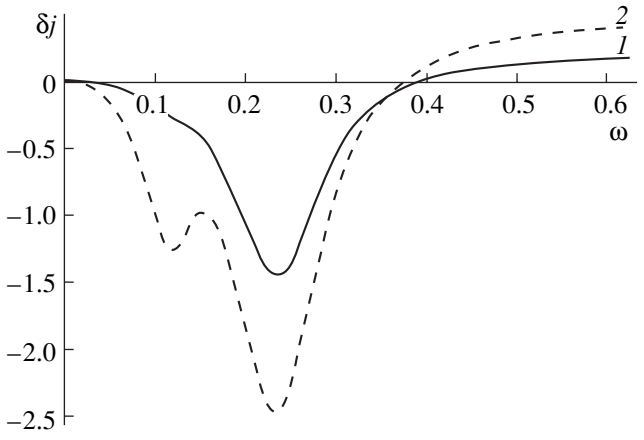

Fig. 4. Dependence of dimensionless steady-state current $\delta j = \left(\frac{1+q}{\sigma E_0} I_0 - 1\right)\frac{2(1+q)}{m^2}$ on the phase modulation frequency calculated using formula (55) for $\Theta = 1$ (curve *1*) and 2 (curve *2*).

exhibits a set of dips with minima at the frequencies $\omega = 1/(\tilde{d}\, l)$; the amplitude of a dip decreases with increasing index l in proportion to Θ^{2l} for small Θ. Figure 4 shows the frequency dependence of the steady-state current calculated from formula (55). It can be seen from Fig. 4 that the frequency dependence of the current for $\Theta < 1$ exhibits only one appreciable minimum at the fundamental frequency $\omega = 1/\tilde{d}$; however, the minimum at the second resonance frequency $\omega = 1/(2\tilde{d})$ rapidly deepens upon a further increase in the phase modulation amplitude, while the amplitude of the first minimum starts to decrease.

For $\Theta \ll 1$, relation (55) assumes a simpler form, in which only the first dip at the fundamental frequency with $l = 1$ is preserved:

$$I_0(\omega) = \frac{\sigma E_0}{1+q}\left\{1 - \frac{m^2}{2(1+q)} + \frac{m^2\Theta^2}{8(1+q)} \times\left[2 - \frac{1}{(1-\omega\tilde{d})^2 + \omega^2} - \frac{1}{(1+\omega\tilde{d})^2 + \omega^2}\right]\right\}. \quad (56)$$

It should be noted that this simple expression correctly describes the situation up to $\Theta \le 1$.

Thus, the frequency dependence of the rectified current to the lowest (second) order in Θ has a dip at the frequency $\omega = 1/\tilde{d}$. The value of current in the low-frequency wing ($\omega \ll 1/\tilde{d}$) of the frequency dependence is smaller than that in the high-frequency wing ($\omega \gg 1/\tilde{d}$), the relative difference of the extreme values being

$$\frac{I_0(\omega = \infty) - I_0(\omega = 0)}{I_0} = \frac{m^2}{2(1+q)}[1 - J_0^2\Theta] \cong \frac{m^2\Theta^2}{4(1+q)}. \quad (57)$$

The frequency dependence of current exhibits an interesting feature in the region of not very strong modulation of phase Θ when relation (56) holds. In this region, all $I_0(\omega)$ curves for different values of Θ intersect at the same point at $\omega = \sqrt{(3\tilde{d}^2 - 1)}/(\tilde{d}^2 + 1)$, while the value of current at this point of intersection coincides with the current $I_0(0)$ at zero frequency. The experimental determination of the position of such a point of intersection makes it possible to find the numerical value of the quality parameter $\tilde{d}$ (of course, only if the Maxwellian time τ_M is known).

Numerical estimates show that the relative variation of current at resonance ($\omega = 1/\tilde{d}$) amounts to tens of percent. Indeed, if we put $m = 0.5$, $\Theta = 0.5$, $q = 0.5$, and $\tilde{d} = 4$–6, (these values are typical of crystals of the type $Bi_{12}GeO_{20}$), we have $I_0(\omega = \tilde{d}^{-1})/I_0(\omega = 0) \cong 0.9$–$0.7$. Thus, the effect of rectification should be easily observed in experiments. Indeed, preliminary measurements [3] show the presence of a minimum in the dependence of direct current on the frequency of oscillations of the interference pattern. Formulas (56) and (57) also open an interesting opportunity of determining the internal field in the sample. As a matter of fact, the internal field in photorefractive crystals of the sillenite group often differs from the calculated field $E_0 = U/L$ because of the voltage drop across nonohmic contacts. The actual field can be determined using various methods (e.g., using the electrooptical effect or probing with a probe beam). It follows from Eqs. (56) and (57), however, that the parameter q, which describes the decrease in the internal field, can be found from the difference in the values of current for $\Omega = 0$ and $\Omega \longrightarrow \infty$. The value of q can also be determined without phase modulation ($\Theta = 0$), but in this case, we must measure the difference in the currents for $m = 0$ and $m \neq 0$. In the latter case, we must either take into account the correction for the change in electrical conductivity due to the variation of the mean intensity of illuminating light with a change in m or ensure the constancy of the average intensity of illumination upon a change in the contrast.

ACKNOWLEDGMENTS

This study was supported by the Russian Foundation for Basic Research, project no. 02-02-17603.

REFERENCES

1. R. F. Kazarinov, R. A. Suris, and B. I. Fuks, Fiz. Tekh. Poluprovodn. (Leningrad) **6** (3), 572 (1972) [Sov. Phys. Semicond. **6**, 500 (1972)].
2. M. P. Petrov, V. V. Bryksin, V. M. Petrov, *et al.*, Phys. Rev. A **60** (3), 2413 (1999).
3. M. P. Petrov, V. V. Bryksin, S. Wevering, and E. Kraetzig, Appl. Phys. B **73**, 669 (2001).
4. V. V. Bryksin and M. P. Petrov, Fiz. Tverd. Tela (St. Petersburg) **40** (8), 1450 (1998) [Phys. Solid State **40**, 1317 (1998)].
5. V. V. Bryksin and M. P. Petrov, Fiz. Tverd. Tela (St. Petersburg) **42** (10), 1808 (2000) [Phys. Solid State **42**, 1854 (2000)].
6. N. V. Kukhtarev, V. B. Markov, S. G. Odulov, *et al.*, Ferroelectrics **22**, 949 (1979).
7. M. P. Petrov, A. P. Paugurt, V. V. Bryksin, *et al.*, Appl. Phys. B **69**, 341 (1999).
8. M. P. Petrov, A. P. Paugurt, V. V. Bryksin, *et al.*, Phys. Rev. Lett. **84** (22), 5114 (2000).

Translated by N. Wadhwa

Physics of the Solid State, Vol. 44, No. 10, 2002, pp. 1880–1884. Translated from Fizika Tverdogo Tela, Vol. 44, No. 10, 2002, pp. 1795–1798.

DEFECTS, DISLOCATIONS, AND PHYSICS OF STRENGTH

Method for Estimating Local Lattice Distortions near a Magnetic Ion Based on the Parameters of the Ligand Hyperfine Interaction: Ce^{3+} in the Fluorite Homologous Series

Ts. A. Gavasheli, D. M. Daraseliya, D. L. Dzhaparidze, R. I. Mirianashvili, O. V. Romelashvili, and T. I. Sanadze

Tbilisi State University, Tbilisi, 380028 Georgia

e-mail: annrom@hotmail.com

Received May 31, 2001; in final form, November 1, 2001

Abstract—A method is suggested for estimating local lattice distortions near a paramagnetic center by using the parameters determined from experimental tensors of the ligand hyperfine interaction with surrounding nuclei through the use of a simple mathematical procedure. In general, a tensor with nine independent components can be unambiguously reduced to nine independent parameters characterizing the hyperfine interaction: the isotropic part, deviations from the symmetric and axially symmetric form, the axially symmetric component (containing dipole and pseudodipole contributions), and the angles defining the bond direction. Under certain physical assumptions, these parameters are used to estimate distortions of the first and second coordination shells of Ce^{3+} in the homologous series CaF_2, SrF_2, and BaF_2. © *2002 MAIK "Nauka/Interperiodica".*

1. INTRODUCTION

Determination of the actual structure of a crystal lattice near a paramagnetic center is of significant interest in solid-state physics. Direct methods of structural analysis are inapplicable in the case of a low impurity concentration. Therefore, indirect methods should be invoked based on an analysis of physical parameters as dependent on the ligand coordinates, such as the crystal field parameters or the ligand hyperfine interaction (LHFI).

In the latter case, the ligand position with respect to the magnetic ion can be accurately determined only in the case of point-dipole interaction. In fact, the LHFI can contain a significant nondipole contribution caused by the covalence and overlap effects even for nuclei of the second and farther coordination shells. It is noteworthy that there is no adequate theory which would allow one to calculate the LHFI nondipole component and separate the pure dipole contribution. Therefore, all attempts to estimate local lattice distortions are in essence reduced to treating experimental data on the LHFI of nuclei of the first and second coordination shells in order to establish its dipole character or to separate the dipole component of the interaction.

Most of the relevant publications are dedicated to rare-earth ions in fluorite-type lattices. Babershke [1] was the first to determine distortions of the cubic Eu^{2+} center in the homologous series CdF_2, CaF_2, SrF_2, and BaF_2 by using the LHFI parameters of the first coordination shell and making a number of significant physical assumptions (which we shall also make in what follows). Later on, the same approach was applied to similar Tm^{2+} and Cd^{3+} centers in the fluorite-type lattices [2, 3].

The distortion pattern around noncubic centers is much more intricate due to the presence of a compensator ion in the nearest neighborhood of the magnetic ion: the latter can be displaced toward the compensator, and the compensator can push the nearest neighbor fluorine ions apart. Baker *et al.* [4] were the first to determine (under some assumptions) the displacement of a magnetic ion and fluorine ions of the second coordination shell around the compensator by using experimental electron–nuclear double resonance (ENDOR) data for the second coordination shell. Subsequently, other authors applied this approach to study distortions of noncubic centers of rare-earth elements.

In the case of distortions of the first coordination shell, Wolfe and Markiewicz [5] have determined the magnetic ion–ligand direction (but not their spacing) for the Yb^{3+} tetragonal center in CaF_2 within a three-parameter LHFI representation, although the symmetry dictates a five-parameter one. However, this approach did not prove advantageous when used for the analogous $CaF_2 : Ce^{3+}$ center [6]. Quite recently, the displacements of fluorine ions of the first coordination shell in the trigonal Cd^{3+} centers in BaF_2 have been determined from LHFI data, crystal field parameters,

and ENDOR data on the hyperfine interaction [7], as well as in trigonal and cubic centers Cd^{3+} and Eu^{2+} in the fluorite homologous series [8, 9]. We note that the authors of [7–9] solved this problem mainly due to (as follows from their results) the compensator ion in trigonal centers causing very weak changes in all the LHFI and crystal field parameters in comparison with the analogous cubic centers. It is obvious that the approach used is applicable only to ions in the *S* state.

In this paper, we suggest a method for estimating the local lattice distortions in the vicinity of a magnetic ion by using the parameters determined from the experimental LHFI tensors through the use of a certain mathematical procedure. We illustrate this method using the example of tetragonal Ce^{3+} centers in the homologous series CaF_2, SrF_2, and BaF_2, since only for this ion are there comprehensive and accurate experimental data on the LHFI.

2. LIGAND HYPERFINE INTERACTION PARAMETERS

We consider the most general case of the nine-component LHFI tensor A_{ik} (which is conventionally measured in hertz) written in the frame of reference of the electron *g* tensor. Following [10], we pass from the tensor A_{ik} to the tensor $B_{ik} = hA_{ik}/(g_n\beta_n g_i\beta)$, where g_n is the nuclear *g* factor, β_n is the nuclear magneton, g_i are the electron *g*-tensor components, and β is the Bohr magneton. The tensor B_{ik} has dimensions m^{-3} and takes into account only the value and geometry of the magnetic ion–ligand bond, since we have excluded the anisotropy of the electron magnetic moment. We separate the isotropic part $B^I_{ik} = (\mathrm{Tr}B_{ik}/3)\delta_{ik}$ from this tensor and designate the components of the isotropic tensor as C_1. The remaining tensor with zero trace can be separated into a symmetric B^S_{ik} and an antisymmetric tensor B^A_{ik}:

$$B^S_{ik} = (B_{ik} + B_{ki})/2 - (\mathrm{Tr}B_{ik})\delta_{ik},$$

$$B^A_{ik} = (B_{ik} - B_{ki})/2.$$

The antisymmetric tensor B^A_{ik} corresponds to a certain axial vector, whose magnitude will be denoted by C_2 and whose polar angles will be designated as θ and φ. By rotating the frame of reference, we bring the tensor B^S_{ik} with zero trace into the diagonal form C^S_{ik}; therefore, we have three components of this tensor and three angles α, β, and γ characterizing the rotation. In this coordinate frame, we select the axis corresponding to the largest positive component of the tensor and separate the tensor into two axially symmetrical parts

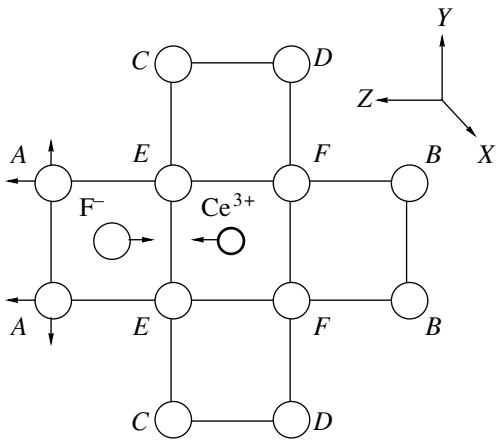

Projection of the nearest neighborhood of Ce^{3+} ion onto the (001) plane.

with mutually perpendicular symmetry axes and zero traces [11]:

$$C^S_{ik} = C_3\begin{vmatrix} 2 & 0 & 0 \\ 0 & -1 & 0 \\ 0 & 0 & -1 \end{vmatrix} + C_4\begin{vmatrix} -1 & 0 & 0 \\ 0 & -1 & 0 \\ 0 & 0 & 2 \end{vmatrix}.$$

Here, C_3 and C_4 are positive by definition and $C_4 > C_3$. Thus, in general, the nine-component tensor B_{ik} is reduced to nine independent parameters: five angles (θ, φ, α, β, γ) and four parameters C_1–C_4.

If the LHFI is a pure dipole–dipole interaction, we have $C_1 = C_2 = C_3 = 0$ and $C_4 = 1/r^3$, where *r* is the magnetic-ion–nucleus distance and the angles α, β, and γ define the bond direction. The parameters C_1–C_3 are completely defined by the nondipolar part, of the LHFI tensor; C_1 characterizes the isotropic part and C_2 and C_3 characterize deviations from the symmetric and axially symmetric form, respectively. The parameter C_4 contains the dipolar and so-called pseudodipolar covalent contributions. For the cubic centers, we have $C_2 = C_3 = 0$, while C_1 and C_4 are similar to A_s and A_p. An advantage of the method suggested is that it allows pictorial separation of particular characteristics of the interaction, which are absolutely indistinguishable in initial LHFI tensors. These characteristics make it possible to compare the data on different (nonequivalent) nuclei with each other and with the case of dipole–dipole interaction, as well as to compare different magnetic centers.

3. DISTORTIONS DETERMINED FROM THE LHFI FOR THE SECOND COORDINATION SHELL

Let us illustrate the application of the technique described above using the example of the second coor-

Table 1. Components of the LHFI tensors (MHz) of nuclei of the second coordination shell in $CaF_2 : Ce^{3+}$ (the parenthetical numbers are the errors in the last digit)

Component	Nucleus			
	A	*B*	*C*	*D*
A_{xx}	−0.375(5)	−0.366(5)	0.851(2)	0.737(2)
A_{xy}	0.196(7)	0.118(7)	0.476(6)	0.431(6)
A_{xz}	0.504(20)	0.406(20)	0.421(10)	0.485(10)
A_{yx}	0.196(10)	0.118(7)	0.476(6)	0.431(6)
A_{yy}	−0.375(5)	−0.366(5)	−0.408(15)	−0.379(15)
A_{yz}	0.504(20)	0.406(20)	0.112(30)	0.147(30)
A_{zx}	1.052(10)	0.881(10)	0.925(20)	1.065(20)
A_{zy}	1.052(10)	0.881(10)	0.246(10)	0.323(70)
A_{zz}	1.736(5)	1.648(5)	−0.954(4)	−0.786(5)

Table 2. LHFI parameters (nm^{-3}) and displacements (nm) of nuclei of the *A*–*D* types in the second coordination shell of $CaF_2 : Ce^{3+}$

Component	Nucleus			
	A	*B*	*C*	*D*
C_1	0.3(1)	0.1(1)	0.1(1)	0.0(1)
C_2	0.3(3)	0.1(3)	0	0
C_3	0.2(1)	0.1(1)	0.4(3)	0.2(1)
C_4	11.2(1)	9.8(1)	11.1(1)	10.5(1)
θ	27.6(3)	24.4(4)	74.5(4)	70.4(4)
φ	45	45	18.3(3)	18.6(4)
ΔX	0.010(2)	0.001(2)	0.001(2)	0.000(3)
ΔY	0.010(2)	0.001(2)	0.001(2)	0.001(3)
ΔZ	−0.012(2)	0.017(2)	−0.016(3)	0.018(3)

dination shell of the tetragonal $CaF_2 : Ce^{3+}$ center. The figure displays the projection of this paramagnetic complex onto the (100) plane. The compensator ion causes the following effect. Twenty-four fluorine ions of the second coordination shell are partitioned into four nonequivalent groups: type-*A* and type-*B* groups contain four ions each, and type-*C* and type-*D* groups contain eight ions each. From symmetry considerations, it follows that the LHFI of nuclei *A*, *B* and the LHFI of nuclei *C*, *D* are characterized by five and nine independent components, respectively. Baker *et al.* [4] presented tensors only for nuclei *A* and *B*; for this reason, we carried out more accurate measurements (Table 1). Having applied the technique described above to the tensors listed in Table 1, we obtained the corresponding LHFI parameters (Table 2). One can see that the nondipolar interaction parameters C_1–C_3 are smaller than C_4 by two orders of magnitude, which allows us to consider these tensors to be of a pure dipolar nature. Furthermore, the nuclei *A*–*D* are virtually equivalent. It should be emphasized that these properties cannot be detected by considering the tensors themselves (see Table 1). The parameters C_4 make it possible to determine the magnetic-ion–nucleus distance independently for each of the *A*–*D* groups. Table 2 lists the changes in coordinates of nuclei *A*–*D* in the *XYZ* frame with its origin at the magnetic ion with respect to the equilibrium frame of reference related to the cube center. We note that the error in the quantities found includes the probable nondipolar contribution to C_4 under the assumption that this contribution does not exceed the root-mean-square value of the parameters C_1–C_3.

One readily sees that $\Delta X = \Delta Y = 0$ for nuclei *B*, *C*, and *D* to within the experimental error (see figure); ΔZ increases for groups *B* and *D* but decreases for *C* by the same value. Hence, the coordinate changes can be explained only by the fact that Ce^{3+} is displaced toward the compensator ion by $\delta = 0.17(3)$ Å, while the nuclei themselves remain at their sites. As for nuclei *A*, the compensator ion pushes them apart by $\varepsilon_z = 0.05(5)$ Å along the *Z* axis and by $\varepsilon_x = \varepsilon_y = 0.10(3)$ Å (taking into account the symmetry of the center). Baker *et al.* [4] assumed these nuclei to be displaced along each of the three axes by the same amount and found that $\varepsilon_x = \varepsilon_y = \varepsilon_z = 0.11$ Å, while the displacement of the Ce^{3+} ion itself is $\delta = 0.16$ Å. Our result seems to be more reasonable physically, since Ca and F ions are densely packed along the cube body diagonals. On the whole, the distortion pattern described in terms of the LHFI parameters is more accurate than that determined immediately from the experimental data, since the nondipolar interaction component is (at least in part) eliminated from the parameter C_4.

4. DISTORTIONS OF THE FIRST COORDINATION SHELL OF Ce^{3+}

We also attempted to apply our technique to nuclei of the first coordination shell of Ce^{3+} in the fluorite homologous series, since noncubic centers here remain poorly studied. These nuclei are classified into two nonequivalent groups: four nuclei of type *E* on the compensator ion side and four nuclei of type *F* on the opposite side; their LHFI is described by tensors with five independent components. The relevant experimental data are presented in [4, 12, 13]. The LHFI parameters calculated from these tensors are listed in Table 3. One readily sees that the parameters C_1–C_3 are very large; hence, C_4 contains a fairly large covalent contribution.

To estimate distortions of the first coordination shell, the dipolar contribution must be separated from C_4.

Using the Babershke approach [1], we assumed that the contribution from nondipolar interaction to C_4 in the fluorite homologous series is proportional to the quantity $[(C_1^2 + C_2^2 + C_3^2)/3]^{1/2}$ (which is the measure of covalence) for all the nuclei of the first coordination shell. We calculated the proportionality factor for $CaF_2 : Ce^{3+}$ after subtracting the dipolar component from C_4; the dipolar component was calculated under the assumption that the distance from Ce^{3+} to the fluorine nuclei of type *E* on the compensator side is equal to the sum of their ionic radii (2.36 Å). Taking into account that the ionic radii of Ca^{2+} and Ce^{3+} almost coincide and that the Ce^{3+} ion is displaced toward the compensator ion, such an assumption is well founded. Using the calculated coefficient of proportionality, we separated out the dipolar component of C_4 for all three crystals and determined the distances R_E and R_F of nuclei of types *E* and *F*, respectively, to the Ce^{3+} ion. These distances are listed in Table 3 and compared with the corresponding distances R_0 in the undistorted lattice.

As is evident from Table 3, the distances R_E are very close to 2.36 Å, i.e., to the sum of the Ce^{3+} and F ionic radii. This means that Ce^{3+} ions in all three lattices are kept close to the fluorine ions on the compensator side. The distance R_F on the opposite side increases (Table 3) but to a lesser extent than follows from the lattice parameter increase. Hence, the fluorine nuclei are displaced toward Ce^{3+}; this displacement increases as one goes from CaF_2 to BaF_2.

In its symmetry, the LHFI of the compensator ion is described by an axially symmetric tensor and is characterized by two parameters, C_1 and C_4. Table 3 lists the distances R_{comp} from the Ce^{3+} ion (taking its displacement into account) to the compensator ion calculated under the assumption that the latter remains in the equilibrium position, which is not evident. Assuming this condition to be met in CaF_2 and using the same technique as that applied to the nuclei of the first coordination shell, the Ce^{3+}–compensator distance R_{comp} can be determined in the SrF_2 and BaF_2 lattices. The corresponding results are given in Table 3. As expected, the compensator ion is displaced toward Ce^{3+} due to their mutual attraction.

Table 3 clarifies the qualitative pattern of distortions of the first coordination shell: the angle θ exceeds its equilibrium value 54.7° for nuclei of type *E* and is smaller than this value for nuclei of type *F* (on the opposite side). This means that because of the attraction between the Ce^{3+} and compensator ions, the *E*-type fluorine ions between them are "squeezed out," whereas the lattice is contracted on the opposite side. However, these angles seem to be underestimated for nuclei of the *E* and *F* types, since their values do not conform to the Ce^{3+} displacement corresponding to the distortions of the second coordination shell (Table 2). This discrepancy may be due to the very large value of C_3 (characterizing the deviation of the LHFI from its axially symmetric form), which is specific to the LHFI of the Ce^{3+} ion; such disagreement is absent for other rare-earth ions.

Table 3. LHFI parameters C_i (nm^{-3}) and θ (angle degrees) of the *E*- and *F*-type nuclei of the first coordination shell of Ce^{3+} and of the compensator ion

Nucleus	Parameter	CaF_2	SrF_2	BaF_2
111	C_1	9.8(1)	12.7(1)	15.4(1)
	C_2	22.2(3)	23.1(3)	26.0(1)
	C_3	60.0(1)	55.4(1)	52.6(1)
	C_4	107.0(2)	103.2(2)	101.2(1)
	θ	55.1(1)	56.9(1)	58.5(1)
$\bar{1}\bar{1}\bar{1}$	C_1	8.5(1)	7.9(1)	7.4(1)
	C_2	16.9(3)	19.0(3)	22.1(1)
	C_3	53.1(1)	45.8(1)	40.7(1)
	C_4	93.8(2)	86.6(2)	82.0(1)
	θ	44.5(1)	45.0(1)	45.8(1)
	R_E	0.236	0.238	0.240
	R_F	0.246	0.252	0.256
	R_0	0.236	0.250	0.268
002 (compensatorion)	C_1	41.2(1)	32.4(1)	21.6(1)
	C_4	64.9(2)	59.6(2)	52.7(1)
	R'_{comp}	0.255(1)	0.271(1)	0.290(1)
	R_{comp}	0.255(1)	0.261(1)	0.271(1)

In summary, we note that our technique, in which the experimentally determined LHFI tensors are expressed in terms of the parameters introduced in this paper, allows one to estimate the local lattice distortions produced by any paramagnetic ion in any crystal.

REFERENCES

1. K. Babershke, Z. Phys. **252**, 1 (1972).
2. C. H. Anderson, P. Call, J. Stott, and W. Hayes, Phys. Rev. B **11** (9), 3305 (1975).
3. J. M. Baker and T. Christidis, J. Phys. C **10** (7), 1059 (1977).
4. J. M. Baker, E. R. Davies, and J. P. Hurrel, Proc. R. Soc. London, Ser. A **308**, 403 (1968).
5. J. P. Wolfe and R. S. Markiewicz, Phys. Rev. Lett. **30** (22), 1104 (1976).
6. B. R. McGarvey, J. Chem. Phys. **65** (3), 955 (1976).

7. A. D. Gorlov, V. B. Guseva, A. P. Potapov, and A. I. Rokeakh, Fiz. Tverd. Tela (St. Petersburg) **43** (3), 456 (2001) [Phys. Solid State **43**, 473 (2001)].
8. A. D. Gorlov and A. P. Potapov, Fiz. Tverd. Tela (St. Petersburg) **42** (1), 49 (2000) [Phys. Solid State **42**, 51 (2000)].
9. A. D. Gorlov, V. B. Guseva, A. Yu. Zakharov, *et al.*, Fiz. Tverd. Tela (St. Petersburg) **40** (12), 2172 (1998) [Phys. Solid State **40**, 1969 (1998)].
10. T. I. Sanadze and G. R. Khutsishvili, in *Problems of Magnetic Resonance* (Nauka, Moscow, 1978), pp. 206–225.
11. A. Carrington and A. D. McLachlan, *Introduction to Magnetic Resonance with Applications to Chemistry and Chemical Physics* (Harper and Row, New York, 1967; Mir, Moscow, 1970).
12. B. G. Berulava and R. I. Mirianashvili, Phys. Status Solidi B **127**, K69 (1985).
13. R. P. Akhaladze, R. I. Mirianashvili, and T. I. Sanadze, Izv. Akad. Nauk SSSR, Ser. Fiz. **47** (12), 2319 (1983).

Translated by A. Kazantsev

Physics of the Solid State, Vol. 44, No. 10, 2002, pp. 1885–1888. Translated from Fizika Tverdogo Tela, Vol. 44, No. 10, 2002, pp. 1799–1801.

DEFECTS, DISLOCATIONS, AND PHYSICS OF STRENGTH

Motion of Dislocations through Ensembles of Forest Dislocations and Point Obstacles upon the Simultaneous Action of Static and Cyclic Loads

B. M. Loginov, A. N. Proskurnin, and E. V. Vershinin

Kaluga Branch, Bauman Moscow State Technical University, ul. Bazhenova 4, Kaluga, 248600 Russia

e-mail: loginov@kaluga.ru

Received December 11, 2001; in final form, January 15, 2002

Abstract—Methods of computer simulation developed for hcp crystals were used to analyze the motion of gliding dislocations through composite ensembles of points obstacles and vibrating forest dislocations. It is shown that the possibility for forest dislocations to suffer forced vibrations increases the transparency of a composite ensemble. It was established that as the amplitude of dislocation vibrations reaches a certain limit depending on the strength of point obstacles, such obstacles in a composite ensemble almost completely lose their ability to hinder the motion of gliding dislocations. © *2002 MAIK "Nauka/Interperiodica".*

INTRODUCTION

The deformation strengthening and plastic flow of crystals is substantially determined by the interaction of gliding dislocations with random ensembles of defects. The most typical ensembles of such defects are ensembles of points obstacles and the so-called forest dislocations. A theoretical investigation of the processes of dislocation interactions with such ensembles using analytical methods proves to be ineffective because of the multiple character of interactions and complex geometrical statistics. Upon experimental investigations, the effects of isolated factors on the occurring processes can be distinguished and analyzed only in rare, exclusive cases [1–4]. At the same time, the experience of recent decades shows that the methods of computer simulations can serve as a fine tool for systematic studies of the processes of interaction of gliding dislocations with random ensembles of obstacles of various origin. In [5, 6], computer simulation was used to analyze the effect of the flexibility of forest dislocations on the forest transparency to moving dislocations. In [7], the processes of motion of gliding dislocations through composite ensembles of forest dislocations and point obstacles were investigated. In [8], the processes of motion of gliding dislocations through a vibrating dislocation forest were analyzed. The present work is a continuation of the above investigations and is devoted to an analysis of the results of simulation of the processes of motion of gliding dislocations through composite ensembles of point obstacles and vibrating forest dislocations.

1. MODEL

The simulation was performed as applied to hcp crystals (Fig. 1). We considered the motion of a probe edge dislocation with a Burgers vector $\mathbf{b} = 1/3\,[\bar{1}2\bar{1}0]$ in the basal plane (0001) under the effect of an external shear stress. The dislocation forest consisted of 12 types of screw dislocations with Burgers vectors $\mathbf{b} = 1/3\,\langle\bar{2}113\rangle$ located on second-order pyramid planes $\{2\bar{1}\bar{1}2\}$ with the same density of occupation for each type.

The strength of point obstacles was characterized by the critical angle of circumventing φ_{cr}.

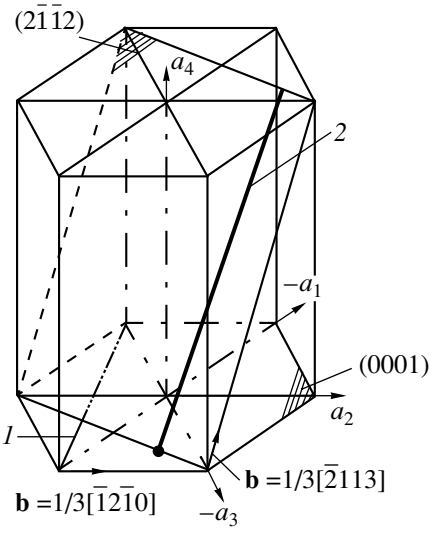

Fig. 1. A schematic of dislocations in hcp crystals (a forest dislocation located only in one plane (2$\bar{1}\bar{1}$2) is shown): (*1*) probe gliding dislocation and (*2*) forest dislocation.

1063-7834/02/4410-1885$22.00 © 2002 MAIK "Nauka/Interperiodica"

The coordinates of the points of intersection of forest dislocations with the plane of motion of the probe dislocation, as well as the coordinates of point obstacles, were specified in a random manner.

The direction and the plane of application of an external periodic load were $[10\bar{1}0]$ and $(10\bar{1}0)$, respectively. In this case, the Schmid factor in the slip system of the probe dislocation proved to be zero; i.e., the basal dislocation was not subjected to the direct action of the periodic load. At the same time, eight types of forest dislocations belonged to slip systems for which the Schmid factor was equal to $m = \pm\frac{\sqrt{3}c}{4\sqrt{a^2 + c^2}}$ (here, a and c are the lattice parameters), and four types of dislocations belonged to slip systems with $m = 0$. It is assumed that, under the effect of the periodic external load, the forest dislocations execute forced periodic vibrations in their slip planes, remaining rectilinear and retaining the initial orientation with respect to the line of intersection of their slip plane with the slip plane of the probe dislocation. We considered synchronous periodic vibrations of the forest dislocations with a zero initial phase and with a vibration amplitude proportional to the Schmid factor.

The motion of a probe gliding dislocation through a composite ensemble of obstacles was considered in a quasi-static approximation. In this case, the problem reduces to finding sequences of obstacles such that, at a fixed level of an external shear stress, they resisted the motion of a gliding dislocation for the entire period of vibration of forest dislocations.

The simulation was performed under the following assumptions:

(1) the probe gliding dislocation is flexible; its shape for each fixed value of the phase of vibrating forest dislocations is determined by the external shear stress and the total field of internal stresses generated by the forest dislocations;

(2) the self-action of a gliding dislocation is taken into account in the linear-tension approximation;

(3) the formation of jogs and recombination zones upon the intersection of a gliding dislocation with forest dislocations is ignored;

(4) to exclude the effect of the edge of the simulation domain on the motion of the probe dislocation, periodic boundary conditions were used;

(5) the level of the external shear stress at which the gliding dislocation passes through the simulation domain is assumed to represent the critical stress for passage τ_{cr}.

In terms of the above assumptions, the equilibrium configuration of the gliding dislocation at a given level of the external shear stress τ_{yz}^{ex} and for all values of the phase of vibrating forest dislocations ($|\psi| \le \pi/2$) should be described by the following equation:

$$T\kappa(x_j, y_j, 0) = b\left\{\tau_{yz}^{ex} + \sum_D \tau_{yz}^{in}[(x_j - x_i), (y_j - y_i), 0]\right\}, \quad (1)$$

where $T = Gb^2/2$; G is the shear modulus; b is the Burgers vector of the gliding dislocation; $\kappa(x_j, y_j, 0)$ is the local curvature of the gliding dislocation at the point with coordinates $(x_j, y_j, 0)$; and $\tau_{yz}^{in}[(x_j - x_i), (y_j - y_i), 0]$ is the internal stress at the point $(x_j, y_j, 0)$ generated by a forest dislocation located at the point $(x_j, y_j, 0)$. The region D over which summation was performed was determined according to the Predvoditelev–Stratan criterion [9]. Note that at the points of intersection of the probe dislocation with forest dislocations, the right-hand side of Eq. (1) has singularities. In the vicinities of the singular points, the solution to Eq. (1) was sought in the form of a power series with irrational exponents, whose magnitudes depended on the type of forest dislocations [10]. In the regions between obstacles, the equilibrium configuration of the gliding dislocation was constructed using the radius-of-curvature method [10], in which the shape of the dislocation was approximated by segments of circles that were joined without breaks. The radii of these circles at the points with the coordinates $(x_j, y_j, 0)$ were determined by Eq. (1).

The procedure of finding the solution to Eq. (1) represents a modification of previously developed techniques of constructing equilibrium configurations of gliding dislocations moving through immobile composite ensembles [7] or through a forest of vibrating dislocations [8].

The parameters of simulation were chosen as applied to zinc crystals; i.e., $b = |\mathbf{a}| = 2.66 \times 10^{-10}$ m, $|\mathbf{c}| = 4.94 \times 10^{-10}$ m, and $G = 3.83 \times 10^{10}$ N m^{-2}. The simulation was performed for composite ensembles of forest dislocations and point obstacles with varying strengths φ_{cr} and densities ρ_p of point obstacles and a constant density of forest dislocations $\rho_f = 4 \times 10^{10}$ m^{-2}.

2. RESULTS AND DISCUSSIONS

The dependences of the critical stress for passage τ_{cr} on the relative amplitude of vibrations of forest dislocations A/λ (where $\lambda = \rho_f^{-1/2}$) obtained for various composite ensembles of forest dislocations and point obstacles are shown in Fig. 2. Curves *1–3* in Fig. 2a correspond to the $\tau_{cr}(A/\lambda)$ dependences for composite ensembles consisting of forest dislocations and point obstacles of strength $\varphi_{cr} = 2.7925$ rad at various values of the relative concentration of point obstacles in composite ensembles. It can be seen that in all cases the effect of point obstacles in a composite ensemble on the

critical stress for passage manifests itself only in a range of the relative amplitudes of vibrations of 0–0.08. The greater the magnitude of the relative concentration of point obstacles in a composite ensemble, the greater the level of the critical stress for passage τ_{cr}. However, an increase in the amplitude of vibrations of forest dislocations leads to a decrease in the ability of point obstacles to resist the motion of gliding dislocations. Beginning from a relative amplitude of vibrations $A/\lambda = 0.08$, point obstacles almost completely stop rendering any resistance to gliding dislocations that move through composite ensembles. It is seen from Fig. 2a that at $A/\lambda \geq 0.08$ the character of the $\tau_{cr}(A/\lambda)$ functions for the composite ensembles of forest dislocation and point obstacles under consideration completely corresponds to the dependence obtained for the corresponding single-component ensembles of forest dislocations.

Thus, the results displayed in Fig. 2a suggest that the relative amplitude of vibrations of forest dislocations at which a break in the $\tau_{cr}(A/\lambda)$ dependences appears is directly caused by the strength of point obstacles in the composite ensemble. To test this hypothesis, we simulated the processes of motion of gliding dislocations through composite ensembles of forest dislocations and point obstacles of various strength.

Figure 2b displays the variation of the critical stress for passage τ_{cr} as a function of the relative amplitude of vibrations of forest dislocations A/λ obtained for composite ensembles of forest dislocations and point obstacles of various strengths. In accordance with [7], the characteristics of single-component ensembles of point obstacles were chosen in such a way that at $A/\lambda = 0$ the single-component ensembles of point obstacles of various strengths contributed equally to the deformation strengthening of corresponding dislocation ensembles. It can be seen that, in this case as well, an increase in the amplitude of vibrations of forest dislocations leads to a decrease in the ability of point obstacles to render resistance to the motion of gliding dislocations through composite ensembles. However, now, the point obstacles, in accordance with their strength, stop rendering resistance to the motion of gliding dislocations at different relative amplitudes of vibrations of forest dislocations. The results obtained permitted us to establish that weak point obstacles, characterized by a strength $\varphi_{cr} = 2.8798$ rad, stop rendering noticeable resistance to the motion of gliding dislocations through composite ensembles beginning from a value of the relative amplitude of vibrations of forest dislocations equal to 0.04. However, as the strength of point obstacles increases to $\varphi_{cr} = 2.6878$ rad, their effect on the resistance to the motion of gliding dislocations in a composite ensemble proves to be noticeable up to the relative amplitudes of vibrations equal to 0.10. Thus, the whole body of the results obtained shows that the relative amplitude of vibrations of forest dislocations in a composite ensemble at which there is a break in the $\tau_{cr}(A/\lambda)$ dependence is directly related to the strength of point obstacles that enter into the composite ensemble.

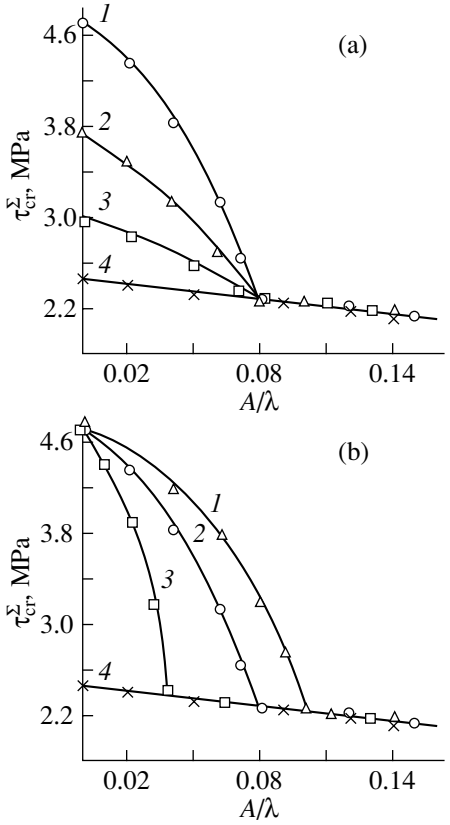

Fig. 2. Variations of the critical stress for passage τ_{cr} as functions of the relative amplitude of vibrations of forest dislocations A/λ for various composite ensembles of forest dislocations and point obstacles of strength φ_{cr} and density ρ_p: (a) $\varphi_{cr} = 2.7925$ rad, (*1*) $\rho_p = 3.75 \times 10^{13}$, (*2*) 1.81×10^{13}, and (*3*) 0.63×10^{13} m^{-2}; (b) (*1*) $\varphi_{cr} = 2.6878$ rad, $\rho_p = 1.88 \times 10^{13}$ m^{-2}; (*2*) $\varphi_{cr} = 2.7925$ rad, $\rho_p = 3.75 \times 10^{13}$ m^{-2}; and (*3*) $\varphi_{cr} = 2.8798$ rad, $\rho_p = 6.83 \times 10^{13}$ m^{-2}. In all the cases, the density of forest dislocations ρ_f was 4.0×10^{10} m^{-2}. Curves (*4*) in both (a) and (b) represent dependences obtained for the motion of gliding dislocations through corresponding single-component ensembles of forest dislocations.

REFERENCES

1. B. I. Smirnov, *Dislocation Structure and Crystal Strengthening* (Nauka, Leningrad, 1981).
2. I. N. Zimkin, T. V. Samoĭlova, and B. I. Smirnov, Fiz. Tverd. Tela (Leningrad) **17** (6), 1841 (1975) [Sov. Phys. Solid State **17**, 1208 (1975)].
3. I. N. Zimkin, T. V. Samoĭlova, and B. I. Smirnov, Fiz. Tverd. Tela (Leningrad) **20** (12), 3703 (1978) [Sov. Phys. Solid State **20**, 2141 (1978)].

4. V. V. Shpeĭzman, V. I. Nikolaev, B. I. Smirnov, *et al.*, Fiz. Tverd. Tela (St. Petersburg) **40** (9), 1639 (1998) [Phys. Solid State **40**, 1489 (1998)].
5. B. M. Loginov and A. A. Predvoditelev, Fiz. Tverd. Tela (Leningrad) **23** (1), 112 (1981) [Sov. Phys. Solid State **23**, 63 (1981)].
6. A. A. Predvoditelev and B. M. Loginov, Fiz. Tverd. Tela (Leningrad) **25** (10), 3181 (1983) [Sov. Phys. Solid State **25**, 1835 (1983)].
7. B. M. Loginov and S. V. Tolstykh, Fiz. Tverd. Tela (St. Petersburg) **35** (2), 469 (1993) [Phys. Solid State **35**, 242 (1993)].
8. B. M. Loginov and V. T. Degtyarev, Phys. Status Solidi A **120**, 387 (1990).
9. I. V. Stratan and A. A. Predvoditelev, Fiz. Tverd. Tela (Leningrad) **12** (7), 2141 (1970) [Sov. Phys. Solid State **12**, 1702 (1971)].
10. A. A. Predvoditelev and G. I. Nichugovskiĭ, Kristallografiya **17** (1), 166 (1972) [Sov. Phys. Crystallogr. **17**, 132 (1972)].

Translated by S. Gorin

Physics of the Solid State, Vol. 44, No. 10, 2002, pp. 1889–1897. Translated from Fizika Tverdogo Tela, Vol. 44, No. 10, 2002, pp. 1802–1810.

MAGNETISM AND FERROELECTRICITY

Electron Transport in Granular Amorphous Silicon Dioxide Films with Ferromagnetic Nanoparticles Placed in a Magnetic Field

L. V. Lutsev*, Yu. E. Kalinin, A. V. Sitnikov**, and O. V. Stogneĭ****

** Domen Research & Development Institute, St. Petersburg, 196084 Russia*
e-mail: lutsev@domen.ru
*** Voronezh State Technical University, Moskovskiĭ pr. 14, Voronezh, 394026 Russia*
e-mail: kalinin@ns1.vstu.ac.ru
Received November 13, 2001

Abstract—Electron transport in amorphous silicon dioxide films with embedded nanoparticles (Co, Nb, Ta) was studied. The mean number of localized states in the interparticle tunneling channel was derived from the temperature dependence of conductivity for various grain concentrations under the assumption of the electron transport being governed by resonance tunneling in a chain of localized states between grains. To confirm the assumption of the inelastic character of tunneling, the dependences of the magnetoresistance on grain concentration, temperature, and magnetic field were studied. Accepting the single-orbital model, where the intergrain tunneling magnetoresistance is determined by *s*–*s* tunneling, it was found that the existence of weakly split localized states in the tunneling channel results in a lack of magnetoresistance saturation in strong magnetic fields. The combined effect of a decrease in the *s*–*s* tunneling coefficient and of growth in the probability of inelastic electron spin scattering with increasing length of the chain of localized states between particles in which the electron is tunneling accounts for the characteristic temperature–concentration dependences of the magnetoresistance. The experimental observation of these features provides an argument for the electron transport in *a*-SiO_2(Co,Nb,Ta) structures being governed by inelastic resonance tunneling through intergrain localized states. *© 2002 MAIK "Nauka/Interperiodica".*

1. INTRODUCTION

Electron transport under a magnetic field, which occurs in granular structures with ferromagnetic nanoparticles (grains) embedded in an insulating matrix, exhibits a number of properties that distinguish them markedly from bulk amorphous and crystalline materials. Among these properties are temperature anomalies in the giant magnetoresistance associated with Coulomb blockade [1], the anomalous Hall effect in the tunneling-conduction regime [2, 3], and long-term relaxation of magnetization and tunneling magnetoresistance [4].

The purpose of this study was to investigate the effect of localized states in a matrix on the magnetoresistance of granular structures. The experimental studies were performed on granular films of amorphous silicon dioxide with embedded $Co_{86}Nb_{12}Ta_2$ ferromagnetic nanoparticles. The metallic phase (grains) was present in concentrations for which the granular structure was below the percolation threshold. In this case, tunneling between grains provides a major contribution to electron transport. The tunneling can have either elastic or inelastic character and proceed via localized states in the matrix. The number of localized states was calculated in terms of a model relating the inelastic resonance tunneling between grains via a chain of localized states in an amorphous matrix to the temperature dependence of conductivity [5, 6]. According to this model, the exponent of the temperature dependence of conductivity in a channel containing *n* localized states near the Fermi level is fully determined by *n*.

The experimental studies of magnetoresistance were conducted at 77 and 295 K in magnetic fields *H* ranging from 0 to 25 kOe. The magnetoresistance was found to be negative. It depends on the magnetic field only weakly and is small for $H < 2$ kOe. For $H > 2$ kOe, there exists a magnetic field interval within which the variation of the magnetoresistance of a granular structure with its metallic-phase concentration corresponding to the percolation threshold region is the strongest. A further increase in the field saturates the magnetoresistance. In granular structures with lower metallic phase concentrations, the magnetoresistance saturation effect in the magnetic field range covered is either considerably weaker or is altogether absent. The temperature-induced variation of the magnetoresistance at low grain concentrations was found to be substantially larger than that observed in structures near the percolation threshold. In structures with low grain concentrations, the magnetoresistance at low temperatures (T = 77 K) reaches higher levels than that in granular structures near the percolation threshold. As shown in this

study, most of the above properties of the magnetoresistance can be attributed to spin-dependent tunneling via localized states in the matrix. The experimental findings are treated in terms of the tunneling-magnetoresistance model developed in [7, 8].

2. TEMPERATURE DEPENDENCE OF THE CONDUCTIVITY AND THE NUMBER OF LOCALIZED STATES IN THE MATRIX

The nature of the temperature dependence of conductivity in granular structures remains an open problem. Experimental studies suggest that the conductivity σ of granular structures scales with temperature as

$$-\ln\sigma \propto T^{-\alpha} \tag{1}$$

with $\alpha = 1/2$ [9, 10]. Various models have been proposed to explain relation (1). In particular, the 1/2 power law can be treated as a manifestation of a Coulomb gap in the density of electron states $g(E)$ in the grains, where the density of states vanishes as $g(E) \propto (E - E_F)^2$ near the Fermi energy E_F. A Coulomb gap opens in disordered systems as a result of Coulomb interaction between grains [11, 12]. An essential factor is the presence of a large random potential, which causes recharging of the originally neutral grains in the ground state of the system [13]. A gap opens when the random potential becomes comparable in magnitude to the particle charge energy. However, the gap model operates only at low temperatures. It was shown in [14] that the 1/2 power law can be a consequence of grain size scatter.

In this study, we employ a theoretical model of inelastic tunneling through amorphous layers [5, 6] to derive Eq. (1). According to this model, the observed experimental temperature dependences of the conductivity are accounted for by resonance tunneling in a chain of localized states in the amorphous layer between tunneling junctions. Because a grain contains a sufficiently large number of atoms ($N \sim 1000$), this theoretical model is applicable to determination of the character of electron transport between metallic particles in granular structures. Another favorable factor is that the Coulomb energy between grains can give rise to the formation of quasi-stable one-dimensional conduction channels [15]. This model was used to interpret the temperature dependences of one-electron transport under Coulomb blockade conditions in [16]. The localized states can originate from defects in the matrix structure and grain–matrix interfaces. The existence of these states brings about a sharp increase in the barrier tunneling transmittance. According to the model proposed in [5, 6], inelastic resonance tunneling in channels containing localized states near the Fermi level with an energy scatter of about kT plays a noticeable part in the conduction mechanism. The temperature dependence of conductivity in a channel containing n impurities follows a power law [5],

$$\sigma_n = P\left(\frac{\Lambda^2}{\rho_0 c^5}\right)^{(n-1)/(n+1)} \frac{(ga^2n^2l)^n T^{\gamma_n} E^{\beta_n}}{al} \times \exp\left[\frac{-2l}{a(n+1)}\right], \tag{2}$$

where a is the radius of the localized state, l is the mean distance between grains, $\gamma_n = n - 2/(n+1)$, $\beta_n = 2n/(n+1)$, P is a coefficient, Λ is the deformation potential constant, ρ_0 is the density of the matrix material, c is the velocity of sound, g is the density of localized states, and E is the depth of a localized state in the barrier region. The mean conductivity between grains is a sum,

$$\sigma^{(gr)} = \sum_n \sigma_n. \tag{3}$$

As the temperature increases, inelastic channels with a larger number of impurities become operable. As shown in [5], there exists a temperature interval $[T_n, T_{n+1}]$ within which the largest contribution to the conductivity in Eq. (3) comes from one term σ_n. In this interval, the temperature dependence of the conductivity $\sigma^{(gr)}$ in Eq. (3) can be approximated by a power law with an exponent γ_n. For $T > T^*$, where T^* is given by the relation

$$\ln(T^* gal^2) \approx -\left(\frac{l}{a}\right)^{1/3},$$

Eq. (3) should include contributions due to several channels; as a result, the conductivity $\sigma^{(gr)}$ will now be determined by the contributions from channels for which the number n is close to the mean number $\langle n \rangle$ of localized states between grains. In this case [5],

$$\ln\sigma^{(gr)} \propto -\left[\frac{2l}{a}\ln\left(\frac{1}{gal^2T}\right)\right]^{1/2}. \tag{4}$$

For certain values of the radius of the localized state a and distances between grains l falling in the range in which $gal^2T \approx 1$, $\sigma^{(gr)}$ calculated from Eq. (4) to the first order in $1/T$ exhibits temperature dependence (1) with $\alpha = 1/2$. Similar results were obtained in the model of hopping conduction in metal–semiconductor–metal junctions proposed in [17].

An increase in intergrain distance results in a rise of the number of channels and of impurities in them. As $n \longrightarrow \infty$, the total conductivity over all channels transfers from resonance tunneling to the hopping conduction regime, which is described by Mott's law [18] having the form of Eq. (1) with $\alpha = 1/4$.

Below the percolation threshold, the total conductivity σ of a granular structure is dominated by the tunneling conductivity between grains $\sigma^{(gr)}$ or, if the grains form limited conducting clusters, by the conductivity of

the clusters and the tunneling conductivity between them $\sigma^{(gr)}$. Because the cluster conductivity is considerably larger than the tunneling conductivity, we shall assume, as a first approximation, that the conductivity σ of a granular structure in the temperature interval $[T_n, T_{n+1}]$ depends on temperature in a power law, which is described by the expression for $\sigma^{(gr)}$ with $n = \langle n \rangle$ (the structure-averaged number of localized states in the tunneling channels between grains). Approximating the experimental temperature dependences of conductivity by power-law relations with an exponent γ and taking into account Eq. (2), we can determine the average number of localized states $\langle n \rangle$ that participate in electron transport in a granular structure at a given temperature:

$$\langle n \rangle = \frac{1}{2}[\gamma - 1 + (\gamma^2 + 2\gamma + 9)^{1/2}]. \quad (5)$$

This approach was used in [19] to find $\langle n \rangle$ for an *a*-C:H(Co) structure.

Experimental determination of the number of localized states from the temperature dependences of conductivity was performed on films of amorphous silicon dioxide, *a*-SiO_2, with ferromagnetic $Co_{86}Nb_{12}Ta_2$ nanoparticles. These films with composition $(a\text{-}SiO_2)_{100-x}$ + $(Ci_{86}Nb_{12}Ta_2)_x$ were grown on fixed corundum-based ceramic substrates through Ar-ion beam cosputtering of SiO_2 and a $Co_{86}Nb_{12}Ta_2$ alloy. The film thicknesses ranged from 4.0 to 5.1 μm. The metallic phase concentrations x varied in the range 22.4–63 at. % and corresponded to structures with grain concentrations below the percolation threshold. The average grain size increased with concentration from 2.0 nm for x = 22.4 at. % to 5 nm for x = 63 at. % (Fig. 1). The dark inclusions in Fig. 1 identify grains of the metallic alloy, and the bright background corresponds to the dielectric phase of silicon dioxide.

Figure 2 plots concentration dependences of the electrical resistivity $\rho = \sigma^{-1}$ of $(a\text{-}SiO_2)_{100-x}$ + $(Ci_{86}Nb_{12}Ta_2)_x$ granular films measured at room temperature on samples in the original state and after heat treatment. The films were annealed in vacuum at a pressure of ~10 μTorr at T = 400°C for 30 min. After the heat treatment, the concentration dependences of the electrical resistivity assumed an *S* shaped form characteristic of percolation systems. We note that annealing of granular structures results in an increase in the electrical resistivity for compositions with a low concentration of the metallic phase and in its decrease for large x, near the percolation threshold. After annealing, the percolation threshold shifts toward lower concentrations x.

The temperature dependence of the conductivity of nonannealed samples was measured with the current flowing in the film plane (horizontal symmetry) at a voltage of 0.1 V under cooling. To reveal the power law, relative temperature dependences are plotted in Fig. 3 on a log–log scale. The origin is placed at the conductivity σ_0 at T_0 = 292 K. The average number of localized states $\langle n \rangle$ in the tunneling channels between isolated conducting clusters as a function of grain concentration was derived from the exponent γ of the temperature dependences of conductivity with the use of Eq. (5) and is plotted in Fig. 4. We readily see that $\langle n \rangle$ grows fairly rapidly with increasing concentration x.

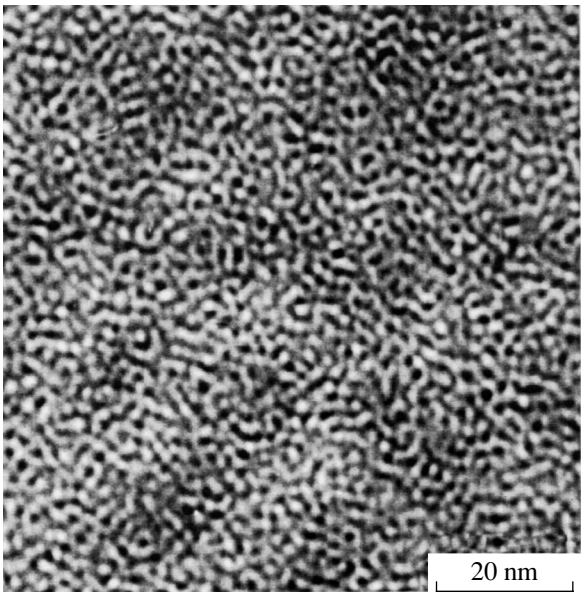

Fig. 1. Microstructure of an $(a\text{-}SiO_2)_{100-x}$ + $(Co_{86}Nb_{12}Ta_2)_x$ granular film with x = 63 at. %.

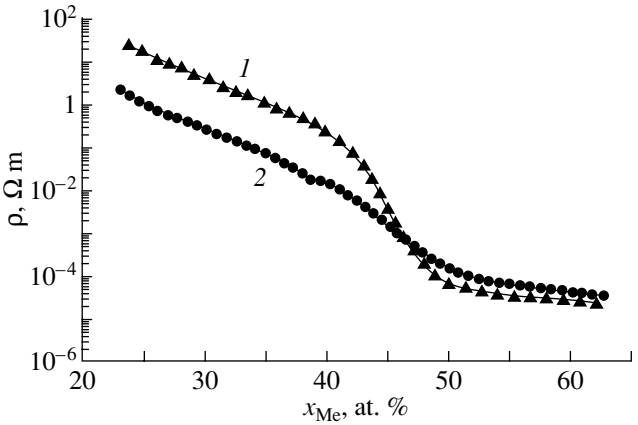

Fig. 2. Electrical resistivity ρ of an $(a\text{-}SiO_2)_{100-x}$ + $(Co_{86}Nb_{12}Ta_2)_x$ granular structure as a function of metallic phase concentration x (*1*) after annealing and (*2*) before annealing.

3. MAGNETORESISTANCE

Localized states in an insulating matrix exert a considerable effect on spin-polarized electron transport.

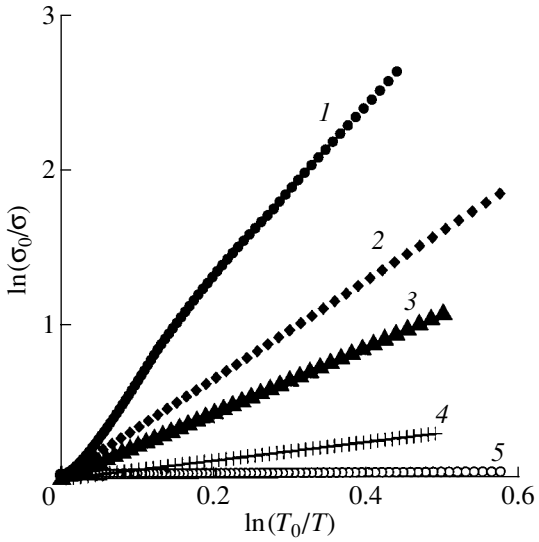

Fig. 3. Relative temperature dependences of the conductivity of a-SiO_2(Co, Nb, Ta) nonannealed samples plotted for various grain concentrations x (at. %): (*1*) 22.4, (*2*) 31.7, (*3*) 41.9, (*4*) 54.5, and (*5*) 61.7.

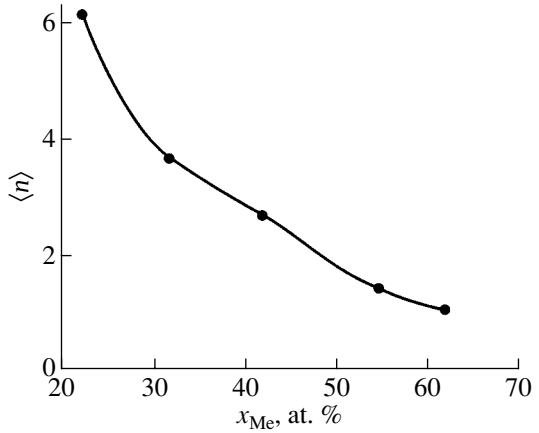

Fig. 4. Mean number of localized states $\langle n \rangle$ in the tunneling channels between grains plotted vs. metallic phase concentration x in nonannealed a-SiO_2(Co,Nb,Ta) samples.

Although the conductivity involving tunneling between ferromagnetic metals increases with impurity concentration in the insulating matrix, the tunneling magnetoresistance decreases down to 4% [20, 21]. The sharp drop in magnetoresistance is favored by the multitude of impurity resonance states, which results in a decrease in the polarization of tunneling electrons, as well as by the random distribution of the impurities from which the electrons are scattered. At the same time, the magnetoresistance of tunneling junctions in the presence of paramagnetic impurities can be higher than that in the same structure but without impurities [22].

We define the junction magnetoresistance (JMR) by the relation [8]

$$\text{JMR} = \frac{R(H) - R(0)}{R(0)} = \frac{\sigma(0) - \sigma(H)}{\sigma(H)}, \qquad (6)$$

where $R(0)$ and $R(H)$ are the resistances between junctions without a field and in a magnetic field H, respectively. The magnetoresistance measurements on nonannealed a-SiO_2(Co, Nb, Ta) granular structures were conducted at T = 77 and 295 K with horizontally arranged electrical contacts in magnetic fields that were oriented perpendicular to the film plane and varied from 0 to 25 kOe. Figure 5 shows the dependence of JMR on applied magnetic field measured at 295 K on structures with different grain concentrations. The magnetoresistance was negative; i.e., the resistance between junctions decreased with increasing field. No hysteresis phenomena were observed within the experimental accuracy. In magnetic fields up to 2 kOe, the JMR varied little and was very small. In the field interval 2–7 kOe, the variation of the resistance with magnetic field was the strongest. The variation of the resistance in the interval 2–7 kOe in structures which had high concentrations of $Co_{86}Nb_{12}Ta_2$ metallic grains (x = 53–56 at. %) and were close to the percolation threshold was more pronounced than that in structures with lower grain concentrations. As the field was increased further, JMR saturation set in structures with grain concentrations near the percolation threshold. In structures with lower metallic phase concentrations, the magnetoresistance saturation effect was either much less pronounced or altogether absent.

Temperature measurements of the magnetoresistance were conducted in magnetic fields close to H = 3 kOe. We measured the derivative of the relative resistance with respect to the field $\chi = -dR/RdH$. Figure 6 presents concentration dependences of χ measured at T = 77 and 295 K. Interestingly, in structures with low grain concentrations, the temperature-induced variations in χ and, hence, in JMR are larger than those in structures with metallic phase concentrations near the percolation threshold. We note that the value of JMR at T = 77 K is considerably higher in structures with lower grain concentrations.

4. DISCUSSION OF RESULTS

We shall address the experimentally revealed features of spin-dependent tunneling in granular structures in terms of the magnetoresistance tunneling model [7, 8]. We assume that (i) the electron spin is conserved in tunneling between grains, (ii) tunneling between any two grains is not affected by other grains, and (iii) electrons tunnel from the Fermi level of one grain to that of another. Under these conditions, the conductivity of the

channel between two grains for polarization $\nu = \uparrow, \downarrow$ can be written as [7, 8]

$$\sigma^{(\mathrm{gr})\nu} = \frac{4e^2}{h}\mathrm{Tr}[T_{10}^{\nu}\mathrm{Im}g_{00}^{\nu\nu}(E_\mathrm{F})][T_{01}^{\nu}\mathrm{Im}g_{11}^{\nu\nu}(E_\mathrm{F})]. \quad (7)$$

In Eq. (7), $g_{00}^{\nu\nu}$ and $g_{11}^{\nu\nu}$ are the $\nu\nu$ projections of the one-electron Green's functions for two isolated adjacent grains with indices 0 and 1; ν is the spin index of a tunneling electron; $T_{10}^{\nu} = T_{01}^{\nu+}$ are transition matrices;

$$g_{kk}^{\nu\nu'}(E_\mathrm{F}) = \lim_{E\to E_\mathrm{F},\,\varepsilon\to+0}\langle E_\mathrm{F}, N, \nu|[E - \mathcal{H}(\mathbf{S}_k\mathbf{H}) + i\varepsilon\,\mathrm{sgn}(E - E_\mathrm{F})]^{-1}|E_\mathrm{F}, N', \nu'\rangle,$$

where $k = 0, 1$; $\mathcal{H}$ is the Hamiltonian of an electron in a grain, which includes the interaction of the spin of a tunneling electron with that of a grain and the interaction of the grain spin with magnetic field $\mathbf{H}$; $\mathbf{S}_k$ is the spin of the kth grain; and N and N' are quantum numbers of electrons residing on the Fermi level E_F in a grain. The quantities $g_{00}^{\nu\nu}$, $g_{11}^{\nu\nu}$, T_{10}^{ν}, and T_{01}^{ν} are matrices in the space of quantum numbers N. The trace Tr means that summation is performed over these quantum numbers. The transition matrices T_{10}^{ν} and T_{01}^{ν} are related to the hopping integrals $t_{10}^{\nu} = t_{01}^{\nu+}$, which are determined by electron wave function overlap between two grains, through the Dyson equation

$$\begin{pmatrix} T_{00}^{\nu} & T_{01}^{\nu} \\ T_{10}^{\nu} & T_{11}^{\nu} \end{pmatrix} = \begin{pmatrix} 0 & t_{01} \\ t_{10} & 0 \end{pmatrix} + \begin{pmatrix} T_{00}^{\nu} & T_{01}^{\nu} \\ T_{10}^{\nu} & T_{11}^{\nu} \end{pmatrix}\begin{pmatrix} g_{00}^{\nu\nu} & 0 \\ 0 & g_{11}^{\nu\nu} \end{pmatrix}\begin{pmatrix} 0 & t_{01} \\ t_{10} & 0 \end{pmatrix}. \quad (8)$$

It follows from Eq. (8) that

$$T_{01}^{\nu} = t_{01}(I - g_{11}^{\nu\nu}t_{10}g_{00}^{\nu\nu}t_{01})^{-1},$$

where I is the identity matrix in the space of quantum numbers N of an electron at the Fermi level in a grain. The sum of spin-dependent conductivities (7) yields the conductivity between grains defined by Eq. (3):

$$\sigma^{(\mathrm{gr})} = \sigma^{(\mathrm{gr})\uparrow} + \sigma^{(\mathrm{gr})\downarrow}. \quad (9)$$

In the granular structures studied by us, the wave functions of electrons residing at the Fermi level in a (Co, Nb, Ta) grain are determined by *s*, *p*, and *d* outer-shell electrons of the metals contained in a grain. For the wave functions of electrons in two adjacent grains 0 and 1, made up of linear combinations of products of certain atomic orbitals, the overlap integral is proportional to [7, 23]

$$C_{\lambda_0\lambda_1\mu}l^{-(\lambda_0+\lambda_1+1)},$$

where l is the distance between grains; $C_{\lambda\nu\mu}$ is a distance-independent constant; $\lambda_0, \lambda_1 = 0, 1, 2$ (for *s*, *p*, *d* orbitals, respectively) are the orbital indices of the atomic wave functions involved in the expressions for the wave functions of electrons in a grain; and $\mu = \sigma, \pi, \delta, \ldots$ specifies the projection of the total angular momenta of atomic orbitals for two grains. If the dis-

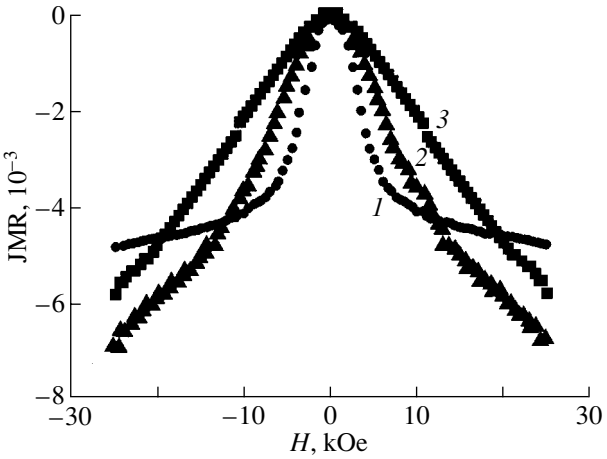

Fig. 5. Junction magnetoresistance (JMR) of a nonannealed *a*-SiO_2(Co, Nb, Ta) granular structure plotted vs. external magnetic field H for various grain concentrations x (at. %): (*1*) 54.5, (*2*) 41.9, and (*3*) 31.7.

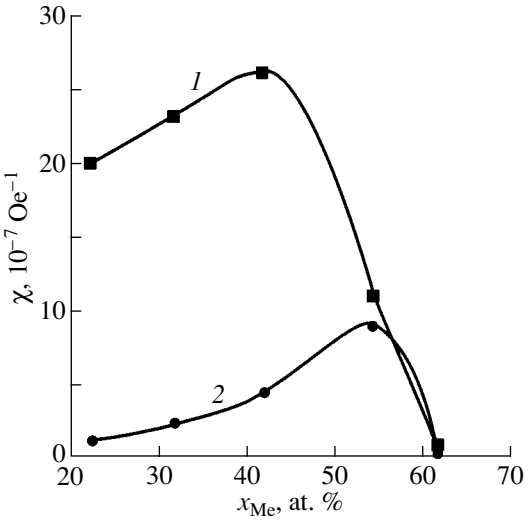

Fig. 6. Derivative of the relative electrical resistivity with respect to magnetic field χ measured at $H = 3$ kOe as a function of metallic phase concentration x in a nonannealed *a*-SiO_2(Co, Nb, Ta) granular structure at (*1*) 77 and (*2*) 295 K.

tance l between two neighboring grains exceeds a certain value (for Co atoms and for tunneling through a vacuum gap between two Co electrodes [7], this value is approximately equal to a monatomic cobalt layer), the overlap integrals of wave functions derived from s orbitals of metal atoms are the largest. Hence, as a first approximation, the set of quantum numbers N of the electrons at the Fermi level in Eqs. (7) and (8) can be chosen to consist of quantum numbers N_s of the wave functions derived from the s orbitals. This approximation is referred to as the single-orbital model, and, accordingly, the tunneling between grains is defined as s–s tunneling [7]. The applicability of the single-orbital approximation is limited by the magnitude of the spin–orbit coupling (which accounts for part of the d-orbital wave functions being admixed to the s wave functions) and by the intergrain distance. For small distances l, the s–p, s–d, p–d, … tunneling are added to the s–s tunneling, which can substantially increase the magnetoresistance under certain conditions [7, 24]. In this case, we should transfer to a multiorbital approximation.

The JMR defined by Eq. (6) is determined by the magnetic field dependence of the conductivity of the granular structure. According to the above assumption, the conductivity of a granular structure is proportional to the average conductivity of tunneling channels between grains, $\sigma \propto \sigma^{(gr)}$. The effect of a magnetic field H on $\sigma^{(gr)}$ in Eq. (9) manifests itself through variation of Green's functions $g_{00}^{\nu\nu}$ and $g_{11}^{\nu\nu}$ in Eqs. (7) and (8) and depends on the mutual orientation of the grain spins. In the molecular-field approximation in the case of $|\mathbf{S}_0| = |\mathbf{S}_1| = S$, the spin orientation with respect to one another is given by the correlation function [25]

$$\frac{\langle \mathbf{S}_0 \mathbf{S}_1 \rangle}{S^2} = L^2(\xi), \tag{10}$$

where $L(\xi) = \coth\xi - \xi^{-1}$ is the Langevin function.

If the grains are ferromagnetically coupled, ξ is a root of the equation [25]

$$\xi = \frac{\gamma_L \mu_B S H}{kT} + \frac{3T_M}{T} L(\xi),$$

where γ_L is the Landé factor, μ_B is the Bohr magneton, and T_M is the transition temperature from the superparamagnetic to ferromagnetic state of the granular structure.

In the superparamagnetic case, we have

$$\xi = \frac{\gamma_L \mu_B S H}{kT}.$$

Let us see how the experimentally observed features in the magnetoresistance can be explained in terms of the above model and tunneling through localized states in a matrix.

4.1. Increase in |JMR| in Structures with Lower Grain Concentrations Relative to |JMR| of Structures near the Percolation Threshold

This effect is observed to occur at $T = 77$ K in the concentration range $x = 42$–62 at. % (Fig. 6). The dependence of tunneling magnetoresistance TMR = –JMR/(1 + JMR) on the s–s tunneling coefficient t_{01} was studied in [7] in the case where the TMR is determined by the difference between the state in which the junction spins are antiparallel ($H = 0$) and the state with parallel junction spins ($H \gg 0$). Using Eqs. (7)–(9) and taking into account the band structure of the junction material, it was shown in [7] that in the case of Co electrodes, TMR decreases sharply as one crosses over from the metallic to tunneling regime. After the TMR has passed a minimum, which corresponds to a monatomic insulating spacer sandwiched between ferromagnetic metals, the TMR grows again as t_{01} is increased still further. The growth in TMR correlates in order of magnitude with the increase in the junction magnetoresistance |JMR| that takes place in granular structures with the metallic-phase concentration decreasing in the concentration interval 42–62 at. %, because the tunneling channel length between grains increases with decreasing grain concentration.

4.2. JMR Saturation in High Fields in Structures near the Percolation Threshold and the Absence of JMR Saturation in Structures with Low Grain Concentrations (Fig. 5)

The absence of saturation, which manifests itself as a logarithmic dependence of magnetoresistance on a strong magnetic field, is associated in [26] with a large scatter of nonspherical grains nanocomposite in shape, from strongly elongated to flattened. It was assumed in [26] that the grains in the structures near the percolation threshold and the grains in structures with low metallic-phase concentrations should differ in shape. This should become manifest in specific features of the magnetoresistance in strong magnetic fields. Let us consider the magnetic fields acting on a grain. The spin $\mathbf{S}$ of a (Co, Nb, Ta) grain derives from the d electrons of the outer shells of metal atoms. The internal magnetic field $\mathbf{H}^{(0)}$ acting on the d-electron spins of the grains will be the sum of the external field $\mathbf{H}$ and the field $\mathbf{H}^{(gr)}$ generated by the granular structure: $\mathbf{H}^{(0)} = \mathbf{H} + \mathbf{H}^{(gr)}$. The field $\mathbf{H}^{(gr)}$ is, in turn, the sum of grain interaction field $\mathbf{H}^{(int)}$, grain shape anisotropy field $\mathbf{H}^{(a)}$, and the spin interaction field between the grain d electrons and the impurities in the matrix $\mathbf{H}^{(loc)}$:

$$\mathbf{H}^{(gr)} = \mathbf{H}^{(int)} + \mathbf{H}^{(a)} + \mathbf{H}^{(loc)}. \tag{11}$$

The demagnetizing grain field $\mathbf{H}^{(a)}$ is connected with the grain magnetization $4\pi\mathbf{M}^{(gr)}$ through the relation $\mathbf{H}^{(a)} = 4\pi N\mathbf{M}^{(gr)}$, where N is the demagnetizing coefficient tensor [27]. This field should not exceed, in order

of magnitude, the magnetization $4\pi\mathbf{M}^{(gr)}$, which in the case of (Co, Nb, Ta) grains is less than 17.9 kG (the magnetization of cobalt). Because a logarithmic dependence of magnetoresistance on field H was observed in [26] in magnetic fields considerably in excess of $4\pi\mathbf{M}^{(gr)}$, grain shape anisotropy cannot account for the logarithmic behavior (i.e., the absence of saturation) of magnetoresistance in the granular structures studied. Furthermore, there is no experimental evidence that the grains in nanocomposites with different metallic phase concentrations differ in shape.

The model described above permits one to understand why the presence of localized states in a matrix can bring about a lack of magnetoresistance saturation in granular structures subjected to strong magnetic fields. A decrease in the metallic phase concentration gives rise to an increase in the number of localized states $\langle n\rangle$ supporting spin-dependent resonance tunneling between grains (Fig. 4). Spin-polarized electron transport depends on the exchange splitting ΔE of the localized states via which an electron is tunneling and on the mutual spin orientation of the two adjacent grains, which is determined by the correlation function in Eq. (10). If in a granular structure the splitting is $\Delta E > kT$ and the grain spin correlation function does not vary (the case of a strong magnetic field and of parallel grain spins), then magnetic field will not affect the polarization of a localized state and the magnetoresistance. In this case, after the spins have become parallel, the magnetoresistance will not vary and saturation will set in. If the grain concentration is low, the chain of localized states in a long conductivity channel between grains will contain weakly split levels with $\Delta E \ll kT$ that are located far away from the grains. As the magnetic field H increases from 0 to $(kT - \Delta E)/\mu_B$, the weakly split localized states will gradually become polarized and the tunneling conductivity will increase. This becomes manifest in a lack of magnetoresistance saturation for $H < (kT - \Delta E)/\mu_B$ in structures with low grain concentrations.

It should also be pointed out that exchange splitting of the levels of localized states gives rise not only to features in the magnetoresistance but also to a considerable growth in the relaxation parameter of spin excitations in granular structures [28].

4.3. Growth of the Temperature-Induced Magnetoresistance Variation with Decreasing Grain Concentration

This effect is readily revealed by comparing the concentration dependences of χ measured at $T = 77$ and 295 K (Fig. 6). In terms of the above model, temperature can influence the conductivity $\sigma^{(gr)\nu}$ of the intergrain channel with polarization ν through (i) variation of the spin correlation function between two neighboring grains, which is defined by Eq. (10) and enters the Green's functions $g_{00}^{\nu\nu}$ and $g_{11}^{\nu\nu}$ in Eq. (7), and (ii) inelastic spin scattering of an electron tunneling in the chain of localized states between grains. In the latter case, differently polarized tunneling channels are coupled and, when using Eq. (7), one should take into account transition matrices T_{10}^{ν} and T_{01}^{ν} with $\nu = \uparrow$ and $\downarrow$. An increase in the length of the chain of localized states in which an electron is tunneling results in an increase in the inelastic electron spin scattering probability. Because the |JMR| increases with decreasing grain concentration x (see above), the increase in inelastic electron spin scattering probability with increasing channel length at nonzero temperature must give rise to a specific concentration dependence, namely, a rise in the magnetoresistance with the concentration decreasing from the percolation threshold x_{perc} to a certain concentration x_m and then passing through a maximum at x_m and then a falloff of magnetoresistance with x decreasing from x_m to zero. Such a concentration dependence has been observed in a-SiO_2(Ni) granular structures [29]. At the concentration x_m, the two factors (the concentration-induced growth of |JMR| and the increase in inelastic electron spin scattering probability with increasing temperature) cancel each other. As the temperature decreases, the magnetoresistance grows and the position of the maximum, x_m, should shift toward lower values of x.

We experimentally studied films in the superparamagnetic state. If the external magnetic field H is higher than the field $H^{(int)}$, which is determined by the exchange and dipole–dipole interaction of grains, then, to the first order in the ratio of these fields, for $T > T_M$, the grain spin correlation functions (10) will have the same form for all concentrations and the temperature and concentration dependences will be governed by the specific features determined by the inelastic tunneling spin scattering. These features, as pointed out earlier, are the presence of a maximum in magnetoresistance at $x = x_m$, an increase in the temperature-induced magnetoresistance variation with decreasing x, and a shift in x_m toward lower values of x with decreasing temperature. These effects were observed experimentally, which suggests that electron transport in the structures studied involves inelastic resonance tunneling in a chain of localized states between grains.

4.4. Small Variation of Magnetoresistance in Weak Fields (Fig. 5)

The grain shape anisotropy, the exchange spin coupling between the grains and impurities in the matrix, and interaction between the grains [field $\mathbf{H}^{(int)}$] result in a nonzero internal field $\mathbf{H}^{(gr)}$ (11) determined by the granular structure. This field adds to the external field $\mathbf{H}$; as a result, in order to take it into account in the above model, one must make the replacement $H \longrightarrow H^{(0)} = |\mathbf{H} + \mathbf{H}^{(gr)}|$ in the correlation functions (10). Because the internal field has an arbitrary orientation,

the field $H^{(0)}$ for $H < H^{(gr)}$ is determined primarily by the field $H^{(gr)}$, which brings about only a small change in the correlation function (10) and the conductivity in Eq. (7). From the experimental JMR relations displayed in Fig. 5 it follows that $H^{(gr)} \approx 2$ kOe.

4.5. Effect of Annealing, Resulting in an Increase in the Electrical Resistivity at Low Grain Concentrations and in a Decrease in the Resistivity at Grain Concentrations near the Percolation Threshold

The effect of annealing on the resistivity of granular structures (Fig. 2) can be accounted for within the model developed above. As a first approximation, a granular structure can be considered to be a percolation system that can be fitted by two limiting models depending on the conductivities of grain clusters σ_{Me} and of the matrix σ_b. One of these models describes the case of $\sigma_b = 0$ (the ant limit); the other, the case of $\sigma_{Me} = \infty$ (the termite limit) [18, 30, 31]. Percolation systems are characterized by the existence of a certain percolation threshold x_{perc} and a scaling dependence of the total conductivity on the metallic phase concentration in the form $\sigma \sim (x - x_{perc})^{\mu}$. If the conductivity ratio $\sigma_{Me}/\sigma_b = \rho_b/\rho_{Me}$ is neither infinite nor zero, there is no certain percolation threshold. The threshold spreads out, and one can only speak confidently of the region of the percolation threshold [30, 31]. The percolation region can be determined only from a change in the behavior of the temperature dependences of conductivity, more specifically, from a transition from a nonmetallic type of conductivity to a metallic type. For nonannealed *a*-SiO_2(Co, Nb, Ta) samples (Fig. 3), this region lies approximately in the grain concentration interval 57–62 at. %.

Annealing of granular structures initiates two processes.

(a) Annealing reduces the number of defects in the matrix, thus reducing the number of localized states in the tunneling channels between the grains and the transmittance of the tunneling barrier. The conductivity of the matrix σ_b, which is equal to $\sigma^{(gr)}$ in Eq. (9), decreases.

(b) Annealing gives rise to a structural relaxation of the metallic phase. The grains can grow larger and coalesce. This increases the cluster conductivity σ_{Me}.

At low grain concentrations, the first process predominates and annealing entails an increase in the total electrical resistivity of *a*-SiO_2(Co, Nb, Ta) granular structures (Fig. 2). At high concentrations, the second process operates and results in a decrease in the resistivity. The *S*-shaped resistivity curve obtained for annealed samples suggests that annealed granular structures approach the termite limit with $\sigma_{Me} = \infty$.

We may note in concluding this section that using the *s–s* tunneling approximation for interpretation of the magnetoresistance in the composite under study is valid, because an amorphous $Co_{86}Nb_{12}Ta_2$ metallic alloy has a close-to-zero magnetostriction. In $(CoFeB)_x(SiO_n)_{1-x}$ composites, metallic grains possess magnetostriction $\lambda \approx 30 \times 10^{-6}$, which is evidence of an effect of magnetic field on the *d* electrons. In this case, the *s–d* tunneling is admixed to the *s–s* tunneling, which increases the magnetoresistance by nearly an order of magnitude [32].

5. CONCLUSIONS

Thus, we can make the following conclusions:

(1) The existence of weakly split localized states in the intergrain tunneling conductivity channel results in a lack of magnetoresistance saturation in strong magnetic fields in granular structures with low grain concentrations.

(2) An increase in the intergrain chain length of localized states in which electrons are tunneling results in (i) a decrease in the *s–s* tunneling coefficient, thus increasing the |JMR|, and (ii) a growth in the probability of inelastic spin scattering of the tunneling electron, thus reducing the |JMR|. The combined effect of these two factors in granular structures residing in the superparamagnetic state gives rise to the following features in the temperature and concentration dependences: (i) the presence of a maximum in magnetoresistance at a certain grain concentration x_m; (ii) an increase in the temperature-induced variations in magnetoresistance with decreasing x for $x < x_m$; and (iii) a shift in x_m toward lower concentrations with decreasing temperature.

(3) The presence of characteristic features in the concentration dependences of the magnetoresistance at various temperatures and the lack of magnetoresistance saturation in strong magnetic fields in *a*-SiO_2(Co,Nb,Ta) granular films suggest that electron transport occurs here via inelastic resonance tunneling in an intergrain chain of localized states in the *a*-SiO_2 matrix. While one cannot exclude the possibility that the temperature dependence of the conductivity in granular structures can be approximated by the models proposed in [13, 14], analysis of the behavior of the magnetoresistance shows that inelastic resonance tunneling through intergrain localized states provides a certain contribution to the temperature dependence of the conductivity in the films studied.

ACKNOWLEDGMENTS

This study was supported by the Russian Foundation for Basic Research, project no. 99-02-17071.

REFERENCES

1. S. Mitani, K. Takanashi, K. Yakushiji, and H. Fujimori, J. Appl. Phys. **83** (11), 6524 (1998).

2. B. A. Aronzon, A. B. Granovskiĭ, D. Yu. Kovalev, *et al.*, Pis'ma Zh. Éksp. Teor. Fiz. **71** (11), 687 (2000) [JETP Lett. **71**, 469 (2000)].
3. B. A. Aronzon, D. Yu. Kovalev, A. N. Lagar'kov, *et al.*, Pis'ma Zh. Éksp. Teor. Fiz. **70** (2), 87 (1999) [JETP Lett. **70**, 90 (1999)].
4. E. Z. Meĭlikhov, Zh. Éksp. Teor. Fiz. **117** (6), 1136 (2000) [JETP **90**, 987 (2000)].
5. L. I. Glazman and K. A. Matveev, Zh. Éksp. Teor. Fiz. **94** (6), 332 (1988) [Sov. Phys. JETP **67**, 1276 (1988)].
6. L. I. Glazman and R. I. Shekhter, Zh. Éksp. Teor. Fiz. **94** (1), 292 (1988) [Sov. Phys. JETP **67**, 1462 (1988)].
7. J. Mathon, Phys. Rev. B **56** (18), 11810 (1997).
8. J. S. Moodera and G. Mathon, J. Magn. Magn. Mater. **200**, 248 (1999).
9. Ping Sheng, B. Abeles, and Y. Arie, Phys. Rev. Lett. **31** (1), 44 (1973).
10. Ping Sheng, Philos. Mag. B **65** (3), 357 (1992).
11. A. Möbius, M. Richter, and B. Drittler, Phys. Rev. B **45** (20), 11568 (1992).
12. E. Cuevas, M. Ortuño, and J. Ruiz, Phys. Rev. Lett. **71** (12), 1871 (1993).
13. D. A. Zakheim, I. V. Rozhansky, I. P. Smirnova, and S. A. Gurevich, Zh. Éksp. Teor. Fiz. **118** (3), 637 (2000) [JETP **91**, 553 (2000)].
14. E. Z. Meĭlikhov, Zh. Éksp. Teor. Fiz. **115** (4), 1484 (1999) [JETP **88**, 819 (1999)].
15. S. V. Vyshenski, Pis'ma Zh. Éksp. Teor. Fiz. **61** (1–2), 105 (1995) [JETP Lett. **61**, 111 (1995)].
16. L. V. Litvin, V. A. Kolosanov, D. G. Baksheev, *et al.*, Pis'ma Zh. Éksp. Teor. Fiz. **72** (5), 388 (2000) [JETP Lett. **72**, 264 (2000)].
17. A. V. Tartakovskiĭ, M. V. Fistul', M. É. Raĭkh, and I. M. Ruzin, Fiz. Tekh. Poluprovodn. (Leningrad) **21** (4), 603 (1987) [Sov. Phys. Semicond. **21**, 370 (1987)].
18. B. I. Shklovskiĭ and A. L. Efros, *Electronic Properties of Doped Semiconductors* (Nauka, Moscow, 1979; Springer, New York, 1984).
19. L. V. Lutsev, T. K. Zvonareva, and V. M. Lebedev, Pis'ma Zh. Tekh. Fiz. **27** (15), 84 (2001) [Tech. Phys. Lett. **27**, 659 (2001)].
20. E. Yu. Tsymbal and D. G. Pettifor, Phys. Rev. B **58** (1), 432 (1998).
21. A. M. Bratkovsky, Phys. Rev. B **56** (5), 2344 (1997).
22. A. V. Vedyaev, D. A. Bagrets, A. A. Bagrets, and B. Dieni, in *Proceedings of the XVII International School-Workshop "Novel Magnetic Materials for Microelectronics," Moscow, 2000*, p. 622.
23. A. S. Davydov, *Quantum Mechanics* (Nauka, Moscow, 1973; Pergamon, Oxford, 1976).
24. E. Yu. Tsymbal and D. G. Pettifor, J. Phys.: Condens. Matter **9** (30), L411 (1997).
25. J. S. Helman and B. Abeles, Phys. Rev. Lett. **37** (21), 1429 (1976).
26. E. Z. Meĭlikhov, B. Raquet, and H. Rakoto, Zh. Éksp. Teor. Fiz. **119** (5), 937 (2001) [JETP **92**, 816 (2001)].
27. A. G. Gurevich and G. A. Melkov, *Magnetic Oscillations and Waves* (Nauka, Moscow, 1994).
28. L. V. Lutsev, Fiz. Tverd. Tela (St. Petersburg) **44** (1), 95 (2002) [Phys. Solid State **44**, 102 (2002)].
29. J. I. Gittleman, Y. Goldstein, and S. Bozowski, Phys. Rev. B **5** (9), 3609 (1972).
30. A. Bunde, A. Coniglio, D. C. Hong, and H. E. Stanley, J. Phys. A **18**, L137 (1985).
31. D. C. Hong, H. E. Stanley, A. Coniglio, and A. Bunde, Phys. Rev. B **33** (7), 4564 (1986).
32. Yu. E. Kalinin, A. V. Sitnikov, O. V. Stognei, *et al.*, Mater. Sci. Eng. A **304–306**, 941 (2001).

Translated by G. Skrebtsov

Physics of the Solid State, Vol. 44, No. 10, 2002, pp. 1898–1906. Translated from Fizika Tverdogo Tela, Vol. 44, No. 10, 2002, pp. 1811–1818.

MAGNETISM AND FERROELECTRICITY

Bismuth-Induced Enhancement of Magneto-Optical Effects in Iron Garnets: A Theoretical Analysis

A. S. Moskvin and A. V. Zenkov

Ural State University, pr. Lenina 51, Yekaterinburg, 620083 Russia

e-mail: andreas@r66.ru

Received October 1, 2001; in final form, November 19, 2001

Abstract—A semiquantitative model of circular magneto-optical effects in iron garnets is constructed within the concept of charge-transfer transitions and the existing qualitative notions. In the framework of the proposed model, the drastic enhancement of circular magneto-optical effects in $R_3Fe_5O_{12}$ iron garnets containing impurities of Bi^{3+} or Pb^{2+} ions is explained by the increase in the oxygen contribution to the spin–orbit coupling constant of the $(FeO_6)^{9-}$ and $(FeO_4)^{5-}$ complexes (the main magneto-optically active centers in iron garnets). This increase is associated with the covalent admixture of the Bi^{3+} (or Pb^{2+}) 6*p* orbitals (with a giant one-electron spin–orbit coupling constant) to the oxygen 2*p* orbitals. The influence of the substitution does not reduce to an enhancement of the oxygen spin–orbit interaction alone but also leads to the appearance of the effective anisotropic tensor contributions to the spin–orbit interaction and circular magneto-optical effects. These contributions to the magneto-optical effects in garnets are estimated. The influence of an inhomogeneous bismuth distribution on the magneto-optical effects in $Y_{3-x}Bi_xFe_5O_{12}$ garnets is investigated using computer simulation. Analysis of the available experimental data on the magneto-optical effects in garnets confirms the validity of the theoretical model proposed. © *2002 MAIK "Nauka/Interperiodica".*

1. INTRODUCTION

As is known, circular magneto-optical effects in $R_3Fe_5O_{12}$ iron garnets (where *R* is a rare-earth element) drastically increase even at a relatively low content of Bi^{3+} or Pb^{2+} isoelectronic ions replacing rare-earth ions in the iron garnet lattice. Attempts have been repeatedly made to explain this phenomenon [1–3]; however, the problem, as before, remains topical. In particular, Scott *et al.* [1] considered the following possible reasons for this enhancement in lead-containing yttrium iron garnets: (1) the s^2–$sp(^1S_0$–$^3P_1)$ intraatomic interconfigurational transition in the Pb^{2+} ion, (2) the photoinduced electron exchange between Fe^{3+} and Fe^{4+} ions (the Fe^{4+} ion forms as a result of charge compensation for the Pb^{2+} ion), and (3) the charge-transfer transition between the Pb^{2+} cation and anions.

The important disadvantage of the aforementioned *ad hoc* hypotheses is their inapplicability to the explanation of the bismuth-induced enhancement of the magneto-optical effects, which undeniably should have the same origin as the lead-induced enhancement. Actually, hypothesis (2) is obviously inadequate in the case of bismuth. Mechanism (3) essentially depends on the energy level structure of ions in crystals and, hence, should lead to different results for bismuth- and lead-substituted garnets. At the same time, the analysis of the difference spectra obtained by subtracting the spectrum of pure garnet from the spectra of bismuth- or lead-substituted garnets indicates that the impurities of these ions almost identically affect the spectral anomalies of circular magneto-optical effects in the near-UV range. This circumstance is also a serious argument against hypothesis (1), because the fundamental transition in the Bi^{3+} ion ($\hbar\omega_0 \approx 4.3$ eV [4]) occurs too far from the range $\hbar\omega_0 \approx 3$ eV in which the influence of the Bi^{3+} impurity is already pronounced (the corresponding transition in the Pb^{2+} ion occurs at a considerably lower energy).[1]

A more promising hypothesis was proposed, particularly, in [5] (even though only at a qualitative level). According to this hypothesis, the enhancement of the circular magneto-optical effects in bismuth-substituted and lead-substituted iron garnets is explained in terms of the covalent admixture of 6*p* orbitals of Bi^{3+} and Pb^{2+} ions to the oxygen 2*p* orbital. It should be noted that the 6*p* orbitals of Bi^{3+} and Pb^{2+} ions are characterized by the giant one-electron spin–orbit coupling constants ζ_{6p}, which for the 6*p* shells of the Bi^{3+} and Pb^{2+} ions are equal to 17000 and 14500 cm^{-1}, respectively [2].[2]

In the present work, we developed this idea and constructed the semiquantitative model described

[1] Therefore, in the near-UV range $\hbar\omega_0 \approx 3$–4 eV, the contribution of this transition in the Bi^{3+} ion to magneto-optical effects can manifest itself only as a monotonic change in the intensity of spectral lines associated with other mechanisms. Note that the closer the corresponding line to the line of the fundamental transition, the larger the change in the intensity. However, such a monotonic change is not observed in actuality.

[2] Hereafter, for brevity, we will consider only bismuth, even though all the inferences pertain equally to lead.

below. This paper is a logical continuation of our earlier work [5].

2. SPIN–ORBIT INTERACTION IN THE PRESENCE OF BISMUTH IMPURITIES

Owing to the $2p(O^{2-})$–$6p(Bi^{3+})$ electron shell overlap and the virtual transfer of a $2p$ electron of an O^{2-} ion to the $6p$ vacant shell of a Bi^{3+} ion, the wave function of the outer $2p$ electrons of the O^{2-} ion nearest to the Bi^{3+} ion involves the admixture of its $6p$ states; that is,

$$\varphi_{2pm} \longrightarrow \psi_{2pm} = \varphi_{2pm} - \sum_{m'} \langle 6pm'|2pm\rangle^* \varphi_{6pm'}, \quad (1)$$

where φ_{2p} and φ_{6p} are the atomic wave functions. The $2p$–$6p$ overlap integral $\langle 6pm'|2pm\rangle^* = \langle 2pm|6pm'\rangle$ can be represented in the form

$$\langle 2pm|6pm'\rangle = \sum_{kq} (-1)^{1-m} \times \begin{pmatrix} 1 & k & 1 \\ -m & q & m' \end{pmatrix} \gamma_k C_q^k(\mathbf{R}). \quad (2)$$

Here, $\begin{pmatrix} \cdots \\ \cdots \end{pmatrix}$ is the $3j$ Wigner symbol [6]; C_q^k is the spherical tensor of rank k (the rank is necessarily even and can be equal to 0 and 2, see Section 5), which is given by the formula

$$C_q^k = \sqrt{\frac{4\pi}{2k+1}} Y_{kq},$$

Y_{kq} is the spherical function; $\mathbf{R}$ is the unit vector aligned along the O–Bi bond; and γ_k is the covalence parameter.

The linear combinations of the quantities γ_0 and γ_2 corresponding to the covalence parameters for the σ and π bonds are more convenient to use in calculations; that is,

$$\langle 6p_z|2p_z\rangle \equiv \langle 6p0|2p0\rangle \equiv \gamma_\sigma = \frac{1}{\sqrt{3}}\gamma_0 - \frac{2}{\sqrt{30}}\gamma_2,$$

$$\langle 6p_x|2p_x\rangle \equiv \langle 6p \pm 1|2p \pm 1\rangle \equiv \gamma_\pi = \frac{1}{\sqrt{3}}\gamma_0 + \frac{2}{\sqrt{30}}\gamma_2.$$

As a result of the covalence effects, the virtual transfer of the O $2p$ electron to the Bi $6p$ vacant shell with the strong spin–orbit interaction described by the operator

$$V_{so} = \zeta_{6p} \sum_{\alpha=1}^{3} (-1)^\alpha \hat{l}_\alpha \hat{s}_{-\alpha} \quad (3)$$

(the scalar product of the orbital angular momentum $\hat{\mathbf{l}}$ into the spin angular momentum $\hat{\mathbf{s}}$ is written in spherical components [6]) leads to an enhancement of the spin–orbit interaction on the oxygen ion as well. However, the influence of the bismuth impurity does not reduce to the above "trivial" effect and the spin–orbit interaction structure itself undergoes a change and acquires an anisotropic tensor character.

Consideration of the matrix element $\langle 2pm_1|V_{so}|2pm_2\rangle$ of operator (3) between the hybrid wave functions ψ_{2pm} (1) results in the operator of the effective spin–orbit interaction on the oxygen ion:

$$V_{so}^{\text{eff}}(2p) = V_{so} + \Delta V_{so}^{\text{iso}} + \Delta V_{so}^{\text{an}}. \quad (4)$$

The terms entering into expression (4) have the following meaning:

$$V_{so} = \zeta_{2p}(\mathbf{l}\cdot\mathbf{s}) \quad (5)$$

is the operator of the conventional spin–orbit interaction (observed in the absence of the bismuth impurity) and $\Delta V_{so}^{\text{iso}}$ is the isotropic addition to V_{so} due to the bismuth-induced increment $\Delta\zeta_{2p}$ of the effective spin–orbit coupling constant for the $2p$ shell; that is,

$$\Delta V_{so}^{\text{iso}} = \Delta\zeta_{2p}(\mathbf{l}\cdot\mathbf{s}), \quad (6)$$

where

$$\Delta\zeta_{2p} = \frac{1}{3}\gamma_\pi(2\gamma_\sigma + \gamma_\pi)\zeta_{6p}. \quad (7)$$

From relationship (7), with the use of the reasonable approximate parameters $|\gamma_\sigma| = |\gamma_\pi| \approx 0.4$ (see Section 4), we obtain $\Delta\zeta_{2p} \approx 4000$ cm^{-1} per Bi^{3+} ion. This value is one order of magnitude larger than the one-electron spin–orbit coupling constant for iron ($\zeta_{3d} \approx 420$ cm^{-1} [7]) and provides competing "iron" and "oxygen" contributions to the spin–orbit interaction (see Section 3).

The term $\Delta V_{so}^{\text{an}}$ in expression (4) is the anisotropic addition to V_{so}. This addition has a tensor character and can be represented in the irreducible tensor form as the convolution of the spherical tensor with the tensor product of the orbital and spin angular momentum operators; that is,

$$\Delta V_{so}^{\text{an}} = \sqrt{\frac{2}{3}}\gamma_\pi(\gamma_\pi - \gamma_\sigma)(C^2(\mathbf{R})\cdot[\mathbf{l}\times\mathbf{s}]^2)_0^0\zeta_{6p}. \quad (8)$$

In the Cartesian coordinates, the term $\Delta V_{so}^{\text{an}}$ takes the form

$$\Delta V_{so}^{\text{an}} = \lambda_{ij} l_i s_j.$$

Here, the effective spin–orbit interaction tensor λ_{ij}—an analog of the constant λ in the relationship $V_{so} = \lambda(\mathbf{l}\cdot\mathbf{s})$ written in the traditional form—is defined as

$$\lambda_{ij} = \gamma_\pi(\gamma_\sigma - \gamma_\pi)\zeta_{6p}\left(R_i R_j - \frac{1}{3}\delta_{ij}\right).$$

Table 1. Characteristics of the charge-transfer states and charge-transfer transitions in octahedral (nos. 1–6) and tetrahedral (nos. 7–13) complexes in iron garnets

No.	Charge-transfer transition [9]	Effective Landé factor g_L^* [9]	Effective spin–orbit coupling constant λ [9]	Energy, eV		Oscillator strength f**, 10^{-3}	Half-width of the line Γ**, eV
				SP DV-X_α calculations [9]	processing of the spectra of $Y_{3-x}Bi_xFe_5O_{12}$ [2]		
1	$t_{2u} \longrightarrow t_{2g}$	$-\frac{1}{2} - \frac{1}{4}$	$\frac{1}{10}\zeta_{3d} + \frac{1}{20}\zeta_{2p}$	3.1	2.78	1.5	0.2
2	$t_{1u}(\pi) \longrightarrow t_{2g}$	$\frac{1}{2} - \frac{1}{4}$	$-\frac{1}{10}\zeta_{3d} + \frac{1}{20}\zeta_{2p}$	3.9	3.6	40	0.3
3	$t_{2u} \longrightarrow e_g$	$0 + \frac{1}{4}$	$-\frac{1}{20}\zeta_{2p}$	4.4	4.3	60	0.3
4	$t_{1u}(\sigma) \longrightarrow t_{2g}$	$\frac{1}{2} + 0$	$-\frac{1}{10}\zeta_{3d}$	5.1	4.8	50	0.3
5	$t_{1u}(\pi) \longrightarrow e_g$	$0 - \frac{1}{4}$	$\frac{1}{20}\zeta_{2p}$	5.3	–****	–****	–****
6***	$t_{1u}(\sigma) \longrightarrow e_g$	0 + 0	0 + 0	6.4	–****	–****	–****
7	$1t_1 \longrightarrow 2e$	0 + 0.30	$-0.06\zeta_{2p}$	3.4	3.4	10	0.4
8	$6t_2 \longrightarrow 2e$	−0.01 + 0.05	$0.002\zeta_{3d} - 0.01\zeta_{2p}$	4.3	4.6	40	0.3
9	$1t_1 \longrightarrow 7t_2$	0.42 – 0.41	$-0.09\zeta_{3d} + 0.08\zeta_{2p}$	4.5	–****	–****	–****
10	$5t_2 \longrightarrow 2e$	−0.07 + 0.13	$0.02\zeta_{3d} - 0.03\zeta_{2p}$	5.0	–****	–****	–****
11	$6t_2 \longrightarrow 7t_2$	−0.43 + 0.16	$0.09\zeta_{3d} - 0.03\zeta_{2p}$	5.4	5.1	185	0.3
12	$1e \longrightarrow 7t_2$	−0.42 + 0.11	$0.09\zeta_{3d} - 0.02\zeta_{2p}$	5.6	–****	–****	–****
13	$5t_2 \longrightarrow 7t_2$	−0.49 + 0.24	$0.10\zeta_{3d} - 0.05\zeta_{2p}$	6.0	–****	–****	–****

* The Landé orbital factors are represented as the sum of the 3*d* contribution (the first term) and the ligand 2*p* contribution.

** The data are given for $Y_3Fe_5O_{12}$.

*** The charge-transfer state corresponding to this transition makes a nonzero contribution to the circular magneto-optical effects only within the mixing mechanism [10].

**** The transition is disregarded when simulating the experimental spectra, because it either occurs outside the range of measurements (nos. 5, 6, 12, and 13) or is so close to the included transition that their lines virtually coincide with each other (nos. 9, 10).

3. MICROSCOPIC MECHANISMS OF MAGNETO-OPTICAL EFFECTS IN IRON GARNETS

From the foregoing, it follows that, the influence of the Bi^{3+} ions on the circular magneto-optical effects in iron garnets substantially depends on the O 2*p* states in the $(FeO_6)^{9-}$ and $(FeO_4)^{5-}$ complexes, which are the main magneto-optically active centers in iron garnets.[3] This is a forcible argument in favor of the hypothesis that transitions [of the type ${}^6A_{1g}$–${}^6T_{1u}$ in the $(FeO_6)^{9-}$ complex or ${}^6A_1$–${}^6T_2$ in the $(FeO_4)^{5-}$ complex] occur with charge-transfer between the ligand (O^{2-} ion) and the central Fe^{3+} ion of the complex [8–10]; these transitions are predominantly responsible for the magneto-optical properties of ferrites, because only this approach naturally takes into account the role of ligand states in the magneto-optical effects in ferrites.

The state of the charge-transfer complex is characterized by the presence of two unfilled shells, namely, the ligand 2*p* shell and 3*d* shell. Correspondingly, the effective spin–orbit coupling constant λ for the complex involves two terms

$$\lambda = \lambda(2p) + \lambda(3d). \quad (9)$$

The constants λ calculated for different charge-transfer states in the $(FeO_6)^{9-}$ and $(FeO_4)^{5-}$ complexes are listed in Table 1. The calculations were performed according to the procedure described in our previous work [9]. The increment [formula (7)] in the constant ζ_{2p} due to ΔV_{so}^{iso} [formula (6)] leads to an increase in the oxygen contribution $\lambda(2p)$ in expression (9).[4] This results in an

[3] Apart from the processes under consideration, the $3d(Fe^{3+})$–$6p(Bi^{3+})$ hybridization is also theoretically possible. However, in this case, too, the oxygen ion serves as a coupling agent. The order of smallness of the contribution of this mechanism is $\sim\gamma$.

[4] Note that the one-electron constant ζ_{2p} is not equivalent to the constant λ characterizing the many-electron state of the complex.

increase in the so-called ferromagnetic contribution [the first two terms in formula (10) given below] to the gyration vector **g** of iron garnets. The ferromagnetic contribution is proportional to the ferromagnetic vectors $\mathbf{m}_a$ and $\mathbf{m}_d$ for the *a* and *d* sublattices of garnet and arises from the orbital splitting and mixing [10] of the excited ${}^6T_{1u}({}^6T_2)$ charge-transfer states under the influence of spin–orbit interaction. The gyration vector is written as

$$\mathbf{g} = A_a\mathbf{m}_a + A_d\mathbf{m}_d + C\mathbf{H} \tag{10}$$

(where A_a, A_d, and C are the proportionality coefficients).

At the same time, the bismuth impurity does not affect the last term in relationship (10) for the gyration vector. This term is the field contribution, which is proportional to the external magnetic field **H** and results from the orbital splitting and mixing of the excited ${}^6T_{1u}({}^6T_2)$ charge-transfer states at the expense of the orbital part of the Zeeman interaction $V_Z = \mu_B g_L(\mathbf{L}\cdot\mathbf{H})$. However, the oxygen states originally play an important role in the formation of the field contribution to the gyration vector **g**, since the effective Landé orbital factors $g_L(2p)$ and $g_L(3d)$ are comparable in magnitude (see Table 1).

In the case of the ferromagnetic contribution, the transitions whose constants λ for the excited charge-transfer states contain only the oxygen component $\lambda(2p)$ [for example, transitions nos. 3 and 5 in the $(FeO_6)^{9-}$ complex (Table 1)] do not considerably contribute to the vector **g**, because $\lambda(2p)$ is substantially less than $\lambda(3d)$. However, in bismuth-substituted iron garnets, these transitions make an appreciable contribution owing to a manifold increase in the constant $\lambda(2p)$.

By contrast, the substitution only slightly affects the charge-transfer transitions in which the final state is characterized by the constant λ determined only by the 3*d* subsystem of molecular orbitals of the complex [for example, transition no. 4 in the $(FeO_6)^{9-}$ complex (see Table 1)].

The relationship (required for further consideration in Sections 4 and 5) that describes the ferromagnetic contribution to the gyration vector (10) of iron garnets due to the charge-transfer transitions in octahedral and tetrahedral complexes (with the subscripts *a* and *d*, respectively) within the splitting mechanism [10] has the form

$$\mathbf{g}_{a,d} = 2\sum_{j={}^6T_{1u},\,{}^6T_2}\frac{\pi e^2 L N_{a,d}}{\hbar m_e \omega_{0j}} \times \lambda^j\langle\mathbf{S}\rangle f_j\frac{\partial F_1(\omega,\omega_{0j},\Gamma_j)}{\partial\omega_{0j}}. \tag{11}$$

Here, $L = [n_0^2 + 2)/3]^2$ is the Lorentz–Lorenz factor, $N_{a,d}$ is the concentration of Fe^{3+} ions at the *a* and *d* sites, λ^j is the spin–orbit coupling constant for the *j*th excited charge-transfer state, f_j is the oscillator strength of the transition, and $\langle\mathbf{S}\rangle$ is the mean spin. The dispersion function F_1 is defined as

$$F_1(\omega,\omega_0,\Gamma) = \frac{2(\omega + i\Gamma)}{(\omega + i\Gamma)^2 - \omega_0^2},$$

where ω_0 is the resonance frequency and Γ is the half-width of the line of the transition.

In the framework of the splitting mechanism, the field contribution to the gyration vector **g** is represented by the formula

$$\mathbf{g}_{a,d} = 2\sum_{j={}^6T_{1u},\,{}^6T_2}\frac{\pi e^2 L N_{a,d}}{\hbar m_e \omega_{0j}} \times \mu_B g_L^j \mathbf{H} f_j\frac{\partial F_1(\omega,\omega_{0j},\Gamma_j)}{\partial\omega_{0j}}, \tag{12}$$

where g_L^j is the effective Landé orbital factor for the *j*th charge-transfer state.

Finally, we note that bismuth can affect the quadratic (in magnetization) magneto-optical effects in garnets. Within the second order of the perturbation theory, the contribution from the orbital splitting of the excited ${}^6T_{1u}$ states due to the spin–orbit interaction to the polarizability tensor of the $(FeO_6)^{9-}$ complex is written as [11]

$$\alpha_{kl} = \frac{1}{2\sqrt{3}}\sum_{j={}^6T_{1u}}\frac{e^2(\lambda^j)^2 f_j}{\hbar^2 m_e\omega_{0j}} \times\left\langle S_kS_l - \frac{1}{3}S(S+1)\right\rangle\frac{\partial^2 F_2(\omega,\omega_{0j},\Gamma_j)}{\partial\omega_{0j}^2}, \tag{13}$$

where the dispersion function is represented as

$$F_2(\omega,\omega_0,\Gamma) = \frac{2\omega_0}{(\omega + i\Gamma)^2 - \omega_0^2}.$$

Therefore, the bismuth-induced increment of the spin–orbit coupling constant λ^j of the complex leads to an increase in the linear magnetic birefringence, in addition to the circular magnetic birefringence [note that the effect should be even more pronounced, because, unlike formula (11), the constant λ^j in formula (13) is squared].

On the other hand, the magnetic linear birefringence can be associated not only with the spin–orbit interaction but with a low-symmetry crystal field as well. The crystal field is responsible for the anisotropic elastooptical contribution to α_{kl} [11]. This contribution is insensitive to bismuth, but a strong distortion produced by bismuth in the crystal lattice affects the parameters of the low-symmetry crystal field, and, hence, the above

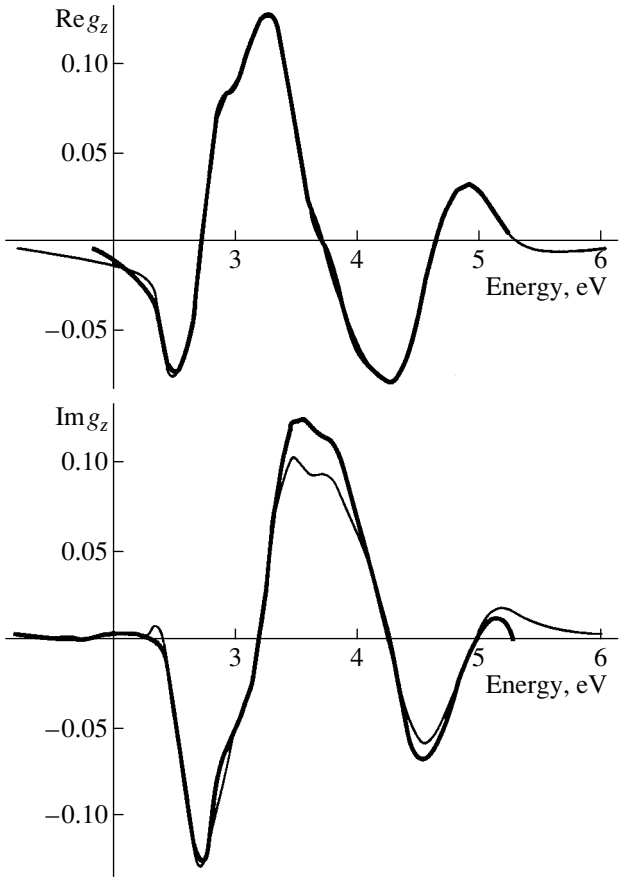

Spectral dependences of the real and imaginary parts of the z component of the gyration vector for $Y_{2.2}Bi_{0.8}Fe_5O_{12}$ garnet. Thick lines are the experimental data taken from [2], and thin lines represent the results of their theoretical treatment.

contribution, in actual fact, also depends on the bismuth concentration, even though the character of this dependence is not so clear as in the case of α_{kl} [see formula (13)].

4. THEORETICAL ANALYSIS OF EXPERIMENTAL SPECTRA

Now, we describe the procedure used in the present work for the theoretical treatment of optical and magneto-optical spectra of iron garnets.

The use of relationships (11)–(13) requires knowledge of the oscillator strengths f_j for the charge-transfer transitions. In order to obtain these strengths, we visually fitted the spectral dependence of the imaginary part $\mathrm{Im}\alpha_0^0$ of the diagonal component of the irreducible polarizability tensor, which determines the isotropic absorption in $Y_3Fe_5O_{12}$ garnet. The fitting was performed with due regard for the data on the real and imaginary parts of the permittivity $\varepsilon_0 = \varepsilon_0' + i\varepsilon_0''$ [2]. In cubic dielectrics, the quantities α_0^0 and ε_0 obey the Clausius–Mossotti equation

$$\frac{\varepsilon_0 - 1}{\varepsilon_0 + 2} = \frac{4\pi}{3} N\alpha_0^0.$$

From this formula, we have

$$\frac{4\pi}{3} N\mathrm{Im}\alpha_0^0 = \frac{3\varepsilon_0''}{(\varepsilon_0' + 2)^2 + (\varepsilon_0'')^2}. \qquad (14)$$

The imaginary part $\mathrm{Im}\alpha_0^0$ is represented by the expression

$$\mathrm{Im}\alpha_0^0 = -\sum_j \frac{e^2\hbar f_j}{2m_e\omega_{0j}} \mathrm{Im}F_2(\omega, \omega_{0j}, \Gamma_j), \qquad (15)$$

which was used for the results of the fitting.

In this way, we derived the values of f_j, ω_{0j}, and Γ_j (Table 1). Since spectrum (14) is weakly structured, the half-widths Γ_j, for the most part, were determined by fitting the off-diagonal part of ε[1]; this was done, however, consistently with spectrum (14).

Within the theory of charge-transfer transitions, the experimental spectra $g_z(\omega)$ of the z component of the gyration vector for bismuth-substituted iron garnets of the $Y_{3-x}Bi_xFe_5O_{12}$ type (x = 0.25, 0.8, and 1.0) [2] were theoretically processed with due regard for allowed and a number of forbidden charger-transfer transitions in the octahedral and tetrahedral complexes. The treatment was carried out according to the Mathematica-4 software package with the use of the transition frequencies ω_{0j}, the half-widths Γ_j of lines, and other parameters characteristic of yttrium iron garnets (Table 1). Consideration was given to the contributions from the mechanism of splitting of states (with the dispersion dependence $\propto \frac{\partial F_1}{\partial \omega_0}$) and the contributions from the mechanism of their mixing (with the dispersion dependence $\propto F_1$). The figure shows the model fitting dependence $\mathrm{Re}g_z(\omega)$ and the dependence $\mathrm{Im}g_z(\omega)$ calculated with the same parameters for $Y_{2.2}Bi_{0.8}Fe_5O_{12}$ (thin lines) and the experimental dependences (thick lines) taken from [2].[5] It can be seen that the results of model calculations and the experimental data are in good agreement over a wide spectral range (2–5 eV). This counts in favor of the hypothesis that the contribution of charge-transfer transitions plays the dominant role in circular magneto-optical effects in iron garnets.

The results of the simulation make it possible to estimate the values of $\Delta\zeta_{2p}$ at different bismuth concen-

[5] The quantities Re**g** and Im**g** cannot be approximated with the same accuracy, because the dependences Re$g(\omega)$ and Im$g(\omega)$ themselves result from experimental data processing in the framework of an approximate computational algorithm.

trations x in $Y_{3-x}Bi_xFe_5O_{12}$ garnet. Note that the model "macroscopically observed" values of $\Delta\zeta_{2p}^{\text{mod}}$ as a consequence of their dependence on the concentration and distribution of Bi^{3+} ions over the crystal lattice differ from the "microscopic" $\Delta\zeta_{2p}$ values calculated from formula (7).

By assuming that the Bi^{3+} ions are uniformly distributed over the crystal bulk and occupy either of the two **c** positions nearest to a particular O^{2-} ion with equal probability (determined by the relative concentration $\xi = x/3$), we obtain

$$\Delta\zeta_{2p}^{\text{mod}} = \Delta\zeta_{2p}[P_2(1) + 2P_2(2)],$$

where $P_n(k)$ is the probability that, among existing n positions, k positions are occupied. For the binomial probability distribution $P_n(k) = C_n^k \xi^k (1-\xi)^{n-k}$ (where C_n^k is the number of combinations), with allowance made for eight Bi^{3+}–O^{2-} bonds for each Bi^{3+} ion, we finally have

$$\Delta\zeta_{2p}^{\text{mod}}(x) = \frac{16}{3}x\Delta\zeta_{2p}. \quad (16)$$

Therefore, within the simplest model, which ignores selective ordering of Bi^{3+} impurity ions over the crystal lattice, the increment $\Delta\zeta_{2p}^{\text{mod}}$ and, hence, the enhancement of circular magneto-optical effects in iron garnets appear to be linearly dependent on the bismuth concentration.

The covalence parameters γ_σ and γ_π can be estimated from formulas (7), (11), and (16) with the data presented in Table 1. For example, the simulation with the use of expression (11) for the charge-transfer transition with the lowest energy ($\hbar\omega_0 = 3.4$ eV) in the tetrahedral complex at $x = 0.25$ gives the "fitting" spin–orbit coupling constant $\lambda^{\text{mod}} = -380\ \text{cm}^{-1} = -0.06\Delta\zeta_{2p}^{\text{mod}}$ (Table 1). Then, from relationship (16), we find $\Delta\zeta_{2p} \approx 4700\ \text{cm}^{-1}$. Within the rough approximation of equality between the covalence parameters $|\gamma_\sigma| = |\gamma_\pi| \equiv \gamma$, these parameters can be easily evaluated from relationship (7). At different bismuth concentrations, we obtain reasonable parameters, which are listed in Table 2.

Note that the parameter γ decreases with an increase in the bismuth content in iron garnets. One of the reasons for this decrease can be a change in the geometry of Bi–O bonds due to a distortion of the lattice by bismuth. The inclusion of these distortions and the possible inhomogeneous distribution of bismuth over the sample bulk will lead to a deviation of the concentration dependence of the circular magneto-optical effects in iron garnets from linear behavior.

Table 2. Covalence parameters at different bismuth concentration in yttrium iron garnet

x	γ
0.25	0.53
0.8	0.47
1.0	0.42

5. THE ROLE OF TENSOR CONTRIBUTIONS TO MAGNETO-OPTICAL EFFECTS IN IRON GARNETS

According to the Kramers–Heisenberg relation in the irreducible tensor form [10], the contribution of charge-transfer allowed electric dipole transitions of the ${}^6A_{1g}$–${}^6T_{1u}$ (${}^6S$–${}^6P$) type to the components α_p^1 of the antisymmetric part of the polarizability tensor $\hat{\alpha}$ for the $(FeO_6)^{9-}$ complex is written as

$$\alpha_p^1 = \frac{1}{\hbar}\sum_{j={}^6T_{1u}}\sum_{r_1,r_2}\sum_{m_1,m_2}\begin{bmatrix}1 & 1 & 1\\ r_1 & r_2 & p\end{bmatrix}\langle 00|d_{r_1}|1m_1\rangle \times \langle 1m_1|V_{so}|1m_2\rangle\langle 1m_2|d_{r_2}|00\rangle\frac{\partial F_1(\omega,\omega_{0j},\Gamma_j)}{\partial\omega_0}, \quad (17)$$

where $\begin{bmatrix}\cdots\\ \cdots\end{bmatrix}$ is the Clebsch–Gordan coefficient and d_r is the component of the electric dipole moment. After transformations (see the Appendix), we obtain

$$\alpha_p^1 = \frac{\sqrt{2}}{\hbar}\sum_{\substack{k_1,k_2\\ k,q\\ \alpha}}(-1)^{-p+k+k_1}(2k+1)\gamma_{k_1}\gamma_{k_2} \times C_{-q}^k(\mathbf{R})s_{-\alpha}|\langle 0\|d\|1\rangle|^2\begin{pmatrix}k_1 & k_2 & k\\ 0 & 0 & 0\end{pmatrix} \times\frac{\partial F_1}{\partial\omega_0}\zeta_{6p}\begin{pmatrix}k & 1 & 1\\ q & p & \alpha\end{pmatrix}\begin{Bmatrix}k & 1 & 1\\ k_2 & 1 & 1\\ k_1 & 1 & 1\end{Bmatrix}, \quad (18)$$

where $\langle 0\|d\|1\rangle$ is the reduced matrix element of the electric dipole moment **d** and $\begin{Bmatrix}\cdots\\ \cdots\\ \cdots\end{Bmatrix}$ is the 9j symbol [6].

It should be noted that the other variant of the relation between the moments results in expression (8).

From physical considerations, the index k is even, because, otherwise, the spatial inversion $\mathbf{R} \longrightarrow -\mathbf{R}$

would lead to a change in the sign of $C^k(\mathbf{R})$ and, hence, in the sign of expression (18). The triangle rule for the 9*j* symbols and the requirement for the parity of the sum of the elements of the upper row in $\begin{pmatrix} k_1 & k_2 & k_3 \\ 0 & 0 & 0 \end{pmatrix}$ allow for only the indices $k = 0$ and 2. In this case, the index $k = 0$ corresponds to the isotropic scalar relation between the antisymmetric part of the polarizability tensor $\hat{\alpha}$ and the mean spin $\langle \hat{\mathbf{s}} \rangle$ [compare with formula (6)], whereas the anisotropic tensor contribution to α^1 [compare with formula (8)] can be derived at $k = 2$.

The corresponding formulas are as follows:

$$\begin{aligned}\boldsymbol{\alpha} &= \frac{\sqrt{2}}{\hbar}\left[-\frac{1}{9}\gamma_0^2 + \frac{1}{90}\gamma_2^2\right]|\langle 0\|d\|1\rangle|^2 \frac{\partial F_1}{\partial \omega_0}\zeta_{6p}\langle \mathbf{s}\rangle \\ &= -\frac{\sqrt{2}}{9\hbar}\gamma_\pi(\gamma_\pi + 2\gamma_\sigma)|\langle 0\|d\|1\rangle|^2 \frac{\partial F_1}{\partial \omega_0}\zeta_{6p}\langle \mathbf{s}\rangle;\end{aligned} \tag{19}$$

for the isotropic contribution,

$$\begin{aligned}\alpha_p^1 &= \frac{5\sqrt{2}}{\hbar}\frac{\partial F_1}{\partial \omega_0}\zeta_{6p}|\langle 0\|d\|1\rangle|^2 \\ &\times \sum_{k_1,k_2=0,1,2}\ \sum_{q=-2}^{2}\ \sum_{\alpha=-1}^{1}(-1)^{-p+k_1}\begin{pmatrix} 2 & 1 & 1 \\ q & p & \alpha \end{pmatrix} \\ &\times \begin{Bmatrix} 2 & 1 & 1 \\ k_2 & 1 & 1 \\ k_1 & 1 & 1 \end{Bmatrix}\gamma_{k_1}\gamma_{k_2}C^2_{-q}(\mathbf{R})s_{-\alpha}\begin{pmatrix} k_1 & k_2 & 2 \\ 0 & 0 & 0 \end{pmatrix};\end{aligned} \tag{20}$$

for the anisotropic contribution, and

$$\boldsymbol{\alpha} = \frac{\sqrt{2}}{6\hbar}\gamma_\pi(\gamma_\sigma - \gamma_\pi)|\langle 0\|d\|1\rangle|^2 \frac{\partial F_1}{\partial \omega_0}\zeta_{6p}\hat{\Lambda}\langle \mathbf{s}\rangle, \tag{21}$$

for the anisotropic contribution in the Cartesian coordinates. Here, the tensor $\hat{\Lambda}$ has the form

$$\begin{pmatrix} \sin^2\theta\cos 2\varphi - \frac{1}{3}(3\cos^2\theta - 1) & \sin^2\theta\sin 2\varphi & \sin 2\theta\cos\varphi \\ \sin^2\theta\sin 2\varphi & -\sin^2\theta\cos 2\varphi - \frac{1}{3}(3\cos^2\theta - 1) & \sin 2\theta\sin\varphi \\ \sin 2\theta\cos\varphi & \sin 2\theta\sin\varphi & \frac{2}{3}(3\cos^2\theta - 1) \end{pmatrix},$$

where θ and φ are the polar angles of the unit vector **R** aligned along the O^{2-}–Bi^{3+} bond.

With the use of formula (21), we calculated the gyration vector $\mathbf{g} = 4\pi NL\boldsymbol{\alpha}$ and the specific Faraday rotation $\theta_F = \frac{\omega}{2n_0 c}\mathrm{Re}(\mathbf{g}\cdot\mathbf{n})$ (where **n** is the unit vector aligned along the direction of propagation of light and n_0 is the mean refractive index of two circularly polarized waves). The calculations were performed using a cubic cluster composed of eight unit cells of iron garnet with the atomic positions taken from [12] and the parameters of perfect $Y_3Fe_5O_{12}$ garnet [13] (the unit cell parameters and the atomic positions were assumed to be independent of the bismuth concentration).

The nearest oxygen ions were determined for each **c** position, and the corresponding contributions to **α** according to relationship (21) were summed. We considered the following variants of occupation of the **c** positions by Bi^{3+} ions.

(1) All the **c** positions in the unit cell of garnet are occupied by Bi^{3+} ions.

(2) Only positions nos. 1–3 and 10–12 and those related to them by the translations {1/2, 1/2, 1/2} are occupied (hereinafter, the position numbering will be given according to [12]).

(3) Only positions nos. 4–9 and those related to them by the translations {1/2, 1/2, 1/2} are occupied.

The second and third cases correspond to a (111)-oriented iron garnet film in which there exist two coextensive sets of crystallographically nonequivalent **c** positions.

The calculations demonstrate that the contribution of the Bi^{3+} ions in positions nos. 4–9 and equivalent positions to **α** is approximately eight times larger than that from the Bi^{3+} ions in positions nos. 1–3 and 10–12 and equivalent positions (undeniably, the sum of these contributions coincides with that calculated in the first case).

The specific Faraday rotation θ_F calculated using the obtained data with parameters characteristic of charge-transfer electric dipole transitions in iron garnets at a wavelength of 0.6 μm is of the order of 6×10^3 deg/cm for the "anisotropic" mechanism. The "isotropic" mechanism (19) leads to the specific Faraday rotation $\theta_F \approx 3 \times 10^5$ deg/cm, which is more than one order of magnitude larger than the contribution of the usual spin–orbit interaction (11).

In closing, we dwell on the important approximation used in the present work. This approximation consists in neglecting the vibronic structure of the charge-transfer states, the vibronic mechanism of charge-transfer transitions, and also different interactions in the charge-transfer states. Our approximation accounts only for the electronic components of the wave functions. The achieved accuracy of model calculations does not exclude a small vibronic reduction (by ~10%) in the matrix elements of orbital operators. This reduction is the manifestation of vibronic interactions and can lead to a decrease (potentially rather noticeable) in the magnitude of purely electronic values of such parameters as g_L and λ. Note that the vibronic reduction of the bismuth-induced contribution to the spin–orbit coupling constants for the charge-transfer states can radically differ in character from the Fe 3*d* contribution. The consistent inclusion of vibronic interactions for the charge-transfer states is a complex problem due to the presence of two unfilled shells (the predominantly ligand 2*p* shell and the Fe 3*d* shell) in the electronic configurations of these states.

6. CONCLUSIONS

The results of the above analysis can be summarized as follows.

(1) Owing to the contribution from the ligand orbitals of the $(FeO_6)^{9-}$ and $(FeO_4)^{5-}$ complexes, the Bi^{3+} ions induce an effective anisotropic spin–orbit interaction in the charge-transfer states. The parameters of this effective interaction depend on the geometry of the Fe^{3+}–O^{2-}–Bi^{3+} bond, the charge-transfer state type, and the type of the complex (octahedron or tetrahedron).

(2) The bismuth-induced contributions to the circular magneto-optical effects are especially pronounced in the case when the 3*d* contribution is absent (for example, for complexes based on Cu^{2+} ions).

(3) The bismuth impurity virtually does not affect the field contribution to the circular magneto-optical effects.

(4) The bismuth impurity leads to a considerable increase in the anisotropic magnetic birefringence associated with the spin–orbit interaction.

(5) The physically reasonable estimates of the parameters of the theoretical model advanced were obtained using the model fitting of the experimental spectral dependences of the circular magneto-optical effects in bismuth-containing iron garnets.

(6) The bismuth-induced contributions to the magneto-optical effects in iron garnets were theoretically estimated within the proposed model. The contribution of the anisotropic tensor mechanism to the Faraday effect is comparable in magnitude to the conventional ferromagnetic contribution and strongly depends on the specific features in the spatial distribution of bismuth over the iron garnet lattice.

ACKNOWLEDGMENTS

This work was supported in part by the American Foundation for Civilian Research and Development for the promotion of cooperation with scientists from the New Independent States of the former Soviet Union (CRDF), grant no. NREC-005.

APPENDIX

Formula (17) can be rearranged to give

$$\frac{1}{\hbar}\sum_{j={}^6T_{1u}}\sum_{r_1,r_2}\sum_{m_1,m_2}(-1)^{-p}\sqrt{3}\begin{pmatrix}1&1&1\\ r_1&r_2&-p\end{pmatrix}$$

$$\times(-1)^{1-m_1}\frac{1}{\sqrt{3}}\delta_{r_1,-m_1}\langle 1m_1|V_{so}|1m_2\rangle(-1)^{1-m_2}$$

$$\times(-1)^{1-r_2}\frac{1}{\sqrt{3}}\delta_{r_2,m_2}|\langle 0\|d\|1\rangle|^2\frac{\partial F_1(\omega,\omega_{0j},\Gamma_j)}{\partial\omega_0} \quad (22)$$

$$=\frac{1}{\hbar\sqrt{3}}\sum_{j={}^6T_{1u}}\sum_{m_1,m_2}(-1)^{-p-m_1-m_2+1-m_2}\begin{pmatrix}1&1&1\\ -m_1&m_2&-p\end{pmatrix}$$

$$\times\langle 1m_1|V_{so}|1m_2\rangle|\langle 0\|d\|1\rangle|^2\frac{\partial F_1(\omega,\omega_{0j},\Gamma_j)}{\partial\omega_0}.$$

The matrix element of the spin–orbit interaction $\langle 1m_1|V_{so}|1m_2\rangle$ involves the term [see expression (2)]

$$\left\langle\sum_{\substack{k_1,q_1\\ m_1}}(-1)^{1-m_1}\begin{pmatrix}1&k_1&1\\ -m_1&q_1&m_1'\end{pmatrix}\right.$$

$$\times\gamma_{k_1}C^{k_1}_{q_1}(\mathbf{R})\varphi_{6pm_1'}\left|\zeta_{6p}\sum_{\alpha}(-1)^{\alpha}l_\alpha s_{-\alpha}\right| \quad (23)$$

$$\left.\times\sum_{\substack{k_2,q_2\\ m_2'}}(-1)^{1-m_2}\begin{pmatrix}1&k_2&1\\ -m_2&q_2&m_2'\end{pmatrix}\gamma_{k_2}C^{k_2}_{q_2}(\mathbf{R})\varphi_{6pm_2'}\right\rangle.$$

After application of the Wigner–Eckart theorem and a number of transformations, this term takes the form

$$\sum_{\substack{k_1,k_2\\ q_1,q_2}}\sum_{\substack{m_1',m_2'\\ \alpha}}(-1)^{-m_1-m_2+\alpha}\begin{pmatrix}1&k_1&1\\ -m_1&q_1&m_1'\end{pmatrix}$$

$$\times\begin{pmatrix}1&k_2&1\\ -m_2&q_2&m_2'\end{pmatrix}\gamma_{k_1}\gamma_{k_2}(-1)^{q_1}C^{k_1}_{-q_1}(\mathbf{R})C^{k_2}_{q_2}(\mathbf{R}) \quad (24)$$

$$\times(-1)^{1-m_1'}\begin{pmatrix} 1 & 1 & 1 \\ -m_1' & \alpha & m_2' \end{pmatrix}\sqrt{6}s_{-\alpha}\zeta_{6p},$$

where the product of the spherical functions $C^{k_1}_{-q_1}(\mathbf{R})C^{k_2}_{q_2}(\mathbf{R})$ is transformed to the expression

$$\sum_{kq}(2k+1)\begin{pmatrix} k_1 & k_2 & k \\ -q_1 & q_2 & q \end{pmatrix}\begin{pmatrix} k_1 & k_2 & k \\ 0 & 0 & 0 \end{pmatrix}C^k_q{}^*(\mathbf{R}). \quad (25)$$

Taking into account relationships (23)–(25), we obtain the following formula for α^1_p

$$\alpha^1_p = \frac{\sqrt{2}}{\hbar}\sum_{\substack{k_1,k_2\\k,q\\\alpha}}(-1)^{-p+k+k_1+1}(2k+1)\gamma_{k_1}\gamma_{k_2}$$

$$\times C^k_{-q}(\mathbf{R})s_{-\alpha}|\langle 0\|d\|1\rangle|^2\begin{pmatrix} k_1 & k_2 & k \\ 0 & 0 & 0 \end{pmatrix}\frac{\partial F_1}{\partial\omega_0}\zeta_{6p}$$

$$\times\sum_{m_1,m_2q_1,q_2m_1',m_2'}\sum\sum(-1)^{k_1+k_2+q_2-q_1+m_1-m_2+m_2'-m_1'} \quad (26)$$

$$\times\begin{pmatrix} k_2 & k & k_1 \\ -q_2 & -q & q_1 \end{pmatrix}\begin{pmatrix} k_1 & 1 & 1 \\ -q_1 & -m_1' & m_1 \end{pmatrix}$$

$$\times\begin{pmatrix} 1 & 1 & 1 \\ -m_1 & -p & m_2 \end{pmatrix}\begin{pmatrix} 1 & k_2 & 1 \\ -m_2 & q_2 & m_2' \end{pmatrix}\begin{pmatrix} 1 & 1 & 1 \\ -m_2' & -\alpha & m_1' \end{pmatrix}$$

which, for brevity, includes the contribution only from one charge-transfer transition.

The triple sum over the projections of angular momenta in formula (26) according to [6, p. 388] gives relationship (18).

REFERENCES

1. G. B. Scott, D. E. Lacklison, and J. L. Page, Phys. Rev. B **10** (3), 971 (1974).
2. S. Wittekoek, T. J. A. Popma, J. M. Robertson, and P. F. Bongers, Phys. Rev. B **12** (7), 2777 (1975).
3. K. Shinagawa, in *Magnetooptics*, Ed. by S. Sugano and N. Kojima (Springer-Verlag, Berlin, 1999), pp. 137–177.
4. S. Wittekoek and D. E. Lacklison, Phys. Rev. Lett. **28** (12), 740 (1972).
5. A. S. Moskvin and A. V. Zenkov, Solid State Commun. **80** (9), 739 (1991).
6. D. A. Varshalovich, A. N. Moskalev, and V. K. Khersonskii, *Quantum Theory of Angular Momentum* (Nauka, Leningrad, 1975; World Scientific, Singapore, 1988).
7. J. J. Krebs and W. G. Maisch, Phys. Rev. B **4** (3), 757 (1971).
8. A. V. Zenkov and A. S. Moskvin, Fiz. Tverd. Tela (Leningrad) **32** (12), 3674 (1990) [Sov. Phys. Solid State **32**, 2131 (1990)].
9. A. S. Moskvin, A. V. Zenkov, E. I. Yuryeva, and V. A. Gubanov, Physica B (Amsterdam) **168** (1), 187 (1991).
10. E. A. Gan'shina, A. V. Zenkov, S. V. Koptsik, *et al.*, Available from VINITI, No. 788-V90 (Sverdlovsk, 1990).
11. A. V. Zenkov, Author's Abstract of Candidate's Dissertation (Sverdlovsk, 1990).
12. *International Tables for X-ray Crystallography* (Kynoch, Birmingham, 1952), Vol. 1.
13. B. V. Mill', *Magnetic and Crystal Chemical Studies of Ferrites* (Mosk. Gos. Univ., Moscow, 1971), p. 56.

Translated by O. Borovik-Romanova

Physics of the Solid State, Vol. 44, No. 10, 2002, pp. 1907–1915. Translated from Fizika Tverdogo Tela, Vol. 44, No. 10, 2002, pp. 1819–1826.

MAGNETISM AND FERROELECTRICITY

The Nature of Anomalies in the Magnetoresistance of Antiferromagnetic $YBa_2Cu_3O_{6+x}$

A. S. Moskvin and Yu. D. Panov

Ural State University, pr. Lenina 51, Yekaterinburg, 620083 Russia

e-mail: yuri.panov@usu.ru

Received November 22, 2001

Abstract—The characteristic *d*-type angular dependence of the in-plane magnetoresistance on the orientation of the external magnetic field in the (*ab*) plane for the antiferromagnetic tetragonal crystal $YBa_2Cu_3O_{6+x}$ ($x \sim 0.3$) is considered theoretically. This dependence is interpreted in terms of the efficient hole transfer through the low-lying purely oxygen O $2pe_u$ doublet, which is not hybridized with the $b_{1g}(d_{x^2-y^2})$ ground state. The external magnetic field determines the orientation of the strong exchange field acting on the $b_{1g}e_u : {}^3E_u$ triplet state of the hole-type CuO_4 center. The spin–orbit interaction results in orbital polarization of the E_u doublet, which is responsible for the *d*-type spatial anisotropy of the hole transport. The available experimental data make it possible to evaluate the parameter of the effective spin Hamiltonian. The influence of spin-vibronic effects on the hole transfer is analyzed. © *2002 MAIK "Nauka/Interperiodica".*

1. INTRODUCTION

The transport properties of a single hole in strongly correlated antiferromagnetically ordered quasi-two-dimensional cuprates have become the subject of numerous theoretical and experimental investigations. In particular, Ando *et al.* [1] considered a number of specific features of magnetoresistance in heavily underdoped antiferromagnetic crystals $YBa_2Cu_3O_{6+x}$ (x = 0.30 and 0.32). In these systems, the in-plane resistivity ρ_{ab} exhibits an unusual crossover from the metallic behavior in the high-temperature range ($T > 50$ K) to the dielectric behavior in the low-temperature range. Note that the latter behavior is characteristic of neither a simple band model nor an Anderson dielectric.

The following specific features in the in-plane magnetoresistance $\Delta\rho_{ab}/\rho_{ab}$ of samples have been revealed in magnetic fields applied parallel to the CuO_2 plane: an unusual angular dependence of the *d* type ($\propto\cos 2\phi$), an anomalous low-field behavior with a saturation above a clear-cut threshold field, and a hysteresis at low temperatures. At temperatures below 20–25 K, the field dependence of the resistivity ρ_{ab} becomes completely irreversible and the system acquires memory. In the authors' opinion, the above specific features qualitatively indicate that these systems have a ferromagnetically ordered charged stripe structure, which easily rotates in a relatively weak external magnetic field. As the temperature decreases, the stripe dynamics becomes slower and a certain structure similar to a cluster spin glass is formed in the CuO_2 layer.

Janossy *et al.* [2] thoroughly studied the antiferromagnetic domain structure in the dielectric $YBa_2Cu_3O_{6+x}$ ($x < 0.15$) crystal containing 1% Ga^{3+} ions as paramagnetic centers instead of nonmagnetic Y ions. As follows from the EPR data, the easy and hard axes of antiferromagnetic order are aligned along the [100] and [110] directions in the (*ab*) plane. In a zero magnetic field, the number of domains oriented along the two possible easy axes in the single crystal are equal to each other. The external magnetic field applied along the (*ab*) plane leads to the orientational spin flop transition, and virtually all domains at $h > h_{sf} = 5T$ ($T \sim 20$ K) are aligned perpendicularly to the field. Two models of the domain structure were considered in [2]: (i) magnetic domains are separated by charged domain walls inside the (*ab*) plane and (ii) ideal antiferromagnetic planar domains are separated by defect (*ab*) planes. In [2], the authors made the inference that the EPR data qualitatively confirm the validity of the latter model.

In our opinion, the experimental data obtained in [1] are not consistent with the universally accepted Zhang–Rice model of the ground state of a hole-type CuO_4 center in the CuO_2 plane [3]. According to this model, the ground state of a CuO_4 cluster with two $b_{1g}(d_{x^2-y^2})$ holes is the spin orbital singlet ${}^1A_{1g}$, which is well apart in energy from excited two-hole states. However, a simple spin and orbital symmetry of the *s* type suggests tetragonally isotropic *s*-wave transport properties for the well-isolated Zhang–Rice singlet in CuO_2 layers. An unusual *d*-wave magnetoresistance anisotropy observed in dielectric cuprates and also a number of other experimental and theoretical data indicate that the valence multiplet of the hole-type CuO_4 center has a more complex structure as compared to the well-isolated Zhang–Rice singlet, even though it is this singlet

1063-7834/02/4410-1907$22.00

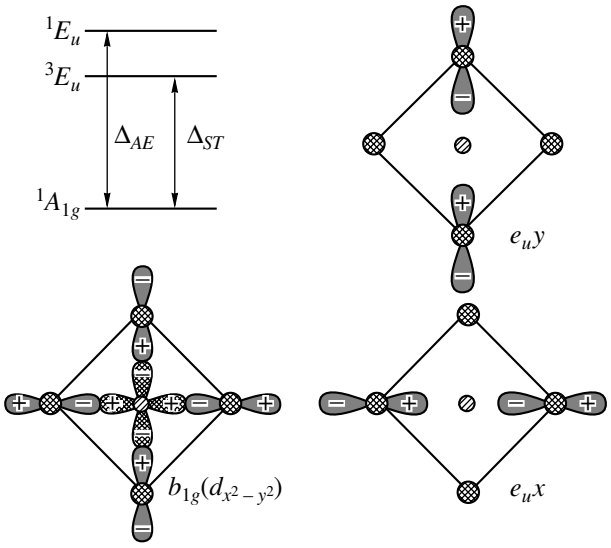

Fig. 1. Energy spectrum of the $(b_{1g}^2)^1A_{1g}$–$(b_{1g}e_u)^{1,3}E_u$ multiplet and the electron density distributions for the b_{1g}, $e_u x$, and $e_u y$ valence states of a hole.

that provides the basis for the majority of the existing model approaches.

The nature of the valence hole states in doped cuprates is of the utmost importance in the problem of high-temperature superconductivity. The solution of this problem will allow one to justify the choice of the appropriate effective Hamiltonian and the possibility of reducing the problem to the simple unambiguous *t*–*J* model or the Hubbard model.

In the present work, we demonstrated that the valence $^1A_{1g}$–^1E_u multiplet model developed in our previous works [4–6] provides a consistent interpretation of the most important result obtained in [1], namely, the *d*-wave magnetoresistance anisotropy in the CuO_2 planes of doped cuprates.

2. THE MODEL OF A VALENCE $^1A_{1g}$–^1E_u MULTIPLET

Within this model, it is assumed that the hole-type CuO_4^{5-} center is characterized by a quasi-degenerate ground state with the $^1A_{1g}$ and ^1E_u terms, which are close in energy and have the configurations b_{1g}^2 and $b_{1g}e_u$, respectively. In other words, it is assumed that an additional hole can be localized in two virtually equivalent states, namely, either in the Cu 3*d*–O 2*p* $b_{1g}(d_{x^2-y^2})$-hybridized state (this leads to the $^1A_{1g}$ Zhang–Rice singlet) or in the purely oxygen nonbonding e_u doublet state. Figure 1 displays the electron density distributions for two valence states, b_{1g} and e_u, of the hole and the qualitative energy spectrum of the valence multiplet.[1] It should be noted that the symmetry of the O $2pe_u x$ and O $2pe_u y$ states coincides with that of the Cu 4*px* and Cu 4*py* states.

In a sense, the valence $(b_{1g}^2)^1A_{1g}$–$(b_{1g}e_u)^1E_u$ multiplet of the hole-type CuO_4^{5-} center suggests the occurrence of a specific state with the copper valence resonant between Cu^{3+} and Cu^{2+} or ionic–covalent bonding [7]. In actual fact, the CuO_4 center with the valence $(b_{1g}^2)^1A_{1g}$–$(b_{1g}e_u)^1E_u$ multiplet is a particular type of the correlation polaron introduced by Goodenough and Zhou [7].

The model under consideration is confirmed by local-density functional calculations [8], first-principles calculations within the unrestricted Hartree–Fock method with self-consistent field for copper–oxygen clusters [9, 10], and a large number of experimental data. As far as we know, one of the first quantitative inferences regarding the competing role of the $b_{1g}(d_{x^2-y^2})$ copper–oxygen-hybridized orbital and the purely oxygen O $2p_\pi$ orbitals in the formation of valence states in the vicinity of the Fermi level in the CuO_2 plane was drawn in [8, 9]. According to [8, 9], it is these orbitals that are responsible for the unusual properties of cuprates in the vicinity of the ground state.

One of the most conclusive pieces of experimental evidence in favor of the valence $^1A_{1g}$–^1E_u multiplet model lies in the fact that the absorption bands with polarization characteristics corresponding to the dipole transitions in the $^1A_{1g}$–^1E_u multiplet are observed in the mid-IR range for doped cuprates [5]. The transition energies ($\sim\Delta_{AE}$) found for different cuprates are equal to several tenths of an electron-volt, which is the typical energy scale for the valence multiplet.

The hole in the e_u state can be antiferromagnetically and ferromagnetically bound to the b_{1g} hole. Therefore, the valence multiplet should include both the $(b_{1g}e_u)^1E_u$ spin singlet and the $(b_{1g}e_u)^3E_u$ spin triplet, whose energy can be even lower in the case of the b_{1g}–e_u ferromagnetic exchange. Actually, the low-lying triplet spin state in the CuO_4^{5-} center in $La_2Cu_{0.5}Li_{0.5}O_4$ with the singlet–triplet splitting $\Delta_{ST} = 0.13$ eV was revealed by Yoshinari *et al.* [11] with the use of ^{63}Cu and ^{65}Cu NQR spectroscopy. An indirect manifestation of valence states of the O $2p\pi$ or e_u type was observed in NMR measurements of the Knight shift in 1 : 2 : 3 YBaCuO systems [12]. In regard to the valence $^1A_{1g}$–^1E_u multiplet model, it is necessary to dwell on the results obtained by Tjeng *et al.* [13]. The authors of this work noted that they "are able to unravel the different

[1] There exist two types of O $2pe_u$ orbitals: e_u^σ and e_u^π. For simplicity, hereafter, we will consider only the e_u^σ orbitals.

spin states in the single-particle excitation spectrum of CuO" antiferromagnet and asserted that the top of the valence band is of pure singlet character, which "provides strong support for the existence and stability of Zhang–Rice singlets in high-T_c superconductors." However, in their photoemission experiment, the authors used the Cu $2p_{3/2}(K_3)$ resonance, which makes it possible to identify uniquely only copper states of photoholes. Consequently, they could not observe the purely oxygen e_u states.

Note that the complex $^1A_{1g}$–$^{1,3}E_u$ structure of the valence multiplet of the two-hole CuO_4^{5-} center should manifest itself in the photoemission spectra, because the odd ^1E_u terms are of particular importance in this case: it is these terms that make a nonzero contribution to the angle-resolved photoemission at $\mathbf{k} = 0$ or, in other words, at the Γ point. In this respect, it should be noted that the photoemission spectra have been experimentally measured for $Sr_2CuO_2Cl_2$ [14, 15] and $Ca_2CuO_2Cl_2$ [16]. In these spectra, the photocurrent of nonzero intensity is clearly observed at the center of the Brillouin zone, which corroborates the $^1A_{1g}$–$^{1,3}E_u$ structure of the valence multiplet in the ground state. As a whole, the valence multiplet model provides a way of consistently explaining the unusual properties of dielectric and superconducting cuprates: the absorption bands in the mid-IR range [5], the pseudo-Jahn–Teller (JT) effect and the related phenomena [6], and the specific spin properties [17].

3. ANOMALIES IN THE TRANSPORT PROPERTIES OF A HOLE IN THE $b_{1g}e_u : {}^3E_u$ STATE IN A MAGNETIC FIELD

The pseudo-Jahn–Teller polaronic nature of the $^1A_{1g}$–^1E_u ground state [6] (the spin singlet) favors its localization. Moreover, allowance should be made for the antiferromagnetic background, which results in a substantial increase in the effective mass of the moving spin singlet. Therefore, the virtually immobile pseudo-Jahn–Teller small singlet polaron is the ground state of the hole. In this situation, the most efficient channel of the hole transfer can be associated with the $b_{1g}e_u : {}^3E_u$ low-lying excited spin triplet. This gives rise to a thermoactivated *p*-type conductivity observed in the majority of lightly doped cuprates.

In order to describe the magnetoresistance effect, let us consider the spin and spin–orbit interactions for the $b_{1g}e_u : {}^3E_u$ spin triplet. The hole in the e_u state is strongly exchange-coupled with the b_{1g} hole on the same CuO_4 center and with the nearest neighbor CuO_4 centers. The spin state of the isolated CuO_4 center in the $b_{1g}e_u$ hole state is represented by two spin operators,

$$\mathbf{S} = \mathbf{s}_{b_{1g}} - \mathbf{s}_{e_u}, \quad \mathbf{V} = \mathbf{s}_{b_{1g}} - \mathbf{s}_{e_u} \tag{1}$$

(where $\mathbf{S}^2 + \mathbf{V}^2 = 3/2$ and $\mathbf{SV} = 0$), and the corresponding order parameters [17]. The E_u orbital doublet can be described using the pseudospin $s = 1/2$ formalism with the Pauli matrices σ_x, σ_y, and σ_z possessing simple transformation properties in the framework of the $E_u x$ and $E_u y$ basis set:[2]

$$\sigma_x = \begin{pmatrix} 0 & 1 \\ 1 & 0 \end{pmatrix} \propto b_{2g}, \quad \sigma_y = \begin{pmatrix} 0 & -i \\ i & 0 \end{pmatrix} \propto a_{2g},$$

$$\sigma_z = \begin{pmatrix} 1 & 0 \\ 0 & -1 \end{pmatrix} \propto b_{1g}.$$

As a consequence, the effective spin Hamiltonian for the ^3E_u spin triplet state of the hole-type center can be written as

$$\begin{aligned} \hat{H}_S &= \lambda S_z \sigma_y + D S_z^2 + a(S_x^2 - S_y^2)\sigma_z \\ &+ b\widetilde{S_x S_y}\sigma_x - \mu_B \mathbf{h}\hat{g}_S \mathbf{S} - 2\mu_B \mathbf{H}_{\text{ex}} \mathbf{S}, \end{aligned} \tag{2}$$

where $\widetilde{S_x S_y} = 1/2(S_x S_y + S_y S_x)$; λ is the effective spin–orbit interaction constant for the ^3E_u term; D, a, and b are the spin anisotropy parameters; g_S is the effective g tensor; $\mathbf{H}_{\text{ex}}$ is the internal effective spin exchange field; and $\mathbf{h}$ is the external magnetic field. For simplicity, hereinafter, we will assume that the CuO_2 layers are perfectly planar, the spin g factor is isotropic, and the external magnetic field is aligned parallel to the CuO_2 plane. Within the strong molecular field approximation, the spin operators can be replaced by the corresponding means

$$\langle S_x^2 - S_y^2 \rangle = \cos 2\Phi, \quad \langle \widetilde{S_x S_y} \rangle = \sin 2\Phi,$$

and the spin Hamiltonian (2) is transformed into the effective Hamiltonian of the spin-induced low-symmetry crystal field, that is,

$$\hat{H}_S = a\cos 2\Phi \sigma_z + b\sin 2\Phi \sigma_x, \tag{3}$$

where Φ is the azimuthal angle determining the orientation of the total magnetic field $\mathbf{H} = \mathbf{H}_{\text{ex}}(\mathbf{h}) + \mathbf{h}$. The eigenvectors and eigenvalues of this simple Hamiltonian have the form

$$\begin{aligned} \Psi_+ &= \cos\alpha|x\rangle + \sin\alpha|y\rangle, \quad \Psi_- = \sin\alpha|x\rangle - \cos\alpha|y\rangle, \\ \tan 2\alpha &= \frac{b}{a}\tan 2\Phi, \quad E_\pm = \pm\Delta(\Phi), \\ \Delta(\Phi) &= [b^2 + (a^2 - b^2)\cos^2 2\Phi]^{1/2}, \end{aligned} \tag{4}$$

where $|x\rangle \equiv |E_u x\rangle$ and $|y\rangle \equiv |E_u y\rangle$. The quantum-mechanical and thermodynamic means of the matrices σ_z and

[2] The standard notation is used for the representations of the point group D_{4h}.

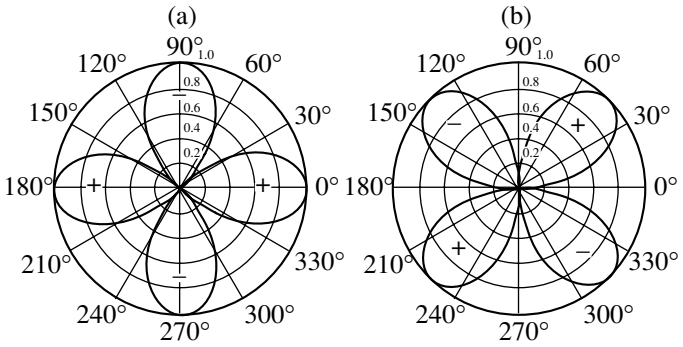

Fig. 2. Angular dependences of the high-temperature spin-induced quadrupole polarization for e_u orbitals of CuO_4 centers: (a) $\langle\langle\sigma_z\rangle\rangle$ and (b) $\langle\langle\sigma_x\rangle\rangle$.

σ_x, which describe the orbital polarization effects (the quadrupolar ordering), are as follows:

$$\langle\sigma_z\rangle_\pm = \langle\Psi_\pm|\sigma_z|\Psi_\pm\rangle = \pm\cos 2\alpha,$$
$$\langle\langle\sigma_z\rangle\rangle = -\frac{a\cos 2\Phi}{\Delta(\Phi)}\tanh\beta\Delta(\Phi), \tag{5}$$
$$\langle\sigma_x\rangle_\pm = \pm\sin 2\alpha, \quad \langle\langle\sigma_x\rangle\rangle = -\frac{b\sin 2\Phi}{\Delta(\Phi)}\tanh\beta\Delta(\Phi),$$

where $\beta = 1/kT$. Note that the dependences of the thermodynamic means $\langle\langle\sigma_z\rangle\rangle$ and $\langle\langle\sigma_x\rangle\rangle$ on the angle Φ exhibit the characteristic *d*-type ($d_{x^2-y^2}$ and d_{xy}, respectively) behavior (see Fig. 2).

Therefore, in the framework of our approximation, the orbital states of the ${}^3E_u$ spin triplet easily change in the external magnetic field or, to put it differently, the model provides an efficient "magnetic orbital" transformation. It is apparent that this induced orbital polarization can be strong only at sufficiently low temperatures. In the high-temperature limit ($|a|$ and $|b| \ll kT$), we have

$$\langle\langle\sigma_z\rangle\rangle \approx -\frac{a}{kT}\cos 2\Phi. \tag{6}$$

It should be noted that Hamiltonian (3) has an exact tetragonal symmetry. However, this Hamiltonian permits us to describe the effects of spontaneous breaking of the tetragonal symmetry individually in the spin and orbital subspaces or, in other words, the effects of spin-induced breaking of the tetragonal symmetry in the space of the $E_u\pm$ orbital states.

Taking into account only the (Cu $3d$–O $2p)_\sigma$ contribution to the transfer of the e_u hole between the E_u states of the nearest CuO_4 clusters, the matrices $\hat{t}(e_u–e_u)$ of the hole transfer integrals $e_u–e_u$ in the basis set $|x, y\rangle$ for the transfer along the [100] and [010] directions can be represented as

$$\hat{t}_a(e_u–e_u) = t_\sigma\begin{pmatrix} 1 & 0 \\ 0 & 0 \end{pmatrix}, \quad \hat{t}_b(e_u–e_u) = t_\sigma\begin{pmatrix} 0 & 0 \\ 0 & 1 \end{pmatrix}$$

where $t_\sigma = t_a(e_ux–e_ux) = t_b(e_uy–e_uy)$. The energy spectra of the e_u hole within the strong coupling approximation for the *nn* transfer consist of two bands, E^x and E^y, formed owing to the transfers $e_ux–e_ux$ and $e_uy–e_uy$; that is,

$$E^x_{\mathbf{k}} = 2t_\sigma\cos(k_xa), \quad E^y_{\mathbf{k}} = 2t_\sigma\cos(k_ya). \tag{7}$$

These one-dimensional bands are characterized by an extremely anisotropic effective mass and describe the one-dimensional motion of the hole along the *a* and *b* directions, respectively. However, it is easy to see that, with due regard for the *x*–*y* (*a*–*b*) exact symmetry, the transport properties are tetragonally isotropic. The spin-induced low-symmetry crystal field (3) leads to the mixing of two bands. Instead of simple relationships for the initial hole transfer integrals, we obtain the matrices of the renormalized hole transfer integrals in the $|\pm\rangle$ basis set, that is,

$$\hat{t}_a(e_u–e_u) = t_\sigma\begin{pmatrix} \cos^2\alpha & \frac{1}{2}\sin 2\alpha \\ \frac{1}{2}\sin 2\alpha & \sin^2\alpha \end{pmatrix},$$
$$\hat{t}_b(e_u–e_u) = t_\sigma\begin{pmatrix} \sin^2\alpha & -\frac{1}{2}\sin 2\alpha \\ -\frac{1}{2}\sin 2\alpha & \cos^2\alpha \end{pmatrix}, \tag{8}$$

where we used expression (5) for the function $\Psi_\pm$.

As a result, simple calculations for the renormalized bands give the expression

$$E^\pm_{\mathbf{k}} = t_+(\mathbf{k}) \mp [t^2_-(\mathbf{k}) + \Delta^2(\Phi) + 2\Delta(\Phi)t_-(\mathbf{k})\cos 2\alpha]^{\frac{1}{2}},$$
$$t_\pm(\mathbf{k}) = t_\sigma(\cos(k_xa) \pm \cos(k_ya)). \tag{9}$$

The tensors of inverse in-plane effective mass for the two bands can be written as

$$\left(\frac{\hat{1}}{\mathbf{m}^*}\right)_\pm = \frac{1}{m^*_0}\left[\mathbf{1} \pm \cos 2\alpha\begin{pmatrix} 1 & 0 \\ 0 & -1 \end{pmatrix}\right], \tag{10}$$

where $m^{*-1}_0 = -t_\sigma 4a^2/\hbar^2$.

Thus, we obtain the spin-induced shift and the spin-induced splitting of the initial bands, which leads to the violation of the *x*–*y* tetragonal symmetry and the

appearance of the spin-dependent anisotropy of the effective mass.

Taking into consideration the proportionality of the one-band conductivity and the tensor of inverse effective mass, we can derive a simple relationship for the in-plane magnetoresistance, that is,

$$\frac{\delta\rho_{a,b}}{\rho_{a,b}} = \langle\cos 2\alpha\rangle = \mp\langle\langle\sigma_z\rangle\rangle, \tag{11}$$

where the upper (lower) sign corresponds to the [100] ([010]) direction. This means that the in-plane magnetoresistance turns out to be related directly to the spin-induced orbital (quadrupole) polarization of the e_u states of the CuO_4 centers. In the strict sense, expression (11) is valid in the high-temperature range $\Delta(\Phi) \ll kT$, in which it reduces to the relationship

$$\frac{\delta\rho_{a,b}}{\rho_{a,b}} \approx \mp\frac{a}{kT}\cos 2\phi. \tag{12}$$

Unlike formula (6), in relationship (12), ϕ is the in-plane azimuthal angle of the external magnetic field **h** and allowance is made for the fact that the field **H** is almost orthogonal to **h**. This extremely simple expression describes all the essential specific features of the magnetoresistance anisotropy in the CuO_2 layers and is the main result of our model. A comparison with the experimental data obtained in [1] for $YBa_2Cu_3O_{6+x}$ ($x \sim 0.3$) indicates that the experimental angular dependence of the magnetoresistance in a sufficiently strong magnetic field exceeding $h_{\text{flop}} \approx 5$ T is well represented by the angular (temperature) dependence (12) at the reasonable spin anisotropy parameter $a \approx +0.1$ K.

4. EFFECT OF LOCAL VIBRONIC INTERACTIONS

Owing to the symmetry, the states of the E_u doublet for the tetragonal CuO_4 cluster are mixed by low-symmetry vibrations of the B_{1g} and B_{2g} type (orthorhombic and rectangular distortions of the square, respectively). Therefore, the observed small deviations of the dependence of the magnetoresistance from the simple relationship $\delta\rho_{ab}/\rho_{ab} \propto \cos 2\phi$ can be caused by the Jahn–Teller effect for the E_u doublet [6]. Note that this can lead to such strong spin-vibronic effects as spin-induced distortions of the CuO_4 center. Let us analyze the simplest variant of including the effect of the local vibronic interactions—the E–b_1–b_2 problem for the e_u hole.

The Hamiltonian of the E–b_1–b_2 problem has the form

$$H_{Ebb} = \sum_i \hbar\omega_i\left(b_i^+ b_i + \frac{1}{2}\right)\hat{I} + \sum_i k_i(b_i^+ + b_i)\hat{\sigma}_i, \quad \hat{\sigma}_1 \equiv \hat{\sigma}_z, \quad \hat{\sigma}_2 \equiv \hat{\sigma}_x, \tag{13}$$

where the second term describes the linear vibronic interaction associated with the symmetrized coordinates $Q_{b_{1g}}$ and $Q_{b_{2g}}$ of the CuO_4 cluster and

$$x_i = \frac{Q_i}{l_i} = \sqrt{\frac{\omega_i}{\hbar}}Q_i, \quad b_i = \frac{1}{\sqrt{2}}\left(x_i + \frac{d}{dx_i}\right), \quad b_i^+ = \frac{1}{\sqrt{2}}\left(x_i - \frac{d}{dx_i}\right).$$

In the case of the weak vibronic coupling $E_i^{JT} \ll \hbar\omega$, the energy and the wave functions of the vibronic ground doublet to the second order of the perturbation theory are given by

$$E_g = \frac{1}{2}(\hbar\omega_1 + \hbar\omega_2) - E_1 - E_2, \quad E_i = k_i^2/\hbar\omega_i, \tag{14}$$

$$\Psi_{+,00} = \left(1 - \frac{\gamma_1}{2} - \frac{\gamma_2}{2}\right)|+, 00\rangle - \sqrt{\gamma_1}|+, 10\rangle - \sqrt{\gamma_2}|-, 01\rangle + \frac{\gamma_1}{\sqrt{2}}|+, 20\rangle + \frac{\gamma_2}{\sqrt{2}}|+, 20\rangle - \sqrt{\gamma_1\gamma_2}\frac{\omega_1 - \omega_2}{\omega_1 + \omega_2}|-, 11\rangle, \tag{15}$$

$$\Psi_{-,00} = \left(1 - \frac{\gamma_1}{2} - \frac{\gamma_2}{2}\right)|-, 00\rangle + \sqrt{\gamma_1}|-, 10\rangle - \sqrt{\gamma_2}|+, 01\rangle + \frac{\gamma_1}{\sqrt{2}}|-, 20\rangle + \frac{\gamma_2}{\sqrt{2}}|-, 02\rangle + \sqrt{\gamma_1\gamma_2}\frac{\omega_1 - \omega_2}{\omega_1 + \omega_2}|+, 11\rangle, \tag{16}$$

where $\gamma_i = E_i/\hbar\omega_i$, $|\sigma, n_1n_2\rangle \equiv |\sigma\rangle|n_1\rangle|n_2\rangle$, $|\sigma\rangle$ are the orbital functions $|+\rangle$ and $|-\rangle$ of the E doublet $\hat{\sigma}_z|\sigma\rangle = \sigma|\sigma\rangle$, and $|n_1\rangle$ and $|n_2\rangle$ are the oscillatory functions corresponding to modes of the symmetries b_{1g} and b_{2g}.

The effective Hamiltonian (3) of the spin-induced low-symmetry crystal field in the basis set $\{\Psi_{+,00}, \Psi_{-,00}\}$ of the vibronic ground doublet takes the form

$$\tilde{V} = \tilde{a}\cos 2\varphi\hat{\sigma}_z + \tilde{b}\sin 2\varphi\hat{\sigma}_x, \quad \tilde{a} = a(1 - 2\gamma_2), \quad \tilde{b} = b(1 - 2\gamma_1). \tag{17}$$

This results in the corresponding modification of relationships (4) for the eigenvectors and eigenvalues, that is,

$$\tilde{\Psi}_+ = \cos\tilde{\alpha}\Psi_{+,00} + \sin\tilde{\alpha}\Psi_{-,00}, \quad \tilde{\Psi}_- = \sin\tilde{\alpha}\Psi_{+,00} - \cos\tilde{\alpha}\Psi_{-,00}, \quad \tilde{E}_\pm = \pm\tilde{\Delta}(\Phi), \quad \tan 2\tilde{\alpha} = \frac{\tilde{b}}{\tilde{a}}\tan 2\Phi, \tag{18}$$

$$\tilde{\Delta}(\Phi) = [\tilde{b}^2 + (\tilde{a}^2 - \tilde{b}^2)\cos^2 2\Phi]^{\frac{1}{2}}.$$

The quantum-mechanical and thermodynamic means are defined by the expressions

$$\begin{aligned}
\langle \sigma_z \rangle_\pm &= \pm(1-2\gamma_2)\cos 2\tilde{\alpha}, \\
\langle\langle \sigma_z \rangle\rangle &= -(1-2\gamma_2)\frac{\tilde{a}\cos 2\Phi}{\tilde{\Delta}(\Phi)}\tanh\beta\tilde{\Delta}(\Phi), \\
\langle \sigma_x \rangle_\pm &= \pm(1-2\gamma_1)\sin 2\tilde{\alpha}, \\
\langle\langle \sigma_x \rangle\rangle &= -(1-2\gamma_1)\frac{\tilde{b}\sin 2\Phi}{\tilde{\Delta}(\Phi)}\tanh\beta\tilde{\Delta}(\Phi), \\
\langle Q_1 \rangle_\pm &= \mp Q_1^{(0)}\cos 2\tilde{\alpha}, \\
\langle\langle Q_1 \rangle\rangle &= Q_1^{(0)}\frac{\tilde{a}\cos 2\Phi}{\tilde{\Delta}(\Phi)}\tanh\beta\tilde{\Delta}(\Phi), \\
\langle Q_2 \rangle_\pm &= \mp Q_2^{(0)}\sin 2\tilde{\alpha}, \\
\langle\langle Q_2 \rangle\rangle &= Q_2^{(0)}\frac{\tilde{b}\sin 2\Phi}{\tilde{\Delta}(\Phi)}\tanh\beta\tilde{\Delta}(\Phi),
\end{aligned} \tag{19}$$

where $Q_i^{(0)} = \sqrt{2\hbar\gamma_i/\omega_i}$. As a consequence, the in-plane magnetoresistance associated with $\langle\langle\sigma_z\rangle\rangle$ is slightly renormalized owing to the vibronic coupling with the vibrational mode b_{2g}.

The situation radically changes in the case of strong vibronic coupling: the terms with a certain symmetry in the effective Hamiltonian vanish completely. Now, we consider in more detail the case of strong vibronic coupling with the b_{1g} vibrations at $E_{b_{1g}}^{JT} \gg E_{b_{2g}}^{JT} \gg \hbar\omega_{b_{1g}}$ and $\hbar\omega_{b_{2g}}$. According to [18], Hamiltonian (13) can be rearranged using the unitary shift transformation $U = \exp[\Sigma_i \alpha_i(b_i^+ - b_i)]$; that is,

$$\begin{aligned}
\tilde{H}_{Ebb} &= U^+ H_{Ebb} U \\
&= \sum_i \hbar\omega_i\left(b_i^+ b_i + \alpha_i(b_i^+ + b_i) + \alpha_i^2 + \frac{1}{2}\right)\hat{I} \\
&\quad + \sum_i k_i(b_i^+ + b_i + 2\alpha_i)\hat{\sigma}_i.
\end{aligned} \tag{20}$$

The parameters α_i are chosen in such a way as to obtain a minimum of the ground-state energy of the system. At $E_1 > E_2$, we have

$$\begin{aligned}
&\alpha_1 = \pm\alpha, \quad \alpha_2 = 0 \quad (\alpha = k_1/\hbar\omega_1); \\
&E_0 = -E_1 + \frac{\hbar\omega_1}{2} + \frac{\hbar\omega_2}{2},
\end{aligned} \tag{21}$$

which corresponds to the states $|\mp, 0^{(\pm)}, 0\rangle$, where $|n_1^{(\pm)}\rangle$ is the oscillator shifted to the point $Q_1 = \pm Q_1^{(0)}$, that is,

$$|n_1^{(\pm)}\rangle = U(\pm\alpha)|n_1\rangle, \quad U(\alpha) = e^{\alpha(b_1^+ - b_1)}. \tag{22}$$

By choosing $\alpha_1 = \alpha$, we obtain

$$\begin{aligned}
\tilde{H}_{Ebb} &= H_0 + H_1, \\
H_0 &= \sum_i \hbar\omega_i\left(b_i^+ b_i + \frac{1}{2}\right)\hat{I} + E_1(\hat{I} + 2\hat{\sigma}_z), \\
H_1 &= k_1(b_1^+ + b_1)(\hat{I} + \hat{\sigma}_z) + k_2(b_2^+ + b_2)\hat{\sigma}_x.
\end{aligned} \tag{23}$$

From here on, H_1 is treated as a perturbation providing corrections to the spectrum H_0. It is interesting to note that the same result can be obtained starting from the basis set of the E–b_1 problem and allowing for $V_{b_2} = k_2(b_2^+ + b_2)\hat{\sigma}_x$ as a perturbation. The oscillatory functions of the vibronic doublets in the basis set of the E–b_1 problem are centered at different minima ($Q_1^{(0)}$ and $-Q_1^{(0)}$) of the adiabatic potential. The matrix elements V_{b_2} involve the factor $e^{-2E_1/\hbar\omega_1} \ll 1$. Therefore, with the aim of accounting for the perturbation, it is necessary to construct the coherent states centered at a given minimum of the adiabatic potential [for example, at $Q_1^{(0)}$] with the use of the states centered at the opposite minimum of the adiabatic potential [at $-Q_1^{(0)}$]. These coherent states are not the eigenfunctions of the E–b_1 problem, as a result of which terms of the type $2k_1(b_1^+ + b_1)$ arise in the effective perturbation operator.

Within the second order of the perturbation theory, we can write

$$\begin{aligned}
E_{n_1 n_2} &= -E_1 + \hbar\omega_1\left(n_1 + \frac{1}{2}\right) + \hbar\omega_2\left(\frac{1}{2} - \frac{E_2}{4E_1 + \hbar\omega_2}\right) \\
&\quad + n_2\hbar\omega_2\left(1 - \frac{8E_1E_2}{(4E_1)^2 - (\hbar\omega_2)^2}\right).
\end{aligned} \tag{24}$$

In the strong coupling limit ($E_{1,2} \gg \omega_{1,2}$), we have

$$\begin{aligned}
E_{n_1 n_2} &= -E_1 + \hbar\omega_1\left(n_1 + \frac{1}{2}\right) + \hbar\omega_2\left(1 - \frac{p}{2}\right)\left(n_2 + \frac{1}{2}\right), \\
p &= E_1/E_2.
\end{aligned} \tag{25}$$

The energy levels (25) are doubly degenerate, and the corresponding states $\Psi_{-, n_1^{(+)}, n_2}$ [centered at $Q_1^{(0)}$] and

$\Psi_{+, n_1^{(-)}, n_2}$ [centered at $-Q_1^{(0)}$] are represented as

$$\Psi_{-, n_1^{(+)}, n_2} = \Psi^{(0)}_{-, n_1^{(+)}, n_2} + \Psi^{(1)}_{-, n_1^{(+)}, n_2} + \Psi^{(2)}_{-, n_1^{(+)}, n_2} + \ldots,$$

$$\Psi^{(0)}_{-, n_1^{(+)}, n_2} = |-, n_1^{(+)}, n_2\rangle,$$

$$\Psi^{(1)}_{-, n_1^{(+)}, n_2} = \frac{k_2\sqrt{n_2+1}}{\hbar\omega'(0,1)}|+, n_1^{(+)}, n_2+1\rangle + \frac{k_2\sqrt{n_2}}{\hbar\omega'(0,-1)}|+, n_1^{(+)}, n_2-1\rangle,$$

$$\Psi^{(2)}_{-, n_1^{(+)}, n_2} = \frac{k_2\sqrt{n_2+1}}{\hbar\omega'(0,1)}\left\{\frac{2k_1\sqrt{n_1+1}}{\hbar\omega'(1,1)}|+, n_1^{(+)}+1, n_2+1\rangle + \frac{2k_1\sqrt{n_1}}{\hbar\omega'(-1,1)}|+, n_1^{(+)}-1, n_2+1\rangle + \frac{k_2\sqrt{n_2+2}}{\hbar\omega(0,2)}|-, n_1^{(+)}, n_2+2\rangle\right\} + \frac{k_2\sqrt{n_2}}{\hbar\omega'(0,-1)}\left\{\frac{2k_1\sqrt{n_1+1}}{\hbar\omega'(1,-1)}|+, n_1^{(+)}+1, n_2-1\rangle + \frac{2k_1\sqrt{n_1}}{\hbar\omega'(-1,-1)}|+, n_1^{(+)}-1, n_2-1\rangle + \frac{k_2\sqrt{n_2-1}}{\hbar\omega(0,-2)}|-, n_1^{(+)}, n_2-2\rangle\right\}, \quad (26)$$

where

$$\omega'(n_1, n_2) = -(4E_1 + n_1\omega_1 + n_2\omega_2),$$
$$\omega(n_1, n_2) = -(n_1\omega_1 + n_2\omega_2).$$

In the relationship for the state $\Psi_{+, n_1^{(-)}, n_2}$, the functions $|+\rangle$ and $|-\rangle$ should be interchanged and $n_1^{(+)}$ should be replaced by $n_1^{(-)}$.

Note that, although the curvature of the adiabatic potential at the points $Q_1^{(0)}$ and $-Q_1^{(0)}$ results in the frequencies ω_1 and $\omega_2\sqrt{1-p}$ of local vibrations and spectrum (25) is similar to the spectrum of the harmonic oscillator with the frequencies ω_1 and $\omega_2(1-p/2)$, the frequency renormalization, in fact, is caused by the vibronic mixing of the states of the electron doublet and does not correspond to the completely factorized Born–Oppenheimer state. The states $\Psi_{-, n_1^{(+)}, n_2}$ and $\Psi_{+, m_1^{(-)}, m_2}$ are not orthogonal, but the overlap integral is proportional to $\exp(-2E/\hbar\omega_1) \ll 1$.

The effective Hamiltonian (3) of the spin-induced low-symmetry crystal field in the basis set $\{\Psi_{+, n_1^{(-)}, n_2}, \Psi_{-, n_1^{(+)}, n_2}\}$ of the vibronic doublet has the form

$$\tilde{V} = (1-\gamma)a\cos 2\Phi\hat{\sigma}_z + D_{n_1n_1}(2\alpha)b\sin 2\Phi\hat{\sigma}_x, \quad (27)$$

where $D_{nn}(2\alpha)$ is the matrix element of the shift operator $\langle n|U(2\alpha)|n\rangle$ [$\langle 0|U(2\alpha)|0\rangle = \exp(-2E_1/\omega_1) \ll 1$ for the ground state] and γ defined as

$$\gamma = \frac{2\hbar\omega_2 E_2}{(4E_1 + \hbar\omega_2)^2} \quad (28)$$

is a correction of the second order to vibronic mixing of the b_{2g} type.

The quantum-mechanical and thermodynamic means over the states $\{\Psi_{+, 0_1^{(-)}, 0_2}, \Psi_{-, 0_1^{(+)}, 0_2}\}$ of the vibronic ground doublet considerably differ from those obtained in the case of weak vibronic coupling [see formulas (19)] and are represented as

$$\begin{aligned}
\langle\sigma_z\rangle_\pm &= \pm(1-\gamma),\\
\langle\langle\sigma_z\rangle\rangle &= -(1-\gamma)\tanh(\beta(1-\gamma)a\cos(2\Phi)),\\
\langle\sigma_x\rangle_\pm &= 0, \quad \langle\langle\sigma_x\rangle\rangle = 0,\\
\langle Q_1\rangle_\pm &= \mp Q_1^{(0)},\\
\langle\langle Q_1\rangle\rangle &= Q_1^{(0)}\tanh(\beta(1-\gamma)a\cos 2\Phi),\\
\langle Q_2\rangle_\pm &= 0, \quad \langle\langle Q_2\rangle\rangle = 0.
\end{aligned} \quad (29)$$

It should be noted that the complete vibronic reduction of the orbital operator σ_x occurs in the case of the strong vibronic coupling. The dependence $\langle\langle\sigma_z\rangle\rangle \propto \cos 2\Phi$ appears owing to the additive contribution from the spin-induced low-symmetry crystal field to the total energy. In the high-temperature limit, we have

$$\begin{aligned}
\langle\langle\sigma_z\rangle\rangle &= -(1-2\gamma)\frac{a\cos 2\Phi}{kT},\\
\langle\langle Q_1\rangle\rangle &= (1-\gamma)Q_1^{(0)}\frac{a\cos 2\Phi}{kT}.
\end{aligned} \quad (30)$$

As in the preceding case of strong vibronic coupling with the b_{1g} mode, the strong vibronic coupling with the b_{2g} vibrations leads to the complete vibronic reduction of the orbital operator σ_z. This results in the disappearance of the asymmetry of the effective mass tensor and in a transfer independent of the angle Φ in the (ab) plane.

Therefore, the renormalization of the parameters a and b in the effective Hamiltonian and, correspondingly, the renormalization of the quantities $\langle\sigma_i\rangle_\pm$ and $\langle\langle\sigma_i\rangle\rangle$ take place in the case of weak vibronic coupling at $E_{JT} \ll \hbar\omega$ (where F_{JT} is the characteristic Jahn–Teller interaction energy and $\hbar\omega$ is the characteristic vibra-

tional energy). For strong vibronic coupling, the double-well adiabatic potential stabilizes one of the orbital modes with symmetry b_{1g} or b_{2g}, which leads to a sharp decrease (vibronic reduction) in the term proportional to $\propto\sigma_x$ or $\propto\sigma_z$ in the effective Hamiltonian (3). In the former case (i.e., reduction in the term proportional to $\propto\sigma_x$), the pattern of two independent one-dimensional bands corresponding to the transfer along the *a* and *b* directions is restored, but the band energy modulation results in the dependence of the magnetoresistance $\delta\rho_{ab}/\rho_{ab} \propto \cos 2\phi$. In the former case, the tensor of inverse effective mass is isotropic and the in-plane magnetoresistance does not depend on ϕ.

5. CONCLUSIONS

Thus, in the present work, we proposed a model that allowed us to interpret the observed anomalous *d*-wave angular dependence of the in-plane magnetoresistance on the direction of the external magnetic field in the (*ab*) plane for the antiferromagnetic tetragonal crystal $YBa_2Cu_3O_{6+x}$ ($x \sim 0.3$). This dependence was explained in terms of efficient hole transfer through the low-lying excited purely oxygen O $2pe_u$ doublet state rather than through the $b_{1g}(d_{x^2-y^2})$ ground state. In the framework of this approach, it was assumed that the ground state of the doped CuO_4 cluster in cuprates can have the ${}^1A_{1g}$–${}^{1,3}E_u$ singlet–triplet structure, which is considerably more complex as compared to the well-isolated ${}^1A_{1g}$ Zhang–Rice singlet. The external magnetic field determines the orientation of the strong exchange field acting on the $b_{1g}e_u : {}^3E_u$ spin triplet state of the hole-type CuO_4 center, and the corresponding spin–orbit interaction results in the particular orbital polarization of the E_u doublet and the spatial anisotropy of the hole transfer. The observed *d*-wave angular dependence of the magnetoresistance on the orientation of the external magnetic field is associated with the shift and the splitting of two one-dimensional bands and the effective-mass anisotropy. In turn, this anisotropy is caused by the effective spin-induced low-symmetry crystal field at the e_u hole. Moreover, consideration was given to the possible influence of the spin-vibronic effects on the hole transfer. It was shown that, depending on the ratio between the model parameters, these effects can lead either to renormalization of the parameters in the effective Hamiltonian or to vibronic reduction of the orbital operators.

In this work, we did not consider important problems concerning the nature of the magnetic anisotropy and the antiferromagnetic domain structure in doped dielectric cuprates. In our opinion, the decisive role in this case is played by the doping-induced nucleation of domains of a new phase whose percolation at $x \geq 0.4$ gives rise to superconductivity [19]. The efficient nucleation of these domains in CuO_2 is favored by a strong in-plane charge inhomogeneity associated, at the minimum, with three linearly ordered *nn* chain oxygen atoms. This is responsible for the quasi-one-dimensional stripelike structure of in-plane domains. The stripelike domains aligned along the [100] and [010] directions produce orthorhombic distortions of the crystal structure in the surrounding antiferromagnetic tetragonal matrix and, thus, induce the corresponding in-plane magnetic anisotropy. Therefore, the CuO_2 layers in underdoped dielectric tetragonal $YBa_2Cu_3O_{6+x}$ crystals can be treated as antiferromagnets with stripe-induced fluctuating in-plane magnetic anisotropy characterized by the competition between the [100] and [010] axes.

Under the conditions of pronounced phase separation with comparable volumes of both phase fractions, the in-plane resistance can be qualitatively represented as the sum of three contributions, namely, the contributions from the semiconductor phase, the stripes, and the contact resistance due to the transfer through the interface. It should be noted that the stripe domains in *p*-doped cuprates can be considered sources of hole carriers (donors) for the semiconductor matrix.

According to ${}^{63}Cu$ and ${}^{65}Cu$ NQR spectroscopy [20], the observed low-temperature magnetic hysteresis and memory effects can be associated with the freezing of the stripe structure at temperatures below $T \approx 20$ K as a result of a sharp retardation of the relaxation through interfaces. It is interesting to note that Niedermayer *et al.* [21] recently found the low-temperature (20–25 K) spin glass transition in the heavily underdoped antiferromagnetic $Y_{1-y}Ca_yBa_2Cu_3O_6$ crystal.

ACKNOWLEDGMENTS

This work was supported in part by the American Foundation for Civilian Research and Development for the promotion of cooperation with scientists from the New Independent States of the former Soviet Union (CRDF) (grant no. N REC-005), the Ministry of Education of the Russian Federation (project no. E00-3.4-280), and the International Association of Assistance for promotion of cooperation with scientists from the New Independent States of the former Soviet Union (project INTAS no. 01-0654).

A.S. Moskvin acknowledges the hospitality of the Max-Planck-Institut für Festkörperforschung at which this work was performed in part.

REFERENCES

1. Y. Ando, A. N. Lavrov, and K. Segawa, Phys. Rev. Lett. **83** (14), 2813 (1999).
2. A. Janossy, F. Simon, T. Feher, *et al.*, Phys. Rev. B **59** (2), 1176 (1999); A. Janossy, F. Simon, and T. Feher, cond-mat/0005275.
3. F. C. Zhang and T. M. Rice, Phys. Rev. B **37** (7), 3759 (1988).

4. A. S. Moskvin, Pis'ma Zh. Éksp. Teor. Fiz. **58** (5), 342 (1993) [JETP Lett. **58**, 345 (1993)]; Physica C (Amsterdam) **282–287**, 1807 (1997); Physica B (Amsterdam) **252** (3), 186 (1998).
5. A. S. Moskvin, N. N. Loshkareva, Yu. P. Sukhorukov, *et al.*, Zh. Éksp. Teor. Fiz. **105** (4), 967 (1994) [JETP **78**, 518 (1994)].
6. A. S. Moskvin and Yu. D. Panov, Zh. Éksp. Teor. Fiz. **111** (2), 644 (1997) [JETP **84**, 354 (1997)]; Phys. Status Solidi B **212** (1), 141 (1999); Fiz. Tverd. Tela (St. Petersburg) **40** (10), 1795 (1998) [Phys. Solid State **40**, 1627 (1998)].
7. J. B. Goodenough and J.-S. Zhou, Phys. Rev. B **49** (6), 4251 (1994).
8. A. K. McMahan, R. M. Martin, and S. Satpathy, Phys. Rev. B **38** (10), 6650 (1988).
9. J. Tanaka, K. Kamiya, and C. Tanaka, Physica C (Amsterdam) **161** (4), 451 (1989).
10. J. Tanaka and C. Tanaka, J. Phys. Chem. Solids **59** (10–12), 1861 (1998).
11. Y. Yoshinari, P. C. Hammel, J. A. Martindale, *et al.*, Phys. Rev. Lett. **77** (10), 2069 (1996).
12. Y. Yoshinari, Physica C (Amsterdam) **276** (1–2), 147 (1997).
13. L. H. Tjeng, B. Sinkovic, N. B. Brookes, *et al.*, Phys. Rev. Lett. **78** (6), 1126 (1997).
14. B. O. Wells, Z.-X. Shen, A. Matsuura, *et al.*, Phys. Rev. Lett. **74** (6), 964 (1995).
15. C. Dürr, S. Legner, R. Hayn, *et al.*, Phys. Rev. B **63** (1), 014505 (2001).
16. F. Ronning, C. Kim, D. L. Feng, *et al.*, cond-mat/9903151; Science **282**, 2067 (1998).
17. A. S. Moskvin and A. S. Ovchinnikov, J. Magn. Magn. Mater. **186** (3), 288 (1998); Physica C (Amsterdam) **296** (3–4), 250 (1998).
18. Y. M. Liu, C. A. Bates, J. L. Dunn, and V. Z. Polinger, J. Phys.: Condens. Matter **8** (37), L523 (1996).
19. A. Furrer, P. Allenshpach, F. Fauth, *et al.*, Physica C (Amsterdam) **235–240**, 261 (1994).
20. M. Matsumura, H. Yamagata, Y. Yamada, *et al.*, J. Phys. Soc. Jpn. **58** (3), 805 (1989).
21. Ch. Niedermayer, C. Bernhard, T. Blasius, *et al.*, Phys. Rev. Lett. **80** (17), 3843 (1998).

Translated by O. Borovik-Romanova

Physics of the Solid State, Vol. 44, No. 10, 2002, pp. 1916–1924. Translated from Fizika Tverdogo Tela, Vol. 44, No. 10, 2002, pp. 1827–1835.

MAGNETISM AND FERROELECTRICITY

Charge Segregation and a Nonuniform Magnetic State in Donor- and Acceptor-Doped $LaMnO_3$

N. N. Loshkareva*, A. V. Korolev*, T. I. Arbuzova*, N. I. Solin*, N. A. Viglin*, I. B. Smolyak*, N. G. Bebenin*, Yu. P. Sukhorukov*, S. V. Naumov*, N. V. Kostromitina*, and A. M. Balbashov**

** Institute of Metal Physics, Ural Division, Russian Academy of Sciences, ul. S. Kovalevskoĭ 18, Yekaterinburg, 620219 Russia*

e-mail: loshkareva@imp.uran.ru

*** Moscow Power Institute, ul. Krasnokazarmennaya 14, Moscow, 105835 Russia*

Received December 11, 2001

Abstract—A coordinated study of the magnetic, electrical, optical, and EPR properties of $LaMnO_3$ single crystals doped by donors (7 at. % Ce) and acceptors (7 at. % Sr) revealed that in all cases, except undoped $LaMnO_3$, charge segregation associated with large-scale crystal-field fluctuations occurs and the magnetic properties originate from the existence of ferromagnetic phase inclusions and localized ferrons in the matrix with a canted magnetic structure. © *2002 MAIK "Nauka/Interperiodica".*

1. INTRODUCTION

An essential feature of strongly correlated systems, in particular, of manganites with colossal magnetoresistance (CMR), is their tendency to phase separation [1–4]. It was initially assumed that the insulating antiferromagnetic matrix in lightly doped manganites contains metallic ferromagnetic drops. At present it seems clear that the real phase separation pattern is more complex. One should discriminate between two mutually connected aspects of this problem. The first of them (electronic) originates from the presence of charge segregation, i.e., of metallic drops in the dielectric matrix, and the second (magnetic) is connected with the character of the magnetic state, which is assigned to either a uniform canted magnetic structure or a two-phase magnetic state. Only a coordinated approach to the investigation of manganites can provide well-founded conclusions.

The effect of light strontium doping (up to $x < 0.17$) on the properties of $LaMnO_3$ has been fairly well studied (see, e.g., [5]). The effect of cerium, which can be quadrivalent and, hence, act as a donor, has been investigated only at heavy doping levels ($x > 0.3$) [6] or with small additions of Ce to manganite of an optimum composition $La_{0.6}Sr_{0.33}Ce_{0.07}MnO_3$ [7]. The present work deals, in a coordinated approach, with $LaMnO_3$ single crystals doped with 7 at. % Ce or Sr ions. We compare measurements of the magnetization, dc and microwave electrical resistivity, EPR, and light absorption in the IR range. Light absorption is used as a quasi-local method applied to systems with charge segregation. The quasilocality is due to the difference between the optical response from the conducting regions and the insulating matrix [8, 9].

2. SAMPLES AND EXPERIMENTAL TECHNIQUES

Single crystals of $LaMnO_3$ (LMO), $La_{0.93}Ce_{0.07}MnO_3$ (LCar), and $La_{0.93}Sr_{0.07}MnO_3$ (LS) were grown by the floating-zone technique with radiative heating [10] in an argon atmosphere, and $La_{0.93}Ce_{0.07}MnO_3$ (LCai) was grown in air. X-ray diffraction studies showed the single crystals to be single phase. The parameters of the orthorhombic lattice (*Pbnm* structure) and the unit cell volume of the crystals are given in the table.

The magnetic measurements in dc ($H \le 50$ kOe) and ac magnetic fields were carried out within a broad temperature range $T = 2$–600 K at the Center of Magnetometry (Institute of Metal Physics, Ural Division, Russian Academy of Sciences) using an MPMS-5XL (Quantum Design) SQUID magnetometer, Faraday magnetic balance, and vibrating-sample magnetometer. The need to take into account the considerable magnetic anisotropy and the twinning structure of the single crystals gave rise to the following features in our experiment. In the magnetically ordered state, the $M(H)$ magnetization curves were measured on unfixed samples; thereby, the magnetic field H was always directed along the easy axis. The data presented below relate to single-crystal samples with the highest magnetization, whose $M(H)$ curves almost coincide with the curves for powder samples prepared by grinding fragments of the single crystals under study. The chosen procedure of sample selection reduces the effect of the twinning structure of single crystals on the results of experiments to a minimum. The experiments carried out on powders do not reveal strong compositional fluctuations from sample to sample.

Structural, magnetic, and electrical parameters of $La_{1-x}A_xMnO_3$ single crystals, where A = Ce and Sr and x = 0.07

Compound	$LaMnO_3$	$La_{0.93}Ce_{0.07}MnO_3$ (Ar)	$La_{0.93}Ce_{0.07}MnO_3$ (air)	$La_{0.93}Sr_{0.07}MnO_3$
a, Å	5.722 ± 0.002	5.727 ± 0.002	5.722 ± 0.002	5.600 ± 0.002
b, Å	5.536	5.534	5.531	5.549
c, Å	7.712	7.705	7.703	7.753
Unit cell volume, Å^3	244.3	244.2	243.8	240.9
T_C, K	133	131	132	122
H_c (T = 2) K, kOe	1.9	2.0	2.1	1.74
M_S at 2 K (H = 0), emu/g	6.58	4.66	4.30	44.75
M_S/M_0	0.073	0.049	0.045	0.473
θ, K				(*O*') 141
	84	76	76	(*O*) 236
μ_{eff}^{exp}, μ_B	6.49	4.98	6.55	(*O*') 7.21
				(*O*) 6.39
μ_{eff}^{theor}, μ_B	4.90	4.98	4.98	4.83
E_a, eV	0.26	0.29	0.28	0.18

The temperature dependence of dc electrical resistivity was measured using the four-probe method. The electrical resistivity at microwave frequencies (9.2 GHz) was studied on samples placed in the antinode of an electric field [11].

Magnetic-resonance measurements were performed on a standard ERS-231 *X*-range (3 cm) spectrometer.

The absorption spectra were studied in the energy region 0.09–0.9 eV on a computerized IKS-21 spectrometer.

3. EXPERIMENTAL RESULTS

3.1. Magnetic Properties

Figure 1 presents field dependences of crystal magnetization measured at 2 K with the magnetic field reduced from its maximum value of H = 50 kOe. The LMO, LCar, and LCai crystals exhibit a linear $M(H)$ dependence with low spontaneous magnetization M_S (see table), with the spontaneous magnetization of the cerium-doped crystals being lower than that of pure $LaMnO_3$. This character of the $M(H)$ relation and the small spontaneous moment are characteristic of both a weak ferromagnet (FM) [12] and an antiferromagnet (AFM) with inclusions of the ferromagnetic phase or with localized magnetic polarons (ferrons), as in EuTe [13]. The field dependence of magnetization, $M(H)$, of the Sr-doped crystal deviates noticeably from being linear, and the spontaneous magnetization is an order of magnitude higher than that of LMO, LCar, and LCai, which cannot be attributed to weak Dzyaloshinski ferromagnetism [14]. The magnetooptic Kerr effect associated with the ferromagnetic contribution [15] is also an order of magnitude larger in LS than in LCai.

The temperature dependence of the real part (χ'_{ac}) of the dynamic magnetic susceptibility of all crystals has a narrow peak (1–2 K wide). Measurements of the temperature dependence of the static susceptibility of LMO, LCar, and LCai samples made in a dc magnetic field H = 250 Oe in the interval 120–140 K revealed a rise in the susceptibility χ of the crystals under cooling, which is obviously connected with the onset of spontaneous magnetization. The position of the inflection point on the $\chi(H)$ curve almost coincides with the temperature of the maximum of (χ'_{ac}), thus permitting one to identify it with the Curie temperature T_C. The values of T_C of the samples studied are listed in the table.

The temperature dependences of magnetization of the LMO, LCar, and LCai samples measured at H =

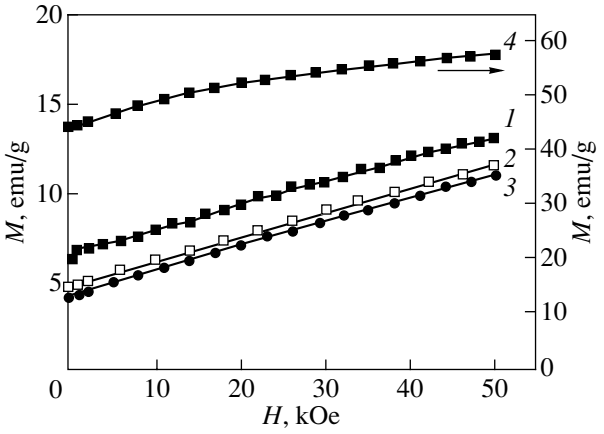

Fig. 1. Magnetization vs. magnetic field plots obtained at T = 2 K. (*1*) LMO, (*2*) LCar, (*3*) LCai, and (*4*) LS.

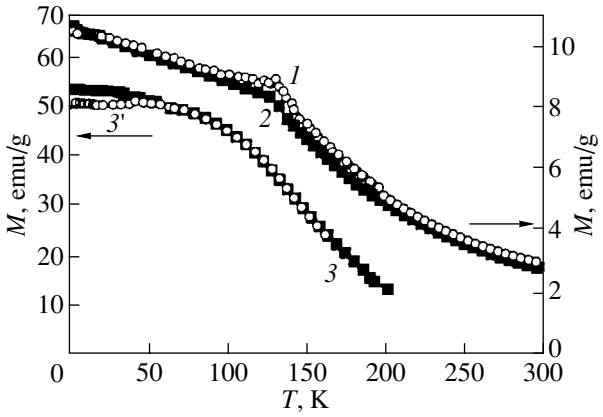

Fig. 2. Temperature dependences of magnetization measured in a magnetic field $H = 50$ kOe. (*1*) LMO, (*2*) LCai, and (*3*, *3*') LS under FC and ZFC conditions, respectively.

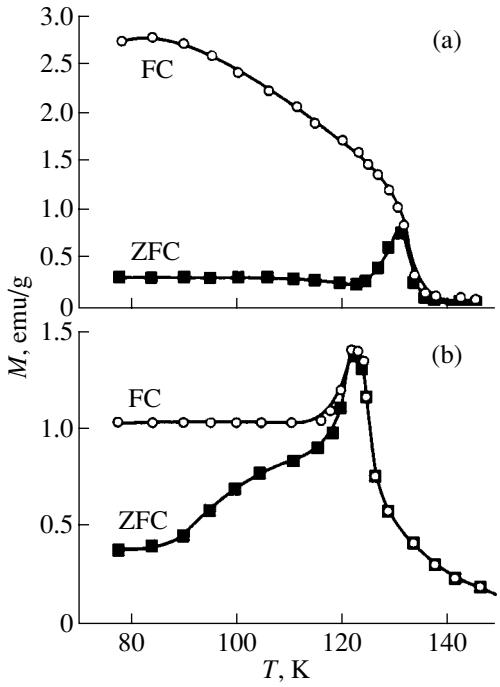

Fig. 3. Temperature dependences of magnetization measured in a magnetic field of 100 Oe in the FC and ZFC regimes for (a) LCai and (b) LS.

50 kOe (Fig. 2) exhibit breaks. These features are associated with the phase transition from the paramagnetic to antiferromagnetic state, because the $M(T)$ relation of ferromagnets in a strong magnetic field is monotonic. Hence, the temperature at which this break is observed may be identified with the Néel temperature T_N. The $M(T, H = 50$ kOe) curve for the LS crystal does not have breaks, and the temperature dependence of magnetization follows a course typical of ferromagnets.

In weak magnetic fields (on the order of 100 Oe), the $M(T)$ curves measured on the LCai and LS single crystals in the field-cooling (FC) and zero-field-cooling (ZFC) regimes differ very strongly (Fig. 3). The magnetization curves taken on undoped LMO and LCar (not shown in Fig. 2) are similar to those for LCai. In LS, the difference between the FC and ZFC magnetizations decreases smoothly with the temperature increasing to T_C, while in LCai this difference decreases sharply near T_C. LCai does not exhibit a magnetization peak near T_C when cooled in a field of 100 Oe, while LS retains the peak down to fields of the order of 5 kOe. We note that the magnetization of $La_{0.99}Sr_{0.01}MnO_3$ reached a maximum in a magnetic field of 2 Oe [16]. The FC and ZFC magnetization curves of Ce-doped crystals are similar to those measured in [17] for the $Ca_{0.9}Sm_{0.1}MnO_3$ manganite in a field of 10 Oe. In the latter study, the $Ca_{1-x}Sm_xMnO_3$ manganites with $0 < x \le 0.12$ were treated at low temperatures and in weak magnetic fields as cluster glasses.

$M(T)$ relations of manganites measured under zero-field- and field-cooling are frequently observed to follow different patterns, which is attributed to the presence of magnetic inhomogeneities (see, e.g., [18]). The higher the applied field, the narrower the temperature interval within which this difference is seen. For the LS crystal in a magnetic field of 50 kOe, a difference between the FC and ZFC magnetization curves is seen to exist for $T < 50$ K (Fig. 2).

All the manganites studied have a fairly broad hysteresis loop at $T = 2$ K. The values of the coercive force at $T = 2$ K are listed in the table. The coercive force H_c of the LS crystal increases monotonically with decreasing temperature (Fig. 4). The other three samples reveal two regions of steep growth in H_c, namely, near T_C and in the low-temperature domain ($T <$ 20–30 K). The growth in H_c at low temperatures is similar to the increase in the coercive force of magnetically inhomogeneous manganites $La_{0.8}Ca_{0.2}MnO_{3-\delta}$] with different oxygen deficiencies [19] and of materials with ferromagnetic grains in a nonferromagnetic matrix [20], wherein the $H_c(T)$ dependence can be assigned to the cluster glass state.

Let us consider the magnetic properties of the manganites under study in the paramagnetic temperature region. The paramagnetic susceptibility of the LCar crystal for temperatures $T > 290$ K follows the Curie–Weiss law $\chi = N\mu_{eff}^2/3k_B(T - \theta)$ with the effective magnetic moment $\mu_{eff} = 4.98\mu_B$ and paramagnetic Curie temperature $\theta = 76$ K (Fig. 5). This implies that the spin correlations accounting for the short-range order persist up to $T \approx 290$ K, which is considerably in excess of the magnetic phase transition temperature. The theoretical value of μ_{eff} was calculated only with the spin moments taken into account, $\mu_{eff} = g\mu_B\sqrt{S(S+1)}$. The calculations were made under the assumption that doping with cerium gives rise to the formation of Mn^{2+} ions ($S =$ 5/2), whereas the doping with strontium is accompa-

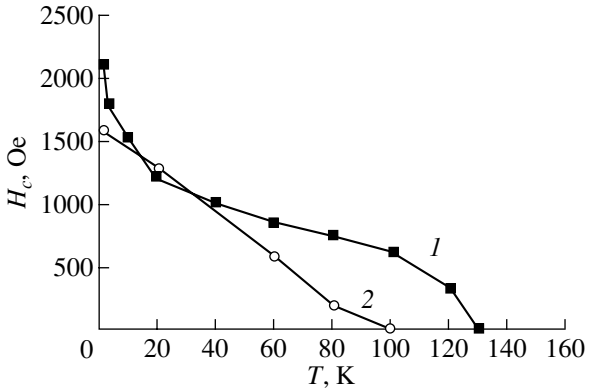

Fig. 4. Temperature dependence of the coercive force for (*1*) LCai and (*2*) LS.

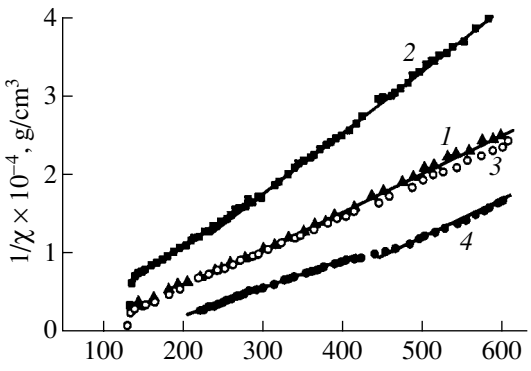

Fig. 5. Temperature dependences of inverse magnetic susceptibility measured in a field H = 2.65 kOe. (*1*) LMO, (*2*) LCar, (*3*) LCai, and (*4*) LS.

nied by the formation of Mn^{4+} ions (S = 2). The agreement between the experimental and theoretical values of the effective magnetic moment and the independence of the magnetic susceptibility on the applied field argue for a purely paramagnetic state of the magnetic ions for temperatures $T > 290$ K. Although the paramagnetic Curie temperature is lower than T_N, $\theta > 0$; nevertheless, this indicates superposition of the ferromagnetic and antiferromagnetic contributions. We note that the paramagnetic Curie temperature is positive for all the crystals (see table), which is due to a strong FM exchange in the *ab* plane (J_1 = 0.83 meV) and a weak AFM exchange along the *c* axis (J_2 = –0.58 meV) [21]. Estimates made from the values of J_1 and J_2 by using the molecular field theory yield θ = 100 K.

The temperature dependences of the inverse susceptibility χ^{-1} of LCai and LMO almost coincide. The effective moment for these crystals is considerably in excess of the theoretical value of μ_{eff} (see table). It may be conjectured that spin correlations between the magnetic manganese ions persist at least up to T = 600 K.

The $\chi^{-1}(T)$ relation for the strontium-doped crystal differs from those obtained for LMO, LCar, and LCai in the clearly pronounced break present at 480 K (Fig. 5). In the temperature region $380 < T < 450$ K, the susceptibility depends on the magnetic field. Apparently, a structural transition from the high-temperature, weakly distorted orthorhombic (pseudocubic) phase *O* to the strongly distorted orthorhombic (Jahn–Teller) phase *O*' occurs near T = 480 K. The susceptibility revealed anomalies at this structural transition for other strontium concentrations in [22]. A similar structural transition is observed to occur in pure LMO at 750 K [22, 23]. The magnitude of the effective magnetic moment in the *O*' phase of LS derived from the slope of the $\chi^{-1}(T)$ plot in the temperature region $200 < T < 380$ K is $\mu_{eff} = 7.21\ \mu_B$, which considerably exceeds the theoretical value 4.83 μ_B. In the *O* phase, the effective magnetic moment is smaller and close to μ_{eff} for LMO and LCai.

3.2. DC and AC Electrical Resistivity

All the single crystals studied reveal a semiconducting character of the temperature dependence of dc electrical resistivity ρ (Fig. 6a). Judging by the sign of their thermopower, all the samples are *p*-type semiconductors at room temperature. In the case of the LMO single crystal, the $\rho(T)$ relation is closely approximated, within a broad range of values of the electrical resistivity ($\rho = 10^2$–$10^6\ \Omega$ cm), by an exponential law $\rho = \rho_0 \exp(E_a/kT)$ with an activation energy E_a = 0.26 eV; at room temperature, $\rho \approx 2 \times 10^3\ \Omega$ cm. The electrical resistivity of cerium-doped samples is higher by an order of magnitude than that of pure $LaMnO_3$. For the same Ce content, the electrical resistivity is larger for the crystal grown in argon than in air. Extrapolating the linear $\log\rho(1/T)$ plots for all crystals from room temperature to very high temperatures ($1/T \longrightarrow 0$) yields, for the prefactor values, $\rho_0 = (1$–$3) \times 10^{-3}\ \Omega$ cm; this expression is characteristic of conduction in delocalized states in a Mott disordered semiconductor [24]. The values of E_a near room temperature are listed in the table for all the crystals studied.

It appears natural to assume that cerium has a valence of +4 and acts as a donor. The increase in resistivity accompanying cerium doping is probably connected with partial compensation of the acceptors, more specifically, the cation vacancies present even in pure $LaMnO_3$ (see Section 3.3). The compensation is the largest in single-crystal LCar. It may be conjectured that crystal growth in air (in an oxygen-containing atmosphere) favors the formation of vacancies on the cation (Mn^{4+} ions) sublattices more than crystal growth in Ar, because an argon atmosphere is more reductive than air.

Hole doping with strontium reduces the electrical resistivity (by nearly two orders of magnitude at room temperature) through a decrease in the activation energy associated with an increase in the Mn^{4+} concentration.

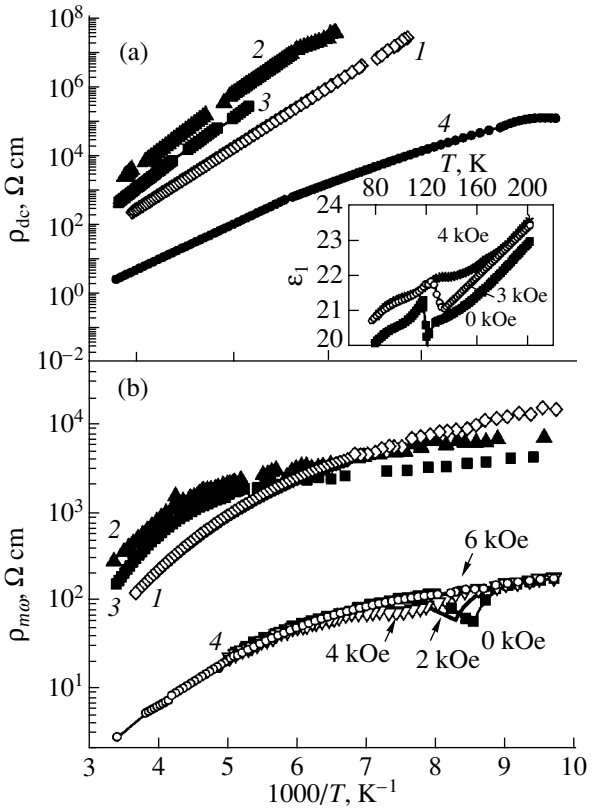

Fig. 6. Temperature dependences of (a) dc and (b) ac electrical resistivity measured for (*1*) LMO, (*2*) LCar, (*3*) LCai, and (*4*) LS. Inset: temperature dependence of the dielectric permittivity of LS.

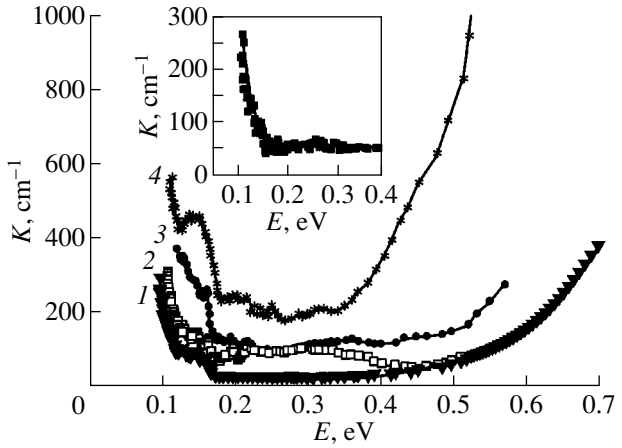

Fig. 7. Absorption spectra measured at $T = 80$ K on single crystals of (*1*) LMO, (*2*) LCar, (*3*) LCai, and (*4*) LS. Inset: difference between absorption spectra of LCai measured at 80 and 130 K.

The temperature dependences of microwave electrical resistivity $\rho_{m\omega}$ at a frequency of 9.2 GHz exhibit monotonic behavior for all single crystals except LS (Fig. 6b), which is similar to what is observed for dc resistivity $\rho(T)$. The ac electrical resistivity is lower than the dc resistivity throughout the temperature range covered. As seen from Fig. 6b, LS exhibits an anomaly in its microwave resistivity near $T_C \approx 122$ K. A jump in the real part ε_1 of the dielectric permittivity occurs in the same temperature interval (see inset to Fig. 6a). Application of a magnetic field shifts the $\rho_{m\omega}$ and ε_1 anomalies toward higher temperatures. The anomalies disappear in magnetic fields above 6 kOe. The temperature behavior of the ac electrical resistivity plotted in Fig. 6b resembles the pattern of dc $\rho(T)$ observed in single crystals with a higher Sr concentration, for instance, in $La_{0.9}Sr_{0.1}MnO_3$ [25].

3.3. Optical Absorption in the Infrared Region

Investigation of optical absorption in the IR region, where the interaction of light with charge carriers becomes manifest, provides evidence for the existence of charge segregation, i.e., concentration of carriers in some regions of the crystal, where the conduction follows a metallic character [8, 15]. This conclusion was drawn from the fact that the quasi-Drude contribution appearing below the Curie temperature in the absorption spectra of manganites, whose resistivity is high and whose temperature dependence has an activated character, cannot be accounted for if a crystal is treated as a homogeneous dielectric medium. In contrast, the optical absorption of polycrystals [8, 26], single crystals [27], and single-crystal films [9] of various manganites finds a natural explanation if one assumes charge segregation to exist. We note that optical-conductivity spectra, which are derived from reflectance spectra using Kramers–Kronig analysis and are widely used in the literature, are only weakly sensitive to the spectral features of lightly doped manganites in the IR region.

As is well known, the purity of a semiconductor single crystal can be judged from the magnitude of the absorption coefficient in the transparency window. The $LaMnO_3$ single crystal under study has a fairly small absorption coefficient, ~40 cm^{-1} at 293 K and ~20 cm^{-1} at 80 K (Fig. 7). At 0.14 eV, LMO and the other crystals exhibit an impurity absorption band originating from the presence of Mn^{4+} ions [9, 27]. The intensity of this band in LMO is the lowest when compared with that in the other crystals. The absorption spectra of Ce-doped crystals have an additional band at ~0.35 eV, which is possibly due to Mn^{2+} ions.

A significant feature of the LMO crystal is a monotonic growth of the transmission of light with cooling (Fig. 8), which indicates a decrease in IR absorption due to carrier freezing-out. The situation for doped single crystals in the region of light-carrier interaction is different; namely, transmission of light by LCar, LCai, and LS decreases when these crystals are cooled below T_C. Actually, this decrease takes place even at higher temperatures, but it is steeper below T_C. The difference between the LCai absorption spectra measured at 80 and 130 K (inset to Fig. 7) indicates the onset of addi-

tional absorption, which grows with decreasing energy, i.e., is quasi-Drude. It is the quasi-Drude (metallic) contribution that accounts for the decrease in transmission of light under cooling below T_C. The appearance of the metallic contribution in light transmission of crystals whose electrical resistivity reaches 10^8 Ω cm at 120 K can be interpreted only in terms of charge carriers being concentrated in highly conducting regions (drops).

3.4. Electron Paramagnetic Resonance

The ion responsible for the magnetic-resonance signal in $LaMnO_3$ is Mn^{3+} [28]. Strontium substitution for lanthanum, as well as the formation of cation defects in crystals grown in air, gives rise to the formation of Mn^{4+} ions. Substitution of Ce^{4+} for La^{3+} can produce Mn^{2+} ions, which have a substantially larger atomic radius than the trivalent ion. All the manganese ions mentioned above have a magnetic moment and produce magnetic resonance signals with different signatures [29, 30]. However, in lanthanum manganites, magnetic resonance signals due to ions in different valence states cannot be separated; as a result, only one line is seen in the paramagnetic region [29]. The width of this line is determined, on the one hand, by exchange interaction (line narrowing) and, on the other, by local fields and distortions, for instance, of the Jahn–Teller type, and by antisymmetric coupling between ions of the Dzyaloshinski–Moriya type (broadening and anisotropy in the linewidth) [31]. According to the literature data, the resonance line of $La_{1-x}Sr_xMnO_3$ narrows with increasing strontium concentration [31]. This observation can be interpreted as enhancement of the exchange interaction between manganese ions caused by an increasing Mn^{4+} ion concentration. At the same time, the parameters of the crystal structure change [5].

Figure 9 plots the resonance linewidth ΔH_{pp} as a function of temperature. For the LMO, LCai, and LCar samples, the linewidth in the paramagnetic region depends on temperature only weakly. Doping with cerium results in an increase in ΔH_{pp}, the linewidth being the largest in the closest compensated LCar sample.

The value of ΔH_{pp} for the LS sample, which exhibits the highest spontaneous magnetization, is smaller than that in the other samples at $T < 300$ K but grows strongly with increasing temperature. Similar dependences were observed earlier in [30, 31]. As pointed out in [30], the EPR linewidth in $La_{0.8}Ca_{0.2}MnO_{3+y}$ is proportional to the electrical conductivity, which is described by the expression $\sigma(T) \propto 1/T\exp(-E_\sigma/k_BT)$ for small-radius polaron hopping. In our case, ΔH_{pp} of the LS crystal in the temperature region 170–300 K can be fitted by a relation of the type $\Delta H_{pp}(T) = A\exp(-E_{pp}/k_BT)$, where the activation energy E_{pp} = 0.20 eV is close to that for the resistivity, E_a = 0.18 eV (see table). It can be assumed that the temperature-induced change in ΔH_{pp} in this sample is caused by spin–lattice relaxation, which is governed by the hole conduction in delocalized states.

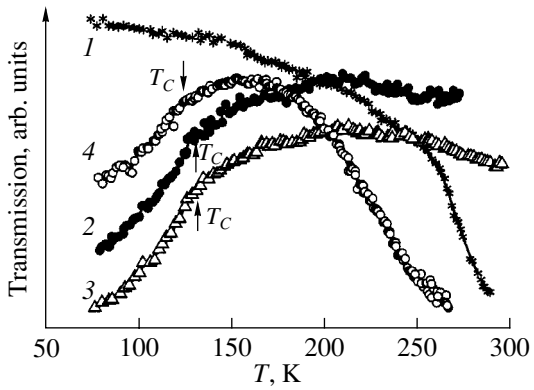

Fig. 8. Temperature dependence of transmission at an energy of 0.14 eV measured for single crystals of (*1*) LMO, (*2*) LCar, (*3*) LCai, and (*4*) LS. The data for different compositions are given on different scales.

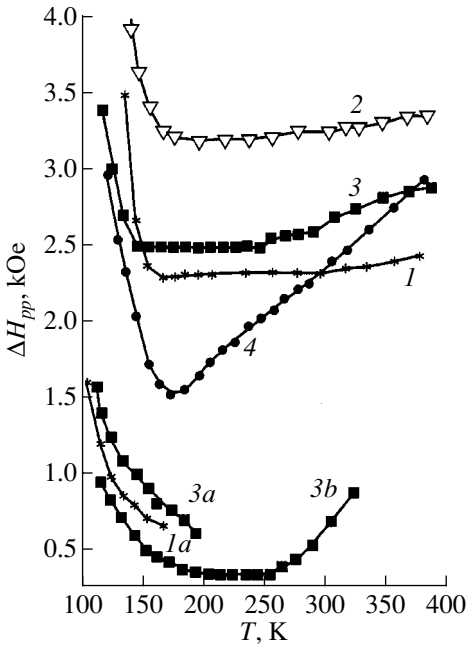

Fig. 9. EPR linewidth for single crystals of (*1*) LMO, (*2*) LCar, (*3*) LCai, and (*4*) LS; (*1a*), (*3a*), and (*3b*) are additional lines obtained for LMO and LCai.

The LCar crystal exhibits one broad line at temperatures from 150 to 400 K (at 300 K, the linewidth $\Delta H_{pp} \approx 3300$ Oe, the resonance field $H_0 \approx 3700$ Oe); this line starts to broaden below 150 K and disappears altogether at $T \approx 130$ K. The magnetic-resonance spectra of the other crystals reveal additional narrow lines; the temperature dependence of their widths is displayed in Fig. 9. For instance, in addition to a broad line (at 300 K, the linewidth $\Delta H_{pp} \approx 2700$ Oe, $H_0 \approx 3600$ Oe),

which also broadens and vanishes below 140 K, the LCai spectrum has two narrow lines, one of which appears below 320 K and the other, at a temperature below 200 K. The appearance of additional lines implies the magnetic inhomogeneity of the samples. It may be conjectured that this state is initiated by the presence of regions with a magnetization differing noticeably from that of the matrix and that these regions are due to the Mn^{4+} ions.

4. DISCUSSION OF RESULTS

4.1. Magnetic State of $LaMnO_3$ and of Doped Crystals

Let us consider the effect of doping on the magnetic properties of $LaMnO_3$ in the region of magnetic ordering. As seen from the table, substitution of 7 at. % strontium for lanthanum results in a fairly strong change in the lattice parameters as compared to those of an undoped crystal, while in the case of cerium, the lattice parameters change only weakly. Nonisovalent doping not only changes the lattice parameters but also modifies the exchange interaction between the manganese ions through the formation of Mn^{4+} ions.

The field and temperature dependences of magnetization (Figs. 1, 2) indicate that the LMO and cerium-doped crystals are antiferromagnets with a weak spontaneous magnetization. Neutron experiments [32] show the LCai crystal to be an antiferromagnet with an *A*-type structure and an exchange integral $J_2 = -0.46$ meV, which is slightly less in absolute value than that for $LaMnO_3$ ($J_2 = -0.58$ meV) [21]. The value of M_S is a small fraction of the maximum magnetization under ferromagnetic ordering of magnetic ions, $M_0 = Ng\mu_B S$, in LMO and LC; here, N is the number of spins per 1 g of the material, g is the g factor, μ_B is the Bohr magneton, and S is the spin moment (see table). The crystal structure allows weak Dzyaloshinski ferromagnetism. The M_S/M_0 ratios for the compounds studied are comparable with the data available for known antiferromagnets with weak ferromagnetism [12]. The decrease in M_S resulting from cerium doping can be due to a decrease in the Dzyaloshinski field, which is caused by the impurity-induced lattice deformation. However, the experimental data on the magnetic properties and EPR presented above imply that the magnetic state of our crystals is nonuniform; hence, the Dzyaloshinski interaction is not the only reason for the onset of spontaneous magnetization even in nominally pure $LaMnO_3$. The close values of T_C and T_N may, in our case, result from different variations in these temperatures under doping. Indeed, neutron data [33, 34] suggest a decrease in T_N and an increase in T_C for $LaMnO_3$ doped by Ca and Sr ions, with T_N and T_C coinciding at low dopant concentrations; for instance, for Ca-doped crystals, this occurs at $x \approx 0.07$.

The totality of our experimental data permits the conclusion that the antiferromagnetic matrix (possibly, with a canted magnetic structure) of nominally pure $LaMnO_3$ and of Ce-doped samples contains inclusions of a ferromagnetic phase (which is probably connected with the formation of metallic drops) and clusters with a large magnetic moment (localized ferrons [13]).

In the LCar sample, where compensation is the closest and, hence, the Mn^{4+} concentration is the lowest, the effective moment is close to its theoretical value (see table) and there are no additional lines in the EPR spectra. This suggests that the number of clusters and inclusions of the ferromagnetic phase in LCar is the smallest. In LCai, the concentration of Mn^{4+} ions is higher than in LCar and, therefore, one may assume the presence of a larger number of clusters and inclusions of the FM phase in the former crystal.

In the LMO sample, the effective magnetic moment substantially exceeds the theoretical value, the EPR spectra contain additional lines, and no metallic drops are observed. It follows that undoped $LaMnO_3$ contains localized ferrons, but there is no ferromagnetic phase. The spontaneous magnetization is determined in this case by the Dzyaloshinski interaction and localized ferrons.

Unfortunately, it does not appear possible to separate the contributions from the ferrons, ferromagnetic regions, and weak ferromagnetism to M_S, because the Dzyaloshinski field can vary strongly when impurities are introduced.

In the Sr-doped crystal, the $M(H)$ relation deviates from a linear course and $M_S/M_0 = 0.47$. At 2 K, the magnetization in a magnetic field of 50 kOe is more than 50% of M_0. The simplest explanation of this consists in that the crystal is actually a mixture of ferro- and antiferromagnetic regions of approximately the same volume; when a magnetic field is applied, the magnetic moment of the antiferromagnetic regions increases and the ferromagnetic phase grows in volume. Neutron scattering experiments show, however, that the situation in lightly doped manganites may be much more complex. According to [33, 34], the manganite single crystals doped by Sr and Ca have a modulated canted magnetic structure, with the canting angle in FM drops being substantially larger than that in the host matrix and depending on the carrier concentration. For instance, in $La_{0.92}Ca_{0.08}MnO_3$ at $T = 15$ K, the spins inside the above regions cant away from their direction in a perfect AFM structure by an angle of 20° and the average canting angle derived from nuclear Bragg peaks is 10° [33]. The average canting angle determined for the $La_{0.94}Sr_{0.06}MnO_3$ crystal (close in composition to our LS crystal) is 13° [34], which corresponds to $M_S/M_0 = 0.23$. It was assumed in [33, 34] that the existence of the modulated canted structure is associated with charge segregation. Our experimental data do not make it possible to make an unambiguous conclusion as to the magnetic state of the LS sample, even though these data do not contradict the interpretation proposed in [33, 34].

4.2. Inhomogeneous State of the Electron Subsystem

The main effect of weak doping by cerium on the manganite electrical properties is a partial compensation of acceptors by donors. Holes (Mn^{4+}) are present even in pure LMO because of cation vacancies, which is indicated by the impurity band at 0.14 eV in the absorption spectra (Fig. 7). We note that photoemission spectroscopy shows that the cerium valence in $La_{0.67}Ce_{0.33}MnO_3$ is larger than 3 but is not 4 [35]; as a result, the concentration of excess electrons is less than that of cerium.

Prior to discussing the origin of the charge and magnetic inhomogeneities in weakly doped manganites, we note that the impurities can be distributed nonuniformly over a sample, particularly at low doping levels (7 at. %). Our measurements made on different samples cut from the same crystal yield similar results; therefore, the manganites studied can be considered to be macroscopically uniform. This does not, however, imply the absence of microinhomogeneities on various scales. Charge segregation, i.e., the presence of carrier-enriched regions separated from one another, can, in particular, set in a crystal. The conductivity increases in the ferromagnetic state, and metallic drops, which do not form a singly-connected region, can appear in the dielectric matrix. In this case, the dc conductivity will be of an activated character at any temperature. The formation of carrier-enriched regions is possibly initiated by clusters of charged impurities. We note that the $\rho(T)$ relation for composite media representing nanosized metallic particles embedded in a dielectric matrix also has an activated character [36].

The anomaly in the $\rho_{m\omega}(T)$ and $\varepsilon_1(T)$ relations observed in the LS crystal near $T_C = 122$ K (Fig. 6) can be assigned to a manifestation of the insulator–metal transition in the drops. Application of a magnetic field shifts the anomaly toward higher temperatures. Manganite single crystals undergoing a metal–insulator transition near the Curie temperature are known to exhibit a resistivity peak, which becomes less sharp and shifts toward higher temperatures [25]. One may, therefore, conjecture that this anomaly in the $\rho_{m\omega}(T)$ curves also originates from the metal–insulator transition, which occurs, however, in small regions of the crystal. In the $\rho(T)$ curves, this anomaly is not seen because of the higher electrical resistivity.

In the low-temperature domain, $T < 125$ K, the microwave resistivity of cerium-doped crystals becomes lower than that of the pure crystal, which indicates the presence of high-conductivity regions.

The formation of metallic drops in samples doped by cerium and strontium can also be deduced from the appearance of a quasi-Drude contribution in the IR absorption spectra of these crystals at low temperatures (see inset to Fig. 7), which is absent in undoped lanthanum manganite. The existence of a metal–insulator transition in drops below T_C is also corroborated by the temperature dependence of the transmission of light in the region where the light interacts with free charge carriers (Fig. 8). Indeed, if a sample were to be in a uniform dielectric state, the absorption of light would decrease with decreasing temperature because of the decreasing conductivity. Hence, the observed drop in the transmission of light under cooling implies the existence of regions in which the conductivity increases, a pattern characteristic of metals. Let us estimate the contribution of metallic drops to the light absorption coefficient. As seen from the M_S/M_0 ratio (see table), the FM regions can amount to a few percent of the sample volume. Experiments carried out on $La_{1-x}Sr_xMnO_3$ single crystals [25] suggest that the volume of the metallic phase is noticeably smaller than that of the ferromagnetic regions; for a rough estimate, we assume that the metallic drops occupy $\sim 10^{-3}$ of the sample volume. Assuming the electrical resistivity of the drops to be approximately $\sim 10^{-3}$ Ω cm, we find $\delta \sim 1$ μm for the skin layer thickness, which corresponds to an absorption coefficient $\delta^{-1} = 10^4$ cm^{-1}. Multiplying this figure by the relative volume of the drops yields ~ 10 cm^{-1} for the estimated contribution of the drops to the absorption coefficient, which agrees in order of magnitude with the experiment.

At first glance, the above interpretation is at odds with the observation that metallic drops form under doping not only by strontium, where the Mn^{4+} concentration increases, but also by cerium, i.e., in the case where the Mn^{4+} concentration decreases and the dc electrical resistivity increases. In actual fact, however, we are dealing here with a heavily doped, closely compensated semiconductor. As shown in [37], due to the presence of large-scale fluctuations under close compensation, the charge carriers form isolated drops, with the carrier concentration inside each drop being high and the electrical conductivity having a metallic character. If the compensation is nearly complete, the material has both electrons and holes, which reside, however, in spatially isolated regions. In this system, the dc conductivity is not metallic. The density of states at the Fermi level, as derived from microwave absorption, can be quite high, whereas the density of states in the band gap can be fairly low, as found from optical absorption. We readily see that this pattern is in full agreement with our experimental data for the low-temperature region when there are no magnetic fluctuations.

Carrier-enriched regions also exist in the paramagnetic state, because they form as a result of fluctuations in the impurity concentration. However, because of the strong scattering from magnetic fluctuations, the carriers should become localized. Obviously enough, the metal–insulator transition in these regions should occur near the Curie temperature; this is in full agreement with the above experimental data.

5. CONCLUSION

Thus, a coordinated study of cerium- and strontium-doped lanthanum manganites shows that doping by di- and quadrivalent ions to low dopant concentrations (7 at. %) yields essentially different results. The magnetic state of cerium-doped crystals is antiferromagnetic with a low spontaneous magnetization, which derives from inclusions of a ferromagnetic phase, localized ferrons, and Dzyaloshinski interaction. The volumes of the ferro- and antiferromagnetic phases in a strontium-doped crystal are nearly equal. In all cases, except pure $LaMnO_3$, charge segregation occurs. The electronic properties agree with these materials being heavily doped and (in the case of cerium doping) closely compensated semiconductors. The existence of regions with metallic conductivity in these crystals is due to large-scale crystal-field fluctuations.

ACKNOWLEDGMENTS

The authors are indebted to M. Hennion and F. Moussa for the neutron diffraction data, É.L. Nagaev for valuable discussions, and E.V. Mostovshchikov for assistance in the measurements.

This study was supported by INTAS (grant no. 97-30253) and, partially, by the Russian Foundation for Basic Research (project no. 00-02-17544).

REFERENCES

1. E. L. Nagaev, Phys. Rep. **346** (6), 388 (2001).
2. E. Dagotto, T. Hotta, and A. Moreo, Phys. Rep. **344**, 1 (2001).
3. M. Yu. Kagan and K. I. Kugel', Usp. Fiz. Nauk **171** (6), 577 (2001).
4. V. M. Loktev and Yu. G. Pogorelov, Fiz. Nizk. Temp. **26** (3), 231 (2000) [Low Temp. Phys. **26**, 171 (2000)].
5. A. A. Mukhin, V. Yu. Ivanov, V. D. Travkin, *et al.*, Pis'ma Zh. Éksp. Teor. Fiz. **68** (4), 331 (1998) [JETP Lett. **68**, 356 (1998)].
6. P. Mandal and S. Das, Phys. Rev. B **56** (23), 15073 (1997).
7. R. I. Zaĭnullina, N. G. Bebenin, V. V. Mashkautsan, *et al.*, Fiz. Tverd. Tela (St. Petersburg) **40** (11), 2085 (1998) [Phys. Solid State **40**, 1889 (1998)].
8. N. N. Loshkareva, Yu. P. Sukhorukov, S. V. Naumov, *et al.*, Pis'ma Zh. Éksp. Teor. Fiz. **68** (1), 89 (1998) [JETP Lett. **68**, 97 (1998)].
9. N. N. Loshkareva, Yu. P. Sukhorukov, E. A. Gan'shina, *et al.*, Zh. Éksp. Teor. Fiz. **119** (3), 533 (2001) [JETP **92**, 462 (2001)].
10. A. M. Balbashov, S. G. Karabashev, Ya. M. Mukovskiy, and S. A. Zverkov, J. Cryst. Growth **167** (1–2), 365 (1996).
11. A. B. Davydov, N. I. Solin, and G. L. Shtrapenin, Defektoskopiya, No. 8, 95 (1982).
12. A. S. Borovik-Romanov, in *Antiferromagnetism and Ferrites* (Fiz.-Mat. Nauki, Moscow, 1962), p. 70.
13. É. L. Nagaev, *Physics of Magnetic Semiconductors* (Nauka, Moscow, 1979).
14. I. E. Dzyaloshinskiĭ, Zh. Éksp. Teor. Fiz. **19**, 960 (1964).
15. N. N. Loshkareva, Yu. P. Sukhorukov, E. V. Mostovshchikova, *et al.*, Zh. Éksp. Teor. Fiz. **121** (2), 412 (2002) [JETP **94**, 350 (2002)].
16. K. Ghosh, R. L. Greene, S. E. Lofland, *et al.*, Phys. Rev. B **58** (13), 8206 (1998).
17. A. Maignan, C. Martin, F. Damay, *et al.*, Phys. Rev. B **58** (5), 2758 (1998).
18. A. V. Korolyov, A. Ye. Arkhipov, V. S. Gaviko, *et al.*, J. Magn. Magn. Mater. **213**, 63 (2000).
19. H. L. Ju and H. Sohn, J. Magn. Magn. Mater. **167**, 200 (1997).
20. F. Conde, C. Gomez-Polo, and A. Hernando, J. Magn. Magn. Mater. **138**, 123 (1994).
21. F. Moussa, M. Hennion, J. Rodriguez-Carvajal, *et al.*, Phys. Rev. B **54** (21), 15149 (1996).
22. M. Paraskevopoulos, F. Mayr, J. Hemberger, *et al.*, J. Phys.: Condens. Matter **12**, 3993 (2000).
23. J.-S. Zhou and J. B. Goodenough, Phys. Rev. B **60** (22), R15002 (1999).
24. N. F. Mott and E. A. Davis, *Electronic Processes in Non-Crystalline Materials* (Clarendon, Oxford, 1979; Mir, Moscow, 1982), Vol. 1.
25. A. Urushibara, Y. Moritomo, T. Arima, *et al.*, Phys. Rev. B **51** (20), 14103 (1995).
26. N. N. Loshkareva, N. I. Solin, Yu. P. Sukhorukov, *et al.*, Physica B **293**, 390 (2001).
27. N. N. Loshkareva, Yu. P. Sukhorukov, É. A. Neĭfel'd, *et al.*, Zh. Éksp. Teor. Fiz. **117** (2), 440 (2000) [JETP **90**, 389 (2000)].
28. E. Granado, N. O. Moreno, A. Garcia, *et al.*, Phys. Rev. B **58** (17), 11435 (1998).
29. S. A. Al'tshuler and B. M. Kozyrev, *Electron Paramagnetic Resonance* (Fizmatgiz, Moscow, 1961; Academic, New York, 1964).
30. A. Shengelaya, Guo-meng Zhao, H. Keller, *et al.*, Phys. Rev. B **61** (9), 5888 (2000).
31. V. A. Ivanshin, J. Deisenhofer, H.-A. Krug von Nidda, *et al.*, Phys. Rev. B **61** (9), 6213 (2000).
32. M. Hennion, private communication.
33. G. Biotteau, M. Hennion, F. Moussa, *et al.*, Phys. Rev. B **64**, 104421 (2001).
34. M. Hennion, F. Moussa, G. Biotteau, *et al.*, Phys. Rev. B **61** (14), 9513 (2000).
35. J.-S. Kang, Y. J. Kim, B. W. Lee, *et al.*, J. Phys.: Condens. Matter **13** (16), 3779 (2001).
36. P. Sheng and B. Abeles, Phys. Rev. Lett. **28** (1), 34 (1972).
37. B. I. Shklovskiĭ and A. L. Efros, *Electronic Properties of Doped Semiconductors* (Nauka, Moscow, 1979; Springer, New York, 1984).

Translated by G. Skrebtsov

Physics of the Solid State, Vol. 44, No. 10, 2002, pp. 1925–1928. Translated from Fizika Tverdogo Tela, Vol. 44, No. 10, 2002, pp. 1836–1839.

MAGNETISM AND FERROELECTRICITY

Magnetic Properties of $Fe_xMn_{1-x}S$ Sulfides Exhibiting the Magnetoresistive Effect

G. A. Petrakovskiĭ*, L. I. Ryabinkina*, G. M. Abramova*, A. D. Balaev*, O. B. Romanova*, G. I. Makovetskiĭ, K. I. Yanushkevich**, and A. I. Galyas****

** Kirensky Institute of Physics, Siberian Division, Russian Academy of Sciences, Akademgorodok, Krasnoyarsk, 660036 Russia*

e-mail: lir@iph.krasn.ru

*** Institute of Solid-State and Semiconductor Physics, National Academy of Belarus, Minsk, 220072 Belarus*

Received December 28, 2001

Abstract—The magnetic, electrical, and thermal (derived from DTA data) properties of $Fe_xMn_{1-x}S$ polycrystalline sulfides ($0 \le x \le 0.38$) synthesized based on α-MnS (NaCl cubic lattice) and exhibiting colossal magnetoresistance were studied. The studies were conducted at temperatures from 77 to 1000 K and magnetic fields of up to 30 kOe. As the degree of cation substitution in the $Fe_xMn_{1-x}S$ system was increased, the magnetic order was found to change from antiferromagnetic to ferromagnetic. In the high-temperature domain (550–850 K), the samples undergo two phase transitions with critical temperatures T_{c_1} and T_{c_2}, which are accompanied by reversible anomalies in the magnetization and thermal (DTA) properties and by a semiconductor–metal transition. *© 2002 MAIK "Nauka/Interperiodica".*

1. INTRODUCTION

The colossal magnetoresistance (CMR) remains an intriguing problem, because a clear understanding of the mechanism of this phenomenon is still lacking. The CMR effect has been revealed recently [1, 2] in new, NaCl-type cubic fcc compounds synthesized on the basis of manganese monosulfide. Materials with a NaCl lattice exhibiting CMR can be exemplified by cation-substituted systems based on europium oxide and chalcogenides [3]. In these compounds, CMR is observed to occur at low temperatures, ≤40 K. In the $Fe_xMn_{1-x}S$ sulfides, negative colossal magnetoresistance is found at temperatures $T \le 200$ K. A possible origin of the CMR is the magnetic and electronic separation of crystallographically similar compounds [2, 3].

2. EXPERIMENTAL TECHNIQUES

The present communication reports on a study of the electrical, magnetic, and thermal (derived from DTA measurements) properties of polycrystalline sulfides $Fe_xMn_{1-x}S$ with compositions $0 \le x \le 0.38$ at temperatures from 77 to 1000 K in magnetic fields of up to 30 kOe. The techniques used to prepare the compounds and to measure their electrical properties are described elsewhere [1, 2]. The magnetic measurements in the range 100–1000 K and in fields of up to 10 kOe were performed using the Faraday method on samples placed in evacuated quartz ampoules. Measurements of the magnetic properties within the 77- to 300-K temperature interval and in fields up to 30 kOe were made in a vibrating-sample, superconducting-coil magnetometer.

X-ray structural measurements of the $Fe_xMn_{1-x}S$ samples thus synthesized ($0 \le x \le 0.38$) showed them to be solid solutions with a NaCl-type structure typical of manganese monosulfide [1, 2]. The fcc lattice parameter decreases as the degree of cation substitution (x) increases, which agrees with the data from [4].

3. EXPERIMENTAL RESULTS AND DISCUSSION

Figure 1 displays temperature dependences of the magnetization (measured in a field of 8.6 kOe) of single-crystal α-MnS (curve *1*) and polycrystalline α-MnS (curve *2*). The magnetic susceptibility of the polycrystalline manganese monosulfide, $\chi_{300\,K} = 6.9 \times 10^{-5}$ cm^3/g, is in agreement with the data from [5, 6] and is higher than that of the single-crystal compound. In the region of the Néel temperature $T_N \sim 150$ K, the temperature-dependent magnetization exhibits a maximum which signals an antiferromagnetic transition. Above the Néel temperature, the inverse magnetic susceptibility $\chi^{-1}(T)$ of the manganese monosulfide follows the Curie–Weiss relation, with the paramagnetic temperature Θ and Curie constant C equal to –450 K and 4.32, respectively. At temperatures above ~450 K, the inverse magnetic susceptibility is seen to deviate from the Curie–Weiss law. According to [7], in this temperature interval, the charge carriers in α-MnS reverse sign. For $T < 450$ K, the manganese monosulfide behaves as a *p*-type semiconductor, with the carrier mobility being $\mu \sim 0.065$ cm^2 V^{-1} s^{-1}. For $T > 450$ K, the carriers are electrons and their mobility increases by an

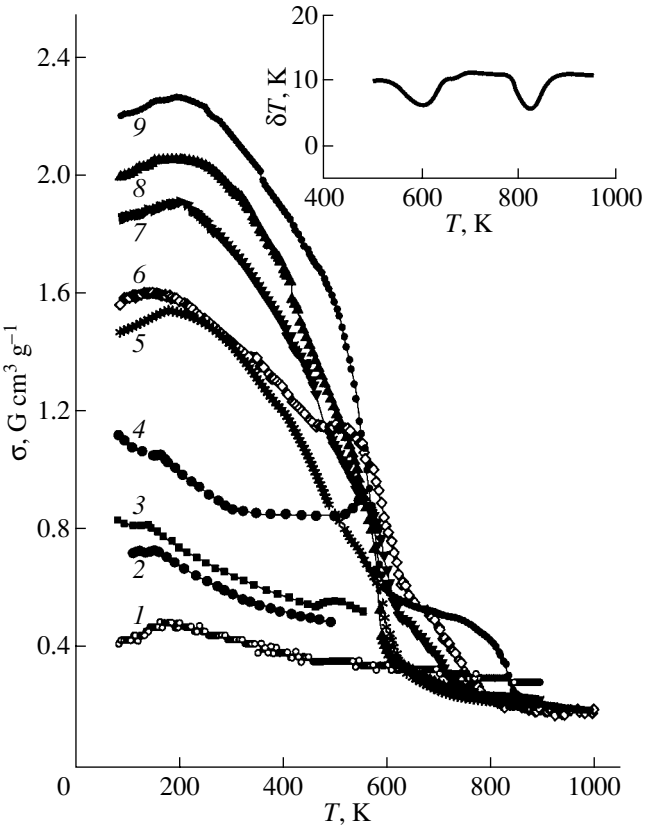

Fig. 1. Temperature dependences of the magnetization of the $Fe_xMn_{1-x}S$ system measured in a field H = 8.6 kOe for different compositions x: (*1*) 0, α-MnS single crystal; (*2*) 0, polycrystalline α-MnS; (*3*) 0.05; (*4*) 0.15; (*5*) 0.25; (*6*) 0.29; (*7*) 0.27; (*8*) 0.32; and (*9*) 0.38. Inset: differential thermal analysis data for $x \sim 0.35$.

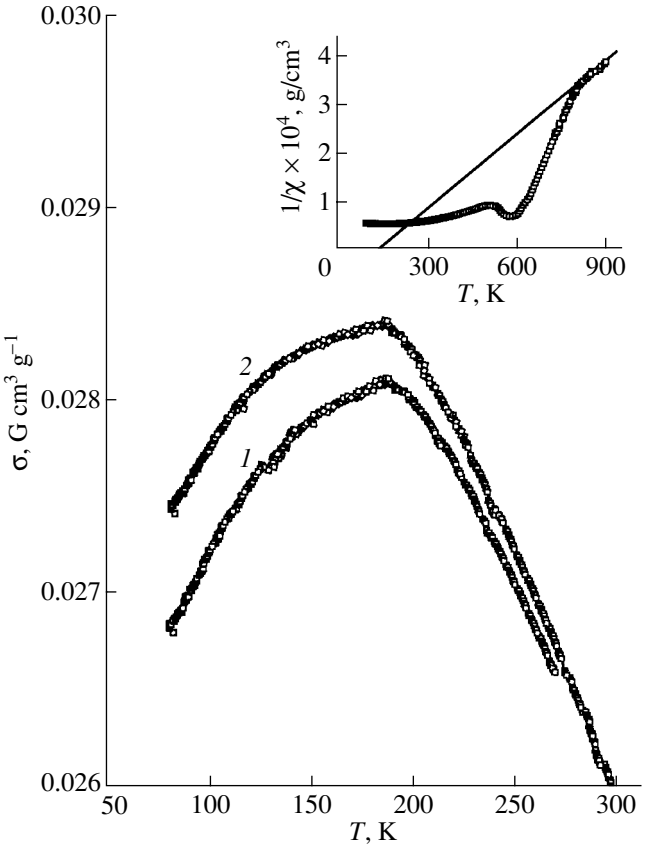

Fig. 2. Temperature dependence of the magnetization of $Fe_{0.2}Mn_{0.8}S$ cooled (*1*) in a zero magnetic field and (*2*) in a field H = 2 kOe. Inset: temperature dependence of inverse magnetic susceptibility for $Fe_{0.25}Mn_{0.75}S$.

order of magnitude. Measurements of the temperature dependence of the magnetization of the cation-substituted $Fe_xMn_{1-x}S$ samples revealed (Fig. 1) that, at low concentrations ($x \le 0.2$), sulfides (similar to manganese monosulfide) undergo an antiferromagnet–paramagnet transition at low temperatures, with the Néel temperature increasing from 150 K (x = 0) to 185 ± 5 K ($x \sim$ 0.2). The behavior of the magnetization $\sigma(T)$ of samples with $x \sim 0.2$ depends on the way in which the sample was cooled, namely, in a nonzero or zero magnetic field (Fig. 2). At $T > T_N$, the magnetic properties of cation-substituted samples with compositions $0.05 \le x \le 0.2$ behave similarly to $\chi^{-1}(T)$ of manganese monosulfide. The temperature dependence of the inverse magnetic susceptibility $\chi^{-1}(T)$is described by the Curie–Weiss law, with the paramagnetic temperature Θ and the Curie constant C increasing to –400 and 10.8 K ($x \sim 0.2$), respectively. For temperatures T > 450 K, samples with $0.05 \le x \le 0.2$ exhibit a deviation from the Curie–Weiss relation. More specifically, the magnetization (Fig. 1) displays an anomaly at a temperature T_{c_1}, which grows from 500 for $x \sim 0.05$ to 580 K for $x \sim 0.2$. For compositions with $x \sim 0.25$, the behavior of the inverse magnetic susceptibility $\chi^{-1}(T)$ in the high-temperature domain is similar to that characteristic of ferrimagnets (see inset to Fig. 2) [8]. The paramagnetic Curie temperature assumes positive values (Θ ~ 106 K for $x \sim 0.25$). The Curie constant becomes smaller, which indicates a decrease in the effective paramagnetic moment (for $x \sim 0.25$, C = 1.69). As seen from Fig. 1, the temperature dependences of the magnetization measured on samples with $0.27 \le x \le 0.38$ in the range 100–1000 K in a field of 8.6 kOe are typical of ferromagnetic compounds. Below ~200 K, the magnetization of these samples decreases with decreasing temperature. In the high-temperature region, the $\sigma(T)$ curve exhibits two magnetization anomalies at the critical temperatures T_{c_1} and T_{c_2}, which are accompanied by anomalies in the thermal (DTA) properties (inset to Fig. 1), thus indicating the occurrence of two phase transitions. At $T_{c_1} \sim$ 550–650 K, in the region of the reversible thermal (derived from DTA data) anomaly, there are anomalies in the electrical resistivity (Fig. 3) and in the fcc lattice parameter [9]. Below T_{c_1}, the resistivity behaves in a manner typical of the Fermi

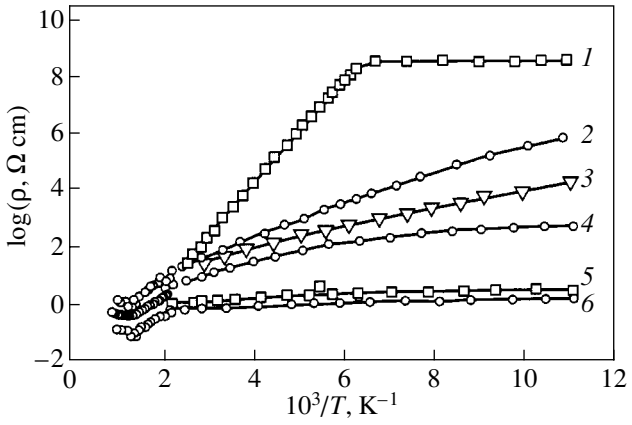

Fig. 3. Temperature dependences of the electrical resistivity of the $Fe_xMn_{1-x}S$ system for different compositions x: (*1*) 0, (*2*) 0.3, (*3*) 0.33, (*4*) 0.36, (*5*) 0.4, and (*6*) 0.5.

glass state and of systems with Anderson localization [10]. The temperature T_{c_2} is the Curie point of sulfides; this temperature increases with increasing concentration x from 730 ($x \sim 0.27$) to 860 K ($x \sim 0.38$). As seen from Fig. 1, the magnetization of the high-temperature paramagnetic phase ($T > T_{c_2}$) of the cation-substituted $Fe_xMn_{1-x}S$ samples is close to that of the paramagnetic phase of single-crystal α-MnS and, for compositions with $x \sim 0.27$, 0.29, and 0.38, virtually does not depend on temperature. According to electrical resistivity measurements, the ferromagnet–paramagnet transition near T_{c_2} is accompanied by a semiconductor–metal change in the conduction character (Fig. 3).

At room temperature, the manganese monosulfide α-MnS is in the paramagnetic state, in which the σ(H) relation is linear (Fig. 4). The σ(H) relations for the cation-substituted $Fe_xMn_{1-x}S$ solid solutions ($0.05 \le x \le 0.2$) measured at room temperature become nonlinear [6], with no hysteresis in the field dependence of the magnetization. As the degree of cation substitution x increases, the ferromagnetic contribution to magnetization increases and samples with $x > 0.2$ exhibit a magnetization hysteresis (Fig. 4), with the coercive force H_c increasing from 0.8 ($x = 0.25$) to 1.2 kOe ($x = 0.29$). The magnetization isotherms σ(H) measured for samples with $0.25 \le x \le 0.27$ at temperatures of 77 and 300 K do not exhibit saturation. As seen from Fig. 4, which displays hysteresis loops, hysteresis is no longer seen in comparatively weak magnetic fields ($H \sim$ 3–5 kOe), but the magnetization does not saturate and continues to grow as the field increase. Such a situation is observed, for instance, in the gadolinium ferrite garnets and can be attributed to the positive component of magnetostriction appearing in strong fields [8]. The magnetization curves obtained on samples with $x \sim 0.29$ are typical of ferromagnets, which is supported by the presence

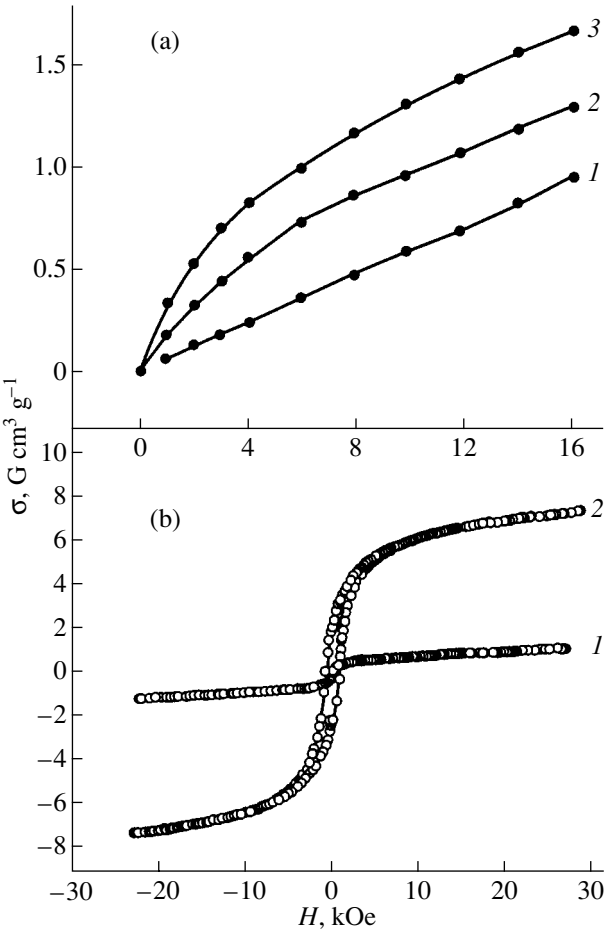

Fig. 4. Field dependences of the magnetization of the $Fe_xMn_{1-x}S$ system for different compositions x (a) at 300 K: (*1*) 0, (*2*) 0.05, and (*3*) 0.2; and (b) at 77 K: (*1*) 0.27 and (*2*) 0.29.

of a hysteresis loop. The same compositions exhibit the maximum colossal magnetoresistance ($\sigma_H \sim$ –450% in a field of 30 kOe at 50 K) [2].

4. CONCLUSION

Thus, studies of the magnetic, electrical, and thermal properties of the $Fe_xMn_{1-x}S$ solid solutions have revealed a sequence of phase transitions (at T_{c_1} and T_{c_2}) in the compositions of the above sulfides exhibiting colossal magnetoresistance. The high-temperature phase ($T > T_{c_2}$) is a paramagnetic metal. At $T \sim T_{c_2}$, a transition to the ferromagnetic state takes place, with the conduction character changing from metallic to semiconducting. The phase transition at T_{c_1}, associated possibly with lattice distortion, is accompanied by a strong increase in the magnetization and by a change in the conduction character of the semiconducting phase.

ACKNOWLEDGMENTS

This study was supported by the Russian Foundation for Basic Research (project no. 00-02-81059 Bel 2000a) and, in part, by the project Eniseĭ-2002 (no. 02-02-97702).

REFERENCES

1. G. A. Petrakovskiĭ, L. I. Ryabinkina, G. M. Abramova, *et al.*, Pis'ma Zh. Éksp. Teor. Fiz. **69** (12), 895 (1999) [JETP Lett. **69**, 949 (1999)].
2. G. A. Petrakovskiĭ, L. I. Ryabinkina, G. M. Abramova, *et al.*, Pis'ma Zh. Éksp. Teor. Fiz. **72** (2), 99 (2000) [JETP Lett. **72**, 70 (2000)].
3. É. L. Nagaev, Usp. Fiz. Nauk **166** (8), 833 (1996) [Phys. Usp. **39**, 781 (1996)].
4. P. Burlet, Le titre de docteur *ès*-sciences physiques (De L'Uneversite de Grenoble, 1968).
5. H. H. Heikens, G. A. Wiegers, and C. F. van Bruggen, Solid State Commun. **24** (3), 205 (1977).
6. G. A. Petrakovskiĭ, S. S. Aplesnin, G. V. Loseva, *et al.*, Fiz. Tverd. Tela (Leningrad) **33** (2), 406 (1991) [Sov. Phys. Solid State **33**, 233 (1991)].
7. H. H. Heikens, C. F. van Bruggen, and C. Haas, J. Phys. Chem. Solids **39** (8), 833 (1978).
8. S. V. Vonsovskiĭ, *Magnetism* (Nauka, Moscow, 1971; Wiley, New York, 1974).
9. G. V. Loseva, L. I. Ryabinkina, and A. A. Smyk, Fiz. Tverd. Tela (Leningrad) **28** (2), 596 (1986) [Sov. Phys. Solid State **28**, 334 (1986)].
10. N. F. Mott and E. A. Davis, *Electronic Processes in Non-Crystalline Materials* (Clarendon, Oxford, 1979; Mir, Moscow, 1982), Vol. 2.

Translated by G. Skrebtsov

Physics of the Solid State, Vol. 44, No. 10, 2002, pp. 1929–1935. Translated from Fizika Tverdogo Tela, Vol. 44, No. 10, 2002, pp. 1840–1846.

MAGNETISM AND FERROELECTRICITY

Piezoelectric Properties of Crystals of Some Protein Aminoacids and Their Related Compounds

V. V. Lemanov*, S. N. Popov*, and G. A. Pankova**

** Ioffe Physicotechnical Institute, Russian Academy of Sciences, Politekhnicheskaya ul. 26, St. Petersburg, 194021 Russia*
e-mail: lemanov@pop.ioffe.rssi.ru

*** Institute of Macromolecular Compounds, Russian Academy of Sciences, Bol'shoĭ pr. 31, St. Petersburg, 199034 Russia*

Received December 29, 2001

Abstract—Growth of single crystals of some protein aminoacids and synthesis and growth of single crystals of their related compounds are reported. The temperature dependence of the integrated piezoelectric response of the single crystals grown was studied in the temperature range 120–320 K. The specific features in the temperature dependence are shown to be due to the enhanced damping of elastic vibrations in the crystals, which originates from the elastic vibrations being coupled to thermally activated rotation of the CH_3 and NH_3 molecular groups. © *2002 MAIK "Nauka/Interperiodica".*

1. INTRODUCTION

Crystals of protein aminoacids of *L* and *D* modifications, as well as of many related compounds, belong to symmetry groups which lack inversion symmetry and, in most cases, to polar symmetry groups [1]. These crystals possess properties whose symmetry is described by odd-rank tensors, such as the pyroelectric effect and spontaneous electrical polarization, piezoelectric effect [2], and optical second harmonic generation [3]. Crystals belonging to the 11 enantiomorphic point groups (lacking mirror reflection planes) also exhibit natural optical gyrotropy (optical activity) described by an axial gyration tensor. Crystals of protein aminoacids of the *L* and *D* modifications are, by definition, enantiomorphic and possess optical activity [4, 5]. The role played by all of the above properties (which are characteristic of low-symmetry systems) in the functioning of living organisms remains unclear; however, investigation of these properties is of profound interest not only in the physics of crystals but also in biophysics (see reviews [6, 7] and references therein).

The present communication reports on measurements of the temperature dependence of the integrated piezoelectric response of single crystals of a number of pure protein aminoacids and of their related compounds.

2. EXPERIMENTAL TECHNIQUES AND RESULTS

Crystals of pure aminoacids and their related compounds were grown under slow cooling of their saturated aqueous solutions. The aminoacids were dissolved in distilled water heated to 40°C (heating *L* aminoacids above 40°C is undesirable, because it may result in racemization, i.e., formation of the *DL* modification).

The temperature variation rates were typically about 1°C/day, and the growth continued, as a rule, for approximately a month. The crystals were seed-pulled.

When synthesizing and growing aminoacid-based compounds, a corresponding amount of inorganic substances was added to the solution. When the solution *pH* was to be changed, acetic acid or an aqueous solution of ammonia was added; these substances do not react with aminoacids and, therefore, are not involved in crystal formation. This was followed by cooling of the solutions to room temperature, filtering, and placing them in a thermostat. In some cases, for instance, when mixing *L* alanine and *DL* alanine with sulfuric, phosphoric, and phosphorous acids, the solubility of the complexes increased considerably. In this case, one first carried out slow evaporation at room temperature until a small amount of nuclei formed. Next, the solution was filtered and cooled slowly.

Tables 1 and 2 list the aminoacids and their related compounds from which single crystals were grown in the present study. Also given are the point symmetry groups of the crystals.

While no attempt was made to attain any particular optimization of the crystal growth conditions (choosing the cooling rate and *pH* of the solvent), we can point out, on the whole, the following features in the growth of crystals of pure aminoacids and their compounds. Large bulk crystals (about 1 cm^3) of α glycine (α-Gly) and *L* alanine (*L*-Ala) were fairly easy to obtain. *DL*-Ala crystals could be prepared only in the form of thin needles. Asparagine monohydrate (*L*-Asn.H_2O) and *DL*-methionine (*DL*-Met) were produced as small bulk crystals (3–5 mm in linear dimensions), *L*-valine (*L*-Val) and *L*-methionine (*L*-Met) formed thin scales,

Table 1. Protein aminoacids, their radicals *R*, and crystal symmetry at $T = 295$ K

Aminoacid	Abbreviation	Radical *R*	Symmetry
α-glycine	α-Gly	H	C_{2h}
γ-glycine	γ-Gly	H	C_3
L-alanine	*L*-Ala	CH_3	D_2
DL-alanine	*DL*-Ala	CH_3	C_{2v}
L-valine	*L*-Val	$CH(CH_3)_2$	C_2
L-isoleucine	*L*-Ile	$CHCH_3CH_2CH_3$	C_2, D_2
L-serine	*L*-Ser	CH_2OH	D_2
L-glutamic acid	*L*-Glu	$(CH_2)_2COOH$	C_2, D_2
L-asparagine	*L*-Asn	CH_2CONH_2	D_2
L-lysine	*L*-Lys	$(CH_2)_4NH_3$	C_2
L-arginine	*L*-Arg	$(CH_2)_3NHC(NH_2)_2$	C_2, D_2
L-methionine	*L*-Met	$(CH_2)_2SCH_3$	C_2

Table 2. Compounds related to protein aminoacids and their symmetry at $T = 295$ K

Compound	Symmetry
$Gly \cdot H_3PO_3$	C_{2h}, C_2 (≤225 K)
$Gly \cdot H_3PO_4$	C_{2h}
$L\text{-}Ala_2 \cdot H_3PO_3 \cdot H_2O$	C_2
$L\text{-}Ala \cdot H_3PO_4$	C_2
$DL\text{-}Ala_2 \cdot H_2SO_4$	C_{2h} (?)
$L\text{-}Val \cdot H_3PO_3$	C_2
$L\text{-}Val_2 \cdot H_3PO_4$	C_2
$L\text{-}Ser_2 \cdot H_3PO_4 \cdot H_2O$	C_{2h} or C_2
$DL\text{-}Ser_2 \cdot H_2SO_4 \cdot H_2O$	D_2
$L\text{-Glu} \cdot Na$	D_2
$L\text{-Lys} \cdot HCl$	C_2
$L\text{-}Arg \cdot H_3PO_4 \cdot H_2O$	C_2

and *L*- and *DL*-isoleucine (*L*- and *DL*-Ile) were produced in the form of thin platelets and needles, respectively. Crystals of *L*-serine (*L*-Ser) grew to form fairly thick plates ($8 \times 5 \times 2$ mm), which were transparent in solution but rapidly turned murky when exposed to air.

We grew single crystals of a number of protein aminoacid compounds (with their composition determined by elemental analysis). Large bulk crystals (about 1 cm^3) of protein aminoacid compounds were obtained for glycine phosphite ($Gly \cdot H_3PO_3$), glycine phosphate ($Gly \cdot H_3PO_4$), and *DL*-diserine sulfate monohydrate ($DL\text{-}Ser_2 \cdot H_2SO_4 \cdot H_2O$). Smaller bulk crystals were prepared for $L\text{-}Ala_2 \cdot H_3PO_3 \cdot H_2O$, $L\text{-Ala} \cdot H_3PO_4$, $DL\text{-}Ala_2 \cdot H_2SO_4$, $L\text{-Lys} \cdot HCl$, and $L\text{-}Ser_2 \cdot H_3PO_4 \cdot H_2O$. Crystals of *L*-valine with H_3PO_3 as an impurity and of $L\text{-Val} \cdot H_3PO_4$ formed scales and needles. Large bulk crystals were obtained for the $L\text{-Arg} \cdot H_3PO_4 \cdot H_2O$ compound [8].

We made an attempt at synthesizing $L\text{-Ala} \cdot CaCl_2$ and $L\text{-Ala} \cdot H_2SO_4$; the crystals obtained were large, but elemental analysis showed them to be pure alanine with a slight addition (about 5 mol %) of $CaCl_2$ and H_2SO_4, respectively.

The piezoelectric response of the crystals was studied using an IS-2 NQR setup. The sample in the form of a crystal or a set of small crystallites was placed in the capacitor of a circuit to which 4-μs-long voltage pulses with a 10-MHz carrier were applied at a pulse repetition frequency of 12 Hz. The maximum voltage amplitude at the circuit was about 4 kV. The piezoelectric response signals were measured with an AI-1024 multichannel analyzer. Radio-frequency pulses excite elastic vibrations of piezoelectric crystals through the inverse piezoelectric effect. After termination of the pulse, elastic vibrations persist for a time on the order of $\Delta t\ (\mu s) \approx 10/\alpha\ (dB/\mu s)$, where α is the elastic wave damping. This sample ringing is detected by the pickup through the direct piezoelectric effect. In crystals of soft materials such as protein aminoacids and their compounds, the elastic wave damping is typically on the order of $\alpha \approx 10^{-1}$ dB/μs at room temperature and a frequency of 10 MHz. This means that the sample ringing time is $\Delta t \approx 100$ μs. By measuring this time, one can estimate the damping. The magnitude of the piezoelectric signal at the instant $\Delta t \approx 0$ is determined by the electromechanical coupling constant; i.e., it depends on the piezoelectric coefficients, elastic moduli, and dielectric permittivities. However, sample ringing in experiments of such type, particularly when using fine powders, has the pattern of random echo signals, where a signal may turn out to be stronger than that preceding it; therefore, the damping of elastic vibrations is determined in this case with a very large error. For this reason, in measurements of the temperature dependence of the piezoelectric response, we recorded the response as integrated over the total ringing time, which depends on both the electromechanical coupling coefficient and the damping of elastic vibrations. We note that the setup used by us possessed a high sensitivity and permitted detection of piezoelectric response signals with an amplitude of about 5×10^{-5} of the piezoelectric response of quartz crystals.

The measured temperature dependences of the integrated piezoelectric response in crystals of protein aminoacids and their related compounds are summed up in Figs. 1–7. The piezoelectric response is given in arbitrary units; nevertheless, the amplitudes of the response of different crystals in each figure are qualitatively matched. At the same time, to make the pattern more revealing, the quantitative relations in the figures are quite frequently distorted. This is manifested most strongly in Fig. 6, where the piezoelectric response signals in *DL*-diserine sulfate monohydrate and in trigly-

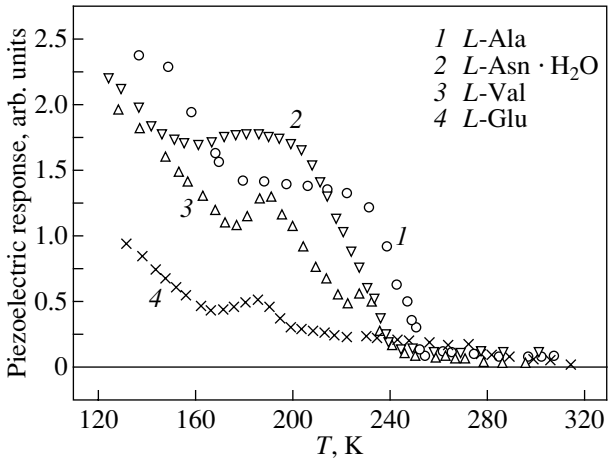

Fig. 1. Temperature dependence of the piezoelectric response in crystals of protein aminoacids of the *L* modification: alanine, asparagine monohydrate, valine, and glutamic acid.

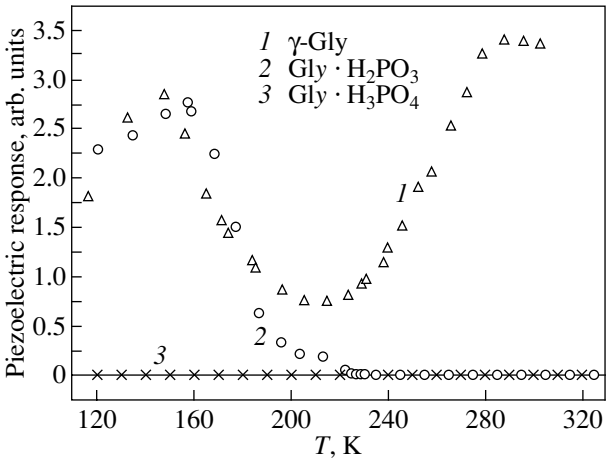

Fig. 2. Piezoelectric response of glycine phosphite, glycine phosphate, and γ-glycine crystals.

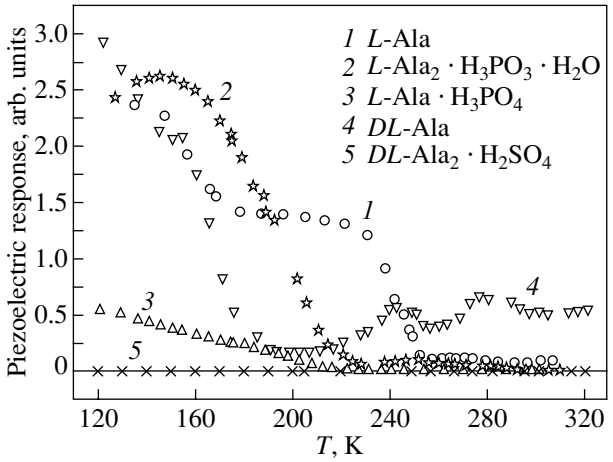

Fig. 3. Piezoelectric response of crystals of *L*-alanine, *L*-dialanine phosphite monohydrate, *L*-alanine phosphate, *DL*-alanine, and *DL*-dialanine sulfate.

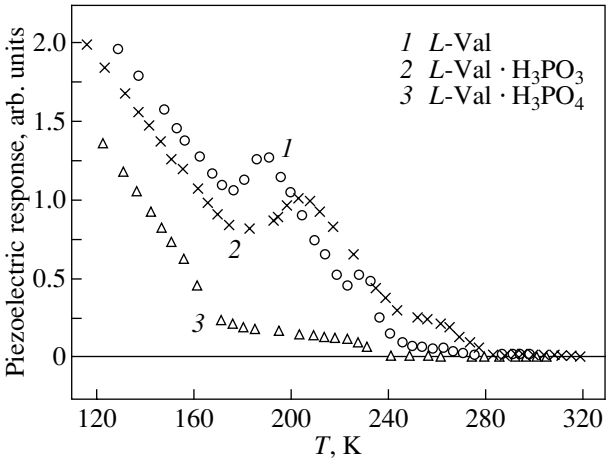

Fig. 4. Piezoelectric response of crystals of *L*-valine, *L*-valine with an addition of H_3PO_3 (about 20 mol %), and *L*-valine phosphate.

cine sulfate are indeed comparable in magnitude, whereas the response signal is substantially weaker in *L*-Lys · HCl (by about two orders of magnitude). On the whole, the piezoelectric response signals for many of the crystals studied are, comparable to those of quartz crystals.

It should be note that the electromechanical coupling coefficients, elastic moduli, piezoelectric coefficients, and components of the dielectric permittivity were measured earlier for crystals of *L*-arginine phosphate monohydrate (*L*-Arg · H_3PO_4 · H_2O) [8]. The largest electromechanical coupling coefficient K_{16} for these crystals was found to be about 22%.

Figure 1 shows the temperature dependences of the piezoelectric response for four aminoacids of the *L* modification. For the glutamic acid, a fine-powder reagent was used; in the other cases, the measurements were performed on the single crystals grown by us. As already pointed out (Table 1), the symmetry of these aminoacids allows for the existence of the piezoelectric effect; this is indeed observed experimentally. As the temperature is lowered, the behavior of the piezoelectric response becomes complex, which will be the subject of the next section.

The temperature dependences of the piezoelectric response are presented graphically in Figs. 2–7 for a number of protein aminoacid compounds.

Figure 2 shows these dependences for glycine phosphite and phosphate crystals (Gly · H_3PO_3, Gly · H_3PO_4). Also presented are data for glycine of the γ

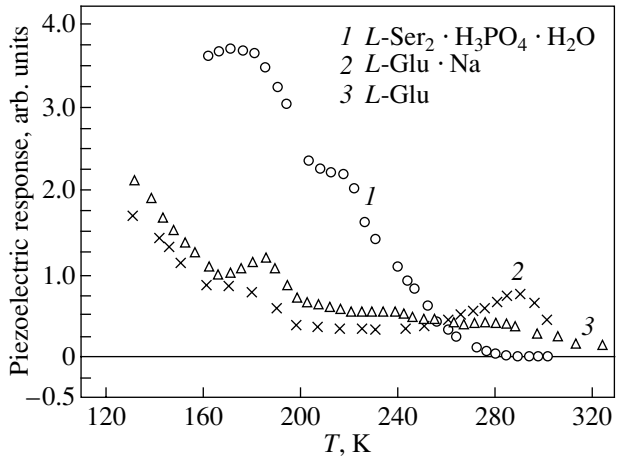

Fig. 5. Piezoelectric response of crystals of *L*-diserine phosphate monohydrate, sodium *L*-glutamate (known as a meat seasoning), and *L*-glutamic acid.

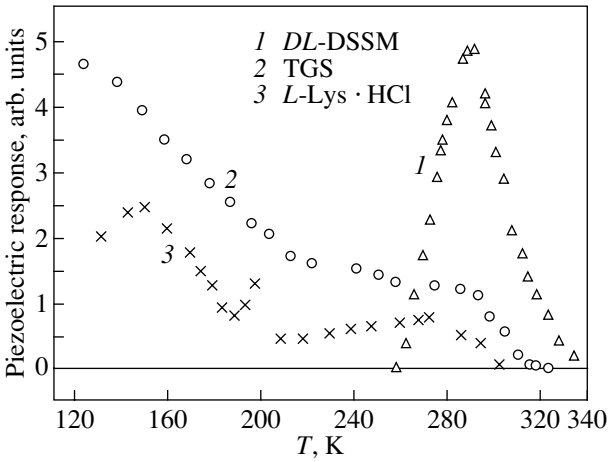

Fig. 6. Piezoelectric response of crystals of *DL*-diserine phosphate monohydrate, triglycine sulfate, and *L*-lysine hydrochloride.

modification (γ-Gly). In accordance with the symmetry of these crystals (Tables 1, 2), the piezoelectric response is observed in Gly · H_3PO_3 and γ-Gly and is not seen in Gly · H_3PO_4. We note that crystals of glycine of the α modification (α-Gly) grown from an aqueous solution do not exhibit the piezoelectric response, as should be expected from symmetry considerations (Table 1); however, α-glycine in the form of a fine powder does show piezoelectric activity, apparently, because of a small amount of γ-Gly impurity [9].

Figures 3 and 4 display the temperature dependences of the piezoelectric response observed in crystals of dialanine phosphite monohydrate (*L*-Ala_2 · H_3PO_3 · H_2O), alanine phosphate (*L*-Ala · H_3PO_4), dialanine sulfate (*DL*-Ala_2 · H_2SO_4), valine with an H_3PO_3 impurity (*L*-Val · H_3PO_3), and valine phosphate (*L*-Val · H_3PO_4). Presented for comparison are data for *L*-alanine and *L*-valine, as well as for *DL*-alanine. Interestingly, crystals of alanine of the *DL* modification belong to the polar symmetry group C_{2v} and should exhibit piezoelectric activity; this is exactly what is observed experimentally. In general, crystals of racemates, i.e., crystals of the *DL* modification, are, as a rule, centrosymmetric, but for some protein aminoacids (for instance, in the case of *DL*-alanine and *DL*-tyrosine [7]) this is not so.

Figure 5 shows data for crystals of diserine phosphate monohydrate (*L*-Ser_2 · H_3PO_4 · H_2O) and of the monosodium salt of glutamic acid, sodium glutamate (*L*-Glu · Na). The latter compound was used in the form of a fine powder, commonly known as the meat seasoning "Korean salt."

The temperature dependence of the piezoelectric response in crystals of *DL*-diserine sulfate monohydrate DSSM (*DL*-Ser_2 · H_2SO_4 · H_2O) and of *L*-lysine hydrochloride (*L*-Lys.HCl) is displayed in Fig. 6, with a plot for triglycine sulfate TGS (Gly_3 · H_2SO_4), a classical ferroelectric, added for comparison. We note that, for DSSM, this dependence exhibits a strong hysteresis [10] and the plot presented in Fig. 6 was measured on a cooled crystal.

Finally, Fig. 7 illustrates the effect of $CaCl_2$ and H_2SO_4 impurity in *L*-alanine crystals on the temperature behavior of the piezoelectric response.

3. DISCUSSION OF RESULTS

The structural formula of protein aminoacids has the form

$$\begin{array}{l} \quad\ \ H \\ NH_2\text{–}C\text{–}COOH\,. \\ \quad\ \ R \end{array}$$

Here, *R* is a radical whose composition and structure are different for various protein aminoacids (see Table 1).

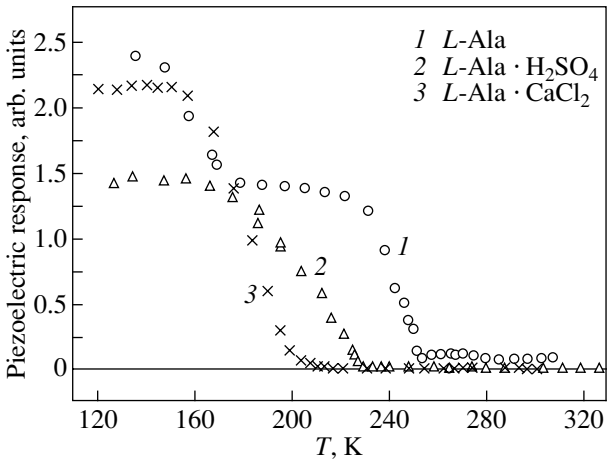

Fig. 7. Piezoelectric response of crystals of *L*-alanine and of *L*-alanine with impurities of H_2SO_4 and $CaCl_2$ (about 5 mol %).

The structure of crystals of protein aminoacids has been considered in many publications. As for their related compounds listed in Table 2, the structures of glycine phosphite ($Gly \cdot H_3PO_3$) [11], *DL*-diserine sulfate monohydrate (*DL*-$Ser_2 \cdot H_2SO_4 \cdot H_2O$) [12], dialanine phosphite monohydrate, and alanine phosphate (*L*-$Ala_2 \cdot H_3PO_3 \cdot H_2O$ and *L*-$Ala \cdot H_3PO_4$) [13] have been revealed presently.

In discussing the experimental temperature dependences of the piezoelectric response (Figs. 1–7), the problem of possible phase transitions in the crystals under study appears to be of most interest. Two of the relations plotted in Figs. 1–7 belong to well-known ferroelectrics, namely, glycine phosphite, with the phase transition point T_c = 224 K [14–16], and triglycine sulfate, with the transition temperature T_c = 322 K. Both crystals are monoclinic, with their symmetry changing from C_{2h} to C_2 at the phase transition. The piezoelectric effect appears in the low-symmetry phase; this was observed experimentally (Figs. 2, 6). A similar behavior of the piezoelectric effect is seen in crystals of dialanine phosphite and alanine phosphate (Fig. 3), valine phosphate (Fig. 4), and diserine phosphate monohydrate (Fig. 5); namely, the piezoelectric response is absent (within the sensitivity of the setup) at room temperature and appears at lower temperatures. However, this behavior of the piezoelectric response may originate not from its absence at room temperature but rather from the small value of the piezoelectric coefficients and/or high damping of the elastic vibrations. Indeed, according to available data [13], crystals of dialanine phosphite and alanine phosphate are piezoelectrically active and belong to the point group symmetry C_2 at room temperature (Table 2).

L-diserine phosphate monohydrate exhibits a very strong rise in the piezoelectric response at 8°C (Fig. 5), but no response is seen at higher temperatures. According to x-ray diffraction measurements, this crystal belongs to the C_{2h} diffraction symmetry class. As follows from diffractograms, the point symmetry group of this crystal may be either C_{2h} or C_2. According to Smolin, the crystal belongs to the polar symmetry group C_2. This means that the strong rise in piezoelectric activity may be associated not with a phase transition but rather with a strong temperature dependence of the electromechanical coupling coefficient or of elastic vibration damping.

We tentatively suggested the existence of a phase transition in *L*-alanine at a temperature of about 170 K [17]. This conclusion was drawn from the temperature dependence of the phonon echo relaxation time and from available data on the nuclear spin–lattice relaxation. As follows from Fig. 1, the piezoelectric response does indeed exhibit some features in this temperature region, but, as will be shown below, these features are not associated with any phase transition.

The Raman spectra measured at room temperature and hydrostatic pressures of up to 2.0 GPa in [18] suggest that *L*-asparagine monohydrate (*L*-$Asn \cdot H_2O$) undergoes three phase transitions. One of them occurs at a pressure of 0.1 GPa. If this transition involves a volume change only, one can expect a transition at normal pressure and at a temperature of about 200 K. However, according to Smolin, the crystal symmetry does not change in the temperature region from 330 to 120 K, which implies that the features seen in this case to occur in the temperature dependence of the piezoelectric response are likewise not associated with a phase transition.

As follows from Fig. 6, the piezoelectric response in crystals of diserine sulfate monohydrate disappears at temperatures near 260 and 340 K, with the low-temperature anomaly being accompanied, as already mentioned, by a noticeable temperature hysteresis [10]. X-ray diffraction measurements carried out at 233 K [12] showed that the principal x-ray reflections are accompanied by satellites that imply one-dimensional incommensurate modulation along the **b** axis (the lattice parameters at this temperature are [12] a = 10.61, b = 21.42, c = 5.90 Å). The modulation wave vector was found to be $\mathbf{q} = 0.23\mathbf{b}^*$, where $\mathbf{b}^*$ is the reciprocal lattice vector. This modulation vector corresponds to a modulation period of about 90 Å. The disappearance of a piezoelectric signal at approximately 260 K (Fig. 6) is possibly associated with a phase transition to the incommensurate phase. Elucidation of the mechanism of this transition requires further study.

Let us now consider the features in the piezoelectric response which are observed primarily in the range 120–240 K in most of the crystals studied (Figs. 1–6). These features become manifest in more or less pronounced minima in the temperature dependences of the piezoelectric response. We believe that these minima originate from an enhancement of damping of elastic vibrations in the crystals. If there are processes in the crystal that are connected in any way with elastic vibrations and, therefore, induce increased damping with a maximum at some temperature, a decrease in the integrated piezoelectric response with a minimum at the same temperature should also take place. It is known that molecular groups in molecular crystals can exhibit hindered rotation whose relaxation is governed by the Arrhenius relation associated with a certain potential barrier. In crystals of protein aminoacids and their related compounds, these groups are CH_3 and NH_3 [19–21] (NH_3^+ groups form in crystals containing zwitterions). This conclusion was drawn from NMR studies performed on a number of protein aminoacids. Investigation of the temperature dependences of proton spin–lattice relaxation made it possible to determine the parameters characterizing the molecular-group rotation. To interpret the features observed by us in the temperature dependences of the piezoelectric response, we shall use the parameters presented in [20]. In the study

cited, the spin–lattice relaxation time T_1 was measured at a frequency of 60 MHz in the temperature range 130–500 K. The observed relaxation features were associated with the hindered rotation of NH_3 (at higher temperatures) and CH_3 (at low temperatures), with the relaxation time depending on temperature according the Arrhenius law

$$\tau = \tau_0 \exp(U/kT), \quad (1)$$

where U is the barrier height.

When the rotation frequency of the NH_3 and CH_3 groups $\omega = 1/\tau$ becomes equal to the NMR frequency, a minimum appears in the temperature dependence of T_1. These experimental data were used in [20] to derive the barrier height U and the attempt frequency $\omega_0 = 1/\tau_0$ for the rotation of the NH_3 and CH_3 groups in a number of protein aminoacids.

The model of hindered molecular-group rotation can be employed in interpreting the features of the piezoelectric response in our crystals.

Molecular rotation in crystals is coupled, as a rule, with elastic lattice strains. In this case, the damping of elastic vibrations is of a relaxation character and described by the expression

$$\alpha = G\Omega^2\tau/(1 + \Omega^2\tau^2), \quad (2)$$

where G is the coupling constant and Ω is the circular frequency of elastic vibrations.

For $\Omega\tau = 1$, the damping is strongest.

As already mentioned, integrated piezoelectric response A decreases with decreasing the electromechanical coupling coefficients and with increasing the elastic-vibration damping α. In general, the electromechanical coupling coefficients (which are determined by the piezoelectric coefficients, elastic moduli, and dielectric permittivities) do not depend strongly on temperature; such dependences are usually monotonic. If we assume that the temperature dependence of the electromechanical coupling coefficients can be neglected within a not very broad temperature interval, the piezoelectric response should be inversely proportional to the elastic-vibration damping:

$$A \propto 1/\alpha \propto (1 + \Omega^2\tau^2)/\Omega^2\tau. \quad (3)$$

It follows from Eq. (3) that the piezoelectric response should be minimum for $\Omega\tau = 1$.

Indeed, as seen from Figs. 1–7, the temperature dependences of the piezoelectric response exhibit more or less distinct minima in many cases; therefore, these minima originate from elastic vibrations being coupled to molecular group rotation. We note that the absence of the piezoelectric response in many crystals at room temperature may also be accounted for by the large damping of elastic waves because they are connected with the rotation of molecular groups.

We shall now use the relaxation parameters U and τ_0 derived from NMR experiments in [20] to calculate the temperature T_{min} corresponding to $\Omega\tau = 1$ (in our case $\Omega = 2\pi \times 10^7$ s^{-1}).

For the case of NH_3 relaxation in α-glycine, it was established in [20] that $U = 0.29$ eV and $\tau_0 = 7 \times 10^{-15}$ s. For such relaxation parameters, the piezoelectric response should have a minimum at $T_{min} = 230$ K, which is in reasonable agreement with the experimental value $T_{min} = 210$ K obtained for γ-glycine (Fig. 2).

Crystals of *L*-alanine do not exhibit distinct minima in the temperature dependence of the piezoelectric response (Fig. 1); therefore, it does not seem possible to make a quantitative comparison with NMR data. There is, however, a certain correlation between our data and the results obtained on nuclear spin–lattice relaxation [19–21].

For *L*-valine, we have [20] $U = 0.39$ eV and $\tau_0 = 3.8 \times 10^{-14}$ s for the NH_3 group rotation and $U = 0.12$ eV and $\tau_0 = 1.89 \times 10^{-12}$ s for the CH_3 groups. For our frequency ($\Omega = 2\pi \times 10^7$ s^{-1}) and these parameters, we find $T_{min} = 352$ K (NH_3) and $T_{min} = 155$ K (CH_3). The former temperature is beyond the temperature range studied by us, and the latter is close to the experimental value $T_{min} = 175$ K (Fig. 1). We note that one should not expect better agreement for our experiments, because the temperature dependence of the electromechanical coupling coefficients also contributes to that of the piezoelectric response.

We can use our experimental data not only for comparison with the results of NMR measurements but also for direct determination of the relaxation parameters with the use of Eqs. (2) or (3) [it would be preferable to use Eq. (2) and consider the minima in the piezoelectric response as maxima in the elastic-vibration damping]. However, the above-mentioned contribution of the temperature dependence of the electromechanical coupling coefficients and the difficulties involved in extracting the background damping of elastic vibrations from our experiments suggest that it is only possible to estimate the relaxation parameters from measurements of the integrated piezoelectric response. In such cases, as is well known, even small errors in determination of the barrier height U can entail substantial errors in determining the prefactor τ_0.

Let us perform such an estimation of the relaxation parameters for *L*-glutamic acid, *DL*-alanine, and *L*-lysine hydrochloride.

L-Glu exhibits one type of relaxation with a minimum of the piezoelectric response at a temperature $T_{min} = 166$ K (Fig. 1). Using the experimental data on the temperature dependence of the piezoelectric response near this temperature and Eq. (2), we find that $U = 0.15$ eV and the average value of τ_0 is roughly 5×10^{-13} s.

For *DL*-alanine, there are two types of relaxation, with the piezoelectric signal minima at the temperatures T_{min} = 255 and 200 K (Fig. 3). In this case, the relaxation parameters are found to be U = 0.35 eV and $\tau_0 \approx 3 \times 10^{-15}$ s for T_{min} = 255 K and U = 0.2 eV and $\tau_0 \approx 10^{-13}$ s for T_{min} = 200 K.

Two types of relaxation are also seen to occur in *L*-Lys.HCl at T_{min} = 215 and 190 K (Fig. 6). The relaxation parameters are U = 0.3 eV, $\tau_0 \approx 5 \times 10^{-15}$ s (T_{min} = 215 K) and U = 0.25 eV, $\tau_0 \approx 10^{-15}$ s (T_{min} = 190 K). There is apparently one more type of low-temperature relaxation at $T_{min} \leq 130$ K.

Obviously enough, a definite conclusion as to the mechanisms of the relaxation and the precise determination of its parameters can be made only from direct ultrasonic measurements of the damping and velocity of ultrasonic waves. Such experiments are being planned at our laboratory.

ACKNOWLEDGMENTS

The authors are indebted to N.V. Zaĭtseva for x-ray diffraction measurements and to Yu. I. Smolin and L.S. Sochava for helpful discussions.

This study was supported in part by the Russian Foundation for Basic Research (project no. 99-02-18307) and the program for the support of leading scientific schools (grant no. 00-15-96754).

REFERENCES

1. G. V. Gurskaya, *The Molecular Structure of Amino Acids: Determination by X-ray Diffraction Analysis* (Nauka, Moscow, 1966; Consultant Bureau, New York, 1968).
2. D. Vasilescu, R. Cornillon, and G. Mallet, Nature **225**, 635 (1970).
3. M. Delfino, Mol. Cryst. Liq. Cryst. **52**, 271 (1978).
4. T. Asahi, H. Utsumi, Y. Itagaki, *et al.*, Acta Crystallogr. A **52**, 766 (1996).
5. T. Asahi, M. Takahashi, and J. Kobayashi, Acta Crystallogr. A **53**, 763 (1997).
6. V. V. Lemanov, *Piezoelectric Materials: Advances in Science, Technology and Applications*, Ed. by C. Galassi *et al.* (Kluwer, Dordrecht, 2000), p. 1.
7. V. V. Lemanov, Ferroelectrics **238**, 211 (2000).
8. I. M. Sil'vestrova, G. N. Nabakhtiani, V. B. Kozin, *et al.*, Kristallografiya **37**, 1535 (1992) [Sov. Phys. Crystallogr. **37**, 831 (1992)].
9. V. V. Lemanov and S. N. Popov, Fiz. Tverd. Tela (St. Petersburg) **40** (6), 1086 (1998) [Phys. Solid State **40**, 991 (1998)].
10. V. V. Lemanov, S. N. Popov, V. V. Bakhurin, and N. V. Zaĭtseva, Fiz. Tverd. Tela (St. Petersburg) **43** (7), 1283 (2001) [Phys. Solid State **43**, 1336 (2001)].
11. M. T. Averbuch-Pouchot, Acta Crystallogr. C **49**, 815 (1993).
12. Yu. I. Smolin, A. E. Lapshin, and I. A. Drozdova, Fiz. Tverd. Tela (St. Petersburg) **44** (10), 1881 (2002) [Phys. Solid State **44**, 1972 (2002)].
13. Yu. I. Smolin, A. E. Lapshin, and G. A. Pankova, Kristallografiya (in press).
14. S. Dacko, Z. Czapla, J. Baran, and M. Drozd, Phys. Lett. A **233**, 217 (1996).
15. E. V. Balashova, V. V. Lemanov, and G. A. Pankova, Fiz. Tverd. Tela (St. Petersburg) **43** (7), 1275 (2001) [Phys. Solid State **43**, 1328 (2001)].
16. E. V. Balashova, V. V. Lemanov, and G. A. Pankova, Ferroelectr. Lett. **29** (1–2) (2001).
17. V. V. Lemanov and S. N. Popov, Fiz. Tverd. Tela (St. Petersburg) **40** (11), 2119 (1998) [Phys. Solid State **40**, 1921 (1998)].
18. A. J. D. Moreno, P. T. C. Freire, F. E. A. Melo, *et al.*, Solid State Commun. **103**, 655 (1997).
19. M. R. Zaripov, *Radiospectroscopy: Collection of Articles* (Nauka, Moscow, 1973), p. 193; British Library. Lending Division RTS 9205 (December 1974).
20. E. R. Andrew, W. S. Hinshaw, M. G. Hutchins, and R. O. I. Sjöblom, Mol. Phys. **31**, 1479 (1976); **32**, 795 (1976).
21. K. Beshah, E. T. Olejniczak, and R. G. Griffin, J. Chem. Phys. **86**, 4730 (1987).

Translated by G. Skrebtsov

Physics of the Solid State, Vol. 44, No. 10, 2002, pp. 1936–1943. Translated from Fizika Tverdogo Tela, Vol. 44, No. 10, 2002, pp. 1847–1854.

LATTICE DYNAMICS AND PHASE TRANSITIONS

Manifestation of Quantum Statistics in Vibrational Dynamics of Poly(ethylene) Crystals

A. I. Slutsker*, V. I. Vettegren*, V. L. Gilyarov*, G. Dadobaev*, V. B. Kulik*, and L. S. Titenkov**

** Ioffe Physicotechnical Institute, Russian Academy of Sciences, Politekhnicheskaya ul. 26, St. Petersburg, 194021 Russia*

*** Moscow State Textile University, Malaya Kaluzhskaya ul. 1, Moscow, 119991 Russia*

e-mail: Alexander.Slutsker@pop.ioffe.rssi.ru

Received November 12, 2001; in final form, December 7, 2001

Abstract—The temperature dependences of the transverse expansion $\varepsilon_\perp(T)$ and the longitudinal contraction $\varepsilon_\parallel(T)$ (with respect to the axes of chain molecules) in large-sized poly(ethylene) (PE) crystal grains ($100 \times 60 \times 60$ nm) are measured using x-ray diffraction in the temperature range 5–380 K. The temperature dependence of the elongation of the molecular skeleton $\varepsilon_C(T)$ is obtained by Raman spectroscopy. It is found that the dependences $\varepsilon_\perp(T)$, $\varepsilon_\parallel(T)$, and $\varepsilon_C(T)$ exhibit a similar specific nonlinear behavior. Analysis of these dependences indicates that the nonlinearity is associated with the quantum statistics of transverse vibrations. The energies and amplitudes of zero-point (at $T = 0$) transverse (torsional and bending) vibrations and the relevant zero-point components $\varepsilon_\parallel(0)$ and $\varepsilon_C(0)$ are estimated. It is revealed that the zero-point components make a considerable contribution to the dynamics of the PE crystal up to the melting temperature (~400 K). © *2002 MAIK "Nauka/Interperiodica".*

1. INTRODUCTION

Quantum effects in vibrational dynamics are characteristic of all solids. They manifest themselves in zero-point (at $T = 0$) vibrations and specific temperature dependences of the vibrational energy, heat capacity, thermal expansion, and other quantities.

The properties of polymer crystals built up of straight-chain molecules significantly differ from those of crystals composed of "usual" low-molecular compounds. The high longitudinal rigidity of the molecular skeleton at a comparatively low transverse rigidity and the weak intermolecular interaction are responsible for the specific features in the molecular dynamics and the related phenomena. These are the difference between the frequencies of longitudinal and transverse vibrations, the negative longitudinal thermal lattice expansion (at a positive transverse expansion), etc. [1].

A large number of works have been devoted to theoretical analysis of the lattice dynamics in polymers [1–4]. However, detailed experimental investigations into the quantum regularities in the dynamics of polymer crystals are very scarce. The aim of the present work was to obtain data on the behavior of the lattice and macromolecules in a large-sized polymer crystal with the use of x-ray diffraction and Raman spectroscopy over a wide range of temperatures (5–380 K).

2. THE OBJECT OF INVESTIGATIONS

The simplest crystallizing polymer—poly(ethylene) (PE) with the polymer molecule structure … $-CH_2-CH_2-CH_2-$… was chosen as the object of investigation.

The experiments were performed with oriented PE samples. The samples were prepared by annealing of preliminarily oriented plates under high pressure.[1] The crystallinity of the samples prepared was more than 95%. The specific features of the samples were large sizes of the crystalline grains and low distortion of their lattice. According to x-ray diffraction measurements, the linear sizes of crystalline grains were equal to 90–100 nm along the molecular axes and 50–60 nm in the transverse direction. The distortions in the longitudinal and transverse directions were as follows: $<1 \times 10^{-4}$ and $\sim 4 \times 10^{-3}$, respectively. The above properties of the crystal lattice appeared to be appropriate for the unambiguous interpretation of the experimental data obtained by x-ray diffraction and Raman spectroscopy.

3. EXPERIMENTAL TECHNIQUE

The positions, intensities, and widths of meridional and equatorial reflections were measured using large-

[1] We are grateful to Yu.A. Zubov (Karpov Research Institute of Physical Chemistry) for supplying the samples used in our experiments and helpful discussions.

angle x-ray diffraction over the temperature range from 5 to 350 K. The measurements were performed on DRON-1 and DRON-3 x-ray diffractometers with the use of filtered CuK_α radiation ($\lambda = 0.154$ nm) and MoK_α radiation ($\lambda = 0.071$ nm). The instrumental angular collimation width was 2′.

The shift in the band at 1129 cm^{-1} (at 293 K) with a variation in the temperature from 90 to 380 K was determined using Raman spectroscopy. The spectra were excited with the 488-nm line of an argon laser (the laser radiation power was 0.1 W) and recorded on a Ramalog-5 spectrometer. The bandwidth of the spectrometer slit in the range 1090–1160 cm^{-1} was equal to 1 cm^{-1} and did not exceed ~0.25 of the half-width of the band at 90 K. For this reason, the distortion of the band shape due to the bandwidth of the spectrometer slit was no more than 10%. With the aim of minimizing dynamic distortions, the scanning rate was no higher than 1 cm^{-1}/min.

4. X-RAY DIFFRACTION DATA

The shifts of the (002) meridional and (110) equatorial reflections with an increase in the temperature from 5 to 350 K were measured using reflections of two orders for the purpose of obtaining more reliable data.

As an illustration, Fig. 1 shows the angular contours of the (002) meridional and (110) equatorial reflections at two temperatures. It is seen that an increase in the temperature results in a shift of the reflections and a decrease in their intensity. It is essential that the reflections shift in different directions: the meridional reflection is displaced toward the large-angle range, whereas the equatorial reflection shifts toward the small-angle range. Similar changes in the positions and intensities of the reflections are observed at other temperatures for two radiation types and reflections of two orders.

The thermal expansion of the PE crystal lattice in the longitudinal and transverse directions was determined using the temperature dependences of the angular position of the reflections. The expansion was calculated from the expression derived by differentiation of the Bragg equation, that is,

$$\varepsilon(T) = \frac{\Delta d(T)}{d} = -\frac{\Delta\varphi_m(T)}{2\tan\varphi_m/2}, \qquad (1)$$

where d and $\Delta d(T)$ are the interplanar distance and its change, respectively; and φ_m and $\Delta\varphi_m(T)$ are the angular position of the reflection and its change with an increase in the temperature, respectively. The value of $\Delta\varphi_m(T)$ is reckoned from φ_m at $T = 0$. This allows us to determine directly only the thermal component of the expansion. The dependences $\varepsilon_\parallel \equiv \Delta d_\parallel(T)/d_\parallel$ and $\varepsilon_\perp \equiv \Delta d_\perp(T)/d_\perp$ are depicted in Fig. 2. Here, the interplanar distance $d_\parallel$ in the longitudinal direction (i.e., along the molecular axes) is the projection of the C–C bond onto the molecular axis ($d_\parallel = 0.127$ nm at 300 K) and $d_\perp$ is

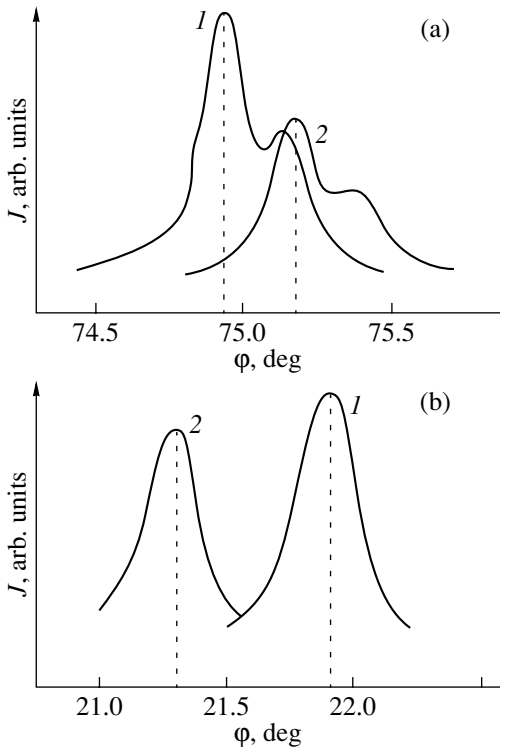

Fig. 1. (a) The (002) meridional and (b) (110) equatorial x-ray reflections (CuK_α radiation) of PE at temperatures of (*1*) 5 and (*2*) 350 K.

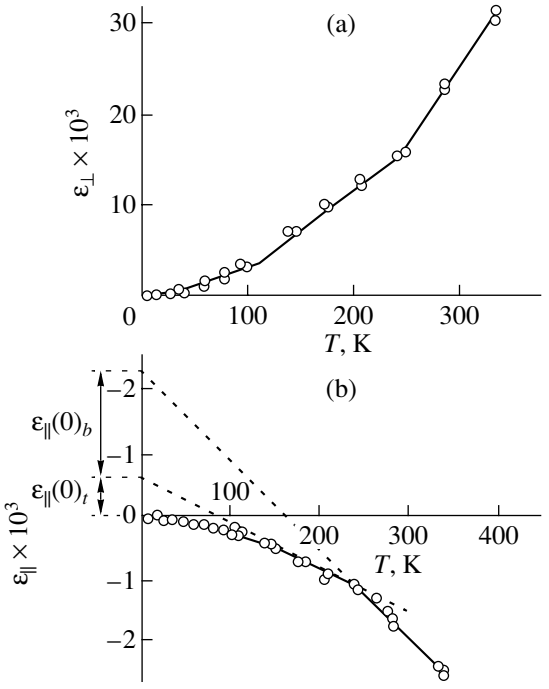

Fig. 2. Temperature dependences of the thermal expansion of the PE lattice in (a) the transverse and (b) longitudinal directions. The curves are obtained using the data on reflections of two orders and two radiation types.

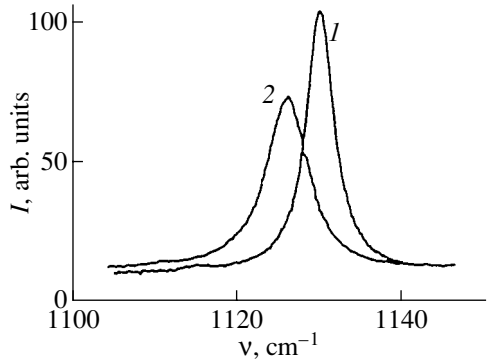

Fig. 3. Intensities of bands at 1130 cm^{-1} in the Raman spectra at temperatures of (*1*) 90 and (*2*) 293 K.

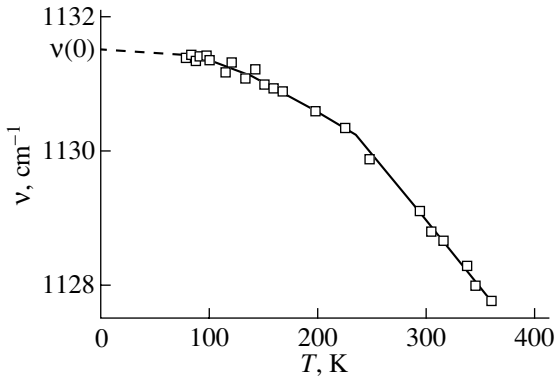

Fig. 4. Temperature dependence of the frequency at a maximum of the band assigned to the stretching vibrations of the C–C bonds in the carbon skeleton of the PE molecules.

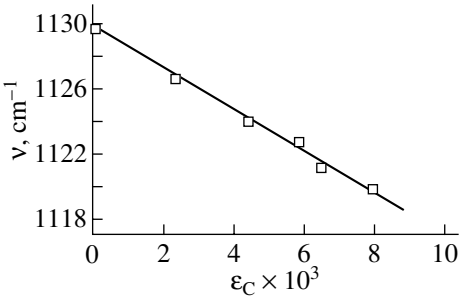

Fig. 5. Dependence of the frequency of the C–C stretching vibrations on the elongation of the carbon skeleton of the PE molecules under a load.

the distance between the molecular axes along different equatorial directions (the mean distance is estimated to be $d_\perp \sim 0.4$ nm at 300 K).

These dependences have different signs: as the temperature increases, the crystal lattice of PE expands in the transverse direction and contracts in the longitudinal direction. A decrease in the longitudinal size of the PE crystal implies that the projection of the macromolecular skeleton contour onto the crystallographic direction [002], i.e., the axial length of the macromolecule, decreases.

Note that the ordinate portion upward from zero but also with negative values of $\varepsilon_\parallel$ in Fig. 2b is intended for estimating the zero-point components of $\varepsilon_\parallel$.

Both dependences exhibit a nonlinear behavior: as the temperature increases, the quantities $\varepsilon_\perp(T)$ and $\varepsilon_\parallel(T)$ only slightly vary at low temperatures and begin to change more steeply at high temperatures.

5. RAMAN SPECTROSCOPIC DATA

The Raman spectra of PE in the range 1050–1150 cm^{-1} at two temperatures (90 and 300 K) are shown in Fig. 3. The band at 1130 cm^{-1} is assigned to the C–C symmetric stretching vibrations in *trans* isomer fragments with a length of no less than 12 CH_2–CH_2 monomer units, i.e., no less than ~1.5 nm [5]. Since the crystallinity of the studied samples is higher than 95% and the crystalline grains in the samples are characterized by a weak distortion, the molecular fragments under consideration reside in the PE crystals.

As can be seen from Fig. 3, an increase in the temperature leads to a shift in the maximum of the band at 1130 cm^{-1} toward the low-frequency range and an increase in its half-width.

The temperature dependence of the frequency $\nu(T)$ at the maximum of the band is nonlinear (Fig. 4): the slope of the dependence tends to zero at $T \longrightarrow 0$ and increases with an increase in the temperature. By extrapolating the dependence $\nu(T)$ to $T = 0$ with the use of the technique proposed in [6, 7], we obtain $\nu(0) = (1131.7 \pm 0.1)$ cm^{-1}.

In [6, 7], the decrease in the frequencies of similar bands with increasing temperature was explained as resulting from the elongation of the macromolecular skeleton (i.e., the increase in the equilibrium values of the CCC bond angles and the C–C bond lengths in the macromolecular skeleton). The frequency shift $\Delta\nu$ and the relative thermal change ε_C in the skeleton length are related by the expression

$$\Delta\nu \equiv \nu(T) - \nu(0) = -G\nu(0)\varepsilon_C, \qquad (2)$$

where $\nu(T)$ and $\nu(0)$ are the vibrational frequencies at a given temperature T and $T \longrightarrow 0$ K, respectively.

In order to determine the Grüneisen parameter G, we examined the shifts of the band at 1130 cm^{-1} and the (002) reflection under uniaxial tensile stress. The loading of the sample was performed with a device providing a constant stress during the recording of the Raman spectra and x-ray diffraction patterns. The shift of the reflection was used to calculate the strain ε_C of the macromolecular skeleton. Then, the frequency of the band at 1130 cm^{-1} was analyzed as a function of ε_C. It can be

seen from Fig. 5 that the frequency decreases in proportion to the relative elongation of the polymer molecule skeleton. The Grüneisen parameter G for the vibration at a frequency of 1130 cm^{-1} was determined from the slope of the straight line and proved to be equal to 1.3.

The shift of the frequency of C–C stretching vibrations under uniaxial tensile stress was investigated theoretically and experimentally in [8–12]. It was established that the frequency decreases proportionally to the stress σ; that is,

$$\Delta\nu(\sigma) = -\alpha\sigma = -\alpha E_C \varepsilon_C, \quad (3)$$

where E_C is the Young modulus of the PE molecule. Analysis of the aforementioned works demonstrates that the most reliable values of α are equal to 5.8–5.9 (cm GPa)$^{-1}$ [8, 12]. It follows from relationships (2) and (3) that the Grüneisen parameter G and the coefficient α are related by the expression

$$G = \frac{\alpha E_C}{\nu(0)}. \quad (4)$$

By substituting the above parameter α and the Young modulus $E_C \sim 240$ GPa [13] into formula (4), we found that the Grüneisen parameter for the vibration at a frequency of 1130 cm^{-1} is equal to 1.3, which coincides with the Grüneisen parameter obtained in our work.

Next, we substitute this value into formula (2) and obtain the expression describing the temperature dependence of the elongation of the carbon skeleton of the PE macromolecules (Fig. 6):

$$\varepsilon_C(T) = -\frac{\Delta\nu(T)}{G\nu(0)}. \quad (5)$$

It is seen from Fig. 6 that the dependence $\varepsilon_C(T)$ exhibits a nonlinear behavior. At temperatures below ~120 K, the length of the PE molecule varies only slightly ($\varepsilon_C < 10^{-4}$). At higher temperatures, the elongation of the carbon skeleton rapidly increases with an increase in the temperature and, at 350 K, reaches $\sim 2 \times 10^{-3}$, which is comparable in magnitude to the decrease in the longitudinal size of the PE crystal (i.e., to the decrease in the axial length of the macromolecule). In this case, the ordinate portion downward from zero with positive values of ε_C is intended for estimating the zero-point components of ε_C.

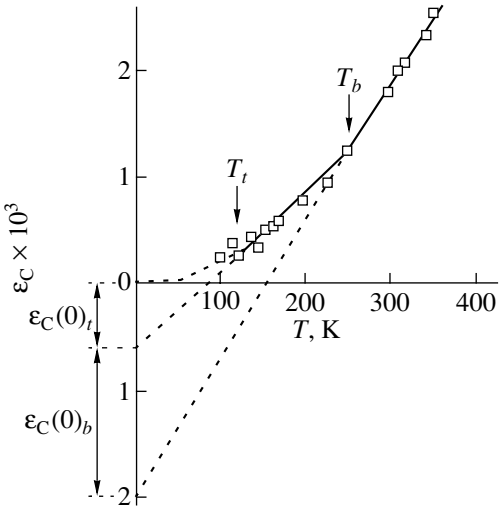

Fig. 6. Temperature dependence of the thermal elongation of the carbon skeleton of the PE molecules.

6. DISCUSSION

6.1. Transverse Vibrations in the PE Crystal

The aforementioned experimental results indicate that the heating leads to an increase in the transverse size of the PE crystal, a decrease in the longitudinal size of the crystal, and an increase in the length of the polymer molecule skeleton.

Within the quasi-harmonic approximation, each vibration of the carbon skeleton of the PE macromolecules can be subdivided into individual modes, namely, two transverse (torsional ν_t and bending ν_b) modes and one longitudinal (stretching ν_s) mode. The maximum frequencies are equal to ~240 cm^{-1} for torsional vibrations, ~520 cm^{-1} for bending vibrations, and ~1200 cm^{-1} for stretching vibrations [5, 14]. The characteristic temperatures $\theta_i \cong h\nu_{max}/k_B$ of these vibrations are as follows: $\theta_i \cong 340$ K, $\theta_b \cong 740$ K, and $\theta_s \cong 1700$ K, respectively. The efficient thermal excitation of the modes is observed at temperatures $T \geq \theta_i/3$.

Thus, only the transverse vibrational modes are thermally excited in the temperature range covered (from 5 to 380 K). Consequently, the transverse expansion of the crystalline-grain lattice $\varepsilon_\perp$, the longitudinal contraction $\varepsilon_\parallel$ of the lattice, and an increase in the length of the carbon skeleton ε_C of macromolecules are caused by the thermal excitation of transverse vibrations.

It needs to be ascertained if the experimental results obtained correlate with the thermal excitation of the transverse vibrations at the above characteristic temperatures. For this purpose, let us determine the temperature dependences of the thermal component of the mean-square amplitude $\overline{\delta_\perp^2}(T)$ and the mean energy $\overline{W}_T(T)$ of the thermal transverse vibrations of the CH_2 groups.

The dependence $\overline{\delta_\perp^2}(T)$ can be obtained from the experimental temperature dependences of the transverse expansion $\varepsilon_\perp(T)$ for the PE crystals (Fig. 2a). The transverse expansion of the unit cell in the PE crystal is characterized by the azimuthal anisotropy due to the mutual arrangement of the planes of the zigzag carbon

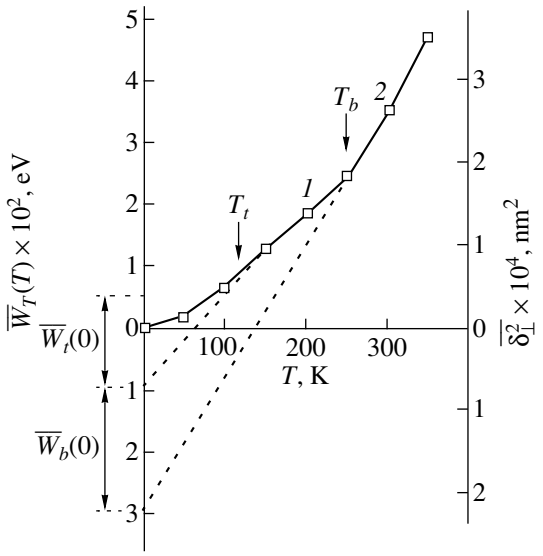

Fig. 7. Temperature dependences of the thermal components of the mean energy $\overline{W}_T$ and the mean-square amplitude $\overline{\delta^2_\perp}(T)$ of transverse molecular vibrations in the PE crystal.

skeleton [15]. In the PE unit cell, the direction [110] is diagonal and the expansion along this direction is approximately the mean of those along the orthogonal directions [200] and [020]. Hence, the mean parameters of the transverse vibrations will be estimated from the expansion along the [110] direction (Fig. 2a).

The transverse expansion of the unit cell in the PE crystal is associated with the anharmonicity of the intermolecular (transverse) interaction.

The anharmonic potential well in which the transverse vibrations of CH_2 groups occur in the lattice can be represented in the form

$$U(\delta_\perp) = \frac{1}{2} f_{\text{eff}} \delta_\perp^2 - \frac{1}{3} g \delta_\perp^3, \tag{6}$$

where $\delta_\perp$ is the displacement of the CH_2 group from an equilibrium position; f_{eff} is the effective coefficient of linear elasticity, which accounts for the rigidity of the molecule with respect to the transverse vibrations and the rigidity of intermolecular (van der Waals) bonds; and g is the anharmonicity coefficient of intermolecular interaction.

From expression (6), we obtain the approximate relationship [16]

$$\overline{\delta^2_\perp} \approx \frac{f_{\text{eff}}}{g} d_\perp \varepsilon_\perp(T), \tag{7}$$

where $\overline{\delta^2_\perp}$ is the mean-square amplitude of the transverse vibrations of the CH_2 group and $d_\perp \approx 0.405$ nm is the distance between the molecular axes (according to the data taken from [15] for the [110] direction and the data obtained from the reflection position in Fig. 1).

The mutual arrangement of CH_2 groups and the interaction between hydrogen atoms of the neighboring molecules (this interaction is responsible for the transverse expansion of the PE lattice) are sufficiently complex in character. Therefore, the subsequent quantitative estimates should be treated as approximate.

Judging from the calculated data on the rigidity of torsional and stretching vibrations [4] and also the experimental [13] and theoretical [15] data on the rigidity of intermolecular bonds, the coefficient f_{eff} is taken to be $f_{\text{eff}} \approx 20$ N/m per CH_2 group.

Reasoning from the experimental data on the heat capacity for crystalline PE [1] and the calculated estimates reported in [5], the coefficient g is assumed to be $g = 7 \times 10^{11}$ N/m^2. The subsequent estimates will be made under the assumption that the coefficients f_{eff} and g are constant over the entire temperature range studied. Then, with the use of expression (7) and the experimental dependence $\varepsilon_\perp(T)$ (Fig. 2a), we obtain the dependence $\overline{\delta^2_\perp}(T)$ shown in Fig. 7. The mean energy of the thermal transverse vibrations of the skeleton atoms (CH_2 groups) can be represented as

$$\overline{W}_T(T) \cong f_{\text{eff}} \overline{\delta^2_\perp}. \tag{8}$$

The energies $\overline{W}_T(T)$ proportional to $\overline{\delta^2_\perp}(T)$ are also presented in Fig. 7. The ordinate portions downward from zero with positive values are intended for use in estimating the zero-point components of $\overline{W}$ and $\overline{\delta^2_\perp}$.

It is seen from Fig. 7 that the dependence $\overline{W}_T(T)$ can be divided into three portions: one curved portion from 0 to ~100 K and two quasi-linear portions from ~100 to ~250 K (portion *1*) and from ~250 to ~350 K (portion *2*).

The behavior of the function $\overline{W}_T(T)$ obtained corresponds to the temperature dependence of the thermal component of the energy of two vibrational modes with different characteristic temperatures. Indeed, it is known that the temperature dependence of the mean energy of single-mode vibrations can be represented in the following form [17]:

$$\overline{W}(T) = \overline{W}(0) + \overline{W}_T(T), \tag{9}$$

where $\overline{W}(0) = k_B \theta_D/4$ is the mean zero-point vibrational energy (θ_D is the characteristic temperature) and $\overline{W}_T(T)$ is the thermal component of the mean vibrational energy, which, at $T \geq \theta_D/3$, can be represented by a quasi-linear dependence with the slope equal to the Boltzmann constant $k_B = 8.6 \times 10^{-5}$ eV/K. The dependence $\overline{W}(T)$ is displayed in Fig. 8 (curve *1*).

In the case when a system is characterized by two vibrational modes with different characteristic temperatures θ_1 and θ_2 ($\theta_1 > \theta_2$), the combined dependence given by $\overline{W} = \overline{W}_1 + \overline{W}_2$ at $T \geq \theta_1/3$ involves two quasi-linear portions with the slopes equal to $\sim k_B$ and $\sim 2k_B$ (Fig. 8, curve *3*).

As can be seen from Fig. 7, the experimental dependence $\overline{W}_T(T)$ is in agreement with the theoretical dependence of the thermal component $\overline{W}_T(T) = \overline{W}(T) - \overline{W}(0)$, which follows from curve *3* in Fig. 8.

First and foremost, it should be noted that the temperatures of the initial points of the quasi-linear portions $T_t \cong 110$ K and $T_b \cong 250$ K are close to the temperatures of the efficient excitation of the torsional (~120 K) and bending (~250 K) vibrations. This allows us to assign the quasi-linear portions depicted in Fig. 7 to the torsional and bending transverse vibrations, respectively.

The slopes determined from the quasi-linear portions of the experimental dependence $\overline{W}_T(T)$ (Fig. 7) are as follows: $\Delta\overline{W}_T(T)/\Delta T \approx 12 \times 10^{-5}$ eV/K for portion *1* and $\Delta\overline{W}_T(T)/\Delta T \approx 23 \times 10^{-5}$ eV/K for portion *2*. It turned out that the slope of portion *1* is close to the Boltzmann constant k_B and the slope of portion *2* is close to $2k_B$. Therefore, the experimental and theoretical dependences $\overline{W}_T(T)$ are in reasonable quantitative agreement.

It is evident that the combined nonlinear dependence $\overline{W}_T(T)$ (Fig. 7) can be interpreted in the following way. At low temperatures (up to ~100 K), the quantum statistics (nonlinear in T) of the transverse vibrations manifests itself. At $T \approx 110$ K, the thermal torsional vibrations are efficiently excited and, as a consequence, the temperature dependence of their energy exhibits classical behavior (linear in T with the slope approximately equal to k_B). In the range ~120–220 K, the bending vibrations are virtually not excited and, hence, do not affect the dependence $\overline{W}_T(T)$ of the torsional vibrations. However, at $T \sim 250$ K, the thermal bending vibrations are efficiently excited and their energy also linearly increases with an increase in T with the slope approximately equal to k_B. As a result, the slope of the dependence at $T \geq 250$ K becomes approximately equal to $2k_B$.

After analyzing the thermal component of the energy of transverse vibrations, we turn to the consideration of the zero-point vibrational energy. As follows from relationship (9) and can be seen from the plots depicted in Fig. 8, the zero-point vibrational energy $\overline{W}(0)$ can be obtained using a linear extrapolation of the dependence $\overline{W}_T(T)$ in the portion at $T \geq \theta_D/3$ and $T = 0$ K. This extrapolation of the portion corresponding to the thermally excited torsional vibrations is shown in Fig. 7. The extrapolation results in the zero-point vibrational energy $\overline{W}_t(0) \approx 0.9 \times 10^{-2}$ eV, which corresponds to the mean-square amplitude of the zero-point vibrations $\overline{\delta_\perp^2}(0)_t \approx 0.7 \times 10^{-4}$ nm^2.

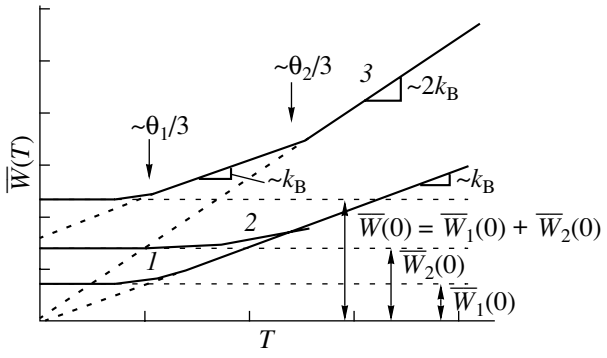

Fig. 8. Schematic temperature dependences of the mean energy of vibrations with characteristic temperatures (*1*) θ_1 and (*2*) θ_2 and (*3*) their combined dependence.

In order to determine the mean zero-point energy $\overline{W}_b(0)$ of bending vibrations, the second quasi-linear portion of the dependence $\overline{W}_T(T)$ is extrapolated to $T = 0$. The difference between the energies obtained by extrapolation of the second and first portions gives the zero-point energy of bending vibrations $\overline{W}_b(0) \approx 2 \times 10^{-2}$ eV. This value corresponds to the mean-square amplitude of the zero-point vibrations $\overline{\delta_\perp^2}(0)_b \approx 1.6 \times 10^{-4}$ nm^2.

From relationship (9), we have $\overline{W}_t(0) \cong 3k_B T_t/4$ and $\overline{W}_b(0) \cong 3k_B T_b/4$. Substitution of $T_t \approx 110$ K and $T_b \approx 250$ K into the above expressions gives $\overline{W}_t(0) \approx 0.8 \times 10^{-2}$ eV and $\overline{W}_b(0) \approx 1.6 \times 10^{-2}$ eV. These zero-point vibrational energies virtually coincide with those determined by extrapolation of the quasi-linear portions in Fig. 8.

6.2. Deformation Effects Induced by Transverse Vibrations in the PE Crystal

6.2.1. Elongation of carbon skeletons of the molecules. If the transverse vibrations are responsible for the elongation of the skeleton of the PE molecules, we should expect a unique relation of $\varepsilon_C(T)$ to the characteristics $\overline{\delta_\perp^2}(T)$ and $\overline{W}_T(T)$ of the transverse vibrations.

Analysis of the curves depicted in Fig. 9 (plotted using the data presented in Figs. 6 and 7) demonstrates that the elongation ε_C is directly proportional to $\overline{\delta_\perp^2}(T)$

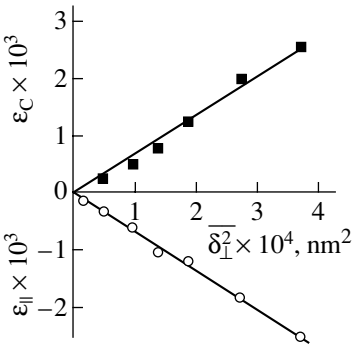

Fig. 9. Dependences of the thermal components of the elongation ε_C of the molecular carbon skeleton and the longitudinal contraction $\varepsilon_\parallel$ of the PE crystal on the thermal component of the mean-square amplitude of transverse vibrations.

[and, correspondingly, to the energy $\overline{W}_T(T)$]. This relation is obvious because the boundaries of the portions (nonlinear and two quasi-linear) in the dependence $\varepsilon_C(T)$, i.e., the temperatures T_t and T_b, coincide with those in the dependence $\overline{\delta_\perp^2}(T)$.

Therefore, the quantum statistics effects revealed in the energy and amplitude of the transverse vibrations also manifest themselves in the elongation of the macromolecular skeleton. Consequently, the zero-point components of the skeleton elongation can be estimated with a procedure similar to that used in analyzing the dependences $\overline{\delta_\perp^2}(T)$ and $\overline{W}_T(T)$.

For this purpose, the linear portions of the dependence $\varepsilon_C(T)$ at $T_t < T < T_b$ and $T > T_b$ in Fig. 6 are extended to intersection with the ordinate axis. The resulting straight-line segments $\varepsilon_C(0)_t$ and $\varepsilon_C(0)_b$ correspond to the contributions of the torsional and bending zero-point vibrations to the elongation of the molecular carbon skeleton. According to our estimates, $\varepsilon_C(0)_t = 0.6 \times 10^{-3}$ and $\varepsilon_C(0)_b = 1.4 \times 10^{-3}$.

6.2.2. Longitudinal contraction of the PE crystal. The longitudinal contraction of the PE crystal can be explained in terms of the decrease in the projection of the macromolecular skeleton onto the molecular axis due to transverse vibrations [2–4]. Since the longitudinal contraction $\varepsilon_\parallel(T)$ is directly proportional to $\overline{\delta_\perp^2}(T)$ (Fig. 9) and the dependence $\varepsilon_\parallel(T)$ exhibits characteristic portions similar to those observed in the dependences $\overline{\delta_\perp^2}(T)$ and $\overline{W}_T(T)$, we can make the inference that the quantum statistics also manifests itself in the longitudinal contraction of the crystal. Hence, the zero-point components of the contraction $\varepsilon_\parallel$, as before, can be estimated by extrapolation.

The linear extrapolation of the quasi-linear portions in the dependence $\varepsilon_\parallel(T)$ to $T = 0$ (Fig. 2b) results in the zero-point contractions $\varepsilon_\parallel(0)_t \approx -0.6 \times 10^{-3}$ and $\varepsilon_\parallel(0)_b \approx -1.5 \times 10^{-3}$ due to the torsional and bending zero-point vibrations, respectively.

6.3. The Ratio of Zero-Point to Thermal Components in the Lattice Dynamics of the PE Crystal

Analysis of the experimental temperature dependences of the transverse expansion, the longitudinal contraction, and the skeleton elongation made it possible to estimate the zero-point (quantum) contributions to these quantities and also to the energy and vibrational amplitude. The results obtained for transverse vibrations of both types—torsional and bending (flexural) modes—are summarized in the table. The zero-point components (i.e., at $T = 0$) and, for comparison, the thermal components at $T = 300$ K are given for each quantity. In addition to the data derived from analyzing the experimental results obtained in the present work

Comparison of the estimated zero-point (quantum) and thermal (at $T = 300$ K) contributions to the mean energy $\overline{W}$ and the mean-square amplitude $\overline{\delta^2}$ of vibrations, the elongation of molecular skeleton ε_C, and the longitudinal lattice contraction $\varepsilon_\parallel$

Vibrations	θ_D, K	$\overline{W}$, 10^{-2} eV		$\overline{\delta_\perp^2}$, 10^{-4} nm^2		ε_C, 10^{-3}		$\varepsilon_\parallel$, 10^{-3}	
		$\overline{W}(0)$	$\overline{W}_T$(300 K)	$\overline{\delta_\perp^2}(0)$	$\overline{\delta_\perp^2}$(300 K)	$\varepsilon_C(0)$	ε_C(300 K)	$\varepsilon_\parallel(0)$	$\varepsilon_\parallel$(300 K)
Torsional	~340	0.9	~3	0.7	~2.4	~0.6	~1.6	–0.6	–1.6
Bending	~740	2	~0.5	1.6	~0.4	~1.4	~0.5	–1.5	–0.5
				$\overline{\delta_\parallel^2}$, 10^{-4} nm^2					
Longitudinal (calculation)	~1700	3.6	0.03	0.14	~0.001	~1	~0.01	+1	+0.01
Total contribution of all vibrations		~6.5	3.5			~3	~2.1	–1.1	–2.1

for the transverse vibrations, the calculated parameters for the longitudinal vibrations of the PE molecules are also presented in the table. The calculations were performed using the characteristic temperature of the longitudinal vibrations $\theta_{\|} \cong 1700$ K and the coefficient of linear elasticity $f_{\|} \cong 400$ N/m [13]. It can be seen from the table that, for the transverse vibrations, the zero-point components of the parameters are comparable to their thermal components (at $T = 300$ K). However, the zero-point components of the parameters for the torsional vibrations are several times smaller than their thermal components, whereas the zero-point components of the parameters for the bending vibrations are several times larger than their thermal components (this is quite reasonable by virtue of the inequality $\theta_b > \theta_t$). By and large, we can note that the contribution of the zero-point transverse vibrations to the lattice dynamics of PE crystals and associated dynamic effects remain significant up to room temperature.

As regards the longitudinal vibrations, which are weakly excited at $T = 300$ K, their effect differs from that of the transverse vibrations. Actually, the energy of zero-point longitudinal vibrations is substantially higher than that of zero-point transverse vibrations but the longitudinal skeleton elongation $\varepsilon_C(0)$ caused by the former vibrations is close to that associated with the latter vibrations. At the same time, compared to the zero-point transverse vibrations, the effect of the zero-point longitudinal vibrations on the longitudinal lattice contraction $\varepsilon_{\|}(0)$ is comparable in magnitude but opposite in sign. For all the parameters of the longitudinal vibrations, the thermal components are appreciably less than the zero-point components.

7. CONCLUSION

Thus, the results of our investigation made it possible to reveal quantum effects in the lattice dynamics of the PE crystal and related phenomena inherent in polymer crystals (such as the longitudinal lattice contraction and the elongation of skeletons in the chain molecules) due to the dominance of transverse vibrations.

Summarizing all the data on transverse and longitudinal vibrations of the PE lattice, we can draw the inference that the zero-point quantum dynamics significantly contributes to the vibrational dynamics of this crystal over the entire temperature range of existence of the PE crystal phase (the melting temperature of PE crystals is equal to 400–410 K [1]).

ACKNOWLEDGMENTS

This work was supported by the Russian Foundation for Basic Research, project no. 00-03-33064a.

REFERENCES

1. Yu. K. Godovskiĭ, *Thermal Physics of Polymers* (Khimiya, Moscow, 1982).
2. I. M. Lifshitz, Zh. Éksp. Teor. Fiz. **22** (4), 475 (1952).
3. F. C. Chen, C. L. Choy, and K. Young, J. Polym. Sci., Polym. Phys. Ed. **18**, 2313 (1980).
4. F. C. Chen, C. L. Choy, S. P. Wang, and K. Young, J. Polym. Sci., Polym. Phys. Ed. **19**, 971 (1980).
5. P. C. Painter, M. Coleman, and J. L. Koenig, *The Theory of Vibrational Spectroscopy and Its Application to the Polymeric Materials* (Wiley, New York, 1986).
6. S. V. Bronnikov, V. I. Vettegren, and S. Ya. Frenkel, Polym. Eng. Sci. **32**, 1204 (1992).
7. V. I. Vettegren, L. S. Titenkov, and S. V. Bronnikov, J. Therm. Anal. **38**, 1031 (1992).
8. R. P. Wool and R. S. Bretzlaff, J. Polym. Sci., Part B: Polym. Phys. **24**, 1039 (1986).
9. D. T. Grubb and Z.-F. Li, Polymer **33**, 2587 (1992).
10. R. J. Meier and H. Vansweefelt, Polymer **36**, 3825 (1995).
11. K. Tashiro, G. Wu, and M. Kobayashi, Polymer **29**, 1768 (1988).
12. L. Berger, Doct. Sci. Tech. These No. 1704 (EPFL, Lausanne, 1997).
13. I. Sakurada, T. Ito, and K. Nakamae, J. Polym. Sci., Part C: Polym. Symp. **15**, 75 (1966).
14. G. J. Safford and A. W. Neumann, Adv. Polym. Sci. **5** (1), 1 (1967).
15. K. Bann, Trans. Faraday Soc. **35**, 482 (1939).
16. J. Frenkel, *Kinetic Theory of Liquids* (Clarendon, Oxford, 1946; Nauka, Leningrad, 1975).
17. J. M. Ziman, *Principles of the Theory of Solids* (Cambridge Univ. Press, Cambridge, 1964; Mir, Moscow, 1966).

Translated by O. Borovik-Romanova

Physics of the Solid State, Vol. 44, No. 10, 2002, pp. 1944–1948. Translated from Fizika Tverdogo Tela, Vol. 44, No. 10, 2002, pp. 1855–1858.

LATTICE DYNAMICS AND PHASE TRANSITIONS

Nuclear Quadrupole Resonance Spectrum and Transition from the Incommensurate Phase to the Commensurate Phase of a Crystal

M. A. Popov

Krasnoyarsk State University, Svobodnyĭ pr. 79, Krasnoyarsk, 660041 Russia

e-mail: rsa@iph.krasn.ru

Received November 26, 2001

Abstract—The relationships describing the nuclear quadrupole resonance spectrum in the vicinity of the transition from the incommensurate phase to the commensurate phase of a crystal are derived in the adiabatic approximation. It is demonstrated that the intensity of the nuclear quadrupole resonance peaks depends on the mutual orientation of the order parameter and the electric field gradient. © *2002 MAIK "Nauka/Interperiodica".*

1. INTRODUCTION

In recent years, crystal structures with an incommensurate phase have been studied extensively [1]. In this phase, the displacements of atoms from their positions in the high-temperature translation-symmetry phase induce a spatial wave whose wave vector does not coincide with any of the high-symmetry (special) points of the Brillouin zone. The loss of translation symmetry is responsible for the specific shape of the nuclear quadrupole resonance (NQR) line (a continuum distribution on the frequency interval determined by the lattice wave amplitude with singularities, at least, at the interval boundaries). This opens up the way to radiospectroscopic detection of the incommensurate phase in the crystal under study [1, 2].

The resonance lines observed in experiments were treated for a long time within the concept of a frozen wave of lattice displacements. The effect of the lattice spin mobility was taken into account nearly twenty years ago. In the first works dealing with this effect, consideration was given to both the slip of a lattice modulation wave over the crystal [3] and thermal fluctuations of the wave phase with a specified Gaussian distribution [4]. The influence of thermal fluctuations on the resonance line has been thoroughly investigated only recently [5–8]. It should be noted that the results obtained in the aforementioned works are applicable only to the plane-wave region of the incommensurate phase of the studied crystal.

In this work, the analysis of the influence of lattice thermal fluctuations on the resonance line was extended to the region of the low-temperature transition from the incommensurate phase to the commensurate phase of a crystal.

2. TRANSITION FROM THE INCOMMENSURATE PHASE TO THE COMMENSURATE PHASE OF A CRYSTAL

In order to describe the properties of the lattice subsystem of a crystal, we will use an incomplete thermodynamic potential which depends on the two-component order parameter (η_1, η_2) [9]; that is,

$$\Phi = \Phi_0 + \int\left\{\frac{A}{2}\eta^2 + \frac{B}{4}\eta^4 + \frac{C}{n}\eta^n\cos(n\varphi) + \frac{D_1}{2}[(\nabla\eta)^2 + \eta^2(\nabla\varphi)^2] - D_2\eta^2\frac{\partial\varphi}{\partial z}\right\}d\mathbf{r}, \quad (1)$$

where $\eta = (\eta_1^2 + \eta_2^2)^{1/2}$, $\tan\varphi = \eta_2/\eta_1$, $A = a(T - T_0)$, $a > 0$, $B > 0$, and $D_1 > 0$; the explicit dependence of the order parameter on the space coordinate and time in the form $\eta_1(\mathbf{r}, t)$ and $\eta_2(\mathbf{r}, t)$ is not presented. In contrast with the cases considered earlier in [5–8], here, we take into account the anisotropy invariant $C\eta^n\cos(n\varphi)/n$. The transition under consideration stems from the competition between the anisotropy invariant and the Lifshitz invariant $D_2\eta^2\partial\varphi/\partial z$ [9].

The extremum conditions for the thermodynamic potential Φ with respect to η and φ, which correspond to an equilibrium state of the crystal, can be written in the following form [10]:

$$\frac{\delta\Phi}{\delta\eta} = A\eta + B\eta^3 + C\eta^{n-1}\cos(n\varphi) + D_1\eta(\nabla\varphi)^2 - 2D_2\eta\frac{\partial\varphi}{\partial z} - D_1\Delta\eta = 0, \quad (2)$$

1063-7834/02/4410-1944$22.00

$$\frac{\delta\Phi}{\delta\varphi} = -C\eta^n\sin(n\varphi) - D_1\nabla(\eta^2\nabla\varphi) + D_2\frac{\partial}{\partial z}\eta^2 = 0, \quad (3)$$

where Δ is the Laplace operator. Since the disturbance of a homogeneous state of the crystal by the Lifshitz invariant is one-dimensional and the transverse deviations with respect to the Z axis in the equilibrium state are ruled out by the condition $D_1 > 0$, conditions (2) and (3) can be reduced to the relationships

$$\begin{aligned}[A\eta + B\eta^3 + D_1\eta\varphi'^2 - 2D_2\eta\varphi' - D_1\eta'']\\ + C\eta^{n-1}\cos(n\varphi) = 0,\end{aligned} \quad (4)$$

and

$$[D_1(\eta^2\varphi')' - D_2(\eta^2)'] + C\eta^n\sin(n\varphi) = 0, \quad (5)$$

where $f' \equiv df/dz$ and $f'' \equiv d^2f/dz^2$.

In the general case, the solution of Eqs. (4) and (5) presents considerable difficulties. At the same time, inside the plane-wave region, in which the contribution of the anisotropy invariant is negligible in comparison with the contributions of the other invariants, the amplitude of the equilibrium lattice wave η does not depend on z [9]. The extension of this behavior of the lattice wave to the whole region of the incommensurate phase is referred to as the constant-amplitude approximation [2]. The condition of its applicability lies in the relative smallness not only of the anisotropy invariant but also of the Lifshitz invariant competing with it. Within this approximation, the equilibrium conditions (4) and (5) take the form

$$A\eta + B\eta^3 = 0, \quad (6)$$

$$D_1\eta^2\varphi'' + C\eta^n\sin(n\varphi) = 0. \quad (7)$$

The solution to Eq. (6) is evident and the solution to Eq. (7) is known from [2]:

$$\begin{aligned}\varphi' &= c_1\sqrt{1 - k_1^2\sin^2(n\varphi/2)},\\ \varphi &= 2\mathrm{am}(nc_1z/2, k_1)/n,\end{aligned} \quad (8)$$

where $\mathrm{am}(x, y)$ is the Jacobian amplitude function and $c_1 = 2\eta^{n/2-1}[C/(nD_1)]^{1/2}/k_1$ (the rotation through the angle $\Delta\varphi = \pi/n$ provides nonnegativity of the coefficient C). The parameter k_1 is determined by minimizing the equilibrium thermodynamic potential in the incommensurate phase after the elimination of the equilibrium phase φ through solution (8); that is,

$$\frac{k_1}{E(k_1)} = \frac{4\eta^{n/2-1}}{\pi D_2}\sqrt{\frac{CD_1}{n}},$$

where $E(k_1)$ is the complete elliptic integral of the second kind.

In order to calculate the NQR spectrum in the adiabatic approximation, we need appropriate expressions for the time pair correlation functions of the lattice. These expressions can be obtained from the dynamic equations [11]

$$\frac{d}{dt}\frac{\delta\Phi}{\delta\dot\eta_m} = -\frac{\delta\Phi}{\delta\eta_m} - \frac{\delta\Psi}{\delta\dot\eta_m},$$

where $\dot f \equiv df/dt$, $\Psi = \int\Gamma(\dot\eta_1^2 + \dot\eta_2^2)\,d\mathbf{r}/2 = \int\Gamma(\dot\eta^2 + \eta^2\dot\varphi^2)\,d\mathbf{r}/2$ is the dissipative function. The thermodynamic potential accounts for both the kinetic contribution $\Delta\Phi_T = \int M(\dot\eta_1^2 + \dot\eta_2^2)\,d\mathbf{r}/2 = \int M(\dot\eta^2 + \eta^2\dot\varphi^2)\,d\mathbf{r}/2$ and the interaction with conjugate fields $\Delta\Phi_h = -\int[\eta_1h_1(t) + \eta_2h_2(t)]\,d\mathbf{r} = -\int[\eta h_\eta(t) + \varphi h_\varphi(t)]\,d\mathbf{r}$. Let us now represent the order parameter as the sum of two terms: the first term corresponds to the equilibrium conditions (6) and (7) (hereafter, denoted by index s), and the second term corresponds to a deviation from equilibrium (hereafter, denoted by index d). In the case when the alternating fields are relatively weak, we expand the dynamic equations in the vicinity of the equilibrium and obtain

$$\begin{aligned}M\ddot\eta_d &= -\{A\eta_d + 3B\eta_s^2\eta_d + D_1\varphi_s'^2\eta_d + 2D_1\eta_s\varphi_s'\varphi_d'\\ &\quad - 2D_2\varphi_s'\eta_d - 2D_2\eta_s\varphi_d' - D_1\Delta\eta_d\\ &\quad + (n-1)C\eta_s^{n-2}\cos(n\varphi_s)\eta_d\\ &\quad - nC\eta_s^{n-1}\sin(n\varphi_s)\varphi_d\} - \Gamma\dot\eta_d + h_\eta(t)\\ &\approx -\{A\eta_d + 3B\eta_s^2\eta_d - D_1\Delta\eta_d\} - \Gamma\dot\eta_d + h_\eta(t),\end{aligned} \quad (9)$$

$$\begin{aligned}M\eta_s^2\ddot\varphi_d &= -\{-2D_1\eta_s\varphi_s'\eta_d' - D_1\eta_s^2\Delta\varphi_d - 2D_1\eta_s\varphi_s''\eta_d\\ &\quad + 2D_2\eta_s\eta_d' - nC\eta_s^{n-1}\sin(n\varphi_s)\eta_d\\ &\quad - nC\eta_s^n\cos(n\varphi_s)\varphi_d\} - \Gamma\eta_s^2\dot\varphi_d + h_\varphi(t)\\ &\approx -\{-D_1\eta_s^2\Delta\varphi_d\} - \Gamma\eta_s^2\dot\varphi_d + h_\varphi(t).\end{aligned} \quad (10)$$

Here, $\ddot f \equiv d^2f/dt^2$ and the expression in braces refers to the restoring force. In the final estimate, the terms of the order of D_2 and C are dropped (by analogy with the constant-amplitude approximation in statics). At the same time, there are no limitations on the steepness of the inhomogeneity φ_d in Eq. (10).

From relationships (9) and (10), we can first calculate the dynamic susceptibilities of the crystal lattice and then, within the framework of the fluctuation-dissipative theorem [11], deduce the desired expressions for the correlation functions. Since the frequencies used in the NQR measurements are small compared to the frequencies of the lattice modes, the left-hand sides of Eqs. (9) and (10) are negligible; i.e., the lattice dynam-

ics at these frequencies can be treated as the relaxation lattice dynamics. As a result, we have

$$\langle \eta_d^2 \rangle_{\mathbf{k}\omega} = \frac{T\Gamma}{[(A_0 + D_1 k^2)^2 + \Gamma^2\omega^2]},$$

$$\langle \varphi_d^2 \rangle_{\mathbf{k}\omega} = \frac{T\Gamma/\eta_s^2}{[D_1^2 k^4 + \Gamma^2\omega^2]}, \quad \langle \eta_d \varphi_d \rangle = 0,$$

where $\langle f_1 f_2 \rangle_{\mathbf{k}\omega} = \int_{-\infty}^{\infty} \langle f_1(\mathbf{r}, t) f_2(0, 0) \rangle \exp[i(\omega t - \mathbf{kr})] d\mathbf{r}\, dt$, $A_0 = A + 3B\eta_s^2$, and the Boltzmann constant is taken equal to unity.

3. THE SHAPE OF THE NUCLEAR QUADRUPOLE RESONANCE LINE

In the adiabatic approximation [11], with allowance made for the crystal inhomogeneity, the resonance line can be described by the expression

$$g(\omega) = V^{-1} \int_{-\infty}^{\infty} \int \left\langle \exp\left\{ i \int_0^t [\omega - \Omega(\mathbf{r}, t')] dt' \right\} \right\rangle dt d\mathbf{r}, \quad (11)$$

where $\Omega(\mathbf{r}, t)$ is the resonance frequency of the spin located at the point $\mathbf{r}$ at the instant of time t. Let us assume that the electric field gradient separates $\eta(t)\cos[\varphi(t) - \theta]$. Then, the lattice fluctuations lead to the following variation in the resonance frequency:

$$\Omega(\mathbf{r}, t) \approx \Omega_0 + \Omega_1 \eta_\theta(t), \quad (12)$$

where

$$\Omega_0 = \Omega(\eta_s \cos(\varphi_s - \theta)), \quad \Omega_1 = \Omega'(\eta_s \cos(\varphi_s - \theta)),$$
$$\Omega'(\eta) \equiv d\Omega(\eta)/d\eta,$$
$$\eta_\theta(t) = \cos(\varphi_s - \theta)\eta_d(t) - \eta_s \sin(\varphi_s - \theta)\varphi_d(t).$$

Taking into account formula (12), the resonance line [described by expression (11)] in the incommensurate phase can be represented within the approach proposed by Anderson [11] as follows:

$$g_{icp}(\omega) = \lambda^{-1} \int_0^{\lambda} \int_{-\infty}^{\infty} \exp\left\{ i(\omega - \Omega_0)t - \Omega_1^2 \int_0^t (t - t') \langle \eta_\theta(t') \eta_\theta(0) \rangle dt' \right\} dt dz$$
$$= \lambda^{-1} \int_0^{\lambda} \int_{-\infty}^{\infty} \exp\left\{ i(\omega - \Omega_0)t - \Omega_1^2 \int_{-\infty}^{\infty} \langle \eta_\theta^2 \rangle_\varepsilon [(1 - \cos(\varepsilon t))/(2\pi\varepsilon^2)] d\varepsilon \right\} dt dz,$$

where

$$\lambda = \int_0^{\lambda} dz = \int_0^{2\pi} \frac{d\varphi}{|\varphi'|} = \frac{4K(k_1)}{c_1}$$

is the lattice wavelength, $K(k_1)$ is the complete elliptic integral of the first kind [2],

$$\langle \eta_\theta^2 \rangle_\varepsilon = \int_{-\theta}^{\infty} \langle \eta_\theta(t) \eta_\theta(0) \rangle \cos(\varepsilon t) dt$$
$$= \frac{V}{8\pi^3} \int (\langle \eta_d^2 \rangle_{\mathbf{k}\varepsilon} \cos^2(\varphi_s - \theta) + \langle \varphi_d^2 \rangle_{\mathbf{k}\varepsilon} \eta_s^2 \sin^2(\varphi_s - \theta)) d\mathbf{k},$$

integration with respect to the wave vectors $\mathbf{k}$ is carried out inside the first Brillouin zone, and V is the volume of the unit cell in the high-temperature phase.

Since the obtained expressions are too cumbersome, we restrict our consideration to an estimate of the integral in the exponent. The main contribution to this integral is made by low-frequency phonons, and the Brillouin zone boundary can be disregarded provided that the integration with respect to the wave vectors is extended to infinity. As a consequence, we obtain the relationship

$$\langle \eta_\theta^2 \rangle_\varepsilon \approx \frac{VT\Gamma}{2\pi(2D_1)^{3/2}} \times \left\{ \frac{\cos^2(\varphi_s - \theta)}{[(A_0^2 + \Gamma^2\varepsilon^2)^{1/2} + A_0]^{1/2}} + \frac{\sin^2(\varphi_s - \theta)}{|\Gamma\varepsilon|^{1/2}} \right\}.$$

The subsequent integral can be interpolated with a relative error of less than 11% with the use of the expression

$$\Omega_1^2 \int_{-\infty}^{\infty} \langle \eta_\theta^2 \rangle_\varepsilon [(1 - \cos(\varepsilon t))/(2\pi\varepsilon^2)] d\varepsilon$$
$$= \gamma(A_0, t)\cos^2(\varphi_s - \theta) + \gamma(0, t)\sin^2(\varphi_s - \theta),$$
$$\gamma(\Delta, t) \approx \frac{\Omega_1^2 VT\Gamma^{1/2} t^{3/2}}{6(\pi D_1)^{3/2}\{1 + [64\Delta t/(9\pi\Gamma)]\}^{1/2}}.$$

The relaxation represented by the function $\gamma(A_0, t)$ is caused by the thermal fluctuations $\eta_d(t)$ of the lattice wave amplitude (amplitudons), and the relaxation described by the function $\gamma(0, t)$ is due to the thermal fluctuations $\varphi_d(t)$ of the wave phase (phasons).

As a result, the relationship describing the resonance line in the incommensurate phase takes the form

$$g_{icp}(\omega) \approx \lambda^{-1}\int_0^{\lambda}\int_0^{\infty}\cos[(\omega-\Omega_0)t] \times \exp[-\gamma(A_0, t)\cos^2(\varphi_s-\theta)-\gamma(0, t)\sin^2(\varphi_s-\theta)]dtdz. \quad (13)$$

If the effect of lattice fluctuations is ignored, i.e., $\gamma(A_0, t) \approx \gamma(0, t) \approx 0$, we obtain the standard relationship for the static model [1, 2]:

$$g_{icp}(\omega) = \frac{2\pi}{\lambda}\sum|\partial\Omega(\eta_s\cos(\varphi_s-\theta))/\partial z|^{-1}. \quad (14)$$

Here, the summation is taken over all the solutions to the equation $\Omega(\eta_s\cos(\varphi_s-\theta)) = \omega$. The continuum distribution of the resonance frequencies (14) exhibits peaks corresponding to its extrema; that is,

$$\partial\Omega(\eta_s\cos(\varphi_s-\theta))/\partial z = -\Omega'(\eta_s\cos(\varphi_s-\theta))\sin(\varphi_s-\theta)\varphi_s' = 0.$$

The frequencies of the peaks that correspond to the condition $\Omega'(\eta_s\cos(\varphi_s-\theta)) = 0$ do not change with temperature, whereas the frequencies of the peaks that satisfy the condition $\sin(\varphi_s-\theta) = 0$ change according to the law $\Omega(\pm\eta_s)$. As the temperature T_c is approached, additional peaks appear in the quasi-continuous distribution in the soliton region. These peaks satisfy the condition $\varphi_s' \approx 0$ at $k_1 \approx 1$ and $|\sin(n\varphi_s/2)| = 1$ and transform into the peaks of the NQR spectrum of the commensurate phase. The influence of amplitudons and phasons on all the peaks observed in the plane-wave region was analyzed earlier in [6, 8]. The influence of amplitudons and phasons on the additional peaks depends on their location on the spectrum.

Similarly, in the commensurate phase, we can obtain the relationship

$$g_{cp}(\omega) = \frac{1}{n}\sum_{\varphi_s}\int_{-\infty}^{\infty}\exp\left\{i(\omega-\Omega_0)t - \Omega_1^2\int_0^t\langle\eta_\theta^2\rangle_\varepsilon[(1-\cos(\varepsilon t))/(2\pi\varepsilon^2)]d\varepsilon\right\}dt \approx \frac{2}{n}\sum_{\varphi_s}\int_0^{\infty}\cos[(\omega-\Omega_0)t] \times \exp[-\gamma(A_0, t)\cos^2(\varphi_s-\theta)-\gamma(A_1, t)\sin^2(\varphi_s-\theta)]dt, \quad (15)$$

where summation is carried out over all solutions of the equation $\cos(n\varphi_s) = -1$ within the limits $0 \le \varphi_s < 2\pi$ and $A_1 = (n-1)C\eta_s^{n-2}$. In this case, the existence of the gap in the spectrum of lattice modes (transverse with respect to the order parameter) due to violation of the continuous symmetry of the crystal (in a homogeneous ordered state) by the anisotropy invariant was taken into account for the commensurate phase.

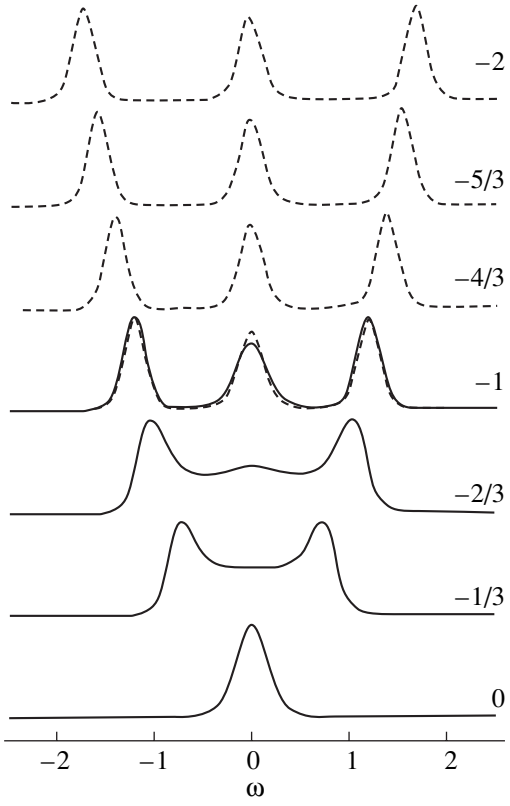

Simulated NQR lines normalized to the intensity for the incommensurate (solid lines) and commensurate (dashed lines) phases. Numbers near the lines are the parameters τ.

4. DISCUSSION

Thus, in the present work, we derived the relationships describing the NQR spectrum in the incommensurate and commensurate phases of the crystal. The figure represents the resonance lines simulated using relationships (13) and (15). In calculations, the convolution was carried out with the Gaussian form $\exp(-\omega^2/2\gamma_g^2)/(2\pi\gamma_g^2)^{1/2}$, which simulates the contribution of the noncritical degrees of freedom of the crystal. The chosen parameters were as follows: $n = 6$, $A = \tau(T_i - T_c)$, $B = D_1 = T = \nu = \Gamma = 1$, $C = 10^{-2}$, $D_2 = \gamma_g = 10^{-1}$, $\Omega(\eta) = \eta$, and $\theta = 0$.

In the case when the temperature decreases to T_c, the continuum contribution vanishes and the difference in the intensity of the peaks manifests itself due to the aforementioned dependence of the broadening effect of thermal fluctuations of the critical degrees of freedom of the crystal on the mutual orientation of the order parameter and the electrical field gradient. The drastic

change in the intensity ratio of the peaks in the vicinity of the temperature T_c does not change their inequality. However, the attenuation of these fluctuations with a further decrease in the temperature leads to equalization of the intensities of peaks, whose width, in this case, is determined by the noncritical degrees of freedom of the crystal.

It should be noted that the obtained discrepancy between the line intensities in the vicinity of the transition to the commensurate phase actually also extends to the transitions from the disordered phase to the commensurate phase, because this discrepancy is associated only with the orientation of the order parameter with respect to the electric field gradient. Observations of this effect are hindered by the insufficient resolution of the spectrum immediately below the transition, unlike the already resolved spectrum of the crystal upon the transition from the incommensurate phase.

ACKNOWLEDGMENTS

I am grateful to A.V. Belokhvostov for his participation in discussions of the results and helpful remarks.

This work was supported by the Krasnoyarsk Region Science Foundation, project no. 9F0139.

REFERENCES

1. H. Z. Cummins, Phys. Rep. **185** (5–6), 211 (1990).
2. *Incommensurate Phases in Dielectrics*, Ed. by R. Blinc and A. Levanyuk (North-Holland, Amsterdam, 1986), Vol. 1.
3. R. Blinc, D. C. Ailion, P. Prelovsek, and V. Rutar, Phys. Rev. Lett. **50** (1), 67 (1983).
4. R. Blinc, F. Milia, B. Topic, and S. Zumer, Phys. Rev. B **29** (7), 4173 (1984).
5. A. M. Fajdiga, T. Apih, J. Dolinsek, *et al.*, Phys. Rev. Lett. **69** (18), 2721 (1992).
6. M. A. Popov, I. P. Aleksandrova, and S. V. Primak, Pis'ma Zh. Éksp. Teor. Fiz. **59** (7), 464 (1994) [JETP Lett. **59**, 485 (1994)].
7. J. Dolinsek, A. M. Fajdiga-Bulat, T. Apih, *et al.*, Phys. Rev. B **50** (14), 9729 (1994).
8. M. A. Popov, Zh. Éksp. Teor. Fiz. **110** (1), 218 (1996) [JETP **83**, 116 (1996)].
9. A. P. Levanyuk and D. G. Sannikov, Fiz. Tverd. Tela (Leningrad) **18** (2), 423 (1976) [Sov. Phys. Solid State **18**, 245 (1976)].
10. L. D. Landau and E. M. Lifshitz, *Course of Theoretical Physics*, Vol. 5: *Statistical Physics* (Nauka, Moscow, 1976; Pergamon, Oxford, 1980), Part 1.
11. P. W. Anderson, J. Phys. Soc. Jpn. **9** (3), 316 (1954).

Translated by O. Moskalev

Physics of the Solid State, Vol. 44, No. 10, 2002, pp. 1949–1953. Translated from Fizika Tverdogo Tela, Vol. 44, No. 10, 2002, pp. 1859–1863.

LATTICE DYNAMICS AND PHASE TRANSITIONS

Effect of Hydrostatic and Chemical Pressure on BaF_2 and $BaF_2 : Eu^{2+}$ Crystals

A. E. Nikiforov, A. Yu. Zakharov, V. A. Chernyshev, M. Yu. Ugryumov, and S. V. Kotomanov

Ural State University, pr. Lenina 51, Yekaterinburg, 620083 Russia

Received July 16, 2001; in final form, November 27, 2001

Abstract—The effect of hydrostatic pressure on a BaF_2 crystal was studied within the shell model in the pairwise potential approximation. The structural phase transition from the cubic to orthorhombic phase was simulated. The behavior of the unit-cell parameters of the α- and β-BaF_2 phases under hydrostatic pressure (from 0 to 12 GPa) was investigated. The fundamental vibration frequencies of BaF_2 under hydrostatic pressure (0–3.5 GPa) were calculated for both phases. The effect of chemical pressure on the BaF_2 crystal was studied by simulating $Ba_{1-x}Me_xF_2$ mixed crystals (*Me* = Ca, Sr). It was shown that at impurity concentrations up to 15–20 at. % the lattice constant varies in the same way as it does when hydrostatic pressure increases to P_c, which corresponds to a phase transition to the orthorhombic phase. The effect of chemical and hydrostatic pressure on $BaF_2 : Eu^{2+}$ doped crystals was also studied. The dependence of the absorption and luminescence zero-phonon line shift on the Eu^{2+}–ligand distance was calculated.© *2002 MAIK "Nauka/Interperiodica".*

1. INTRODUCTION

Barium fluorite BaF_2 is one of the best materials for use in high-energy electromagnetic calorimeters and scintillators [1, 2]; therefore, investigation of the response of this compound to various external factors and of the effect of impurities on its structure and lattice dynamics is not continued importance. Absorption and luminescence spectra of the Eu^{2+}, Sm^{2+}, Yb^{2+}, and Ce^{3+} impurity centers in BaF_2 have been repeatedly studied experimentally [3–5]. Malkin was one of the first to calculate the structure and dynamics of rare-earth (RE) impurity centers in fluorites [6, 7]. Recent publications have reported on studies of impurity centers in mixed crystals, for instance, in $Sr_{1-x}Ba_xF_2 : Eu^{2+}$ [8]. The creation of such mixed systems stems from the need to improve the luminescence and mechanical properties of BaF_2, because one of the shortcomings of this crystal (resulting from its loose structure) is its poor mechanical strength [2]. The effect of hydrostatic pressure on pure barium fluorite was studied experimentally in [9]. The experiment showed that this crystal undergoes a structural phase transition (PT) from the cubic to orthorhombic phase at a pressure of 2.6 GPa and another transition to a lower-symmetry phase at an even higher pressure. Pressure-induced distortions of the crystal lattice, as well as the structural PT, affect the luminescence spectra of impurity ions. A change in the luminescence spectra of the RE impurity ion provides information on the mechanical stresses acting in the crystal [10]. It thus appears important to simulate the effect of hydrostatic and chemical pressure on pure and doped BaF_2 crystals at a microscopic level. These problems are addressed in the present publication.

2. MODEL FOR CRYSTAL ENERGY CALCULATION

The equilibrium ion positions in a crystal can be found by minimizing the lattice energy. Within the shell model and the pairwise potential approximation, the lattice energy can be written as

$$U_{\text{lat}} = \frac{1}{2}\sum_i \sum_{k(\neq i)} V_{ik} + \frac{1}{2}\sum_i \kappa_i \delta_i^2, \tag{1}$$

where $\kappa_i\delta_i$ is the core–shell interaction energy of the *i*th ion and V_{ik} is the interaction energy between the *i*th and *k*th ions, which can be represented in the form

$$V_{ik} = \frac{X_i X_k}{r_{ik}} + \frac{Y_i X_k}{|r_{ik} - \delta_i|} + \frac{X_i Y_k}{|r_{ik} + \delta_k|} + \frac{Y_i Y_k}{|r_{ik} - \delta_i + \delta_k|} + f_{ik}(r_{ik}) + g_{ik}(|r_{ik} - \delta_i + \delta_k|). \tag{2}$$

Here, the function

$$f_{ik}(r) = -A_{ik}\exp(-B_{ik}r)/r \tag{3}$$

describes the short-range screening of the electrostatic interaction between ion cores, the function

$$g_{ik}(r) = C_{ik}\exp(-D_{ik}r) - \lambda_{ik}/r^6 \tag{4}$$

describes the short-range repulsion between the ion shells (which is cast in the form of the Born–Mayer potential) and the van der Waals interaction, X_i and Y_i

Table 1. Ion coordinates in a primitive cell of the α-BaF_2 phase (space group *Pbnm*)

Ion	*X*	*Y*	*Z*
Pb	*U*	*V*	0.25
Pb	0.5 – *U*	*V* + 0.5	0.25
Pb	1 – *U*	1 – *V*	–0.25
Pb	0.5 + *U*	0.5 – *V*	–0.25
F1	U_1	V_1	0.25
F1	0.5 – U_1	V_1 + 0.5	0.25
F1	1 – U_1	1 – V_1	–0.25
F1	0.5 + U_1	0.5 – V_1	–0.25
F2	U_2	V_2	0.25
F2	0.5 – U_2	V_2 + 0.5	0.25
F2	1 – U_2	1 – V_2	–0.25
F2	0.5 + U_2	0.5 – V_2	–0.25

Table 2. Parameters *U* and *V* for a pressure of 4.6 GPa

Ion species	*U*		*V*	
	calc.	exp. [9]	calc.	exp. [9]
Ba	0.110	0.112	0.253	0.259
F1	0.431	0.433	0.354	0.361
F2	0.323	0.320	0.033	0.039

Note: Data are given for the *Pbnm* space group.

are the core and shell charges of the *i*th ion, and r_{ik} is the distance between the cores of the *i*th and *k*th ions. We use here the following values of the core charges: X_F = +5, and $X_{Ca, Sr, Ba, Eu}$ = +8. The values of the pairwise interaction parameters and of the core–shell interaction constants, as well as the methods used to find them, were presented in our previous publications [11–13]. The parameters of the potentials employed make it possible to calculate the lattice constant and the elastic and dielectric constants of MeF_2 (*Me* = Ca, Sr, Ba); the results agree with the respective experimental values to within 10%.

To calculate the structure of an impurity center, the crystal is divided into two parts, namely, the defect region and the remainder of the crystal. The defect region includes the impurity ion and the nearest neighbor ions of the crystal matrix, which can relax within the given symmetry. The ions in the remainder of the crystal are considered to be fixed. The size of the defect region is chosen such that its further increase does not entail substantial changes in ion positions in this region. In our calculations, the defect region included nine coordination shells around the impurity ion. The Coulomb interaction energy of the ions in the defect region with the ions in the remainder of the crystal was calculated following the Ewald method.

To include the effect of hydrostatic pressure, the term *PV* was introduced into Eq. (1) for the crystal energy, where *P* is the external hydrostatic pressure and *V* is the volume of the primitive cell of the crystal; thus, the equilibrium structure is derived from the condition of the minimum not of the crystal energy *E* given by Eq. (1) but rather of the thermodynamic potential *H* = *E* + *PV* The effect of pressure on an impurity crystal was determined in the following way: first, we made a self-consistent calculation of the unit-cell parameters of a pure crystal subjected to pressure, after which the parameters thus obtained were employed in subsequent calculations for an impure crystal.

3. EFFECT OF HYDROSTATIC AND CHEMICAL PRESSURE ON BaF_2

3.1. Effect of Hydrostatic Pressure on the BaF_2 Structure

Two BaF_2 crystal modifications are known: the cubic β phase, whose crystal structure belongs to space group O_h^5, and the orthorhombic α phase with symmetry group D_{2h}^{16}. The orthorhombic phase has a higher density and a higher cation coordination number (this number is nine in the α phase, whereas it is only eight in the β phase). The primitive cell of the orthorhombic phase contains 12 ions (four Ba ions and two symmetry-inequivalent fluorine ion species, namely, four F1 and four F2 ions). All 12 ions occupy the 4*c* positions. The coordinates of ions in a primitive cell are given in Table 1 in fractions of the lattice parameter. As seen from Table 1, the ion coordinates are expressed through the *U*, *V*, U_1, V_1, U_2, and V_2 parameters (space group *Pbnm*). The parameters *U* and *V*, calculated by us for a pressure of 4.6 GPa, are compared with experimental data in Table 2.

At a certain critical pressure P_c, a structural phase transition from the β to α phase occurs. Experiment gives P_c = 2.6 GPa [9].

Our calculations yielded an expression relating the BaF_2 primitive-cell energy to hydrostatic pressure for the cubic and orthorhombic phases (Fig. 1). The minimum lattice energy was found for a given value of pressure. In the cubic phase, the lattice energy was found to be a function of the lattice parameter, and in the orthorhombic phase, this energy was found to depend on three lattice parameters and on the parameters *U*, *V*, U_1, V_1, U_2, and V_2. As seen from Fig. 1, the relation is linear for both phases. According to our calculations, the phase transition occurs at 2.5 GPa. We also predicted a structural phase transition from the β to α phase in CaF_2 (at 2.9 GPa) and SrF_2 (at 3 GPa). Our calculations also yielded the pressure dependences of the BaF_2 lattice parameters for both phases (Fig. 2). The results of the calculations agree well with experiment. According to our calculations, the phase transition from the β to the

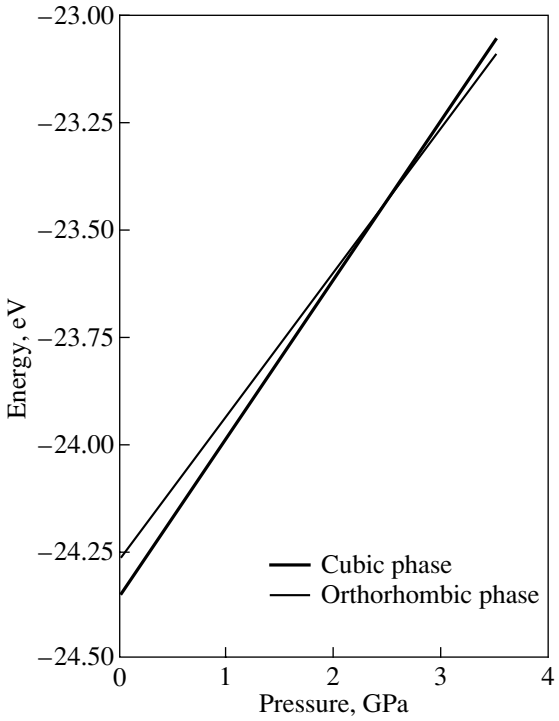

Fig. 1. BaF_2 primitive-cell energy as a function of pressure.

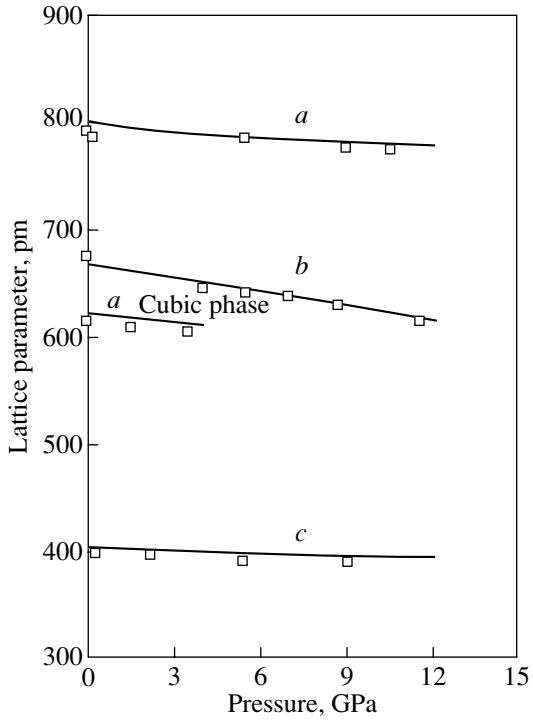

Fig. 2. BaF_2 lattice parameters as a function of pressure. Squares are experimental values [9].

α phase is accompanied by a decrease in the primitive-cell volume by about 10%, which is in accordance with experimental data [9].

3.2. Effect of Hydrostatic Pressure on BaF_2 Fundamental Vibration Frequencies

Studies of fundamental vibration (FV) frequencies of BaF_2 already have a long history [14–16] because this crystal can serve as a basis for creating BaF_2 : *Me* impurity centers (*Me* = Er, Y, Yb, Lu, Eu) and, in addition, BaF_2 possesses a high ionic conductivity in both phases. We found the pressure dependence of FV frequencies for the cubic and orthorhombic phases of BaF_2 (Table 3). The data presented for the orthorhombic phase refer only to the strongest Raman lines observed experimentally [14]. We readily see that the FV frequencies depend linearly on pressure with a positive derivative (this also applies to other frequencies not listed in Table 3).

3.3. Effect of Chemical Pressure on the BaF_2 Crystal Structure

The effect of chemical pressure on the BaF_2 crystal was studied by simulating $Ba_{1-x}Ca_xF_2$ and $Ba_{1-x}Sr_xF_2$ mixed crystals, in which part of the Ba^{2+} ions were replaced isovalently by ions of a smaller radius. The calculations were carried out in accordance with the virtual-crystal method [17]. The cation–fluorine pairwise-interaction parameters are written in the virtual-crystal model as

$$A_{Ba_{1-x}Me_x\text{–F}}(x) = (1-x)A_{\text{Ba–F}} + xA_{Me\text{–F}}, \qquad (5)$$

where $x \in [0, 1]$ is the fraction of the impurity in the original crystal and $A_{Ba_{1-x}Me_x\text{–F}}$ is the pairwise interaction parameter for a lattice site which can be occupied by *Me* (*Me* = Ca, Sr) with a probability *x* and by Ba with a probability $(1 - x)$. The core–shell interaction constant $k_{Ba_{1-x}Me_x}$ is defined in a similar way. Our simulation yielded dependences of the lattice parameter of the $Ba_{1-x}Ca_xF_2$ and $Ba_{1-x}Sr_xF_2$ crystals on concentration *x* (Fig. 3). The results of the calculations can be fitted well using a linear relation which agrees with available experimental data: $\partial a/\partial x = -53.76$ au for $Ba_{1-x}Ca_xF_2$ and $\partial a/\partial x = -31.01$ (–39.59) au for $Ba_{1-x}Sr_xF_2$ (*a* is the

Table 3. Dependence of BaF_2 fundamental vibration frequencies on pressure

Phase	Vibration symmetry	ν_0, cm^{-1}	$\partial\nu/\partial P$, $cm^{-1}\ GPa^{-1}$
Cubic	F_{2g} (calc.)	275	6.5
	F_{2g} (exp. [14])	241	8.5 (±0.6)
	F_{1u} (calc.)	184	6.5
Orthorhombic	A_g (calc.)	91	6.5
	A_g (calc.)	283	6.7

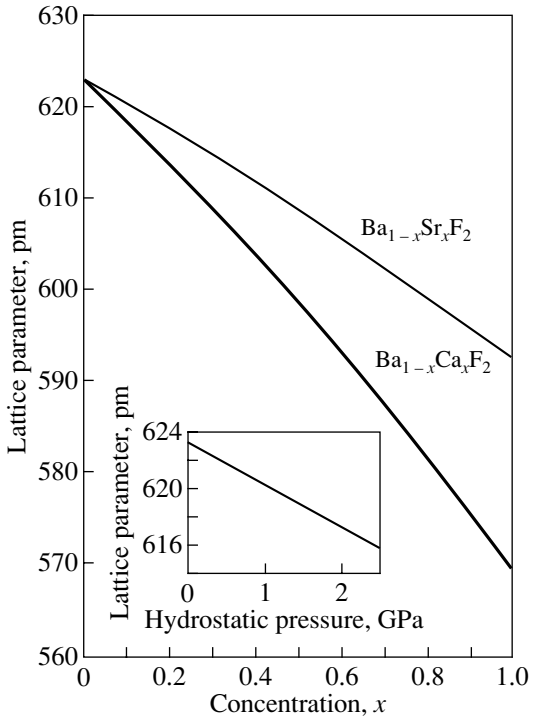

Fig. 3. Lattice parameters of cubic BaF_2 as a function of hydrostatic pressure and impurity concentration x.

lattice parameter, and the experimental data [18] are given in parentheses). A comparison of these relations with the dependence of the lattice parameter of cubic BaF_2 on external hydrostatic pressure (Fig. 3) shows that, up to the phase-transition temperature, the latter dependence follows a course similar to that of the lattice parameter as a function of concentration x for x from 0 to 15–20 at. %. The BaF_2 lattice parameter corresponding to an impurity concentration of 15–20 at. % is equal to that near the phase transition.

4. EFFECT OF HYDROSTATIC AND CHEMICAL PRESSURE ON $BaF_2 : Eu^{2+}$

This part of our study deals with finding a relation between the absorption and luminescence zero-phonon line (ZPL) shift of the Eu^{2+} ion in fluorites and an external force (hydrostatic compression and chemical pressure).

The Eu^{2+} ion in MeF_2 crystals substitutes for the cation and resides at the center of a cube made up of eight fluorine ions. The impurity absorption and luminescence spectra derive from the f^7–f^6d interconfiguration transitions [19] and can serve as indicators of internal strains in a crystal [10, 20] because the excited $\Gamma_8(f^6d)$ level is sensitive to the Eu^{2+}–F^- distance in the crystal.

The different character of Eu^{2+} luminescence in CaF_2, SrF_2, and BaF_2 crystals is connected with different positions of the Γ_8 impurity level with respect to the conduction-band bottom [21]. In CaF_2 and SrF_2, the Γ_8 level lies in the band gap and one observes narrow lines, whereas in BaF_2, the anomalous emission is due to the Γ_8 level being located in the conduction band.

Our calculations suggest that the Eu^{2+}–F^- distance in the $CaF_2 : Eu^{2+}$, $SrF_2 : Eu^{2+}$, and $BaF_2 : Eu^{2+}$ fluorites is linearly related to the external hydrostatic pressure applied to the crystal:

$$\frac{\partial r}{\partial P} = s, \tag{6}$$

where r is the impurity ion–ligand distance and P is the external pressure. Piezospectroscopic experiments show the pressure dependence of frequency in $CaF_2 : Eu^{2+}$ and $SrF_2 : Eu^{2+}$ to be linear [19, 22]:

$$\frac{\partial \nu}{\partial P} = \mu, \tag{7}$$

where ν is the frequency; P is the hydrostatic pressure; and the coefficient μ is –45.1 and –56.9 $cm^{-1}\ GPa^{-1}$ for $CaF_2 : Eu^{2+}$ and $SrF_2 : Eu^{2+}$, respectively. Thus, the dependence of frequency on distance within the given range of Eu^{2+}–F^- distance variation can be considered as linear. Equations (6) and (7) yield the coefficient for this relation:

$$\frac{\partial \nu}{\partial r} = \frac{\mu}{s} = \eta. \tag{8}$$

The coefficient η derived from the data available for $CaF_2 : Eu^{2+}$ and $SrF_2 : Eu^{2+}$ has roughly the same magnitude (9.2×10^3 and $9.6 \times 10^3\ cm^{-1}/au^{-1}$, respectively). The estimation of η from experimental data on Eu^{2+} ZPL frequencies in CaF_2 and SrF_2 [4] yields 1.006×10^4, a value close to the above figures. Thus, we can evaluate the absorption and luminescence ZPL shift of the Eu^{2+} ion in CaF_2, SrF_2, and BaF_2 as a function of the impurity ion–ligand distance by using a linear relationship.

The effect of chemical pressure on $BaF_2 : Eu^{2+}$ was studied by simulating a $Ba_{1-x}Sr_xF_2 : Eu^{2+}$ mixed crystal. The calculations yielded a dependence of the impurity ion–ligand distance on x. The coefficient η (taken equal to $1.006 \times 10^4\ cm^{-1}/au^{-1}$) makes it possible now to obtain the dependence of the ZPL shift on concentration x. According to our estimates, the ZPL shift is proportional to the strontium concentration x with a coefficient $\kappa = -1.010 \times 10^3\ cm^{-1}$. Applying Eq. (8) to mixed crystals is justified, because the nearest neighbor environment of the impurity ion (the F^- ligands) does not change when part of the host cations are replaced by cations of another species. The metal ions are located sufficiently far from the impurity ion, and the short-range interaction between the impurity ion and the metal is disregarded in our model.

The distance between the conduction-band bottom and the Γ_8 level of the Eu^{2+} ion is about 250 cm^{-1} [21]. According to our estimates, this ZPL shift in $Ba_{1-x}Sr_xF_2 : Eu^{2+}$ is reached at an impurity concentration $x \approx 30\%$.

5. CONCLUSION

Thus, we have described the first-order structural phase transition from the cubic to orthorhombic phase induced by pressure in the BaF_2 crystal in terms of the shell model and the pairwise potential approximation. We studied the effect of chemical pressure on the BaF_2 crystal by simulating $Ba_{1-x}Ca_xF_2$ and $Ba_{1-x}Sr_xF_2$ mixed crystals in which part of the Ba^{2+} ions are replaced by ions of a smaller radius. The effect of an impurity on the BaF_2 lattice parameter for concentrations x of up to 15–20 at. % is shown to be similar to that of hydrostatic pressure up to the pressure P_c, at which the phase transition occurs.

The shift of the Eu^{2+} absorption and luminescence ZPL in CaF_2, BaF_2, and SrF_2 crystals was estimated as a function of the Eu^{2+}–ligand distance. According to our calculations, this shift depends linearly on the distance with a coefficient close to 1×10^4 cm^{-1}/au^{-1}.

ACKNOWLEDGMENTS

This study was supported by the Ministry of Education (project no. E00-3.4-227) and CRDF (grant no. REC 005).

REFERENCES

1. M. Kobayashi, M. Isshi, B. P. Sobolev, Z. I. Zhmurova, and E. A. Krivandina, *Solid-State Ionizing-Radiation Detectors* (Ural. Gos. Tekh. Univ., Yekaterinburg, 1997), p. 197.
2. B. P. Sobolev, A. A. Bystrova, E. A. Krivandina, and Z. N. Zhmurova, Inf. Byull. Ross. Fond Fundam. Issled. **5** (2), 111 (1997).
3. P. Dorenbos, R. Visser, C. W. E. van Eijk, *et al.*, Nucl. Instrum. Methods Phys. Res. A **310**, 236 (1991).
4. A. A. Kaplyanskiĭ and P. P. Feofilov, Opt. Spektrosk. **13** (2), 235 (1962).
5. D. L. Wood and W. Kaiser, Phys. Rev. **126** (6), 2079 (1962).
6. B. Z. Malkin, Fiz. Tverd. Tela (Leningrad) **11** (5), 1208 (1969) [Sov. Phys. Solid State **11**, 981 (1969)].
7. Z. I. Ivanenko and B. Z. Malkin, Fiz. Tverd. Tela (Leningrad) **11** (7), 1859 (1969) [Sov. Phys. Solid State **11**, 1498 (1969)].
8. K. Kawano, H. Akahane, R. Nakata, and M. Sumita, J. Alloys Compd. **221**, 218 (1995).
9. J. M. Leger, J. Haines, A. Atouf, and O. Schulte, Phys. Rev. B **52** (18), 13247 (1995).
10. N. S. Sokolov and N. L. Yakovlev, in *Proceedings of the Tenth Feofilov Symposium on Spectroscopy of Crystals Activated by Rare-Earth Transition-Metal Ions*, Ed. by A. I. Ryskin and V. F. Masterov; Proc. SPIE **2706**, 57 (1996).
11. A. E. Nikiforov and S. Yu. Shashkin, *Spectroscopy of Crystals* (Nauka, Leningrad, 1989), p. 274.
12. V. A. Chernyshev, A. D. Gorlov, A. A. Mekhonoshin, *et al.*, Appl. Magn. Reson. **14** (1), 37 (1998).
13. A. D. Gorlov, V. B. Guseva, A. Yu. Zakharov, *et al.*, Fiz. Tverd. Tela (St. Petersburg) **40** (12), 2172 (1998) [Phys. Solid State **40**, 1969 (1998)].
14. J. R. Kessler, E. Monberg, and M. Nikol, J. Chem. Phys. **60** (2), 5057 (1974).
15. R. J. Elliott, W. Hayes, W. G. Kleppmann, *et al.*, Proc. R. Soc. London, Ser. A **360**, 317 (1978).
16. *Physics of Superionic Conductors*, Ed. by M. B. Salamon (Springer, New York, 1979; Zinatne, Riga, 1982).
17. N. J. Ramer and A. M. Rapple, J. Phys. Chem. Solids **61**, 315 (2000).
18. M. Diaz, F. Lahoz, B. Villacampa, *et al.*, J. Lumin. **81**, 53 (1999).
19. A. A. Kaplyanskiĭ and A. K. Przhevuskiĭ, Opt. Spektrosk. **19** (4), 597 (1965).
20. A. A. Kaplyanskiĭ and A. K. Przhevuskiĭ, Opt. Spektrosk. **20** (6), 1045 (1966).
21. D. S. McClure, in *Proceedings of the Tenth Feofilov Symposium on Spectroscopy of Crystals Activated by Rare-Earth Transition-Metal Ions*, Ed. by A. I. Ryskin and V. F. Masterov; Proc. SPIE **2706**, 315 (1996).
22. I. V. Ignat'ev and V. V. Ovsyankin, Opt. Spektrosk. **49** (3), 538 (1980) [Opt. Spectrosc. **49**, 292 (1980)].

Translated by G. Skrebtsov

Physics of the Solid State, Vol. 44, No. 10, 2002, pp. 1954–1960. Translated from Fizika Tverdogo Tela, Vol. 44, No. 10, 2002, pp. 1864–1869.

LATTICE DYNAMICS AND PHASE TRANSITIONS

A Study of the Phase Diagrams of $(NH_4)_3Ga_{1-x}Sc_xF_6$ Ammonium Cryolites

M. V. Gorev*, I. N. Flerov*, A. Tressaud, D. Denu**, A. I. Zaĭtsev*, and V. D. Fokina***

** Kirensky Institute of Physics, Siberian Division, Russian Academy of Sciences, Akademgorodok, Krasnoyarsk, 660036 Russia*

*** Institut de Chimie de la Matiére Condensée de Bordeaux, Pessac, F-33608 France*

e-mail: gorev@iph.krasn.ru

Received December 4, 2001

Abstract—This paper reports on the results of analyzing *p–T* and *x–T* phase diagrams and calorimetric properties of solid solutions in $(NH_4)_3Ga_{1-x}Sc_xF_6$ cryolites with scandium concentrations x = 0.0, 0.1, 0.35, 0.4, 0.6, 0.8, and 1.0. The thermodynamic parameters of the phase transitions observed in the studied compounds are determined. The generalized phase diagram and successive structural transformations in a series of $(NH_4)_3Me^{3+}F_6$ ammonium cryolites are discussed. © *2002 MAIK "Nauka/Interperiodica"*.

1. INTRODUCTION

Crystals of $(NH_4)_3Me^{3+}F_6$ ammonium cryolites in the initial high-temperature phase have a cubic lattice ($Fm\bar{3}m$, Z = 4) in which $Me^{3+}F_6$ and $(NH_4)^+F_6$ fluorine octahedra alternate along the cubic cell edges and holes between octahedra occupied by ammonium ions. As the temperature decreases, all the known ammonium cryolites undergo either single phase transitions or successive phase transitions. Recent extensive studies of ammonium cryolites with the use of different techniques have revealed a number of specific features in these transitions.

It is found that the phase transition temperatures and sequences of distorted phases formed upon phase transitions in ammonium cryolites substantially depend on the size of the trivalent cation Me^{3+}. For example, the ammonium cryolites with large-sized ions Me^{3+} (Me^{3+} = Sc or In) are characterized by a sequence of three phase transitions [1–3]. The cryolite crystals with small-sized ions Me^{3+} (Me^{3+} = Ga, V, Cr, or Fe) undergo only a first-order transition from the cubic phase to the triclinic phase [1, 2, 4]. Moriya *et al.* [5] studied the $(NH_4)_3AlF_6$ crystal with the smallest sized cation Me^{3+} (Me^{3+} = Al) and revealed two successive phase transitions in this compound.

The thermodynamic parameters of the phase transitions in ammonium cryolites have been determined from analyzing the results of heat capacity investigations [1–3, 5–8]. The large entropy change observed upon phase transitions is associated with the significant role played by ordering in structural transformations. According to the model considered in [1, 5, 6], the phase transitions in ammonium cryolites are accompanied by orientational ordering of both fluorine octahedral and ammonium tetrahedral ionic groups.

In the model of rigid fluorine regular octahedra, the fluorine ions in the cubic phase can be located either in the 24*e* positions at the cubic cell edges or in the 192*l* positions. In the latter case, each octahedron has eight equally probable orientations. The ammonium ions in the cubic cell occupy two different crystallographic positions, namely, the 8*c* and 4*b* positions. In the former case, the ammonium ions reside in holes between the octahedra and have only one orientation. In the latter case, the ammonium ions are located inside the octahedra, are disordered in accordance with the symmetry of the occupied site, and have two possible orientations. Therefore, the change in the entropy upon complete orientational ordering of octahedral and tetrahedral ionic groups can be determined as $\Delta S = R(\ln 2 + \ln 8) = R\ln 16$. This is in good agreement with the experimental results obtained for cryolites in [1, 2, 5–7].

The above model of a phase transition associated with simultaneous ordering of octahedra and tetrahedra was confirmed by nuclear magnetic resonance (NMR) investigations of gallium cryolite [9]. It was demonstrated that the spin–lattice relaxation times of both protons and fluorine ions exhibit jumps at the phase transition temperature.

Among the three successive phase transitions $G_0 \longrightarrow G_1 \longrightarrow G_2 \longrightarrow G_3$ observed in scandium cryolites, only the $G_0 \longrightarrow G_1$ phase transition at the temperature T_1 and the $G_1 \longrightarrow G_2$ transition at the temperature T_2 can be associated with orientational ordering, because it is these phase transitions that are accompanied by considerable entropy changes that are close in magnitude to $R\ln 8$ and $R\ln 2$, respectively. Sasaki *et al.* [10] performed an NMR investigation of $(NH_4)_3InF_6$ indium crystals, which can also undergo three successive phase transitions [1], and revealed that the spin–lattice relaxation times show anomalous behavior only

at temperatures T_1 and T_2. It was found that the motion of fluorine ions changes significantly at both temperatures T_1 and T_2. Therefore, the change in the entropy upon phase transition from the cubic phase is due to ordering of ammonium tetrahedra (R ln2) and partial ordering of octahedra (Rln4) [2, 4, 8]. The complete ordering of the octahedra occurs upon the second phase transition ($\Delta S_2 = R\ln 2$). The third phase transition is a clearly defined first-order transition with an extremely large hysteresis and a small change in entropy [2, 8]. It can be assumed that the G_2 and G_3 phases represent two completely ordered variants of the initial phase and differ from each other only in the orientation of tetrahedra in the 4*b* position.

The effect of hydrostatic pressure and a decrease in the size of the Me^{3+} ion bring about a decrease in the unit cell volume of the studied crystal and a change in the interactions in the crystal lattice and, hence, should affect the temperature and sequences of structural transformations. The *p–T* phase diagrams of $(NH_4)_3ScF_6$ and $(NH_4)_3GaF_6$ ammonium cryolites were analyzed in our earlier works [3, 8]. For both compounds studied under pressure, we revealed triple points and changes in the sequence of structural distortions. At high pressures, the scandium cryolite undergoes a direct phase transition $G_0 \longrightarrow G_3$, whereas the gallium cryolite is characterized by a sequence of pressure-induced phase transformations $G_0 \longrightarrow G_4 \longrightarrow G_5 \longrightarrow G_3$. It was assumed that the phase diagram of the gallium cryolite is a continuation of the phase diagram of the scandium cryolite toward the high-pressure range.

The aim of the present work was to reveal the interrelation between different successive structural distortions in ammonium cryolites and to construct a generalized phase diagram, including all the phase transitions observed under atmospheric and higher pressures in $(NH_4)_3Me^{3+}F_6$ crystals. For this purpose, we investigated the heat capacity of $(NH_4)_3Ga_xSc_{1-x}F_6$ solid solutions and analyzed the influence of hydrostatic pressure on the temperature of phase transitions in these compounds.

2. SAMPLE PREPARATION

Solid solutions of $(NH_4)_3Ga_{1-x}Sc_xF_6$ cryolites with scandium concentrations $x = 0.0$, 0.1, 0.35, 0.4, 0.6, 0.8, and 1.0 were prepared in the form of a finely dispersed powder through solid-phase synthesis at a temperature of 600 K. The initial reactants $(NH_4)_3GaF_6$ and $(NH_4)_3ScF_6$ were taken in appropriate molar proportions and placed in platinum tubes, which were then sealed in an argon atmosphere. The compounds synthesized were identified using an x-ray diffractometer. It was established that the samples prepared were crystalline compounds with a cryolite structure. No indications of the presence of the initial compounds (more than 5%) in the resultant solid solutions were revealed. At room temperature, the ammonium compounds with scandium concentrations $x = 0.6$, 0.4, 0.35, and 0.1 had a cubic structure, whereas the solid solution with $x = 0.8$ exhibited monoclinic symmetry, which corresponded to one of the distorted phases of the scandium cryolite. In the last-mentioned sample, the cubic phase was observed at temperatures above ~330 K.

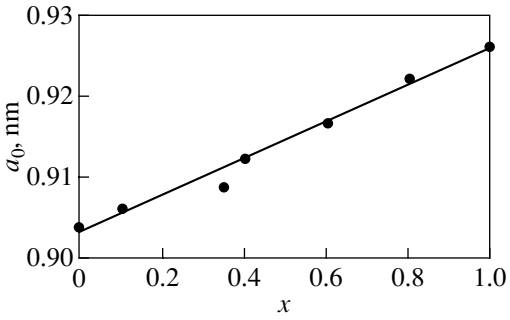

Fig. 1. Dependence of the unit cell parameter a_0 of the cubic phase in $(NH_4)_3Ga_{1-x}Sc_xF_6$ solid solutions on the scandium concentration x.

3. RESULTS AND DISCUSSION

The unit cell parameters a_0 in the cubic phase were calculated from the x-ray diffraction data. According to the Vegard rule [9], a continuous series of solid solutions of two compounds is characterized by a linear relationship between the unit cell parameter a_0 and the concentration x of the solid solution. As can be seen from Fig. 1, the unit cell parameters a_0 of all the studied compounds are well approximated by a straight line. The only exception is the solid solution with $x = 0.35$, for which the deviations from the approximating line are equal to ~0.1 for the concentration x and 0.002 nm for the unit cell parameter. The accuracy in the x-ray diffraction determination of the unit cell parameter a_0 is ~0.001 nm. The problem of accuracy in the determination of the concentration x will be considered below when analyzing the results of the calorimetric measurements.

The results of differential scanning microcalorimetric (DSM) analysis of the solid solutions in the temperature range 150–350 K are displayed in Fig. 2. In this range of temperatures, the initial cryolites undergo phase transitions and mixed cryolites can form distorted phases.

It can be seen from Fig. 2 that the heat capacity of the pure scandium cryolite and mixed compounds with scandium concentrations $x = 0.8$ and 0.6 exhibits three peaks attributed to three phase transitions. As the scandium concentration decreases, the temperature ranges of existence of the intermediate distorted phases G_1 and G_2 become narrower and vanish at concentrations x in the range from 0.6 to 0.4 (Fig. 3). Reasoning from the

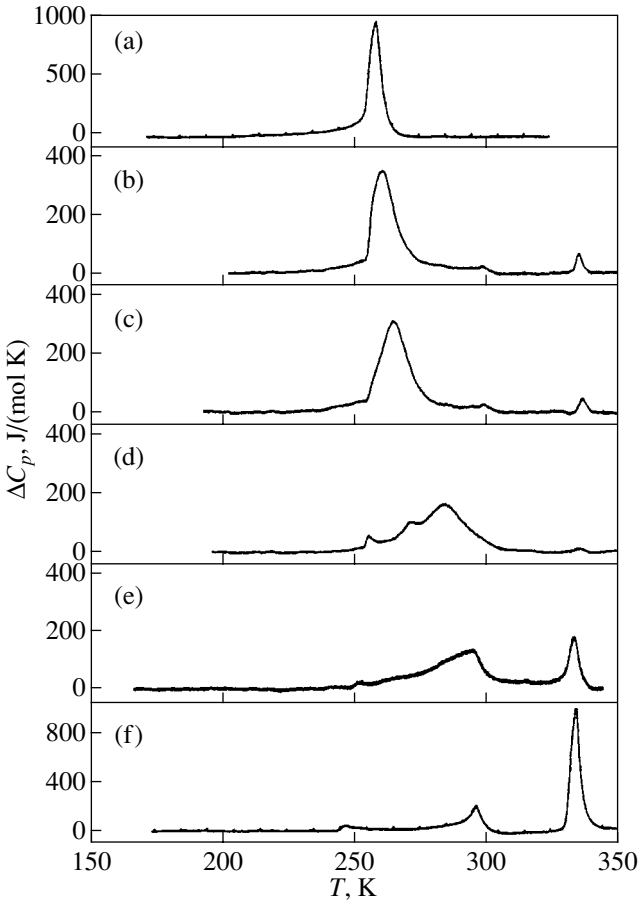

Fig. 2. DSM curves for $(NH_4)_3Ga_{1-x}Sc_xF_6$ solid solutions at different scandium concentrations x: (a) 0, (b) 0.35, (c) 0.4, (d) 0.6, (e) 0.8, and (f) 1.0.

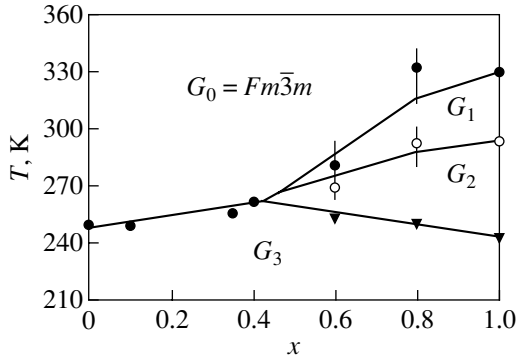

Fig. 3. Dependence of the temperature of phase transitions in $(NH_4)_3Ga_{1-x}Sc_xF_6$ solid solutions on the scandium concentration x.

anomalies observed in the heat capacity (Fig. 2), we can draw the conclusion that the solid solutions with concentrations $x = 0.4$ and 0.35 undergo only one phase transition. However, the DSM curve of the solid solution with $x = 0.4$ has inflection points in the temperature ranges approximately 10 K above and below the temperature of the main maximum in the heat capacity ΔC_p (at ~262 K), which can also be attributed to phase transitions with close temperatures.

It should also be noted that all the studied compounds are characterized by small anomalies in the heat capacity whose temperatures remain constant with a change in the composition of the solid solution. These temperatures are in satisfactory agreement with the phase transition temperatures $T_1 = 330$ K and $T_2 = 291$ K for the scandium cryolite. The latter circumstance indicates that a certain part of $(NH_4)_3ScF_6$ did not react in the course of the solid-phase synthesis. However, as was noted above, the x-ray diffraction analysis did not reveal the initial compounds in the solid solutions to within the accuracy of the analysis. The amount of $(NH_4)_3ScF_6$ which did not enter into the solid-phase reaction according to the results of calorimetric measurements was determined by comparing the enthalpy of the phase transition in the scandium cryolite and the thermal effect observed in the solid solutions at a temperature of 330 K. It was found that, in different samples, the calculated content of unreacted $(NH_4)_3ScF_6$ varies from 1 to 4%; i.e., it is within the sensitivity of the x-ray diffraction method used in our measurements.

The accuracy in the determination of the phase transition temperatures of the solid solutions under investigation (Fig. 3) is not very high because of the considerable smearing and overlapping of the heat capacity anomalies. For this reason, we determined only the total entropy change for the solid solution with $x = 0.6$. In this case, the total entropy change was found to be equal to $2.02R$. The thermodynamic parameters of the phase transitions in solid solutions were determined with due regard for the content of unreacted initial components.

The choice of samples for further comprehensive investigations into the thermodynamic properties was made for the following reasons. In our earlier work [2], we performed a detailed calorimetric analysis of the solid solution with $x = 0.1$ and revealed that this compound undergoes one phase transition similar to the phase transformation in gallium cryolite under atmospheric pressure. Consequently, in the present work, we examined only the effect of hydrostatic pressure on the temperature of the phase transformation in this compound. According to the x–T phase diagram (Fig. 3), the solid solutions with scandium concentrations $x = 0.4$ and 0.6 are close in composition to the points at which the temperature ranges of existence of the intermediate phases G_1 and G_2 vanish. In this respect, the samples with concentrations $x = 0.4$ and 0.6 proved to be the most convenient objects for the investigation of the disappearance of the intermediate phases with a decrease in the volume of the unit cell under pressure. Moreover, the heat capacity of the solid solution with $x = 0.4$ was measured using an adiabatic calorimeter in order to refine the DSM data on the number of phase transitions.

The heat capacity was measured in the course of discrete and continuous heating in the temperature range 80–320 K. A 1.05-g sample was placed in an indium tube, which was then hermetically sealed in a helium atmosphere. The heat capacity of the tube was measured in a separate experiment. The spread of experimental points about the smoothed curve did not exceed 0.5%. As can be seen from Fig. 4, the temperature dependence of the heat capacity, like the DSM curves (Fig. 2c), exhibits a small anomaly at a temperature of ~295 K due to the presence of a minor amount of scandium cryolite in the studied sample. The principal peak of the heat capacity at $T \sim 262$ K also has inflections, which, most likely, can be associated with composition inhomogeneities of the sample, because $(NH_4)_3GaF_6$ and $(NH_4)_3ScF_6$ cryolites in this range of temperatures are characterized by heat capacity anomalies due to phase transitions. However, we cannot rule out the possibility that the second phase transition occurs below the temperature of the main anomaly in the heat capacity. The total entropy change upon the phase transition in the solid solution with $x = 0.4$ is estimated as $\Delta S = (2.6 \pm 0.2)R$ (Fig. 4b). This result is in good agreement with the total changes in the entropy of other cryolites [1–3, 5–8] and the solid solutions studied in the present work (see table).

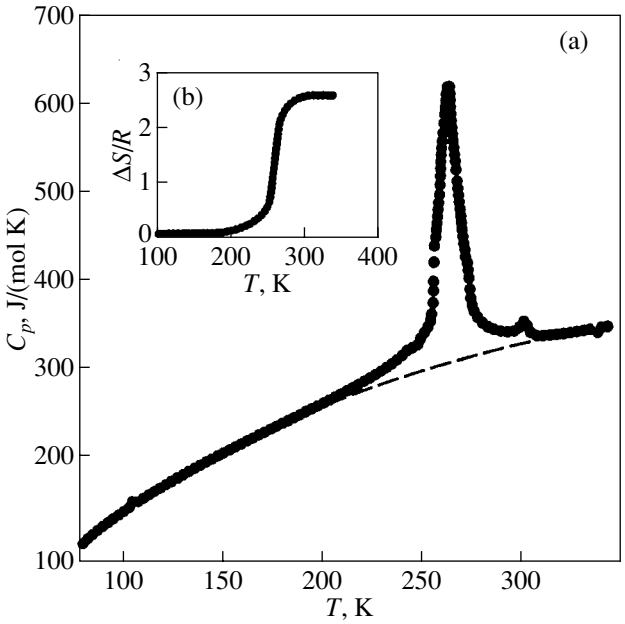

Fig. 4. Temperature dependences of (a) the heat capacity and (b) the entropy change in the $(NH_4)_3Ga_{0.6}Sc_{0.4}F_6$ solid solution. The dashed line shows the lattice heat capacity.

The influence of hydrostatic pressure on the phase transition temperatures was examined with samples weighing approximately 0.2 g. The phase transition temperatures and their changes under pressure were measured using differential thermal analysis [8, 11]. A pressure as high as 0.6 GPa was produced in a chamber of the cylinder–piston type. A mixture of silicone oil and pentane was used as a pressure transmitting medium. In the chamber, the pressure was measured by a manganin resistance pressure gauge and the temperature was measured using a copper–constantan thermocouple. The errors in measurements were equal to $\pm 10^{-3}$ GPa and ±0.3 K, respectively. The reliability of the results obtained was checked by measuring the shifts in the phase transition temperatures with both an increase and a decrease in the hydrostatic pressure. Figure 5 shows the phase diagrams of solid solutions with scandium concentrations $x = 0.4$ and 0.6 and the phase diagrams obtained for $(NH_4)_3GaF_6$ and $(NH_4)_3ScF_6$ cryolites in our earlier work [8]. Since the addition of 10% Sc does not substantially affect the parameters of the phase diagram of the gallium cryolite, it is not shown in the figure.

It is found that the $(NH_4)_3Ga_{0.4}Sc_{0.6}F_6$ cryolite undergoes three phase transitions at $p = 0$; however, the disappearance of the distorted phase G_1 occurs at a lower pressure (0.22 GPa) compared to that in the scandium cryolite (0.52 GPa). The second triple point, at which the G_2 phase disappears, is observed in the experiments under a pressure of 0.38 GPa. For $(NH_4)_3ScF_6$, we succeeded in determining the parameters of this point (1.2 GPa) only through the extrapolation of the phase boundaries $G_0 \longrightarrow G_3$ and $G_2 \longrightarrow G_3$ [8].

The identification of the phase boundaries presents no special problems in any of the studied compounds, except for $(NH_4)_3Ga_{0.6}Sc_{0.4}F_6$. In this compound, as was already noted in analyzing the DSM data, the low-temperature anomaly can be associated with both the second phase transition $G_2 \longrightarrow G_3$ and the presence of small amounts of initial cryolites in the studied sample. This anomaly is small compared to the anomaly observed upon the $G_0 \longrightarrow G_3$ transition from the cubic phase, it is substantially smeared, and it is not observed at pressures above 0.05 GPa. Moreover, this anomaly cannot be assigned with confidence to a phase transformation similar to the $G_2 \longrightarrow G_3$ transition in the scandium cryolite, judging from its temperature behavior with a change in pressure. At a pressure of 0.3 GPa, the boundary between the G_0 and G_3 phases has a clearly defined kink, which, most likely, can be associated with the presence of the triple point characterized by the phase transitions $G_0 \longrightarrow G_3 \longrightarrow G_5$. This assumption is confirmed by the pressure ratio (0.05 GPa) at the triple points for $(NH_4)_3Ga_{0.6}Sc_{0.4}F_6$ and gallium cryolite [8]. The $G_5 \longrightarrow G_3$ phase transition was not observed in our experiments. This can be explained by the insignificant thermal effect and smearing of the heat capacity anomaly at high pressures.

The table presents the quantities dT/dp for all the phase transitions observed in the experiments under pressure.

Thermodynamic parameters of the phase transitions in $(NH_4)_3Ga_{1-x}Sc_xF_6$ cryolites

Phase transition	Thermodynamic parameters	x						
		0	0.1	0.35	0.4	0.6	0.8	1
$G_0 \longrightarrow G_1$	$\Delta S/R$						~1	1.63
	dT/dp, K/GPa					–8.2		–16.4
$G_1 \longrightarrow G_2$	$\Delta S/R$						~1	0.81
	dT/dp, K/GPa					46.4		57.5
$G_2 \longrightarrow G_3$	$\Delta S/R$						~0.05	0.08
	dT/dp, K/GPa					65.2		59.9
$G_0 \longrightarrow G_2$	$\Delta S/R$							
	dT/dp, K/GPa							
$G_0 \longrightarrow G_3$	$\Delta S/R$	2.76	2.56	2.16	2.60			
	dT/dp, K/GPa	–12.1	–6.5		–15.3	–8.1		
$G_0 \longrightarrow G_4$	$\Delta S/R$							
	dT/dp, K/GPa	101.3	100.8					
$G_4 \longrightarrow G_5$	$\Delta S/R$							
	dT/dp, K/GPa	~0	–8.8					
$G_5 \longrightarrow G_3$	$\Delta S/R$							
	dT/dp, K/GPa	–22.5	–26.3					
$G_0 \longrightarrow G_5$	$\Delta S/R$							
	dT/dp, K/GPa	73.1	82.3		60.1			
References		[2.8]	[2]					[2, 8]

Reasoning from the analysis of the entropy changes upon phase transitions and p–T phase diagrams of the studied compounds, we constructed a generalized phase diagram (Fig. 6) including all structural transformations observed in the ammonium cryolites. The dashed lines in Fig. 6 indicate regions corresponding to the experimentally observed phase diagrams of the studied compounds.

The $(NH_4)_3ScF_6$ cryolite is characterized by the largest unit cell volume and, under atmospheric pres-

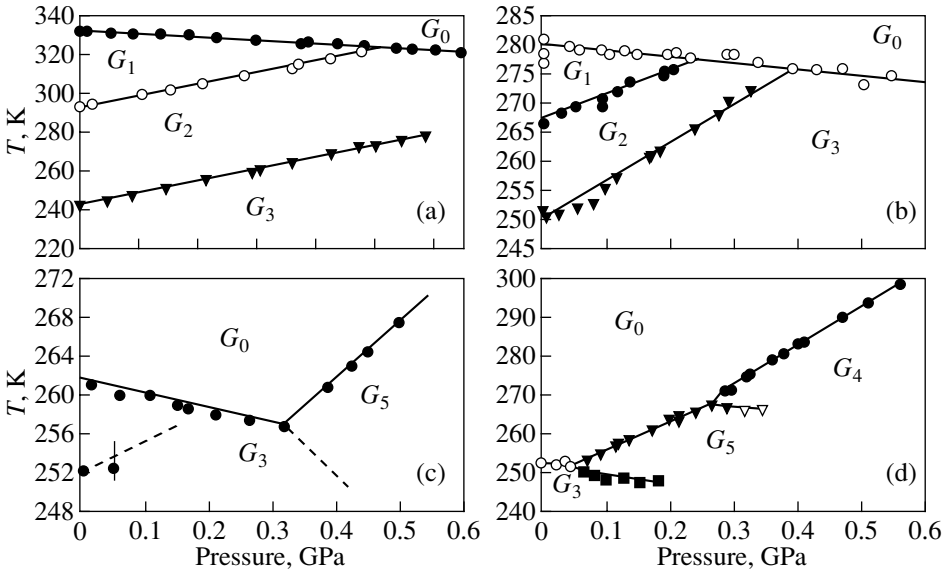

Fig. 5. Phase p–T diagrams for (a) $(NH_4)_3ScF_6$ [8], (b) $(NH_4)_3Ga_{0.4}Sc_{0.6}F_6$, (c) $(NH_4)_3Ga_{0.6}Sc_{0.4}F_6$, and (d) $(NH_4)_3GaF_6$ compounds [8].

sure, undergoes three successive phase transitions $G_0 \longrightarrow G_1 \longrightarrow G_2 \longrightarrow G_3$. The first phase transition is accompanied by the partial ordering of fluorine octahedra ($\Delta S = R\ln 8/2 = 1.4R$). The change in symmetry of the crystallographic positions occupied by ammonium ions inevitably results in complete ordering of ammonium tetrahedra arranged inside the octahedra ($\Delta S = R\ln 2 = 0.7R$). The second phase transition leads to complete ordering of fluorine octahedra ($\Delta S = R\ln 2$). The third phase transition $G_2 \longrightarrow G_3$ is attended by a small entropy change and is unrelated to ordering processes. It seems likely that the third phase transition is a transition between completely ordered phases with different types of ordering of ammonium groups. Preliminary results of investigations into the properties of deuterated cryolites have demonstrated that the deuteration of the initial cryolites substantially affects the temperature of only the third phase transition.

As the pressure increases or, what is the same, the unit cell volume decreases with a decrease in the scandium concentration in the solid solutions, the temperature of the phase transition $G_0 \longrightarrow G_1$ decreases, whereas the temperatures of the other two transitions $G_1 \longrightarrow G_2$ and $G_2 \longrightarrow G_3$ increase. The G_1 and G_2 phases sequentially disappear at two triple points, which are experimentally observed in the scandium cryolite (Fig. 5a) and in the $(NH_4)_3Ga_{0.4}Sc_{0.6}F_6$ solid solution (Fig. 5b). With a further increase in the pressure, the phase transition $G_0 \longrightarrow G_3$ is split at triple points, first, into two phase transitions $G_0 \longrightarrow G_5 \longrightarrow G_3$ and, then, into three phase transitions $G_0 \longrightarrow G_4 \longrightarrow G_5 \longrightarrow G_3$. These sequences of phase transitions and the triple points are observed in the $(NH_4)_3Ga_{0.6}Sc_{0.4}F_6$ solid solution (Fig. 5c) and gallium cryolite (Fig. 5d) in the experiments under pressure.

The occurrence of two different sequences of phase transitions, namely, $G_0 \longrightarrow G_1 \longrightarrow G_2 \longrightarrow G_3$, at low pressures (large parameters a_0 of the cubic unit cell) and $G_0 \longrightarrow G_4 \longrightarrow G_5 \longrightarrow G_3$ at high pressures (small parameters a_0 of the cubic unit cell), can be associated with the presence of two possible variants of partial ordering of octahedral ionic groups in the G_1 phase, as is the case with the distortions (0 0 ψ) and (0 ψ ψ) in elpasolites containing atomic ions A^+ and Me^{3+} [12].

The existing model of phase transitions is based primarily on the experimentally found changes in the entropy and symmetry of crystallographic positions occupied by ordered ions in the initial phase. To the best of our knowledge, there is no reliable experimental evidence for this disordering of octahedra and tetrahedra. Massa *et al.* [13] made an attempt to interpret x-ray diffraction data in the framework of the model of orientationally disordered octahedra for some elpasolites with atomic cations. It was shown that the fluorine ions are displaced from the edge of the cubic unit cell and can occupy the crystallographic positions 96*k*, 96*j*, or 192*l*. Unfortunately, these authors could not uniquely determine the fluorine-occupied position reasoning only from data on the *R* factor, even though they were inclined to choose the variant 96*j* [13]. However, in this case, the phase transition should result in a distortion of the octahedra, which was not supported by experimental results. In our earlier work [12], we demonstrated that elpasolites with atomic cations undergo displacive phase transitions and that the motion of fluorine ions is characterized by substantial anharmonicity and anisotropy rather than by hopping between local disordered positions.

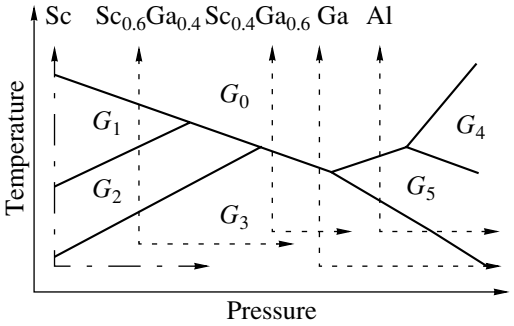

Fig. 6. Generalized phase diagram of $(NH_4)_3Me^{3+}F_6$ ammonium cryolites.

As follows from preliminary x-ray diffraction investigations of the structure of the $(NH_4)_3GaF_6$ ammonium cryolite, the cubic phase can be well refined under the assumption that the fluorine ions are disordered over the 192*l* positions.

For $(NH_4)_3ScF_6$ and $(NH_4)_3GaF_6$ cryolites, the symmetry of disordered phases was analyzed earlier in [3, 14]. It was found that scandium cryolite is characterized by the following sequence of phases: $G_1 = G_{2h}^5(P12_1/n1, Z = 2)$, $G_2 = G_{2h}^3(I12/m1, Z = 16)$, and $G_3 = G_i^1(P\bar{1}, Z = 16)$. The structure of the low-temperature phase in gallium cryolite is identical to that of the G_3 phase in scandium cryolite [14]. We observed the G_4 and G_5 phases in the studied system only under pressure. However, it is quite possible that the G_5 phase corresponds to an intermediate phase in the $(NH_4)_3AlF_6$ cryolite characterized by two phase transitions at $p = 0$ [5]. Unfortunately, the structure of the $(NH_4)_3AlF_6$ cryolite has not been studied thoroughly; it is only known that, at a temperature of 93 K, the structure of $(NH_4)_3AlF_6$ is not cubic [15]. Detailed investigations into the structure of distorted phases and the *p*–*T* phase diagram of this compound could refine the generalized phase diagram and mechanisms of phase transformations in cryolites.

ACKNOWLEDGMENTS

We would like to thank A.D. Vasil'ev for his participation in discussions of the results obtained in our

investigation and helpful speculations regarding the character of disordering of fluorine ions in the cubic phase of $(NH_4)_3GaF_6$.

This work was supported by the International Association of Assistance for the Promotion of Cooperation with Scientists from the New Independent States of the Former Soviet Union (project INTAS no. 97-10177) and the Russian Foundation for Basic Research (project nos. 00-02-16034 and 00-15-96790).

REFERENCES

1. A. Tressaud, S. Khairoun, L. Rabardel, *et al.*, Phys. Status Solidi A **98** (2), 407 (1986).
2. I. N. Flerov, M. V. Gorev, and T. V. Ushakova, Fiz. Tverd. Tela (St. Petersburg) **41** (3), 523 (1999) [Phys. Solid State **41**, 468 (1999)].
3. M. V. Gorev, I. N. Flerov, S. V. Mel'nikova, *et al.*, Izv. Akad. Nauk, Ser. Fiz. **64** (6), 1104 (2000).
4. M. Epple, Thesis (Univ. of Tübingen, Tübingen, 1978).
5. K. Moriya, T. Matsuo, H. Suga, and S. Seki, Bull. Chem. Soc. Jpn. **52** (11), 3152 (1979).
6. K. Moriya, T. Matsuo, H. Suga, and S. Seki, Bull. Chem. Soc. Jpn. **50** (8), 1920 (1977).
7. K. Kobayashi, T. Matsuo, H. Suga, *et al.*, Solid State Commun. **53** (8), 719 (1985).
8. M. V. Gorev, I. N. Flerov, and A. Tressaud, J. Phys.: Condens. Matter **11**, 749 (1999).
9. L. Vegard, Z. Phys. **5**, 17 (1921).
10. A. Sasaki, Y. Furukawa, and D. Nakamura, Ber. Bunsen-Ges. Phys. Chem. **93**, 1142 (1989).
11. M. V. Gorev and I. N. Flerov, Fiz. Tverd. Tela (St. Petersburg) **34** (8), 2614 (1992) [Sov. Phys. Solid State **34**, 1401 (1992)].
12. I. N. Flerov, M. V. Gorev, K. S. Aleksandrov, *et al.*, Mater. Sci. Eng. R **24** (3), 81 (1998).
13. W. Massa, D. Babel, and M. Epple, Rev. Chim. Miner. **23**, 508 (1986).
14. S. V. Mel'nikova, S. V. Misyul', A. F. Bovina, and M. L. Afanas'ev, Fiz. Tverd. Tela (St. Petersburg) **43** (8), 1533 (2001) [Phys. Solid State **43**, 1594 (2001)].
15. E. G. Steward and H. P. Rooksby, Acta Crystallogr. **6**, 49 (1953).

Translated by O. Borovik-Romanova

Physics of the Solid State, Vol. 44, No. 10, 2002, pp. 1961–1966. Translated from Fizika Tverdogo Tela, Vol. 44, No. 10, 2002, pp. 1870–1875.

LATTICE DYNAMICS AND PHASE TRANSITIONS

The Influence of Deuteration on the Phase Transitions in $(NH_4)_3Me^{3+}F_6$ Cryolites (Me^{3+} = Sc and Ga)

I. N. Flerov, M. V. Gorev, M. L. Afanas'ev, and T. V. Ushakova

Kirensky Institute of Physics, Siberian Division, Russian Academy of Sciences, Akademgorodok, Krasnoyarsk, 660036 Russia
e-mail: flerov@ksc.krasn.ru

Received December 4, 2001

Abstract—The heat capacity of partially deuterated crystals with a cryolite structure, namely, $(NH_4)_3ScF_6$ and $(NH_4)_3GaF_6$, is measured in the temperature range from 80 to 370 K. The p–T phase diagrams of these compounds are investigated at pressures up to p = 0.6 GPa. It is revealed that the deuteration does not affect the sequences of phase transitions observed in the proton-containing ammonium cryolites studied earlier. The isotope effect most clearly manifests itself in significant changes in the thermodynamic parameters of the $I12/m1$–$P\bar{1}$ low-temperature transformation in scandium cryolite. *© 2002 MAIK "Nauka/Interperiodica".*

1. INTRODUCTION

Ammonium fluoride cryolites of the general formula $(NH_4)_3Me^{3+}F_6$ with a high-temperature cubic phase ($Fm\bar{3}m$, z = 4) have been studied using different physical methods in sufficient detail [1–6]. The cryolite structure represents a three-dimensional framework consisting of vortex-shared octahedra whose centers are occupied by one of the three $(NH_4)^+$ ions and one Me^{3+} ion in an alternating manner. These ions are located in the crystallographic positions 4*b* and 4*a*, respectively. The other two ammonium ions occupy the 8*c* positions in polyhedral holes formed by faces of the surrounding octahedra. It is established that the size of the Me^{3+} ion substantially affects the sequence and temperature of the phase transitions. For example, the $(NH_4)_3GaF_6$ crystal undergoes one ferroelastic phase transition $Fm\bar{3}m$–$P\bar{1}$ [1, 2, 6], whereas the $(NH_4)_3ScF_6$ crystal can undergo three successive phase transitions $Fm\bar{3}m$–$P12_1/n1$–$I12/m1$–$P\bar{1}$ [2, 5]. It is found that the entropy change associated with the triclinic distortion remains constant irrespective of the sequence of phase transitions. According to the model considered in [1, 2, 4], the octahedral $(Me^{3+}F_6)^-$ and tetrahedral $(NH_4)^+$ ionic groups are disordered in the cubic phase over eight and two equivalent positions, respectively. It should be noted that only the $(NH_4)^+$ tetrahedra located in the 4*b* position at the centers of the $(NH_4)F_6^-$ octahedra are disordered.

As follows from analyzing the results of calorimetric [2] and nuclear magnetic resonance (NMR) [3] measurements, the lowering of symmetry to monoclinic in the $(NH_4)_3ScF_6$ cryolite due to a phase transition at the temperature T_1 can be caused by partial ordering of the octahedra and ordering of the tetrahedra, whereas the phase transition between two monoclinic phases at the temperature T_2 is most likely associated with complete ordering of the octahedra involved. However, the phase transition between the monoclinic and triclinic phases at the temperature T_3 in scandium cryolite cannot be considered to be a transformation of the order–disorder type because of the very small change in the entropy [2]. The question as to the nature of this transition remains open.

One way to verify the assumption regarding the mechanism of phase transitions in ammonium-containing compounds is to examine their deuterated analogs. It is known that hydrogen bonding plays a decisive role in structural transformations, whereas the substitution of deuterons for protons, as a rule, most clearly manifests itself in the behavior of thermodynamic parameters such as the temperature and entropy of the phase transition and sensitivity to external pressures [7].

In particular, the isotope effect proved to be rather significant in cryolite-related compounds of the general formula $(NH_4)_2Me^{4+}Cl_6$ with an antifluorite structure ($Fm\bar{3}m$, z = 4). In the crystal structure of these compounds, the ammonium ions occupy only the 8*c* positions, whereas the second octahedron remains unoccupied. Muraoka and Matsuo [8] revealed that the deuteration of $(NH_4)_2PtCl_6$ crystals undergoing one phase transition at T_1 = 78 K leads to a slight increase in the temperature of this transition (T_1 = 81 K), on the one hand, and induces another phase transition in the vicinity of 38 K, on the other hand. Kume *et al.* [9] observed an even more interesting phenomenon upon deuteration of the $(NH_4)_2TeCl_6$ antifluorite, which undergoes a transition from the cubic phase to the rhombohedral phase at T = 88 K. For the deuterated compound, the temperature of this transition remains virtually unchanged;

however, at temperatures of 47 and 38 K, there occur additional structural transformations into the monoclinic and tetragonal phases, respectively.

According to the model considered in [1, 4], the cryolite structure is characterized by ordered tetrahedra in crystallographic positions with the coordination number CN = 12. However, Parsonage and Stavely [7] demonstrated that the N–H···F hydrogen bond in antifluorites is disordered with respect to the three nearest fluorine atoms forming the octahedron face. One of the possible reasons for the different degrees of ordering of ammonium groups located at the same crystallographic positions (8*c*) in related structures can be the presence or absence of an ammonium ion in the 4*b* position at the center of one of the octahedra.

The purpose of the present work was to elucidate how the substitution of deuterium for hydrogen affects the sequences of phase transitions occurring in $(NH_4)_3ScF_6$ and $(NH_4)_3GaF_6$ cryolites. The results obtained can provide better insight into the role played by ammonium tetrahedra and (or) hydrogen atoms in the mechanism of distortion of the cryolite structure. To the best of our knowledge, similar investigations have never been performed. In the nearest future, the deuterated cryolites will be examined using neutron diffraction with the aim of refining the coordinates of hydrogen atoms in the initial cubic phase and investigating the structures of distorted phases, specifically of those induced by high pressure [2].

2. SAMPLE PREPARATION AND EXPERIMENTAL TECHNIQUES

The deuterated ammonium cryolites were prepared according to the following procedure. First, we synthesized the hydrogen-containing compounds through the dissolution of Sc_2O_3 and Ga_2O_3 oxides and NH_4HF in hydrofluoric acid (50 vol %) at a temperature of 100°C. After the evaporation of the resultant solution, the precipitate was recrystallized from distilled water with the formation of $(NH_4)_3ScF_6$ and $(NH_4)_3GaF_6$ crystalline powders. Then, these powders were subjected to fourfold recrystallization from D_2O.

The degree of deuteration of the samples prepared was determined by comparing the integral intensities of the ^1H NMR signals taken from $(NH_4)_3ScF_6$ and $(NH_4)_3GaF_6$ and the synthesized analogs $(ND_4)_3ScF_6$ and $(ND_4)_3GaF_6$. It turned out that the substitution of deuterium for hydrogen in scandium cryolite is more efficient than that in gallium cryolite. In the former compound, the degree of deuteration was equal to 78%. In the latter compound, the degree of deuteration proved to be appreciably less (only 20%). In our opinion, this can be associated in particular with the fact that gallium cryolite is less soluble in heavy water.

Since the deuteration in the studied compounds is not complete, the question arises as to which crystallographic positions are occupied by ND_4^+ and NH_4^+ ions, whose ionic radii considerably differ from each other. According to the stability criterion of the $Fm\bar{3}m$ structure [10], the larger sized cation should occupy the 8*c* position in a hole between octahedra. Apparently, it is these positions that are occupied by the ND_4^+ groups in the deuterated $(ND_4)_3GaF_6$ cryolite. In the $(ND_4)_3ScF_6$ compound, the ND_4^+ ions most likely occupy the larger part of 8*c* positions and a certain part of 4*b* positions at the centers of the octahedra.

X-ray diffraction analysis of the studied samples revealed that the deuteration of the $(NH_4)_3ScF_6$ cryolite leads to an increase in the volume of the unit cell of the monoclinic phase at room temperature by approximately 0.5%.

Preliminary calorimetric investigations were carried out using a DSM-2M differential scanning calorimeter. These experiments demonstrated that no radical changes occur in the sequences and temperatures of the phase transitions observed in the deuterated compounds.

Precision measurements of the heat capacity were performed on an adiabatic calorimeter over a wide range of temperatures in the course of discrete and continuous heating by analogy with our earlier measurements of the heat capacity of proton-containing ammonium cryolites [11]. The weighed portions of the scandium and gallium cryolites were equal to 1.069 and 0.985 g, respectively.

The pressure–temperature phase diagrams were constructed from the results of investigations into the effect of hydrostatic pressure on the phase transition temperatures measured using differential thermal analysis [2].

3. RESULTS AND DISCUSSION

Figure 1 presents the results of our measurements of the heat capacity $C_p(T)$ for $(ND_4)_3ScF_6$ and $(ND_4)_3GaF_6$ deuterated cryolites over a wide range of temperatures. It can be seen from Fig. 1 that the heat capacity of $(ND_4)_3ScF_6$ and $(ND_4)_3GaF_6$ exhibits three and one anomalies, respectively, due to phase transitions observed earlier in the proton-containing analogs $(NH_4)_3ScF_6$ and $(NH_4)_3GaF_6$ [2, 11]. The phase transition temperatures and the behavior of the heat capacity in the vicinity of these temperatures were refined using continuous heating (cooling) at a low rate of temperature change: $|dT/dt| \approx 2 \times 10^{-2}$ K/min. The quasi-static thermograms depicted in Fig. 2 for both deuterated cryolites upon transition from the cubic phase at the temperature T_1 are typical of first-order transformations. As follows from the table, the deuteration of both cryolites brings about an insignificant increase in the temperature T_1 and temperature hysteresis δT_1. At the same time, the latent heat δH_1 of the phase transition remains

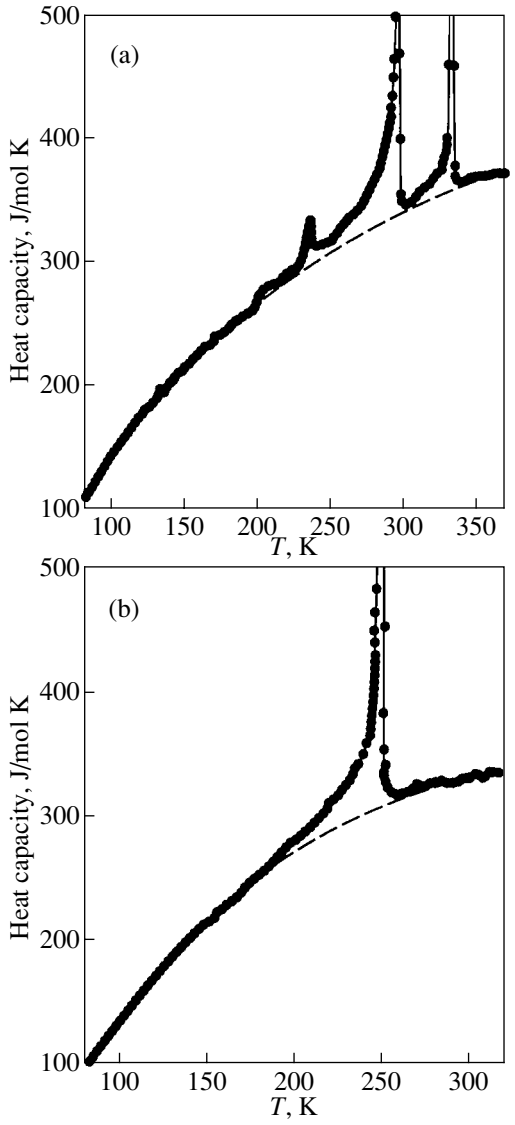

Fig. 1. Temperature dependences of the heat capacity for (a) $(ND_4)_3ScF_6$ and (b) $(ND_4)_3GaF_6$ deuterated cryolites. The dashed line shows the lattice heat capacity.

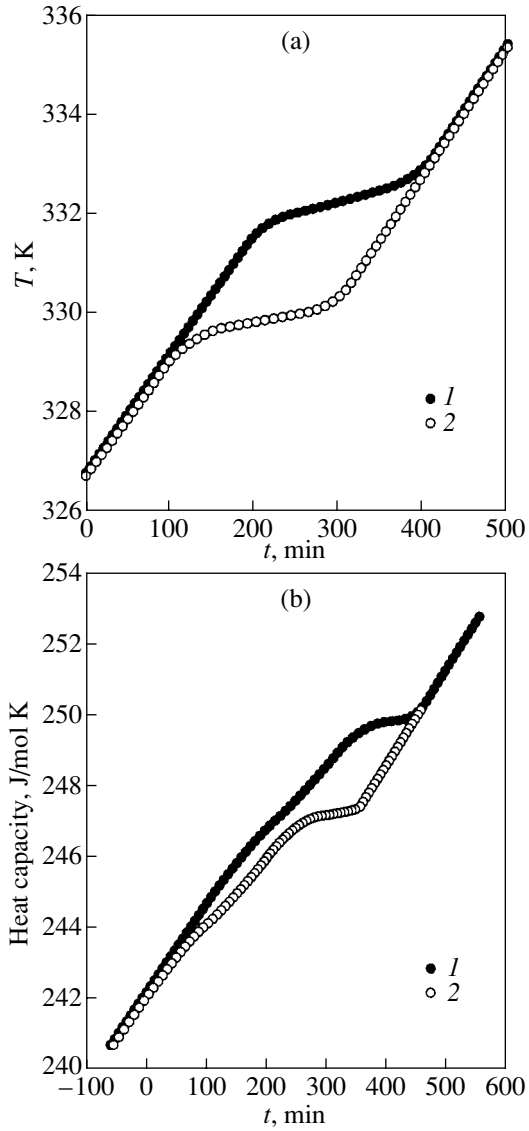

Fig. 2. Thermograms measured in the course of (*1*) heating and (*2*) cooling in the vicinity of the phase transition from the cubic phase in (a) $(ND_4)_3ScF_6$ and (b) $(ND_4)_3GaF_6$ deuterated cryolites.

unchanged within the accuracy in the determination of its magnitude. It is worth noting that the time dependence of the temperature for the deuterated $(ND_4)_3GaF_6$ cryolite exhibits another slight inflection at a temperature of approximately 3 K below T_1. Most likely, this phenomenon can be associated with the inhomogeneity of the studied sample, because no splitting of the heat capacity peak is observed for the considerably smaller volume of the $(ND_4)_3GaF_6$ cryolite studied under pressure (see below).

Since the latent heats of structural transformations in the deuterated $(ND_4)_3ScF_6$ cryolite at temperatures T_2 and T_3 appeared to be rather small, the results of the thermographic measurements were expressed in terms of heat capacity for the benefit of clarity (Fig. 3). It can be seen from the table that, compared to the $(NH_4)_3ScF_6$ compound, the phase transition in the deuterated $(ND_4)_3ScF_6$ cryolite at the temperature T_2 is characterized by an insignificant increase in thermodynamic parameters such as the temperature T_2, its hysteresis δT_2, and the latent heat δH_2 of the phase transition.

The isotopic substitution H $\longrightarrow$ D most strongly affects the thermodynamic parameters of the phase transition at T_3 (see table). This effect more clearly manifests itself in a substantial decrease in the phase transition temperature T_3 and an increase in the temperature hysteresis δT_3.

Thermodynamic parameters of the phase transitions in cryolites

Parameters	$(NH_4)_3ScFe_6$ [2]	$(ND_4)_3ScF_6$	$(NH_4)_3GaF_6$ [2]	$(ND_4)_3GaF_6$
T_1, K	330.8 ± 0.2	332.3 ± 0.2	249.02 ± 0.2	249.9 ± 0.2
δT_1, K	1.8 ± 0.2	2.3 ± 0.1	0.84 ± 0.20	1.0 ± 0.2
δH_1, J/mol	3820 ± 370	3615 ± 350	2690 ± 190	2740 ± 200
$\Delta S_1 R$	1.68 ± 0.13	1.5 ± 0.1	2.77 ± 0.19	2.72 ± 0.20
$\delta S_1/\Delta S_1$	0.83	0.87	0.47	0.49
dT_1/dp, K/GPa	–(16.4 ± 1.3)	–(17.9 ± 0.8)	–(12 ± 20)	~0
T_2, K	293.4 ± 0.2	294.5 ± 0.2		
δT_2, K	0.52 ± 0.15	1.35 ± 0.15		
δH_2, J/mol	160 ± 20	368 ± 90		
$\Delta S_2/R$	0.84 ± 0.06	1.03 ± 0.07		
$\delta S_2/\Delta S_2$	0.08	0.15		
dT_2/dp, K/GPa	57.5 ± 1.7	55.7 ± 0.9		
T_3, K	243.1 ± 0.3	234.5 ± 0.2		
δT_3, K	7.1 ± 0.3	9.9 ± 0.2		
δH_3, J/mol	179 ± 25	250 ± 40		
$\Delta S_3/R$	0.11 ± 0.02	0.14 ± 0.02		
$\delta S_3/\Delta S_3$	0.80	0.92		
dT_3/dp, K/GPa	59.9 ± 1.2	50.1 ± 0.9		

The total entropy change upon successive phase transitions was determined by integrating the function $(\Delta C_p/T)(T)$. In order to calculate the anomalous contribution ΔC_p, we determined the lattice component of the heat capacity $C_{lat}(T)$. For this purpose, the low-temperature and high-temperature portions of the dependence $C_p(T)$ outside the range of phase transition temperatures were approximated using a combination of Debye and Einstein functions. In the temperature range under investigation, the heat capacity is not very sensitive to details of the phonon spectrum due to a relatively low Debye temperature; therefore, the chosen approximation, in our opinion, is entirely justified.

For both deuterated cryolites, the changes in the entropy $\Delta S_i/R$ due to phase transitions are close in magnitude to those for the proton-containing compounds, within the accuracy of the entropy determination (see table). The temperature dependences of the excess entropy are displayed in Fig. 4. It is clearly seen from this figure that a rapid increase in the entropy of the deuterated gallium cryolite $(ND_4)_3GaF_6$ in the temperature range of phase transitions occurs in two steps. At present, the reason for this behavior remains unclear. However, it is quite probable that an examination of $(ND_4)_3GaF_6$ gallium cryolites with a higher degree of deuteration would provide an answer to this problem.

As is known, the degree of closeness of the phase transition to the tricritical point is characterized by a quantity defined as the ratio of the entropy jump at a temperature T_i to the total entropy change $\delta S_i/\Delta S_i$. It follows from the table that, upon deuteration, this quantity increases appreciably only due to phase transitions in the deuterated $(ND_4)_3ScF_6$ cryolite at temperatures T_2 and T_3. This result is in good agreement with the aforementioned substantial increase in the temperature hysteresis of these transformations and indicates that the deuteration of the studied compound leads to a decrease in the degree of closeness of two first-order phase transitions to the tricritical point.

Figure 5 shows the p–T phase diagrams of the deuterated and proton-containing cryolites studied under pressure. It can be seen from the table that, for $(NH_4)_3ScF_6$ and $(ND_4)_3ScF_6$ scandium cryolites, the slopes of the phase boundaries dT_1/dp and dT_2/dp and the coordinates of the triple point observed in the phase diagram virtually coincide. However, in the case of the transition to the triclinic phase at the temperature T_3, the slope dT_3/dp decreases significantly (see table). Judging from the increase in the stability region of the monoclinic phase $I12/m1$ of the deuterated $(ND_4)_3ScF_6$ cryolite, the parameters of the second (hypothetical) triple point (note that, to its right in the p–T phase diagram, there exists only a boundary between the cubic and triclinic phases) should be characterized by a higher pressure and a lower temperature as compared to those of the proton-containing $(NH_4)_3ScF_6$ cryolite.

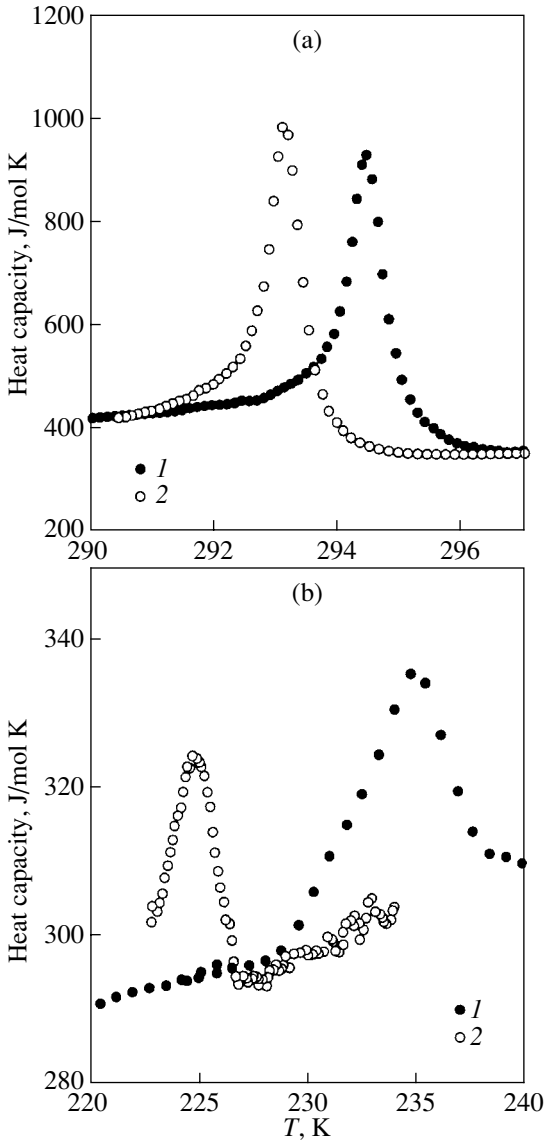

Fig. 3. Temperature dependences of the heat capacity in the vicinity of the phase transitions at temperatures (a) T_2 and (b) T_3 for the $(ND_4)_3ScF_6$ deuterated cryolite upon (*1*) heating and (*2*) cooling.

Upon partial deuteration of the gallium cryolite, no appreciable changes are observed either in the phase transition temperatures under pressure dT_i/dp or in the parameters of the triple points. Unfortunately, for both gallium cryolites, $(NH_4)_3GaF_6$ and $(ND_4)_3GaF_6$, the boundaries between the high-pressure phases were determined reliably only in phase diagram regions of small extent. This circumstance makes the unambiguous interpretation of the constancy of the quantities dT_i/dp with a change in the pressure more difficult. Moreover, the experiments performed under pressure did not reveal anomalies attributed to the aforementioned inflection points in the curves $C_p(T)$ and $T(t)$.

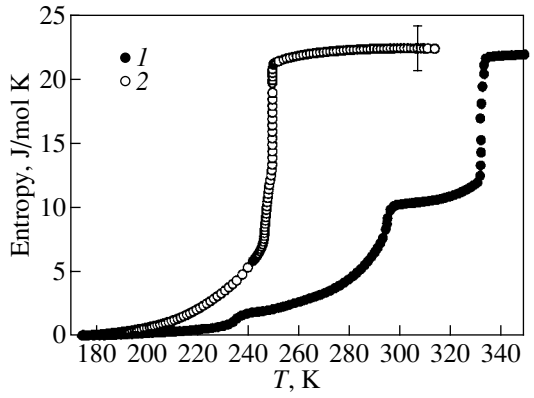

Fig. 4. Temperature dependences of the entropy associated with the phase transitions in (*1*) $(ND_4)_3ScF_6$ and (*2*) $(ND_4)_3GaF_6$ deuterated cryolites.

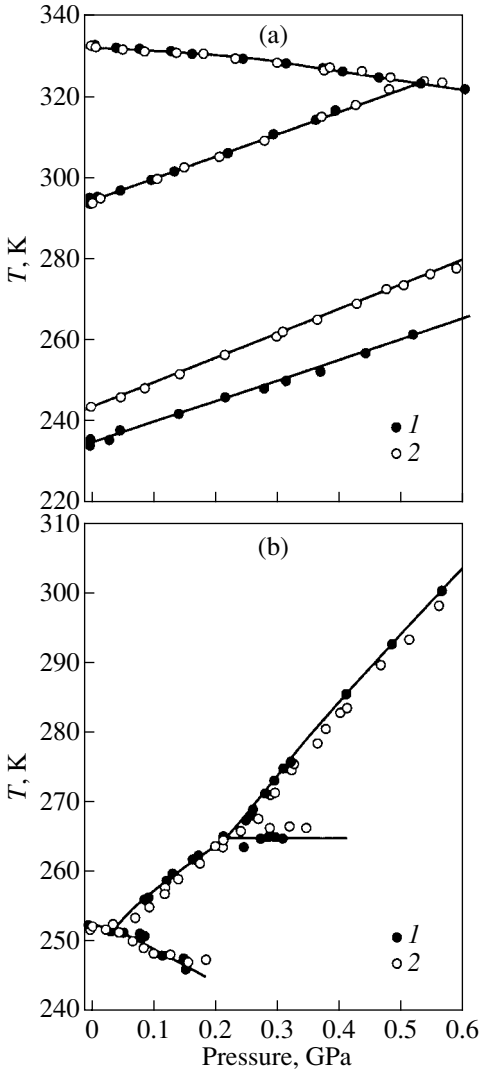

Fig. 5. Phase p–T diagrams for (a) (*1*) $(ND_4)_3ScF_6$ and (*2*) $(NH_4)_3ScF_6$ scandium cryolites and (b) (*1*) $(ND_4)_3GaF_6$ and (*2*) $(NH_4)_3GaF_6$ gallium cryolites.

4. CONCLUSIONS

The main results obtained in the above investigation can be summarized as follows.

(1) The total entropy change $\Sigma\Delta S_i/R$ observed upon a triclinic distortion of the low-temperature phase in $(NH_4)_3ScF_6$ and $(NH_4)_3GaF_6$ cryolites remains unchanged in $(ND_4)_3ScF_6$ and $(ND_4)_3GaF_6$ deuterated compounds, within the accuracy of the measurements, even though the degrees of deuteration of the latter compounds differ significantly. Therefore, it can be assumed that the protons (deuterons) are of little importance in structural ordering associated with considerable changes in the entropy.

(2) The deuteration does not substantially affect the thermodynamic parameters of the phase transitions at temperatures T_1 and T_2. This result confirms the assumption made earlier in [1, 4] that these transformations are due to ordering of ammonium tetrahedra and fluorine octahedra.

(3) The thermodynamic parameters of the $I12_1/m1$–$P\bar{1}$ phase transition in the deuterated scandium cryolite $(ND_4)_3ScF_6$ change considerably as compared to those of the proton-containing scandium compound $(NH_4)_3ScF_6$. This indicates that the structural distortions observed upon this transition are associated with transformations in the subsystem of tetrahedra. The clearly defined transformation revealed at the temperature T_3 can be considered a first-order transition between two completely ordered phases differing only in the orientation of the tetrahedra in the 4*b* positions [7]. This inference is also supported by the insignificant change in the entropy ΔS_3.

ACKNOWLEDGMENTS

This work was supported by the Russian Foundation for Basic Research (project nos. 00-02-16034 and 00-15-96790) and the International Association of Assistance for the Promotion of Cooperation with Scientists from the New Independent States of the Former Soviet Union (project INTAS no. 97-10177).

REFERENCES

1. A. Tressaud, S. Khairoun, L. Rabardel, *et al.*, Phys. Status Solidi A **96**, 407 (1986).
2. M. V. Gorev, I. N. Flerov, and A. Tressaud, J. Phys.: Condens. Matter **11**, 7493 (1999).
3. A. Sasaki, Y. Furukawa, and D. Nakamura, Ber. Bunsen-Ges. Phys. Chem. **93**, 1142 (1989).
4. K. Moriya, T. Matsuo, H. Suga, and S. Seki, Bull. Chem. Soc. Jpn. **52** (11), 3152 (1979).
5. M. V. Gorev, I. N. Flerov, S. V. Mel'nikova, *et al.*, Izv. Akad. Nauk, Ser. Fiz. **64** (6), 1104 (2000).
6. S. V. Mel'nikova, S. V. Misyul', A. F. Bovina, and M. L. Afanas'ev, Fiz. Tverd. Tela (St. Petersburg) **42** (2), 336 (2000) [Phys. Solid State **42**, 345 (2000)].
7. N. G. Parsonage and L. A. Stavely, *Disorder in Crystals* (Oxford Univ. Press, Oxford, 1979; Mir, Moscow, 1982).
8. H. Muraoka and T. Matsuo, Solid State Commun. **93** (6), 529 (1995).
9. Y. Kume, Y. Miyazaki, T. Matsuo, *et al.*, Europhys. Lett. **16** (3), 265 (1991).
10. I. N. Flerov, M. V. Gorev, K. S. Aleksandrov, *et al.*, Mater. Sci. Eng. R **24** (3), 81 (1998).
11. I. N. Flerov, M. V. Gorev, and T. V. Ushakova, Fiz. Tverd. Tela (St. Petersburg) **41** (3), 523 (1999) [Phys. Solid State **41**, 468 (1999)].

Translated by O. Borovik-Romanova

Physics of the Solid State, Vol. 44, No. 10, 2002, pp. 1967–1971. Translated from Fizika Tverdogo Tela, Vol. 44, No. 10, 2002, pp. 1876–1880.

LATTICE DYNAMICS AND PHASE TRANSITIONS

Optical and X-ray Diffraction Investigations of the Symmetry of Distorted Phases of the $(NH_4)_2KGaF_6$ Crystal

S. V. Mel'nikova*, S. V. Misyul', A. F. Bovina*, and M. L. Afanas'ev***

** Kirensky Institute of Physics, Siberian Division, Russian Academy of Sciences, Akademgorodok, Krasnoyarsk, 660036 Russia*

*** Krasnoyarsk State Agricultural University, pr. Mira 88, Krasnoyarsk, 660049 Russia*

e-mail: msv@iph.krasn.ru

Received December 14, 2001

Abstract—Powders and single-crystal plates of different sections of an $(NH_4)_2KGaF_6$ crystal are investigated using polarized light microscopy and x-ray diffraction over a wide temperature range, including the phase transition temperatures. It is established that the sequence of symmetry changes in the crystal under investigation is as follows: O_h^5–$Fm3m$ (Z = 4) ⟷ C_{4h}^5–$I114/m$ (Z = 2) ⟷ C_{2h}^5–$P112_1/n$ (Z = 2). © *2002 MAIK "Nauka/Interperiodica".*

1. INTRODUCTION

Fluoride crystals of the general formula $A_2BMe^{3+}F_6$ with a perovskite-like structure are characterized by a great diversity of phase transitions with a decrease in temperature. Among these compounds, ammonium crystals have attracted particular attention, because the ammonium ions occupy cation positions: *A* and *B* (cryolite) and *A* or *B* (elpasolite). In elpasolite and cryolite crystal cells, these ions can occupy two nonequivalent positions, namely, the position *A* inside a halide octahedron and the position *B* in a hole between octahedra.

Ammonium crystals of the formula $(NH_4)_3Me^{3+}F_6$ (Me^{3+} = Al, Cr, Ga, V, Fe, Sc, or In) with a cryolite structure (space group $Fm3m$, Z = 4) that belong to the family of ammonium perovskite-like compounds have been investigated in sufficient detail. The three-dimensional crystal framework of these compounds is formed by $(NH_4)F_6$ and $Me^{3+}F_6$ octahedra connected by their vertices, and the polyhedra arranged between these octahedra are occupied by ammonium ions. Sasaki *et al.* [1] showed that, in the majority of ammonium cryolites, the transitions from the cubic phase are associated with changes in the orientational motion of two structural groups, namely, $(NH_4)^+$ and $(Me^{3+}F_6)$. Kobayashi *et al.* [2] and Tressaud *et al.* [3] proved that the radius of the Me^{3+} ion affects the number of phase transitions, the sequence of changes in the symmetry upon phase transitions, and the temperature at which the cubic phase loses its stability. The ammonium compounds with a small radius of the trivalent ion ($R_{Me}^{3+} \le R_{Fe}^{3+}$) are characterized by only one phase transition, whereas the compounds with larger sized cations (In or Sc) undergo two or three phase transitions [3–5]. Our recent x-ray diffraction studies on powders and single crystals [6] revealed the following sequence of symmetry changes in the $(NH_4)_3ScF_6$ cryolite: O_h^5–$Fm3m$ (Z = 4) ⟷ C_{2h}^5–$P12_1/n1$ (Z = 2) ⟷ C_{2h}^3–$I12/m1$ (Z = 16) ⟷ C_i^1–$I\bar{1}$ (Z = 16). For the $(NH_4)_3GaF_6$ cryolite with a small-sized trivalent cation Ga^{3+} [7], the sequence of symmetry changes proved to be as follows: O_h^5–$Fm3m$ (Z = 4) ⟷ C_i^1–$I\bar{1}$ (Z = 16). These investigations demonstrated that ammonium cryolites have identical symmetry of the initial and lowest temperature phases; however, the transitions between these phases can occur in a number of ways.

The difference between the ammonium elpasolite $(NH_4)_2KGaF_6$ and the gallium cryolite $(NH_4)_3GaF_6$ lies in the fact that holes between octahedra in the crystal structure of the former compound are occupied by atomic potassium cations rather than by ammonium molecular ions. According to Flerov *et al.* [8], the $(NH_4)_2KGaF_6$ elpasolite exhibits three anomalies in the heat capacity in the temperature range from 80 to 350 K, specifically at T_{01} = 288.5, T_{02} = 250, and T_{03} = 244.5 K. Moreover, reasoning from the thermodynamic characteristics obtained for the $(NH_4)_2KGaF_6$ elpasolite, Flerov *et al.* [8] proposed a different sequence of symmetry changes in this crystal as compared to that in the cryolites studied in [6, 7].

The purpose of the present work was to determine the sequence of symmetry changes (G_0) ⟷ (G_1) ⟷ (G_2) ⟷ (G_3) in the $(NH_4)_2KGaF_6$ crystal. This study was performed by analogy with our previous works [6, 7]. We investigated the twin laws and analyzed the changes observed in the x-ray reflections from powders

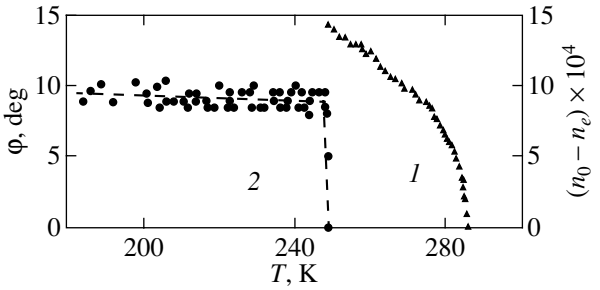

Fig. 1. Temperature dependences of (*1*) the birefringence and (*2*) the rotation angle of the optical indicatrix with respect to the $[110]_0$ direction in the $(NH_4)_2KGaF_6$ crystal.

and oriented single-crystal plates over a wide range of temperatures.

2. SAMPLE PREPARATION

The $(NH_4)_2KGaF_6$ compound was synthesized according to the following procedure. Gallium hydrate $Ga(OH)_3$ was dissolved in hydrofluoric acid HF and was then evaporated almost to dryness. A saturated aqueous solution of $(NH_4)HF_2$ and KHF_2 taken in equivalent amounts was added to the gallium fluoride GaF_3 formed by the above reaction. The resultant polycrystalline compound and a mother solution were placed in a high-pressure bomb. The hermetically sealed bomb was heated to 500 K, allowed to stand for 48 h at this temperature, and was then slowly cooled over ten days to room temperature. The hydrothermal synthesis in the high-pressure bomb resulted in the formation of small-sized (≈30 mm^2), well-faceted crystals of the $(NH_4)_2KGaF_6$ compound. Single-crystal plates of three crystallographic orientations, namely, the $(100)_0$, $(110)_0$, and $(111)_0$ sections cut from these crystals, served as samples in x-ray diffraction and optical investigations (hereafter, the subscript in the designations of the crystallographic planes and directions indicates the type of crystal phase).

3. RESULTS AND DISCUSSION

Thin crystal plates (≈0.05 mm) of different crystallographic sections were examined using a polarizing microscope. It was revealed that, during cooling of the studied samples in the vicinity of the temperature T_{01} = 288 K, the crystal exhibits optical anisotropy and small-sized, poorly defined crystal twins manifest themselves in the form of dark spots. The twin boundaries observed in the $(100)_0$ section are aligned parallel to the $[110]_0$ direction. Extended single-domain regions with pronounced temperature-independent extinctions of reflections along the $[100]_0$ direction are arranged between the spots. In these regions, the birefringence was measured using the Berec compensator technique with an accuracy of ~10^{-4}. Figure 1 illustrates the temperature behavior of the main birefringence $\Delta n = (n_0 - n_e)$ in the $(NH_4)_2KGaF_6$ crystal. It can be seen that the birefringence arises below T_{01} = 288 K, gradually increases with a decrease in the temperature, and reaches $\Delta n = 14 \times 10^{-4}$ in the vicinity of 250 K.

At T_{02} = 250 K, the $(NH_4)_2KGaF_6$ crystal undergoes a first-order phase transition. It is seen that the twin pattern changes drastically. In particular, there arise regions of a new phase with a complex twin structure. In the $(100)_0$ section, this structure is predominantly composed of twins with a preferred orientation of their boundaries along the $[100]_0$ direction, in which the optical indicatrices are rotated through an angle $\pm\varphi$ with respect to the $[110]_0$ direction. Crystal twins with extinctions of the reflections along the $[100]_0$ direction are observed more rarely. The new phase regions are not formed simultaneously throughout the bulk of the sample. Upon cooling, their formation is observed to a temperature of 245 K. At 250 K, the angle φ abruptly increases from zero to 10° and remains nearly constant in the course of cooling (Fig. 1). No additional changes are revealed in the twin pattern in the vicinity of the third anomaly in the heat capacity (T_{03} = 244.5 K).

Judging from the above findings, we can state that the $(NH_4)_2KGaF_6$ crystal is characterized by the following changes in symmetry: cubic (G_0) ⟷ tetragonal (G_1) ⟷ monoclinic (G_3). Analysis of the extinctions of the reflections in different twins of the monoclinic phase indicates that the twofold axis of the unit cell of the monoclinic phase coincides with one of the pseudocubic axes, whereas the other two axes are aligned along the face diagonals. It turned out that both the twin pattern and the sequence of symmetry changes in the $(NH_4)_2KGaF_6$ crystal are closely similar to those observed in the Rb_2KScF_6 elpasolite [9].

X-ray diffraction analysis of the $(NH_4)_2KGaF_6$ crystal was carried out on a DRON-2.0 diffractometer equipped with a URNT-180 low-temperature attachment (CuK_α radiation, graphite monochromator). The measurements were performed over a wide range of temperatures (100–300 K). The samples used in x-ray diffraction investigations were prepared in the form of single-crystal plates of the $(100)_0$, $(110)_0$, and $(111)_0$ sections and powders produced from $(NH_4)_2KGaF_6$ single crystals.

The x-ray reflections taken from the initial phase G_0 correspond to cubic symmetry with a face-centered unit cell F [10]. The unit cell parameters at 293 K are listed in the table. Upon cooling in the temperature range from 288 to 250 K, we observed a very slight broadening of x-ray reflections from single-crystal plates. Unfortunately, in this range of temperatures, we failed to reveal noticeable splittings of reflections that would suffice to determine the symmetry of the G_1 phase from the x-ray diffraction experiment. However, the observed twin pattern indicates that the unit cell of the

Crystallographic characteristics of distorted phases of the $(NH_4)_2KGaF_6$ crystal

Characteristics	G_3	G_1	G_0
Space group	C_{2h}^5–$P112_1/n$	C_{4h}^5–$I114/m$	O_h^5–$Fm3m$
Z	2	2	4
T_{exp}, K	198 K	273 K	293 K
	Unit cell parameters		
$\mathbf{a}_i$, Å	$1/2(\mathbf{a}_0 + \mathbf{b}_0)$ 6.203	$1/2(\mathbf{a}_0 + \mathbf{b}_0)$ 6.256	$\mathbf{a}_0$ 8.850
$\mathbf{b}_i$, Å	$1/2(\mathbf{a}_0 - \mathbf{b}_0)$ 6.252	$1/2(\mathbf{a}_0 - \mathbf{b}_0)$ 6.256	$\mathbf{b}_0$ 8.850
$\mathbf{c}_i$, Å	$\mathbf{c}_0$ 8.928	$\mathbf{c}_0$ 8.847	$\mathbf{c}_0$ 8.850
α, deg	90	90	90
β, deg	90	90	90
γ, deg	89.72	90	90
V, Å^3	346.23	346.22	693.13
(h 0 0)	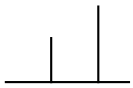		
(h h 0)	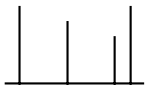		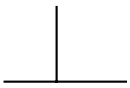
(h h h)	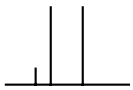		
Presence of superstructure reflections	+	–	–

G_1 phase is characterized by a tetragonal distortion. Moreover, the lack of superstructure reflections in the G_1 phase suggests that the phase transition occurs without a multiple change in the unit cell volume. The parameters and the scheme of crystallographic axis of the Bravais cell in the tetragonal phase of the $(NH_4)_2KGaF_6$ crystal are given in the table.

Upon cooling below the phase transition temperature T_{02} = 250 K, the x-ray diffraction profiles of single-crystal plates and the splittings of reflections in the x-ray powder diffraction patterns change drastically (see table). The cooling of the studied sample leads to the appearance of a set of (h k 0) and (h k l) superstructure reflections for which the sums (h + k), (h + l), and (k + l) are odd numbers and the (h 0 0) and (h h 0) reflections are characterized only by even indices h. The temperature dependence of the (1 0 5) superstructure reflection (Fig. 2) clearly demonstrates that a change in the translational symmetry occurs upon the $G_1 \longrightarrow G_3$ phase transition. The splittings of reflections in the G_3 phase correspond to the monoclinic symmetry (see table).

The temperature dependences of the linear and angular parameters of the unit cell in different phases of the $(NH_4)_2KGaF_6$ crystal were determined from the location of the components of the (6 6 0) reflection. The results obtained are presented in Figs. 3 and 4, respectively. It can be seen from Fig. 3 that, as the temperature decreases, the unit cell parameters remain constant upon the $(G_0) \longleftrightarrow (G_1)$ phase transition but exhibit abrupt jumps at temperatures below T_{02} = 250 K. The

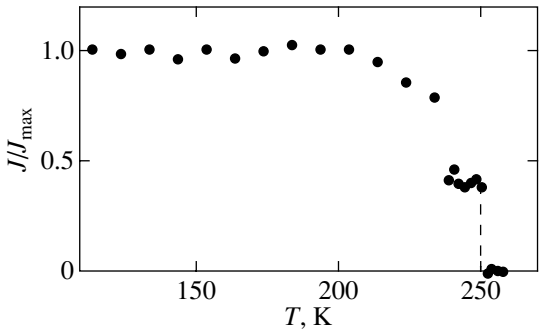

Fig. 2. Temperature behavior of the integral intensity of the (1 0 5) superstructure reflection. The reflection indices are given in the setting and crystallographic axes of the unit cell of the initial cubic phase G_0.

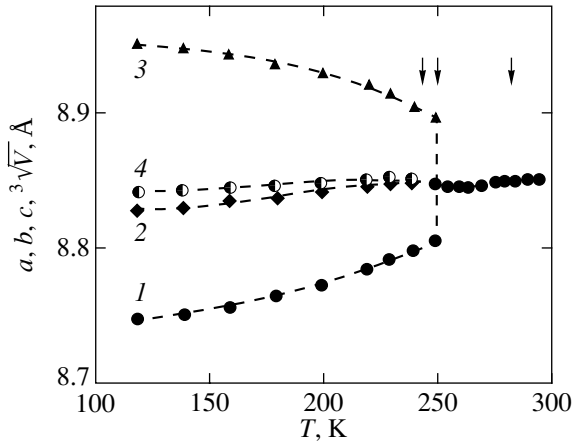

Fig. 3. Temperature dependences of the linear dimensions and the volume of the Bravais cell in the $(NH_4)_2KGaF_6$ crystal: (*1*) $a\sqrt{2}$, (*2*) $b\sqrt{2}$, (*3*) c, and (*4*) $3\sqrt{V}$. The volume of the Bravais cell in the monoclinic and tetragonal phases is doubled.

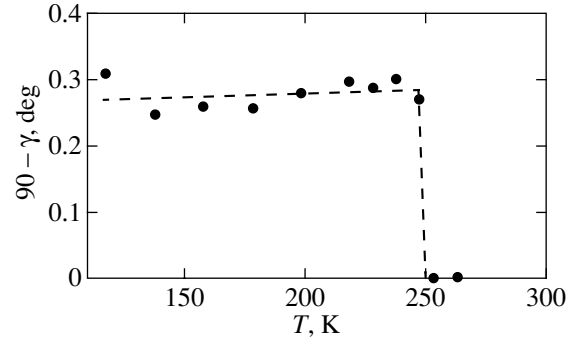

Fig. 4. Temperature dependence of the angular parameter (90° – γ) of the Bravais cell in the $(NH_4)_2KGaF_6$ crystal.

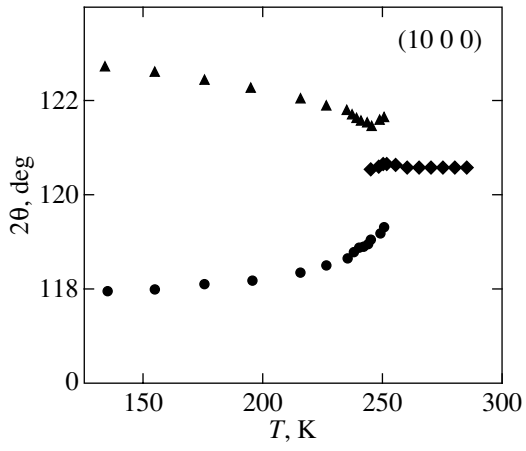

Fig. 5. Positions of the components of the (10 0 0) reflection in the x-ray diffraction pattern at different temperatures (CuK_α radiation).

linear dimension of the monoclinic cell of the $(NH_4)_2KGaF_6$ crystal decreases along the **a** direction and increases along the **c** direction with a decrease in the temperature, whereas the linear parameter along the **b** direction remains virtually unchanged. Upon cooling, the volume of the chosen cell only slightly changes when passing through the temperature T_{02}.

Figure 4 shows the temperature dependence of the angular parameter of the Bravais cell. At T_{02} = 250 K, the deviation of the angular unit-cell parameter from the right angle (90° – γ) abruptly increases from zero to saturation. A similar temperature dependence is observed for the rotation angle φ of the optical indicatrix (Fig. 1).

At temperatures below T_{01} = 288 K, the extinctions of the reflections observed correspond to two tetragonal space groups, namely, *I*4/*mmm* and *I*4/*m*. According to the results of measurements of the birefringence and heat capacity [8], the transformation from the cubic phase into the tetragonal phase is a second-order phase transition. On this basis, we chose the space group *I*114/*m* for the G_1 phase of the $(NH_4)_2KGaF_6$ crystal in the same manner as was done by Flerov *et al.* [9] for the Rb_2KScF_6 crystal. Reasoning from the aforementioned experimental data, for the low-temperature phase G_3, we chose the space group $P112_1/n$, in which the screw axis 2_1 coincides with the $[001]_0$ direction of the unit cell of the initial phase G_0. The parameters of the chosen Bravais cell for the monoclinic phase are listed in the table.

Now, it remains to be seen whether the $(NH_4)_2KGaF_6$ crystal undergoes any transformation in the temperature range from 250 to 245 K (the G_2 phase). In this respect, noteworthy is the temperature dependence of the integral intensity of the (1 0 5) superstructure reflection (Fig. 2). Upon transition from the G_1 phase to the G_2 phase with a decrease in the temperature, the integral intensity of the (1 0 5) superstructure reflection abruptly increases from zero to a certain value, remains nearly constant within a range of approximately 10 K, and increases to saturation only below 240 K. On the one hand, since the intensity of the superstructure reflection accounts for the displacement of atoms in the unit cell with respect to their initial positions, we can assume that an additional transformation of the crystal structure occurs in this range of temperatures ($T < T_{03}$). On the other hand, the intensity of the superstructure reflection depends on the amount of the material involved in the phase transition. In the case when observations in polarized light demonstrate that the phase transition in different parts of the sample occurs at different temperatures just below T_{02}, this circumstance should be reflected in the temperature dependence of the intensity of the reflection under investigation.

Figure 5 depicts the temperature dependence of the components of the (10 0 0) reflection in the x-ray dif-

fraction pattern of the $(100)_0$ section of an oriented plate. At temperatures below 250 K, the (10 0 0) reflection is split into three components. It should be noted that, after the splitting, the intensity of the component observed at the initial position ($2\theta \approx 120.5°$) in the temperature range from 250 to 245 K decreases to zero, whereas the intensities of the other two components increase. In the low-temperature range, this reflection has only two components. Most likely, this finding suggests the coexistence of the G_1 and G_3 phases at these temperatures.

The temperature behavior of the components of the (6 6 6) reflection is also of considerable interest. As the temperature decreases, the number of components of this reflection progressively changes from one component above 250 K to two components in the range 250–245 K and three components below 240 K. Judging from the number of components of the (6 6 6) reflection, we can make the inference that the symmetry of the G_2 phase differs from that of the G_3 phase; furthermore, we can assume that the G_2 phase has the symmetry $P12_1/n1$. In this case, the screw axis 2_1 should be directed along the face diagonal of the cubic cell. However, polarized light microscopy does not confirm this symmetry (Fig. 1). For the proposed variant of symmetry, the rotation angle of the optical indicatrix with respect to the [110] direction must be equal to zero. We believe that the disappearance of one of the components of the (6 6 6) reflection in the temperature range from 250 to 245 K most likely can be associated with the changes in the intensity and width of the other two, stronger components of this reflection in the x-ray diffraction pattern. As a result, the third (weak) component of the reflection is buried in the total profile (see table). One of the possible reasons for the observed changes in the profiles of x-ray reflections is the nucleation and intergrowth of one phase into the other phase, i.e., the intergrowth of the tetragonal phase into the monoclinic phase and vice versa (heating and cooling).

4. CONCLUSION

Thus, the results of the above investigations allowed us to propose the following sequence of symmetry changes in the $(NH_4)_2KGaF_6$ elpasolite: O_h^5–$Fm3m$ ($Z = 4$) $\longleftrightarrow$ C_{4h}^5–$I114/m$ ($Z = 2$) $\longleftrightarrow$ C_{2h}^5–$P112_1/n$ ($Z = 2$). Unfortunately, our investigation did not answer the question regarding additional symmetry changes in the temperature range of existence of the G_2 phase. We made the assumption that two phases coexist at these temperatures. This assumption is supported by the results obtained by Flerov *et al.* [8], who studied the (p–T) phase diagram of the $(NH_4)_2KGaF_6$ elpasolite. These authors demonstrated that, under pressure, the phase transition temperatures T_{02} and T_{03} decrease almost identically [8]: $dT_{02}/dp = -(2.3 \pm 0.3)$ K/GPa and $dT_{03}/dp = -(1.4 \pm 0.4)$ K/GPa. The stability loss temperature of the cubic phase decreases more rapidly with an increase in the pressure: $dT_{01}/dp = -30$ K/GPa.

ACKNOWLEDGMENTS

This work was supported by the Russian Foundation for Basic Research, project nos. 00-02-16034 and 00-15-96790.

REFERENCES

1. A. Sasaki, Y. Furukawa, and D. Nakamura, Ber. Bunsen-Ges. Phys. Chem. **93**, 1142 (1989).
2. K. Kobayashi, T. Matsuo, H. Suga, *et al.*, Solid State Commun. **53** (8), 719 (1985).
3. A. Tressaud, S. Khairoun, L. Rabardel, *et al.*, Phys. Status Solidi A **98** (2), 407 (1986).
4. I. N. Flerov, M. V. Gorev, and T. V. Ushakova, Fiz. Tverd. Tela (St. Petersburg) **41** (3), 523 (1999) [Phys. Solid State **41**, 468 (1999)].
5. M. V. Gorev, I. N. Flerov, and A. Tressaud, J. Phys.: Condens. Matter **11**, 7493 (1999).
6. S. V. Mel'nikova, S. V. Misyul', A. F. Bovina, and M. L. Afanas'ev, Fiz. Tverd. Tela (St. Petersburg) **42** (2), 336 (2000) [Phys. Solid State **42**, 345 (2000)].
7. S. V. Mel'nikova, S. V. Misyul', A. F. Bovina, and M. L. Afanas'ev, Fiz. Tverd. Tela (St. Petersburg) **43** (8), 1533 (2001) [Phys. Solid State **43**, 1594 (2001)].
8. I. N. Flerov, M. V. Gorev, M. L. Afanas'ev, and T. V. Ushakova, Fiz. Tverd. Tela (St. Petersburg) **43** (12), 2209 (2001) [Phys. Solid State **43**, 2301 (2001)].
9. I. N. Flerov, M. V. Gorev, S. V. Mel'nikova, *et al.*, Fiz. Tverd. Tela (Leningrad) **34** (7), 2185 (1992) [Sov. Phys. Solid State **34**, 1168 (1992)].
10. *International Tables for X-ray Crystallography* (Kynoch, Birmingham, 1952), Vol. 1.

Translated by O. Borovik-Romanova

Physics of the Solid State, Vol. 44, No. 10, 2002, pp. 1972–1975. Translated from Fizika Tverdogo Tela, Vol. 44, No. 10, 2002, pp. 1881–1883.

LATTICE DYNAMICS AND PHASE TRANSITIONS

Crystal Structure of Diserinesulfate Monohydrate

Yu. I. Smolin, A. E. Lapshin, and I. A. Drozdova

Grebenshchikov Institute of Silicate Chemistry, Russian Academy of Sciences, ul. Odoevskogo 24/2, St. Petersburg, 199155 Russia

Received December 27, 2001

Abstract—The crystal structure of *DL*-Serine $H_2SO_4 \cdot H_2O$ is determined by single-crystal x-ray diffraction. The intensities of x-ray reflections are measured at three temperatures, namely, 295, 343, and 233 K. The crystal structure of the studied compound is refined using all three sets of intensities. It is demonstrated that, at a temperature of 233 K, the structure transforms into an incommensurately modulated state. This transformation is assumed to be responsible for the disappearance of the piezoresponse at this temperature. © *2002 MAIK "Nauka/Interperiodica".*

1. INTRODUCTION

Owing to their structural features, crystals of inorganic derivatives of proteinic amino acids are of considerable interest to investigators engaged in searching for new pyroelectric and piezoelectric materials and in elucidating the role played by the electrical properties of proteinic amino acids in processes occurring in living organisms.

Lemanov *et al.* [1] described the synthesis of diserinesulfate monohydrate, the growth of diserinesulfate monohydrate single crystals, tentative x-ray structure characteristics, and the temperature dependences of the piezoresponse of diserinesulfate monohydrate crystals. The aim of the present work was to determine the previously uninvestigated crystal structure of diserinesulfate monohydrate [2]. Moreover, we made an attempt to reveal a correlation between the temperature dependences of the piezoelectric characteristics of these crystals and their structural transformations with changes in temperature.

2. EXPERIMENTAL TECHNIQUE

The measurements of the intensities of x-ray reflections were carried out on the same crystal at different temperatures: (i) room temperature (295 K), which corresponds to a sufficiently large piezoresponse; (ii) 233 K, at which the signal disappears; and (iii) 343 K, at which the piezoresponse sharply decreases and tends to zero [1]. The temperatures higher and lower than room temperature were attained by blowing the studied crystal with a jet of dry nitrogen of the specified temperature during the x-ray diffraction experiment. The control system maintained the specified temperature accurate to within ±1 K.

The intensities of x-ray reflections were measured on an automated single-crystal diffractometer operating in a perpendicular beam geometry with layer-by-layer recording (MoK_α radiation, pyrolytic graphite monochromator). The estimation of the integral intensities and correction for the background were performed using an algorithm of the profile analysis. The stability of the crystal was checked by periodic measurements of the intensity of the standard reflection.

It follows from Table 1 that, at all the temperatures, the studied crystal has an orthorhombic structure (space group $P2_12_12_1$). However, the measurements carried out at a temperature of 233 K revealed that the main reflections characterizing the basic cell are accompanied by a small number of first-order and second-order satellite reflections. The positions of the observed satellite reflections indicate a one-dimensional incommensurate modulation along the **b** axis. According to Wolff [3, 4], the positions of the satellite reflections are determined by the vector $\mathbf{H} = h\mathbf{a}^* + k\mathbf{b}^* + l\mathbf{c}^* + m\mathbf{q}$, where m is the order of the satellite reflection and **q** is the wave vector of the modulation.

For the crystal under investigation, the modulation wave vector was determined as $\mathbf{q} = 0.23(1)\mathbf{b}^*$. The coordinates of the non-hydrogen atoms were deter-

Table 1. Selected crystallographic parameters of the studied structures

Structure	*T*, K	*a*, Å	*b*, Å	*c*, Å	*F*(*n k l*)	*R*	Space group
I	295	10.62(1)	21.41(1)	5.89(1)	1791	0.027	$P2_12_12_1$
II	343	10.65(1)	21.39(1)	5.90(1)	1564	0.029	$P2_12_12_1$
III	233	10.61(1)	21.42(1)	5.90(1)	1740	0.026	$P2_12_12_1$

1063-7834/02/4410-1972$22.00

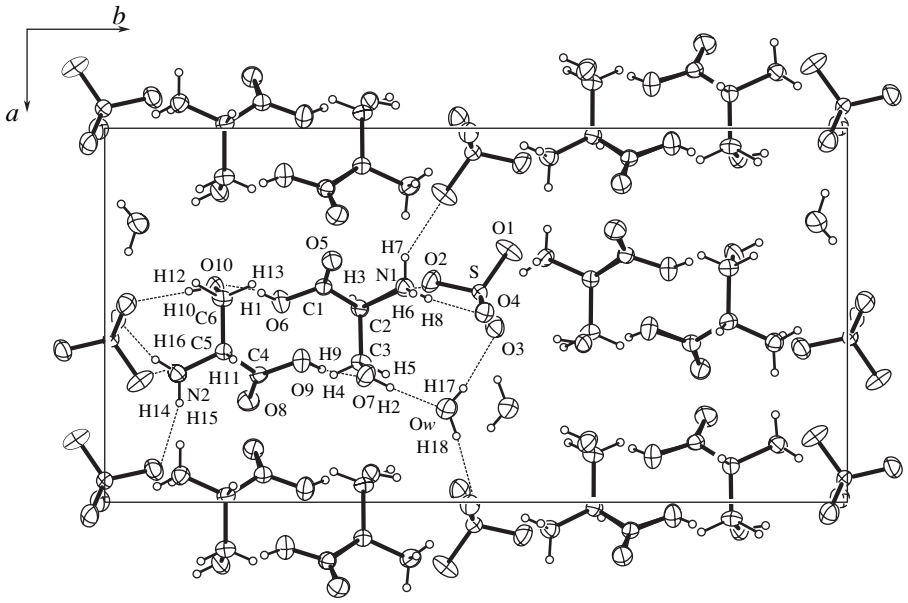

Projection of the crystal structure along the *c* axis.

mined by the direct method with the AREN software package [5] using the $F(h\ k\ l)$ set measured at room temperature. All the hydrogen atoms were located in a series of difference syntheses alternating with the least-squares refinement of the positional and thermal parameters of the atoms with the use of a modified version of the ORFLS program [6] and the weighting function $w = [\sigma^2(F_0) + 0.001F_0^2]^{-1}$; the scattering factors of the neutral atoms were used in the refinement. The thermal parameters were refined in the anisotropic approximation for the non-hydrogen atoms and in the isotropic approximation for the hydrogen atoms. In further refinement, the crystal structures were determined from the measurements performed at temperatures of 233 K (in the basic-cell approximation) and 343 K. Initially, we used the parameters of the non-hydrogen atoms which were obtained for the crystal at room temperature. Then, these parameters were refined by the least-squares method and the parameters of the hydrogen atoms were determined from the electron-density difference syntheses. The final *R* factors are presented in Table 1.

It turned out that the obtained parameters of the atoms differ only slightly from those determined for the crystal structure measured at room temperature. For this reason, Table 2 lists only the atomic coordinates and equivalent thermal parameters for the room-temperature structure (structure **I**).

3. RESULTS AND DISCUSSION

The projection of the crystal structure of diserinesulfate monohydrate along the *c* axis is shown in the figure. It can be seen that the left and right serine molecules are bound in pairs by two strong hydrogen bonds between the hydroxyl ions [O(6)–O(10), 2.627 Å and O(9)–O(7), 2.599 Å], thus forming layers aligned parallel to the *a* axis. These positively charged layers alternate with layers formed by $[SO_4]^{2-}$ ions and water molecules.

Two serine molecules form a group with a local center of symmetry in which the adjacent negatively charged layers consisting of $[SO_4]^{2-}$ ions and water molecules are linked through active NH_3 groups. Consequently, the nitrogen atom of one of the molecules in a pair forms three hydrogen bonds with three $[SO_4]^{2-}$ ions of one layer, whereas the nitrogen atom of the other molecule of this pair is bonded to three sulfate ions of the adjacent layer. In the crystal structure, the water molecules and hydroxyl groups of the serine molecules are also involved in the system of hydrogen bonds. Each water molecule provides hydrogen bonding of a pair of neighboring sulfate ions in the layer and, in turn, is linked to the serine hydroxyl group through the hydrogen bond. The coordination environment of the water molecules is not complete; as a result, the thermal parameter of the oxygen atom of the water molecule is considerably larger than that of the other atoms of the crystal structure. Thus, apart from the electrostatic interaction, the crystal structure is characterized by an extended system of hydrogen bonds. The bond lengths and angles in the serine molecules agree well both with each other and with those determined earlier in [7, 8]. The sulfate ion is a slightly distorted tetrahedron in which all the bond lengths and angles fall in the expected range (1.468–1.491 Å, 108°–111°).

Table 2. Atomic coordinates and thermal parameters in structure **I** (e.s.d.'s are given in parentheses). $B_{eq} = 4/3\Sigma(B_{ij}\, a_i a_j)$

Atom	*x*/*a*	*y*/*b*	*z*/*c*	B_{eq}/B_{iso}, Å^2
S	0.43850(3)	0.50423(1)	0.97266(6)	1.75(1)
N1	0.4252(2)	0.4017(1)	0.4683(3)	2.20(3)
N2	0.6526(2)	0.0940(1)	1.0255(3)	2.20(3)
O1	0.3255(2)	0.5434(1)	0.9521(4)	3.67(4)
O2	0.4094(2)	0.4376(1)	0.9337(3)	2.84(3)
O3	0.5327(2)	0.5249(1)	0.8013(3)	2.90(3)
O4	0.4920(2)	0.5104(1)	1.2059(3)	2.51(3)
O5	0.3540(2)	0.3027(1)	0.7142(3)	2.80(3)
O6	0.4622(2)	0.2342(1)	0.4986(3)	2.90(3)
O7	0.6605(2)	0.3483(1)	0.6619(3)	3.16(3)
O8	0.7282(2)	0.1894(1)	0.7611(3)	3.21(4)
O9	0.6215(2)	0.2613(1)	0.9617(3)	2.89(3)
O10	0.4213(2)	0.1451(1)	0.7969(3)	2.66(3)
O*w*	0.7499(2)	0.4584(1)	0.7170(8)	8.04(9)
C1	0.4229(2)	0.2909(1)	0.5580(3)	1.98(3)
C2	0.4818(2)	0.3405(1)	0.4059(3)	1.93(3)
C3	0.6258(2)	0.3417(1)	0.4305(4)	2.62(4)
C4	0.6585(2)	0.2040(1)	0.9140(3)	2.05(3)
C5	0.5962(2)	0.1567(1)	1.0702(3)	1.97(3)
C6	0.4532(2)	0.1553(1)	1.0307(4)	2.48(3)
H1	0.438(5)	0.207(2)	0.598(6)	2.5(7)
H2	0.694(5)	0.382(2)	0.695(7)	2.5(7)
H3	0.456(4)	0.331(2)	0.258(5)	2.9(5)
H4	0.659(5)	0.305(2)	0.354(7)	2.7(7)
H5	0.657(4)	0.375(2)	0.336(6)	2.1(6)
H6	0.442(4)	0.413(2)	0.594(6)	2.8(6)
H7	0.343(4)	0.402(2)	0.447(6)	2.8(6)
H8	0.456(5)	0.434(2)	0.382(7)	2.6(7)
H9	0.643(5)	0.289(2)	0.860(6)	2.3(7)
H10	0.431(5)	0.109(2)	0.767(7)	2.8(7)
H11	0.615(4)	0.168(2)	1.221(6)	2.3(6)
H12	0.416(4)	0.196(2)	1.078(6)	2.2(6)
H13	0.412(4)	0.118(2)	1.135(6)	2.5(6)
H14	0.643(4)	0.082(2)	0.886(6)	2.3(7)
H15	0.734(5)	0.097(2)	1.044(8)	2.5(7)
H16	0.613(5)	0.065(2)	1.114(7)	2.4(7)
H17	0.697(7)	0.482(3)	0.72(1)	8.(2)
H18	0.872(7)	0.471(3)	0.73(2)	8.(2)

4. CONCLUSION

The above analysis of the three crystal structures formed from the same crystal at different temperatures have demonstrated that these structures are closely similar to one another. However, the incommensurately modulated structure observed at a temperature of 233 K can be considered a new phase and the transition to this phase can be treated as a phase transition. It is assumed that this transition leads to the disappearance of the piezoresponse at the given temperature. The effect manifests itself in the appearance of a relatively small number of satellite reflections. For this reason, we cannot answer the question as to which of the fragments of

the crystal structure is primarily responsible for the incommensurate modulation. We can only note the following circumstance. Although the temperature was decreased by 60 K when we refined the incommensurate structure in the basic-cell approximation, the thermal parameters of the atoms did not decrease; they actually even increased. In our opinion, this suggests a cooperative effect of atomic displacements in the modulated structure. The attenuation of the piezoresponse at a temperature of 343 K most likely can also be associated with the thermal disordering of the crystal structure.

ACKNOWLEDGMENTS

The authors are grateful to V.V. Lemanov for providing the crystals used in our investigation.

This work was supported by the Russian Foundation for Basic Research, project nos. 01-02-17163 and 99-07-90133.

REFERENCES

1. V. V. Lemanov, S. N. Popov, V. V. Bakhurin, and N. V. Zaĭtseva, Fiz. Tverd. Tela (St. Petersburg) **43** (7), 1283 (2001) [Phys. Solid State **43**, 1336 (2001)].
2. *Cambridge Structural Database, Version 1.3* (Cambridge, 2001).
3. P. M. Wolff, Acta Crystallogr. A **30** (4), 777 (1974).
4. P. M. Wolff, Acta Crystallogr. A **33** (3), 493 (1977).
5. V. N. Andrianov, Kristallografiya **32** (1), 228 (1987) [Sov. Phys. Crystallogr. **32**, 130 (1987)].
6. W. R. Busing, K. O. Martin, and H. A. Levy, Report ORNL-TM-305 (Oak Ridge National Laboratory, 1962).
7. T. J. Kistenmacher, G. A. Rand, and E. Marsh, Acta Crystallogr. B **30** (11), 2573 (1974).
8. M. N. Frey, M. S. Lenmann, T. F. Koetzle, and W. C. Hamilton, Acta Crystallogr. B **29** (4), 877 (1973).

Translated by O. Moskalev

Physics of the Solid State, Vol. 44, No. 10, 2002, pp. 1976–1980. Translated from Fizika Tverdogo Tela, Vol. 44, No. 10, 2002, pp. 1884–1887.

LOW-DIMENSIONAL SYSTEMS AND SURFACE PHYSICS

Optical Vibration Modes in (Cd, Pb, Zn)S Quantum Dots in the Langmuir–Blodgett Matrix

A. G. Milekhin*, L. L. Sveshnikova*, S. M. Repinskiĭ*, A. K. Gutakovskiĭ*, M. Friedrich, and D. R. T. Zahn****

** Institute of Semiconductor Physics, Siberian Division, Russian Academy of Sciences, pr. Akademika Lavrent'eva 13, Novosibirsk, 630090 Russia*

*** Institute of Physics, Technical University, Chemnitz, D-09107 Germany*

Received June 26, 2001

Abstract—The structures with CdS, PbS, and ZnS quantum dots produced using the Langmuir–Blodgett method are investigated by infrared (IR) spectroscopy, Raman scattering, and ultraviolet (UV) spectroscopy. The quantum dot size estimated from the UV spectra and high-resolution transmission electron microscopy (HRTEM) falls in the range 2–6 nm. The longitudinal optical (LO) phonons localized in quantum dots and the surface optical vibration modes are revealed in the IR reflection and Raman scattering spectra of the structures under investigation. The frequencies of the surface optical modes are adequately described with allowance made for the effect of localizing optical phonons in the quantum dots.© *2002 MAIK "Nauka/Interperiodica".*

1. INTRODUCTION

In the last decade, low-dimensional semiconductor structures (quantum wells, quantum wires, and quantum dots) have attracted growing interest due to their unusual optical and electronic properties as compared to bulk materials [1, 2]. The optical properties of bulk crystals and thin films are well understood and explained. However, elucidation of the optical properties of low-dimensional structures calls for theoretical and experimental investigations. At present, quantum dots have been produced using a number of techniques, such as self-organization of quantum dots during molecular-beam epitaxy [3], preparation of quantum dots in solutions [4] and glasses [5], colloid chemistry [6], etc.

This paper reports on the results of analyzing the vibrational spectra of CdS, ZnS, and PbS quantum dots formed in the Langmuir–Blodgett matrix.

2. SAMPLE PREPARATION AND EXPERIMENTAL TECHNIQUE

The standard Langmuir–Blodgett technique provides a means of preparing perfect films of Cd, Zn, and Pb behenates. The interaction of metal behenate films with gaseous hydrogen sulfide results in the formation of microcrystals or quantum dots of Cd, Zn, and Pb sulfides [7, 8]. In the present work, films of cadmium, zinc, and lead behenates were deposited onto aluminum-coated silicon substrates. The aluminum layer served as a mirror for measuring the reflection spectra. The thickness of the Langmuir–Blodgett films used in the experiments was 400 monolayers (1.2 μm). The as-prepared Langmuir–Blodgett films were treated with hydrogen sulfide for 3 h under a pressure ranging from 50 to 100 Torr. As a result, the CdS, ZnS, and PbS quantum dots were formed in the behenic acid matrix according to the reaction

$$Me(C_{21}H_{43}COO)_2 + H_2S = MeS + 2C_{21}H_{43}COOH, \quad (1)$$

where *Me* = Cd, Zn, or Pb.

The infrared (IR) reflection spectra of the studied structures were recorded on Bruker-IFS66 and IFS113v IR Fourier spectrometers with a glancing angle of incidence ($\theta \approx 75°$) in *p*-polarized light. The IR spectrum of an aluminum mirror deposited onto a silicon substrate served as a reference spectrum. The resolution was 2 cm^{-1} over the entire spectral range. The number of scans was equal to 500.

The experiments on Raman scattering were carried out using a Dilor XY800 spectrometer in a backscattering geometry with the excitation by Ar^+ and Kr^+ lasers in the wavelength range 514.5–457.9 nm (2.41–2.71 eV) with a power of 40 mW. The resolution was equal to 2.9 cm^{-1} over the entire spectral range.

The ultraviolet (UV) absorption spectra were recorded on a Specord M-40 UV spectrometer in the wavelength range 250–800 nm with a spectral resolution of 10 cm^{-1}.

The experiments on high-resolution transmission electron microscopy (HRTEM) were performed using a JEM-400EX (JEOL) electron microscope with an accelerating voltage of 400 keV. The point resolution was 0.165 nm. The experiment was described in detail earlier in [9].

1063-7834/02/4410-1976$22.00

3. RESULTS AND DISCUSSION

In order to estimate the quantum dot size, we measured the UV absorption spectra of the structures under investigation. The UV absorption spectra of the structures with CdS, ZnS, and PbS quantum dots are displayed in Fig. 1. These spectra exhibit specific features (indicated by arrows) at 390, 270, and 255 nm, respectively, due to the 1*se*–1*sh* band-to-band transitions in the quantum dots. The vertical lines correspond to the band gaps in bulk CdS and ZnS. The band gap of PbS is equal to 0.4 eV (not shown in Fig. 1).

Within a simple model based on the effective mass approximation, we can estimate the mean size of spherical quantum dots as a function of the energy of the 1*se*–1*sh* transitions [10]:

$$E_{1se-1sh} = E_g + \frac{2\eta^2\pi^2}{D^2}\left[\frac{1}{m_e} + \frac{1}{m_h}\right] - \frac{3.56e^2}{\varepsilon D}. \qquad (2)$$

Here, D is the diameter of the quantum dot, E_g is the band gap, ε is the permittivity, and m_e and m_h are the electron and hole effective masses in the bulk of the material forming the quantum dot, respectively. The calculated dependences are shown in Fig. 2. The hatched regions correspond to the 1*se*–1*sh* transition energies determined, to within the experimental error, from the UV absorption spectra. The mean size of ZnS, CdS, and PbS quantum dots, which was determined from the comparison of the experimental and calculated data, was equal to 2.8 ± 0.2, 3.2 ± 0.1, and 4.2 ± 0.2 nm, respectively.

For comparison, the quantum dots were examined using high-resolution transmission electron microscopy. The HRTEM images of the studied samples are displayed in Fig. 3. The dark-field region corresponds to PbS (Fig. 3a) and CdS (Fig. 3b) quantum dots, and the bright-field region corresponds to the behenic acid matrix. It can be seen from Fig. 3 that the quantum dots have a nearly spherical shape. The mean size of CdS and PbS quantum dots is equal to (3 ± 1) and (4 ± 2) nm, respectively. Thus, the data obtained from analyzing the UV absorption spectra and HRTEM images are in good agreement.

Analysis of the interplanar spacings demonstrated that the PbS quantum dots exhibit a cubic structure, whereas the CdS quantum dots have a wurtzite-type hexagonal structure. We failed to observe a diffraction pattern of ZnS quantum dots. This can be explained by a small (less than 0.1%) volume fraction of crystal particles. Moreover, the small particle size leads to a considerable broadening of the diffraction peaks attributed to quantum dots, which, in turn, makes their visualization against the background of the diffraction pattern of the amorphous matrix of the Langmuir–Blodgett film rather difficult.

The vibrational spectrum of the structures prepared was examined using Raman and IR spectroscopy. Since the selection rules are different for Raman and IR spectroscopy, these methods of analyzing the vibrational spectrum complement each other.

Figure 4 depicts the Raman spectra of the structures with quantum dots in the frequency range of crystal lat-

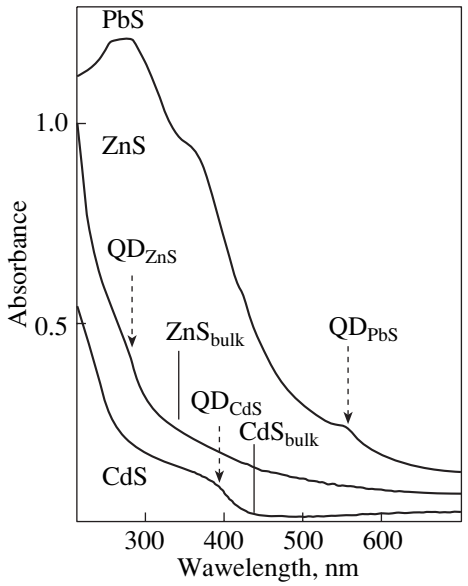

Fig. 1. Experimental UV absorption spectra of the structures with CdS, ZnS, and PbS quantum dots. Vertical solid lines correspond the band gaps of the materials forming quantum dots. The band gap in PbS is 0.4 eV (not shown in the figure). Vertical dashed arrows indicate the 1*se*–1*sh* transition energies in the quantum dots.

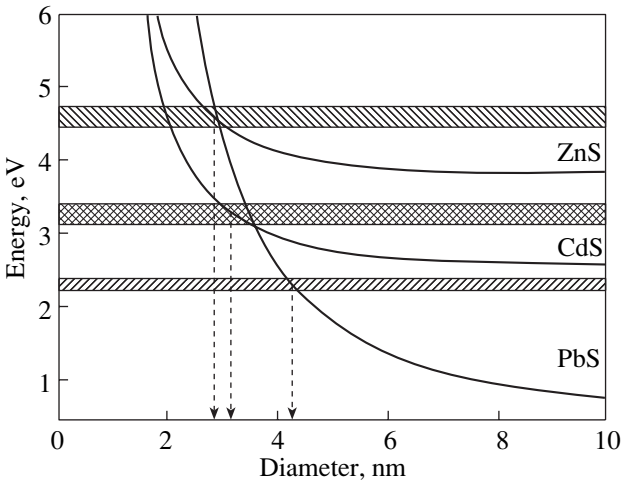

Fig. 2. Calculated energy of the 1*se*–1*sh* transitions in ZnS, CdS, and PbS quantum dots as a function of the quantum dot diameter. The hatched regions correspond to the 1*se*–1*sh* transition energies determined from the UV absorption spectra.

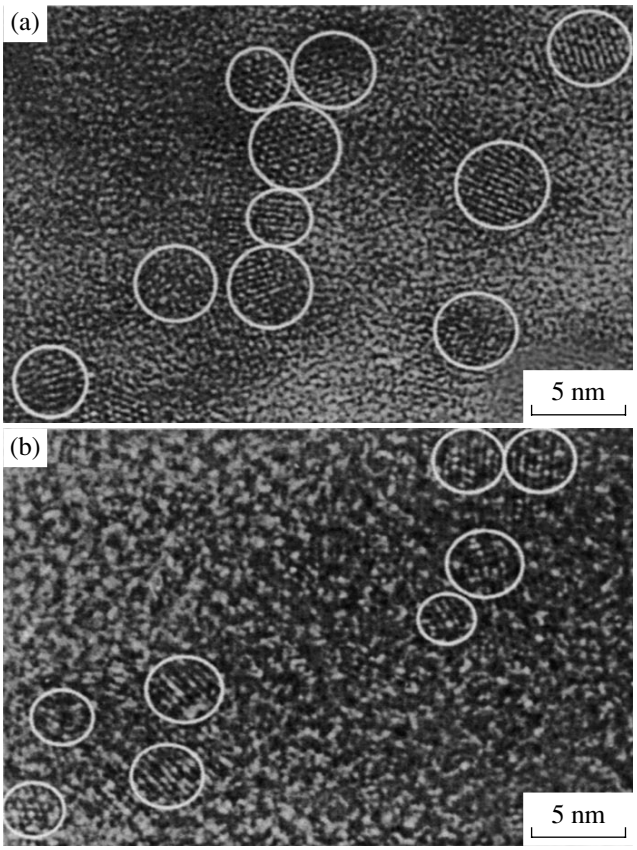

Fig. 3. HRTEM images of the studied samples. The dark-field region corresponds to (a) CdS and (b) PbS quantum dots. The bright-field region corresponds to the behenic acid matrix.

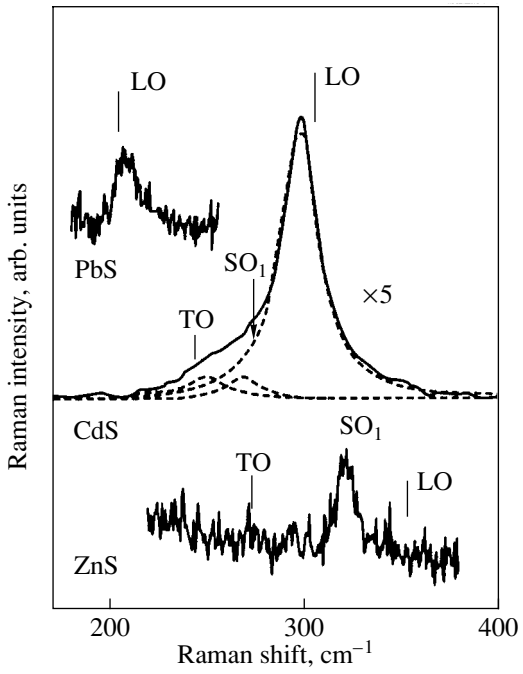

Fig. 4. Experimental Raman scattering spectra of the studied structures with quantum dots in the frequency range of lattice vibrations of ZnS, CdS, and PbS materials forming the quantum dots. Vertical lines indicate the frequencies of the LO and TO phonons in the bulk materials.

tice vibrations of the materials forming the quantum dots. The vertical lines indicate the frequencies of the transverse optical (TO) and longitudinal optical (LO) phonons in the bulk crystals. It can be seen from Fig. 4 that the frequency positions of the experimental Raman lines differ from the frequencies of the optical phonons of the materials forming the quantum dots. Two effects can be responsible for this behavior. These are the effect of localization of optical phonons and Raman scattering by surface optical phonons in quantum dots. The frequencies of the observed Raman lines of the studied structures with PbS and CdS quantum dots differ from the frequencies of the LO phonons in the bulk materials and amount to 207 and 297 cm^{-1}, respectively. These values exceed the frequency of the LO phonon in PbS (205 cm^{-1}) [11] and are less than that of the LO phonon in CdS (303 cm^{-1}) [12]. The difference between the experimental phonon frequencies in the structures with quantum dots and the frequencies in the bulk materials can be explained by the effect of localizing optical phonons in the quantum dots. Under the assumption that the low-dimensional quantum dots have a spherical shape, the wave vector of the localized optical phonons is determined by the expression $q = \pi m/d$. Here, m is the quantum number of the localized mode and d is the diameter of the quantum dot. The dispersion of $\omega(q)$ of the LO phonons in CdS is negative. Hence, the frequency of the first localized mode (LO_1) is less than that of the bulk material. A decrease in the frequency of the LO_1 mode as compared to the frequency of the LO phonon in single-crystal CdS is observed experimentally (Fig. 4). In addition to the intense line, the Raman spectrum exhibits a low-frequency shoulder due to scattering by TO phonons and surface optical (SO_1) phonons of the CdS quantum dots. Figure 4 also illustrates the decomposition of the Raman spectrum into three components, which are represented by Lorentzian curves.

For spherical quantum dots, the surface modes should satisfy the following relationship [13]:

$$\frac{\varepsilon_1(\omega)}{\varepsilon_m} = -1 - \frac{1}{l}. \qquad (3)$$

Here, $\varepsilon_1(\omega)$, $\varepsilon_m = 2.4$, and l are the dielectric function of the material of the quantum dot, the dielectric constant of the Langmuir–Blodgett, and the number of the surface mode, respectively. The calculated frequency of the SO_1 mode with due regard for the effect of localiz-

ing optical phonons in CdS quantum dots [14] is equal to 272 cm^{-1}. This value is in good agreement with the frequency determined from the decomposition of the Raman spectrum (269 cm^{-1}).

The dispersion of LO phonons in the PbS crystal is a nonmonotonic function. The dispersion is positive in the range of wave vectors $q = (0–0.6)\pi/a_0$, where a_0 is the lattice parameter of PbS [15]. This behavior of the dispersion leads to the experimentally observed increase in frequency of the LO_1 mode as compared to the frequency of the LO phonon in bulk PbS. The asymmetric shape of the Raman line in the spectra of the studied structures with PbS quantum dots can be caused by the contribution of higher-order localized modes ($m > 1$) to Raman scattering.

The Raman spectra of the structures with ZnS quantum dots contain a single line at a frequency of 320 cm^{-1}, which differs significantly from the frequencies of the TO and LO phonons; hence, this line cannot be interpreted as a localized mode. Most likely, it is associated with the surface vibration modes. This assumption is confirmed by the fact that the calculated frequency of the SO_1 mode (316 cm^{-1}) coincides with the experimental value. As in the case of CdS quantum dots, the overestimated value of the calculated frequency of the SO_1 mode can be a consequence of the effect of localizing optical phonons in the quantum dots. This effect was disregarded in our calculations, because data on the frequencies of the TO and LO phonons in ZnS quantum dots were not available. The Raman spectra of the structures with ZnS quantum dots do not exhibit lines associated with optical phonons. This confirms the inference made from electron microscopy that the ZnS quantum dots have small sizes. For small-sized quantum dots, the ratio of the surface atoms to the bulk atoms is relatively large. In the case when the number of surface atoms becomes comparable or even larger than that in the bulk of the quantum dots, the contribution of the surface layers to Raman scattering becomes significant. Moreover, no optical phonons were observed in the IR reflection spectra for all the studied structures. Figure 5 shows the IR reflection spectra in the frequency range of lattice eigenmodes for the materials forming quantum dots. It can be seen from Fig. 5 that the specific features associated with the surface optical modes are located in the range between the frequencies of the TO and LO phonons. The calculated frequencies of the SO_1 modes are indicated by arrows in Fig. 5. These frequencies are in good agreement both with the reflectance minima found from the IR spectra and with the SO_1 mode frequencies determined from the Raman spectra. The IR spectrum of the structure with PbS quantum dots exhibits a reflectance minimum at a frequency of approximately 275 cm^{-1}, which exceeds the frequency of any vibration of the crystal lattice. The former frequency is close to the sum of frequencies of the TO and LO phonons (67 + 205 cm^{-1}) in the PbS crystal. Therefore, this feature can be associated with two-phonon processes.

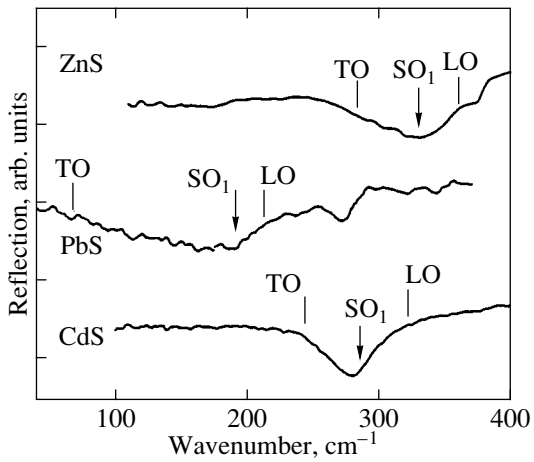

Fig. 5. Experimental IR reflection spectra of the studied structures with quantum dots. Vertical lines and arrows indicate the frequencies of the LO and TO phonons in the bulk materials and the SO_1 modes in the quantum dots, respectively.

4. CONCLUSIONS

Thus, we performed a systematic investigation into the optical properties of the structures with ZnS, CdS, and PbS quantum dots produced using the Langmuir–Blodgett method. Analysis of the IR and Raman spectra revealed lines attributed to both the optical phonons localized in the quantum dots and surface optical phonons. It was shown that the surface optical phonons are adequately described within the model of electromagnetic surface modes in spherical microcrystals. The experiments on high-resolution electron microscopy demonstrated that the quantum dots have a nearly spherical shape; therefore, the model used is quite adequate. The quantum dot size was determined from the experimental data on electron microscopy and UV spectroscopy in combination with the appropriate calculations.

ACKNOWLEDGMENTS

This work was supported by the Russian Foundation for Basic Research, project no. 01-03-32796.

REFERENCES

1. G. Bastard, *Wave Mechanics Applied to Semiconductor Heterostructures* (Halsted Press, New York, 1988).
2. *Science and Engineering of One- and Zero-Dimensional Semiconductors*, Ed. by S. P. Beaumont and C. M. Sotomayor Torres (Plenum, New York, 1990), NATO ASI Ser., Ser. B: Phys., Vol. 214.

3. D. Leonard, M. K. Krishnamurthy, C. M. Reeves, *et al.*, Appl. Phys. Lett. **63**, 3203 (1993).
4. J. Xu, H. Mao, and Y. Du, J. Vac. Sci. Technol. B **15**, 1465 (1997).
5. G. Scamarcio, M. Lugara, and D. Manno, Phys. Rev. B **45**, 13792 (1992).
6. P. V. Kamat and D. Meisel, *Semiconductors Nanoclusters* (Elsevier, New York, 1996), Vol. 103.
7. S. M. Repinskiĭ, L. L. Sveshnikova, and Yu. I. Khapov, Zh. Fiz. Khim. **72**, 829 (1998).
8. S. M. Repinskiĭ, L. L. Sveshnikova, Yu. I. Khapov, *et al.*, Zh. Fiz. Khim. **73**, 1199 (1999).
9. A. K. Gutakovskiĭ, L. D. Pokrovskiĭ, S. M. Repinskiĭ, and L. L. Sveshnikova, Zh. Strukt. Khim. **40**, 589 (1999).
10. L. E. Brus, J. Chem. Phys. **80**, 4403 (1984).
11. *Landolt–Börnstein: Numerical Data and Functional Relationships in Science and Technology* (Springer-Verlag, Berlin, 1982).
12. O. Zelaya-Angel, F. de L. Castillo-Alvarado, J. Avendano-Lopez, *et al.*, Solid State Commun. **104**, 161 (1997).
13. P. A. Knipp and T. L. Reinecke, Phys. Rev. B **46**, 10310 (1992).
14. A. Milekhin, M. Friedrich, D. R. T. Zahn, *et al.*, Appl. Phys. A **69**, 97 (1999).
15. T. D. Krauss, F. W. Wise, and D. B. Tanner, Phys. Rev. Lett. **76**, 1376 (1996).

Translated by N. Korovin

Physics of the Solid State, Vol. 44, No. 10, 2002, pp. 1981–1987. Translated from Fizika Tverdogo Tela, Vol. 44, No. 10, 2002, pp. 1888–1894.

LOW-DIMENSIONAL SYSTEMS AND SURFACE PHYSICS

The Normal Mode Spectrum in a Two-Dimensional Lattice of Neutral Atoms

A. V. Okomel'kov

Institute of the Physics of Microstructures, Russian Academy of Sciences, Nizhni Novgorod, 603600 Russia

e-mail: okom@ipm.sci-nnov.ru

Received July 10, 2001; in final form, December 6, 2001

Abstract—The acoustic phonon spectrum in a two-dimensional lattice composed of neutral atoms is considered. It is demonstrated that the normal mode spectrum in a two-dimensional rectangular lattice cannot be obtained only with inclusion of the interaction between the nearest neighbors. The discrete equations describing normal modes are derived and analyzed. The possibility of forming the anisotropic spectra of elementary excitations is investigated for different parameters of the interatomic interaction potential. It is shown that the anisotropy of the phonon spectra in two-dimensional systems can manifest itself in different kinetic effects in which the electron–phonon interaction plays the decisive role. *© 2002 MAIK "Nauka/Interperiodica".*

1. INTRODUCTION

Acoustic phonons in solids and their spectrum have attracted the particular attention of many researchers for a long time (see, for example, [1, 2]). The simplest approach to the solution of this problem is based on the model of propagation of longitudinal modes along a one-dimensional string consisting of neutral atoms. Let us assume that u_i is the displacement of the ith particle from an equilibrium position. Then, the equation of motion for this particle can be written in the following form (it is assumed that the masses of all the particles are equal to m [1]):

$$m\ddot{u}_i = \beta(u_{i+1} - 2u_i + u_{i-1}), \quad (1)$$

where β is the elastic modulus [1]. As is known [1], the solution of Eq. (1) in the form

$$u_n = A\exp\{i(qna - \omega t)\} \quad (2)$$

leads to the following dispersion relation for acoustic phonons (quasiparticles traveling along the string without attenuation):

$$\omega(q) = \sqrt{4\beta/m}|\sin(qa/2)|, \quad \omega(-q) = \omega(q). \quad (3)$$

In this case, the highest lattice vibration frequency is defined as $\omega_m = \sqrt{4\beta/m}$.

Analysis of the normal mode spectrum in the case of a two-dimensional atomic lattice is of considerable interest for the following reasons. At present, the properties of quasi-two-dimensional (layered) systems, such as $La_{2-x}Sr_xCu_2O_4$, $Bi_2Sr_2CaCuO_{6+\delta}$, and related compounds, have been studied extensively [3–8]. This is associated, to some extent, with the high-temperature superconductivity observed in these compounds, which, in turn, provides impetus for a large number of studies concerned with different properties of layered compounds in superconducting and normal states. According to experimental data on electron photoemission, the superconducting order parameter in high-T_c compounds exhibits strong anisotropy [9, 10]. In this respect, it is of interest to investigate the anisotropy of the phonon spectra under the assumption that carrier pairing in high-T_c compounds occurs via the traditional electron–phonon interaction mechanism. On this basis, the anisotropy of the order parameter can be explained in terms of anisotropic phonon spectra.

The purpose of the present work was to demonstrate the existence of anisotropy of the phonon spectra at certain parameters of the interatomic interaction potential. The generalization of the aforementioned quasi-one-dimensional model to the two-dimensional case with the aim of obtaining the acoustic phonon spectrum involves considerable difficulties. These difficulties reside in the fact that, in the case of a rectangular atomic lattice, the inclusion of the interparticle interaction only with the nearest neighbors in the equations of motion does not lead to an appropriate phonon spectrum. This problem was also considered. The discrete equations describing normal modes in a two-dimensional system were derived, and their dependence on the parameters of the interatomic interaction potential was analyzed.

2. INTERACTION OF NEUTRAL ATOMS IN A TWO-DIMENSIONAL RECTANGULAR LATTICE

Let us consider phonon modes in a two-dimensional rectangular atomic lattice. When analyzing the formation of normal modes in a two-dimensional system comprised of neutral atoms, our prime interest is in the anisotropy of the normal mode spectra. This is an important problem, because the anisotropy of the

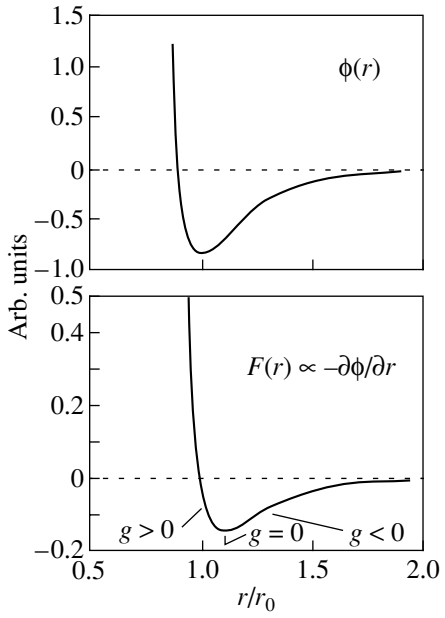

Fig. 1. Qualitative forms of the interaction potential $\phi(r)$ and the interaction force $F(r) \propto -\partial\phi/\partial r$ for the case of two neutral atoms. The coordinate r is normalized to the coordinate r_0 of the minimum of the potential $\phi(r)$. Three different regions are shown in the graph $F(r)$: (i) the region with $g > 0$, in which the attractive force between two particles increases in magnitude with an increase in the distance r; (ii) the region with $g = 0$, in which the attractive force between two particles only slightly varies with distance r; and (iii) the region with $g < 0$, in which the attractive force between two particles decreases in magnitude with an increase in the distance r. The potential $\phi(r)$ can significantly change depending on the constants A_1 and A_2 in formula (4).

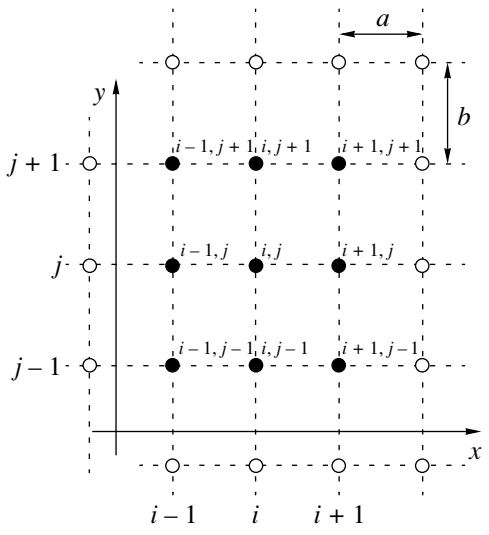

Fig. 2. Schematic drawing of the rectangular lattice. The equations of motion of a particle with the coordinates (i, j) are derived taking into account, first, four and, then, eight nearest neighbor particles denoted by closed circles; a and b are the interparticle distances along the x and y axes, respectively.

phonon spectra can manifest itself in different effects associated with the dominant contribution of the electron–phonon interaction.

2.1. Interaction between the nearest neighbor particles. The simplest potential of the pair interaction between neutral atoms can be represented by the Lennard-Jones potential

$$\phi(r) = \frac{A_1}{r^{12}} - \frac{A_2}{r^6}. \quad (4)$$

Figure 1 depicts potential (4) as a function of the interparticle distance r (the parameter r_0 corresponds to a minimum of the pair interaction potential) and the force of the pair interaction between particles $F(r) \propto -\partial\phi/\partial r$. The graph of the function $F(r)$ at $r > r_0$ can be divided into three regions: $g > 0$, $g = 0$, and $g < 0$ (the physical meaning of this separation will be discussed below).

Now, we assume that the rectangular lattice has the parameters a and b. We consider a model of interaction between the nearest neighbor particles in which the equations of motion of each particle (i, j) will be derived with allowance made for the interaction of this particle with only the four nearest neighbor particles $(i + 1, j)$, $(i - 1, j)$, $(i, j + 1)$, and $(i, j - 1)$ (Fig. 2). First, we will analyze the interaction between the two particles (i, j) and $(i + 1, j)$. For this purpose, we use the scheme depicted in Fig. 3. Let $u_{i,j}$ and $u_{i+1,j}$ be the x components of the particle displacement and $v_{i,j}$ and $v_{i+1,j}$ be the y components of the particle displacement. The interparticle distance squared (Fig. 3) is given by

$$r^2_{(i,j);(i+1,j)} = (a + u_{i+1,j} - u_{i,j})^2 + (v_{i+1,j} - v_{i,j})^2. \quad (5)$$

For the angle φ between the vector $\mathbf{r}_{(i,j);(i+1,j)}$ and the x axis, we have

$$\sin\varphi \approx (v_{i+1,j} - v_{i,j})/a, \quad \cos\varphi \approx 1. \quad (6)$$

The magnitude of the force acting on the particle (i, j) from the particle $(i + 1, j)$ can be written in the form

$$F_{(i,j)(i+1,j)} = \left|\tilde{\alpha}\{\sqrt{(a + u_{i+1,j} - u_{i,j})^2 + (v_{i+1,j} - v_{i,j})^2} - a\}\right| \approx \tilde{\alpha}|u_{i+1,j} - u_{i,j}|, \quad (7)$$

where $\tilde{\alpha}$ is a constant.

The projections of this force onto the coordinate axes in the approximation linear in the particle displacement are represented by the relationships

$$F_x\{(i, j)(i + 1, j)\} = \tilde{\alpha}(u_{i+1,j} - u_{i,j}), \quad (8)$$

$$F_y\{(i, j)(i + 1, j)\} = 0. \quad (9)$$

The sign in relationship (8) can be easily checked as follows. For $u_{i,j} = 0$ and $u_{i+1,j} > 0$, the interparticle distance becomes larger than the equilibrium distance a and, in accordance with the pair interaction potential [for example, potential (4)], the interaction between

particles is governed by the attractive forces. For $u_{i,j} = 0$ and $u_{i+1,j} < 0$ the interaction between particles is governed by the repulsive forces. The projections of the forces acting on the particle (i, j) from the other particles can be represented in a similar manner.

Finally, it is easy to deduce the equations of motion of a particle at the site (n, m) in terms of dimensionless variables. To accomplish this, we choose the characteristic dimension frequency $\omega^* = (\tilde{\alpha}/m)^{1/2}$ and change over to the dimensionless variables $\omega^* t \longrightarrow t$ and $\gamma = \tilde{\beta}/\tilde{\alpha}$. As a result, we obtain

$$\begin{aligned} \ddot{u}_{n,m} &= u_{n+1,m} - 2u_{n,m} + u_{n-1,m}, \\ \ddot{v}_{n,m} &= \gamma(v_{n,m+1} - 2v_{n,m} + v_{n,m-1}). \end{aligned} \tag{10}$$

Note that, within the above approximation, we derived independent equations for the functions u and v. In order to obtain the dispersion relations for modes in this system, we consider a set of equations in the case of an infinite plane. The solutions to the set of equations (10) are traditionally sought in the form

$$\begin{aligned} u_{n,m} &= A\exp\{i(k_x na + k_y mb - \omega t)\}, \\ v_{n,m} &= B\exp\{i(k_x na + k_y mb - \omega t)\}. \end{aligned} \tag{11}$$

Substitution of expressions (11) into formulas (10) gives two independent equations,

$$\omega^2 = 4\sin^2(k_x a/2), \quad \omega^2 = 4\gamma\sin^2(k_y b/2). \tag{12}$$

In order to satisfy the existence conditions for the undamped modes described by expressions (11), Eqs. (12) must have real solutions ω at real k_x and k_y. Let us introduce the dimensionless variables $x = k_x a/2$, $y = k_y a/2$, and $\alpha = a/b$. In this case, we have $k_y b/2 = (k_y a/2)(b/a) = y/\alpha$. Note that, as usual, only the undamped modes with wave vectors from the first Brillouin zone have physical meaning; that is,

$$-\pi/2 \le x \le \pi/2, \quad -\alpha\pi/2 \le y \le \alpha\pi/2. \tag{13}$$

In terms of these variables, Eqs. (12) in the polar coordinates $\mathbf{r}(x, y) \longrightarrow \mathbf{r}(r, \varphi)$ (where $x = r\cos\varphi$ and $y = r\sin\varphi$) take the form

$$\omega^2 = 4\sin^2(r\cos\varphi), \quad \omega^2 = 4\gamma\sin^2\left(\frac{r}{\alpha}\sin\varphi\right). \tag{14}$$

Figure 4 presents real solutions to Eqs. (14), namely, the real values ($\mathrm{Re}\,\omega$) of two branches of the dispersion curves $\omega_1(\varphi)$ and $\omega_2(\varphi)$ at different parameters. It should be noted that two branches ($\mathrm{Re}\,\omega_1$ and $\mathrm{Re}\,\omega_2$) correspond to undamped modes by virtue of the fulfillment of the equality $\mathrm{Im}\,\omega_1 = \mathrm{Im}\,\omega_2 = 0$. Consequently, within the approximation of the interaction between the nearest neighbor particles, we obtained intersecting curves.

The occurrence of intersecting dispersion curves is associated both with the symmetry of a rectangular lattice and with the approximation according to which the interaction between the nearest neighbor particles is taken into account. Within this approximation, the equations for projections of the particle displacement are decoupled and the atomic vibrations along the x and y axes prove to be independent. Note that this decoupling of equations of motions is not a specific feature of the two-dimensional case and also takes place in a three-dimensional lattice. However, the aforementioned intersection of the dispersion curves is invalid from the standpoint of general physics. In this regard, in order to obtain appropriate dispersion curves, it is necessary either to deal with lattices of more complex symmetry or to allow for interactions with other atoms if we restrict our consideration to the case of a rectangular lattice. As a result, the equations for the displacements u and v appear to be coupled (inseparable). This situation can be illustrated by considering the interaction of the particle under investigation with the next (more distant) four neighbors in a rectangular lattice.

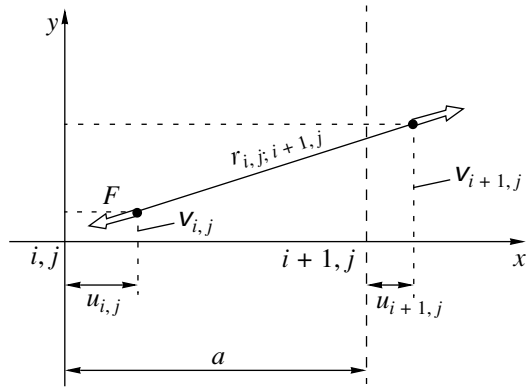

Fig. 3. Scheme illustrating the interaction between two particles (i, j) and $(i+1, j)$.

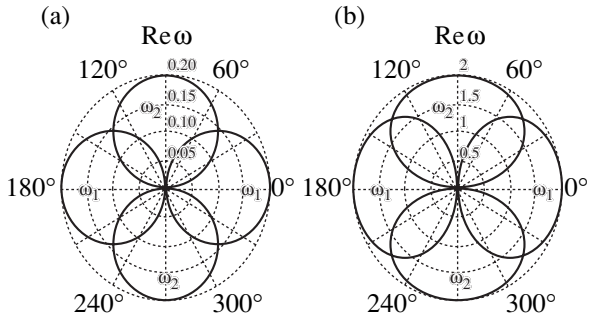

Fig. 4. Real solutions of Eqs. (14) in the form of graphs of the functions $\omega_1(\varphi)$ and $\omega_2(\varphi)$ in the polar coordinates at different parameters: (a) $\alpha = 1$, $\gamma = 1$, and $r = 0.1$ and (b) $\alpha = 1$, $\gamma = 1$, and $r = 1.5$.

2.2. Interaction with eight nearest neighbor particles. Now, we take into account the interaction with eight nearest neighbor particles, as is schematically

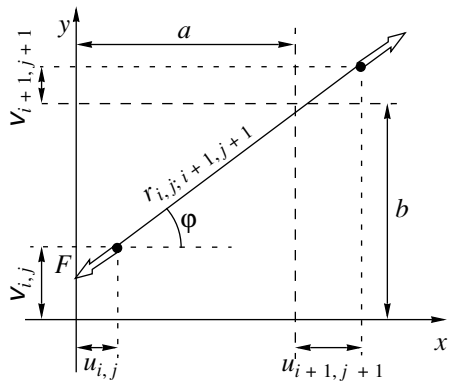

Fig. 5. Scheme illustrating the interaction between particles (i, j) and $(i+1, j+1)$.

shown in Fig. 2. First, we consider a "diagonal" interaction between the particles (i, j) and $(i+1, j+1)$. By calculating the projections of the interaction force between these particles onto the coordinate axes, it is easy to obtain similar expressions for interaction forces between other particles. The schematic diagram of this interaction is depicted in Fig. 5. All the calculations are performed within the approximation linear in the particle displacement.

The distance between the particles (i, j) and $(i+1, j+1)$ can be determined from the formula

$$\begin{aligned} r^2_{(i,j)(i+1,j+1)} &= (a + u_{i+1,j+1} - u_{i,j})^2 \\ &+ (b + v_{i+1,j+1} - v_{i,j})^2 \approx (a^2 + b^2) \\ &+ 2a(u_{i+1,j+1} - u_{i,j}) + 2b(v_{i+1,j+1} - v_{i,j}). \end{aligned} \quad (15)$$

The nearest neighbor particles (i.e., the four particles considered above) occupy positions approximately corresponding to a minimum of the pair interaction potential ϕ (the point $r = r_0$ in Fig. 1), whereas the interaction of the particle (i, j) with more distant particles [including the diagonal particles $(i+1, j+1)$, $(i+1, j-1)$, $(i-1, j+1)$, and $(i-1, j-1)$] is governed by the attractive forces (see also Fig. 1).

The normal mode spectra are affected by the parameters of the pair interaction potential. For simplicity, instead of considering potential (4), we write the following expression for the interparticle interaction force:

$$\begin{aligned} &F\{(i, j)(i+1, j+1)\} \\ &\simeq F(r = \sqrt{a^2 + b^2}) + \left.\frac{\partial F}{\partial \mathbf{r}}\right|_{r=\sqrt{a^2+b^2}} \delta\mathbf{r}. \end{aligned} \quad (16)$$

By designating $F(r = \sqrt{a^2 + b^2}) = F_0 > 0$ (in this case, the interparticle interaction is determined by the attractive forces), we obtain

$$\left|\frac{\partial F}{\partial \mathbf{r}}\right|_{r=\sqrt{a^2+b^2}} = F_0 g (a^2 + b^2)^{-1/2}.$$

Here, we introduced the constant g, which can be positive, negative, and equal to zero depending on the parameters of the interatomic interaction potential. The corresponding regions ($g > 0$, $g = 0$, and $g < 0$) are schematically shown in Fig. 1. It should be noted that, for the pair interaction potential depicted in Fig. 1, the diagonal interaction is characterized by $g < 0$ (at $a = b$, $r = r_0$ is the nearest neighbor distance and the diagonal distance is determined to be $r_0\sqrt{2} \approx 1.41 r_0$). However, for the other parameters of the pair interaction potential in the case when the minimum of the interparticle interaction force $F(r)$ is shifted toward the right (toward the range $r \geq r_0\sqrt{2}$), the condition $g \geq 0$ can also be satisfied. The introduced constants F_0 and g will be used instead of the parameters of potential (4). The difference resides only in the fact that the physical meaning of these constants is more evident (recall that we are dealing here only with small deviations of particles from the equilibrium position). As a result, we can write the expression

$$\begin{aligned} &F\{(i, j)(i+1, j+1)\} = F_0 \\ &\times \left\{1 + \frac{ga(u_{i+1,j+1} - u_{i,j})}{(a^2 + b^2)} + \frac{gb(v_{i+1,j+1} - v_{i,j})}{(a^2 + b^2)}\right\}. \end{aligned} \quad (17)$$

Substituting the expressions for $\cos\varphi$ and $\sin\varphi$ gives the following relationships for projections of the interparticle interaction forces onto the coordinate axes in the linear approximation:

$$\begin{aligned} F_x\{(i, j)(i+1, j+1)\} &= F\{(i, j)(i+1, j+1)\}\cos\varphi \\ &\approx \frac{F_0 a}{\sqrt{a^2 + b^2}}\left\{1 + \frac{(b^2 + ga^2)}{a(a^2 + b^2)}(u_{i+1,j+1} - u_{i,j})\right. \\ &\left. + \frac{b(g-1)}{(a^2 + b^2)}(v_{i+1,j+1} - v_{i,j})\right\}, \end{aligned} \quad (18)$$

$$\begin{aligned} F_y\{(i, j)(i+1, j+1)\} &= F\{(i, j)(i+1, j+1)\}\sin\varphi \\ &\approx \frac{F_0 b}{\sqrt{a^2 + b^2}}\left\{1 + \frac{a(g-1)}{(a^2 + b^2)}(u_{i+1,j+1} - u_{i,j})\right. \\ &\left. + \frac{(a^2 + gb^2)}{b(a^2 + b^2)}(v_{i+1,j+1} - v_{i,j})\right\}. \end{aligned} \quad (19)$$

The expressions for projections of the forces acting on the particle (i, j) from the other particles can be represented in a similar manner. After summation of the projections of the forces acting on the particle (i, j), we

obtain the following equations for the displacements $u_{i,j}$ and $v_{i,j}$, which now cease to be independent:

$$m\ddot{u}_{i,j} = \tilde{\alpha}(u_{i+1,j} - 2u_{i,j} + u_{i-1,j}) + \frac{F_0 ab}{(a^2+b^2)^{3/2}} \times \left\{ \frac{(b^2+ga^2)}{ab}[(u_{i+1,j+1} - 2u_{i,j} + u_{i-1,j-1}) + (u_{i+1,j-1} - 2u_{i,j} + u_{i-1,j+1}) + (g-1) \times [(v_{i+1,j+1} + v_{i-1,j-1}) - (v_{i+1,j-1} + v_{i-1,j+1})] \right\}, \quad (20)$$

$$m\ddot{v}_{i,j} = \tilde{\beta}(v_{i,j+1} - 2v_{i,j} + v_{i,j-1}) + \frac{F_0 ab}{(a^2+b^2)^{3/2}} \times \left\{ \frac{(a^2+gb^2)}{ab}[(v_{i+1,j+1} - 2v_{i,j} + v_{i-1,j-1}) + (v_{i+1,j-1} - 2v_{i,j} + v_{i-1,j+1}) + (g-1) \times [(u_{i+1,j+1} + u_{i-1,j-1}) - (u_{i+1,j-1} + u_{i-1,j+1})] \right\}. \quad (21)$$

Next, we change over to the dimensionless variables $\omega^* = (\tilde{\alpha}/m)^{1/2}$, $\omega^* t \longrightarrow t$, $\alpha = a/b$, $\gamma = \tilde{\beta}/\tilde{\alpha}$, and $F = F_0 ab/[\tilde{\alpha}(a^2+b^2)^{3/2}]$ and substitute solutions (11) into Eqs. (20) and (21). From the condition that the determinant of the system of algebraic equations is equal to zero, we obtain the dispersion relation

$$\omega^4 - 2\omega^2 2\left\{ \sin^2 x + \gamma \sin^2\left(\frac{y}{\alpha}\right) + \frac{F}{\alpha}(1+g)(1+\alpha^2) \times \left[\sin^2\left(x+\frac{y}{\alpha}\right) + \sin^2\left(x-\frac{y}{\alpha}\right)\right]\right\} + 16\left\{ \sin^2 x + \frac{F}{\alpha}(1+g\alpha^2) \times \left[\sin^2\left(x+\frac{y}{\alpha}\right) + \sin^2\left(x-\frac{y}{\alpha}\right)\right]\right\} \times \left\{ \gamma \sin^2\left(\frac{y}{\alpha}\right) + \frac{F}{\alpha}(\alpha^2+g)\left[\sin^2\left(x+\frac{y}{\alpha}\right) + \sin^2\left(x-\frac{y}{\alpha}\right)\right]\right\} - \left[4F(g-1)\sin(2x)\sin\left(\frac{2y}{\alpha}\right)\right]^2 = 0, \quad (22)$$

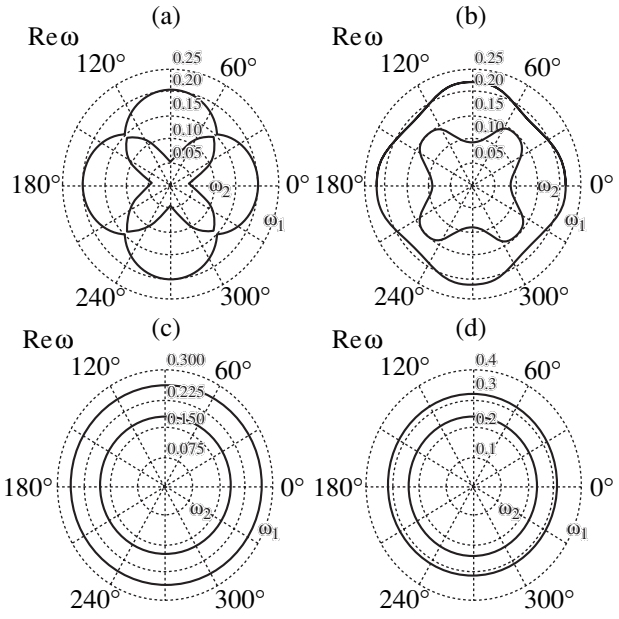

Fig. 6. Real solutions of Eq. (22) in the form of graphs of the functions $\omega_1(\varphi)$ and $\omega_2(\varphi)$ in the polar coordinates at $\alpha = 1$, $\gamma = 1$, and $r = 0.1$ and different parameters F and g: (a) $F = 0.03$ and $g = 0.03$, (b) $F = 0.1$ and $g = 0.1$, (c) $F = 0.3$ and $g = 0.3$, and (d) $F = 0.5$ and $g = 0.5$. In all cases, Eq. (22) has real solutions; i.e., $\mathrm{Im}\omega = 0$.

which is a biquadratic equation with respect to ω. The solutions to Eq. (22) can easily be represented in the analytical form and can be analyzed using numerical calculations. Let us consider the angular dependences of the dispersion curves at specified magnitudes of the wave numbers. For this purpose, we change over to the polar coordinates in the momentum space $\mathbf{r}(x, y) \longrightarrow \mathbf{r}(r, \varphi)$. Equation (22) has two complex solutions, namely, ω_1 and ω_2. These solutions in the polar coordinates at different parameters of the interatomic interaction potential are displayed in Figs. 6–9.

It can be seen that Eq. (22) at $F = 0$ transforms into the set of equations (14), which leads to degenerate solutions similar to those shown in Fig. 4. Figures 6a–6d illustrate the removal of degeneracy in the normal mode spectrum of acoustic phonons. It should be noted that, in the case under consideration, we have $g > 0$; i.e., the interparticle interaction potential is smoother than that depicted in Fig. 1. This means that the interaction potential between the particles separated by a diagonal distance (for a square lattice, $r = r_0\sqrt{2}$) is characterized by the parameter $g > 0$. The real solutions of Eq. (22) represented in Figs. 6a–6d correspond to progressively increasing parameters of the interparticle interaction. For a weak interaction (Fig. 6a), the degeneracy is removed and the dispersion curves are split. However, in this case, Eq. (22) retains the real solutions ω_1 and ω_2. The enhancement of the interparticle interaction (Fig. 6c) leads to a more pronounced splitting of the

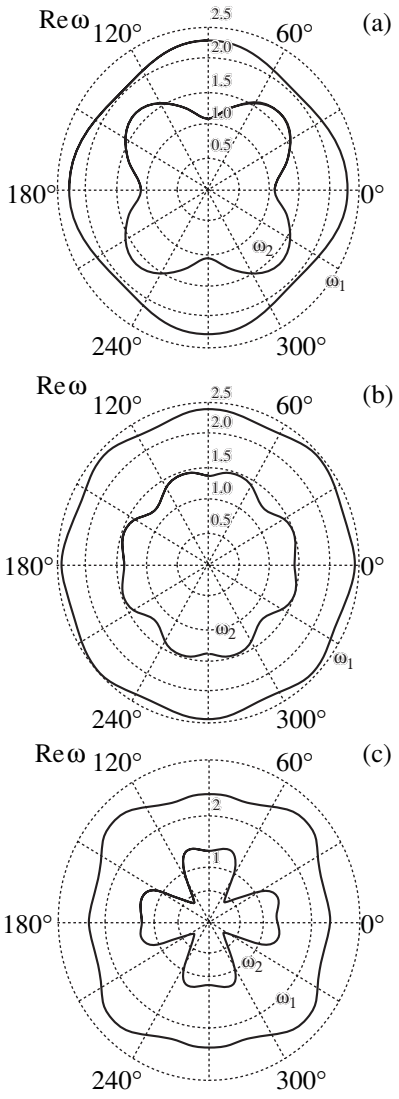

Fig. 7. Real solutions of Eq. (22) in the form of graphs of the functions $\omega_1(\varphi)$ and $\omega_2(\varphi)$ in the polar coordinates at $\alpha = 1$, $\gamma = 1$, and $r = 1.5$ and different parameters F and g: (a) $F = 0.2$ and $g = -0.2$, (b) $F = 0.5$ and $g = -0.5$, and (c) $F = 0.7$ and $g = -0.7$. In all cases, Eq. (22) has real solutions; i.e., $\mathrm{Im}\,\omega = 0$.

dispersion curves; as a result, we obtain two real isotropic modes (Figs. 6c, 6d). Note that the separation between the modes ω_1 and ω_2 in Fig. 6d slightly decreases. It is evident that, within the above approximation [see Eq. (22)], the dispersion curves should intersect each other with a considerable increase in the interaction parameters F and g. This implies that, at large parameters F and g, the approximation accounting for the interaction between an atom and eight nearest neighbor atoms becomes invalid. Hence, in order to obtain appropriate dispersion curves, it is necessary to take into account more distant particles. Consequently, in the case under investigation (Fig. 6), we obtained a reasonable result: the diagonal interaction brings about

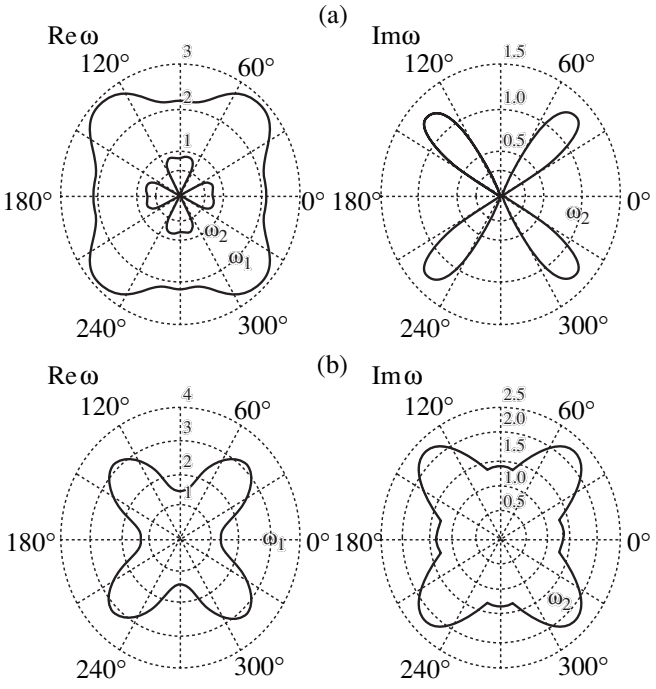

Fig. 8. Solutions of Eq. (22) in the polar coordinates at $\alpha = 1$, $\gamma = 1$, and $r = 1.5$ and different parameters F and g: (a) $F = 0.9$ and $g = -0.9$ (in this case, $\mathrm{Im}\,\omega_1 = 0$) and (b) $F = 1.2$ and $g = -1.2$ (in this case, $\mathrm{Re}\,\omega_2 = 0$ and $\mathrm{Im}\,\omega_1 = 0$).

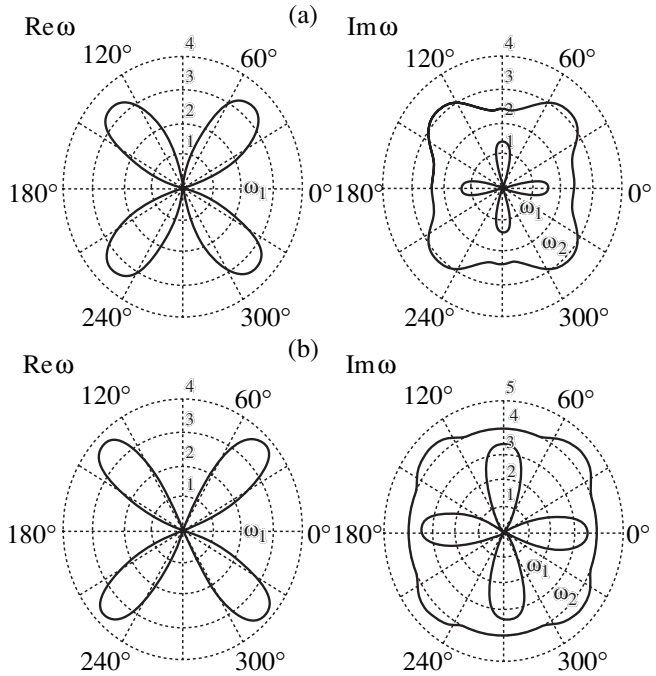

Fig. 9. Solutions of Eq. (22) in the polar coordinates at $\alpha = 1$, $\gamma = 1$, and $r = 1.5$ and different parameters F and g: (a) $F = 1.5$ and $g = -1.5$ (in this case, $\mathrm{Re}\,\omega_2 = 0$) and (b) $F = 2$ and $g = -2$ (in this case, $\mathrm{Re}\,\omega_2 = 0$).

the removal of degeneracy and the formation of a spectrum consisting of two modes.

More complex anisotropic spectra can be observed at $g < 0$ (this case approximately corresponds to the pair interaction potential depicted in Fig. 1: at $r = r_0\sqrt{2}$, we have $g < 0$). In this situation, an increase in the parameters of the interparticle interaction potential initially, as before, results in a splitting of the modes (Fig. 7a). A further increase in the parameters of the interaction potential leads to the formation of a nearly isotropic two-mode spectrum (Fig. 7b). Next, one spectral mode (ω_2) becomes strongly anisotropic (Fig. 7c); however, both solutions remain real. With a further increase in the parameters F and $|g|$ (Fig. 8), as soon as $\mathrm{Re}\,\omega_2$ (in the directions corresponding to 45°) vanishes, the imaginary part appears in the solution ω_2 (Fig. 8a) and the real part $\mathrm{Re}\,\omega_2$ begins to decrease. Then, $\mathrm{Re}\,\omega_2$ vanishes (Fig. 8b), whereas the $\mathrm{Re}\,\omega_1$ becomes strongly anisotropic. As a result (Fig. 9), the solution ω_1 includes real and imaginary parts (but in different directions: if the condition $\mathrm{Re}\,\omega_1 \neq 0$ is satisfied in a certain direction φ, we have $\mathrm{Im}\,\omega_1 = 0$, and, vice versa, at $\mathrm{Re}\,\omega_1 = 0$, we obtain $\mathrm{Im}\,\omega_1 \neq 0$). Note that the second solution (ω_2) is purely imaginary.

Thus, our analysis of the two-dimensional acoustic phonon modes demonstrated that the strongly anisotropic normal mode spectra can be obtained even in the case of a square lattice at certain parameters of the pair interaction potential.

3. CONCLUSIONS

In this work, we considered the formation of the normal mode spectrum in two-dimensional rectangular lattices composed of neutral atoms. The investigation of the normal mode spectra in two-dimensional systems is essential to the understanding of the mechanism responsible for the formation of these spectra and the elucidation of the experimentally observed anisotropy of different physical properties. The anisotropy of normal modes is associated primarily with short-wavelength undamped excitations. The consideration of these excitations necessitates discrete models (treatment of difference equations) and cannot be reduced to a continuum limit (to differential spatial operators). It should be remembered that the changeover to the spatial differential operators becomes possible only for functions describing a discrete lattice in the case when their spatial scales are considerably larger than the characteristic scale of discreteness (for a regular discrete lattice, this is the lattice spacing). Although part of the mode spectrum under investigation corresponds to long-wavelength modes, the overall pattern is more intricate.

It has been demonstrated that the allowance made for diagonal interactions between particles in a primitive rectangular atomic lattice leads to the removal of degeneracy in the normal mode spectrum. At certain parameters of the interatomic interaction potential, the normal mode spectra can exhibit strong anisotropy. The anisotropy of the phonon spectra can manifest itself in different kinetic effects in which the electron–phonon interaction plays the decisive role. The elucidation of this anisotropy can provide better insight into the origin of the anisotropy of the superconducting order parameter within the framework of the traditional mechanism of charged-particle pairing due to electron–phonon interaction.

REFERENCES

1. Frank J. Blatt, *Physics of Electronic Conduction in Solids* (McGraw-Hill, New York, 1968).
2. J. A. Reissland, *The Physics of Phonons* (Wiley, London, 1973).
3. C. W. Chu, J. Supercond. **12** (1), 85 (1999).
4. D. T. Jover, H. Wilhelm, R. J. Wijngaarden, and R. S. Liu, Phys. Rev. B **55** (17), 11832 (1997).
5. C. W. Chu, Y. Y. Xue, Z. L. Du, *et al.*, Science **277** (5), 1081 (1997).
6. J. M. Tranquada, J. D. Axe, N. Ichikawa, *et al.*, Phys. Rev. Lett. **78** (2), 338 (1997).
7. A. Bianconi, M. Lusignoli, N. L. Saini, *et al.*, Phys. Rev. B **54** (6), 4310 (1996).
8. Y. Ando, A. N. Lavrov, and K. Segawa, Phys. Rev. Lett. **83** (14), 2813 (1999).
9. J. Mesot, M. R. Norman, H. Ding, *et al.*, Phys. Rev. Lett. **83** (4), 840 (1999).
10. A. Kaminski, J. Mesot, H. Fretwell, *et al.*, Phys. Rev. Lett. **84** (8), 1788 (2000).

Translated by O. Borovik-Romanova

Physics of the Solid State, Vol. 44, No. 10, 2002, pp. 1988–1992. Translated from Fizika Tverdogo Tela, Vol. 44, No. 10, 2002, pp. 1895–1899.

LOW-DIMENSIONAL SYSTEMS AND SURFACE PHYSICS

Dispersionless Polaritons at Symmetrically Oriented Surfaces of Biaxial Crystals

V. I. Alshits and V. N. Lyubimov

Shubnikov Institute of Crystallography, Russian Academy of Sciences, Leninskiĭ pr. 59, Moscow, 117333 Russia

e-mail: alshits@ns.crys.ras.ru

Received December 17, 2001

Abstract—A set of dispersion relations is derived for surface polaritons in optically biaxial crystals at the surfaces parallel to the symmetry planes of the permittivity tensor ε. The domains of existence, as well as the sectors of the propagation directions of dispersionless surface polaritons which arise at positive components of the tensor ε, are analyzed. Three nonoverlapping domains of the dielectric-anisotropy parameters where dispersionless polaritons can exist are found for weakly anisotropic crystals. In each of these domains, polaritons exist at two different mutually orthogonal surfaces of the crystal. In optically biaxial crystals, in contrast to optically uniaxial media, polaritons arise not only in positive but also in negative crystals. The evolution of the optical-axis configuration is traced as the anisotropy parameters vary in the domains of existence of polaritons. © *2002 MAIK "Nauka/Interperiodica".*

1. INTRODUCTION

There are two types of surface polaritons (surface electromagnetic waves) in crystals. First, there are dispersion polaritons existing at negative components of the permittivity tensor ε [1–7], which takes place near resonant frequencies. Second, polaritons can arise due to dielectric anisotropy of the crystal in the case of positive ε components, when the frequency dispersion is insignificant. Such polaritons, referred to as dispersionless, were earlier considered only in optically uniaxial crystals [8–10].

In this paper, we consider dispersionless polaritons in optically biaxial crystals at the surfaces parallel to the symmetry planes of the permittivity tensor ε of the crystal. A general set of equations is derived to describe surface electromagnetic waves. On this basis, the conditions of a polariton's existence are analyzed in the approximation of small dielectric anisotropy.

2. BASIC RELATIONS

We consider the interface between a biaxial crystal with the permittivity tensor ε and an adjacent isotropic medium with the permittivity ε_0. The frame of reference is chosen such that the *z* axis is normal to the interface (Fig. 1). In general, the magnetic component of the wave field of a polariton localized near the *xy* surface is written as

$$\mathbf{H}(\mathbf{r}, t) = \mathbf{H}(z)\exp\left[i\frac{\omega}{c}(\mathbf{nr} - ct)\right], \quad \mathbf{n} = n(\cos\varphi, \sin\varphi, 0), \tag{1}$$

where $\mathbf{r} = (x, y, z)$ is the radius vector of a point, *t* is the time, ω is the frequency, *c* is the speed of light in vacuum, and $\mathbf{n} = (c/\omega)\mathbf{k}$ is the polariton refraction vector ($\mathbf{k}$ is the wavevector parallel to the surface). The magnitude of the refraction vector *n* defines the polariton phase velocity $v = c/n$. The angle φ specifies the polariton propagation direction along the surface. The electric component $\mathbf{E}(\mathbf{r}, t)$ of the wave field is written similarly to Eq. (1).

The wave field of the polariton in the crystal ($z \geq 0$) is a two-partial surface wave which corresponds to the vector amplitude in Eq. (1) given by

$$\mathbf{H}(z) = a_+\mathbf{H}_+\exp\left(-\frac{\omega}{c}p_+z\right) + a_-\mathbf{H}_-\exp\left(-\frac{\omega}{c}p_-z\right). \tag{2}$$

In the isotropic medium ($z \leq 0$) adjacent to the crystal, the wave field amplitude is written as

$$\mathbf{H}(z) = a\mathbf{H}\exp\left(\frac{\omega}{c}pz\right). \tag{3}$$

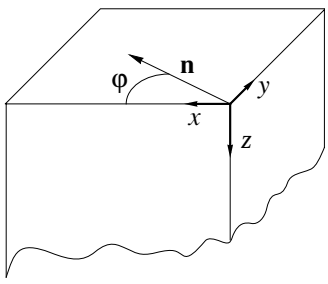

Fig. 1. Frame of reference and the orientation of the polariton refraction vector **n** at the crystal surface.

In Eqs. (2) and (3), $\mathbf{H}_\pm$ and $\mathbf{H}$ are the polarization vectors, $p_\pm$ and p are the parameters of wave field localization near the interface between the crystal and the isotropic medium, and $a_\pm$ and a are the amplitude coefficients; relations between these coefficients are determined from the boundary conditions, i.e., from the requirement of the tangential components of the electric and magnetic fields being continuous at the interface.

The polarization vectors $\mathbf{H}_\pm$ and $\mathbf{E}_\pm$ in the crystal, parameters $p_\pm$, and components n comply with the Maxwell equations

$$\begin{aligned} \mathbf{E}_\pm &= \boldsymbol{\eta}(\mathbf{H}_\pm \times \mathbf{n}_\pm), \quad \mathbf{H}_\pm = \mathbf{n}_\pm \times \mathbf{E}_\pm, \\ \mathbf{n}_\pm &= \mathbf{n} + ip_\pm \mathbf{q}, \quad \mathbf{q} = (0, 0, 1), \end{aligned} \tag{4}$$

where $\boldsymbol{\eta}$ is the tensor inverse to the permittivity tensor $\boldsymbol{\varepsilon}$. The use of the tensor $\boldsymbol{\eta} = \boldsymbol{\varepsilon}^{-1}$ instead of $\boldsymbol{\varepsilon}$ simplifies further algebraic analysis and appears to be preferred (see, e.g., [11, 12]). The symmetry planes of these two tensors and the directions of their eigenvectors are identical. Once the coordinate axes are directed along the tensor $\boldsymbol{\eta}$ eigenvectors, this tensor can be written in the following form, in which the spherical and anisotropic components are explicitly separated:

$$\boldsymbol{\eta} = \eta \mathbf{I} + \begin{bmatrix} \delta_1 & 0 & 0 \\ 0 & 0 & 0 \\ 0 & 0 & \delta_3 \end{bmatrix}. \tag{5}$$

Here, $\mathbf{I}$ is the unit tensor. We will take the tensor $\boldsymbol{\eta}$ in the form of Eq. (5) and consider the case when the xy surface of the crystal is parallel to one of the symmetry planes of the tensor $\boldsymbol{\varepsilon}$.

Maxwell's equations for the isotropic medium contiguous to the crystal are reduced to relations similar to Eqs. (4):

$$\begin{aligned} \mathbf{E} &= \varepsilon_0^{-1}(\mathbf{H} \times \mathbf{n}_0), \quad \mathbf{H} = \mathbf{n}_0 \times \mathbf{E}, \\ \mathbf{n}_0 &= \mathbf{n} - ip\mathbf{q}. \end{aligned} \tag{6}$$

3. DISPERSION RELATIONS

Equations (4) make it possible to relate the components of the refraction vector $\mathbf{n}$ in Eq. (1) to the parameters $p_\pm$ of wave field localization in the crystal; i.e.,

$$\begin{aligned} &n^2 - p_\pm^2 \\ &+ \frac{1}{\eta}\left\{1 - \frac{1}{2}[\delta_3 n_1^2 + (\delta_1 + \delta_3)n_2^2 - \delta_1 p_\pm^2 \pm \mu_\pm]\right\} = 0, \end{aligned} \tag{7}$$

where either plus or minus signs should be chosen and the following parameters are introduced:

$$\begin{aligned} \mu_\pm &\equiv R(p_\pm)R(-p_\pm) \\ &= \sqrt{[\delta_3 n_1^2 + (\delta_3 - \delta_1)n_2^2 + \delta_1 p_\pm^2]^2 - 4\delta_1\delta_3 n_1^2 p_\pm^2}, \end{aligned} \tag{8}$$

$$R(p_\pm) = \sqrt{(\sqrt{\delta_3}n_1 - \sqrt{\delta_1}p_\pm)^2 + (\delta_3 - \delta_1)n_2^2}. \tag{9}$$

Using Eqs. (6), the parameter p of wave field localization in the medium adjacent to the crystal can be explicitly expressed in terms of the magnitude of the refraction vector n:

$$p^2 = n^2 - \varepsilon_0. \tag{10}$$

In further analysis, it will be convenient to measure the inverse permittivity ε_0^{-1} from the spherical component η of tensor $\boldsymbol{\eta}$ in Eq. (5): $\varepsilon_0^{-1} = \eta + \delta$. In this case, the set of usual boundary conditions is reduced to the following equation relating the localization parameters $p_\pm$ and p to the refraction vector components:

$$\begin{aligned} &F_+F_-(f + g\delta + g_1\delta_1 + h\delta\delta_1) - G_+G_- \\ &\times(\tilde{f} + \tilde{g}\delta + \tilde{g}_1\delta_1 + \tilde{h}\delta\delta_1) + (p_+ - p_-)n_1 \\ &\times[\sqrt{\delta_1/\delta_3}G_+F_-(\bar{f} + \bar{g}\delta + \bar{g}_1\delta_1 + \bar{h}\delta\delta_1) \\ &- \sqrt{\delta_1\delta_3}F_+G_-p^2n^2(\eta + \delta)] = 0. \end{aligned} \tag{11}$$

Here, the following notation is introduced:

$$F_\pm = R(p_\pm) + R(-p_\pm), \quad G_\pm = R(p_\pm) - R(-p_\pm), \tag{12}$$

$$\left.\begin{aligned} f &= (p + p_+)[p_- + p(n^2 - p_-^2)\eta]n^2\eta \\ g &= p[p_- + p(n^2 - p_-^2)\eta]n^2 \\ g_1 &= p[p(n_2^2 - p_-^2) + p_+(n^2 - p_-^2)]n^2\eta \\ &+ p_+p_-(1 + p^2\eta)n_1^2 \\ h &= p^2[(n_2^2 - p_-^2)n^2 + p_+p_-n_1^2]. \end{aligned}\right\} \tag{13}$$

It should be borne in mind that

$$\begin{aligned} f \longrightarrow \tilde{f}, \quad g \longrightarrow \tilde{g}, \quad g_1 \longrightarrow \tilde{g}_1, \\ h \longrightarrow \tilde{h} \text{ at } p_\pm \longrightarrow p_\mp. \end{aligned} \tag{14}$$

The other parameters in Eq. (11) are given by

$$\left.\begin{aligned} \bar{f} &= \{p_+p_- + p[(p + p_+ + p_-)n^2 + pp_+p_-]\eta\}\eta \\ \bar{g} &= p^2(n^2 + p_+p_-)\eta \\ \bar{g}_1 &= p(p_+ + p_-)n^2\eta + (n_2^2 + p_+p_-)(1 + p^2\eta) \\ \bar{h} &= p^2(n_2^2 + p_+p_-). \end{aligned}\right\} \tag{15}$$

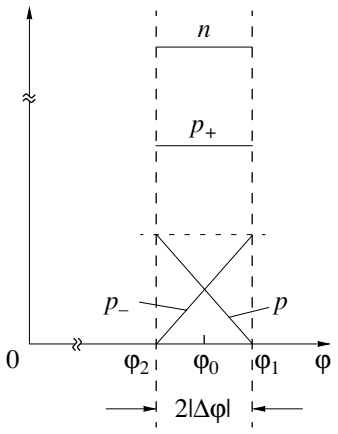

Fig. 2. Basic parameters of polaritons in weakly anisotropic crystals as functions of the angle φ in the existence sector $|\varphi - \varphi_0| < |\Delta\varphi|$ in the case of $\delta_1 > 0$; at $\delta_1 < 0$, the permutations $p \longleftrightarrow p_-$ and $\varphi_1 \longleftrightarrow \varphi_2$ should be made.

The set of equations (7), (10), and (11), complemented by Eqs. (8), (9), and (12)–(15), forms a closed set of dispersion relations from which the polariton parameters of interest (n, $p_\pm$, p) can be found as functions of the inverse permittivities of media and the propagation direction. These relations are universal and allow one to describe both dispersion and dispersionless polaritons and to go over to the results obtained for optically uniaxial media [9, 10] (see below). In this limiting case, the partial waves with parameters specified by the plus and minus signs transform into ordinary and extraordinary waves, respectively.

It is clear that at $\delta_1 = \delta_3 = \delta = 0$ the dielectric properties of the crystal should be precisely the same as the properties of the adjacent isotropic medium and the interface disappears. At $\eta > 0$ and small values of δ_1, δ_3, and δ (the case of weak dielectric anisotropy of the crystal), the components of the tensor $\boldsymbol{\eta}$ in Eq. (5) remain positive, which corresponds to dispersionless polaritons. After small-parameter expansion, the set of dispersion relations allows analytical treatment, which is performed below.

4. POLARITONS IN WEAKLY ANISOTROPIC BIAXIAL CRYSTALS

4.1. Basic Parameters of Polaritons

In the case under consideration, polaritons exist in a narrow sector of propagation directions. In the zeroth approximation, the orientation of this sector is given by the angle

$$\varphi_0 = \arcsin\sqrt{\delta/\delta_1}. \tag{16}$$

Within this sector, the parameters n and p_+ vary very weakly and can be considered to be constant:

$$n^2 = 1/\eta, \tag{17a}$$

$$p_+ = \sqrt{\delta_3 - \delta}/\eta \tag{17b}$$

(see Fig. 2). Let the sector boundaries be given by

$$\varphi_{1,2} = \varphi_0 \pm \Delta\varphi. \tag{18}$$

One of the sector boundaries is defined by the condition $p = 0$, corresponding to the propagation of a bulk wave in the isotropic medium adjacent to the crystal:

$$\varphi_1 = \varphi_0 + \Delta\varphi,$$
$$\Delta\varphi = \frac{\delta_1^3}{2(\delta_3 - \delta)\eta^2}\sin^3\varphi_0\cos^3\varphi_0. \tag{19}$$

The parameter p_- at this boundary is given by

$$p_- = \frac{\delta_1^2}{p_+\eta^3}\sin^2\varphi_0\cos^2\varphi_0. \tag{20}$$

The other (second) sector boundary $\varphi_2 = \varphi_0 - \Delta\varphi$ meets the condition $p_- = 0$ corresponding to bulk-wave propagation in the crystal. Thus, the width of the sector of polariton propagation directions is $2|\Delta\varphi|$. The parameter p at the second boundary of the sector is defined by the same equation as the parameter p_- at the first boundary, i.e., by formula (20). Comparison of the localization parameters given by Eqs. (17b) and (20) shows that the parameter p_+, on the one hand, and the parameters p and p_-, on the other hand, are quantities of different orders of smallness:

$$p, p_- \ll p_+ \ll 1. \tag{21}$$

These inequalities indicate that the partial wave corresponding to p_+ is much more localized than the others. Therefore, the effective localization depth of the wave field in Eqs. (2) and (3) is, in fact, defined by only two parameters, p and p_-. However, this conclusion, as well as inequalities (21), is valid until the difference $\delta_3 - \delta$ is no longer small in comparison with δ_3 and δ. As is evident from Eq. (17b), at $\delta_3 = \delta$, we have $p_+ = 0$; i.e., the partial wave corresponding to p_+ is a nonlocalized bulk wave in this case.

4.2. Domains of Existence of Polaritons

The conditions of existence of surface polaritons follow from Eqs. (16) and (17b) and are given by the following inequalities, which should be met by the material characteristics of the media:

$$0 \le \delta/\delta_1 \le 1, \quad \delta_3 - \delta \ge 0. \tag{22}$$

At $\delta > 0$, the domain of existence of surface polaritons is determined by the condition

$$\delta_1 \ge \delta > 0, \quad \delta_3 \ge \delta > 0. \tag{23}$$

In this case, in the line $\delta_1 = \delta_3$, which is the bisectrix of the quadrant shown in Fig. 3a in the plane (δ_1, δ_3), the tensor $\boldsymbol{\eta}$ in Eq. (5) characterizes a uniaxial crystal

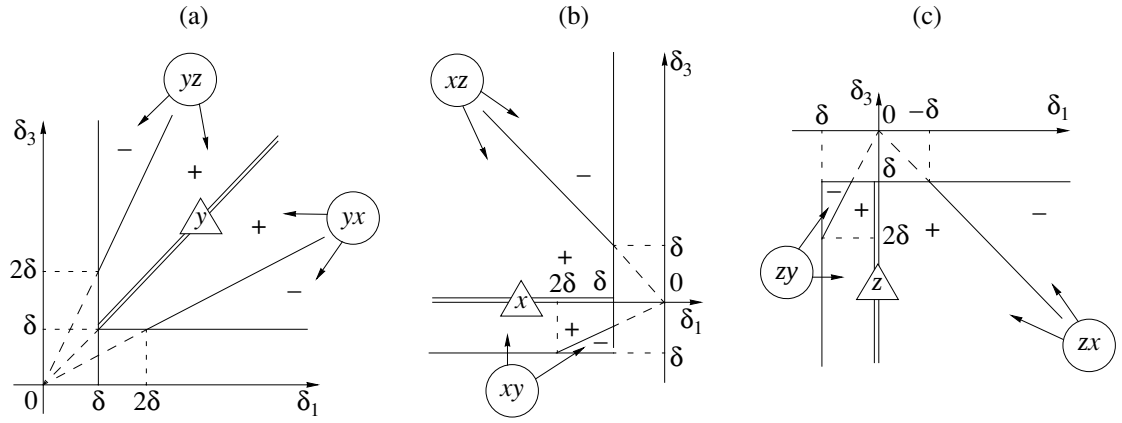

Fig. 3. Domains of existence of polaritons at the surfaces (a) *xy* and *yz* when $\delta > 0$, (b) *xy* and *zx* when $\delta < 0$, and (c) *yz* and *zx* when $\delta < 0$; in these three cases, the bisectrix between the optical axes coincides with the *y*, *x*, and *z* directions, respectively. The plus and minus signs correspond to optically positive and negative crystals, respectively; circles indicate the planes in which the optical axes lie. Double lines correspond to uniaxial media, and triangles indicate the optical-axis directions.

whose optical axis is parallel to the *y* axis. This corresponds to the case [as follows from inequalities (23)] where the optical axis coincides with the major semiaxis of the ellipsoid of the permittivity tensor $\boldsymbol{\varepsilon}$ of the crystal. By definition, such a uniaxial crystal is positive (see [12]). As one leaves the bisectrix $\delta_1 = \delta_3$, the crystal becomes biaxial: the optical axis is split into two optical axes lying in the *yx* or *yz* plane (Fig. 3a). The crystal remains positive until the angle between the optical axes exceeds 90°. It is easy to verify that the optical sign of the crystal reverses in the lines $\delta_3 = \delta_1/2$ and $\delta_3 = 2\delta_1$. As is known [9, 10], surface polaritons cannot exist in optically negative uniaxial crystals. From the above consideration, it follows that this is not the case for biaxial crystals.

At $\delta < 0$, inequalities (22), which define the domain of existence of surface polaritons, are reduced to the inequalities

$$\delta_1 \le \delta \le \delta_3. \tag{24}$$

The corresponding region in the plane (δ_1, δ_3) is shown in Fig. 3b. In this case, the crystal becomes uniaxial, with the optical axis along the *x* axis in the $\delta_3 = 0$ line belonging to the sector of optically positive crystals. The sector boundaries are defined by the lines $\delta_3 = \delta_1/2$ and $\delta_3 = -\delta_1$.

In the particular cases when $\delta = 0$ or $\delta = \delta_1$, we have $\Delta\varphi = 0$; i.e., the sector collapses into a straight line parallel to the *x* or *y* directions, respectively. In this case, bulk waves propagate in both the isotropic medium and the crystal, since $p = p_- = 0$ and the partial-wave amplitude characterized by the parameter p_+ (17b) vanishes.

5. POLARITONS AT DIFFERENT CRYSTAL SURFACES

The results of the analysis carried out for the *xy* surface of the crystal can be used to consider polaritons at other surfaces parallel to the symmetry planes of the inverse permittivity tensor, i.e., at the *yz* and *zx* surfaces. For example, for the *yz* surface, only the following substitutions should be made in all the relations:

$$\eta \longrightarrow \eta + \delta_3, \quad \delta_1 \longrightarrow -\delta_3, \quad \delta_3 \longrightarrow \delta_1 - \delta_3, \quad \delta \longrightarrow \delta - \delta_3. \tag{25}$$

For the *zx* surface, results are obtained through the substitution

$$\eta \longrightarrow \eta + \delta_1, \quad \delta_1 \longrightarrow \delta_3 - \delta_1, \quad \delta_3 \longrightarrow -\delta_1, \quad \delta \longrightarrow \delta - \delta_1. \tag{26}$$

The domains of a polariton's existence at the *yz* surface are shown in Fig. 3a (at $\delta > 0$) and in Fig. 3c (at $\delta < 0$). At the *zx* surface, polaritons can propagate only at $\delta < 0$ and the corresponding domains of existence of the polaritons in the same plane (δ_1, δ_3) belong to the quadrants displayed in Figs. 3b and 3c. In other words, each of the regions shown in Fig. 3 defines the range of the parameter values in which polaritons can propagate in two mutually orthogonal crystal surfaces. However, the conditions of existence cannot be simultaneously met in all three mutually orthogonal symmetry planes.

6. CONCLUSION

We emphasize that both the existence itself of dispersionless polaritons and all their features are caused by the dielectric anisotropy of crystals alone. This property distinguishes the polaritons under study from dis-

persion polaritons [1–7], which can also exist in isotropic media (but only near resonant frequencies).

It turns out that the conditions of existence of dispersionless polaritons in various mutually orthogonal surfaces parallel to the symmetry planes of the tensor $\boldsymbol{\varepsilon}$ of an optically biaxial crystal correlate with each other; at the same set of parameters belonging to one of the three domains of their existence (Fig. 3), polaritons can propagate along either of the two certain mutually perpendicular crystal surfaces. In the case of biaxial crystals, in contrast to uniaxial crystals, the polaritons under consideration can exist not only in optically positive but also in optically negative crystals.

REFERENCES

1. *Surface Polaritons: Electromagnetic Waves at Surfaces and Interfaces*, Ed. by V. M. Agranovich and D. L. Mills (North-Holland, Amsterdam, 1982; Nauka, Moscow, 1985).
2. V. N. Lyubimov and D. G. Sannikov, Fiz. Tverd. Tela (Leningrad) **14** (3), 675 (1972) [Sov. Phys. Solid State **14**, 575 (1972)].
3. V. V. Bryskin, D. N. Mirlin, and Yu. A. Firsov, Usp. Fiz. Nauk **113** (1), 29 (1974) [Sov. Phys. Usp. **17**, 305 (1974)].
4. V. M. Agranovich, Usp. Fiz. Nauk **115** (2), 199 (1975) [Sov. Phys. Usp. **18**, 99 (1975)]; Usp. Fiz. Nauk **126** (4), 677 (1978) [Sov. Phys. Usp. **21**, 995 (1978)].
5. G. A. Puchkovskaya, V. L. Strizhevskii, Yu. A. Frolkov, *et al.*, Phys. Status Solidi B **89** (1), 27 (1978).
6. V. N. Lyubimov, Zh. Prikl. Spektrosk. **33** (5), 913 (1980).
7. V. I. Alshits, V. N. Lyubimov, and L. A. Shuvalov, Fiz. Tverd. Tela (St. Petersburg) **43** (7), 1322 (2001) [Phys. Solid State **43**, 1377 (2001)].
8. F. N. Marchevskiĭ, V. L. Strizhevskiĭ, and S. V. Strizhevskiĭ, Fiz. Tverd. Tela (Leningrad) **26** (5), 1501 (1984) [Sov. Phys. Solid State **26**, 911 (1984)].
9. M. I. D'yakonov, Zh. Éksp. Teor. Fiz. **94** (4), 119 (1988) [Sov. Phys. JETP **67**, 714 (1988)].
10. V. I. Alshits and V. N. Lyubimov, Fiz. Tverd. Tela (St. Petersburg) **44** (2), 371 (2002) [Phys. Solid State **44**, 386 (2002)].
11. F. I. Fedorov, *Theory of Gyrotropy* (Nauka i Tekhnika, Minsk, 1976).
12. Yu. I. Sirotin and M. P. Shaskolskaya, *Fundamentals of Crystal Physics* (Nauka, Moscow, 1975; Mir, Moscow, 1982).

Translated by A. Kazantsev

Physics of the Solid State, Vol. 44, No. 10, 2002, pp. 1993–2000. Translated from Fizika Tverdogo Tela, Vol. 44, No. 10, 2002, pp. 1900–1907.

POLYMERS AND LIQUID CRYSTALS

Dipole Moment and Mobility of Molecules in Nematic Liquid Crystals of the 4-*n*-Butyl Ester of [4'-*n*-Hexyloxyphenyl] Benzoic Acid in the Absence of External Orienting Fields

T. P. Stepanova, A. É. Bursian, and V. M. Denisov

Institute of Macromolecular Compounds, Russian Academy of Sciences, Bol'shoĭ pr. 31, St. Petersburg, 199004 Russia

e-mail: tams@imc.macro.ru

Received June 14, 2001; in final form, January 15, 2002

Abstract—Dielectric polarization was studied in a nematic liquid crystal of the 4-*n*-butyl ester of [4'-*n*-hexyloxyphenyl] benzoic acid (BE[HOP]BA) in the absence of external orienting fields in the isotropic and mesophase states in a frequency range of 10^3–10^7 Hz. In the isotropic melt, three regions of dielectric absorption of a relaxation origin were revealed. It is shown that two of them are related to a reorientation motion of individual molecules about the longitudinal axes (process I) and about the short axes (process II). Processes I and II have relaxation times $\tau \sim 10^{-9}$ and 10^{-8} s and activation energies $\Delta U \sim 16$ and 23 kcal/mol, respectively; the energy of activation of process II in the liquid-crystal phase increases to $\Delta U \sim 38$ kcal/mol. In the isotropic melt, in addition to processes I and II, process III occurs in the low-frequency range, which is characterized by greater relaxation times $\tau \sim 10^{-7}$ s and an activation energy $\Delta U \sim 28$ kcal/mol. In order to establish the nature of process III, temperature dependences of the dipole moments and Kirkwood correlation factor g were studied in both BE[HOP]BA phases. The magnitude of the Kirkwood factor in the isotropic phase of the BE[HOP]BA near the transition temperature from the mesomorphic state ($g \sim 0.88$) indicates the retention of the orientational ordering of molecules of the low-molecular liquid crystal and the compensation of their dipole moments intrinsic to the liquid-crystal state. This circumstance suggests that the third process of the relaxation of dipole polarization is due to a cooperative mode of motion of molecules in mesophase nuclei in the isotropic melt. © *2002 MAIK "Nauka/Interperiodica"*.

1. INTRODUCTION

The investigation of molecular interactions in low-molecular liquid crystals (LLC) is important because they are promising materials for the incorporation into the chemical structure of polymer macromolecules.

Molecular groups or mesogenic fragments that are LLCs in their chemical nature, can enter into the structure of the main or side chains of macromolecules. Their presence may be responsible for conformational and dynamical properties of macrochains. In this connection, LLCs may be used as models in studying molecular interactions in liquid-crystal (LC) polymers [1–3]. In our previous studies of dipole moments and dielectric relaxation of linear and comb-shaped polymers with mesogenic fragments in the side or main chains [4–7], several modes of molecular motion caused by the kinetic properties of mesogenic fragments were revealed. Along with small-scale modes of molecular motion (relaxation times $\tau \sim 10^{-9}$ s) related to a reorientation motion of "partial" dipole moments of individual molecular groups in a mesogenic fragment, dielectric dispersion with large relaxation times ($\tau \sim 10^{-6}$ s) is fixed in macromolecular coils. We consider this type of mobility as a cooperative mode of reorientational motion of mesogenic fragments in nuclei of their ordered mutual arrangement that occurs even in dilute solutions of LC polymers. The study of conformation properties of isolated macromolecules of LC polymers with a comb-shaped structure suggests the presence of ordering of mesogenic fragments inside a macromolecular coil [8, 9]. The magnitudes of the Kirkwood correlation factor g ($g = [\langle M^2 \rangle / N]/\mu_0^2$, where $\langle M^2 \rangle$ is the mean-square dipole moment of a macromolecule, N is the number of monomer units in a macromolecule, and μ_0^2 is the square of the dipole moment of a free monomer unit) in these polymers turned out to be close to the values of g in anisotropic solutions of LLCs whose structure is close to that of the mesogenic fragment in a macromolecule.

In this connection, in the isotropic melt of an LLC, one should expect the presence of heterophase fluctuations inside the homophase environment above the temperature of transition from the LC into the isotropic phase. Frenkel' notes in his work devoted to the study of heterophase fluctuations [10] that in the vicinity of phase-transition points (by temperature or pressure), which are determined by the conditions of thermodynamic equilibrium between the corresponding phases, heterogeneous or "heterophase" fluctuations can arise.

Relaxation times τ and activation energies Δ*U* for the process of relaxation of dipole polarization in 4-*n*-butyl ether of [4'-*n*-hexyloxyphenyl] benzoic acid

State	Isotropic phase, $T = 50°C$			LC phase, $T = 27°C$	
Process	I	II_A	III	I	II_B
τ, s	4.6×10^{-9}	2.6×10^{-8}	8.6×10^{-7}	5.7×10^{-8}	9.5×10^{-7}
Δ*U*, kcal/mol	16	23	28	16	38

The appearance of nuclei of a new phase inside a virtually homogeneous substance occurs upon cooling or heating, i.e., in the thermodynamically unstable state.

The use of the dielectric-polarization method for the investigation of the mechanisms of intramolecular interactions, which manifest themselves in molecular characteristics and properties such as the polarizability, dipole moments, molecular dynamics (the relaxation times for dipole polarization and the activation energies) gives information on the anisotropy of intermolecular interactions, which, in turn, cause the mesogenic nature of the substance on the whole.

As was shown in our previous work [11], the dielectric-polarization method is a sensitive tool for revealing changes in the dynamics of molecules depending on the character of intermolecular interactions in the system. Therefore, this method was used to clarify whether there are ordered domains (clusters) in the isotropic state of LLCs in the absence of a constant external orienting field.

In this work, we used the dielectric-polarization method to study the molecular motion and internal rotation in a thermotropic LLC, namely, in the 4-*n*-butyl ester of [4'-*n*-hexyloxyphenyl] benzoic acid (BE[HOP]BA), in the isotropic melt and in the mesophase state.

As follows from [12], where the structure of low-molecular crystals was considered in connection with the type of the mesophase they form, the BE[HOP]BA refers to the class of typical thermotropic nematic crystals.

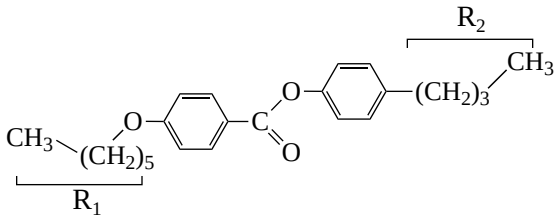

Fig. 1. Chemical formula of a thermotropic nematic liquid crystal of 4-*n*-butyl ether of [4'-*n*-hexyloxyphenyl] benzoic acid (BE[HOP]BA): R_1–O–Ph–COO–Ph–R_2, where Ph is the phenyl radical and R is the alkyl radicals (R_1, the hexyl, and R_2, the butyl radicals).

2. EXPERIMENTAL

The identification of the molecular structure of the BE[HOP]BA was performed based on the spectra of proton magnetic resonance. The spectrum was recorded on an AC-200 Bruker spectrometer (working frequency 200 MHz) for a 5% solution in $CDCl_3$ at room temperature. When identifying signals, the increments of the substituents of aromatic structures and the correlation tables of screening constants were taken into account. The spectrum and the signal identification are shown in Fig. 2.

Dielectric measurements were performed in airtight glass cells (weighing bottles) with a rigid system of platinum plate or coaxial cylindrical electrodes. No other structural materials were present in the interelectrode space. The cells used in this work are constructive modifications of our previously described cell for measuring dielectric constants of liquids [13]. The reservoir of the cells is supplied with a "jacket" (made as an integer part of the reservoir) for passing a thermostating liquid. Through the cell lid with a system of electrodes, a glass tube was also mounted to introduce a thermocouple into the cell. The electric capacitance of the capacitors was $C_0 = 4.53$ pF (platinum plates with a spacing between the electrodes $\delta = 0.12$ cm) and $C_0 = 3.65$ pF (cylindrical surfaces with $\delta = 0.2$ cm) with the filling volumes ~0.5 and ~1 cm^3, respectively. The BE[HOP]BA in the reservoir of the capacitor was first melted to the isotropic-liquid state, after which the reservoir was covered with a lid with a sealed-in system of electrodes. The temperature inside the capacitor was maintained using a U-8 thermostat to an accuracy of 0.1 K. During the measurements of the dielectric constant and dielectric losses, the BE[HOP]BA was heated to 80°C and cooled at a rate of 0.5 K/min after holding at a fixed temperature for 20–30 min. The transparency of the measuring dielectric cell permitted us to visually determine the temperatures of phase transitions in the BE[HOP]BA, which were equal to 29 and ~44°C for the transition of the crystal into the LC state and further into the isotropic melt, respectively. The static dielectric constant ε was determined in a capacitor with $C_0 = 4.53$ pF using a TESLA BM484 bridge ($f = 1.592 \times 10^3$ Hz) ± 0.001. The density ρ of BE[HOP]BA was measured to within to an accuracy of at least ±0.0002 g/cm^3 by using the float method [14].

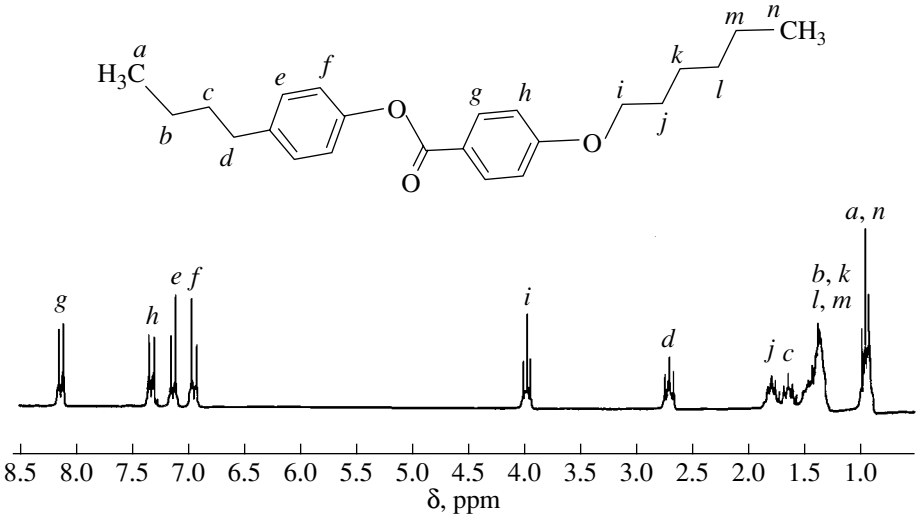

Fig. 2. Proton magnetic resonance spectrum of the BE[HOP]BA.

The dipole moment was calculated by the Onsager formula [15]

$$[(\varepsilon - n^2)(2\varepsilon + n^2)]/[\varepsilon(n^2 + 2)^2] = (4/3)(\pi N/M)\rho(\mu^2/3kT), \quad (1)$$

where ε, n, ρ, μ, and M are the dielectric constant, the refractive index, the density, the dipole moment, and the molecular weight of BE[HOP]BA, respectively; T is the temperature in Kelvins; k is the Boltzmann constant; and N is Avogadro's number.

The refractive index of BE[HOP]BA was determined using the expression for the molar refraction R

$$R = (M/\rho)(n^2 - 1)/(n^2 + 2). \quad (2)$$

The magnitude of the molar refraction was calculated based on the molar refractions of the bonds in the BE[HOP]BA molecule [16].

The dielectric losses were determined in a capacitor with $C_0 = 3.65$ pF using a BM-560 Q meter and a Novocontrol broadband dielectric converter in a frequency range of 10^3–10^7 Hz to an accuracy of at least ±0.5%. The relaxation time and the activation energy of the dipole polarization were determined from the Arrhenius equation

$$\tau = \tau_0 \exp(\Delta U/kT). \quad (3)$$

3. RESULTS AND DISCUSSION

3.1. Dipole Moment of BE[HOP]BA

Measurements of the electric capacitance of the capacitor filled by the BE[HOP]BA were performed upon heating and cooling. The results of these measurements are given in Fig. 3. Segment *1* of the curve corresponds to the transition of the substance from the solid into the LC state. This transition is fixed at $T = 29$°C. Since the nematic liquid crystals are characterized by only one spatial direction of orientational ordering of molecules, the transition into the isotropic melt in the absence of external orienting fields is accompanied by a gradual change in the dielectric parameters. Thus, in the nematic the temperature of transition into the isotropic state can be fixed by the change in the slope of the temperature dependence of the dielectric constant. It is seen that the change in the temperature coefficient of the dielectric constant occurs at a temperature of ~43–44°C. This temperature region corresponds to the nematic–isotropic-melt phase transition in the BE[HOP]BA. It is also seen from Fig. 3 that upon cooling of the isotropic melt (segments *3*, *2*, and *4* of the curve), the BE[HOP]BA passes under chosen experi-

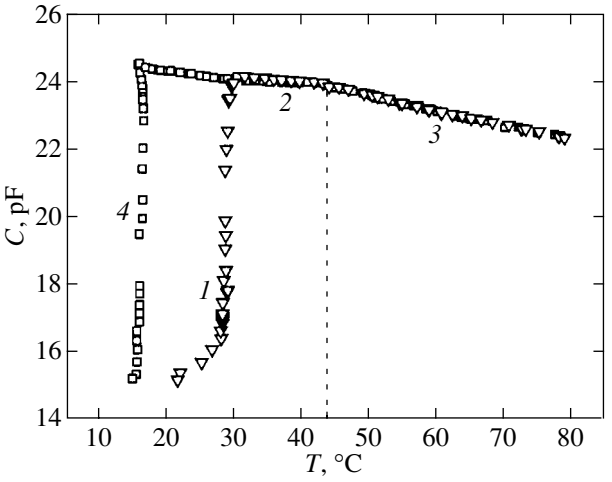

Fig. 3. Temperature dependence of the electrical capacitance of the capacitor filled with the BE[HOP]BA: (*1*), (*2*), (*3*) upon heating and (*3*), (*2*), (*4*) upon cooling.

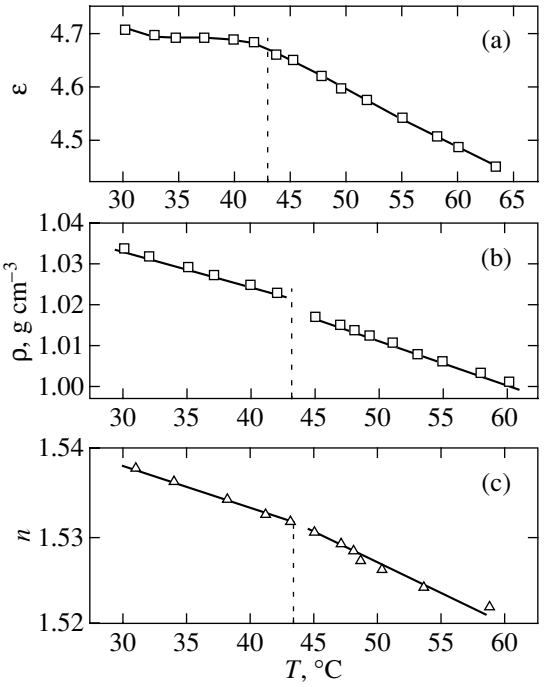

Fig. 4. (a) Dielectric constant ε, (b) density ρ, and (c) refractive index *n* of the BE[HOP]BA as functions of temperature.

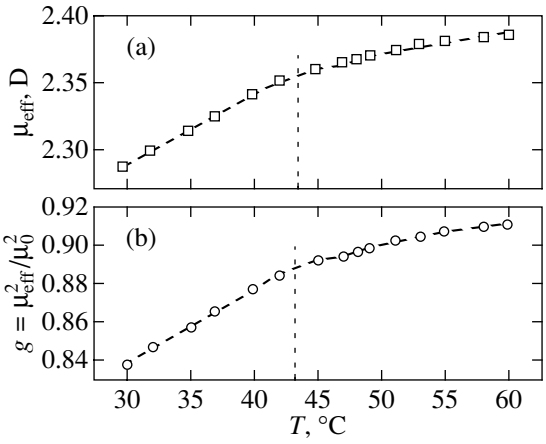

Fig. 5. (a) The dipole μ_{eff} moment and (b) the correlation factor $g = \mu_{eff}^2/\mu_0^2$ of the BE[HOP]BA as functions of temperature.

mental conditions into the solid state at a temperature of ~16°C; i.e., it can easily be supercooled.

Figure 4 displays the temperature dependences of the dielectric constant ε, density ρ, and refractive index *n* of the BE[HOP]BA in the range of 30–65°C. It is seen that the nematic–isotropic-melt transition temperature is fixed as a change in the temperature coefficients of these dependences in the various phases of the BE[HOP]BA in the same temperature range of ~43–44°C. Using the data shown in Fig. 4 and formula (1), we calculated the effective molecular dipole moments of BE[HOP]BA, μ_{eff}. Because of specific intermolecular interactions in BE[HOP]BA, the magnitude of μ_{eff}, according to the Onsager theory of polarization, should differ from the true value of the dipole moment of an isolated molecule in "vacuum," μ_0. Figure 5a shows the μ_{eff} values depending on the temperature; μ_{eff} = 2.28 D at 30°C and increases to μ_{eff} = 2.35 D at 42°C. It is seen from Fig. 5a that the temperature coefficient of the dipole moment of the BE[HOP]BA changes upon transition from the isotropic to the liquid-crystal state. The values of the dipole moment in the isotropic state are greater than in the mesomorphic state (μ_{eff} = 2.38 D at 60°C).

To estimate the dipole moment of an isolated molecule, μ_0, we calculated the geometry of the molecule by a semiempirical quantum-mechanical method PM3 using a HYPERCHEM 5.0 program [17]. The length of the BE[HOP]BA molecule in the ultimately extended *trans* conformation (with respect to the arrangement of the alkyl radicals to the molecule axis) is 24.4 Å. The width of the molecule is approximately 5.0 Å and the thickness depends on the mutual arrangement of the benzene rings and can change from 1.8 (upon the parallel arrangement of the rings) to 5.0 Å (upon their mutually perpendicular arrangement). In our case, with allowance for the van der Waals radii, the maximally extended *trans* conformation of the molecule can be described as a cylinder of length L = 26.7 Å and diameter D = 7.3 Å. The calculation of the ultimately extended *cis* conformation gives close values for the length of the model cylinder and its diameter (L = 26.5 Å and D = 7.6 Å).

As can be seen from Fig. 1, the BE[HOP]BA molecule contains several polar groups; their dipole moments were determined in [18]. The central portion of the molecule contains a polar ester group –COO– with a dipole moment ~1.9 D, as well as a polar group Ph–O–C– with a dipole moment ~1.28 D; the dipole moment of the Ph–R group is ~0.36 D. We calculated the dipole moments for the *cis* and *trans* conformations of the BE[HOP]BA molecules for the case of free internal motion of these partial dipole moments. They are 2.49 D for the *trans* conformation and 2.47 D for the *cis* conformation. Thus, we can accept a value $\mu_0 \sim 2.5$ D for the approximate value of the molecular dipole moment of the BE[HOP]BA in "vacuum." Using this value, we calculated the factor of correlation in the orientations of the dipole moments g (Kirkwood factor [19]) by the formula

$$g = \mu_{eff}^2/\mu_0^2. \quad (4)$$

These data are given in Fig. 5b. It is seen from Figs. 5a and 5b that in both BE[HOP]BA phases we obtain $\mu_{eff} < \mu_0 \sim 2.5$ D and $g < 1$. The correlation factor increases with temperature: g = 0.84–0.88 in the LC phase and 0.89–0.91 in the isotropic melt of the BE[HOP]BA. The values of g smaller than unity unam-

biguously indicate a preferred intermolecular packing with a compensation of molecular dipole moments. With increasing temperature, the intensity of thermal motion increases and the orientational ordering of BE[HOP]BA molecules should decrease. In this case, the mutual compensation of molecular dipole moments also decreases and the magnitudes of μ_{eff} and g increase. In the isotropic melt, the rate of increasing μ and g with temperature decreases and their magnitudes tend to constant values $\mu = 2.38$ D and $g = 0.91$. In the vicinity of the transition of the LLC into the isotropic melt ($T \sim 44$°C), the correlation factor remains less than unity, $g \sim 0.88$–0.89. This may indicate the retention in the isotropic melt of domains with an ordered arrangement of the long axes of the anisodiametric BE[HOP]BA molecules with respect to one another and the compensation of their molecular dipole moments. A change in the molecular dipole moments of BE[HOP]BA with temperature agrees with the results of the investigation of spin–spin nuclear magnetic relaxation in the BE[HOP]BA in the isotropic melt [20].[1] In the present work, we estimated the parameter of local order in clusters of BE[HOP]BA which were considered, following the Frenkel' theory [10], as nuclei of the nematic phase in the continuum of the isotropic liquid.

Thus, the investigation of dipole moments of the NLC BE[HOP]BA showed the presence of orientational ordering of BE[HOP]BA molecules both in the liquid-crystal state and in the isotropic melt in the absence of external orienting fields. The conformational and steric properties of BE[HOP]BA molecules determine the character of their molecular ordering characterized by the compensation of molecular dipole moments.

3.2. Molecular Mobility in BE[HOP]BA

Consider data on the relaxation of the dipole polarization of the BE[HOP]BA in the isotropic melt and in the LC state in the absence of external orienting fields.

As an example, Fig. 6 displays the variation of the dielectric loss tangent as a function of the temperature and frequency. Dashed lines in the figure correspond to temperatures at which there occur phase transitions from the isotropic melt into the liquid-crystal state (at ~43°C) and from the liquid-crystal into the crystalline state (at ~24.5°C).[2] It is seen from Fig. 6 that in the liquid-crystal and isotropic phases, in all temperature

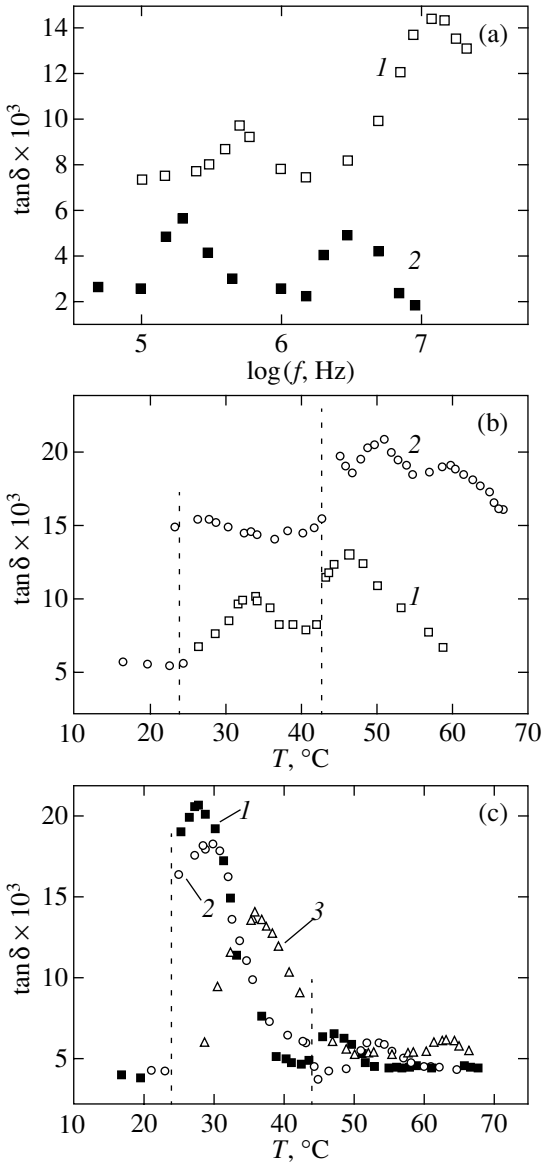

Fig. 6. Variation of the dielectric loss tangent tanδ of BE[HOP]BA as functions of (a) frequency and (b), (c) temperature: (a) (*1*) in the isotropic melt at 57°C and (*2*) in the LC state at 27°C; (b) (*1*) at 5 and (*2*) 21 MHz; and (c) (*1*) at 0.15, (*2*) 0.3, and (*3*) 1 MHz.

dependences of the dielectric losses, processes of relaxation of dipole polarization manifest themselves.

Figure 7 shows (in Arrhenius coordinates $-\log\tau$ vs. T^{-1}) data on the relaxation times of dipole polarization τ as determined from the frequency or temperature position of $\tan\delta_{max}$. It is seen from Fig. 7 that, in the frequency and temperature ranges used in this work, the relaxation times exhibit dependences of three types, I, II, and III. In the range of the highest frequencies, the $-\log\tau$ vs. T^{-1} dependence (process I) is common for both phases of the BE[HOP]BA and can be designated as I_{AB}. The dependence of the relaxation time for pro-

[1] Note that, when writing the structural formula and the name of the NLC investigated in [20], a misprint crept. In [20] and in the present work, the same material was studied, namely, the low-molecular liquid crystal 4-*n*-butyl ether of [4'-*n*-hexyloxyphenyl] benzoic acid (BE[HOP]BA).

[2] The BE[HOP]BA can easily be supercooled. The temperature range of its LC state may be expanded into the region of even negative temperatures [21]. In our work, we used this capability of the BE[HOP]BA for the investigation of the dielectric constant (Section 1) and the frequency dependence of dielectric losses in the range of low frequencies in the LC phase (see below).

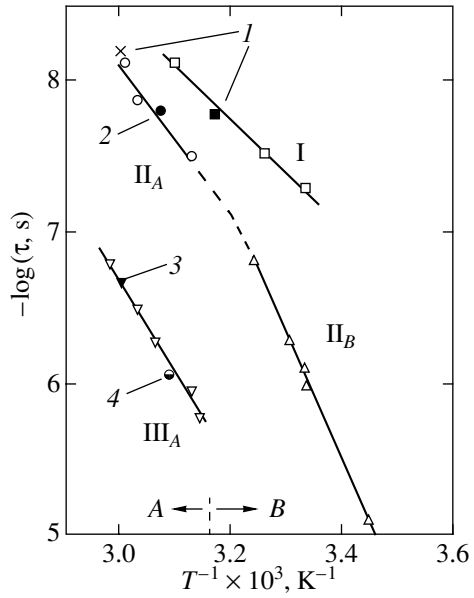

Fig. 7. Relaxation time τ of dipole polarization in the BE[HOP]BA depending on the temperature: (*A*) in the isotropic phase and (*B*) in the LC phase; (*1*) according to [21]; (*2*) calculated value of τ; (*3*) according to [22]; and (*4*) according to [23].

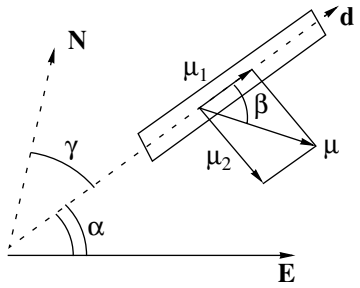

Fig. 8. A schematic of a polar rodlike molecule of an LLC in an electric field **E**: **μ**, **μ**$_1$, and **μ**$_2$ are the molecular dipole moment and its longitudinal and transverse projections on the molecule axis **d**; **N** is the direction of the macroscopic ordering of molecules; and α, β, and γ are the angles between the vectors, (**d**, **E**), (**μ**, **d**), and (**N**, **d**), respectively.

cess II is of a more complex nature. The temperature coefficient of this process suffers a rather sharp change upon the transition of the BE[HOP]BA from the isotropic state into the LC state and can be represented by two linear dependences, namely, II$_A$ in the isotropic phase *A* and II$_B$ in the LC phase *B*. The –logτ vs. T^{-1} dependence in the low-frequency range in the isotropic phase can be considered as process III$_A$. The linear character of the temperature dependences of the times of dielectric relaxation τ permits us to determine, using Arrhenius equation (3), the activation energies of all the relaxation processes given in Fig. 7. The parameters of these processes, i.e., the relaxation times and the activation energies (τ and Δ*U*) in the liquid-crystal and isotropic phases are given in the table. As is seen from the table and Fig. 7, the activation energy Δ*U* of process I does not change upon the transition from the isotropic into liquid-crystal state and is Δ*U* ~ 16 kcal/mol. At the same time, the energy of activation for process II changes by a factor of almost 1.5. Let us compare the parameters of processes I and II for the isotropic state. As is seen from the table, the parameters of the dipole relaxation of BE[HOP]BA in the isotropic phase (relaxation times of processes I and II and the activation energies Δ*U*) are typical of the reorientation motion of anisodiametric molecules about the longitudinal and transverse axes in LLCs [24–28]. The appearance of these modes of motion of rodlike molecules in an electric field is illustrated schematically in Fig. 8. If the total molecular dipole moment **μ** makes an angle β with the long axis of the molecule **d**, as in the case of the BE[HOP]BA [21], then in an external electric field *E* whose direction makes an arbitrary angle α with the long axis of the molecule **d**, the parallel (**μ**$_1$) and perpendicular (**μ**$_2$) components of the dipole moment **μ** have the following projections onto the direction **E**:

$$\boldsymbol{\mu}_{1E} = \boldsymbol{\mu}\cos\angle(\boldsymbol{\mu}, \mathbf{d})\cos\angle(\mathbf{d}, \mathbf{E}) = \boldsymbol{\mu}\cos\angle\beta\cos\angle\alpha,$$

$$\boldsymbol{\mu}_{2E} = \boldsymbol{\mu}\sin\angle(\boldsymbol{\mu}, \mathbf{d})\sin\angle(\mathbf{d}, \mathbf{E}) = \boldsymbol{\mu}\sin\angle\beta\sin\angle\alpha,$$

μ$_{1E}$ and **μ**$_{2E}$ are dielectrically active labels and, therefore, in accordance with the modern concepts of dielectric polarization in thermotropic NLCs [29, 30], we should expect the existence of two orientation-related mechanisms of relaxation of dipole polarization. However, the parameters of these relaxation processes (τ and Δ*U*) should suffer different changes upon the transition from the isotropic melt into the liquid-crystal state. In an anisotropic liquid state, a reorientation of polar molecules under the effect of an electric field is mainly connected with overcoming potential barriers that support the orientational order. Maser and Meier [31] were the first to report the existence of high-frequency and low-frequency relaxation in NLC para-azoxyanisole and demonstrated the difference in the retarding effect of the nematic potential on the rotation of molecules about the short and long molecular axes.

Approximating the BE[HOP]BA molecule by a cylinder with maximum dimensions (length $L \approx 27$ Å and diameter $D \approx 7.6$ Å) and using the data given in Section 3.1, we calculated the times of relaxation of the molecule about the short axis by the Boersma formula [32]

$$\tau = \pi\eta L^3/6kT[\ln(L/b) - \gamma],$$

where η is the viscosity of the substance, *L* and $b = D/2$ are the dimensions of the cylinder (*L* is the length and *D* is the diameter), and $\gamma \sim 0.9$.

The relaxation time of the cylinder was calculated at $T = 326$ K, at which the BE[HOP]BA represents an isotropic melt. Its viscosity as determined by a standard

Ubbelohde viscometer is 9.5 cP at this temperature.[3] To calculate the viscosity of the BE[HOP]BA, we used the experimental values of its density (see Section 2). The calculated relaxation time is 20 ns. This value of the relaxation time satisfies dependence II_A in Fig. 7. Thus, process II of the relaxation of dipole polarization is caused by the rotation of BE[HOP]BA as a whole about the short axis.

It is seen from Fig. 7 that the relaxation times are smaller for process I than for process II. We may assume that process I is due to the rotation of the BE[HOP]BA molecule as a whole about the long axis and to the intramolecular rotations of polar molecular groups. These reorientation motions should not be substantially affected (in the first approximation) by the mesomorphic potential. The rotation of molecules about the short axis in the LC phase undergoes an additional retardation due to the nematic potential. In the LC phase, the relaxation times for both types of motion differ substantially (see table). The data obtained agree well with the results of the investigation of the dielectric relaxation of LLCs with a similar molecular structure and dimensions reported in [21–23, 26]. Some of these results are given in Fig. 7.

Along with the processes of relaxation of dipole polarization I and II caused by the motion of a molecule as a whole, the experimental data show that one more process of dielectric relaxation (Fig. 7, process III) occurs in the isotropic melt of the BE[HOP]BA, which manifests itself in the low-frequency range. As is seen from the table, it is characterized by enhanced (as compared to the above-considered processes I and II in the isotropic state) values of the activation energy and relaxation time.

As was noted in the beginning of this paper, the processes of dielectric relaxation with such high values of the relaxation times and activation energies (along with the processes that occur via local mechanisms) were observed in our previous works devoted studying comb-shaped and linear polymers even in dilute solutions [7, 33]. The nature of such processes was ascribed (by both us and other researchers [34–36]) to a cooperative motion of molecular fragments (containing mesogenic or other fragments with functional groups that exhibit the capacity to specific intra- or intermolecular interactions) that form nuclei of supramolecular structures.

Thus, the method of relaxation of dielectric polarization is a source of information on the kinetic properties of molecules as well as on the intra- and intermolecular interactions in both liquid-crystal polymers and in low-molecular liquid crystals. The presence of nuclei of a mesophase (heterophase fluctuations) on both microscopic (in the isotropic melt of LLCs) and macromolecular (in solutions of polymeric liquid crystals) levels is a characteristic phenomenon for the substances with an anisodiametric molecular structure because of the anisotropic molecular interactions that lead to local orientational ordering even in the absence of external orienting fields.

The above analysis of the data on the investigation of the BE[HOP]BA by the methods of dielectric polarization and the results of the investigations of the BE[HOP]BA by nuclear magnetic relaxation [20] suggest that process III is caused by a cooperative reorientation motion of molecules in clusters of fluctuational nature, which take place in the isotropic melt of low-molecular liquid-crystal substances.

[3] The experimental determination of the viscosity of the BE[HOP]BA was performed by É.P. Astapenko.

ACKNOWLEDGMENTS

This work was supported in part by the Russian Foundation for Basic Research, project no. 97-03-32658. We are grateful to T.I. Borisova for helpful discussion of the results of this work and useful remarks.

REFERENCES

1. *Liquid-Crystalline Polymers*, Ed. by N. A. Platé (Khimiya, Moscow, 1988).
2. N. A. Platé and V. P. Shibaev, *Comb-shaped Polymers and Liquid Crystals* (Nauka, Moscow, 1980).
3. *Molecular Dynamics and Theory of Broadband Spectroscopy*, Ed. by M. Evans, G. J. Evans, W. T. Coffey, and P. Grigollini (Wiley, New York, 1982).
4. T. I. Borisova, T. P. Stepanova, Ya. S. Freĭdzon, *et al.*, Vysokomol. Soedin., Ser. A **30** (8), 1754 (1988).
5. T. P. Stepanova, L. L. Burshteĭn, T. I. Borisova, and V. P. Shibaev, Vysokomol. Soedin., Ser. A **35** (6), 658 (1993).
6. T. I. Borisova, L. L. Burshteĭn, N. A. Nikonorova, *et al.*, Vysokomol. Soedin., Ser. A **40** (1), 38 (1998).
7. T. P. Stepanova and L. L. Burshtein, Chin. J. Polym. Sci. **14** (1), 1 (1996).
8. T. I. Borisova, L. L. Burshteĭn, T. P. Spepanova, *et al.*, Vysokomol. Soedin., Ser. A **28** (5), 1031 (1986); Vysokomol. Soedin., Ser. B **28** (9), 673 (1986).
9. T. I. Borisova, L. L. Burshteĭn, V. P. Malinovskaya, *et al.*, Vysokomol. Soedin., Ser. B **32** (6), 406 (1990).
10. J. Frenkel, J. Chem. Phys. **7** (7), 538 (1939).
11. T. I. Borisova, L. L. Burshtein, T. P. Stepanova, and N. A. Nikonorova, Int. J. Polym. Mater. **22**, 103 (1993).
12. V. A. Usol'tseva, Zh. Vses. Khim. O-va. **28** (2), 2 (1983).
13. T. P. Stepanova and L. L. Burshteĭn, USSR Inventor's Certificate No. 1023233.
14. A. I. Shatenshteĭn, E. A. Yakovleva, U. N. Zvyagintseva, Ya. M. Varshavskiĭ, E. A. Izrailevich, and N. M. Dykhno, *Isotopic Analysis of Water* (Akad. Nauk SSSR, Moscow, 1957), Chap. 6, p. 86.
15. L. Onsager, J. Chem. Soc. **58**, 1486 (1936).
16. M. V. Vol'kenshtein, *Configurational Statistics of Polymeric Chains* (Akad. Nauk SSSR, Moscow, 1959; Interscience, New York, 1963).
17. HyperChem(TM), Hypercube, Inc., 1115 NW 4th Street, Gainesville, Florida 32601, USA.

18. R. T. Kliingbiel, D. J. Genova, T. R. Criswell, and J. P. van Meter, J. Am. Chem. Soc. **96**, 7651 (1974).
19. J. G. Kirkwood, J. Chem. Phys. **7**, 911 (1939).
20. E. R. Gasilova, V. A. Shevelev, and S. Ya. Frenkel, Liq. Crys. **27** (5), 573 (2000); **27** (5), 579 (2000).
21. V. N. Tsvetkov and E. I. Ryumtsev, Zh. Vses. Khim. O-va. **28** (2), 94 (1983).
22. H. Kresse, J. Pietscher, H.-J. Deutscher, *et al.*, Z. Phys. Chem. (Leipzig) **259** (4), 779 (1978).
23. H. Kresse, Fortschr. Phys. **30** (10), 507 (1982).
24. H. Kresse, A. Wiegeleben, and D. Demus, Cryst. Res. Technol. **15**, 334 (1980).
25. H. Kresse and B. Gagejwska, Phys. Status Solidi A **64**, 161 (1981).
26. H. Kresse, Adv. Liq. Cryst. **6**, 109 (1983).
27. H. Kresse, H. Schmalfuss, B. Gestblom, *et al.*, Liq. Cryst. **23**, 891 (1997).
28. M. Schadt, J. Chem. Phys. **56** (4), 1494 (1972).
29. P. de Gennes, *The Physics of Liquid Crystals* (Clarendon, Oxford, 1974; Mir, Moscow, 1977).
30. W. H. de Jeu, *Physical Properties of Liquid Crystalline Materials* (Gordon and Breach, New York, 1980; Mir, Moscow, 1982).
31. W. Maser and G. Meier, Z. Naturforsch. A **16**, 1200 (1961).
32. S. Boersma, J. Chem. Phys. **32** (6), 1626 (1960).
33. T. P. Stepanova, L. L. Burshteĭn, T. I. Borisova, *et al.*, Vysokomol. Soedin., Ser. A **39** (4), 606 (1997).
34. T. P. Stepanova, L. L. Burshteĭn, T. I. Borisova, and V. P. Shibaev, Vysokomol. Soedin., Ser. A **35** (6), 658 (1993).
35. E. V. Anufrieva, V. D. Pautov, Ya. S. Freĭdzon, and V. P. Shibaev, Vysokomol. Soedin., Ser. A **19** (12), 755 (1977).
36. V. N. Tsvetkov, E. I. Ryumtsev, and I. N. Shtennikova, Vysokomol. Soedin., Ser. A **13** (2), 506 (1971).

Translated by S. Gorin

Physics of the Solid State, Vol. 44, No. 10, 2002, pp. 2001–2008. Translated from Fizika Tverdogo Tela, Vol. 44, No. 10, 2002, pp. 1908–1914.

FULLERENES AND ATOMIC CLUSTERS

Small-Angle X-ray Scattering in a Carbon–Sulfur Nanocomposite Produced from Bulk Nanoporous Carbon

É. A. Smorgonskaya*, R. N. Kyutt*, V. B. Shuman*, A. M. Danishevskiĭ*, S. K. Gordeev, and A. V. Grechinskaya****

** Ioffe Physicotechnical Institute, Russian Academy of Sciences, Politekhnicheskaya ul. 26, St. Petersburg, 194021 Russia*

*** Central Research Institute of Materials, St. Petersburg, 191014 Russia*

Received December 25, 2001

Abstract—A new nanocomposite material containing approximately 50 vol % S is prepared by filling pores of bulk nanoporous carbon samples with sulfur. The initial nanoporous carbon samples are synthesized from polycrystalline α-SiC through the chemical reaction. A comparative investigation of small-angle x-ray scattering (SAXS) is performed for the prepared nanocomposite and the initial material. The possible changes in the scattering power of the initial material upon filling of its pores with sulfur are considered in the framework of a simple model. The regularities revealed are used to interpret the experimentally observed changes in the scattering power. The size distribution functions of incorporated sulfur nanoclusters in the nanocomposite (or filled nanopores in the initial material) are determined within the Guinier approximation. It is demonstrated that the smallest sized pores (8–16 Å) remain unfilled, whereas the filling factor for larger sized pores can reach several ten percent by volume. The conditions favorable for small-angle x-ray scattering upon filling of the nanopores are analyzed. © *2002 MAIK "Nauka/Interperiodica".*

1. INTRODUCTION

It is known that nanoporous carbon, which is referred to sometimes as nanocluster carbon, can be prepared in the form of bulk samples with a specified shape according to an original technique involving high-temperature chlorination of carbide powders subjected to preliminary special heat treatment [1–4]. As follows from data on the adsorption [1], nanoporous carbon is characterized by a high nanoporosity (up to 45 vol % at a total porosity as large as 70 vol %) and high nanopore size uniformity. The characteristic size of nanopores depends on the initial carbide. For example, the nanopore size estimated within the slit pore model for nanoporous carbon produced from a polycrystalline α-SiC powder is approximately equal to 8 Å. Owing to these specific features and many other interesting physical and physicochemical properties, nanoporous carbon holds promise as a host material for use in designing a new class of nanocomposites through the filling of pores with guest materials of different nature. At present, the synthesis and examination of composites based on carbon nanocluster materials is a topical direction in the physics and technology of condensed matter [5].

In the present work, we prepared the new nanocomposite material with the use of the host–guest method of filling bulk nanoporous carbon pores with sulfur and performed a small-angle x-ray scattering (SAXS) investigation into the size characteristics of incorporated sulfur nanoclusters. Earlier [6], we used the SAXS technique to examine the nanoporous carbon materials synthesized from different carbides. The distribution functions of structural nanoinhomogeneities over sizes (or gyration radii R_g) and the characteristic gyration radii R_g were determined from analyzing the small-angle x-ray scattering curves $I(s)$ in the framework of the Guinier model. Here, I is the SAXS intensity, $s = 4\pi\sin\vartheta/\lambda$ is the scattering vector magnitude, 2ϑ is the scattering angle, and λ is the x-ray radiation wavelength. However, in the case of highly porous materials, such as nanoporous carbon with comparable volumes of nanopores and nanoclusters of the carbon skeleton, it is difficult to uniquely assign the aforementioned distribution functions and characteristic gyration radii to either nanopores or nanoclusters, because one or the other can contribute to scattering. Actually, the intensity of small-angle x-ray scattering by inhomogeneities with the volume v and the concentration N is proportional to the square of the corresponding electron density fluctuations $\Delta\rho \equiv \rho - \bar{\rho}$ with respect to the mean electron density $\bar{\rho}$, that is,

$$I(s) \propto |\Delta\rho|^2 N v^2, \tag{1}$$

and, hence, does not depend on the sign of $\Delta\rho$ (in the framework of the Guinier model, the inhomogeneity shape is disregarded and $v \propto R_g^3$). If the electron densities ρ_C and ρ_{np} are assigned to nanoclusters and nanopores, the mean electron density $\bar{\rho}$ can be defined as

$$\bar{\rho} = (1-\alpha)\rho_C + \alpha\rho_{np}, \tag{2}$$

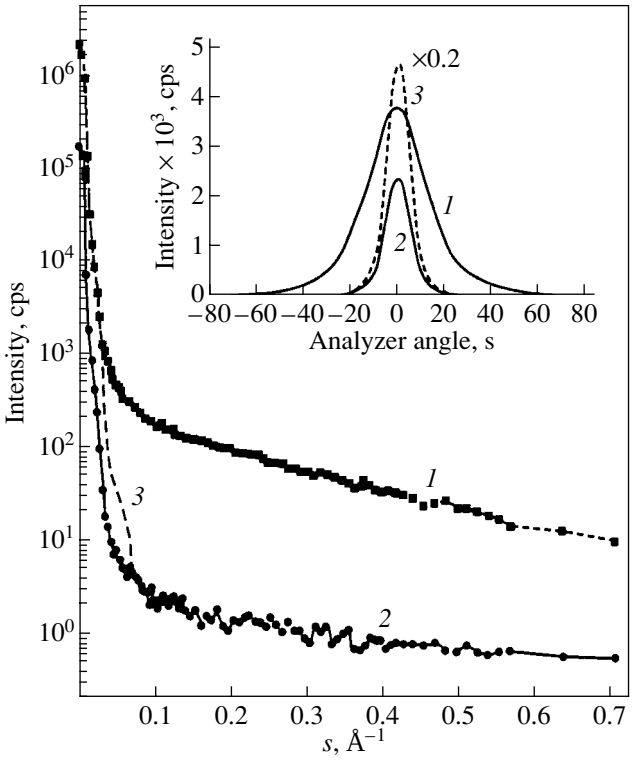

Fig. 1. Experimental dependences of the intensity of x-ray radiation passed through samples of the studied materials on the scattering vector magnitude. Materials: (*1*) the initial nanoporous carbon prior to filling of pores with sulfur (L_1 = 1.05 mm) and (*2*) the nanocomposite prepared by filling nanoporous carbon pores with sulfur (L_2 = 0.35 mm). (*3*) Distribution of the primary-beam intensity in the entrance slit plane. The inset shows the angular distributions of the intensity at ultrasmall scattering angles (the designations of the curves are the same).

where $\alpha = V_{np}/V$ is the degree of nanoporosity, i.e., the volume fraction of nanopores with the total volume $V_{np} \equiv N_{np}v_{np}$ in the sample of volume V. It follows from expressions (1) and (2) that, at $\alpha \lesssim 0.5$, the intensity of small-angle x-ray scattering by nanoclusters and nanopores can be represented by the relationship $I(s) \propto |\rho_C|^2$. Therefore, the nanoclusters and pores at comparable volumes can make comparable contributions to small-angle x-ray scattering. The introduction of sulfur makes it possible to change (to increase) the electron density ρ_{np}, thus changing the contrast $|\rho_{np} - \rho_C|$ between nanopores and the nanoporous carbon skeleton and, correspondingly, the magnitude of electron density fluctuations $|\Delta\rho|$. Analysis of the changes observed in the SAXS curve can provide an answer to the question regarding the size characteristics of nanopores filling with sulfur in nanoporous carbon upon formation of the nanocomposite material. In particular, Plavnik *et al.* [7, 8] used a similar contrast-variation procedure in the SAXS investigation of adsorption, desorption, and mass transfer in porous carbon adsorbents.

The introduction of sulfur into nanoporous carbon is of special interest as a possible efficient method of modifying the properties of materials. Recently [9], sulfur introduced in the course of evaporation was used to prepare composite films based on nanocrystalline carbon.

2. SAMPLE PREPARATION AND EXPERIMENTAL TECHNIQUE

The initial bulk nanoporous carbon samples in the form of plane-parallel pellets of thickness $L_1 \sim 1$ mm were prepared from a polycrystalline α-SiC powder [1–4]. In order to introduce sulfur, the samples were immersed in a boiling solution of sulfur in toluene. The treatment time was approximately equal to 2 h. Then, the samples were held in air at a temperature of ~150°C with the aim of removing toluene traces and excess sulfur from the sample surface. Upon filling with sulfur, the sample weight increased by a factor of more than two. The estimates made with due regard for the density of solid (orthorhombic, stable at room temperature, or amorphous) sulfur $d_S \sim 2.0$ g/cm^3 showed that the fraction of the pore space filled with sulfur exceeded 70 vol % of the total pore volume. The impregnation of the samples for more than 2 h did not lead to a further increase in the sulfur content in the composite material. This indicated that the filling of pores reached saturation.

For measurements of the SAXS intensity, the sulfur-saturated nanoporous carbon samples were ground to a thickness L_2 = 0.25–0.35 mm. The SAXS intensity for the nanoporous carbon–sulfur nanocomposite and the initial nanoporous carbon samples, for the most part, were measured in the scattering angle range $0° < 2\vartheta < 10°$ on a double-crystal diffractometer with a germanium crystal monochromator [(111) reflection] in an x-ray transmission geometry (2ϑ scan mode). The divergence of the incident beam was equal to 20″. The geometric parameters of the setup (the widths of the collimating slit and entrance slit of the detector) ensured an angular resolution of 0.16° for the recorded signal [6].

Moreover, the measurements were carried out with a high angular resolution of 7″. This permitted us to obtain the SAXS curves at ultrasmall scattering angles ($2\vartheta < 100''$). The measuring setup involved an analyzer—a Π-shaped perfect silicon crystal (instead of the entrance slit)—in which the x-ray beam underwent a quintuple reflection from the (111) planes. A similar crystal was used as a monochromator. In this case, the width of the incident beam was equal to 7″.

3. RESULTS

Figure 1 shows typical experimental distributions of the intensity of radiation passed through the nanoporous carbon–sulfur nanocomposite sample (curve *2*) in comparison with the initial sample (curve *1*). The dis-

tribution of the x-ray beam intensity in the entrance slit plane in the absence of samples (curve *3*) is also depicted in this figure. The thicknesses of the nanocomposite and initial samples in the case under consideration are $L_2 = 0.35$ mm and $L_1 = 1.05$ mm, respectively; hence, the ratio between the sample volumes is as follows: $V_2/V_1 = L_2/L_1 \approx 1/3$. The total porosity of the initial nanoporous carbon is estimated to be $V_p/V_1 = 62$ vol %, where V_p is the total volume of all pores. Upon sulfur saturation, the relative change in the density of the material is determined as $(d_2 - d_1)/d_1 = (3m_2 - m_1)/m_1 = 106.2\%$, where m_1 and $3m_2$ are the masses of the initial sample of volume V_1 and the nanocomposite sample of the same volume, respectively. The fraction of the total pore volume filled with sulfur, i.e., the total filling factor of pores in the sample under investigation, is found to be $\beta_{tot} = V_S/V_p \approx 74.8$ vol %, and the fraction of the total sample volume filled with sulfur is $V_S/V_1 \approx 46$ vol %.

It can be seen from Fig. 1 that the filling of pores leads to a drastic decrease in the recorded intensity (by one and a half or two orders of magnitude) over the entire angle range covered. This decrease is associated, first, with a decrease in the scattering volume (by a factor of approximately three) of the nanocomposite sample, second, with an increase in the x-ray radiation absorption loss in the sample, and, third, with a change in the scattering power of the nanocomposite as compared to that of the initial nanoporous carbon. Since, as was noted above, our prime interest is in the last effect, its contribution to the intensity in analyzing the experimental data presented in Fig. 1 should be separated from the contributions of the other two factors. It is characteristic that the introduction of sulfur results not only in a decrease in the intensity but also in a change in the shape of the angular distribution of the intensity, which indicates a change in the parameters of structural nanoinhomogeneities responsible for the small-angle x-ray scattering.

The suppression of scattering upon the introduction of sulfur clearly manifests itself at ultrasmall scattering angles 2ϑ (see inset in Fig. 1). The half-width of the beam passed through the nanocomposite sample is estimated as $w_2 \approx 10''$ (curve *2* in the inset), which only slightly exceeds the half-width of the incident beam $w_3 \approx 9''$ (curve *3* in the inset). At the same time, the scattering from the initial sample brings about a threefold broadening with the half-width $w_1 \approx 27''$ (curve *1* in the inset). Note that the radiation attenuation factors $K = I(0)/I_0(0)$ (where I and I_0 are the intensities of the passed and incident beams at $2\vartheta = 0$, respectively) estimated for measurements at ultrasmall angles (with the analyzer) are appreciably larger than those estimated for the main experiment with the entrance slit (Fig. 1), because a substantial part of the scattered radiation arriving at the entrance slit is not recorded in the case of the analyzer.

With the aim of analyzing the changes in the small-angle x-ray scattering due to the introduction of sulfur, we first obtained the true SAXS curves for both samples over a wide range of s. For this purpose, the experimental curves depicted in Fig. 1 were corrected for the finite height of the entrance slit and the contribution made to the observed signal by the primary beam, which passed through the sample without scattering and weakened through the absorption. The calculations were carried out according to the procedure proposed in our earlier work [10]. The true SAXS curves $i_1(s)$ for the initial nanoporous carbon (curve *1*) and $i_2(s)$ for the nanocomposite (curve *2*), which correspond to the same volume V_1 of both materials and the same radiation attenuation factor K_1, are represented in Fig. 2 on the log–log scale. The true SAXS curve $i_2(s)$ for the nanocomposite was renormalized using the normalizing factor V_1K_1/V_2K_2. This renormalization permits one to compensate for the difference in the measured intensities of the signals from the studied samples due to the difference in their volumes and absorption loss and, thus, to separate the effect caused only by the change in the scattering upon introduction of sulfur. In essence, the dependences $i_1(s)$ and $i_2(s)$ within a constant factor characterize the scattering power per unit volume of the studied materials, and the difference $\delta i(s) = i_2(s) - i_1(s)$ accounts for the change in the scattering power of nanoporous carbon upon filling of its nanopores with sulfur. It can be seen that, upon introduction of sulfur into nanoporous carbon, the scattering intensity per unit volume decreases [$\delta i(s) < 0$] in a larger portion ($0 < s < 0.45$ Å^{-1}) of the angle range studied and slightly increases [$\delta i(s) > 0$] only in the terminal portion ($s > 0.45$ Å^{-1}) of this range; i.e., the introduction of sulfur leads to a clearly pronounced change in the shape of the scattering curve. Figure 2 also shows the dependence of the magnitude of the difference $\delta i(s)$ (curve *3*).

4. DISCUSSION

Under the assumption that sulfur filling the pore space of the initial nanoporous carbon is in the solid state in the nanocomposite (see Section 2), the sulfur density d_S appears to be very close to the carbon skeleton density, which, as a rule, is considered to be approximately equal to the graphite density $d_C \sim 2.1$ g/cm^3. In this case, it is easy to demonstrate that the electron densities of sulfur and the carbon skeleton turn out to be close to each other. Indeed, the electron density ρ and the density d of the monoatomic medium are related by the expression

$$\rho = (d/A)n, \qquad (3)$$

where A is the atomic weight and n is the number of electrons per atom. Since the densities of solid sulfur and the carbon skeleton are estimated to be $d_S \approx d_C$ and $(A/n)_S = (A/n)_C$ ($A = 32$ au and $n = 16$ for sulfur and $A = 12$ au and $n = 6$ for carbon), we obtain $\rho_S \approx \rho_C$. There-

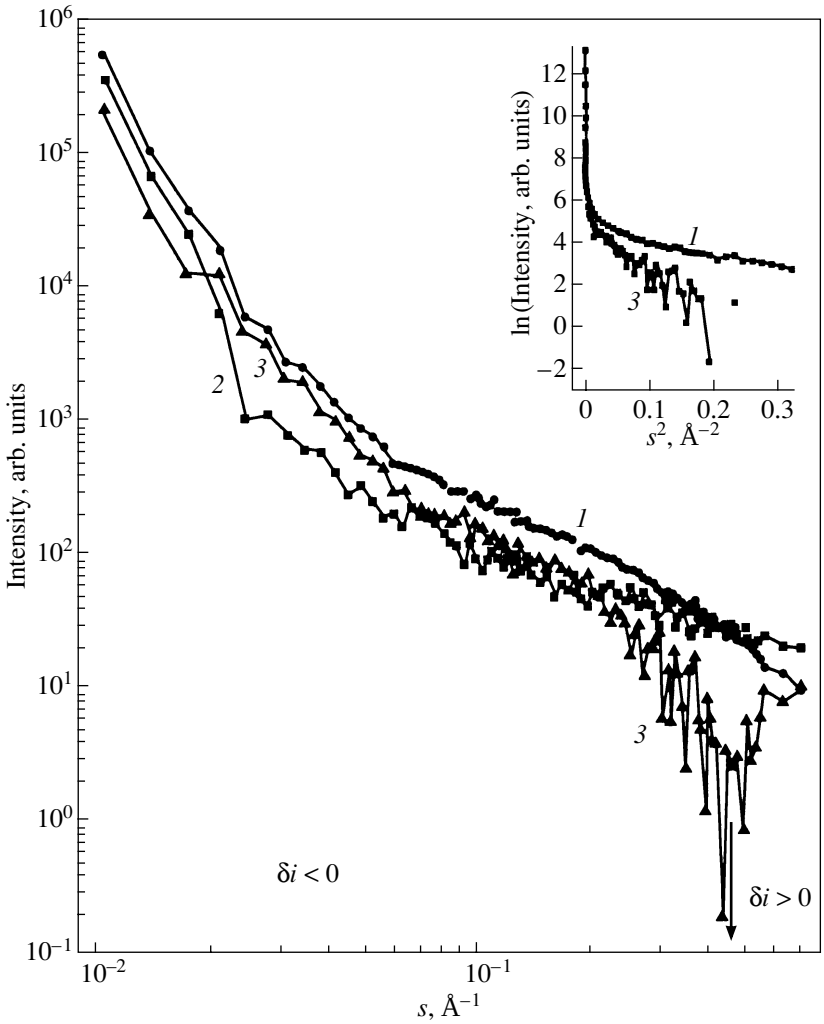

Fig. 2. True scattering powers of the studied materials: (*1*) the initial nanoporous carbon prior to filling of pores with sulfur [the SAXS intensity $i_1(s)$ for a nanoporous carbon sample of volume V_1 with the attenuation factor K_1] and (*2*) the nanocomposite prepared by filling nanoporous carbon pores with sulfur [the SAXS intensity $i_2(s)$ is reduced to the volume V_1 and the attenuation factor K_1]. (*3*) Difference curve $|\delta i(s)| = |i_2(s) - i_1(s)|$. The inset shows curves *1* and *3* in the Guinier coordinates [curve *3* in the range $\delta i(s) < 0$].

fore, the electron density contrast between pores filled 100 percent with sulfur and the carbon skeleton is close to zero: $|\rho_C - \rho_S| \approx 0$.

Let us consider in more detail the possible changes in the scattering power of the initial nanoporous material upon filling of its nanopores with a material whose electron density is identical to that of the main skeleton. For simplicity, we assume that the electron density scattering fluctuations have the same volume v (a monodisperse system). According to formula (1), the change in the scattering power of the material due to these fluctuations can be written in the form

$$\delta i \propto |\Delta\rho_2|^2 V_{2fl} - |\Delta\rho_1|^2 V_{1fl}, \quad (4)$$

where V_{1fl} and V_{2fl} are the total volumes of fluctuations prior to and after filling with sulfur, respectively. Next, for definiteness, we assume that the fluctuations under consideration are empty nanopores with the same volume v_{np}. Hence, it follows from formula (2) that the scattering by these nanopores in the initial nanoporous carbon is determined by the electron density fluctuations

$$\Delta\rho_1 = -(1-\alpha)\rho_C. \quad (5)$$

If the fraction of the total volume of nanopores fully filled with sulfur is designated as β ($0 \le \beta \le 1$ is the filling factor of nanopores), the mean electron density of the medium increases compared to that of the initial medium and the electron density fluctuations corresponding to the nanopores remaining empty in the nanocomposite can be described by the expression

$$\Delta\rho_2 = -(1-\alpha)\rho_C - \alpha\beta\rho_S. \quad (6)$$

Since, for the nanopores, we have $V_{1fl} \propto \alpha$ and $V_{2fl} \propto \alpha(1 - \beta)$, relationship (4) with due regard for the approximate equality $\rho_S \approx \rho_C$ takes the form

$$\delta i_{np} \propto \{[1 - \alpha(1 - \beta)]^2(1 - \beta) - (1 - \alpha)^2\}\alpha\rho_S^2. \quad (7)$$

Relationship (7) describes the change in the scattering by empty nanopores as a result of a decrease in the degree of nanoporosity and an increase in the mean electron density of the medium upon introduction of sulfur. Figure 3a illustrates the change in the scattering power of the nanocomposite upon scattering by empty nanopores δi_{np} [according to formula (7)] as a function of the filling factor β for materials with different degrees of initial nanoporosity α. It can be seen that, in the case when the nanoporosity of the initial material is not very high (curves *1*–*3*), the scattering power associated with nanopores always decreases as the nanopores are filled with sulfur: $\delta i_{np} < 0$. On the other hand, for materials with a high degree of nanoporosity (curves *4*, *5*), there exists a certain range of the filling factors β in which the scattering by nanopores becomes enhanced: $\delta i_{np} > 0$. Note that the effect of an increase in the contrast between the empty nanopores and the medium on the scattering dominates over the effect of a decrease in the number of empty pores. As should be expected, in the limiting case when all the nanopores are filled ($\beta \longrightarrow 1$), the intensity of small-angle x-ray scattering by these pores in the nanocomposite tends to zero; i.e., δi_{np} approaches the scattering power i_1. In the other limiting case, at $\beta \longrightarrow 0$, all the nanopores are empty and $\delta i_{np} \longrightarrow 0$.

Similarly, we can consider the change in the scattering power $\delta i_{nc}(s)$ of the material upon small-angle x-ray scattering by nanoclusters of volume v_{nc}. In this case, instead of relationship (7), we obtain the relationship

$$\delta i_{nc} \propto \{(1 - \beta)^2[1 - \alpha(1 - \beta)] - (1 - \alpha)\}\alpha^2\rho_S^2. \quad (8)$$

The change in the scattering power δi_{nc} as a function of the factor β of filling of nanopores with sulfur at different degrees of initial nanoporosity α [in accordance with relationship (8)] is illustrated in Fig. 3b. As can be seen, the filling of nanopores with sulfur leads to the suppression of small-angle x-ray scattering by nanoclusters at any values of α and β. In this case, the effect of a decrease in the contrast between clusters and the medium on the small-angle x-ray scattering is more pronounced than that of an increase in the solid phase volume.

The combined effect of pore filling is governed by the ratio between the volumes of individual nanopores and nanoclusters, that is,

$$\delta i \propto \delta i_{np} + (v_{nc}/v_{np})\delta i_{nc}. \quad (9)$$

Figure 3c illustrates the change in the scattering power δi [according to formula (9)] as a function of the filling factor β for nanocomposites with different ratios $v_{nc}/v_{np} \leq 1$ at a constant high degree of initial nanoporosity ($\alpha = 0.45$), which is actual for nanoporous carbon. It is seen that, for sufficiently large factors β, the scattering power of the nanocomposite should be lower than that of the initial nanoporous carbon ($\delta i < 0$) at any values of β and v_{nc}/v_{np} and the difference $|\delta i|$ increases with an increase in the ratio v_{nc}/v_{np}. However, when the values of v_{nc}/v_{np} and β are not very high, the scattering power of the nanocomposite can appear to be somewhat higher than that of the initial nanoporous carbon ($\delta i > 0$). The simple estimates made using formulas (7)–(9) show that this effect can occur precisely in the case of highly nanoporous carbon and becomes weak or does not manifest itself at all for lower values of α ($\alpha \lesssim 0.4$).

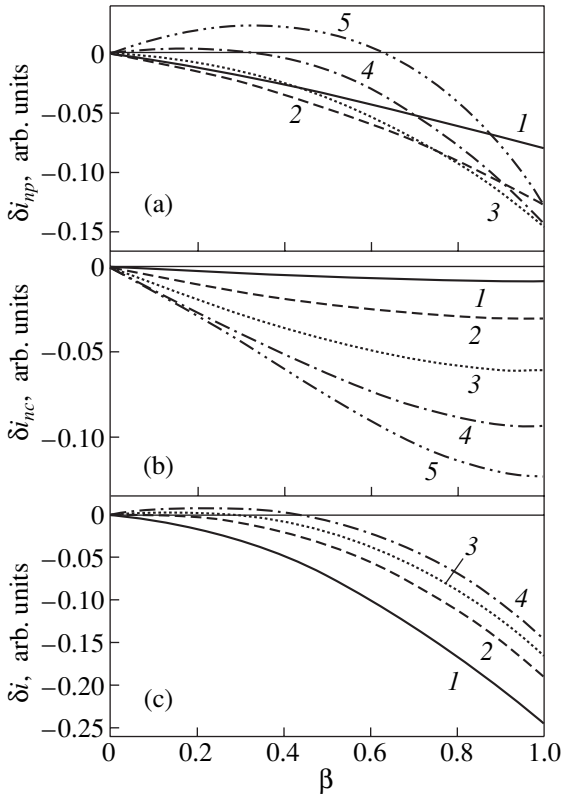

Fig. 3. Change in the scattering power of the nanocomposite upon scattering by (a) empty nanopores, (b) nanoclusters, and (c) empty nanopores and nanoclusters as a function of the factor β of filling of nanopores with sulfur for (a, b) different degrees of nanoporosity α of the initial nanoporous carbon and (c) different ratios v_{nc}/v_{np} of the cluster volume to the pore volume at $\alpha = 0.45$. Degree of nanoporosity α: (a, b) (*1*) 0.1, (*2*) 0.2, (*3*) 0.3, (*4*) 0.4, and (*5*) 0.5. Volume ratio v_{nc}/v_{np}: (c) (*1*) 1, (2) 0.5, (*3*) 0.25, and (*4*) 0.1.

The results obtained within the proposed model should be compared with the experimental data with due regard for the fact that the initial nanoporous carbon is a polydisperse system, even though it has a narrow size distribution of scattering fragments [1, 6]. The filling factor β in a polydisperse system can depend on the nanopore size, which is disregarded in the model. Moreover, the model ignores the possibility that the

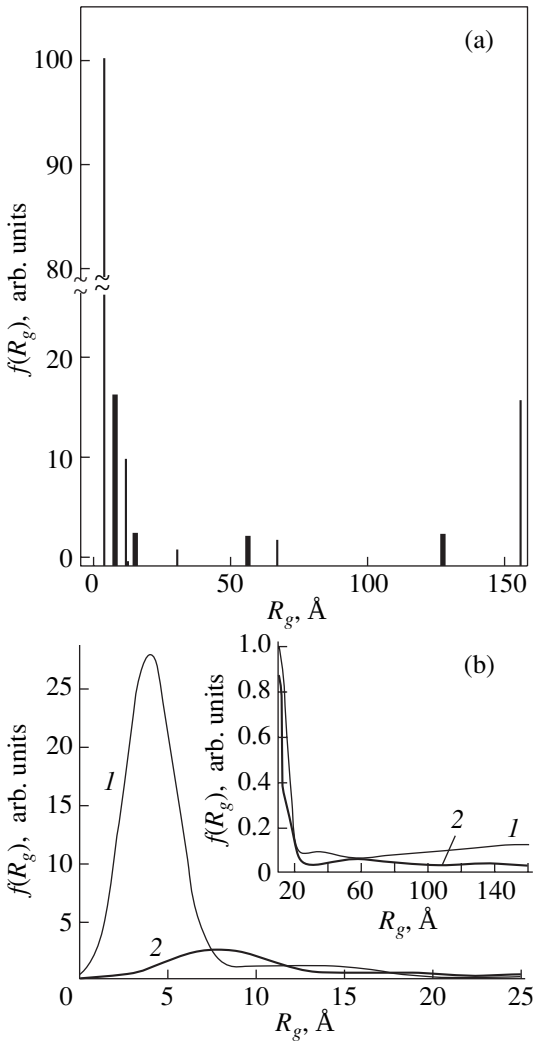

Fig. 4. Size distribution functions for nanoinhomogeneities (a) with discrete Guinier radii and (b) with due regard for the variance of the Guinier radii (see text). Thin lines [$f_1(R_g)$] and curves *1* [$F_1(R_g)$] correspond to nanopores in the initial nanoporous carbon, and thick lines [$f_2(R_g)$] and curves *2* [$F_2(R_g)$] refer to sulfur nanoclusters (sulfur-filled pores in the initial nanoporous carbon).

volume of particular pores can be filled not fully but in part. This can lead to an increase in the concentration of pores with smaller volumes and a decrease in the total volume of the pore space. However, the above results can be qualitatively used for interpreting the experimental data presented in Fig. 2. As was noted above, the difference curve $|\delta i(s)|$ (curve *3* in Fig. 2) involves two portions, namely, $\delta i(s) < 0$ and $\delta i(s) > 0$. The former portion can be associated with the decrease in the total volume of empty nanopores and the decrease in the contrast between filled nanopores and the carbon skeleton to approximately zero due to the formation of sulfur nanoclusters in the pores. The latter portion can be attributed to empty nanopores that remain in the nanocomposite and are characterized by a higher scattering intensity as compared to the initial nanoporous carbon. Therefore, the difference curve in the range $\delta i(s) < 0$, in essence, corresponds to scattering by sulfur nanoclusters incorporated into the nanocomposite. Analysis of this curve can provide information on the size characteristics of these nanoclusters or, what is the same, the size characteristics of the sulfur-filled nanopores in the initial nanoporous carbon.

The difference curve *3* at $\delta i(s) < 0$ (Fig. 2) was analyzed within the Guinier approximation. Curve *3* (Fig. 2) reconstructed in the Guinier coordinates (Fig. 2, curve *3* in the inset) was decomposed into the linear components $\ln|\delta i_k(s)| \propto s^2$ (where $k = 1, 2, \ldots$). Each component corresponds to scattering by nanoinhomogeneities that have a particular gyration radius R_{gk} ($sR_{gk} < 1$) and make up a certain volume fraction $m_k(R_{gk})$. The quantities R_{gk} and $m_k(R_{gk})$ were determined according to the procedure described in detail in our earlier work [6]. The SAXS curve for the initial nanoporous carbon was processed in a similar manner (curves *1* in Fig. 2 and in the inset in this figure).

The discrete functions of the distribution over gyration radii $f(R_g) = \sum_k m(R_g)\delta(R_g - R_{gk})$ for sulfur nanoclusters in the nanocomposite (thick lines) and the scattering fragments in the initial nanoporous carbon (thin lines) are displayed in Fig. 4a in the form of a set of vertical segments with a height proportional to $m_k(R_{gk})$. Here, $\delta(R_g - R_{gk})$ is the Dirac delta function ($\int_{-\infty}^{\infty} \delta(R_g - R_{gk})\delta R_g = 1$). As a result, we have

$$\int_{-\infty}^{\infty} m(R_g)\delta(R_g - R_{gk})dR_g = m_k(R_{gk}).$$

Figure 4b shows the continuous distribution functions

$$F(R_g) = \frac{2}{\sqrt{\pi}}\sum_k \frac{m_k}{R_{gk}}\exp\left[-\frac{(R_g - R_{gk})^2}{R_{gk}^2}\right],$$

which are derived by replacing the delta functions in the expression for $f(R_g)$ by Gaussian functions normalized to unity under the assumption that the gyration radii of scattering fragments are characterized by the spread (variance) ΔR_{gk} about the corresponding discrete radii R_{gk} such that $\Delta R_{gk} \sim R_{gk}$. The functions $f_2(R_g)$ and $f_1(R_g)$ (Fig. 4a), or the functions $F_2(R_g)$ and $F_1(R_g)$ (curves *2*, *1* in Fig. 4b), correspond to sulfur-filled nanopores in nanoporous carbon (or to sulfur nanoclusters in the nanocomposite) and nanoinhomogeneities in the initial nanoporous carbon, respectively, and exhibit similar behavior. This similarity indicates that the functions with subscript 1 account for the distribution of empty nanopores in the initial nanoporous carbon. On the other hand, the difference in the behavior of the functions with subscripts 1 and 2 suggests that not all the nanopores in nanoporous carbon are filled. In this

case, the factor of filling of nanopores with sulfur, depending on their size, can be roughly estimated from the formula

$$\beta(R_g) = F_2(R_g)/F_1(R_g). \quad (10)$$

As is seen from Fig. 4b, the largest difference between the functions $F_2(R_g)$ and $F_1(R_g)$ is observed for the smallest sized nanopores. The distribution $F_1(R_g)$ exhibits a sharp maximum at $R_{gm} \sim 4.1$ Å. This indicates a high size uniformity of the nanopores and agrees well with the absorption data [1] and the SAXS data obtained in our previous work [6]. Furthermore, the most probable nanopore size, which is approximately equal to 8.2 Å ($\sim 2R_{gm}$), virtually coincides with that estimated in [1]. This confirms the inference that the functions $f_1(R_g)$ and $F_1(R_g)$ describe the distribution of nanopores. At the same time, the most probable gyration radius of the sulfur-filled nanopores in the nanocomposite is approximately equal to 7.7 Å. It can be seen from Fig. 4 that the smallest sized nanopores in the nanocomposite remain virtually unfilled and have the filling factor $\beta(R_g) \ll 1$. At $R_g > 7.7$ Å, the functions $F_2(R_g)$ and $F_1(R_g)$ approach each other, so that the filling factor $\beta(R_g)$ can be as large as tens of percent and can even become close to unity (see inset in Fig. 4b). Note that, as is seen from Fig. 4b, the inequality $F_2(R_g) > F_1(R_g)$ holds in the size range $R_g = 7$–11 Å. In the framework of our model, this inequality implies $\beta(R_g) > 1$ and has no physical meaning. It can be assumed that this inequality is a consequence of the above effect associated with the partial filling of larger sized nanopores. As a result, the number of sulfur nanoclusters with these sizes in the nanocomposite can appear to be larger than the number of nanopores with the same sizes in the initial nanoporous carbon. We also cannot rule out that this inequality results merely from the approximate determination of the functions $f(R_g)$ and $F(R_g)$.

From the results obtained, we can roughly estimate the total filling factor of nanopores $\beta_{np} = V_{n\mathrm{S}}/V_{np}$, where $V_{n\mathrm{S}} = \sum_k m_k^{(S)}$ is the volume of the sulfur-filled nanopores in the nanocomposite and $V_{np} = \sum_k m_k^{(np)}$ is the volume of the empty nanopores in the initial nanoporous carbon. The estimates give the filling factor $\beta_{np} \sim 15$ vol %, which is appreciably less than the aforementioned factor β_{tot} obtained from the weighing of the samples prior to and after the introduction of sulfur. Therefore, sulfur in considerable amounts fills the larger sized so-called micropores and macropores also contained in the initial nanoporous carbon [1].

It should be noted that the most probable size of sulfur nanoclusters approximately corresponds to the size of the unit cell of orthorhombic sulfur. In this respect, it is reasonable to assume that, in the best case, only individual sulfur atoms (the atomic radius of sulfur is equal to 1.04 Å) or molecular fragments of the S_2, S_4, S_6, and S_8 types without subsequent formation of a crystal or amorphous structure can be incorporated into the smallest sized pores of nanoporous carbon during the introduction of sulfur. These pores can be filled only in part or remain completely unfilled. In the latter case, according to the model, an increase in the mean electron density of the material upon introduction of sulfur leads to an enhancement of scattering by empty nanopores. This is actually observed in the experiment at the values of $s > 0.45$ Å^{-1}, which correspond to the smallest sized nanopores (Fig. 2). In the case of partial filling, the content of very small-sized pores in the nanocomposite can appear to be higher than that in the initial nanoporous carbon, because, as was already noted, the larger sized (but less accessible to sulfur) nanopores can change over to the group of small-sized nanopores. This effect can also be responsible for the enhancement of scattering at $s > 0.45$ Å^{-1}.

5. CONCLUSIONS

Thus, the carbon–sulfur nanocomposite with comparable contents of the major and introduced components was prepared using a simple method of filling pores of nanoporous carbon with sulfur from a boiling toluene solution. The high total degree of filling of the pore space with sulfur (~75 vol %) in this filling method most likely can be associated with the capillary suction of the solution into open pores of nanoporous carbon. This process becomes efficient with an increase in the temperature to the boiling point due to a decrease in the surface tension and an increase in the wetting of pore walls. A comparative investigation of small-angle x-ray scattering was carried out for the nanocomposite and initial nanoporous carbon. The possible changes in the scattering power of the studied material upon filling of nanopores with sulfur were analyzed in the framework of a simple model. It was demonstrated that, owing to the decrease in the contrast between filled nanopores and the carbon skeleton to approximately zero, the introduction of sulfur brings about a considerable decrease in the scattering power. This permitted us to determine the size distribution function of incorporated sulfur clusters in the nanocomposite and, thus, to judge the size distribution of pores that turned out to be filled in the initial nanoporous carbon. Moreover, we made the inference that the size characteristics of structural inhomogeneities in nanoporous carbon refer primarily to the nanopores. A comparison of the experimental and theoretical results showed that the smallest sized nanopores (8–16 Å), which constitute the greater part of the total nanopore volume in the initial nanoporous carbon, remain empty or, possibly, are partly filled with small-sized molecular sulfur fragments. The intensity of scattering by empty pores in the nanocomposite as a denser medium is higher than that in the initial nanoporous carbon. The enhancement of small-angle x-ray scattering even with a decrease in the total volume of nanopores of appropriate size is characteristic of highly

porous initial materials upon introduction of filling agents comparable in density and can be observed even at moderate filling factors. For low degrees of nanoporosity and low densities of filling agents, for example, in experiments with carbon adsorbents [7, 8], the adsorption invariably leads to a decrease in the SAXS intensity.

ACKNOWLEDGMENTS

This work was supported by the International Association of Assistance for the promotion of cooperation with scientists from the New Independent States of the former Soviet Union (project INTAS no. 00-761), the Russian Foundation for Basic Research (project no. 99-02-17984), and the State Scientific and Technical Program "Topical Directions in the Physics of Condensed Matter: Fullerenes and Atomic Clusters" of the Ministry of Science and Technology of the Russian Federation.

REFERENCES

1. S. K. Gordeev and A. V. Vartanova, Zh. Prikl. Khim. **66** (7), 1080 (1994); **66** (9), 1375 (1994).
2. S. K. Gordeev, A. V. Vartanova, S. G. Zhukov, *et al.*, RF Patent No. 2026735, Byull. Izobret., No. 2 (1995).
3. S. K. Gordeev, R. G. Avarbz, A. E. Kravtjik, *et al.*, Int. Patent Publ. under PCT. Int. Classification CO4B 30/00, 35/52. Publ. Number WO98/54111 (1998).
4. R. G. Avarbz, A. V. Vartanova, S. K. Gordeev, *et al.*, US Patent No. 5876787 (1999).
5. *Science and Technology of Carbon Nanotubes*, Ed. by K. Tanaka, T. Yamabe, and K. Fukui (Elsevier, Amsterdam, 1999).
6. R. N. Kyutt, É. A. Smorgonskaya, S. K. Gordeev, *et al.*, Fiz. Tverd. Tela (St. Petersburg) **41** (5), 891 (1999) [Phys. Solid State **41**, 808 (1999)]; Fiz. Tverd. Tela (St. Petersburg) **41** (8), 1484 (1999) [Phys. Solid State **41**, 1359 (1999)].
7. G. M. Plavnik, T. P. Puryaeva, and M. M. Dubinin, Izv. Akad. Nauk, Ser. Khim., No. 7, 628 (1993).
8. G. M. Plavnik and T. P. Puryaeva, in *Proceedings of the I National Conference on Application of X-ray and Synchrotron Radiation, Neutrons, and Electrons to Research in Materials (RSNÉ'97), Dubna, 1997*, Vol. II, p. 149.
9. S. Gupta, B. R. Weiner, B. L. Weiss, and G. Morell, in *Abstracts of International Conference of the Materials Research Society, 2001, San-Francisco, 2001*, W6-9, p. 388.
10. É. A. Smorgonskaya, R. N. Kyutt, S. K. Gordeev, *et al.*, Fiz. Tverd. Tela (St. Petersburg) **42** (6), 132 (2000) [Phys. Solid State **42**, 1176 (2000)].

Translated by O. Borovik-Romanova

Physics of the Solid State, Vol. 44, No. 10, 2002, pp. 2009–2012. Translated from Fizika Tverdogo Tela, Vol. 44, No. 10, 2002, pp. 1915–1918.

FULLERENES AND ATOMIC CLUSTERS

Effect of Magnetic Field on the Microplastic Strain Rate for C_{60} Single Crystals

B. I. Smirnov*, V. V. Shpeĭzman*, N. N. Peschanskaya*, and R. K. Nikolaev**

** Ioffe Physicotechnical Institute, Russian Academy of Sciences, Politekhnicheskaya ul. 26, St. Petersburg, 194021 Russia*
e-mail: shpeizm.v@mail.ioffe.ru

*** Institute of Solid-State Physics, Russian Academy of Sciences, Chernogolovka, Moscow oblast, 142432 Russia*

Received March 1, 2002

Abstract—Microplastic deformation in a magnetic field and in a zero field, as well as after preliminary action of a magnetic field on C_{60} crystals, is studied with the help of a laser interferometer, which makes it possible to measure the strain rate on the basis of linear displacements of 0.15 μm. It is shown that the introduction of a sample into the field and its removal from a field of 0.2 T directly during sample deformation lead to a change in the strain rate, the decrease in the rate being accompanied by a brief interruption of deformation. The sign of the effect depends on temperature: the magnetic field accelerates deformation at room temperature and slows it down at 100 K. Preliminary holding of a sample in a field of 0.2 or 2 T produces a similar effect on the strain rate. Possible reasons for the observed manifestations of the magnetoplastic effect in C_{60} and the relation between the sign of the effect and the phase transition at 260 K are considered. © *2002 MAIK "Nauka/Interperiodica".*

1. INTRODUCTION

Interest in the magnetoplastic effect (MPE) in various dielectrics has increased in recent years (see, for example, review [1] and publications devoted to alkali-halide crystals [2, 3], ferroelectric crystal $NaNO_2$ [4], and fullerite C_{60} [5]). It is emphasized that the MPE exhibits different features in different crystals. For example, the effect of increasing strain rate in a magnetic field was observed in [4] only in a certain interval of strain rates, while in [5] sign reversal of the MPE was detected at the phase-transition temperature $T_c \approx 260$ K of C_{60} samples by measuring their microhardness at room temperature after the preliminary action of a short magnetic field pulse at various temperatures. For brittle low-strength crystals such as fullerites, investigation of their mechanical properties in the inelastic region is apparently confined to measurements of the microhardness and the rate of damped microplastic strain. The main difference between these two methods is that the former method reflects the properties of the crystal surface, while the latter is associated with the properties of the bulk of the crystal; for this reason, the latter method is less sensitive to possible effects of the environment on the surface. In addition, analysis of the microplastic strain rate also makes it possible to separate the effect of the preliminary action of a magnetic field (i.e., the influence on the structural state of the crystal) and the effect exerted on the rate directly during loading. In order to distinguish between these effects, we will refer to the former effect as the magnetoplastic aftereffect (MPA) and to the latter effect as the magnetoplastic effect. In this work, both these effects were studied experimentally on C_{60} crystals using the method of laser interferometry for measuring the rate and magnitude of microplastic strain.

2. EXPERIMENTAL TECHNIQUE

Fullerite C_{60} single crystals were grown from the vapor phase from the initial material in the form of tiny C_{60} crystals preliminarily purified by multiple vacuum sublimation. The single crystals were grown under the following conditions: the sublimation temperature was 873 K, the crystallization temperature was 813 K, and the growth time was 8–12 h. Well-faceted C_{60} single crystals grown with the help of such a technique had a mass up to 30 mg and a size up to several millimeters. Since the crystals were subsequently subjected to uniaxial compression, we chose crystals with two symmetrically arranged parallel faces for the convenience of loading. The distance between these faces (the dimension along the direction of the compressing force or the sample height) was 2–2.5 mm; the mean cross-section area perpendicular to the force was 8–9 mm^2.

The interferometric method of strain recording in time in the form of consecutive beats [6] used by us here makes it possible to measure the strain rate $\dot{\varepsilon}$ on the basis of small variations in the sample length with an error not exceeding 5%. One beat on the interferogram corresponds to the deformation increment $|\Delta l| = 0.3$ μm. The strain rate in this work was determined by measuring the duration of a half-period, i.e., on the base $|\Delta l| = 0.15$ μm using the formula $\dot{\varepsilon} = \lambda\nu/2l_0$, where $\lambda = 0.63$ μm is the wavelength of laser radiation, ν is the

Table 1. The change in the strain rate of a C_{60} crystal after a 4-h holding in a magnetic field of 2 T at 293 and 77 K

No.	Conditions of tests and preliminary action	Strain rate $\dot{\varepsilon}$, 10^{-5} s^{-1} (σ = 0.3 MPa, T = 293 K)
1	Initial crystal	0.14
2	4-h holding in the field at 290 K	1.06
3	No. 2 + four days rest in a zero field	0.16
4	4-h holding in the field at 77 K	0.09
5	No. 4 + four days rest in a zero field	0.20

Table 2. The change in the strain rate of a C_{60} crystal after holding for different periods of time in a magnetic field of 0.2 T at 293 K

No.	Conditions of tests and preliminary action	Strain rate $\dot{\varepsilon}$, 10^{-5} s^{-1} (σ = 0.3 MPa, T = 293 K)
1	6-day holding at B = 0.2 T	0.2
2	20-day holding at B = 0.2 T	0.8
3	No. 2 + deformation at σ = 0.3 MPa for 22 min	0.19
4	No. 3 + two days rest in a zero field	0.12
5	No. 4 + 20-day holding at B = 0.2 T	0.16
6	No. 5 + 35-day holding at B = 0.2 T	0.45

Note: All measurements except No. 4 were carried out in a field of B = 0.2 T.

frequency of beats, and l_0 is the sample dimension in the direction of the force.

In experiments with a magnetic field, we used two permanent magnets, one of which provided a field with magnetic induction B = 0.2 T and could be displaced such that the sample intended for compression tests was in a magnetic field or in a zero field, while the other magnet, with induction 2 T, was used only for preliminary holding of samples in a magnetic field.

3. EXPERIMENTAL RESULTS AND DISCUSSION

Experiments with preliminary holding of C_{60} crystals at 293 K in a magnetic field proved that the MPA is manifested in an increase in the microplastic strain rate, which is determined by a number of factors: the magnitude of the magnetic field, the time of sample holding in the magnetic field, the "rest" time (between the action of the field and loading), and the magnetic and stress history of the crystal. Let us list the main properties of the MPA. The larger the magnetic induction and the longer the field-exposure time, the stronger the effect. Its magnitude decreases upon an increase in the rest time, and holding under loading considerably accelerates this decrease. If we try to revive the effect after the action of loading has completely suppressed it, we must increase the exposure time in a field of the same strength, or increase the magnetic induction, or hold the sample for a long time in a zero magnetic field without loading.

Some typical examples of manifestation of the MPA and its peculiar features at room temperature are demonstrated in Tables 1 and 2 and in Fig. 1. Table 1 shows the strain rates measured after the same period following the application of a load for a C_{60} crystal subjected consecutively to the following operations: holding in a magnetic field, loading in a field and in a zero field, and rest. It can be seen from Tables 1 and 2 that after holding the sample in a magnetic field of induction of 2 T for 4 h or in a field of induction of 0.2 T for 20 days, the strain rate under a stress σ = 0.3 MPa increases by a factor of 6–8 (rows 2 in Tables 1, 2). However, 2–4 days of rest returns the sample to the initial state (see row 3 in Table 1 and row 4 in Table 2). The variation of the strain rate with time for σ = 0.3 MPa and the effect of repeated action of a magnetic field are illustrated in Fig. 1. When the crystal was unloaded at a low strain rate and was then held again in a magnetic field, the time of holding in a field of the same strength had to be increased more than twofold in order to detect increases in the initial strain rate (see rows 4–6 in Table 2). As the time of loading is increased, the strain rate decreases nonuniformly and rather slowly compared to analogous decreases in other brittle materials, in which a close-to-zero strain rate is attained after $|\Delta l_0|$ = 1–2 μm [7]. The restoration (relaxation) of the structure occurs even more slowly: the reproduction of the MPA effect requires weeks. It should be noted that the relaxation processes associated only with mechanical action are characterized by much higher rates. For example, the intervals between loadings in the recording of the temperature dependence of the strain rate in [8] were only a few minutes long. Thus, the effect of the loading time on the duration of rest required for the recovery of the initial state observed by us in this study indicates that structural rearrangements in C_{60} under the effect of loading and a magnetic field are interrelated but that this relation is not of the simple additive type.

Table 1 also contains the results of studying MPA after holding the sample in a magnetic field of B = 2 T at 77 K for 4 h. It can be seen that the sign of the effect is opposite to that of the MPA observed after holding in a magnetic field at room temperature: the magnetic field slows down the deformation process, while prolonged rest returns the sample to the initial state (i.e., the rest increases the strain rate).

Figure 2 shows the results of analysis of MPE by using the standard method for this effect, namely, by rapidly introducing the sample into a magnetic field or withdrawing it from the field during creep. This proce-

dure can be repeated several times, as long as the creep is noticeable. The stress σ in these experiments was 0.7 MPa. The creep curves recorded at temperatures above (293 K) and below (100–110 K) the temperature of the phase transition from the face-centered cubic lattice to the simple cubic lattice (fcc–sc transitions) were compared. Since we could not ensure thermal stabilization in the latter case, the absolute values of the strain rate might be slightly exaggerated, which, however, should not affect the change in the strain rate at the moment of jumpwise variation of the magnetic field. It can be seen from Fig. 2 that each variation of the magnetic induction leads to a change in the creep rate. The increase in the rate starts immediately after the jump in *B*, while in the case of the rate decreasing after a jump in *B*, the creep is first terminated and then deformation continues at a lower rate than before the jump. A similar effect was observed earlier in an analysis of the thermal-activation characteristics of deformation and internal stresses using the differential method under jumps in stress, temperature, or strain rate leading to decreases in the rate. In some cases, even a negative creep was observed, i.e., the direction of the sample deformation was opposite to the direction of the force [9, 10]. The existence of "deformation delay" (incubation period) has been used as an indication of a change in the structure and internal stresses accompanying jumps [10] in numerous discussions (in 1970–1980) on the possibility of applying differential methods in determining the activation characteristics of deformation. Subsequently, a similar deformation delay was observed during the investigation of microplasticity of high-temperature superconductors at the instant of their transition from the superconducting to the normal state under the action of a transport current or a magnetic field [11]. The delay was usually attributed to the presence of opposite internal stresses for whose decrease (structure rearrangement) a certain time is needed; during this time, the acting stresses are insufficient for the continuation of deformation under new conditions. For example, it was assumed in [11] that the time was spent in increasing the number of dislocations in a pileup in order to compensate for the electron component of the resistance to the motion of dislocations (which appears in the normal state). The observation of an incubation period in the studies described here can also be easily explained since the time of structural rearrangements in C_{60} crystals is quite long (see Tables 1, 2).

Comparison of the MPEs at temperatures above and below the fcc–sc transition indicates that there is a considerable difference between the effects (Fig. 2). At room temperature, the magnetic field accelerates the deformation of the fcc lattice of fullerite C_{60}, while in the sc lattice (at 110 K), the MPE has the opposite sign. This result correlates with the change in the sign of the microhardness increment at the phase transition point under the action of a magnetic field pulse determined in [5]. According to the authors of [5], this can be due to there being different effects produced by a magnetic field on sc and fcc structures, as well as to the effect of the field on the phase-transition kinetics. The latter is unlikely for the fields used in our experiments. Control experiments in which we compared the spectra obtained with the help of differential scanning calorimetry (DSC) for samples before and after the action of a magnetic field with $B = 2$ T did not reveal any variations of the peak in the phase-transition region. In our opinion, it is preferable to explain this effect in terms of different actions of a magnetic field on sc and fcc structures. However, these factors should probably not be opposed since, for example, preliminary compression of C_{60} at temperatures of 293 and 77 K [12] produced different effects on the crystal structure, which could be judged from a considerable broadening of the DSC peak at 260 K after compression at 293 K, while the change in the peak shape after compression at 77 K was insignificant.

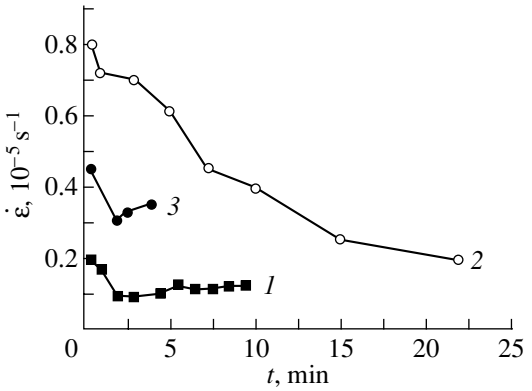

Fig. 1. Variation of microplastic strain rate as a function of the time of action of loading at $\sigma = 0.3$ MPa after preliminary holding in a magnetic field of 0.2 T for (*1*) 6, (*2*) 20, and (*3*) 20 + 35 days. Curve *3* corresponds to repeated loading of sample *2* after 2 day rest in a zero field and holding in a magnetic field.

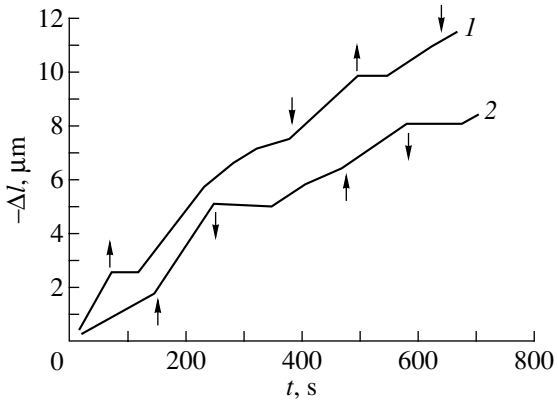

Fig. 2. Compression curves for a C_{60} crystal at (*1*) 100 and (*2*) 290 K and $\sigma = 0.7$ MPa. Arrows indicate the instants of application (↑) and removal (↓) of the magnetic field.

In most experiments, weak magnetic fields were observed to increase the strain rate of nonmagnetic materials, which is usually attributed to a change in the structure of the dislocation core or to suppression of the interaction between dislocations and stoppers under the action of a field [1]. The former reason proposed in [13] to explain the peculiarities in the temperature dependence of microhardness of C_{60} can be used in our case to interpret the MPE at room temperature but cannot explain the remaining effects.

As regards the change in the structure of stoppers under the action of a magnetic field weakening their coupling with dislocations, this mechanism can be used in explaining both the MPE and MPA at $T > T_c$; however, in the case of MPA, this mechanism appears to be more efficient since the time of action of the field for producing this effect in the two cases differs significantly. According to the hypothesis put forth in [5, 12], the fact that a magnetic field decreases the strain rate at $T < T_c$ (which is confirmed by the MPA and MPE) could be due to the effect of redistribution of C_{60} molecules with pentagon and hexagon configurations on the dissipation of energy of a moving dislocation or on the rearrangement of the stopper structure.

4. CONCLUSION

Thus, we have established that the rate of microplastic strain of C_{60} crystals changes under the effect of a magnetic field applied preliminarily or acting directly in the course of deformation. It is confirmed that this change has opposite signs at temperatures above and below the fcc–sc phase transition temperature T_c, which is in accord with the microhardness data [5]. A delay in deformation is detected when a C_{60} sample is introduced in a magnetic field at $T < T_c$ and when it is removed from the field at $T > T_c$.

ACKNOWLEDGMENTS

This study was supported by the state program on fullerenes of the Ministry of Industry, Science, and Technology of the Russian Federation and by the Russian Foundation for Basic Research (project no. 00-01-00482).

REFERENCES

1. Yu. I. Golovin and R. B. Morgunov, Materialovedenie, Nos. 3–6, 2 (2000).
2. A. A. Urusovskaya, V. I. Al'shits, N. N. Bekkauer, and A. E. Smirnov, Fiz. Tverd. Tela (St. Petersburg) **42** (2), 267 (2000) [Phys. Solid State **42**, 274 (2000)].
3. V. I. Al'shits, A. A. Urusovskaya, A. E. Smirnov, and N. N. Bekkauer, Fiz. Tverd. Tela (St. Petersburg) **42** (2), 270 (2000) [Phys. Solid State **42**, 277 (2000)].
4. B. I. Smirnov, N. N. Peschanskaya, and V. I. Nikolaev, Fiz. Tverd. Tela (St. Petersburg) **43** (12), 2154 (2001) [Phys. Solid State **43**, 2250 (2001)].
5. Yu. A. Osip'yan, Yu. I. Golovin, R. B. Morgunov, *et al.*, Fiz. Tverd. Tela (St. Petersburg) **43** (7), 1333 (2001) [Phys. Solid State **43**, 1389 (2001)].
6. N. N. Peschanskaya, A. B. Sinani, V. V. Shpeĭzman, and P. N. Yakushev, Izv. Ross. Akad. Nauk, Ser. Fiz. **63** (9), 882 (1999).
7. N. A. Zlatin, N. N. Peschanskaya, and V. V. Shpeĭzman, Zh. Tekh. Fiz. **57** (7), 1438 (1987) [Sov. Phys. Tech. Phys. **32**, 857 (1987)].
8. V. V. Shpeĭzman, N. N. Peschanskaya, V. M. Egorov, *et al.*, Fiz. Tverd. Tela (St. Petersburg) **42** (9), 1721 (2000) [Phys. Solid State **42**, 1771 (2000)].
9. A. Ivens and R. Roulings, in *Thermically Activated Processes in Crystals* (Mir, Moscow, 1973), p. 172.
10. P. W. Davies and B. Wilshire, Scr. Metall. **5** (6), 475 (1971).
11. V. V. Shpeĭzman, B. I. Smirnov, N. N. Peschanskaya, and L. K. Markov, Fiz. Tverd. Tela (Leningrad) **33** (7), 2198 (1991) [Sov. Phys. Solid State **33**, 1238 (1991)].
12. V. M. Egorov, V. I. Nikolaev, R. K. Nikolaev, *et al.*, Fiz. Tverd. Tela (St. Petersburg) **41** (3), 550 (1999) [Phys. Solid State **41**, 494 (1999)].
13. V. D. Natsik, S. V. Lubenets, and L. S. Fomenko, Fiz. Nizk. Temp. **22** (3), 337 (1996) [Low Temp. Phys. **22**, 264 (1996)].

Translated by N. Wadhwa